Graz University of Technology

FAULT SLIP ANALYSIS AND MORPHOTECTONIC ANALYSIS OF THE KORALPE (EASTERN ALPS)

Gerald Pischinger
Mag.rer.nat.

Doctoral Thesis

for obtaining the academic degree of Doktor der Naturwissenschaften

Institute of Applied Geosciences
Graz University of Technology

Supervisors:
Ao.Univ.-Prof. Dr.phil. Franz-Josef Brosch
Univ.-Prof. Mag.rer.nat. Dr.rer.nat. Walter Kurz
Ao.Univ.-Prof. Mag.rer.nat. Dr.rer.nat. Gerd Rantitsch

Graz, 12. Oktober 2012

Für Karin, Theresa & Eva

Danksagung

Diese Arbeit wäre nicht denkbar ohne die Unterstützung, die ich von zahlreichen Seiten erhalten habe. In fachlicher Hinsicht gilt dies vor allem für mein Betreuer „Dreigestirn“, Franz-Josef Brosch, Walter Kurz und last „but not least“ Gerd Rantitsch.

Gedankt sei auch den Kolleginnen und Kollegen, die mich auf der TU Graz, an der MU Leoben aber auch bei meiner Arbeit auf den diversen Baustellen rund um die Koralpe fachlich und moralisch unterstützt (oder gepiesackt) haben. Einige wenige seien dabei aufgezählt: Andreas Wölfler, Robert Rabitsch, Qian Liu, Kurt Klima, Christine Latal, Anni Pendl, Peter Schreiber, Doris Reischenbacher und Florian Mittermayer, sowie Sabine Wurzwaller, Wolfgang Bacher, Richard Otto und Gerhard Sulzbacher (der überhaupt an allem schuld ist ☺!). Es war nicht immer ganz einfach „nein“ zu sagen wenn die Buschenschänken der Weststeiermark und des Lavanttals riefen… (Sulzi!).

Des Weiteren sei der TU Graz als Arbeitgeber gedankt. Finanzielle Unterstützung erfolgte auch im Rahmen des Forschungsprojektes P-17697-N10 vom FWF (Projektleitung Walter Kurz). Die Österreichische Gesellschaft für Geomechanik hat die Geländearbeiten finanziell unterstützt. Danke!

Der 3G ZT GmbH sei als Arbeitgeber dafür gedankt, dass ich im Rahmen des Koralmtunnelprojektes und anderer Projekte meine Brötchen verdienen durfte.

Der Zugang zu bzw. die Verwendung von Daten der Arbeiten zum Koralmtunnel wurde dankenswerterweise von der ÖBB-Infrastruktur AG, Projektleitung Koralmbahn 3 (Mag. Ing. Gerhard Harer) ermöglicht.

Herr Doktor Lenhardt von der ZAMG stellte dankenswerterweise einen Erdbebenkatalog für das Projektgebiet zur Verfügung. Die ehemalige ÖSAG (Ing. Lorber) stellte die geologische Dokumentation des Gräberntunnels zur Verfügung. Das Amt der Kärntner Landesregierung (Harald Oswalder, MSc) ebenso wie das Amt der steiermärkischen Landesregierung (DI Alfred Nagelschmied) ermöglichten den Zugang zu GIS-Daten.

Last but not least sei meiner Familie gedankt, ohne deren Rückhalt das Leben nur halb so schön wäre!

Statutory declaration

I declare that I have authored this thesis independently, that I have not used other than the declared sources / resources, and that I have explicitly marked all material which has been quoted either literally or by content from the used sources.

……. ……..

(date) (signature)

Abstract

This thesis consist of a first part (Chapter 3) analysing the fault slip and a second part dealing with the morphotectonics of the Koralpe (Chapter 4).

The Paleogene and Neogene evolution of Austroalpine basement units east of the Tauern Window is characterised by the formation of two major sets of faults: (1) ESE–WNW- to E–W-trending faults, associated with ENE- and NNW-trending conjugate structures and (2) N–S to NNE-SSW striking structures, mainly acting as high-angle normal faults and often associated with E-dipping low-angle normal faults along the western margin of the Styrian Basin. Together with the stratigraphic evolution of the Styrian and Lavanttal Basins and the related subsidence histories a tectonic evolution may be reconstructed for this part of the Eastern Alps. In the southern part of the Koralpe, WNW-trending fractures were activated as dextral strike-slip faults, associated with the evolution of WNW-trending troughs filled up with coarse block debris. W- to WNW-trending fractures were reactivated as normal faults, indicating N–S extension. It is assumed that these phases resulted in subsidence and block debris sedimentation in Karpatian and Badenian times (ca. 17–13 Ma). In the Western Styrian Basin no Sarmatian (13–11.5 Ma) sediments are observed; Pannonian (11.5 to 7.1 Ma) sediments are restricted to the Eastern Styrian Basin. This indicates that the Koralpe and the Western Styrian Basin were affected by post-Sarmatian uplift, coinciding with a re-activation of N-trending normal faults along the eastern margin of the Koralpe. Therefore, we suggest that the final uplift of the Koralpe, partly together with the Western Styrian Basin, occurred during the early Pannonian (at approximately 10 Ma). The elevation of clastic deposits indicates that the basement was elevated by approximately 800 m during this phase, associated with an additional phase of E–W-directed extension accommodated by N–S striking normal faults.

A possible neotectonic control of the western and southern mountain front of the Koralpe is deducible from the visualizations of digital elevation data and mountain front sinuosity. However, neotectonic activity of the Lavanttal fault is not large enough to leave a clear trace within the large debris fans at the eastern margin of the Lavanttal Basin and the Lavant River is forced to the western side of the basin.

The eastern mountain front of the Koralpe is tectonically inactive. Gorges indicate a lowering of the base level. Such gorges are observed all around the Styrian Basin too.

The comparison with the elevation data of the Alps shows that the Koralpe belongs to a fault-bounded zone of low relief and low slope gradient east of the Tauern Window. Hypsometric integral and curve for the Koralpe indicate a mature equilibrium landscape. The Koralpe is characterised by large areas of low relief and low slope angle, especially in the north and the east. Here, they do not represent isolated levels of planation but form continuous zones. Therefore, these planation surfaces are proposed to represent remnants of a single paleolandscape with a probable Upper Miocene to Pliocene age.

The Koralpe's geomorphology is fundamentally controlled by the penetrative metamorphic foliation, causing anisotropic rock properties. Orientation of foliation controls especially slope inclination and orientation. In the eastern and central Koralpe, orientation and shape of slopes accentuates the underlying large scale fold structure. On the contrary, the northern Koralpe is characterized by plateau formation due to a frequently nearly horizontal foliation.

Morphological impact of faults and fault zones is verifiable in certain locations. However, the morphological impact of faults within the interior of the Koralpe is difficult to discern from the one caused by other structures or lithological contrasts. Hence, it seems not probable that fault related neotectonic activity could possibly be identified from specific landforms in the Koralpe's interior.

The river pattern of the Koralpe exhibits strong evidence of structural controls too. The presence of wind gaps and angular river knees underline the importance of stream capture processes for the development of the Koralpe's drainage system. Stream capture is also reflected in the asymmetric shape of some of the catchments. Paleorivers may be inferred in several places from aligned wind gaps and linear valleys, indicating a reorganisation of drainage from a N-S direction to a WNW-ESE direction. Pliocene shift of the Drau (Drava) to its present position triggered a renewed reorganisation by stream capture to southwards directed drainage. The systematic changes in river orientation in the eastern Koralpe and at the entrance into the Styrian Basin constrain superposition of consequent river stretches from the former sedimentary cover of the Koralpe onto the basement.

Knickpoints are frequently present in the longitudinal river profiles of the Koralpe. Most of the knickpoints are associated with low concavity indices and located within a belt of high stream gradient index surrounding the Koralpe. This advocates changes in base level as a common cause for knickpoint origin. However, some of the knickpoints are clearly associated to contrasts in lithology. Multi-causality of knick point origin is therefore a probable scenario for the Koralpe.

Tilting of the Koralpe is mainly advocated by its asymmetric topography. However, such a topography is not present in the northern Koralpe, indicating that this part was not tilted. The necessary differential movements between these two regions could have been accommodated by WNW-ESE striking fault zones encountered during tunnelling in the northern Koralpe. Tilting of the Koralpe is not reflected in a preferred asymmetry of catchments. However, several basin shape indices and also the channel index yield elongated basins for the western Koralpe, which could be interpreted as a result of tilting to the east.

Zusammenfassung

Diese Arbeit besteht aus zwei Teilen. Im ersten Teil (Kapitel 3) wird mit Hilfe von Störungsflächendaten die Sprödtektonik und im zweiten Teil (Kapitel 4) die Morphotektonik der Koralpe behandelt.

Die paläogene und neogene Entwicklung der ostalpinen Grundgebirgseinheiten östlich des Tauern Fensters ist durch zwei Hauptstörungsrichtungen gekennzeichnet: (1) OSO-WNW bis O-W streichende Störungen mit konjugierten ONO bis NNW streichenden Elementen und (2) N-S bis NNO-SSW streichende, hauptsächlich als steile Abschiebungen ausgebildete Störungen. Letztere werden vor allem zum Steirischen Becken hin von ostfallenden „low angle“ Störungen begleitet. Unter Berücksichtigung der Entwicklung des Steirischen und des Lavanttaler Beckens lässt sich die tektonische Entwicklung dieses Teils der Ostalpen rekonstruieren. In der südlichen Koralpe werden WNW streichende Störungen als dextrale Seitenverschiebungen aktiviert. Diese Störungen werden im Karpat und Baden (ca. 17-13 Ma) durch Extension in N-S Richtung als Abschiebungen reaktiviert und ermöglichen Subsidenz und die Ausbildung von langgezogenen, mit Blockschutt gefüllten Trögen. Sedimente des Sarmat (13-11,5 Ma) und des Pannon (11,5-7,1 Ma) sind im Weststeirischen Becken nicht erhalten und beschränken sich auf das Oststeirische Becken. Dies indiziert post-sarmatische Hebung im Bereich des Weststeirischen Beckens und eine Reaktivierung von N streichenden Abschiebungen entlang des östlichen Randes der Koralpe. Die finale Hebung der Koralpe, z. T. gemeinsam mit dem Weststeirischen Becken erfolgte daher vermutlich im frühen Pannon (~10 Ma). Die Höhenlage der Grobklastika deutet darauf hin, dass die Koralpe während dieser Phase, die von W-O gerichteter Extension an N-S streichenden Störungen gekennzeichnet ist, um ca. 800 m gehoben wurde.

Die von Dreiecksfacetten begleiteten und in den Höhenmodellen klar erkennbaren, linearen, durch niedrige Sinuosität gekennzeichneten Gebirgsfronten deuten auf neotektonische Aktivität im Bereich der Lavanttal Störung und des Drautals. Diese Aktivität ist jedoch nicht groß genug um die Bewegungszone klar in den Schuttfächern des östlichen Lavanttales abzupausen. Die Lavant wird durch diese mächtigen Schuttfächer an den westlichen Beckenrand gedrängt.

Der östliche Gebirgsrand ist klar als tektonisch inaktiv zu bezeichnen. Systematisch auftretende Schluchten deuten auf Veränderungen im Vorflutniveau. Solche Schluchten kennzeichnen den gesamten Rand des Steirischen Beckens.

Ein Vergleich mit Geländemodellen der Alpen zeigt, dass die Koralpe Teil einer störungsbegrenzten, durch geringes Relief und niedrige Hangneigungen gekennzeichneten Zone östlichen des Tauern Fensters ist. Dies spiegelt sich auch in der hypsometrischen Kurve und im hypsometrischen Integral der Koralpe wieder, die beide auf eine reife, ausgeglichene Landschaft deuten. Große Bereiche mit ausgeglichenem Relief und niedrigen Hangneigungen kennzeichnen vor allem die nördliche und östliche Koralpe. Sie bilden jedoch nicht isolierte Verebnungsniveaus

(„Fluren“), sondern bilden zusammenhängende Zonen. Sie werden daher als Reste einer obermiozänen bis pliozänen Paläolandschaft interpretiert.

Die Morphologie der Koralpe wird grundlegend durch die penetrative Schieferung und die damit verbundene mechanische Anisotropie beeinflusst. So werden die Orientierung und Neigung der Hänge verbreitet durch die Schieferung bestimmt. Ebenso spiegelt die Morphologie der zentralen Koralpe deutlich die Großfaltenstruktur wieder. In der nördlichen Koralpe hingegen begünstigt die flache Schieferung Plateaubildung. Ein Zusammenhang zwischen Störungszonen und Geomorphologie lässt sich bereichsweise nachweisen. Ohne entsprechende Untergrundaufschlüsse ist der Zusammenhang nur schwer verifizierbar, da auch andere Strukturen oder lithologische Unterschiede ähnliche Morphologieelemente bedingen können. Es kann daher nicht davon ausgegangen werden, dass sich durch Neotektonik bedingte Landformen im Inneren der Koralpe nachweisen lassen.

Das Entwässerungsnetz der Koralpe wird ebenfalls weitgehend strukturell kontrolliert. Trockentalreste und Talknickpunkte untermauern die Bedeutung von Anzapfungsprozessen für die Entwicklung des Entwässerungsnetzes. Paläoflüsse lassen sich bereichsweise ableiten und indizieren einen Wechsel von einer N-S zu einer ESE gerichteten Entwässerung. Die pliozäne Verlagerung der Drau (Drava) in ihr heutiges Tal verursachte eine erneute Anzapfung von Süden her. Systematische Talknicke in der östlichen Koralpe und am Übergang vom Kristallin in das Steirische Becken deuten daraufhin, dass eine in den ehemals überlagernden Sedimenten konsequent angelegte Entwässerungsrichtung dem Kristallin aufgeprägt wurde.

Zahlreiche Knickpunkte kennzeichnen die Flußprofile der Koralpe. Die meisten davon sind durch einen niedrigen „concavity index“ gekennzeichnet und finden sich in einem die Koralpe umgebenden Gürtel der durch hohe Flußgradienten gekennzeichnet ist. Einige dieser Knickpunkte sind jedoch eindeutig lithologisch bedingt. Die Entstehung der Knickpunkte lässt sich somit nicht auf Veränderungen des Vorflutniveaus reduzieren und die Multikausalität ihrer Entstehung muss betont werden.

Die Kippung der Koralpe wird meistens mit ihrer asymmetrischen Topographie begründet. Diese fehlt jedoch in der nördlichen Koralpe und eine Kippung lässt sich hier nicht nachweisen. Die Akkommodierung dieser differentiellen Bewegungen könnte entlang von WNW-ESE streichenden Störungszonen erfolgt sein, die im Zuge von Untertagebauarbeiten in der nördlichen Koralpe angetroffen wurden. Die Kippung spiegelt sich nicht in einer bevorzugten Asymmetrie der Einzugsgebiete der Koralpe wieder. Anhand von Indexwerten lassen sich jedoch in der westlichen Koralpe stärker gestreckte Einzugsgebiete nachweisen, was auf eine Kippung nach Osten hinweist.

Contents

1 INTRODUCTION

1.1 MOTIVATION

Motivation for this research is nourished by the geological experiences I made during field and drill core mapping for the Koralmtunnel project during the late 1990ies and the first decade of the new millennium and during the geological documentation of the Herzogbergtunnel in the northern Koralpe. These works showed that the Koralpe is largely a white spot with regards to its brittle tectonic history. At the Herzogberg Tunnel the two largest faults were nicely mirrored in the geomorphology and during field mapping for the Koralmtunnel geomorphology was frequently used to advocate the identification of faults (Figure 1-1). However, core drilling showed that not every morphological indicator is necessarily linked to a cataclastic fault. These experiences fostered my interest for the tectonics and geomorphology of the Koralpe. The opportunity for funded work at Graz University of Technology finally allowed me to jump into these waters.

1.2 PROBLEM STATEMENT

The presence of cataclastic fault zones plays a major role for the feasibility of subsurface infrastructure projects (tunnels, caverns, high risk waste disposals etc.). These zones of weakness most times influence the overall stability of subsurface excavations and the hydrogeology of the rock mass of interest. Hence the feasibility and the costs of a project are directly linked to the problems connected with the occurrence of such fault zones. For example, a tunnel boring machine (TBM) designed for an intact rock mass with favourable mechanical properties may get stuck when encountering a cataclastic fault zone with low mechanical properties and eventually high water inflow (Barton, 2000). The presence of a brittle fault zone may require extensive grouting measures to seal a subsurface structure against water inflows or may even be a knock-out criterion for certain types of structures (e.g. a radioactive waste disposal). Large deformations and instabilities up to complete collapse of a tunnel are possible scenarios for tunnel headings in faulted rocks resp. active fault zones (Brox and Hagedorn, 1999).

Consequently, knowledge about the regional fault pattern, the style of faulting, the associated fault rocks, the responsible tectonic regime and possible neotectonic activities form an important base for the engineering geological work in the course of an underground construction project (Schneider, 1997; Bürgi and Parriaux, 1999; Harer and Riedmüller, 1999; Löw et al., 1999; Brosch et al., 2001; Laws, 2001; Lützenkirchen, 2003).

The Koralpe Range (Figure 1-2) at the eastern margin of the Alps forms a barrier between South-Eastern Austria (Province of Styria) and Southern Austria (Province of Carinthia), resp. between Eastern Europe and Italy. The construction of roads across this mountain range has been a tedious task for centuries, culminating in the construction of a highway from the 1980s onwards. The last decade of the last millennium brought a general trend towards the construction of new, resp. the

renovation of existing railway corridors across the Alps. During this period, a high capacity railway, crossing the Koralpe Range had been initiated, including the Koralm Tunnel project (Figure 1-2).

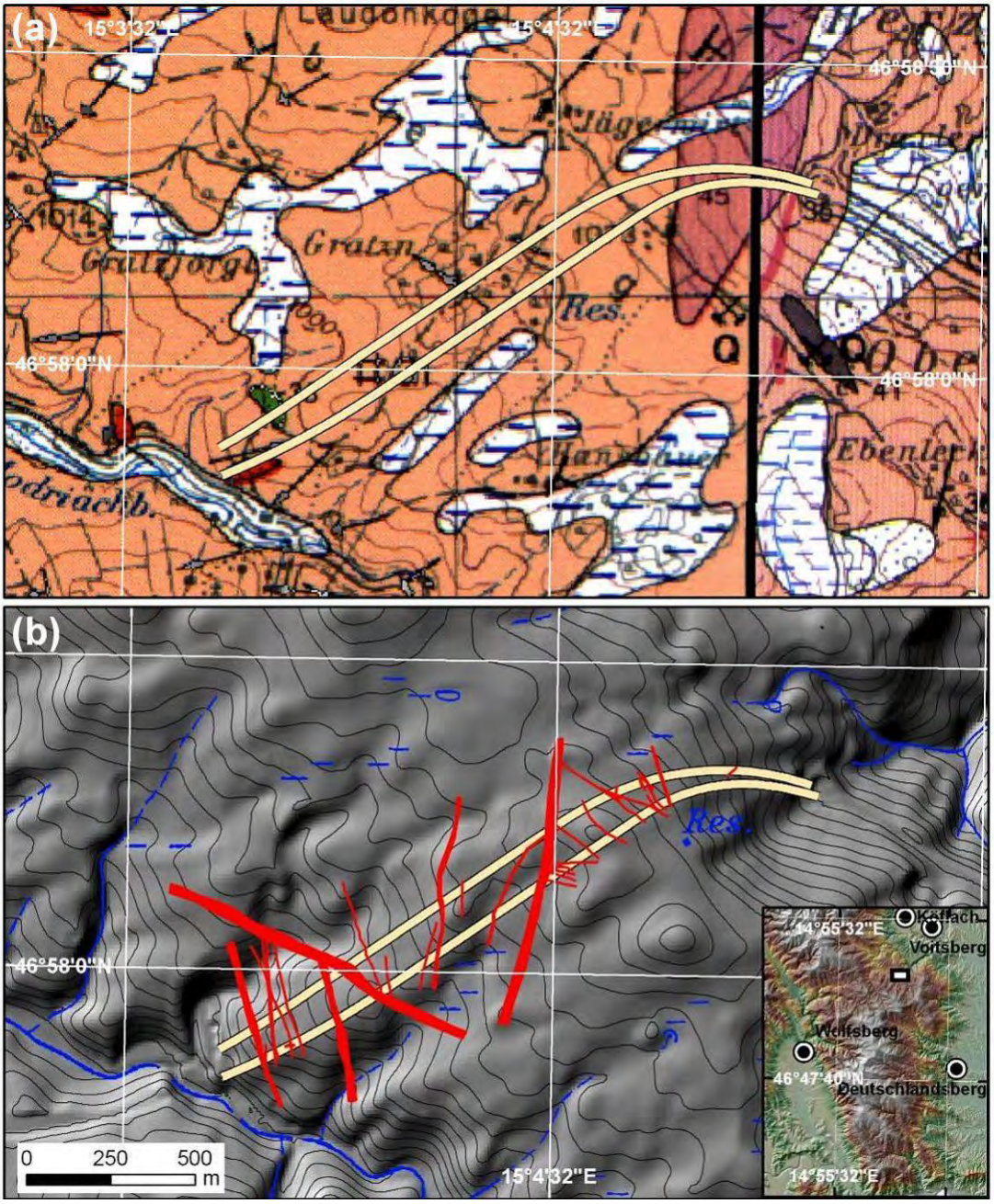

Figure 1-1: (a) Detail of the geological map of the Austrian Geological Survey sheets 188 and 189 of the area around the Herzogberg Tunnel (b) Faults mapped on tunnel level (horizontal section, faults not projected to surface), contour lines and hillshade are added to emphasise the morphological impact of the main faults. See insert in the lower right corner for location of the Herzogberg Tunnel (white rectangle).

During the early stages of the Koralm Tunnel project, the study of the regional geological literature and maps revealed missing important information about the faulting-related tectonics of this area: The geological maps show large differences in the regional distribution of faults. The geological maps of the Austrian Geological Survey 188 Wolfsberg and 189 Deutschlandsberg (Beck-Mannagetta, 1980; Beck-Mannagetta et al., 1991) as well as 162 Köflach (Becker, 1979) only show sparse faults and fault zones (Figure 1-1). Over large areas faults have not been mapped. In contrast to these maps, a pronounced network of faults is mapped in sheet no. 205 St. Paul im Lavanttal (Kleinschmidt et al., 1989) directly south of sheet 188. Lineaments (as indicators for faults) were mapped from remote sensed data by Tollmann (1976), by Buchroithner (1984) and by Peresson and Decker (1998). Especially the latter two studies show a high lineament density, contrasting the present regional geological maps. Evidence for pronounced faulting in this area comes from subsurface infrastructure projects (Fürlinger, 1978; Litscher, 1978; Riedmüller and Schwaighofer, 1978; Brosch, 1982; Brosch, 1983; Klima et al., 1988; Schmitz et al., 1989; Graf et al., 2001; Steidl et al., 2001; Neumüller et al., 2003). Besides these references, only few papers deal with the regional brittle tectonics of the Koralpe (e.g. Neubauer, 1991).

In the west, the Koralpe is bounded by a prominent fault zone, the Lavanttal Fault Zone (Figure 1-3 and Figure 1-4). This fault zone is part of the Pöls-Lavanttal fault system and has been recognized as a major tectonic fault zone, discussed for more than 110 years (Höfer, 1894; Kieslinger, 1928a; Tollmann, 1969; Metz, 1976; Kurz et al., 2011). More contemporary authors describe the Lavanttal Fault Zone mostly as an outcome of Miocene lateral extrusion (Ratschbacher et al., 1991a; 1991b) of the Eastern Alps (Frisch et al., 2000a). Detailed structural geological field work about the brittle tectonic structures of the Koralpe Range, resp. the Lavanttal fault was not present at the beginning of site investigations for the Koralm Tunnel (Peresson and Decker, 1998). The sedimentary evolution and the tectonics of the adjacent Lavanttal Basin (Figure 1-2, Beck-Mannagetta, 1952) have recently been highlighted by Reischenbacher and Sachsenhofer (2006; 2012), Reischenbacher et al. (2007) and Reischenbacher (2008). Evidence for the present tectonic regime of the Pöls – Lavanttal fault system from earthquake fault plane solutions has been published by Reinecker & Lenhardt (1999) and Reinecker (2000). The neotectonic regime has also been analysed by GPS measurements (Vrabec et al., 2006; Haslinger et al., 2007; Caporali et al., 2009).

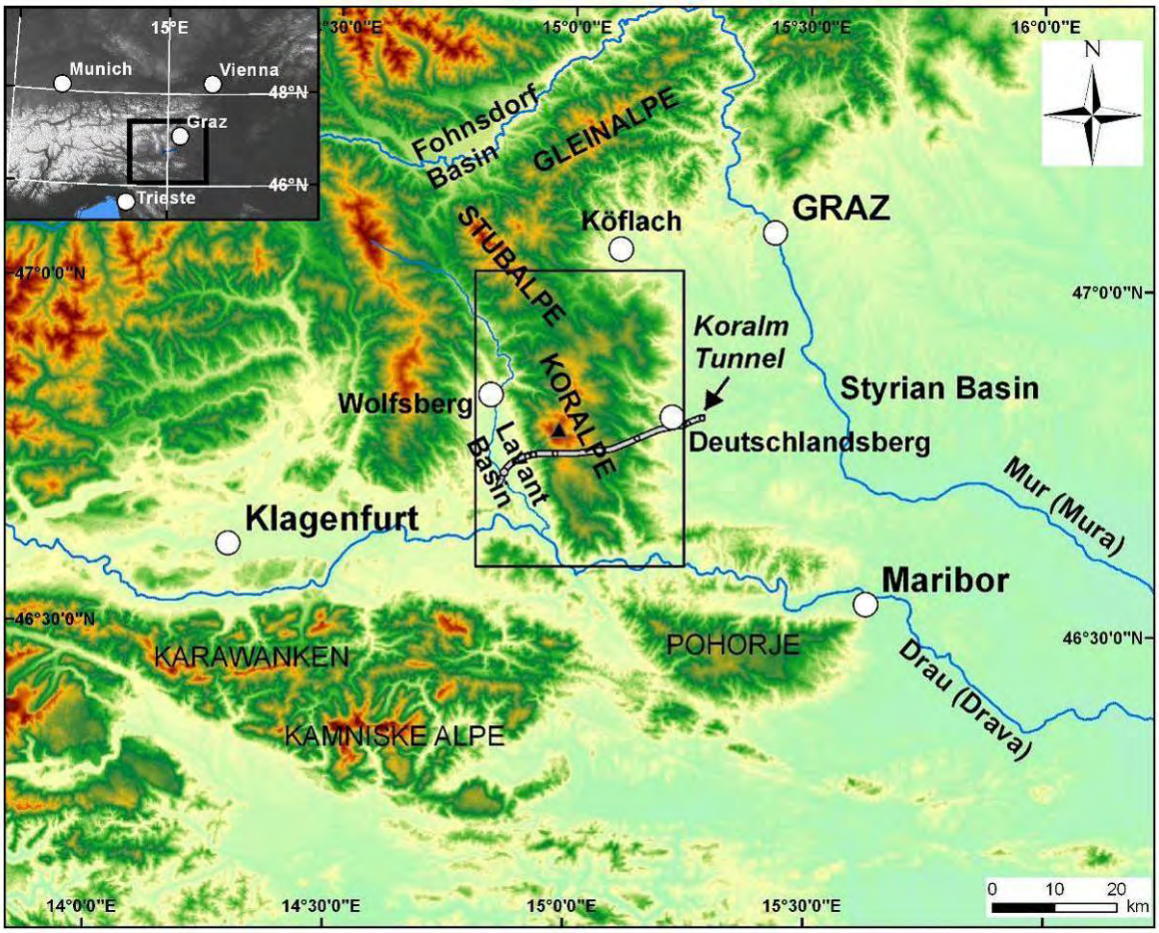

Figure 1-2: Overview of the working area (see insert). The black triangle marks the highest peak of the range (Großer Speikkogel 2140 m). DEM derived from 96m SRTM data (http://srtm.csi.cgiar.org/).

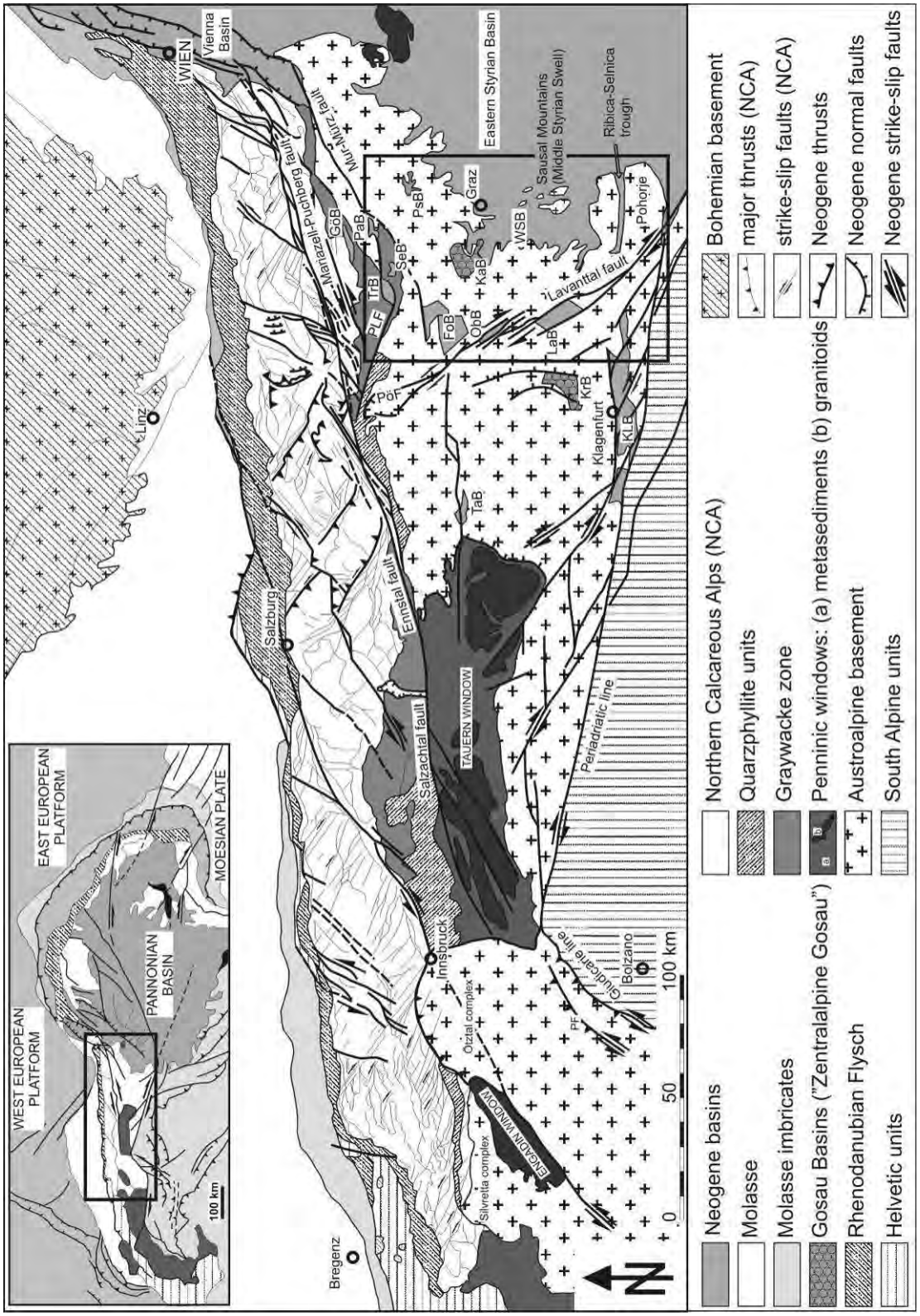

Figure 1-3: Tectonic map of the Eastern Alps displaying major and minor Paleogene to Neogene fault systems (after Linzer et al., 2002). PLF=Palten – Liesing fault; PöF=Pöls fault; GöB=Göriach Basin; PaB=Parschlug Basin; SeB=Seegraben Basin; PSB=Passail Basin; FoB=Fohnsdorf Basin; ObB=Obdach Basin; LaB=Lavanttal Basin; TaB=Tamsweg Basin; TrB=Trofaiach Basin; KLB=Klagenfurt Basin; WSB=Western Styrian Basin; KrB=Krappfeld Gosau Basin; KaB=Kainach Gosau Basin.

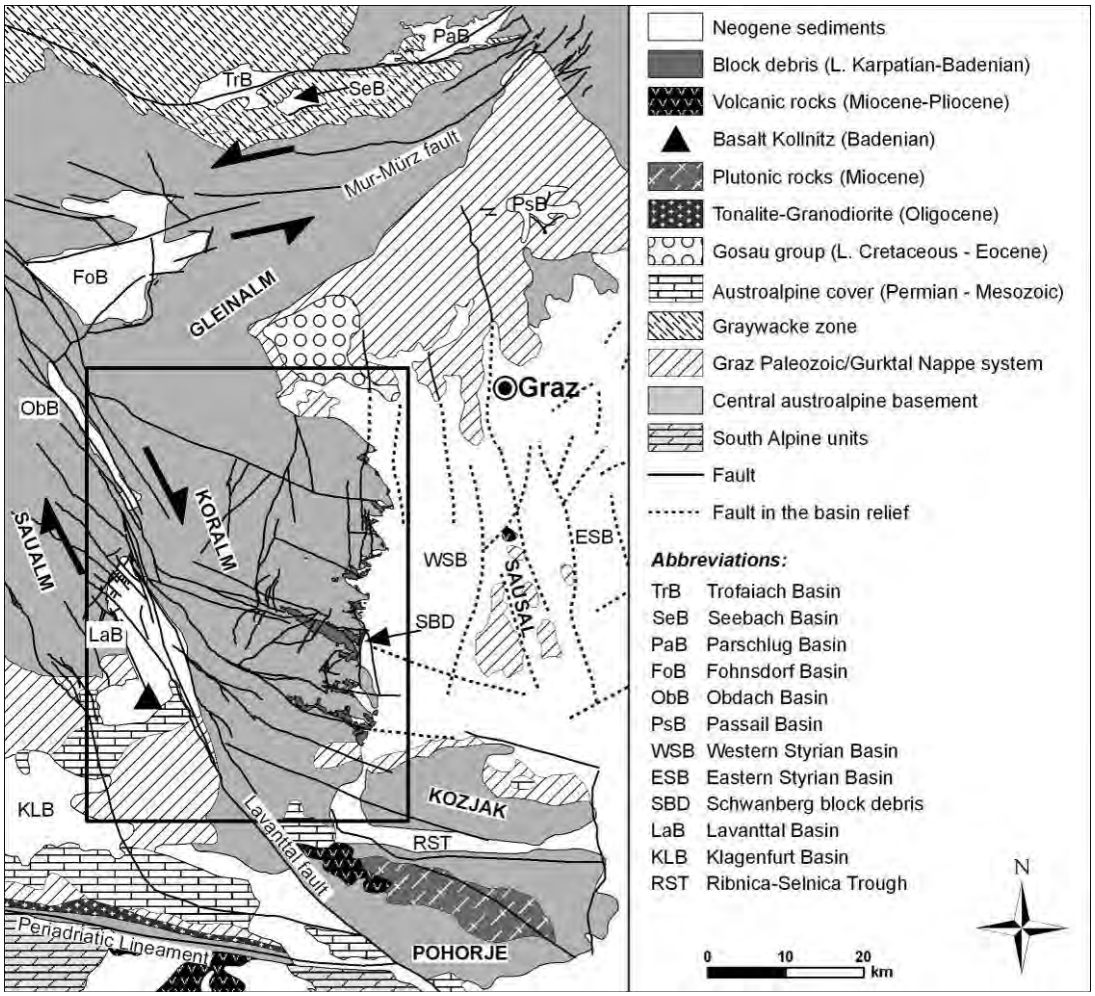

Figure 1-4: Geological map of the Koralpe and adjacent areas, including the main faults activated during the Miocene. Rectangle marks working area. Map compiled from Beck-Mannagetta, 1952; Weissenbach, 1978a; Weissenbach, 1978b; Becker, 1979; Beck-Mannagetta, 1980; Kröll, 1988; Beck-Mannagetta et al., 1991; Egger et al., 1999; 1999; Strauss et al., 2001; Beck-Mannagetta and Stingl, 2002, mappings by 3G ZT GmbH (courtesy of ÖBB Infrastruktur Bau GmbH) and own mappings.

One main reason for the described lack of information is the outcrop situation. Large areas of the Koralpe are weathered intensely. That is due to the fact, that only the summit region was covered by small local glaciers during the Pleistocene glaciation (Morawetz, 1952; Beck-Mannagetta, 1953; Van Husen, 1987). Weathering resulted in the accumulation of thick slope debris hiding the bed rock (Figure 1-5). This is especially true along mechanical weak fault zones, which are prone to intense weathering. They are consequently badly preserved in outcrops, if they are exposed at all (Cladouhos, 1999; Riedmüller et al., 2001), especially in humid regions (Faulkner et al., 2008). Additionally, the focus of many researchers was on the Pre-Paleogene history of the Koralpe.

Considering the structural and lithological controls of landforms, their understanding becomes a helpful tool to identify hidden subsurface structures. This is essentially true in areas like the Koralpe, where an often thick cover of slope debris, resulting from intense weathering, and a dense vegetation cover hide the bedrock geology (Figure 1-5).

Figure 1-5: Slope debris blanket in the northern Koralpe (Mitterberg). Vertical height is approximately 5 m.

Nevertheless, the geomorphological expression of fault zones enables us to identify such zones even in areas with sparse outcrops. Apart from “classic” landforms controlled by fault activity (see Chapter 3.1.1.3; Ramsay and Huber, 1987; Bloom, 1998; Summerfield 2000; Scheidegger, 2004; Twiss and Moores, 2007) topographical features at a wide range of scales can be used as indicators for the presence of a fault (zone). Such indicators may be morphological saddles, flat and/or wet areas, abrupt changes in the orientation of river courses or ridges, or in the gradient of a slope, forming “a network of differentially eroded zones on both fault lines and joints” (Bloom, 1998).

The application of modern morphometric techniques for surface classification in digital elevation models (DEM) can help to identify indicator landforms (Wood, 1996; Bolongaro-Crevenna et al., 2005; Jordan et al., 2005; Schmidt and Andrew, 2005).

With the availability of very detailed DEMs these techniques support early stage site investigations for large infrastructure projects. Despite all advances in this field, geological field mapping and human interpretation of landforms remain as fundamental tools to allow a genetic explanation. This is especially true as similar morphological features may have different causes.

To asses landscape evolution several techniques have been brought forward from the fields of tectonic geomorphology resp. morphotectonics (Burbank and Anderson, 2001; Keller and Pinter, 2002) exploring the concurrent activity of endogenic (tectonic) and exogenic (surface) processes (Bull and McFadden, 1977; Keller, 1986; Mayer, 1986; Wells et al., 1988; Snyder et al., 2000; Wobus et al., 2003; Scheidegger, 2004; Zovoili et al., 2004). The interaction of these processes formed the earth's morphology. Climate, weathering, erosion and isostatic rebound are supposed to be linked by positive feedback mechanisms (Molnar and England, 1990). The interaction of these processes forms the core of "tectonic geomorphology" or "morphotectonics" (Burbank and Anderson, 2001), more generally defined as the relation of landscape morphology to tectonics (Scheidegger, 2004).

However, the actual topography of a region is not only controlled by structure it is additionally strongly influenced by the mechanical and structural properties of the main lithologies and their distribution (Kühni and Pfiffner, 2001).

1.3 SCOPES

This thesis is aimed to improve the knowledge about the tectonics of the Koralpe under semi-brittle to brittle conditions. Additionally, it tries to analyse the morphological imprint of the tectonic events on the present day landscape. This is essential because the results of field mapping in an area like the Koralpe depend fundamentally on the understanding of its present geomorphology. A better understanding of the relations of structure and geomorphology leads to a more reliable interpretation of geological field data for engineering purposes.

The following methods are applied:

- Mapping of brittle tectonic structures.
- Kinematical reconstruction of the brittle structures, as documented in outcrops, tunnels and exploratory core drillings to identify the deformation mechanisms.
- Estimation of the paleostress axes on the basis of kinematic indicators.
- Identification of lineaments from digital elevation models (DEM), digital terrain models (DTM), if possible with the support of other remote sensing data (SAR, Landsat TM, aerial photographies).
- Morphotectonic analysis of the Koralpe by applying digital morphometry including hypsometry, digital elevation analysis and morphotectonic index values.
- Characterisation of the drainage system of the Koralpe including longitudinal river profiles, drainage pattern and catchment shape.
- Identification and description of geomorphological characteristics linked to brittle faulting to facilitate the identification of faults in an area with sparse outcrops and strong weathering.

This thesis is divided into two parts. Part one deals with the brittle tectonics, part two focuses on the geomorphology of the Koralpe and the morphotectonic aspects.

The fault slip data analysis (Chapter 3) and parts of the morphotectonic analysis (Chapter 4) were published in the Swiss Journal of Geosciences (Pischinger et al., 2008; Rantitsch et al., 2009).

2 GEOMORPHOLOGICAL AND GEOLOGICAL SETTING

2.1.1 PHYSIOGRAPHY AND GEOMORPHOLOGY

2.1.1.1 TOPOGRAPHIC EVOLUTION

The morphogenesis of the Eastern Alps is thought to have started in Oligocene times, 30 Ma before present, when the collision of the Adriatic and the European plates was largely completed (Frisch et al., 2000b). However, analysis of Alpine topography gives evidence, that it is still far off from geomorphic equilibrium and the formation of the present topography of the Alps may only have begun 5-6 Ma b.p. (Hergarten et al., 2010). According to Frisch (2000b), a hilly landscape prevailed in Oligocene times east of the Tauern Window and the Austroalpine basement rocks of the Koralpe were not yet exposed. Erosion of this cover of low grade metamorphic rocks led to the sedimentation of the Augenstein Formation in the Northern Calcareous Alps (Frisch et al., 2001). Before the onset of lateral extrusion, drainage in the eastern part of the Eastern Alps was directed towards the north (Frisch et al., 2000b). With starting lateral extrusion of the Eastern Alps at the Oligocene/Miocene boundary a fundamental reorganisation of drainage occurred (Ratschbacher et al., 1991b; Frisch et al., 2000a), with the main rivers following the evolving W-E trending faults. Further, due to surface uplift of the Tauern Window and the Niedere Tauern the main water divide was shifted towards the north around the Early / Middle Miocene boundary (Frisch et al., 2000b). At this time the Austroalpine basement rocks must have already been exposed to erosion. This is reflected in the sedimentary content of the fault-related, orogen parallel valleys (Frisch et al., 2000b). Wagner et al. (2011) suggested that the Styrian Basin and the surrounding part of the Eastern Alps (bordered by the Mur-Mürz fault and the Lavanttal fault and subsumed under the term “Styrian Block”) underwent a common evolution since the end of the Miocene. According to Wagner et al. (2011) subsidence is documented for the basin parts up to the Sarmatian (~12.5 Ma). Fluctuating subsidence and uplift due to fragmentation and/or Horst-Graben formation characterises the Styrian Block up to the Upper Pannonian, from where on Wagner et al. (2011) assume continuous uplift. Incision rates derived from the river Mur are 125mm/Ma for the last 4 Ma (Wagner et al., 2010a), with higher rates before ~2.5 Ma (~250mm/Ma) and ~40mm/Ma up to the present. The higher rates are reasoned with surface uplift and effects of stream piracy. Surface uplift during the last 4 Ma is thought to have rejuvenated the topography of the Styrian Block (Wagner et al., 2010a). Tectonic disturbances are rarely traceable in the profiles of the Eastern Alp’s main rivers and most major knick points are related to the last glacial maximum (Robl et al., 2008). However, Robl et al. (2008) note evidence for “late” orogenic uplift in the Koralpe, indicated by stream power variations along the Koralpe’s rivers.

The pre-extrusion landscape is preserved in remnants east of the Tauern Window including the Koralpe. Winkler-Hermaden (1957) and others (Götzinger, 1913; Seefeldner, 1926; Tollmann, 1968) described this and other paleosurface levels (“Fluren”) as piedmont benchlands (Penck, 1924). They assigned these levels to different periods of the Miocene (Table 1). According to Winkler-Hermaden (1957), denudational paleosurfaces in the Koralpe are preserved only from the Quaternary

period and not from the Miocene. The latter are only preserved as downward shifted surfaces, parallel to the original ones. However, Frisch et al (2000b) reject Winkler-Hermaden's (1957) concept of planation surfaces of similar altitude correlated across fault bounded valleys. They discard the interpretation of a Piedmont benchland ("Rumpf- oder Piedmondtreppe") sensu Penck (1924) due to geochronological and tectonical considerations. Dunkl and Frisch (2002) suggested that the Koralpe was covered by sediments of the Pannonian Basin during Middle and Late Miocene times. According to Summerfield (1991), Penck's concept is generally not tenable, as major factors like climate and lithology are not considered. Recently cosmogenic derived denudation rates for the Koralpe (Legrain et al., 2011), burial ages of cave sediments from the nearby Palaeozoic of Graz (Wagner et al., 2010b) and (U-Th)/He ages (Wölfler et al., 2010, Kurz et al., 2011), constrain the exhumation history of this region from the late Miocene to present. Wagner (2010b) correlated different cave levels to Winkler-Hermaden's planation surfaces (Table 1). He assumes that these levels can be correlated within the entire "Styrian Block".

Level	Elevation a.s.l. [m]		Proposed age (Winkler-Hermaden, 1957)		Proposed age (Frisch et al. 2000b)		Minimum age (cave sediments) (Wagner et al, 2011)	
	from	to	Stage	[Ma]	Synonym	Age	Stage	[Ma]
Kor	1700	2000	Upper Sarmatian	~12	Nock surface	Early Miocene		
Wolscheneck	1500	1700	Lower Pannonian	~11				
Glashütten	1100	1400	Middle Pannonian	~10-9				
Trahütten	900	1000	Uppermost Pannonian	~8			Dacium	~4
Hochstraden	650	850	Uppermost Pliocene	~2.5-1.8			Romanian/Dacian	~3.4

Diss_Fluren.xls

Table 1: Paleosurface levels in the region of the Koralpe after Winkler-Hermaden (1957) and correlation to Frisch et al. (2000b) and Wagner et al. (2011).

2.1.1.2 GEOMORPHOLOGICAL CHARACTERISTICS

The Koralpe forms an asymmetrically shaped mountain range in a W-E directed profile view (Figure 2-1), bordered in the west by the Lavant valley and in the east and northeast dipping below the Styrian Basin. To the north it passes into the mountain ranges of the Stub- and Gleinalpe (Figure 1-2 & Figure 1-4). Towards the south, the Koralpe is separated by the river Drau (Drava) from the Pohorje range (Figure 1-2 & Figure 1-4). The highest elevation is 2140 m (Großer Speikkogel, Figure 1-2). The western slope is generally WSW dipping and drains into the river Lavant. Within a horizontal distance of approx. 4 to 5 km, the altitude rises by approx. 1700 m. Deeply incising, ENE-WSW to NE-SW trending creeks, flanked by steep, mainly NW to SW dipping slopes, interrupt this escarpment (Figure 2-1, Profiles 2 to 4). The slope angles along these creeks are frequently larger than 25° (Figure 2-2). Morphological saddles (Peucker and Douglas, 1975) subdivide the WSW-ENE trending ridges of the western realm in NNW-SSE direction (Figure 2-3).

The eastern realm drains towards the Styrian Basin and is morphologically subdivided by WNW-ESE to NW-SE trending valleys and ridges. Steeper slope angles are mainly concentrated along the valleys and the crests of the separating ridges. The

eastern Koralpe has a width in WNW-ESE direction of approx. 12 to 16 km. The maximum difference in elevation is 1772 m from the highest point, the Speikkogel (2140 m), to Deutschlandsberg (368 m).

The northern part of the Koralpe forms a depression between the northern Lavant valley (Bad St. Leonhard Basin) and the Styrian Basin (Figure 2-1). The Teigitsch is the main creek draining this area towards the Styrian Basin. Its course is characterised by several pronounced changes in its drainage direction (Figure 2-1). Especially east of the Herzogberg it forms a deeply incising gorge before reaching the Styrian Basin. Towards the west the northern Koralpe is drained by the Waldensteinbach, into the Twimberg gorge of the Lavant River, This gorge connects the Bad St. Leonhard and the Lavanttal Basin.

The southern part of the Koralpe (south of the line Großer Speikkogel – Wolschenek, see Figure 2-1 for location) drains southwards to the Slovenian part of the Drau (Drava) river. Morphologically it can be subdivided into a northern area with gentler slopes and a southern escarpment towards the Drau (Drava). Here, slope gradients exceed frequently 20° (Figure 2-2).

The asymmetric shaped W-E cross-section of the Koralpe has already been noted by Winkler-Hermaden (1957). Neubauer and Genser (1990) and Ratschbacher (1991b) explained this feature by block rotation due to Miocene lateral extrusion of the Eastern Alps and associated crustal thinning east of the Tauern Window. For the period of lateral extrusion, significant synsedimentary rotations around an vertical axis in counter clockwise direction (CCW) are inferred from paleomagnetic data measured in the surrounding intramontane basins (Márton et al., 2000; 2002). This is followed by an estimated post-Sarmatian CCW rotation of approximately 30°(Márton et al., 2000). This CCW rotation can be explained by higher lateral displacements along the southern border of the extruding Eastern Alps (the Periadriatic Lineament) than along the northern boundary (Salzach-Ennstal-Mariazell Puchberg fault, Márton et al., 2000; Wölfler et al., 2011).

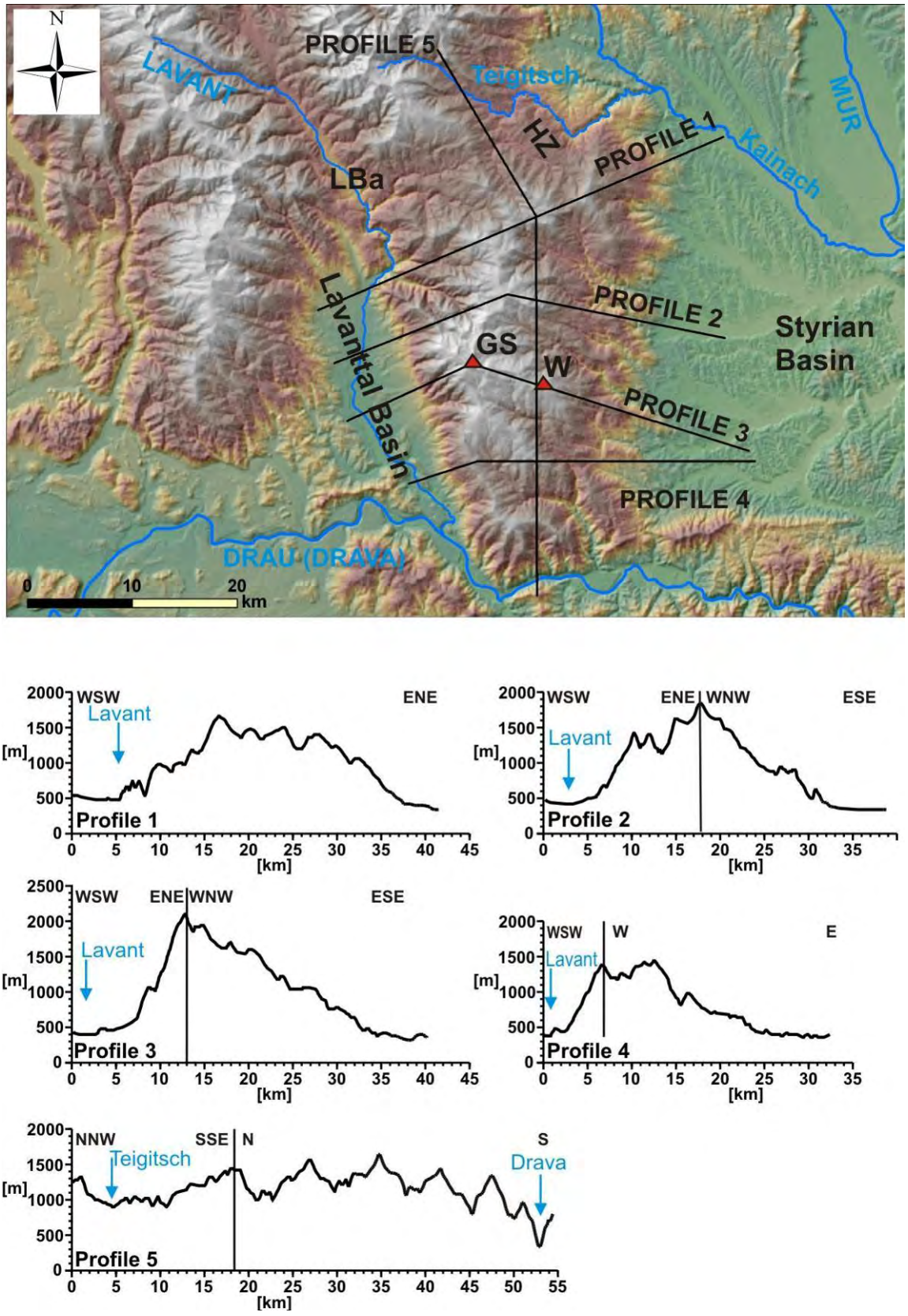

Figure 2-1: Location of topographic profiles and topographic profiles through the project area. DEM derived from 96m SRTM data. Red triangles in the map mark summits mentioned in the text. Black lines in the profiles mark change in profile direction (LBa…Bad St. Leonhard Basin, HZ…Herzogberg, GS…Großer Speikkogel, W…Wolschenek).

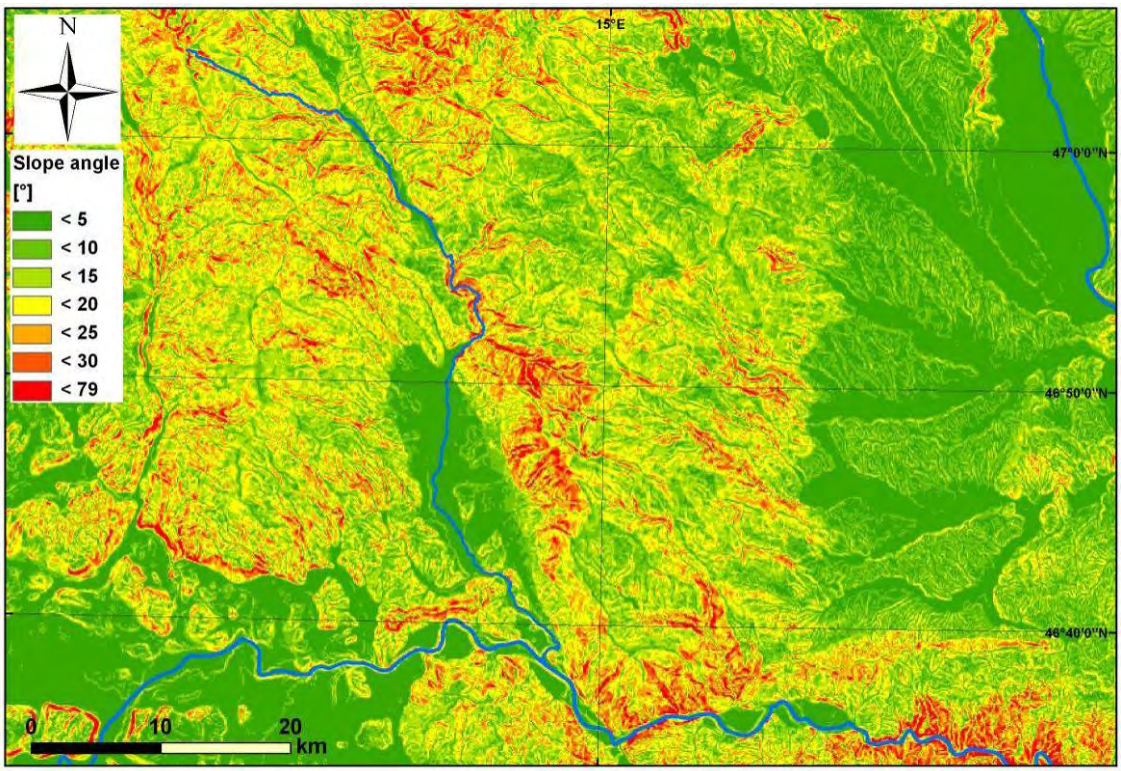

Figure 2-2: Slope angles calculated from 96m SRTM DEM with ArcGIS Spatial Analyst.

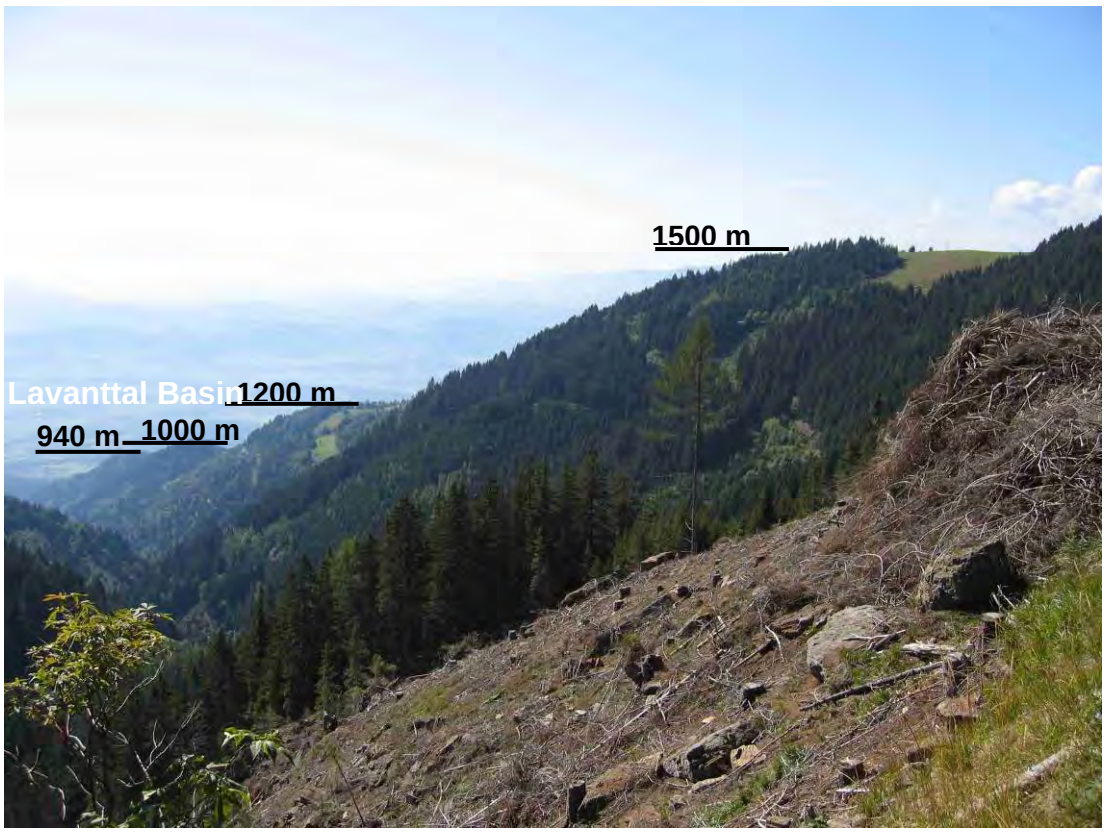

Figure 2-3: Western realm of the Koralpe - view towards NW to Goding and the Lavanttal Basin, the slope is structured by flat areas often interpreted as results of differential weathering of areas weakened by fault activity.

2.1.2 GEOLOGICAL SETTING

The largest part of the working area is situated in the Koralpe Range as part of the polymetamorphic basement of the Eastern Alps. It is bordered by Neogene and Quaternary sediments of the Lavanttal and Styrian Basin. The basement rocks comprise mainly mica schist, paragneiss and mylonite ("Plattengneis"). Subordinately marble, silicate bearing marble, quartzite, amphibolite, eclogite and pegmatite to pegmatite gneiss are incorporated in this metasedimentary succession (Kieslinger, 1928b; Homann, 1962; Kleinschmidt and Ritter, 1976; Pacher and Riepl, 1978; Becker, 1979; Becker, 1980; Beck-Mannagetta, 1980; 1980b; Heritsch, 1980a; Frank et al., 1983; Krohe, 1987; Beck-Mannagetta et al., 1991; Beck-Mannagetta and Stingl, 2002).

The Koralpe forms a dome structure with an approximately E-W- trending axis (Kurz et al., 2002) reflecting the orientation of the penetrative foliation, dipping to the south in the southern part of the Koralpe Range and the Plankogel Complex, and to the north to northeast in the northern parts. In the central part, the penetrative foliation has a subhorizontal orientation. Generally, the foliation is parallel to the lithological and tectonic boundaries, in particular along the southern and northern/northeastern margin of the Koralpe Range. Isoclinal folding of the foliation can be observed in the Plattengneis, with approx. N-S trending fold axes, parallel to the stretching lineation (Kurz et al., 2002). Consecutive folding with approx. W-E trending fold axes created open syn- and antiforms (Kurz et al., 2002; Putz et al., 2006).

The Koralpe and the adjacent high grade metamorphic units Saualpe, Gleinalpe, and Pohorje are parts of the Lower Austroalpine unit and, according to Schmid et al. (2004), are assigned to the Koralpe-Wölz high-pressure nappe system of the Austroalpine basement. Alternatively, these units are assigned to the "Middle" Austroalpine unit (Tollmann, 1959; 1963; 1977; Neubauer and Höck, 2000). The units within the Koralpe, Pohorje, Saualpe, and Gleinalpe expose high-grade metamorphic units (Tenczer and Stüwe, 2003) being incorporated into the Austroalpine nappe stack during Early Cretaceous times (Frank, 1987; Krohe, 1987).

The Koralpe-Wölz nappe system is overlain tectonically by the very low- to low-grade Graz Paleozoic and the Gurktal Nappe, both being part of the Upper Austroalpine Drauzug-Gurktal nappe system (Schmid et al. 2004). These units are transgressive and unconformably overlain by Gosau sediments of Late Cretaceous to Eocene age (Neubauer et al., 1995; Ebner and Rantitsch, 2000 resp. Figure 1-3, Figure 1-4).

The major part of the Austroalpine nappe pile in the Eastern Alps was already near to the surface during Neogene times, as indicated by zircon and apatite fission track data, referred to as "Cold Spots" by Hejl (1997). One of these "Cold Spots" is represented by the Koralpe Range (Figure 1-3, Figure 1-4).

2.1.2.1 PRE-CENOZOIC HISTORY

The pre-Cenozoic evolution of the Koralpe is very well documented by detailed petrological and structural studies, in particular from Permian to Late Cretaceous times (Gregurek, 1997, Habler and Thöni 2001, Kurz et al. 2002, Kurz and Fritz 2003, Schuster and Kurz 2005). This period is characterized by a poly-metamorphic history with indications of pre-Alpine events (Frank et al., 1983). Amphibolite to eclogite facies conditions were reached during the Lower Cretaceous (Eo-Alpine event). At least three metamorphic events (Variscan, Permian and Cretaceous) are constrained by detailed geochronological work (e.g. Frank et al., 1987; Thöni and Miller, 1996; Habler and Thöni, 2001).

Nappe stacking, HP metamorphism and subsequent exhumation of HP units occurred during Cretaceous times and are summarized as Eo-Alpine evolution (Kurz and Fritz, 2003). At upper crustal levels, the exhumation of the Koralpe Range was accommodated by low-angle normal faults along its southern and north-eastern margins (e.g. Rantitsch and Mali, 2006). Extension triggered the formation of the Gosau sedimentary basins (Figure 1-4) during Late Cretaceous times (Neubauer et al., 1995; Ebner and Rantitsch, 2000; Rantitsch et al., 2005). However, the Koralpe Range was not exhumed to the surface at that time as indicated by the absence of Koralpe-derived pebbles in the Gosau deposits (Gollner et al., 1987; Neubauer et al., 1995).

2.1.2.2 LATE CRETACEOUS AND CENOZOIC EVOLUTION

The Late Cretaceous to Paleogene tectono-metamorphic evolution of the Koralpe and adjacent areas is discussed by Bojar et al. (2001), Fritz et al. (2002), Kurz & Fritz (2003), Rantitsch et al. (2005) and Krenn et al. (2008). However, the recognition of post-Eoalpine structures and metamorphic assemblages is hampered by the fact that Cretaceous to Paleogene structural elements are frequently overprinted by Miocene structures. However, geochronological and tectono-metamorphic arguments give strong evidence that the evolution during the latest Cretaceous and Paleogene played a major role in Alpine tectonics (Kurz and Fritz, 2003): (1) Major Early Cretaceous thrusts are overprinted and sealed by upper greenschist- to amphibolite-facies metamorphism and tectonics. (2) Large rock volumes within the eastern sectors of the Eastern Alps cooled down below ca. 250°C already in Cretaceous times. (3) A large number of geochronological mineral formation ages, previously interpreted to date Eo- Alpine nappe stacking, cluster around ca. 80 Ma and may easily be re-interpreted in terms of strike-slip and/or extensional tectonics. In particular, sets of ductile strike slip and normal faults along the southern margin of Austroalpine units (Kurz and Fritz, 2003) are frequently obliterated by younger tectonic events along the Periadriatic Lineament (Figure 1-3).

The actual structural shape and topography of the Eastern Alps including the Koralpe started to evolve around the Early/Late Oligocene boundary, where, after the Adria/Europe collision, nappe stacking and crustal thickening reached its culmination (Ratschbacher et al., 1991b; Frisch et al., 1998; Frisch et al., 2000a). As a consequence of the break-off of the subducted Penninic oceanic slab, calc-alkaline intrusions and mafic dykes line up along the Periadriatic lineament (von Blanckenburg and Davies, 1995). This coincides with the onset of coarse clastic sedimentation in the Molasse basin of the central and western Eastern Alps and indicates a massive uplift of the Alps (Frisch et al., 2000a).

Along its margins, the Koralpe is surrounded by distinct faults. In particular, low-angle normal faults form the northeastern and southern margins of the Koralpe. The western margin is formed by the NNW-trending Lavanttal fault (Figure 1-3, Figure 1-4). This strike slip fault is part of the Pöls-Lavanttal fault system (Reinecker, 2000; Frisch et al., 2000a). Along the Lavanttal segment, a dextral offset of approximately 10 km was estimated from displaced lithological units. The vertical offset is 4-5 km, whereby the eastern block (Koralpe) was up-faulted (Frisch et al., 2000a). Near its southern termination, the Lavanttal fault cuts and offsets the Periadriatic fault by about 20 km. Fault displacement and substantial block movement resulted in the formation of a number of Early Miocene intramontane basins including the Lavanttal Basin, the Obdach Basin (=Bad St. Leonhard Basin) and the Fohnsdorf Basin (Figure 1-4, Frisch et al., 1998; Reinecker, 2000; Sachsenhofer et al., 2000; Strauss et al., 2001; Reischenbacher, 2008). Sedimentation in the Styrian Basin started at the same time, approximately 18 Ma before present (Sachsenhofer, 1996). Sedimentation ceased in most of the intramontane basins within the Badenian around 12 Ma (Frisch et al., 2000a), but continued in the Styrian Basin (Gross et al., 2007).

The Lavanttal Basin and Obdach Basin formed along left-handed oversteps of the Lavanttal fault. The nature of the Lavanttal Basin is probably an oblique graben structure formed in a transtensional regime (Frisch et al., 2000a; Reischenbacher, 2008) during Karpatian and Early Badenian pull-apart phases (Reischenbacher and Sachsenhofer, 2012). Modelling of seismic and gravity data yield a depth of ~2000 m for the Lavanttal Basin (Reischenbacher and Sachsenhofer, 2012). The Lavanttal fault is assumed to be active since the Early Miocene with peaks in activity between 18-16 Ma and 14-12 Ma (Reinecker 2000). Vertical displacement along the Lavanttal fault around 10-12 Ma probably caused the separation of the Lavanttal and the Styrian Basin (Kurz et al., 2011).

The largest part of the eastern margin of the Koralpe is covered by Miocene sediments of the western Styrian Basin (Figure 1-3). However, brittle faults and fault-related cataclastic rocks were detected by cored drillings located at the eastern margin of the Koralpe (Brosch et al., 2001; Vanek et al., 2001; Pischinger et al., 2005; 2006). Brittle structures related to the latest evolution of the Koralpe were analyzed by Vanek et al. (2001) during the site investigations for the Koralm Tunnel. The few results of tectonic and stress-strain analyses may be correlated with the Neogene tectonic evolution of the Eastern Alps including N-S- directed extension, re-oriented and replaced by E-W extension and subsequent E-W compression.

Following the descriptions above, the latest clearly documented metamorphic event within the Koralpe is the amphibolite facies overprint which occurred approximately 90 Ma before present. Subsequent cooling is poorly documented. This comprises exhumation, tectonic uplift and surface uplift.

Data show that crustal stretching, extension and the formation of the Gosau Basins of the Eastern Alps east of the Tauern Window („Zentralalpine Gosau“) coincide with the exhumation of crystalline basement complexes of the Austroalpine unit (Figure 1-3, Neubauer et al., 1995). Exhumation resulted in cooling from initial epidote-amphibolite and upper greenschist facies conditions to temperatures below 300°C at the beginning of the Paleogene. Sphene, zircon and apatite fission track data from the Gleinalpe area, indicate cooling to temperatures below 200-250°C at 65 Ma (Neubauer et al., 1995). The northern part of the Koralpe cooled to temperatures below 200°C already during Late Cretaceous times (Hejl, 1997; 1998). Hence, these regions were already near (approximately 5 to 8 km) to the surface during the Cenozoic. Towards the south, apatite fission track ages within the Koralpe gradually become younger. This indicates that the southern parts were exhumed later. In the central part of the Koralpe these ages range from approximately 50 to 37 Ma (Hejl, 1998; Rabitsch et al., 2007; Wölfler et al., 2010). Approximately 31 Ma are reported from the southern margin of the Koralpe, approx. 26 Ma from the western margin (Hejl, 1998). Two apatite fission track ages from the central part of the Koralpe, close to the Lavanttal fault, show cooling below approximately 120°C between 28.5 and 18 Ma. West of the Lavanttal fault, apatite fission track ages range from approx. 27 to 12 Ma (Puch, 1995). In the Pohorje region early to mid-Miocene cooling of both magmatic and metamorphic rocks is indicated by zircon fission track ages of 26-19 Ma (Fodor and POSIHU Research Group, 2003). U-Th/He thermochronometry indicates an exhumation event younger than 10 Ma (Kurz et al., 2009; Wölfler et al., 2010). Brittle deformation takes place in the upper 15 km of the earth’s crust (Sibson, 1977). Transition from brittle to the quasi plastic deformation regime occurs, according to Sibson (1977), at temperatures between 250 and 350°C. So the thermochronological data can be correlated with the deformation regime and indicate that brittle deformation in the Koralpe may have started already more than 50 Ma from present.

Indirect evidence for the Neogene evolution of the Koralpe may be provided by the sedimentary record within the adjacent sedimentary basins (in particular the Styrian and Lavanttal Basins; Figure 1-3, Figure 1-4 & Figure 2-4, for a summary see Ebner and Sachsenhofer 1995, Sachsenhofer et al. 1997, 2001 and Reischenbacher and Sachsenhofer, 2012). Subsidence in the Styrian Basin started probably at 18 Ma (Ottnangian stage of the Central Paratethys paleogeographic realm, Piller et al., 2007, Figure 2-4), followed by a phase of transgression in the Early Karpatian. In the latest Karpatian block-tilting of the Koralpe led to the re-organisation of the basin architecture (Styrian unconformity, Friebe, 1990; Friebe, 1991). This coincided with an eustatic sea level low stand, thus forming a tectonically enhanced sequence boundary. In the southern part of the western Styrian Basin, close to the Pohorje Mountains (Figure 1-3), early Miocene sediments lacking a thermal overprint contain apatite grains showing a cooling age of approx. 19 Ma (Eggenburgian), only 1-2 Ma

older than the time of deposition (Sachsenhofer et al., 1998). The cooling rate of the Austroalpine source was very fast, pointing to tectonic denudation (Sachsenhofer et al., 1998).

The earliest Badenian (approx. 16 Ma) is characterised by shallow marine conditions. Fluvial sedimentation with debris flow sediments was restricted to the western margin of the basin, i.e. close to the eastern margin of the Koralpe ("Schwanberger Blockschutt", Winkler, 1926; Nebert, 1989). Synsedimentary normal faults indicating W-E extension have been documented by Friebe 1990 in the vicinity of the Southern Styrian Swell. A major sea-level drop at the end of Badenian times (approx. 13 Ma) caused the progradation of (braided-) delta deposits into the western part of the Styrian Basin, followed by a new phase of transgression during the Sarmatian (13-11.5 Ma). This marine influence prevailed up to the Early Pannonian (Sachsenhofer, 1996). Limnic and fluviatile sediments replaced this marine period, and from Late Pannonian times onwards, the terrestric sedimentary influence increased due to continuing uplift.

The early stage of subsidence in the Styrian Basin was accompanied by volcanism, which started in the Karpatian and lasted up to the early Badenian (Balogh et al., 1994; Reinecker, 2000).

Sedimentation in the Lavanttal Basin (Figure 2-4) started with fluvial sediments of the Karpatian, separated by the Styrian unconformity from the lacustrine to marine Lower Badenian Mühldorf Formation (Reischenbacher and Sachsenhofer, 2012). The isolated Basalt of Kollnitz in the Lavanttal Basin yielded a K/Ar age of 14.9 Ma (Lippolt et al., 1975). Separated by a erosional unconformity the Early Sarmatian follows with brackish and limnic sediments (Beck-Mannagetta, 1952), until the end of the Early Sarmatian. Thin freshwater sediments of the Upper Sarmatian follow above an erosion surface. Fluvial sediments of a probable Pannonian age were deposited above. Their different depositional environments mirror an increase in relief caused by tectonic activities (Reischenbacher and Sachsenhofer, 2012). Basin inversion follows. Reischenbacher and Sachsenhofer (2012) assign it to the Plio- to Pleistocene, which is characterised by terrestrial sediments (Figure 2-4).

To the north of the project area, the Fohnsdorf Basin (Figure 1-3, Figure 1-4) formed along the sinistral Mur-Mürz fault during the onset of lateral extrusion as an asymmetric pull-apart basin (Sachsenhofer et al., 2000). The sedimentary evolution (Figure 2-4) is subdivided in a pull-apart phase from Karpatian to early Late Badenian times and in a half-graben phase during Late Badenian times (Strauss et al., 2001).

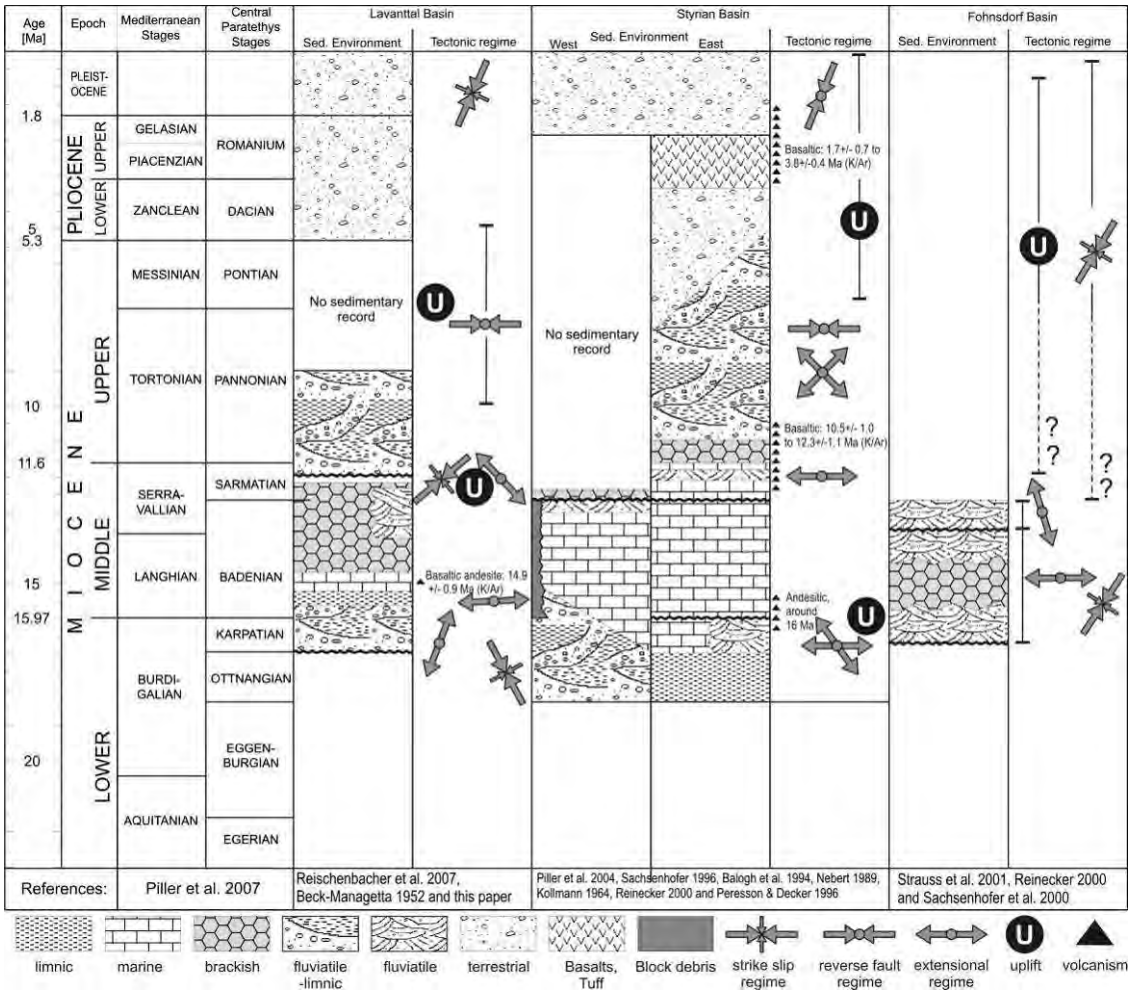

Figure 2-4: Comparison of the sedimentary evolution and tectonic regime for the Lavanttal, the Styrian and the Fohnsdorf Basin from the lower Miocene up to the Pleistocene. Grey filled arrows indicate orientation of paleostress tensors (West is left page margin and east is right page margin).

2.1.2.3 NEOTECTONICS AND PRESENT DAY STRESS FIELD

Neotectonic activity along the Lavanttal fault, the Mur-Mürz fault and the other major faults formed during Neogene extrusion is confirmed by geomorphology (e.g. Popotnig et al., 2007; Popotnig, 2009) and numerous recorded earthquakes (Reinecker and Lenhardt, 1999; Reinecker, 2000), especially in the vicinity of the Mur valley. Focal plane solutions show clear dextral sense of movement for the Lavanttal fault (Reinecker and Lenhardt, 1999). This is reflected in the data of the World Stress Map (Heidbach et al., 2009). For the Styrian Basin the World Stress Map contains only one datum from borehole breakouts with a NNW-SSE directed maximum horizontal compressional stress. No measurements from the Koralpe itself are contained. In situ stress measurements by hydraulic fracturing (Haimson, 1993; Fairhurst, 2003; Haimson and Cornet, 2003), the RACOS® method (Braun, 2003) and borehole breakouts (Fairhurst, 2003; Reinecker et al., 2003; Zoback et al., 2003; Tingay et al., 2008) from the site investigations of the Koralmtunnel yielded WNW-ESE to NNE-SSW directed maximum horizontal compressional stress (Goricki and

Harer, 2004; Übleis, 2007). Borehole breakouts were judged to yield the most consistent orientation of the maximum horizontal compressional stress (Figure 2-5).

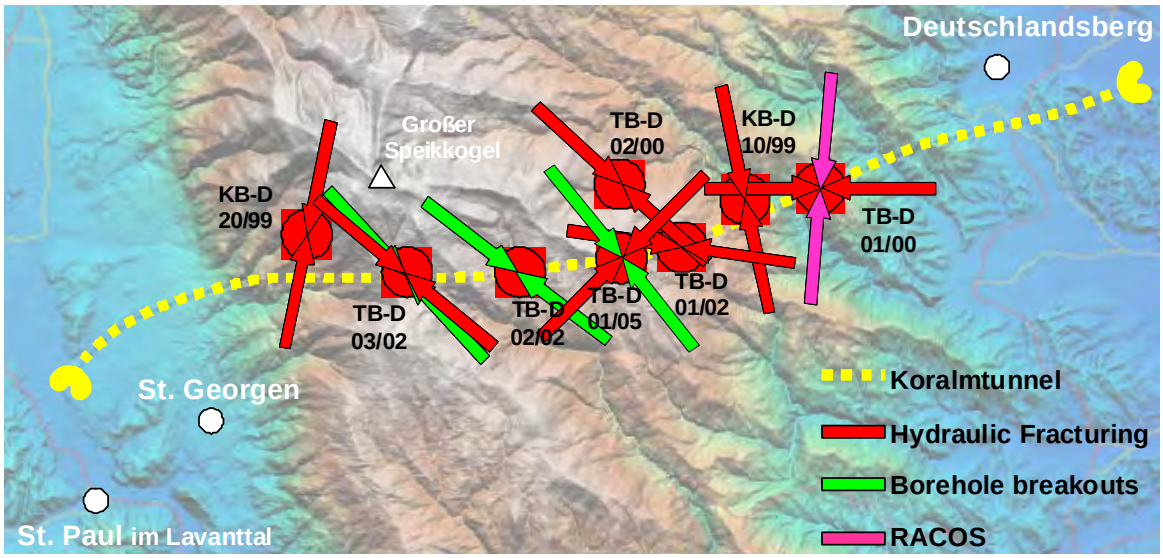

Figure 2-5: Orientation of the maximum horizontal compressional stress in the Koralpe as derived from hydraulic fracturing, borehole breakouts and RACOS method. Figure modified after Goricki and Harer (2004) and Übleis (2007).

The horizontal slip rate of the Lavanttal fault is, according to GPS measurements, around 1 mm/year (Vrabec et al., 2006). GPS measurements indicate an ongoing eastward horizontal displacement of the Miocene extrusion block east of the Tauern Window, bounded by the Periadriatic Lineament and the Salzach-Ennstal-Mariazell Puchberg fault, of approximately 1 to 1.3 mm/year (Vrabec et al., 2006; Caporali et al., 2008). This is confirmed by intra plate velocities (reference plate is the Eurasian plate) derived from permanent GPS stations (Haslinger et al., 2007). These measurements show ENE to E directed velocity vectors for the stations located in the Styrian and Vienna Basin. The vectors derived from stations in the vicinity of the Koralpe (Deutschlandsberg, Völkermarkt, Treibach/Althofen) are directed towards the north, except of Bad St. Leonhard with an ESE vector indicating a resumption of extrusion tectonics after the Pannonian to Pliocene stress field inversion (see chapter 3.3). GPS measurements showed a sudden change in horizontal velocity of 1.5 +/- 0.2 mm/yr within 20 km of an E-W profile from the Tauern Window to the Pannonian Basin (Caporali et al., 2009). The location of the drop in velocity coincides with the crossing of the Lavanttal fault and coincides with a pronounced rise of the Moho depth (Brückl et al., 2007). According to Caporali et al. (2009), the Lavanttal fault marks the change between dominant indentation kinematics to the West and dominant extrusion kinematics to the East.

Vertical movements in the Eastern Alps have been documented by repeated precise levellings (Reinecker, 2000; Székely et al., 2002). These measurements indicate slight subsidence for the area of the Koralpe if the reference point in the Bohemian massif is considered stable. However, geomorphological and sedimentological constraints from the Molasse indicate a slightly uplifting Bohemian massif (Székely et

al., 2002). Consequently the Koralpe would be neutral with respect to vertical movements. This is confirmed by vertical GPS velocities (Haslinger et al., 2007) too.

2.2 PREVIOUS WORK ON BRITTLE TECTONIC STRUCTURES IN THE PROJECT AREA

One of the oldest studies dealing with the brittle tectonics of the Koralpe is Stiny's (1925) work about jointing (Stiny uses the term "joint" in a non-genetic sense) in the area of the Teigitsch river. He parallels mapped "joint" directions with six main regional fault resp. lineament directions ("Baulinien"). Stiny relates the direction of the different segments of the Teigitsch to these faults resp. discontinuity systems. Additionally he described the presence of gravel layers (with Triassic limestone pebbles!) on levels far above the Styrian Basin and deduced a tectonic offset.

The presence of Neogene faults was already anticipated by Winkler (1926), who related the genesis of block debris to fault activity. Most of his work is linked to geomorphological and sedimentological questions.

The structure of the Koralpe and, for the first time, the Lavanttal Fault Zone are discussed by Kieslinger (1928a; 1928b). He mentioned important NE trending joints ("Nordostsprünge") which are partly widened to Pegmatite dikes. To his opinion the filled joints are older than "jungalpidisch" (Neo-Alpine), pointing out that some were reactivated later than the movement along the Lavanttal Fault Zone. Kieslinger also stated that the western slope of the Koralpe was uplifted during several tectonic events reaching up into present times. He called the southern margin of the Koralpe "Draugraben", characterized by a tectonic syncline, lowered by steeply dipping faults. Young horizontal displacements were mentioned for this area. For the eastern slope of the Koralpe, tectonic subsidence, compensated by series of faults, was concluded from geomorphological constraints. The polyphase tectonic evolution of the margins of the Koralpe was also emphasised.

The presence of Neogene faulting and its relation to the morphology of the Koralpe was discussed by Beck-Managetta (1948). He named SE-NW trending joints as the most frequent elements of young (Neogene), brittle tectonics ("Bruchtektonik"). A map depicts several faults ("Verwerfungen und Flexuren") at the eastern margin of the Koralpe trending SW-NE and N-S.

Metz (1976) divided the Lavanttal Fault Zone into a northern segment between the Fohnsdorf Basin and Twimberg and a southern segment south of Twimberg. He points out similarities to the "Görtschitztal" fault system further to the west (Figure 1-4).

From the 1970s onwards scientific studies about (brittle) fault zones were related primarily to infrastructure projects and to mapping projects (Kleinschmidt et al., 1989). Litscher (1978) described a large WNW-ESE striking, S dipping fault ("Jauksattel Störung"), which is offset (?) by a N-S striking, E dipping fault ("Kesselbach-Krumbach Störung") encountered during the site investigations for a dam in the

southern Koralpe. According to clay mineral analysis of Riedmüller & Schwaighofer (1978), these faults can be assigned to two different tectonic events (Litscher, 1978).

At the south-western slopes of the Koralpe, the Kleinschmidt group (1972-1985) mapped a pronounced fault pattern parallel to the Lavanttal fault with cataclasite, tectonic breccia and partly quartz dikes resp. veins (Sandau, 1981; Kleinschmidt et al., 1989). N-NNE to S-SSW striking faults with predominately downfaulted eastern block were mapped south of the village Soboth (Kleinschmidt and Ritter, 1976). W-E trending faults were only subordinately found.

Brosch (1983) presented structural data from the excavation of the Kalcherkogel tunnel in the northern Koralpe. He described three fold generations and a dense fault pattern. Normal faulting with N-S resp. WNW-ESE directed extension is the dominant brittle tectonic regime. WNW-ESE and N-S trending, steeply dipping, partly conjugated faults prevail. Foliation planes were frequently activated as faults, underlining the importance of rock anisotropy for brittle deformation. The morphology of the Kalcherkogel clearly reflects the fault pattern mapped on tunnel level. This is comparable to results from the Herzogbergtunnel (Figure 1-1 b).

Mähr (1990) investigated the microstructural evolution of cataclasites along two shear zones. Progressing cataclasis results in the formation of fault rocks with a high proportion of clay and clay minerals. Within the same research project, Koch (1990) analysed clay minerals in hydrothermally altered shear zones.

Neubauer (1991) distinguished three generations of undeformed extensional veins, postdating the last foliation in the Sau- and Koralpe. Vein minerals document a change from amphibolite to greenschist facies. The extension directions are WSW-ENE, W-E and NW-SE from the oldest to the youngest.

During the site investigation for the Koralm Tunnel extensive geological field mapping and consecutive core drilling campaigns were performed to improve the knowledge about the rock mass conditions, the fault zones and the hydrogeological conditions. Additionally, aerial photographies, satellite images (Landsat TM, Spot-Pan) and DEM data were analysed to detect lineament patterns and consecutive faults in the alignment corridor (Peresson and Decker, 1998). Brittle tectonic features and associated kinematic indicators were analysed in several boreholes (Brosch et al., 2001; Vanek et al., 2001; Egger, 2007; Übleis, 2007). All these data were used for route selection within the alignment corridor. Furthermore these data attributed to the geological model during further project stages (Steidl et al., 2001).

3 FAULT SLIP DATA ANALYSIS

3.1 DEFINITION OF TERMS AND METHODS

3.1.1 FAULTS AND FAULT ZONES

3.1.1.1 BRITTLE DEFORMATION

Brittle deformation in the upper crust (Sibson, 1977) is reflected in the presence of microfractures on the microscale up to large scale fault zones with the associated fault rocks. According to Sibson (1977), the transition from brittle deformation to ductile deformation takes place in a depth from 10 – 15 km at a temperature range from 250 to 350° C. It marks a zone where the influence of increasing temperature starts to prevail over the effect of increasing pressure (Suppe, 1985).

Different definitions can be found for the term “brittle deformation”. According to Suppe (1985), it is “defined as strongly pressure-dependent deformation involving an increase in volume as a result of cracking and it includes fracture and frictional sliding”. Mandl (2000) defines a macroscopic deformation process as “brittle” if it is rate – independent and strain softening in the post-peak region.

3.1.1.2 BRITTLE DEFORMATION – FRACTURE TYPES – FRACTURE MODES – FAULT TYPES

Fractures are defined by three basic characteristics: they have two parallel walls that meet at the fracture front, these walls are approximately planar and the relative displacement of originally adjacent points across the fracture is small compared to the overall fracture length (Pollard and Aydin, 1988). Two basic fracture types are generally distinguished: extension and shear fractures (e.g. Twiss and Moores, 2007). For extension fractures the opening displacements are perpendicular to the fracture walls (mode I). For shear fractures two end members are possible for fracture propagation: displacement perpendicular to the propagation front (“in-plane shear”, mode II) and displacement parallel to the propagation front (“out-of-plane shear, mode III, Pollard and Aydin, 1988).

Mandl (2000) defines four basic failure modes (Figure 3-1) based on the concept of the maximum differential stress. He distinguishes two types of tension fractures: The first forms under uniaxial extension (“tension joint”), the second under uniaxial compression with the fracture forming parallel to the direction of the maximum vertical effective stress (“joint”). Compressional shear fractures (“fault”) form under general compressional confining stresses. Dilatational shear fractures (“hybrid extension/shear fracture”) form under a compressional maximum shear stress and a negative (tensile) confining stress (oblique extension fracture sensu Twiss and Moores, 2007).

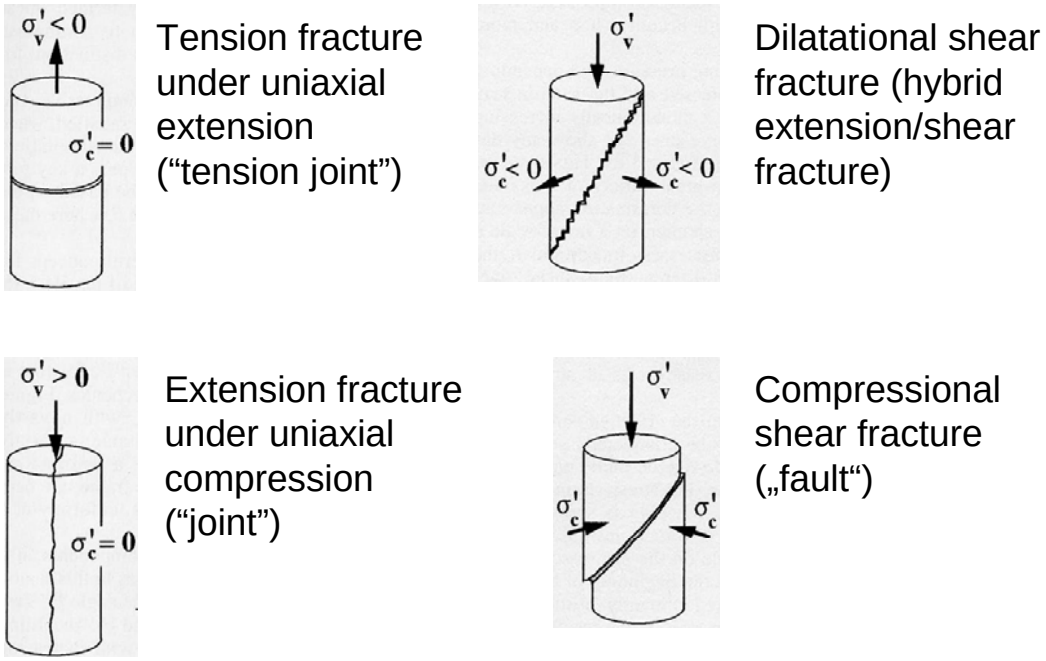

Figure 3-1: Basic failure modes (after Mandl, 2000; $\sigma_v^{'}$ …effective vertical stress, $\sigma_c^{'}$ …effective confining stress)

Pollard and Aydin (1988) suggested the use of the term "joint" only for those fractures where evidence for dominating mode I displacement can be deduced from field observations. Where such is missing the term "fracture" should be used.

The three basic types of faults (Figure 3-2), their geometry and their relation to the driving stresses have been described in the classic book of Anderson (1951). Normal faults show a relative downward displacement of the hanging wall with the maximum stress (σ_1) in a vertical orientation and a minimum horizontal stress (σ_3). The intermediate stress axis (σ_2) is horizontal and parallel to the fault plane. In the case of thrust or reverse faults σ_1 is horizontal and σ_3 is vertical resulting in an upward displacement of the hanging wall block. Strike slip faults are characterized horizontal displacements, σ_1 and σ_3 are horizontal.

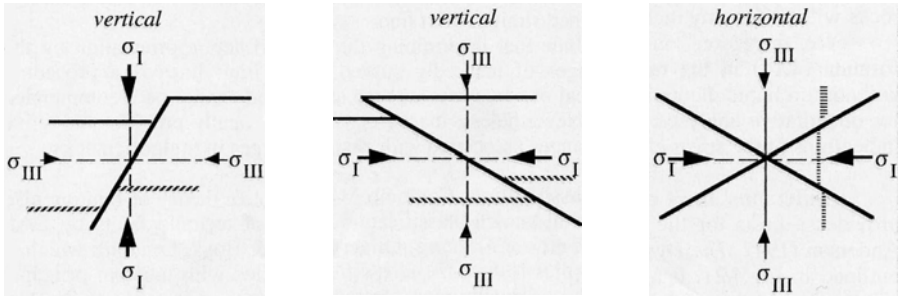

normal fault **thrust fault** **strike-slip fault**

Figure 3-2: The three basic fault types, their geometry and relation to the driving stresses as described by Anderson 1951 (after Mandl 2000).

3.1.1.3 FAULTS AND ASSOCIATED MORPHOLOGICAL FEATURES

Faults, especially recently active ones, often leave a pronounced imprint on the landscape. The associated geomorphological features are often clear indicators for the underlying faulting mechanisms. In the case of major normal faults we may expect pronounced fault scarps (Figure 3-3) in a stair case array, forming a basin margin fault (Peacock et al., 2000). The fault scarps are deeply incised by the drainage system. Perched terraces may be found along these valleys (Ramsay and Huber, 1987). Alluvial fans form at the mouth of these valleys in the “hanging wall” region. Areas of pronounced normal faulting may exhibit a typical array of morphological highs and lows called “horst and graben” structure (Peacock et al., 2000). Complex zones of transfer faults may interrupt the typical horst and graben morphology (Burbank and Anderson, 2003).

For faults with a predominating strike-slip component there may be no contrast in the elevation of the two adjacent fault blocks (Figure 3-4). Nevertheless, linear fault scarps are developed associated with linear valleys or troughs and shutter ridges. Rivers crossing an active strike-slip fault may be deflected or even beheaded by the lateral offset (Ramsay and Huber, 1987; Burbank and Anderson, 2001). Water may be trapped in depressions along the strike-slip faults and form sag ponds.

Figure 3-3: Fault scarp of a normal fault in the Awash Graben (Ethiopia). Note slope debris cover on the hanging wall side of the fault, sheltering the scarp against erosion (arrow indicates geologists for reference scale, picture courtesy of K. Klima).

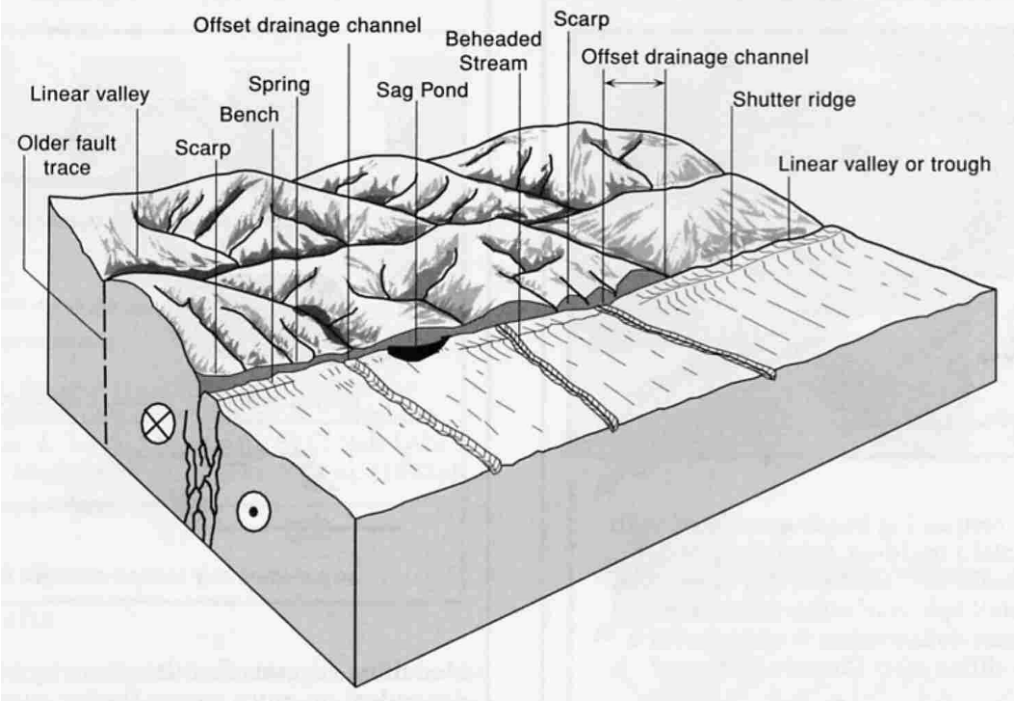

Figure 3-4: Morphological features associated with a strike slip fault (from Burbank and Anderson 2003)

Figure 3-5: Glarus thrust in Switzerland – the thrust is recognisable as a clear horizontal line separating darker rocks from light grey rocks. A simple sedimentary contact could produce a similar morphological expression (photo from http://earth.geology.yale.edu/~brandon/Misc/Glarus_thrust.JPG; Date of accession: 05-09-2009).

Active thrust faults may produce major linear fault scarps too, associated with the development of topography in the hanging wall. Mountain fronts along inactive thrusts may exhibit more irregular slopes than normal and strike-slip fault bounded mountain ranges (Ramsay and Huber, 1987). Active folding and thrusting may result in the deflection of streams (Burbank and Anderson, 2003). Erosion of low angle thrusts (often more or less parallel to sedimentary bedding or metamorphic foliation) may produce morphological expressions comparable to the ones produced by erosion of horizontally bedded rocks (Figure 3-5).

3.1.1.4 BRITTLE FAULT ROCKS – NOMENCLATURE

Faulting frequently produces a variety of associated rocks. Several nomenclatures for brittle fault rocks do exist in scientific literature (e.g. Sibson, 1977; Wise et al., 1984; Heitzmann, 1985; Schmid and Handy, 1991; Cladouhos, 1999b; e.g. Brodie et al., 2002; Twiss and Moores, 2007) resp. engineering geology (e.g. Brekke and Howard, 1973; Zhang et al., 1986; Riedmüller et al., 2001) but none has been finally agreed on (Twiss and Moores, 2007). Generally, the different classifications vary between non-genetic and genetic classifications (Schmid and Handy, 1991). Problems arise from the fact that fault rocks show a very wide range of appearance and transitions between different types of fault rocks are gradually, so all descriptions have their shortcomings. One example is the use of the words cohesive and incohesive. Clay rich fault rocks ("fault gouge") in its natural state exhibit a pronounced cohesion. But nearly always they are classified as incohesive fault rocks. Another example for the problems associated with fault rock classification is the use of foliation as a classifier. Fault gouge is often described to be unfoliated, hence field studies and laboratory experiments have shown that fault gouge can exhibit a distinct foliation (Chester et al., 1985).

Sibson (1977) discriminated different fault rock types based on four criteria: fabric (random fabric resp. foliated), cohesive-incohesive and proportion and nature of the matrix. Sibson generally labels brittle fault rocks as characterized by random fabric. Wise et al. (1984) name fault rocks "fault-related rocks" and classify them according to their rate of strain and their rate of recovery. The term "cataclasite" is used to subsume all non-foliated fault rocks related to brittle faults. Cataclasites are described to be non-foliated. Heitzmann (1985) described fault rocks as metamorphic rocks with a deformational fabric and establishes a descriptive classification. He distinguishes four main groups of fault rocks: Kakirite (≈ fault gouge), pseudotachylite, cataclasite and mylonite. The matrix proportion and the presence of fabric (foliation) are used as main classification criteria. The different fault rocks are related to the deformation mechanisms leading to their formation. Kakirites are described as soil like or incohesive rocks with a random fabric, which is inconsistent to the original definition (Mitchell, 1985). The other three fault rock types are labelled as "Festgesteine" (German for rocks exhibiting a pronounced strength / cohesion, coherent rocks). Cataclasites are described to exhibit generally a random fabric but may have foliation.

Following outcrop observations and the results of laboratory experiments Chester et al., 1985 Sibson's classification scheme from 1977 has been amended by with the term "foliated gouge" Scholz, 1990.

Schmid and Handy (1991) propose a classification based on the deformation mechanisms, the rate of recovery, and the strain rate. Fault rocks resulting from brittle deformation are here generally termed "cataclastic fault rocks". They are subdivided on the one hand into fault breccia and fault gouge and on the other hand into cataclasite. Cataclastic flow (Passchier and Trouw, 1996) is the main deformation mechanism for these rocks. In cataclasites, dislocation glide and/or solution-precipitation may locally contribute to the strain. Cataclasites are described to be cohesive and sometimes foliated. Contrarily to this, fault breccia and fault gouge are described as cohesionless and unfoliated. The terms cohesive and cohesionless are used here to describe their cohesiveness during faulting, hence post-tectonic cementation may be present in fault breccias and fault gouge outcrops. All cataclastic fault rocks show a reduced grain size.

Twiss and Moores (2007) proposed a classification scheme, which includes the clast size and the matrix. Brittle fault rocks are subsumed under the term "cataclastic rocks". Four main categories are used: the breccia series (megabreccia, breccia and microbreccia), gouge, cataclasite and pseudotachylite. According to Twiss and Moores (2007), cataclastic rocks usually lack internal planar and linear structures.

A classification scheme of fault rocks is given by Meschede (1994) which is based on the classifications of Wise et al. (1984) and Heitzmann (1985). Here, fault rocks are generally termed "rocks with deformational fabrics". Brittle fault rocks are divided into kakirite, cataclasite and pseudotachylite. Following Heitzmann (1985) the term kakirite is used to subsume tectonic breccias, crush breccias and flour-like fault rocks formed under an extremely brittle regime. Cataclasites are again described as fault rocks with a random, often "chaotic" fabric. Only in cataclasites with a matrix proportion >90% (ultracataclasite), a parallel texture may be developed by cataclastic flow. Fabric, clast/matrix proportion, manifestation of faults (brittle/ductile) and the genetic processes involved are used to classify the different fault rock types.

The IUGS subcommission on the systematics of metamorphic rocks a proposed a nomenclature of structural terms and fault rock terms (Brodie et al., 2002; 2007). This proposal includes a subdivision into cohesive and incohesive fault rocks (Figure 3-6). Incohesive fault rocks are further subdivided into clay-rich and clay-poor cataclasites, where foliation may be used for a further subdivision of the incohesive fault rocks.

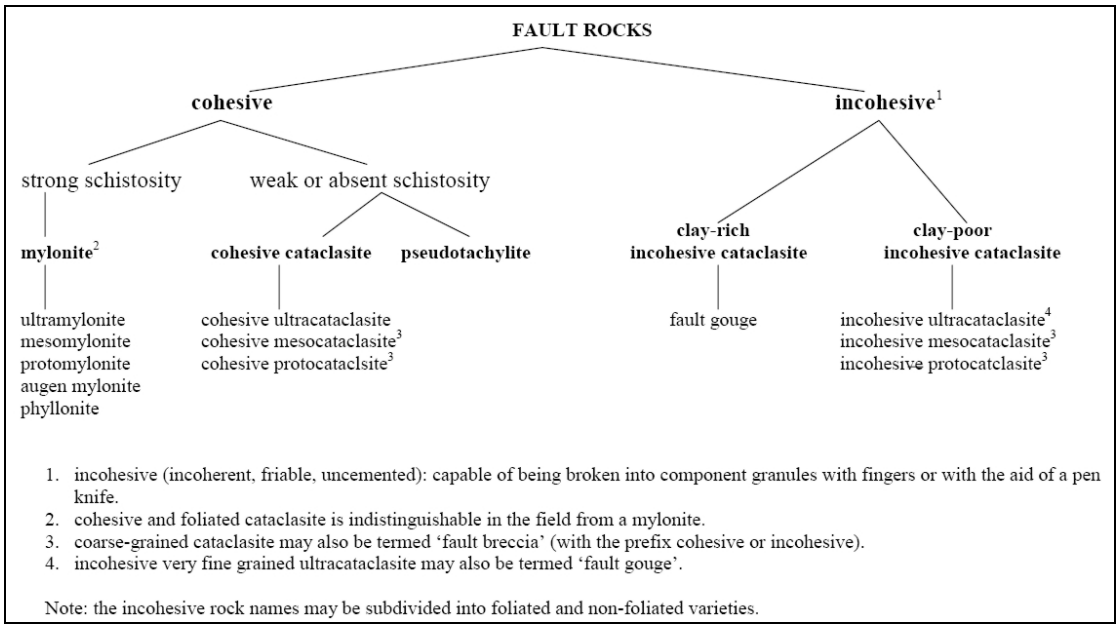

Figure 3-6: Fault rock classification scheme, proposed by the IUGS Subcommission on the Systematics of Metamorphic rocks Brodie et al., 2002.

Several engineering geological classifications have been brought forward in addition to the classifications described above. In the following the ones by Brekke and Howard (1973), Zhang et al. (1986), Riedmüller et al. (2001) and Bürgi et al. (2001) are discussed. As a main difference to the classifications described at the beginning of this chapter, these classifications mostly lack the genetic context resp. the tendency to integrate the genetic aspects.

Brekke and Howard (1973) established a "tentative classification for fault gouge material", linked to the potential behaviour of fault gouge material in underground excavations. Five categories were distinguished based on the dominant material in the gouge:

- Swelling clay
- Inactive clay
- Chlorite, talc, graphite, serpentine
- Crushed rock fragments or sand like gouge
- Porous or flaky calcite, gypsum

Zhang et al. (1986) reviewed existing nomenclature schemes and postulate three principles for an engineering geological classification of fault rocks:

- It should be based on the petrological classification of fault rocks.

- The engineering geological properties of fault rocks, the similarity of engineering geological properties must be taken as the criterion for the classification of fault rocks.

- The classification should be simple, clear and convenient to use. The signs for classification should therefore enable a distinction of the different fault rock types in the field.

Consequently, Zhang et al. (1986) developed a classification based on the degree of consolidation and the grading composition.

Riedmüller et al. (2001) proposed an engineering geological classification scheme for cataclastic rocks, based on experiences from geotechnical projects and on the research work of Medley (1994), Lindquist and Goodman (1994), Lindquist (1994a) and Wakabayashi and Medley (2004). This classification scheme distinguishes primarily between cohesion-less (soil like material) and cohesive cataclastic rocks (Figure 3-7). Cohesion-less cataclasites are classified according to the proportion of blocks resp. matrix. If the block proportion is lower than 25% the particle size of the matrix becomes the main classification parameter. The differentiation of the matrix follows the procedures defined in soil mechanics (unified soil classification system, American Society for Testing and Materials). Cohesive cataclasites are classified according to their type of cement, as the degree of cementation and the type of cementation are thought to be geotechnically more relevant than the size of clasts.

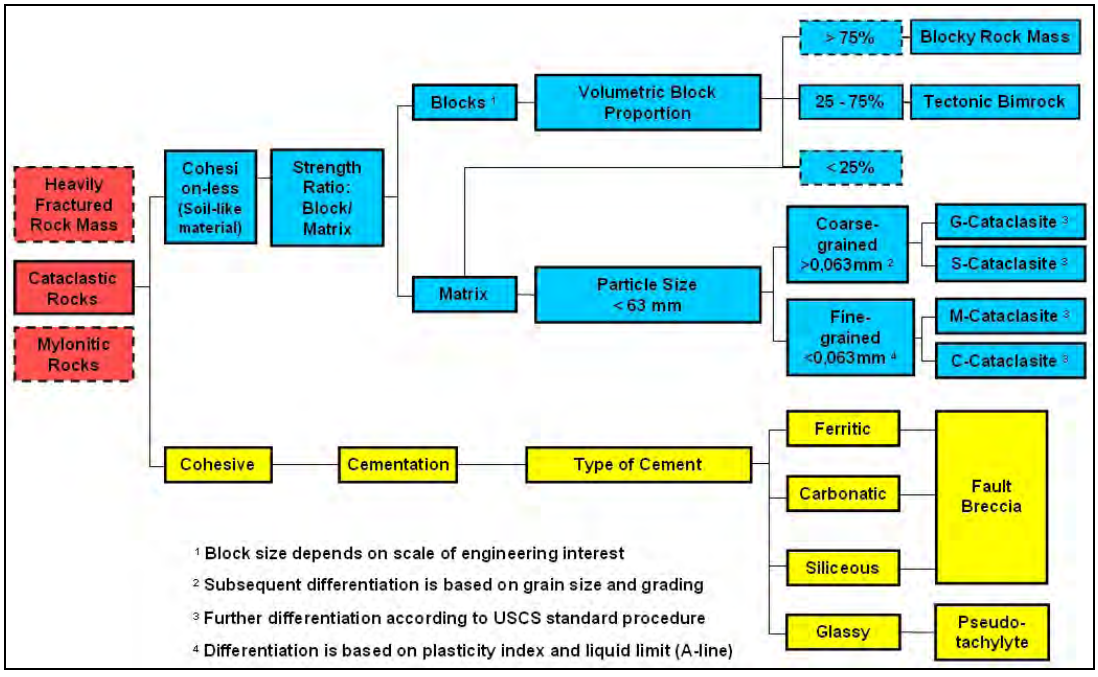

Figure 3-7: Engineering geological classification of cataclastic rocks (fault rocks) Riedmüller et al., 2001.

Bürgi et al. (2001) introduced a new quantitative method to characterize weak cataclastic rocks. Characterization is based on the mineralogical composition and the rock fabric (clast and discontinuity properties). The mineralogical composition is

determined by X-ray diffraction and the mean weighted Vickers hardness is determined as well. The rock fabric is characterised by the texture coefficient TC (Howarth and Rowlands, 1986) and a newly developed matrix coefficient MC. The matrix coefficient is a discontinuity parameter including the linear roughness of discontinuities, the mean trace length, the trace line density and an orientation factor. The proposed combination of these indices is called “mineralogical and structural index” (MSI). A regression analysis showed a significant correlation of the MSI to the mechanical properties of the analysed samples. The authors emphasize that their method is still conceptual and propose a use parallel to the geological strength index (GSI) for very weak and sheared rock masses (Hoek et al., 1998). The research work was performed on a restricted range of scales (drill cores, thin sections).

For the present study the nomenclature of Brodie et al (2002, 2007) was used.

3.1.2 FAULT SLIP DATA ANALYSIS

Fault slip data analysis attempts to deduce kinematic (strain related) or dynamic (stress related) data from fault plane orientations and their associated slip vectors (Blenkinsop, 2006). Fault slip analysis methods have been source for debates about their validity and their interpretation (Pollard et al., 1993; Twiss and Unruh, 1998; Gapais et al., 2000). Blenkinsop (2006) summarized the major problems associated with fault slip analysis: Fault slip data resulting from different tectonic events may be difficult or even impossible to separate. Faults may be reoriented or rotated during a single or successive deformation phases. Distribution of stress, strain and strain rate tensors may vary during a single deformation event. Several methods anticipate that slip occurs in the direction of maximum resolved shear stress (e.g. Angelier, 1994) assuming that the Wallace-Bott Hypothesis (Wallace, 1951; Bott, 1959) is valid. This may not be true in all cases. (Nieto-Samaniego and Alaniz-Alvarez, 1997). Finally it is debatable whether the kinematic or the dynamic approach should be used for fault slip analysis. Twiss and Unruh (1998) pointed out, that on a local scale fault-slip data define the local principal strain axes and not the local principal stress axes. On a large scale P and T axis maxima do not provide accurate solutions for strain rate or stress. However Blenkinsop (2006) showed in an analysis of fault slip data from the spectacular 100 km long rupture of the 1999 Chi-Chi earthquake along the Chelongpu fault (Taiwan) that both kinematic and dynamic analysis yielded results compatible to seismological and GPS data. Results from both methods showed regional variations which can be related to slip vector rotation and stress field pattern variations. Regular field mapping mostly does not show such spectacular phenomena and one is rarely being confronted with fault slip data readily measurable along a major fault zone. Fortunately, data from small scale fault planes yield considerable coincidence with bounding master faults regarding the orientation of the horizontal stress axes (Ghisetti, 2000). Ghisetti (2000) additionally notes that in her Californian working area small faults only rarely show the same orientations and mechanisms as the adjacent master faults. Thus, fault slip analysis can yield valuable information, but only if the uncertainties associated with data mapping and analysis are taken into account.

Nowadays, mapping of fault slip data is regarded as a standard technique in structural geology (Angelier, 1994; Goldsworthy and Jackson, 2001; Liu-Zeng et al., 2006; Lopes Cardozo and Behrmann, 2006; Orife and Lisle, 2006), despite all problems associated with it. It is not yet a standard technique in engineering geological field work (Brosch et al., 2001), despite the benefits it can have on the assessment of the tectonic situation of a site.

In the following chapters the methods used in fault data collection and analysis are outlined.

3.1.2.1 KINEMATIC INDICATORS

The kinematics of a fault is characterized by the orientation of the fault plane, the orientation of the slip direction and the sense of slip (Marrett and Allmendinger, 1990). Kinematic indicators allow a determination of the sense of shear of a fault. Classic indicators are the offset of marker horizons and the presence of drag folds (Angelier, 1994; Grasemann et al., 2003; 2005). Indicators related to a fault plane may be classified into indicators linked to secondary fractures and shear-sense structures not linked to secondary fractures (Petit, 1987). A more detailed classification into eleven groups of kinematic indicators is given by Doblas (1998).

- SECONDARY FRACTURE ELEMENTS

Secondary fractures develop frequently along fault planes or in shear zones respectively (Logan et al., 1979; Petit, 1987; Meschede, 1994; Doblas, 1998; Friedman et al., 1998). Following Logan et al. (1979) four fracture types are associated to a fault plane (Y-shear) or a shear zone in experimental fault gouges (Figure 3-8).The experiments by Logan et al. (1979) indicate that the so called “Riedel” fractures (R_1 and R_2) are the first to develop in the course of ongoing deformation. R_1 and R_2 may be explained as conjugated shear fractures (“Coulomb fractures”) with R_1 oriented in an acute (α in Figure 3-8) and R_2 in an obtuse angle to the Y shear. The experiments described yielded 12° to 18° as a mean value of α and 50° to 57° for β. These values may be used as a help for classification, but may show in nature a wide range of values (Mandl, 2000). P shears are synthetic secondary fractures of reverse faulting type with respect to the Y-shear. T-features are tensile fractures indicating the direction of the maximum stress axis σ_1. X-shears have first been described by Logan et al. (1979) and represent antithetic fractures with normal fault character with respect to the Y-shear. A detailed review and suggestions for classification of secondary fracture indicators can be found e.g. in Doblas (1998) and Petit (1987).

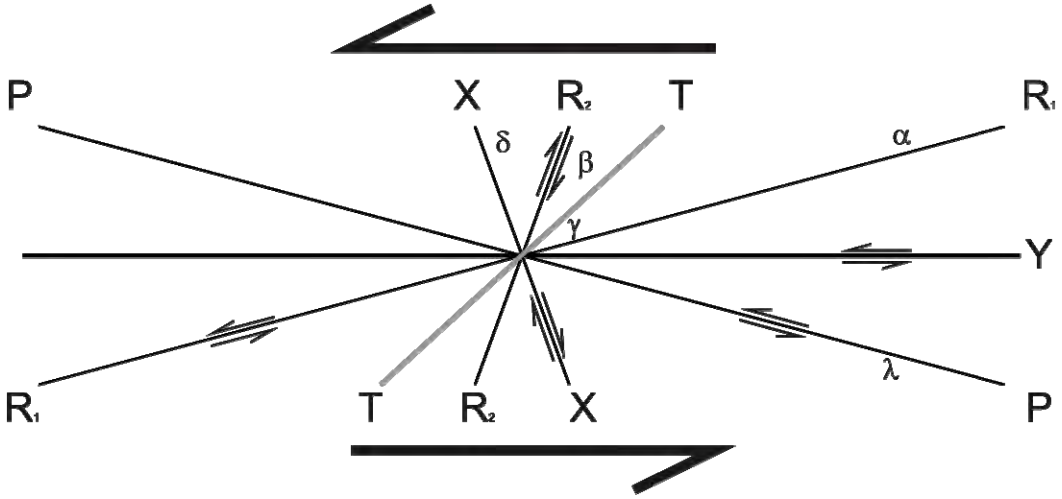

Figure 3-8: Fracture pattern and terminology as described for experimental shear zones after Logan et al. 1979.

- KINEMATIC INDICATORS NOT LINKED TO SECONDARY FRACTURES

This group includes prominent indicators like mineral fibres (frequently calcite, quartz or chlorite) along steps in the shear plane (Petit, 1987; Angelier, 1994; Doblas, 1998). Mineral fibres are abundantly found in marble or limestone or in the vicinity of these rocks and form most times very clear kinematic markers (Figure 3-9). Stylolitic peaks (called slickolites if the peaks are oblique to the surface) resulting from pressure solution processes (Angelier, 1994; Meschede, 1994) form another classic indicator. In the working area they are restricted to some marble quarries (Figure 3-10).

More frequently encountered are step-like asperities without crystal growth fibres (Figure 3-11), alternating polished (striated) and rough facets (Angelier, 1994).

Another classic kinematic indicator is the offset of marker horizons, yet it may be misleading as it only yields the sense and amount of displacement in the section of observation. The measurement of a striation on the respective fault plane may help to resolve the sense of shear of the fault. Caution has to be taken in the case of repetitive markers, especially in combination with a limited exposure size.

If a marker element is offset, other types of kinematic indicators may develop additionally or prior to the offset. These features may be summarized as flanking structures (Passchier, 2001). Drag folds are one example for flanking structures. Fault drag may be subdivided into normal drag and reverse drag (Grasemann et al., 2005). Normal drag results in the formation of markers that are bent convexly into the direction of shear, whereas reverse drag produces markers that are concave in the direction of shear (Figure 3-22 b). Grasemann et al. (2005) showed that whether normal or reverse drag develops is mainly controlled by the angle between the marker and the fault, with high angles favouring reverse drag.

Figure 3-9: Calcite fibres on fault plane in a marble quarry near Twimberg (Carinthia) with a sinistral sense of shear (missing block downwards to the right), orientation of plane is 278/84 with striation 194/45. For location refer to Figure 3-17 a, outcrop ID is 175.

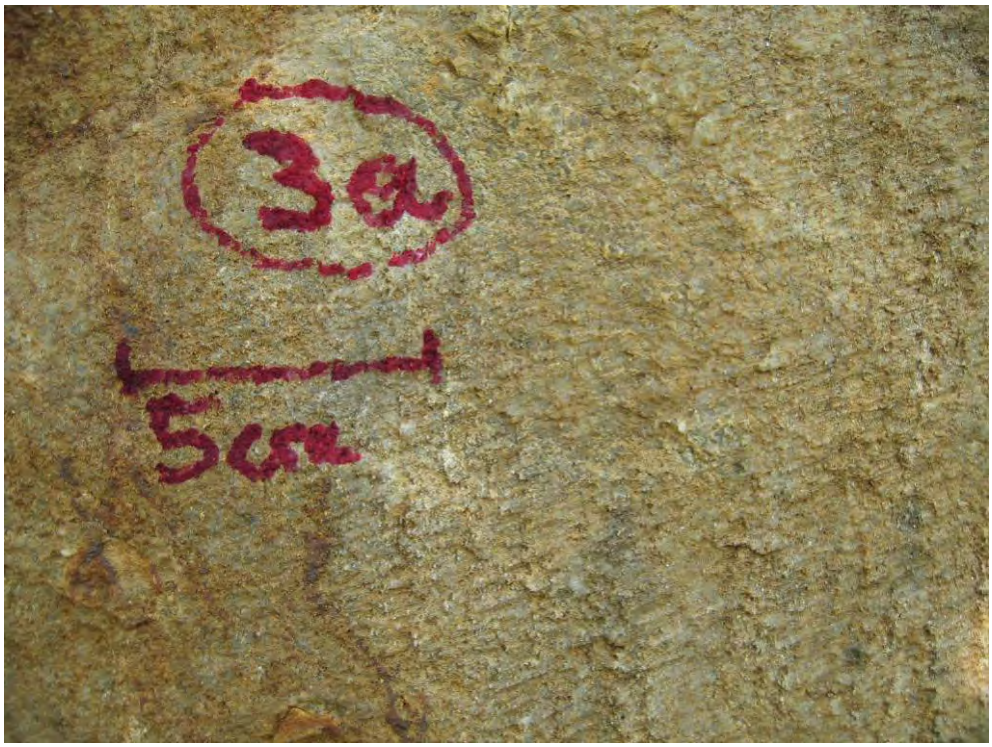

Figure 3-10: Oblique stylolites ("slickolite") in a marble quarry south of the Wildbach (Styria). Orientation of plane is 308/89, slickolite orientation is 198/04, indicating a SSW-NNE oriented maximum stress axis. For location refer to Figure 3-17 a, outcrop ID is 186.

Figure 3-11: Hanging wall of a stepped slickenside in mica schist with normal fault kinematics. Orientation of plane is200/86 with striation 206/84, location is Brandgraben near Weinebene. For location refer to Figure 3-17 c, outcrop ID is 8.

3.1.2.2 KINEMATIC INDICATORS IN BRITTLE SHEAR ZONES

Abundant kinematic indicators in brittle shear zones are secondary fractures as described in chapter 3.1.2.1 and in Figure 3-8 (Logan et al., 1979; Friedman et al., 1998). The most frequent secondary fractures found in shear zones are Riedel (R_1) fractures oriented in an acute angle to the boundaries and shears parallel to the boundaries of the zone (Y-shear). Both exhibit the same sense of shear as the shear zone. These repetitive features are summarized as shear band fabric (Chester and Logan, 1998). As they are frequently offsetting other fabric elements they are regarded as reliable kinematic indicators (Chester and Logan, 1987). Riedel shears may exhibit a sigmoidal shape in sections parallel to the shear direction () due to rotation during progressive deformation (Hoogerduijn Strating and Vissers, 1998).

A feature frequently described for clay gouges is a foliation fabric (Chester et al., 1985; Rutter et al., 1986; Chester and Logan, 1987), often sigmoidal and comparable to SC fabric in natural mylonites (Lister and Snoke, 1984). This foliation is marked by a preferred alignment of phyllosilicates (Rutter et al., 1986) dipping into the opposite direction as the R_1 fractures. In the case of metamorphic rocks the pre-existing foliation is often preserved within shear zones and activated as shear planes.

As both foliation and Riedel shears may exhibit a sigmoidal shape a differentiation between them may not be possible without the presence of other shear sense indicators (especially in the outcrop).

Pre-existing fabrics like foliation or bedding may be subjected to drag folding within the shear zone.

3.1.3 PALEO STRESS CALCULATION METHODS

Fault plane – striation pairs may be used to determine the orientation of the three principal stress axes that lead to the observed shear fracture pattern. The methods are based on the fundamentals of fracture mechanics and some basic assumptions and simplifications Meschede, 1994). In this work the graphical P/T method (Turner, 1953), the Right Dihedra method (Angelier and Mechler, 1977) as well as the Numerical Direct Inversion method (NDA, Angelier and Goguel, 1979) were used and are briefly described below.

Figure 3-12: SE dipping shear zone with sigmoidal Riedel (R_1) shears in the eastern Koralpe (Outcrop ID is 84, for location refer to Figure 3-20 c). Schmidt net shows shear planes mapped in this outcrop.

3.1.3.1 PT-METHOD

The P-T method (Turner, 1953) is a graphical, stereo net based method to determine the theoretical compression axis (P), extension axis (T) and intermediate axis (I) for each fault plane – striation pair (Figure 3-13). This method assumes that all analysed fractures develop independently from each other under homogenous deformation conditions in an isotropic medium (Meschede, 1994).

Calculation parameters are the azimuth and dip angle of a fault plane, the respective azimuth and plunge of the striation, shear sense. The quality of the shear sense determination was recorded for each data set during field mapping. Data sets with a

low quality were only used for the analysis if they seem plausible in the context of the high quality data. Bivalent data sets (sets with unknown sense of shear) are not used. Additionally the material specific empirical angle of friction α (angle between compression axis and fault plane) has to be known or estimated for the given rock type. In this work α was assumed to range between 30 to 40°. The resultant orientations of an analysed fault plane data set are used to calculate the mean kinematic axes by means of directional statistics (Wallbrecher, 1986; Meschede, 1994).

The P-T calculations were performed with the Tectonics FP program (Reiter and Acs, 1996-2007). Data sets were checked for erroneous data and separated into sets with consistent kinematics if necessary. Separation was most times performed in the field or was based on the field mapping results. If a separation based on field mapping was not possible, separation was performed according to the kinematic consistency of the data set.

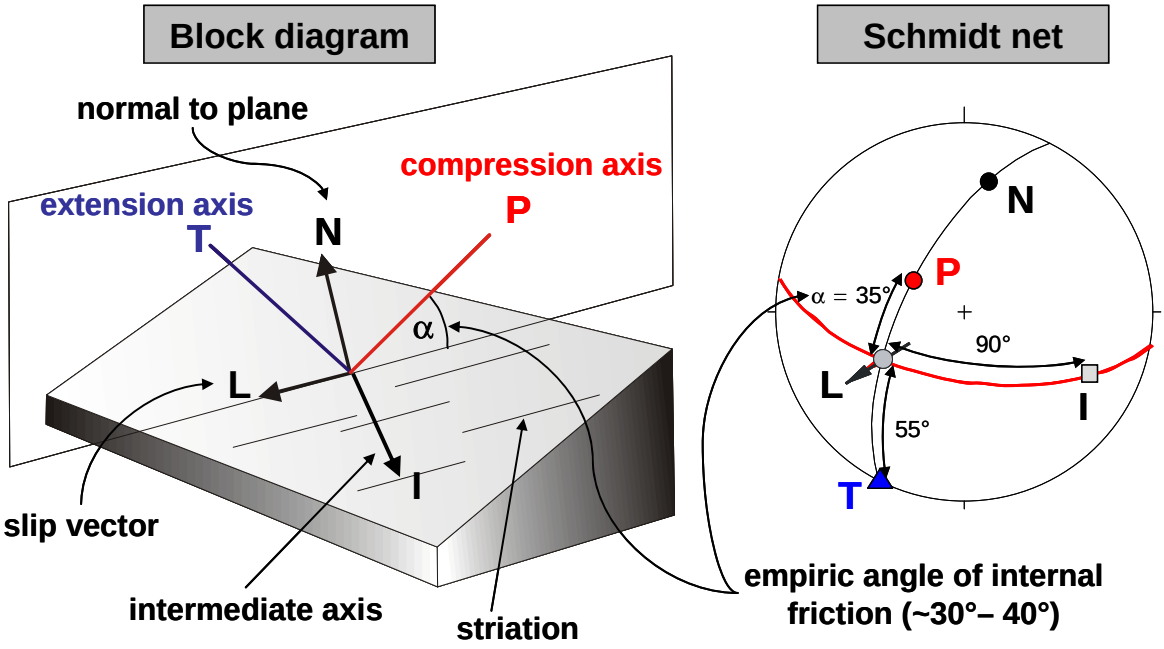

Figure 3-13: Schematic block diagram (after Meschede (1994)) and the respective Schmid net (Lambert projection). The P/T method uses the concept of theoretical compression (P) and extension (T) axes for a fault plane with striation.

3.1.3.2 RIGHT DIHEDRA METHOD

The Right Dihedra method (Angelier and Mechler, 1977) uses a similar graphical method as used in seismology for focal mechanism analysis (Angelier, 1994), here called the fault focal plane mechanism (Figure 3-14b). The method relies on the principle to distinguish between a compressional and an extensional dihedron for a given fault – striation - shear sense datum with the help of an auxiliary plane perpendicular to the fault plane and the striation (Figure 3-14a). The maximum stress

axis σ_1 is to be found in the compressional, the minimum stress axis σ_3 in the extensional dihedron. If we determine these dihedrons for each datum of our data set we are able to isolate the areas were σ_1 and σ_3 are located (Figure 3-15). This method implies that all faults of a data set formed in the same stress regime and the acceptance of the extended Wallace-Bott (Wallace, 1951; Bott, 1959) hypothesis (Angelier, 1994). To approximate the stress axes orientation this method necessitates data sets with a certain variation in the orientation of the fault planes and their striations to confine the remaining residual area. A high scatter in the input data may result in an uniform distribution of the resulting probability numbers, indicating either the presence of two or more fault populations in the data set, or rotational deformation within a shear zone or local variations of the stress field Meschede, 1994.

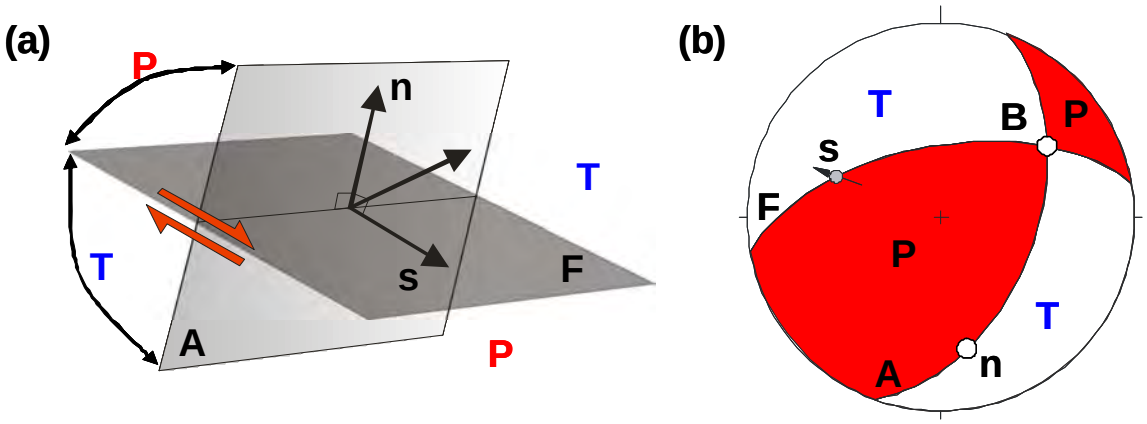

Figure 3-14: Right Dihedra Method (after Angelier, 1994): (a) Schematic diagram and (b) the fault focal plane mechanism for a sinistral normal fault. (F…fault plane; A…auxiliary plane; n…normal to fault plane; S…unit slip vector in (a), sinistral slickenside lineation in (b); B…intersection of planes A and F; P…compressional dihedron; T…extensional dihedron.).

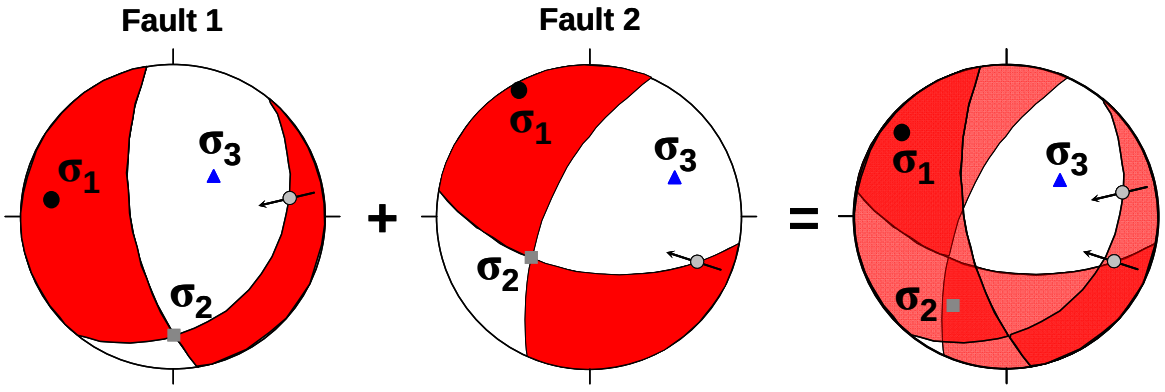

Figure 3-15: Right Dihedra Method: Successive overlay of fault focal plane mechanisms narrows the possible location for the principle stress axes (after Meschede, 1994).

3.1.3.3 DIRECT INVERSION METHOD

The Direct Inversion Method (Angelier and Goguel, 1979) is a mathematical method to determine the stress tensor ("inverse problem", Angelier, 1994) for a given fault set with known sense of slip. It uses a least-square criterion to minimize the deviation of the calculated shear stress direction from the direction of a measured fault striation (Meschede, 1994). This methods yields the stress tensor with the three principal stress axes and the ratio of the stress differences R (Meschede, 1994). The calculations were performed with the Tectonics FP program (Reiter and Acs, 1996-2007) which uses a solution of Sperner et al. (1993). The program substitutes bivalent shear sense with a reverse shear sense, which may result in a flip of σ_1 and σ_3 if too many bivalent data sets are used. A histogram showing the deviation of the measured striation from the calculated orientation of the maximum shear stress is used to assess the fluctuation of the data. Dimensionless Mohr circle diagrams allow an additional control of the calculation results. A regular distribution of the data points is interpreted as a good result. Prevailing low shear stress values indicate a data set dominated by one data set (Meschede, 1994), for which the method should not be used.

3.2 RESULTS - BRITTLE STRUCTURES AND THEIR INTERPRETATION

Morphologically the eastern slope of the Koralpe is characterised by valleys of two main orientations, either trending N-S or WNW-ESE; the widest of the latter contains the Schwanberg block debris (Figure 1-4; Winkler, 1926). These morphological features coincide with two main sets of brittle structures, in particular fault zones and slickensides. Therefore it is assumed that the course of most valleys is structurally controlled, a feature already noted by Stiny (1925) for the northern Koralpe. The main faults, together with conjugated secondary fractures, were repeatedly activated during distinct deformational phases.

Two sets of map-scale faults can be distinguished; their strike directions range from E to SE and N to NE, respectively (Figure 1-4). In general, the E- trending ones are partly covered by block debris, crosscut and displaced by NNE-trending faults (Figure 1-4). The contact of the Koralpe with the Miocene sediments of the Western Styrian Basin is badly exposed, as are assumed normal fault zones forming the eastern margin of the Koralpe.

The contact of the metamorphic rocks with the covering sediments was temporally exposed during the excavation of the Koralm pilot tunnel. At this location the eastern margin of the Koralpe is formed by an approx. 1 m thick cataclastic shear zone with normal fault kinematics (Figure 3-16). The amount of displacement was not exposed. The shear zone comprises fine-grained cohesive cataclasites (sensu Brodie et al., 2007) with a fragment size of approximately 0.5 to 5 cm; the fragments are embedded within a matrix with predominating grain sizes of 0.2 to 0.5 mm (Figure 3-16). A highly fractured damage zone with highly variable thickness (several decimetres to several meters), partly grading into a block-in-matrix rock (sensu Medley, 1994), characterises the footwall. In the hanging wall the shear zone is covered by slightly

compacted cross-bedded, undeformed sands of probable Late Karpatian to Early Badenian age (Nebert, 1989; Beck-Mannagetta et al., 1991).

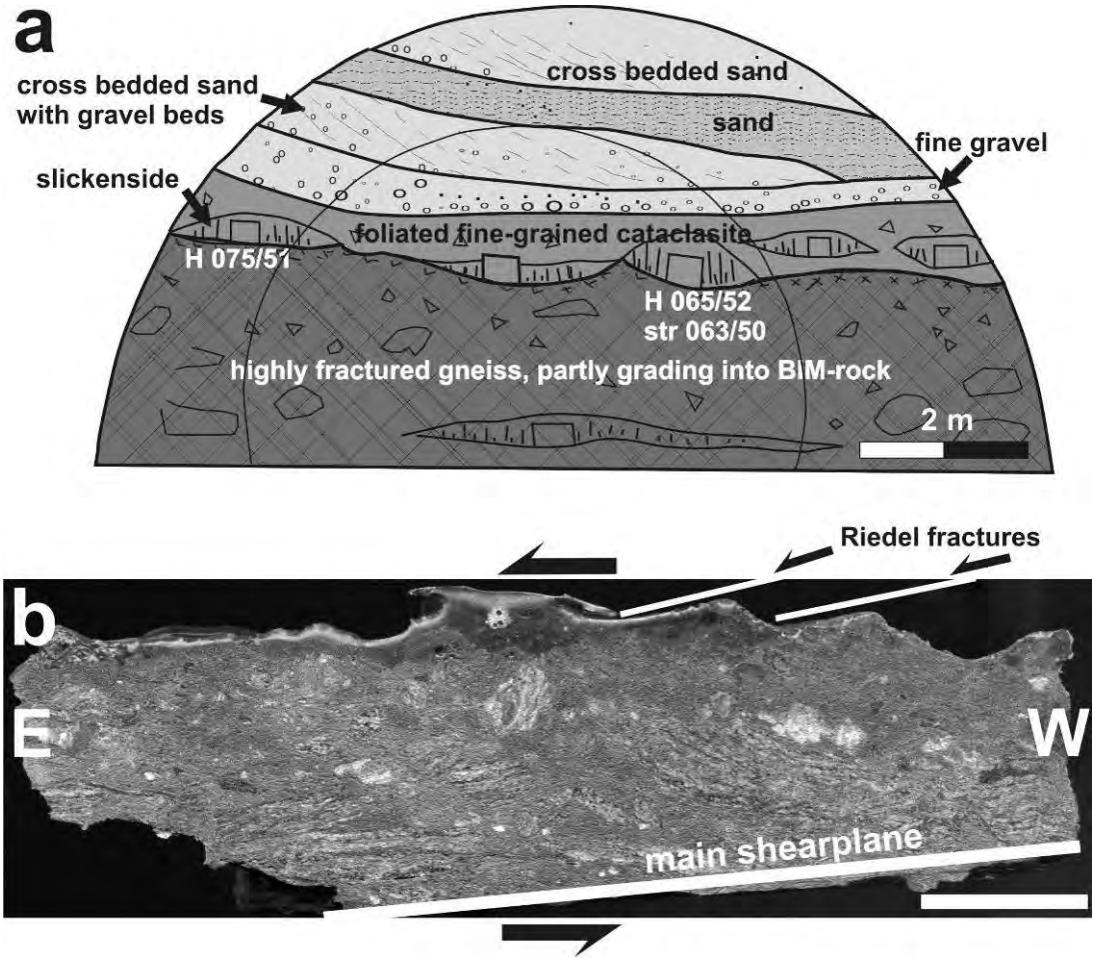

Figure 3-16: a - Contact between a cataclastic shear zone and slightly compacted, but undeformed Badenian (?) sand along the eastern margin of the Koralpe, as exposed within the pilot tunnel "Leibenfeld" at station 130m (view is towards east, approx. 12 m wide and 5.5 m high); the cataclastic shear zone rock in the footwall of the sediments is dipping to the east, slickenside striae are plunging subparallel to the fault dip (normal sense of shear); H: slickensided fault plane, str: striation, BIM-rock: Block-in-matrix rock (refer to text for nomenclature). b – Polished section of a hand specimen of the cataclasite with gravel-sized, angular to slightly rounded fragments of gneiss in a fine-grained, foliated matrix, Riedel fractures support top to east sense of shear. Main shear plane is the same as slickenside in Figure 4a. (Scale bar in the lower right is 3 cm long)

At the scale of a few decimetres to meters, the sequence of displacements along distinct faults can be derived from crosscutting relationships both in outcrops and drill cores. However, these relationships are restricted to a few key outcrops that provide the basis for the structural analysis at sites with incomplete information about the relative deformation sequence. This sequence comprises four major events of brittle deformation, referred to as D1 to D4. The coordinates of outcrop locations with

detailed data on the orientation of the evaluated principal stress axes are summarised in Table 13 (Appendix).

D1 can be subdivided into two sub-phases. D1-1 related structures are restricted to distinct domains. Locally, E to ESE striking sub-vertical fractures were activated as dextral strike-slip faults. These are associated with conjugate N to NW- trending dextral, and NNE- trending sinistral strike-slip faults (Figure 3-17 a, b). A detailed analysis shows that either ESE and N- trending, or (N)NW and NNE- trending faults occur as conjugate fracture sets. Locally, NW- trending fractures with dextral displacement occur as single sets. The complete assemblage can be geometrically interpreted to represent ESE- trending Y (main)-, E- trending P-, (N)NW- trending R- (Riedel), and NNE-trending R'- fractures. The results from the analysis of paleostress orientations show a sub-horizontal NNW-SSE orientation of σ1 and a sub-horizontal orientation of σ3 in ENE-WSW- direction (Figure 3-17 a, b). Major D1-1- related, ESE-trending faults form the tectonic basis for the consecutive deposition of the Schwanberg block debris, mainly consisting of components derived from the adjacent basement. These deposits have already been described by Winkler (1926), who postulated already a connection to fault activity. According to Nebert (1989), sedimentation of these deposits started during the Late Karpatian / Early Badenian (Figure 2-4). In general, the base of the block debris is formed by highly disintegrated host rock, often accompanied by tectonic breccias and cataclasites. The basement protoliths (mainly garnet mica-schist and schistose garnet-bearing gneiss) show severe alteration and deformational overprint of the penetrative fabrics along distinct semi-ductile shear zones. The basement protolith is intensely retrogressed; biotite is mainly replaced by stilpnomelane, plagioclase is mainly replaced by epidote-zoisite and calcite (Egger, 2007). Besides the alteration, veins and cracks filled by calcite and subordinate quartz, white mica, and zeolite indicates the presence of hydrothermal fluids during faulting. The thickness of the deposits was acquired by both reflexion seismology and several drillings penetrating the contact between the block debris and the underlying basement during the site investigations for the Koralm Tunnel. Sediment thickness amounts to approximately 180 meters in the central part, and decreases to 80 meters towards the margins of the Schwanberg block debris basin. The sedimentary base of the deposits is at an altitude of approximately 600 meters in the central parts, and approximately 700 meters close to the margins of the block debris basin. Hence the base of the debris is situated 300 to 400 meters higher than the present top of the western part of the Styrian Basin (Egger, 2007).

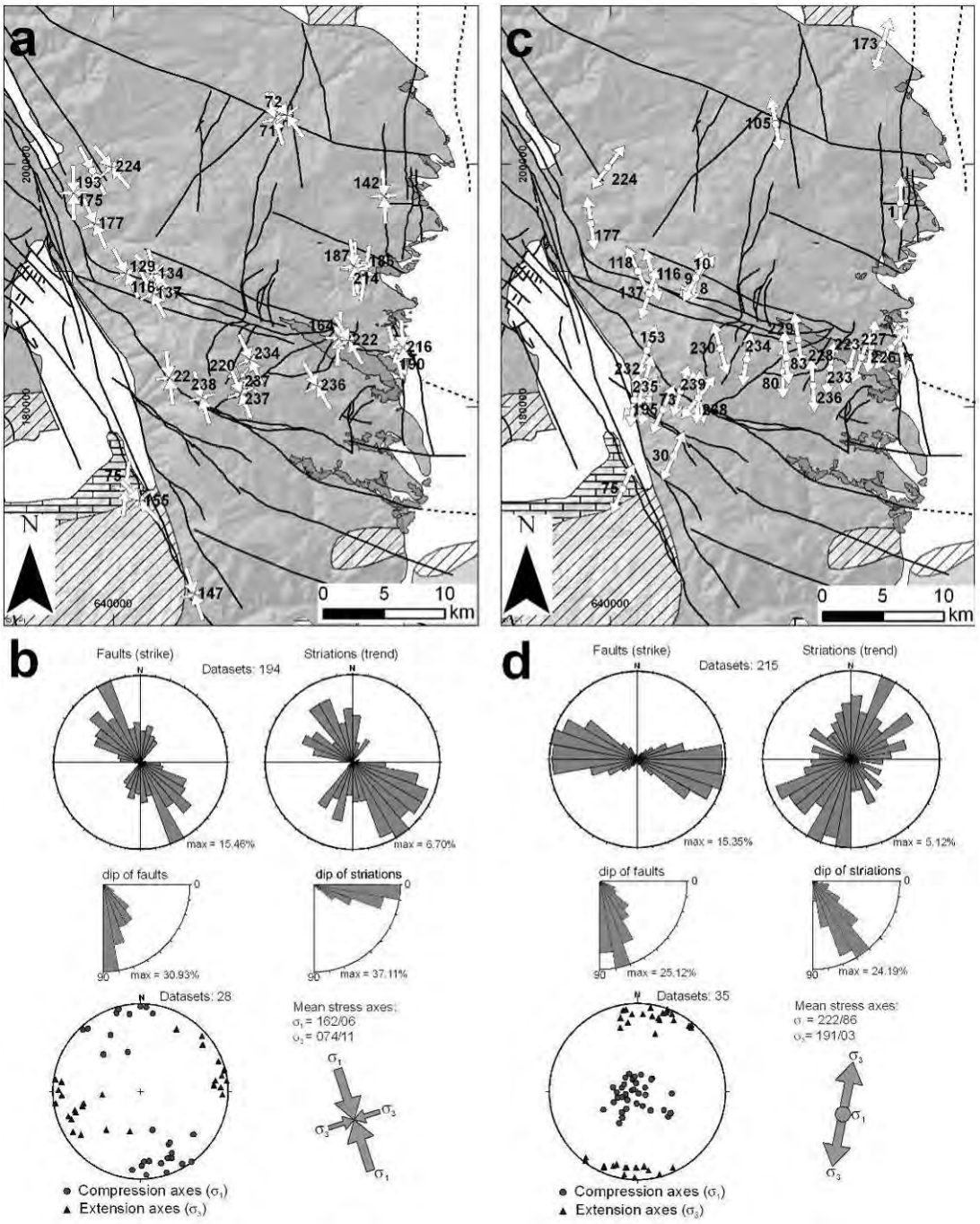

Figure 3-17: a - Orientation of σ_1 (large arrows) and σ_3 (small arrows) related to $D_{1\text{-}1}$; labelled numbers refer to Table 13(Appendix). b - Rose diagrams with strike and dip of fault planes and trend of striations; orientation of σ_1 (filled circles) and σ_3 (triangles) of $D_{1\text{-}1}$- related tensors with mean maximum and minimum principal stress axes. c - Orientation of σ_1 (large arrows) and σ_3 (small arrows) related to $D_{1\text{-}2}$; labelled numbers refer to Table 13(Appendix). d - Rose diagrams with strike and dip of fault planes and trend of striations; orientation of σ_1 (filled circles) and σ_3 (triangles) of $D_{1\text{-}2}$- related tensors with mean maximum and minimum principal stress axes. Refer to Figure 2 for legend of geological units. Grid is in Austrian BMN M34 system.

The ESE striking dextral strike-slip shears were reactivated during D1-2 as conjugate high-angle normal faults. This is indicated by sub-vertical striae associated with top-down displacement criteria overprinting the D1-1–related sub-horizontal striae (Figure 3-17 d). These high-angle normal faults are better preserved than the previous strike-slip faults and are locally associated with the development of cm-thick fault gouges. The main valleys and ridges parallel these WNW-ESE oriented structures. D1-2–related normal faults crosscutting the lower parts of the Schwanberg block debris have been observed in drill cores (Egger 2007). The high-angle faults are additionally associated with sub-vertical, ESE striking extensional veins and open fractures, indicating (N)NE-(S)SW- directed extension. This interpretation is supported by the paleo-principal stress orientations, i.e. σ1 with a sub-vertical orientation, σ3 with a (N)NE – (S)SW orientation (Figure 3-17 c).

Most of the brittle structures observed in the Koralpe are related to D2. They dominate both in surface exposures and in drill cores. The slickensides strike NNW-SSE, the major set steeply dipping towards E, and minor conjugate sets dipping to the W (Figure 3-18). Slickenside - related striae plunge subparallel or slightly oblique to the slickenside dip direction and kinematic indicators confirm normal faulting. In the field these shear fractures are locally associated with sub-vertical extensional veins arranged within an en echelon geometry, mainly filled with quartz or calcite. As seen particularly in drill cores, sub-vertical open en echelon fissures strike in a N-S direction. Altogether, these structures are related to general E-W- directed extension; The results from the analyses of paleostress orientations show a sub-vertical orientation of σ1, and a sub-horizontal orientation of σ3 in E-W to ESE-WNW-direction, locally shifting to a (N)NW-(S)SE orientation (Figure 3-18).

These high-angle structures are associated with E- dipping low-angle normal faults and shear zones. The latter formed by the reactivation of the penetrative foliation, mainly within smoothly dipping Plattengneis domains. These shear zones are accompanied by cataclastic fault rocks, consisting of very fine grained quartz, white mica and biotite in the matrix with incorporated broken grains of feldspar or cm to decimetre large protolith fragments (Figure 3-19 a). The damage zone (sensu Chester & Logan 1986; Caine et al. 1996) adjacent to the low-angle shear zones is characterised by the formation of closely, millimetre- to centimetre- spaced fractures, 5-20 cm in length, at high angles (70-90°) to the fault zone boundaries, bounding distinct rhombohedral blocks. The fracture-bound blocks show antithetic bookshelf rotation referring to the displacement along the low-angle shear zones, and associated to normal displacement along the high-angle fractures, too (Figure 3-19 b). Locally these low angle shear zones are associated with antithetic W- dipping conjugate high-angle normal faults (Figure 3-19 a). Synthetic sets of high-angle fractures continuously curve into the dip direction of the low-angle shear zones and form listric normal faults. Towards the lower tip line the high-angle faults show the development of cataclasites. High disintegration of the protolith may be observed along antithetic high-angle faults, too; in most cases, however, the original structure of the protolith can still be identified, irrespective of the slight alteration of the protolith. This alteration is characterised by the enrichment of feldspar and biotite. Around the

upper tip area, the high-angle faults may split up into splays, typically forming horse-tail structures.

N-S striking D2- related major faults crosscut both previously formed E- to SE trending faults and the block debris deposits of Schwanberg. Locally, the block debris is crosscut by distinct brittle shear zones, a few centimetres wide, as well as by slickensides, indicating a post-sedimentary (re-)activation of distinct faults.

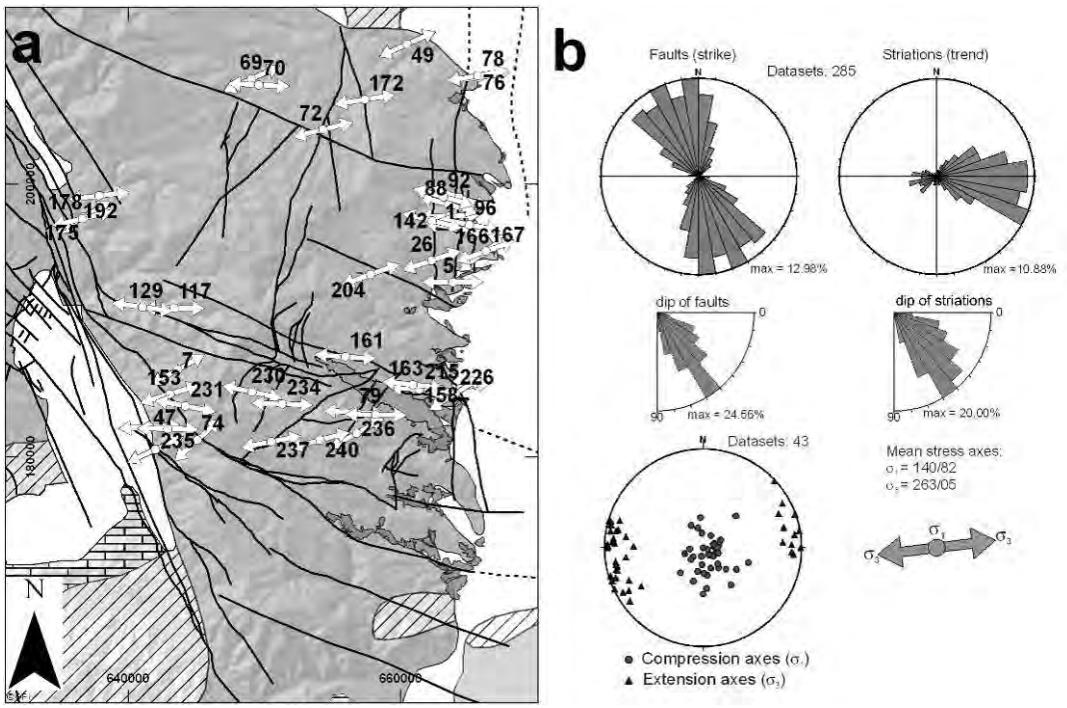

Figure 3-18: a - Orientation of σ_1 (large arrows) and σ_3 (small arrows) related to D_2; Labelled numbers refer to Table 13 (Appendix). b - Rose diagrams with strike and dip of fault planes and trend of striations; orientation of σ_1 (filled circles) and σ_3 (triangles) of D_2- related tensors with mean maximum and minimum principal stress axes. Refer to Figure 2 for legend of geological units. Grid is in Austrian BMN M34 system.

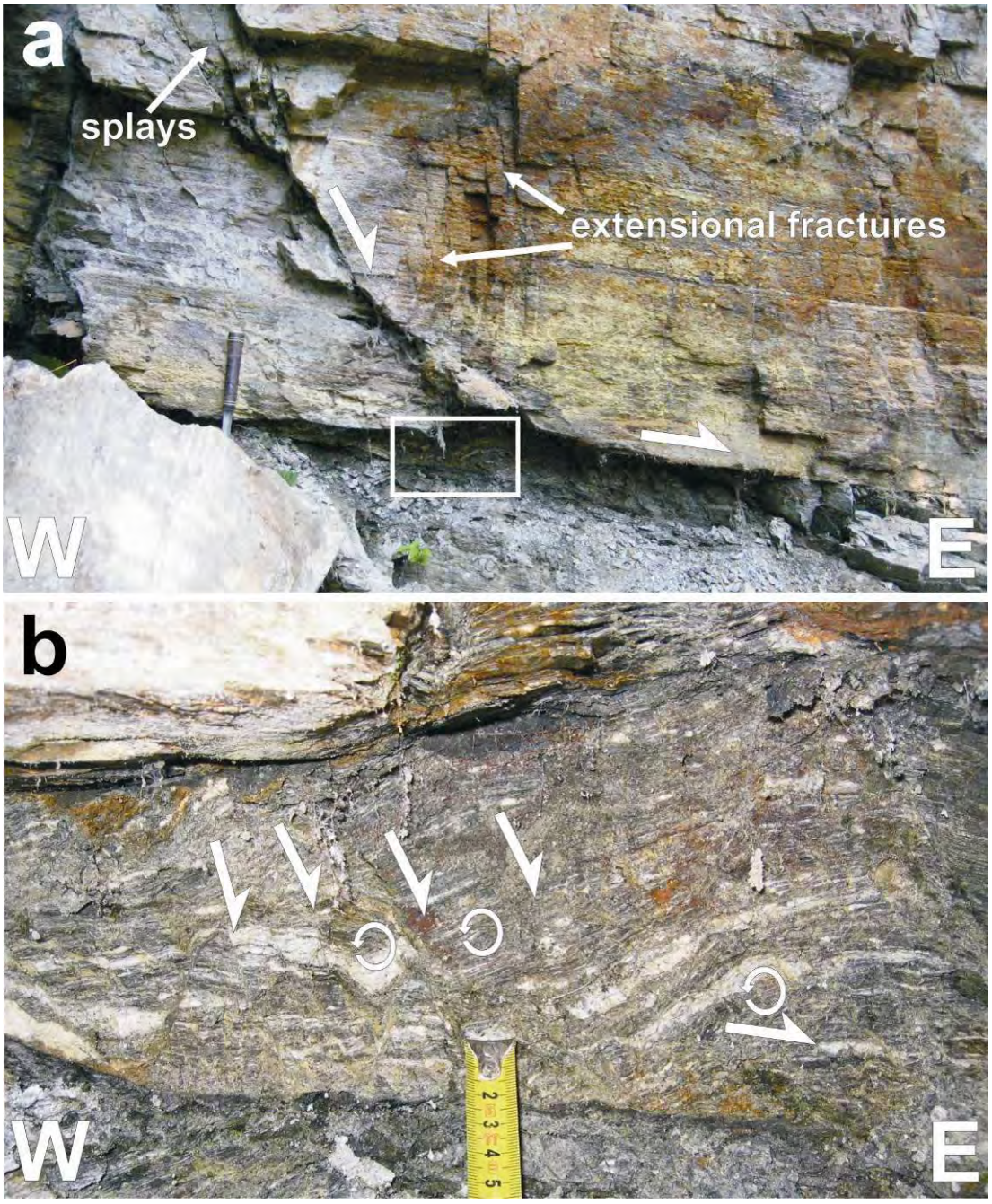

Figure 3-19: a - Listric cataclastic shear zone dipping towards E, passing into a shear zone parallel to the foliation of the Plattengneis. White rectangle indicates location of Figure 4b, use hammer handle for scale (approx. 18 cm). b - High-angle fractures associated with foliation parallel cataclastic shear zones with shear-related antithetic rotation of fracture-bound fragments (Outcrop-ID: 96, NW of Stainz / Styria).

D3 is characterised by a sub-horizontal orientation of the minimum principal stress σ3 in SE-NW direction (Figure 3-20). Locally, E-W trending fractures are activated as sinistral shears. Additionally ENE- and NNW- striking subvertical fractures are activated as strike slip planes with sinistral and dextral sense of shear, respectively. A detailed analysis of single stations shows that (E)NE- and N- to NW- trending fractures may occur as conjugate shears. The complete assemblage is interpreted to represent E- trending Y-, NE- trending R-, and (N)NW- trending R'- fractures (Figure

3-20 a, c). The analysis of paleostress orientations for this deformational event (D3-1) indicates a sub-horizontal NE-SW orientation of the maximum, and a sub-horizontal NW-SE orientation of the minimum principal stress axis (σ1 and σ3, respectively) (Figure 3-20 a, b). Locally, mainly along restraining bends along E-W- striking strike slip faults, σ3 shifts to a subvertical orientation. This indicates inversion of previously formed E-trending faults and the related block debris basins. However, these orientations are poorly constrained because of lack of sufficient data due to subsequent reactivation of fault planes.

SSE to S striking fractures were reactivated as oblique high-angle normal faults with striae dipping toward NW and SE, respectively (D3-2) Figure 3-20 d). Foliation planes slightly dipping to the E were activated as oblique low- angle normal faults as well. Paleostress orientation analysis of the fault-striae data related to this deformational phase yields a sub-vertical orientation of σ1 and a sub-horizontal orientation of σ3 in SE-NW direction (Figure 3-20 c, d).

Especially sub-horizontal and slightly E- and W- dipping pre-existing foliation planes as well as E- and W- vergent low-angle normal faults were finally re-activated as low-angle reverse faults (thrusts) as can be deduced from associated slickensides and striae indicating reverse to oblique reverse slip (D4; Figure 3-21). The displacements range from of a few centimetres to decimetres. The analysis of paleo-principal stress orientations indicates sub-horizontal σ1 in E-W direction, and sub-vertical σ3 (Figure 3-21). E-W oriented compression is additionally indicated by the development of kink bands (Figure 3-22 a) and the reverse drag of the pre-existing foliation forming s- type flanking folds (Figure 3-22 b) in terms of Grasemann et al. (2003).

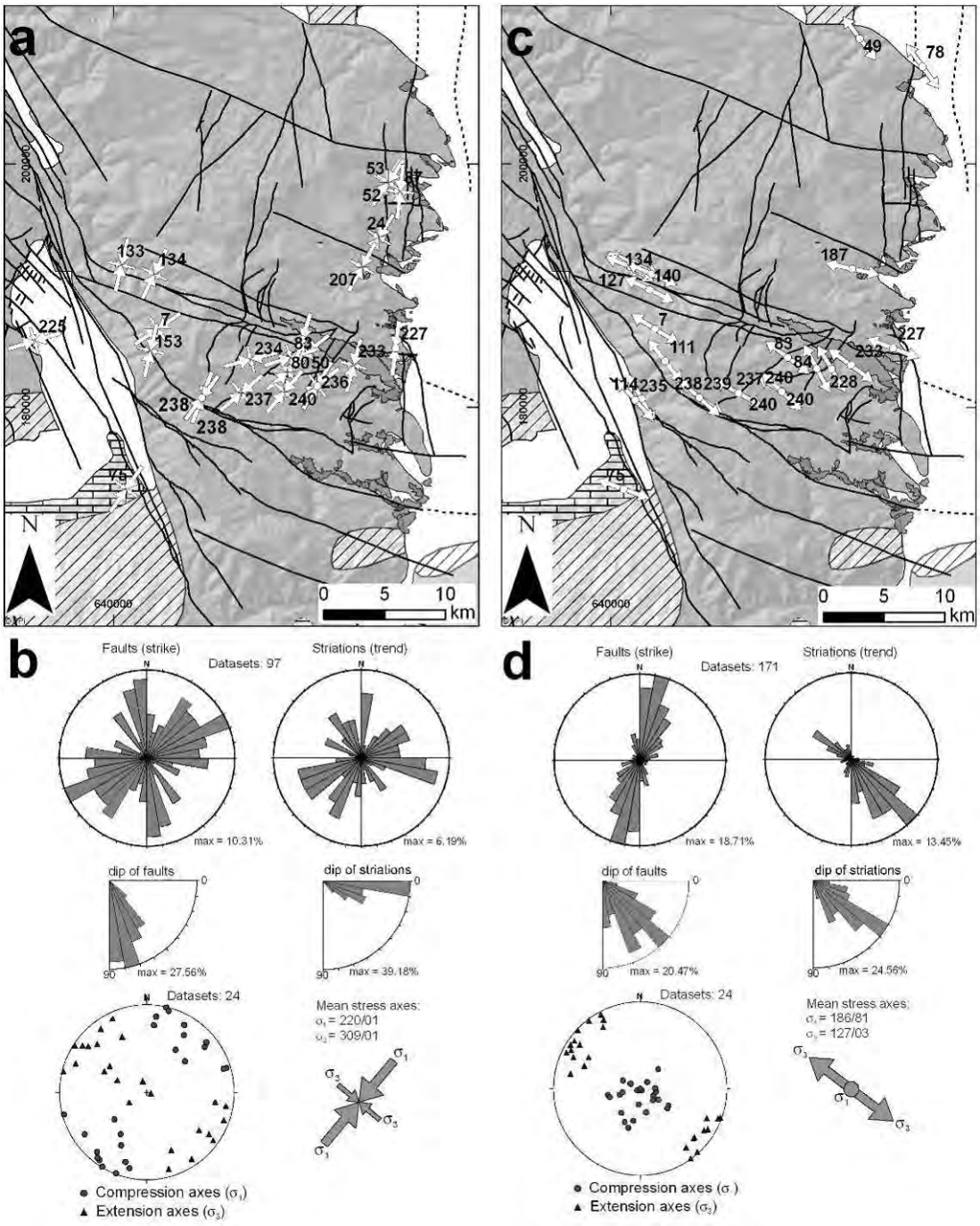

Figure 3-20: a - Orientation of σ_1 (large arrows) and σ_3 (small arrows) related to $D_{3\text{-}1}$; Labelled numbers refer to Table 13 (Appendix). b - Rose diagrams with strike and dip of fault planes and trend of striations; orientation of σ_1 (filled circles) and σ_3 (triangles) of $D_{3\text{-}1}$- related tensors with mean maximum and minimum principal stress axes. c - Orientation of σ_1 (large arrows) and σ_3 (small arrows) related to $D_{3\text{-}2}$; labelled numbers refer to Table 13 (Appendix). d - Rose diagrams with strike and dip of fault planes and trend of striations; orientation of σ_1 (filled circles) and σ_3 (triangles) of $D_{3\text{-}2}$- related tensors with mean maximum and minimum principal stress axes. Refer to Figure 2 for legend of geological units. Grid is in Austrian BMN M34 system.

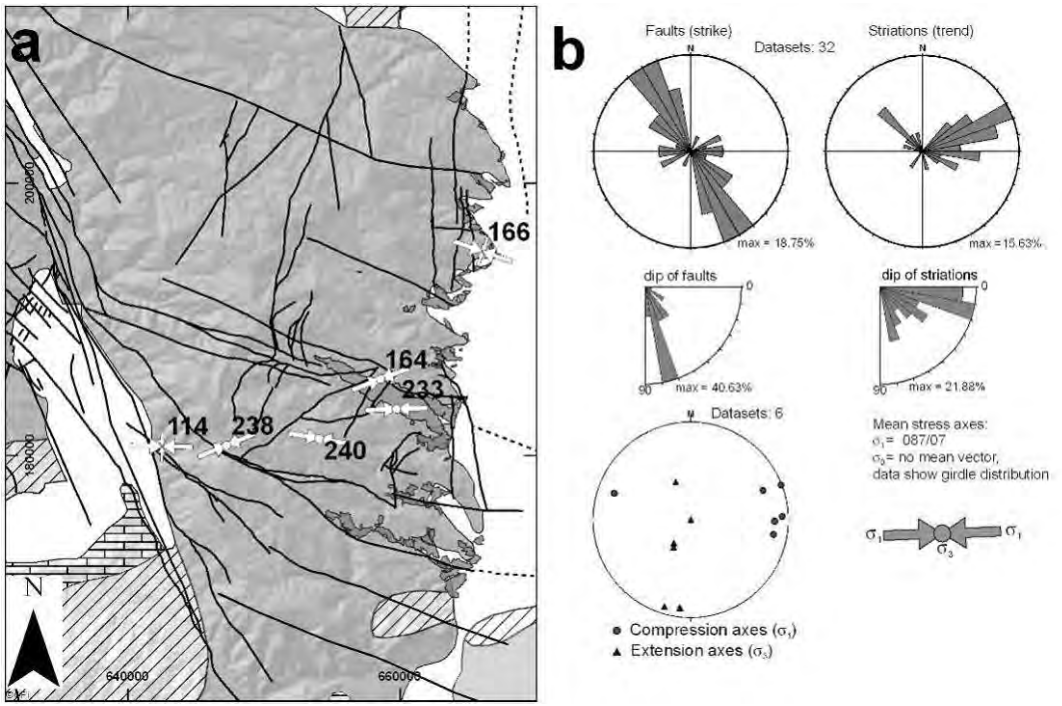

Figure 3-21: a - Orientation of σ_1 (large arrows) and σ_3 (small arrows) related to D_4; labelled numbers refer to Table 1. b - Rose diagrams with strike and dip of fault planes and trend of striations; orientation of σ_1 (filled circles) and σ_3 (triangles) of D_4- related tensors with mean maximum and minimum principal stress axes. Refer to Figure 2 for legend of geological units. Grid is in Austrian BMN M34 system.

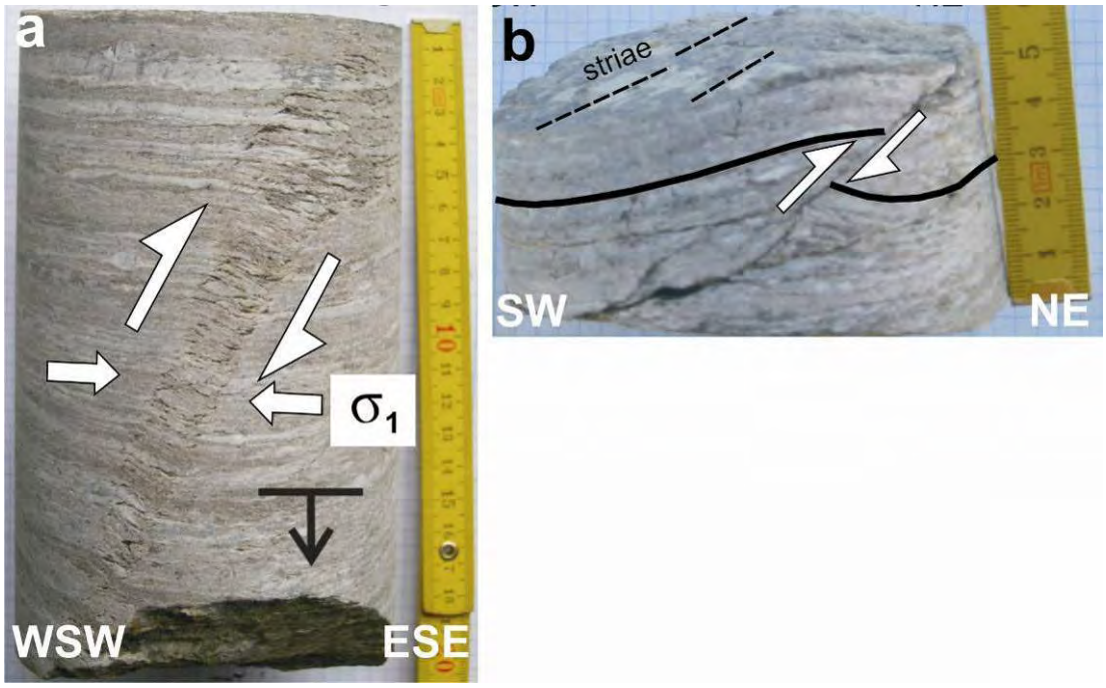

Figure 3-22: D_4- related structures: kink band (a) and s- type flanking folds with reverse drag of foliation (b), both indicating top-to-the E reverse sense of shear; a - from drilling TB-D01/05, depth 303,8 m, specimen is 20 cm long; b - from drilling TB-D01/05, depth 291,9 m, vertical length of specimen is 6 cm (after Übleis, 2007.

3.3 DISCUSSION

The evolution of the Koralpe and the adjacent sedimentary basins, during the Paleogene is not well known due to the sporadic sedimentary record and the rather low abundance of geochronological data from this period. The Miocene tectonic evolution is better documented for the sedimentary basins, in particular the Styrian and the Lavanttal Basin, located to the east and west of the Koralpe, respectively. However, the Paleogene and Neogene evolution of the Koralpe still lacks a detailed documentation.

In general, the Koralpe was transected by two major sets of faults, coinciding with the general Miocene fault pattern of the Eastern Alps (compare e.g. Ratschbacher et al., 1991b; Decker, 1996; Neubauer et al., 2000). These are:

1. ESE-WNW- to E-W- trending faults, associated with ENE- and NNW-trending conjugate structures;

2. N- to NNE-striking faults, mainly acting as high-angle normal faults, often associated with E-dipping low-angle normal faults along the western margin of the Styrian Basin.

These fault sets were repeatedly activated during the Miocene, resulting in a complex pattern of fault interferences. Detailed timing of distinct phases of faulting still remains difficult due to the lack of geochronological data directly dating fault activity, and the lack of exposed interference with sedimentary deposits. Especially along the eastern margin of the Koralpe, previously formed E- trending faults and associated structures were covered or sealed by syn- to post- tectonic sediments and may hardly be traced toward east into the Styrian Basin. However, together with the stratigraphic and paleogeographic evolution of the Styrian and Lavanttal Basins and the related subsidence histories (see, for example Weber and Weiss, 1983; Ebner and Sachsenhofer, 1995; Sachsenhofer et al., 1997; Sachsenhofer et al., 1998; Dunkl et al., 2005; Vrabec and Fodor, 2005) a rough structural evolution, not provided so far, may be reconstructed for this part of the Eastern Alps.

In general, the Koralpe, adjacent basement units north and south of it, and the Styrian Basin are bordered by two major confining fault zones: the ESE-trending Periadriatic fault with dextral sense of displacement in the south, and a system of ENE- trending sinistral fault zones in the north (e.g. Neubauer et al. 2000) (Figure 3-23). These are linked by the NNW- trending Lavanttal fault system west of the Koralpe (Figure 3-23). The evolution of the Styrian Basin can be subdivided into an Early Miocene (Ottnangian to Karpatian: approximately 18-17Ma) syn-rift phase and a subsequent post-rift phase (Ebner & Sachsenhofer 1995). During the syn-rift phase, there is a close genetic relation between basin formation and the formation of pull apart structures along predominately E- trending strike slip zones (Ebner & Sachsenhofer 1995; Sachsenhofer et al. 1997, 1998).

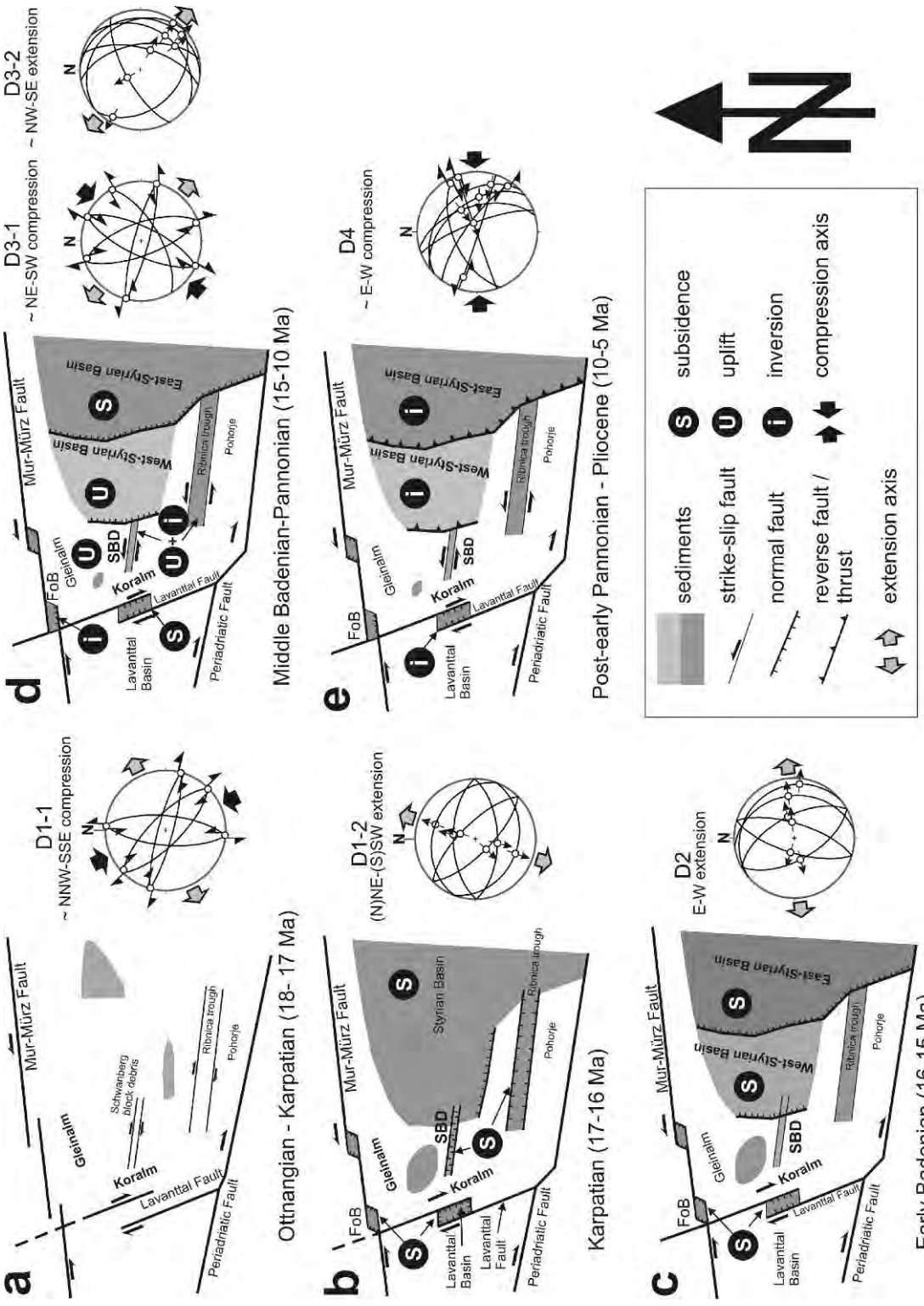

Figure 3-23: Scheme of the tectonic evolution of the central southern Koralpe and the adjacent Styrian Basin during the Miocene. Schematic Angelier plots indicate orientation of principal stress axes in the realm of the Koralpe as inferred from fault slip analysis and do not consider rotation by successive tectonic events (FoB=Fohnsdorf Basin; SBD=Schwanberg block debris. Sketch is not to scale)

During a first phase of deformation (D1-1) WNW-ESE- striking fractures were activated as dextral strike-slip faults in the southern part of the Koralpe (Ottnangian to

Karpatian: approximately 18-17Ma) (Figure 3-23 a). In domains characterised by overlapping fault segments this was associated with the evolution of WNW- trending troughs filled up with coarse block debris, e.g. the block debris of Schwanberg. This evolution continued with subsequent reactivation of E-W to WNW-ESE striking crustal fractures as normal faults, indicating (N)NE-(S)SW directed extension (D1-2, Figure 3-23 b) and crosscutting the lowermost parts of the block debris (Egger 2007), indicating partly synsedimentary faulting. The southern part of the Western Styrian Basin (Figure 1-3, Figure 1-4) was characterised by a fan-delta sedimentation in a fault-controlled setting with 1000- to 2000 m thick coarse conglomerates close to the eastern margin of the Koralpe, too (Nebert, 1983; Ebner and Sachsenhofer, 1995). The oldest sedimentation cycle (Lower Ottnangian) of these succession shows strong influence of strike slip faulting (Nebert, 1983) and pronounced tilting of the beds. Tilting has been documented for the rest of the succession too, but becomes progressively less pronounced (Nebert, 1983). It is assumed that the onset of this phase documents subsidence of the Styrian Basin in the time span from 18 to 16 Ma ago.

A similar tectonic evolution at a larger scale, with the development of an E- trending, fault-bounded trough (Ribnica-Selnica trough), may be observed along the northern margin of the Pohorje Massif (Figure 1-3, Figure 1-4, Figure 3-23 b, Sachsenhofer et al., 1998). Trough subsidence coincided with the exhumation of the Pohorje pluton showing a Miocene intrusion age (Fodor et al., 2008). During Middle Miocene time the Pohorje already supplied sediment into the surrounding basins with nearly synsedimentary apatite cooling ages, indicating fast, tectonic denudation (Sachsenhofer at al. 1998; Dunkl et al. 2005). This phase of tectonic denudation by N-S- directed extension may therefore coincide with the climax of subsidence of the Styrian Basin during latest Karpatian times (approximately 17 Ma) (Sachsenhofer et al. 1997). The NNW- trending segments of the Lavanttal fault system were activated by dextral displacement (Fig. 11a), resulting in the formation of the Lavanttal Basin in a pull-apart manner (D1-1, 18-17 Ma) with subsequent subsidence due to NE-SW extension (D1-2, 17-16 Ma) (Figure 3-23 b).

E-W- directed extension (D2) during the Badenian (approx. 16-13 Ma) disintegrated the Styrian Basin into distinct sub-basins. Tilting of crustal blocks resulted in the separation of the western from the eastern Styrian Basin (Figure 3-23 c) by the Middle Styrian Swell (Sausal Mountains, Figure 1-3 and Figure 1-4). The Western Styrian Basin is characterised by a lagoonal environment with siliciclastic sediments (Gross et al., 2007), also along the previously formed E-W- trending troughs, and shows coarse grained alluvial and coastal deposits during this age. This phase of extension may also coincide with normal faulting along the eastern margin of the Koralpe, and mainly oblique normal displacement along the Lavanttal fault. Related uplift of the Koralpe resulted in the separation of the Lavanttal Basin from the Styrian Basin.

Along the northern margin of the central Eastern Alps, this time span is characterised by the formation of pull apart basins along the Mur-Mürz fault system, in particular the Fohnsdorf Basin (e.g. Sachsenhofer et al., 2000; Strauss et al., 2001) and the

Trofaiach Basin (e.g. Nievoll, 1985, Figure 1-3, Figure 1-4). The well documented sedimentary evolution of the Fohnsdorf basin provides additional time constraints on the tectonic evolution of the Koralpe. Subsidence occurred along ENE- trending sinistral strike-slip faults and NE-SW to N-S trending normal faults during the Late Karpatian/Early Badenian, followed by N-S extension and normal faulting along the southern basin margin during the Middle/Late Badenian. Simultaneous dextral displacement and subsidence along the Lavanttal fault system allowed temporary marine influx from the Lavanttal basin towards north during the Early Badenian (Strauss et al., 2001). Post-Middle Badenian NNW-SSE directed shortening resulted in inversion of the Fohnsdorf Basin.

A sea level low stand at the Badenian/Sarmatian boundary caused erosional unconformities in parts of the Eastern Styrian Basin and the progradation of fluvial and deltaic sequences toward east (Ebner and Sachsenhofer, 1995). The early Sarmatian (approximately 13 Ma) is marked by a transgressional phase, with deposition of shallow marine sediments. Northward propagation of sedimentation occurred mainly along N-trending fault zones. In the Western Styrian Basin Sarmatian sediments have only been observed in its northwesternmost parts (Kollmann, 1964; Flügel and Neubauer, 1984). The lack of equivalent sediments in the rest of the Western Styrian Basin may result from erosion linked to Post-Sarmatian uplift. This is in accordance with the view of Dunkl et al. (2005) that the Eastern Alps between the Tauern Window and the Pannonian basin were covered by sediments more widely during the Early-Middle Miocene than is recorded by the sediments still preserved today. Pannonian (11.5 to 7.1 Ma) sediments are restricted to the Eastern Styrian Basin and grade from fine-grained marine sands and marl to coarse grained siliciclastics related to alluvial fans during the early Pannonian (Ebner & Sachsenhofer 1995). A similar evolution can be observed in the Lavanttal Basin as well (e.g. Weber & Weiss 1983). This was associated with local inversion of E-trending troughs and the re-activation of E- trending and NNW- trending faults by sinistral and dextral displacement, respectively, due to NE- directed compression (D3-1). Subsequent (S)SE-(N)NW- directed extension (D3-2) caused the reactivation of N-trending normal faults along the eastern margin of the Koralpe and the Middle Styrian Swell, and of the Lavanttal fault by dextral normal oblique displacement (Figure 3-23 d).

During the Late Pannonian to Pliocene the entire Styrian and Lavanttal Basin became an erosional domain, interpreted to coincide with a phase of basin inversion (D4) (Figure 3-23 e). This phase is correlated to the inversion of low-angle normal faults along the eastern margin of the Koralpe, related to E-W- directed compression indicated by a sub-horizontal E-W- orientation of the maximum principal paleostress axes. Previously formed E-W striking structures probably were reactivated as tear faults, showing either dextral or sinistral displacement.

This structural succession, constrained by the sedimentary evolution of adjacent basins (Kuhlemann et al., 2002), indicates that the Koralpe basement and the Western Styrian Basin were affected by post- Sarmatian uplift with respect to the Eastern Styrian Basin. For the timing of uplift this opens two possible interpretations:

(1) Uplift was mainly related to tilting of crustal blocks along east-directed normal or oblique normal faults and contemporaneous to basin subsidence (compare Dunkl et al. 2005). This resulted in uplift of the Koralpe, including the Schwanberg block debris and Miocene deposits in the northern part of the Koralpe, above the top of the Western Styrian Basin (Figure 3-23 d). The main final uplift of the Koralpe, partly together with the Western Styrian Basin, occurred during the Sarmatian.

(2) Uplift was related to W- directed inversion during the Pannonian and resulted in erosion of Sarmatian sediments in the western Styrian basin. However, as inversion affected the Styrian basin entirely it seems not to be a plausible mechanism for explaining the separation of the Styrian Basin into domains of distinct subsidence. Therefore, a model of extension-related uplift during the Sarmatian, according to (1), is favoured.

Irrespective of the mode of uplift the Koralpe was elevated by a minimum amount of approximately 800m during this phase. This can be deduced from the present position of the Schwanberg block debris. These clastics are at an altitude of ± 1100m today, in contrast to the top of the Styrian Basin, having an average altitude of ± 300m. This was accompanied by the development of a pronounced relief resulting in enhanced erosion and subsequent deposition of coarse-grained clastics in the Lavanttal and Eastern Styrian Basin (Gross et al., 2007; Reischenbacher, 2008).

The formation of the main fault sets in the Koralpe also reflects the structural evolution of an eastward extruding block with increasing width away from the central part of the Eastern Alpine orogen during orogen-parallel escape (e.g. Ratschbacher et al., 1989; Ratschbacher et al., 1991b; Neubauer et al., 2000, Figure 3-24). This evolution is mainly governed by the N to NNE directed (Rosenberg et al., 2007), oblique indentation of a rigid indenter represented by the Southalpine (Figure 1-3) accompanied with maximum shortening in the central Eastern Alps, and a continuous decrease of shortening toward east. According to Kuhlemann et al. (2003) this deformation episode occurred between 21 and 12 Ma. Additionally to these “intra-Alpine” forces (Froitzheim et al., 2008) subduction in the Carpathians exerted a pull force on the upper-plate lithosphere (Peresson and Decker, 1997). In the eastern part of the Eastern Alps, this extruding block is mainly characterised by strike-slip faulting along confining WSW-ENE and WNW-ESE trending wrench faults. Pull-apart basins form at oversteps of the different fault segments and accommodate displacement along these strike-slip faults (Figure 3-24). The eastward increasing width of the extruding wedge implies that progressive lateral displacement causes dilatancy within the extrusion wedge. This dilatancy is accommodated by N-S- directed extension perpendicular to the overall displacement direction. This process may be reflected in the re-activation of previously formed E- trending strike-slip faults and by the formation of additional E- trending extensional structures (Figure 3-24).

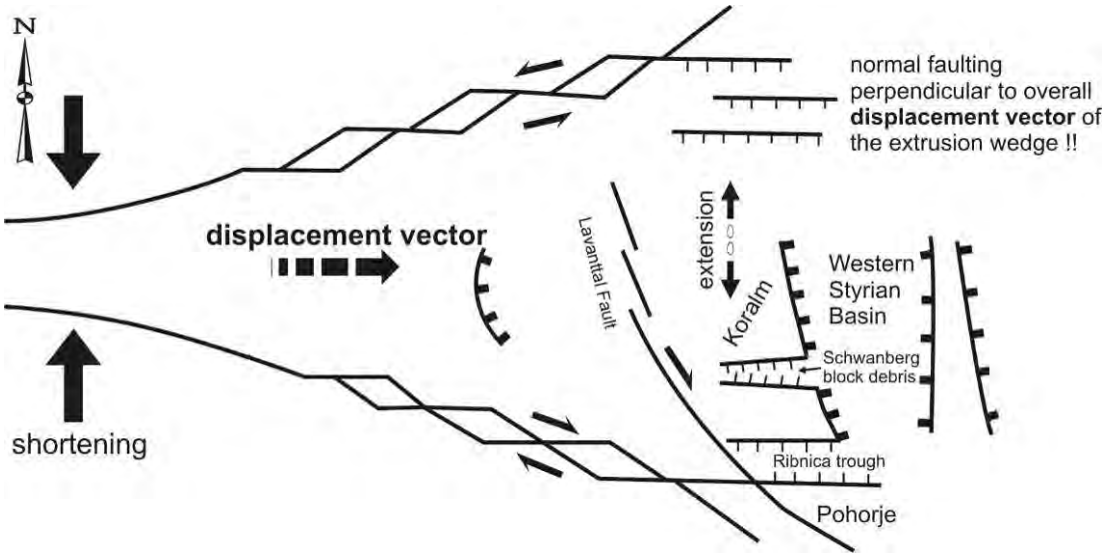

Figure 3-24: Scheme showing the development of the fault pattern and related structures within an orogen-parallel extruding wedge, widening toward the direction of displacement. Sketch is not to scale (Modified after Neubauer et al. 2000).

The D1 – D3 paleostress orientation patterns may be mistaken as a clockwise rotation of the minimum principal stress (σ3) from a NE-SW to a NW-SE orientation (Figure 3-23 a-d). However, this shift in principal stress orientation may be related to counter clockwise rotation of crustal blocks, as suggested by paleomagnetic data indicating counter clockwise block rotation in the eastern part of the Eastern Alps by 30° to 40° from approximately 17 to-13 Ma (Fodor et al. 1998; Márton et al. 2000, 2002; Kuhlemann et al. 2003). Consequently, the apparent rotation of the regional stress field resulted from passive rotation of the evaluated stress tensors. The subsequent inversion of the regional stress field to E-W oriented compression (Figure 3-23e) was described all over the eastern part of the Eastern Alps and the Pannonian Basin (Peresson & Decker 1997) and is interpreted to represent the far-field response of a phase of "soft continental collision" in the Eastern Carpathians. According to Peresson & Decker (1997), deformed Pannonian strata in the eastern Styrian Basin indicate that this paleostress regime may have started at 9 Ma and lasted approximately until 6 Ma.

3.4 CONCLUSIONS

1) The structural evolution of the Koralpe during the Neogene is determined by the development of two main fault sets: (a) E- to ESE-trending faults formed as strike slip faults with dextral sense of shear, linked by (b) approximately N-trending normal faults. Fault-related E- trending troughs were filled with block debris ("Schwanberger Blockschutt"). Sedimentary deposits up to the Early/Middle Badenian are mainly related to E-W- striking faults.

2) During (N)NW-(S)SE- directed compression the E-trending structures were reactivated as high-angle normal faults or oblique normal faults, indicating a phase of (N)NE-(S)SW extension.

3) Main uplift of the Koralpe did not occur before the late Middle Miocene (Sarmatian).

4) Pannonian sedimentation was restricted to the Eastern Styrian Basin; this suggests uplift of the Western Styrian Basin together with the Koralpe and the block debris at post-Sarmatian times. This is mainly related to displacement along E-dipping low-angle normal faults during a phase of E-W- to SE-NW- directed extension. The Koralpe was elevated by approximately 800 meters during this phase.

5) E-W directed contraction resulted in the reactivation of former low-angle normal faults as W- directed reverse faults, and the re-activation of E- trending structures as related tear faults. This coincides with the inversion of the Styrian Basin.

4 MORPHOTECTONIC ANALYSIS[1]

4.1 DATA

4.1.1 DIGITAL ELEVATION DATA

Two digital elevation data sources (see Table 2) were used. A DEM is an ordered array of numbers that represents the spatial distribution of elevations above some arbitrary datum in a landscape (Moore et al., 1991). Frequently the term “digital terrain model (DTM)” is used as a synonym. However, following Florinsky (1998) a DTM is defined as “a digital representation of variables relating to a topographic surface” and this incorporates the term DEM as well as other topography related digital representations like slope, aspect or curvature. Thus the DEM provides the input data needed to produce all other types of DTMs (Florinsky, 1998).

Name	Spatial resolution [m]	Source
Digital elevation data from space shuttle radar topographic mission (SRTM)	96.36	http://srtm.csi.cgiar.org/
DGM R10	10	Bundesamt für Eich und Vermessungswesen resp. Amt der Steiermärkischen Landesregierung Landesbaudirektion – geographische Informationssysteme
Aerial photographies	2.5 (scale 1:5000, colour images)	Bundesamt für Eich und Vermessungswesen
	0.5 (scale 1:10.000, black and white images)	Amt der Steiermärkischen Landesregierung Landesregierung Landesbaudirektion – geographische Informationssysteme
		Amt der Kärntner Landesregierung, Abteilung 15 Umweltschutz, Unterabteilung Geologie und Bodenschutz
Landsat ETM+ scenes path190 row 27 (2001-05-24) and path 190 row 28 (2000-09-10)	14.25	http://glcf.umiacs.umd.edu
Radarsat scene	5	Joanneum Research Forschungsgesellschaft mbH

Diss_Tab remote sensing.xls

Table 2: Digital elevation data and remote sensing data used in this work

The DEM derived from the Space Shuttle Radar Topographic Mission (SRTM) data set has a spatial resolution of approximately 96 m (3 arc seconds) and is derived from radar interferometry. This DEM was used for a general topographical overview.

[1] This section has partly been published in the Swiss Journal of Geosciences (doi 10.1007/s00015-009-1305-5)

The 10 m DEM, provided by the Bundesamt für Eich und Vermessungswesen (BEV) is the product of photogrammetric analysis of black and white, as well as coloured aerial photographies with an approx. scale of 1:30.000 and 1:15.000 respectively. The accuracy of these interpolated elevation values ranges from +/- 1 m to +/-3 m in an open and flat landscape and from +/- 5 m to +/- 20 m in a forested or mountainous area (BEV, 2006). For the areas on Slovenian territory in the southern parts of the project area (north of the Drau / Drava), the DEM was interpolated from manually digitized 20 m contour intervals of 1:50.000 topographic maps and merged with the 10 m elevation model. The georeferenced contour lines were crosschecked with the adjacent contour lines interpolated from the 10 m DEM and if necessary manually adjusted to avoid systematic step-like errors along the seam. Despite different approaches in joining the two data sets the seam is still visible especially in elevation derivatives like hillshades. No further effort was put on improving this effect as to my opinion a known, clear irregularity is easier to be excluded from analysis as a masked one. The final 10 m DEM includes parts of the Saualpe, the Stubalpe, the Lavanttal Basin, the Styrian Basin and parts of the Drau (Drava) valley in the south.

The digital elevation data were used to produce hillshades, contour maps, 3D surfaces and grey resp. colour scale images. Hillshading was performed with ArcGIS 9.1 software for different azimuths and altitudes of illumination to allow a more reliable identification of lineaments. The elevation data were also used for morphometric and morphotectonic analysis of the project area.

4.1.2 REMOTE SENSING DATA

Remote Sensing data other than elevation data where used supplementary for the identification and interpretation of morphological features like lineaments or anthropogenic structures. The data used include Landsat Enhanced Mapper scenes, a Radarsat scene and aerial photographies as black & white and partly as colour images (Table 2). All data were georeferenced in the Austrian Bundesmeldenetz M34 system, if not already provided in this system. Transformation was done with ArcGIS implemented transformation tools. Resolution of the data sets, the providing institutions as well as path and row of the scenes and date of acquisition are listed in Table 2.

4.1.3 GEOLOGICAL MAPS

Different geological maps where used in this study to derive basic informations about lithology and structure. These were 1:50.000 maps of the Geological Survey of Austria (Becker, 1979; Beck-Mannagetta, 1980; Kleinschmidt et al., 1989; Beck-Mannagetta et al., 1991; Beck-Mannagetta and Stingl, 2002), own mappings and maps for the Koralmtunnel project by 3g Gruppe Geotechnik Graz ZT GmbH for the ÖBB Infrastruktur AG (used with permission).

4.2 METHODS

The methodological approach follows partly the scheme proposed by Jordan et al. (2005) and Székely (2001). In a first step, the elevation data were analysed visually. Further on, their distribution and some statistical measures of distribution were determined, followed by hypsometric analysis. Lineaments were mapped to detect fault zones or subsurface structures. The drainage system, catchment properties and longitudinal river profiles were analysed.

4.2.1 VISUALIZATION OF ELEVATION DATA

The elevation data were visualized in the ArcGIS environment as grey and colour scale images and as shaded relief images ("hillshade"). Additionally, combinations of these images with variable transparency were used to support perception of topographical features. Hillshades generated with varying illumination direction and altitude were used to identify linear structures (lineaments). Furthermore, contour lines with different spacing were calculated to visualize the topography. Contour lines were also used for mapping the stream courses in the uppermost reaches of a catchment. Topographic cross sections were extracted from the DEM data (Figure 2-1) to allow a better understanding of the 3D morphology of the project area.

4.2.2 ELEVATION ANALYSIS AND HYPSOMETRY

Elevation analysis was performed on the 10 m DEM. As a first step, descriptive statistics and the hypsometric integral (H_i) were estimated for the entire DEM of the project area and a DEM clipped to the outcropping basement rocks and the morphological units. Additionally a relief map was calculated for the entire DEM.

To describe the data distribution of elevation, maximum and minimum values, mean, median, standard deviation and range (=relief) were estimated. Székely (2001) defines relief as "the difference between largest and smallest elevations within a geometric shape". This definition corresponds to the term "local relief" as used by Smith (1935) and Wood (1996). For the present analysis, relief was calculated for the entire data set including the adjacent basin regions, the data set clipped to the margins of the basement rocks of the Koralpe, and for the individual catchments. It forms one parameter for the calculation of the hypsometric integral and equivalent elevation-relief ratio (see below). Relief was calculated in the ArcGIS environment using the neighbourhood statistics function of the Spatial Analyst toolbox for circular windows with 100 m, 200 m and 500 m radius. This procedure enhances the flatter areas in the central parts of the Koralpe and the more gorge like tributaries along the margins. Additionally the scale dependency of this parameter (Székely, 2001), increasing with size of the window used, can be shown.

Hypsometry is the study of the distribution of ground surface area, or horizontal cross-sectional area of a landmass as a function of elevation (Strahler 1952). It describes the area-altitude relationship of a portion of the earth's surface. To compare different areas, hypsometric curves are calculated (Figure 4-1). The shape of the curve is specific for a drainage basin and together with the value of the hypsometric integral H_i

it may be an indicator for the maturity of a landscape (Strahler, 1952; Keller and Pinter, 2002). H_i is defined as the area below the hypsometric curve (e.g. Keller and Pinter, 2002). It lies between 0.25 and 0.75 for most drainage basins, where high values indicate large parts and low values indicate small parts of land at high elevations (Summerfield 1991). Pike and Wilson (1971) showed that H_i is equal to the elevation-relief ratio E which is defined as

E=(Mean elevation – Minimum elevation) / (Max elevation – Minimum elevation).

Strahler (1952) showed that the H_i correlates inversely to basin relief, slope, and stream gradient. Lifton & Chase (1992) found in a tectonical active region a negative correlation of H_i with tectonic activity and a clear influence of tectonic activity across the mountain-piedmont junction at all scales. This is explained by a lack of time for landscape dissection by low order streams in tectonically active parts of the mountain front. Strahler (1952) showed that geological factors (structure, lithology) influence the hypsometry of a catchment. He falsified the hypothesis that catchments over the same bedrocks show similar integrals and he found a clear influence of lithology in areas with horizontal strata and contrasting rock strength.

Hypsometry has widely been used to assess the influence of exogenic and endogenic factors on landscape development (Lifton and Chase, 1992; Hurtrez et al., 1999; Chen et al., 2003). Hurtrez et al. (1999) showed that the hypsometry is not sensitive to the resolution of DEMs. However, their results indicate a dependence on the basin characteristics and a relationship to basin area. Following their findings larger basins should have relatively less basin area at low elevations. This is consistent with Willgoose and Hancock (1998), who showed that hypsometry reflects landscape runoff and erosion processes and is strongly dependent on channel network and catchment geometry. Further, the width to length ratio of the catchment influences the shape of the hypsometric curve, but does not affect the hypsometric integral (Willgoose and Hancock, 1998). According to these authors, the hypsometric curve is scale dependent. Hurtrez et al. (1999) suggested that the scale dependency is related to the acting of both, river and hillslope processes in catchments of different scales, where hillslope processes dominate in smaller catchments. Further, a positive correlation was found between H_i and the mean uplift rate in different basins. Walcott & Summerfield (2008) analysed the scale dependence of hypsometric integrals too, however they did not find a correlation with “any measures of basin-scale, e.g., basin area, basin shape and basin relief”. In their analysis of basins along the passive continental margin of southeast Africa they detected a strong variation of H_i with location. For basins of a Strahler order 5 or less they suggested differences in erodibility (lithology) as the main cause. For basins of Strahler order 6 this could not be verified. The Strahler stream order (Strahler, 1957), based on Gravelius (1914) and Horton (Horton, 1945) terms a segment with no tributaries as a first order segment. If it joins another first order segment it becomes a second order segment, until it joins another second order segment. Then it becomes a third order segment and so on (Figure 4-2).

The use of the hypsometric curve and of H_i as a proxy of landscape evolution as proposed by Strahler (1952) is questioned by several authors. Summerfield (1991) proposed that this may only be valid for small catchments, because the "areal distribution of elevation" in large catchments may be altered by tectonic uplift or subsidence and sea-level changes over time. Because of the scale dependency of H_i, its use as a proxy of landscape evolution stage has been denied by Hurtrez et al. (1999). Ohmori (1993) proposed, that Hi indicates rather the state of the fluvial processes acting in a basin than the stage of the geomorphic cycle.

Harlin (1978) introduced a method to describe the hypsometric curve with the help of its statistical moments, suggesting that this procedure has a much greater potential for quantitative landform analysis than the use of the integral value alone. Luo (2000; 2002) used this method to characterize landforms dominated by groundwater-sapping processes and for the hypsometric characterization of watersheds on Earth and Mars.

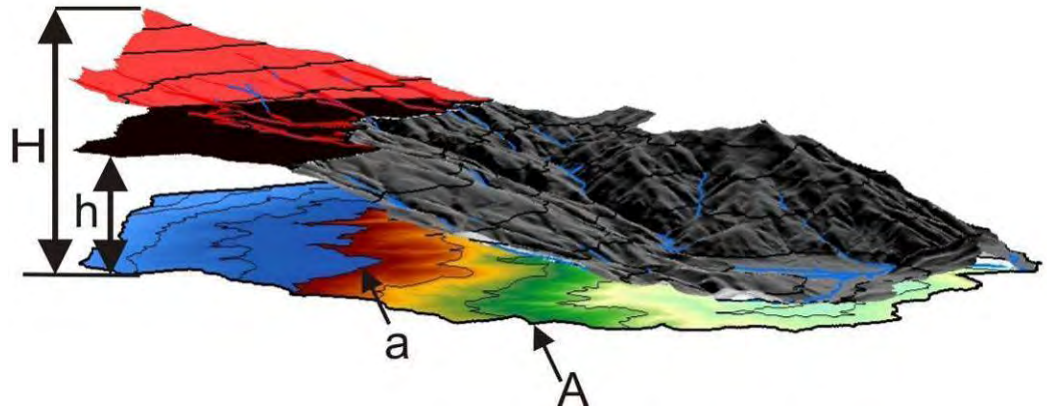

(a)

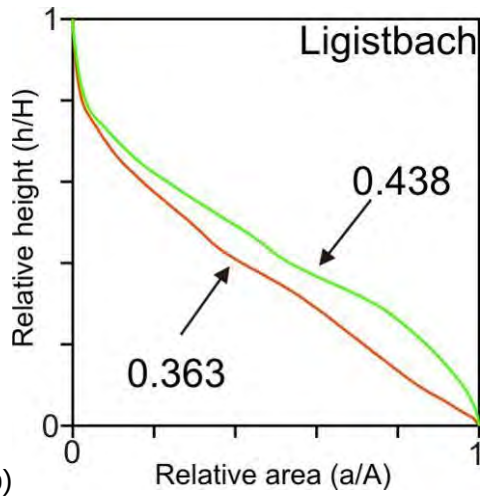

(b)

Figure 4-1: (a) Perspective view of the catchment of the Ligistbach from the Koralpe demonstrating the variables involved in the calculation of the hypsometric curves and the hypsometric integral H_i resp. the elevation-relief ratio E. A=the total projected area of the catchment; a=projected area of the catchment above a certain height h, H is the total relief of the catchment. (b) Hypsometric curves for the catchment of the Ligistbach and the respective H_i values. The green curve is for the catchment entirely in basement rocks, the red one represents also data from Neogene and Quaternary sediments.

In the present study, the hypsometric curves were extracted from the 10 m DEM in the ArcGIS environment following Luo (1998). First the DEM was reclassified in a certain interval (e.g. 20 m). The attribute table of the reclassified DEM gives the number of raster cells in each elevation class and the multiplication with cell size gives the area of a class. The relative area data (a/A) and the relative height data (h/H) were used to plot the curves (refer to Figure 4-1 for description of the variables). Hypsometric curves and H_i values were determined for the entire DEM and also for the DEM clipped to the outcropping basement rocks of the Koralpe. Similarly they were determined for all catchments analysed. On the eastern slopes of the Koralpe some of the streams reach significantly beyond the available DEM and therefore their hypsometric curves and H_i values only represent the truncated basins.

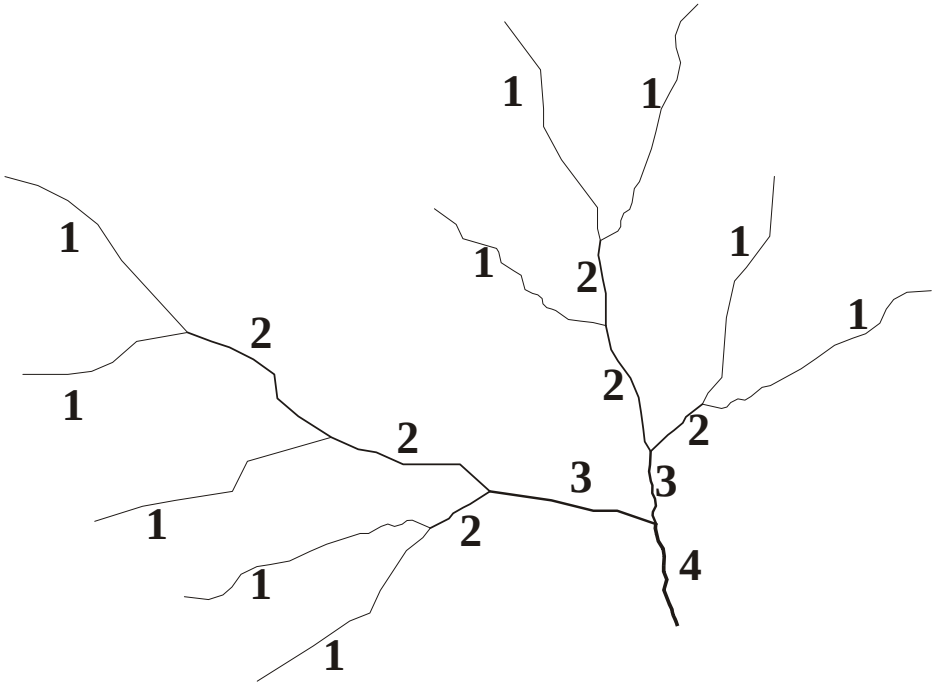

Figure 4-2: Stream order scheme after Strahler (1957).

4.2.3 ELEVATION DERIVATIVES – SLOPE GRADIENT, ASPECT AND CURVATURE

Derivatives of elevation used are *slope gradient* (or slope angle), *slope aspect* and *curvature*. These parameters are attributes of the earths surface and require the incorporation of a neighbourhood for their calculation (Evans, 1981). They have widely been used in geomorphometry, landscape classification and morphotectonics (e.g. Florinsky, 1996; Wood, 1996; 1998; 2000; Kühni and Pfiffner, 2001; Székely, 2001; Bolongaro-Crevenna et al., 2005; Jordan et al., 2005; Jelinek, 2006) and their extraction from elevation data is a standard raster GIS procedure. Slope describes the inclination of the land surface in a chosen observation window. In the ArcGIS environment, slope is calculated for a 3x3 cell neighbourhood and can be expressed in degrees or as percentage. In this work, slope is given in degrees. Its spatial distribution reflects mass movements, areas of planation (paleosurfaces), areas of

sedimentation or enhanced erosion. Additionally, slope angle is a parameter that can be used to detect fault scarps. Szekely (2001) showed that the slope histogram of 2-D sections may exhibit typical shapes for distinct landforms like U-shaped valleys or plateaus.

Figure 4-3: Asymmetric ridge with "Dip slope" in the eastern realm of the Koralpe (Glashüttenkogel, view towards ESE. Foliation is dipping towards NNW with approx. 20°).

Aspect can be described as the orientation of the slope in degrees clockwise from the north in direction of the maximum slope gradient. For hydrological applications, aspect defines the direction in which water flows (Zevenbergen and Thorne, 1987). In morphotectonics, aspect indicates the dominant slope orientation. Structurally controlled slopes may result from the presence of fault structures or other inclined planar structures like bedding or foliation ("dip slopes"). Exposed fault scarps form linear slopes of uniform orientation, degrading with ongoing erosion to triangular facets, especially if the displacement vector includes a significant normal faulting component (Keller and Pinter, 2002). Differential weathering of inclined strata with contrasting rock mass strength may mould the more resistant strata as asymmetric ridges (Figure 4-3) called "hogbacks" on more steeply inclined strata and "cuestas" on flatly dipping beds (Hamblin and Christiansen, 1995). Aspect is undefined in the case of horizontal slopes and therefore should not be regarded as independent of the slope gradient (Evans, 1981).

Curvature describes the rate of change of slope (second derivative of elevation) and aspect (Moore et al., 1991). It has two components, the plan and the profile curvature (Evans, 1981). Curvature may be classified as rectilinear, convex and concave, so

with respect to plan and profile curvature nine classes of hill slope forms are distinguished (Figure 4-4). In ArcGIS a negative profile curvature indicates a convex profile, values equal to zero are linear and positive values are indicative for a concave profile form. Plan curvature is positive for convex (convex contour line), negative for concave and zero for linear shapes. Reasonable values are, according to the ArcGIS help files, in the range of -4 to +4 for rugged mountains. Plan curvature has a significant effect on slope wash. In concave areas, flow is concentrated and enhances erosion (Summerfield 1991). Plan curvature marks breaks in aspect, which may identify morphological features like ridges or valleys (Jordan, 2003). Profile curvature helps to delineate breaks in the slope angle which may be indicative for the presence of faults (Jordan et al., 2005). The acceleration or deceleration of flow is controlled by profile curvature (Florinsky, 2000). Florinsky (1996) has shown that lineaments revealed in plan curvature maps may represent faults with predominating horizontal slip vector. Profile curvature showed to be more sensitive for the detection of faults with a vertical displacement vector. Lineaments detected in both curvature maps could be related to an oblique slip vector (Florinsky, 1996). In the present study, the curvatures were calculated in the ArcGIS environment, using the 3D Analyst. Smoothing of the curvature maps improved the visual impression marginally, especially as the pronounced net of (forestry) roads, which is incorporated in the elevation data, is still clearly visible in the maps. As curvature is especially sensitive to noise (Jordan, 2003), smoothing of the input DEM was performed, as proposed by Jordan (2003), by applying two times a 3x3 moving average low pass filter.

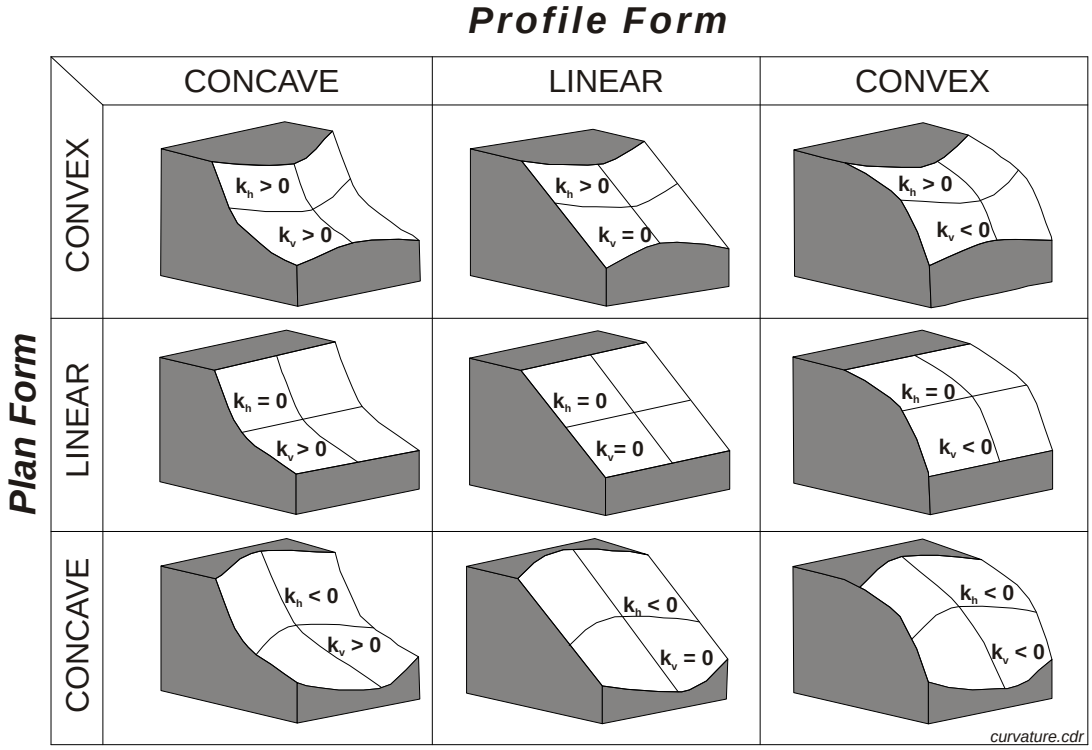

Figure 4-4: Classification of slope forms by plan and profile Curvature. (Modified from Summerfield (1991) and Florinsky (2000) (k_h…. Plan curvature, k_v….Profile Curvature).

4.2.4 LINEAMENT ANALYSIS

Several definitions exist for the frequently used term “lineament”. Hobbs (1904, 1912) defined a lineament as *“a significant line of landscape which reveals the hidden architecture of rock basement”*. O’Leary’s (1976) definition is more detailed and again points out the relation to the subsurface: *"a mappable simple or composite linear feature of a surface whose parts are aligned in a rectilinear or slightly curvilinear relationship and which differs distinctly from the pattern of the adjacent features and presumably reflects a sub-surface phenomenon".* A further definition describes them as *“long, often subtle linear arrangements of various topographic, tonal, geological and even geophysical and geochemical features”* (Drury, 1993). Drury (1993) proposed the term “linear feature” for a short (< 5% of image size) line in images. Often the term lineament is used in a specific structural geological context, as geological structures (e.g. faults, folds, bedding, and foliation) are frequently reflected as linear morphological features. Lineament analyses have also been performed for the mapping of glacial landforms (Barnett and Shirota, 2004; Smith and Clark, 2005). In the present analysis, the term “lineament” is used primarily to detect possible fault zones and other linear reflections of geological structures. Linear structures clearly related to human activities like roads, buildings, high voltage power lines or forestry operations were omitted from the analysis.

Lineaments can be mapped by visual interpretation (Leber et al., 1997; Massironi, 1999; Smith and Clark, 2005) or by digital techniques (Koike et al., 1995; Gülcan, 2005). The more frequently used visual interpretation is of course prone to subjectivity (Raghavan et al., 1993; Gupta, 2003). whereas automated methods may identify a significant number of lineaments without relevance (Gupta, 2003). An overview of methods and a summary of previous work can be found in Gülcan (2005).

Typical parameters derived are length and orientation of lineaments, as well as different measures for lineament density (Casas et al., 2000; Gupta, 2003; Kim et al., 2004; Ekneligoda and Henkel, 2006). For this study, lineament orientation, length distribution, relation of orientation and length, as well as a description of the regional distribution of lineaments with the help of simple maps and density maps were determined.

Frequently used data sources for lineament mapping are aerial (stereoscopic) photographs and satellite images. With increasing availability of digital elevation data in different resolutions, the use of DEMs and DEM derivatives has become an additional data source (Leber et al., 1997; Jordan et al., 2005; Smith and Clark, 2005; Arenas Abarca, 2006).

A lineament analysis covering entire Austria and therefore the Koralpe too was published by Buchroithner (1984). The lineaments were mapped from Landsat MSS images in scale 1:500.000. A much more detailed lineament analysis was done by Peresson and Decker (1998) during the early stages of the site investigation for the Koralm Tunnel. This work incorporated a DEM (50 m grid), a Spot-Pan black & white satellite scene (10 m ground resolution), a Landsat TM scene (band combination 7-4-

2 with 30 m resolution) and digitised boundaries of lithological units. A primary shortcoming of Peresson and Decker's (1998) analysis is the quality of the input data with respect to data artefacts (striping) and resolution of the input DEM. Resolution merging of the multispectral and the panchromatic satellite image proved valuable in the non forested regions of the Koralpe summit, however no improvement was achieved in forested areas, which cover the largest part.

The approach used by these authors was also used in this analysis. Input data were the space shuttle radar topographic mission (SRTM) elevation model and a 10 m DEM. Derivative hillshades were calculated for illumination azimuth intervals of 45° starting in the north (0°) to avoid unwanted suppression of lineaments parallel to the illumination direction (Mark, 1992; Smith and Clark, 2005). Mark's (1992) approach of creating a multidirectional, oblique weighted relief image was used to reduce directional bias. Angles of 45° and 65° were chosen as altitude for the illumination source. Combinations of those hillshades with adjusted transparency and the colour-coded DEM were also used. Additionally a Landsat ETM+ mosaic with a merged resolution of 14.25 m and a Radarsat scene (resolution 5m) were used as supplementary data for lineament mapping. The lineaments were mapped in different scales. Black and white (B&W) aerial photographies as well as colour aerial photographies provided were used in this analysis. Additionally, layers containing structural information like roads, buildings and others were used to exclude artificial, human related linear features.

As the appearance of a lineament is dependent on the scale of observation (Gupta, 2003), lineaments were mapped at several scales. A combined 1:50.000 and 1:25.000 scale mapping was done on the 10 m DEM. Furthermore mapping at a scale of 1:200.000 was performed on the 10 m DEM. Mapping on the 96 m DEM was performed at a 1:100.000 scale.

4.2.5 DRAINAGE SYSTEM ANALYSIS

Drainage systems are the result of multiple, interacting processes. Besides the exogenic processes, bedrock lithology and structure as well as endogenic processes play a major role in the development of drainage basins.

The balance between these processes is very sensitive to any kind of disturbance (Keller & Pinter 2002). Hence, active tectonic processes may be reflected in the structure of drainage systems. According to Burbank and Anderson (2001), drainage systems may record deformation events from the Holocene (<10 ka) to intermediate time scales (<400 ka, Pleistocene, approx. time of Mindel glaciation). Tectonic controls may be reflected by the shape of river courses, river patterns or basin form.

The analysis of the drainage system in this work includes the extraction of the drainage pattern from the 10 m resolution DEM and the delineation of the individual catchments. This was done by using ArcGIS 9.1 software. Prior to the extraction, a depressionless DEM was created with the Hydrology tools of the ArcGIS Spatial Analyst. This was followed by the calculation of “Flow Direction” and “Flow Accumulation”. “Flow Direction” is determined by finding the direction of the steepest descent from each cell (Jenson and Domingue, 1988). The “Flow Direction” raster is further used to calculate “Flow Accumulation”. “Flow Accumulation” is defined as the number of cells flowing into a cell (Jenson and Domingue, 1988). The stream grid was determined by using a conditional if/else evaluation (“Con” tool in the Spatial Analyst extension), assigning a raster cell value of 1, if a threshold value of cells flowing into a cell is exceeded and a “no data” value for all other cells. This threshold is thought to mark the limit above which a stream starts to flow. The resultant stream pattern was compared to the stream pattern raster layer provided by the BEV (equivalent to the one from 1:50.000 topographical maps) and the threshold value was optimized in several steps to the value which yielded the best visual fit. A value of >0.03 km² was found to yield the best results. 71 catchments were delineated by manually defining their pour points (Figure 4-5). For 53 of these catchments longitudinal river profiles were extracted with the help of the Easy Profiler V 9.1 tool (Huang, 2006) using the Douglas-Poiker generalisation algorithm (Douglas and Peucker, 1973), which uses only those points along the river which define segment boundaries. The longitudinal profiles were analysed with respect to the presence of knickpoints in their course. Knickpoints were visually identified. Additionally, the concavity index C_A (Snow and Slingerland, 1987) and the stream gradient index SL (Hack, 1973) were calculated for the longitudinal river profiles.

4.2.5.1 GORGES

A gorge is defined as a “deep and narrow vertically sided valley” (Whitten and Brooks, 1972). In this work the term gorge is also used for vallies with steep, but not vertical sides and abundant cliffs.

Generally two types of gorges can be distinguished: Gorges cutting through a topographical barrier ("transverse gorge" sensu Scheidegger, 2004) and gorges reaching into a mountain range, generally in an obtuse angle to the mountain front ("watershed gorge" sensu Scheidegger, 2004). Transverse drainage is defined as a river cutting transversally across geological structures like mountain ranges, fold belts, or the regional tectonic fabric (Oberlander, 1984; Stokes and Mather, 2003; Scheidegger, 2004; Stokes et al., 2008). Gorges in such a setting may be caused by several mechanisms (Stokes et al., 2008): Stream capture by headward erosion, antecedence and superposition. A river is said to be "antecedent", if it maintains its course across a rising area (Twidale, 2004; Stokes et al., 2008). Superposition means that a river removes a sedimentary cover and becomes imprinted on a structurally and/or lithologically different geological unit (Oberlander, 1984; Twidale, 2004; Stokes et al., 2008).

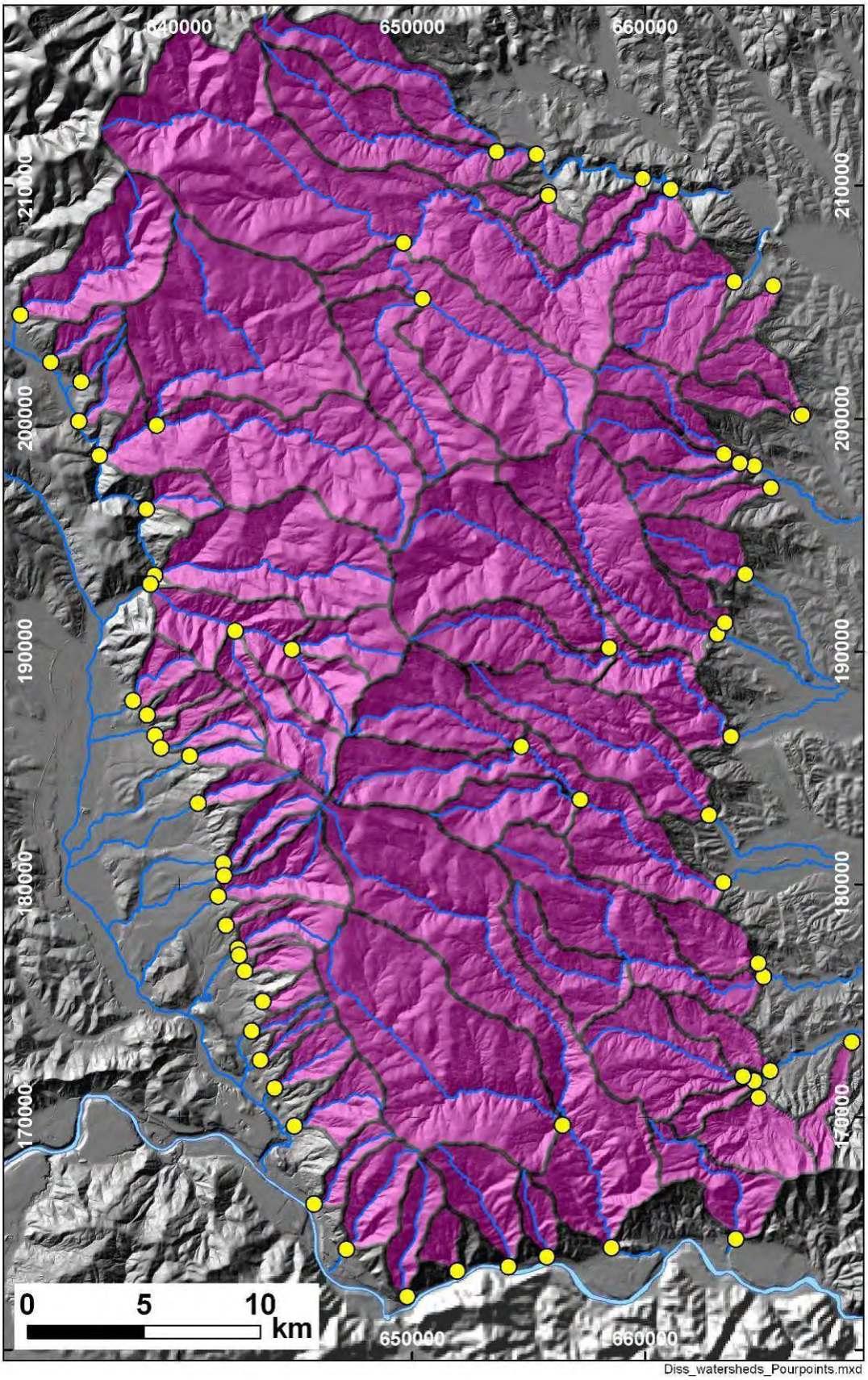

Figure 4-5: Catchments of the Koralpe (truncated to the basement rocks) and their pour points (yellow points).

4.2.5.2 STREAM AND DRAINAGE PATTERNS

In this work “stream pattern” is defined as the design formed by a single drainageway and “drainage pattern“ is defined as the design formed by the aggregate of drainageways in an area regardless of whether they are occupied by permanent streams (Howard, 1967).

Stream and drainage patterns do not only provide clues to fracture patterns and bedrock type, but they may also assist in unravelling local and regional geological chronology (Twidale, 2004). The description of basic drainage patterns and their interpretation goes back to the paper of Zernitz (1932). Later papers (e.g. Howard, 1967; Twidale, 2004) are based on this work and present some modifications, as transitions between different basic drainage patterns are quite frequent in nature. Structurally controlled drainage patterns with a possible relevance for alpine areas are trellis, rectangular and contorted (Figure 4-6). Structural control of stream patterns may also be revealed by directional statistics of river courses and lineaments or measurements of geological structures (Scheidegger, 2004). The analysis of stream patterns includes the identification of angular river bends (abrupt changes in drainage direction). Additionally the channel index (Mueller, 1968) was calculated as a simple measure for the deviation of the main stream of a catchment from the general drainage direction. It is defined as the ratio of the stream length L_c to the length of the line connecting source (projected to the drainage boundary) and outpour point L_a (Figure 4-7). According to Mueller (1968), the channel index can be described as an index of total sinuosity, including hydraulic and topographic sinuosity.

4.2.5.3 BASIN SHAPE AND SYMMETRY

Basin shape may be an indicator for regional tilting or for structural resp. lithological controls. In tectonically active mountain ranges, drainage basins frequently show an elongated form (e.g. Bull, 2009). Basin shape is often described by index values (Horton, 1932; Morisawa, 1958; Cannon, 1976; Vörösmarty et al., 2000). An overview of the numerous different basin shape measures is given by Zavoianu (1985) and, more critically, by Jarvis (1981). Jarvis (1981) stresses the chaos in terminology, where the same indices may be used under different names. Additionally he points out that several ratios of long- to short-axis lengths are identical to each other or are related by similar mathematical relations. For example Vörösmarty (2000) introduced a basin shape index to describe basin elongation, which can be directly deduced from Schumm’s (1956) elongation ratio. Frequently basin shape is related to distinct reference shapes like a circle or an ellipse. In some of the indices (e.g. circularity ratio RC, Miller, 1953) basin perimeter is used despite its fractal, scale dependent nature (Bárdossy and Schmidt, 2002). Despite these possible pitfalls, shape indices may be useful to compare the morphology of basins and to reveal tectonic influences. Basin shape may also be described in terms of symmetry, taking the main river as a symmetry axis. Basin asymmetry may result from regional tilting followed by a shift of rivers towards the downwards moving edge of the basin (Hare and Gardner, 1984; Cox, 1994).

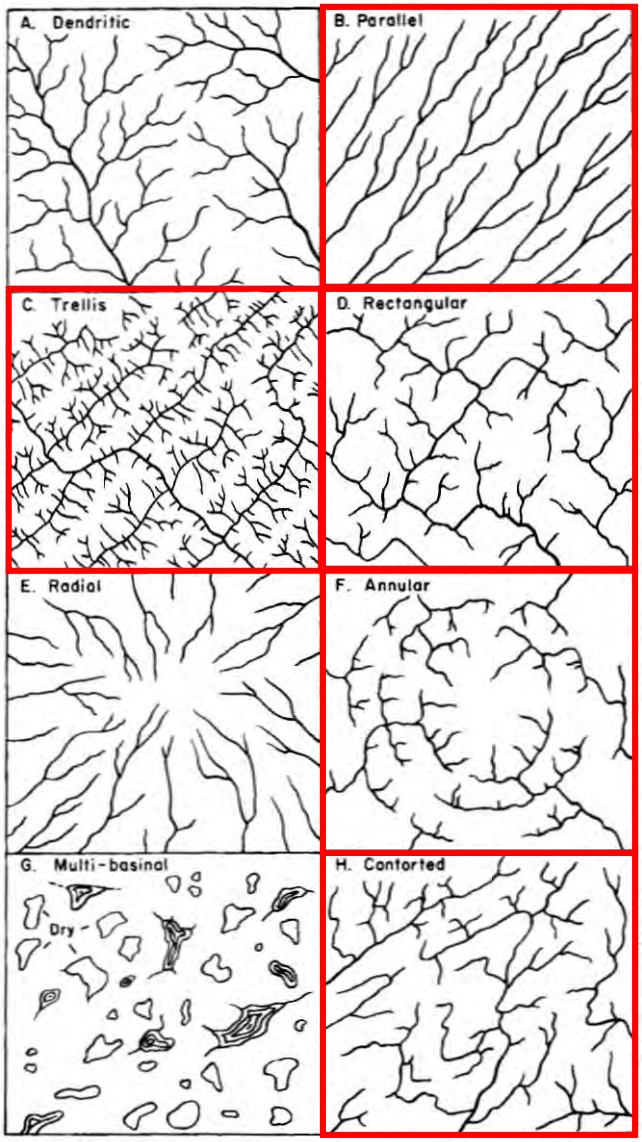

Figure 4-6: Basic drainage patterns after Howard (1967) (Bloom, 1998, Figure 12-15). Patterns with structural controls are highlighted by red squares: (a) Dendritic, (b) Parallel, (c) Trellis, (d) Rectangular, (e) Radial, (f) Annular, (g) Multi-basinal, (h) Contorted.

The following measures are used in this study: The *basin asymmetry factor AF* (Hare and Gardner, 1984), the *elongation ratio* E_r (Schumm, 1956), the *basin ellipse ratio or ellipticity index* (Stoddart, 1965) and the *form factor* (Horton, 1932).

The *basin asymmetry factor AF* is defined as the ratio of the area of the right basin half (view downstream) and the area of the entire basin times hundred (Figure 4-8). AF may help to reveal tilting perpendicular to the main drainage direction (Keller and Pinter, 2002). A value >50 indicates tilt to the left, with the area of the right basin half larger than the left basin half. Values around 50 indicate a symmetric drainage basin, whereas values <50 indicate a tilt to the right. However basin asymmetry does not necessarily result from tilting but may also be caused by rock structure (bedding planes, foliation) or by differences in vegetation or weathering within the basin (Keller and Pinter, 2002). A modified asymmetry factor AF_{mod} was introduced, by simply converting AF into values ranging from 0 to 50. An $AF_{mod} = 0$ indicates a symmetric basin. The higher the value the more asymmetric the basin is. For multidirectional drainage, like in the case of the Koralpe, AF_{mod} facilitates the comparison of catchments draining into different directions. The orientation of a possible tilt is expressed by the azimuth of the vector perpendicular to the general drainage direction in the direction of the possible tilt. It was plotted as an arrow together with AF and AF_{mod} to facilitate the detection of regional trends of asymmetry resp. tilt (Figure 4-8).

Schumms (1956) *elongation ratio* E_r is defined as the quotient of the diameter of a circle with the same area as the basin and the maximum basin length L_a. E_r measures the similarity of a basin to a circle. The higher E_r gets, the more the catchment resembles a circle (Vörösmarty et al., 2000). Vörösmarty et al. (2000) note for stream orders 1 to 6 a global mean value of 0.52 to 0.82.

The shape of a basin is is also compared to the shape of an ellipse (“basin ellipse”, Figure 4-7). The long axis of the ellipse L_a is defined as the line connecting the source at the watershed boundary with the outlet point, the short axis L_b is defined as the maximum width of the basin perpendicular to L_a. The ratio of these axes has been termed “*ellipticity index*” by Stoddart (1965) and was used for the description of the shape of atolls. In this study this index is called “*basin axes ratio*”. The smaller L_a / L_b, the more elongated the basin is parallel to L_a. Values larger than 1 indicate an elongation perpendicular to L_a.

Hortons (1932) *form factor F* is calculated by the ratio of the drainage basin area A_b to the squared basin length L_a. F equals 1 for a square and approaches a theoretical value of 1.273 for a perfect circle (Zavoianu, 1985). The lower the value the more elongated the basin is.

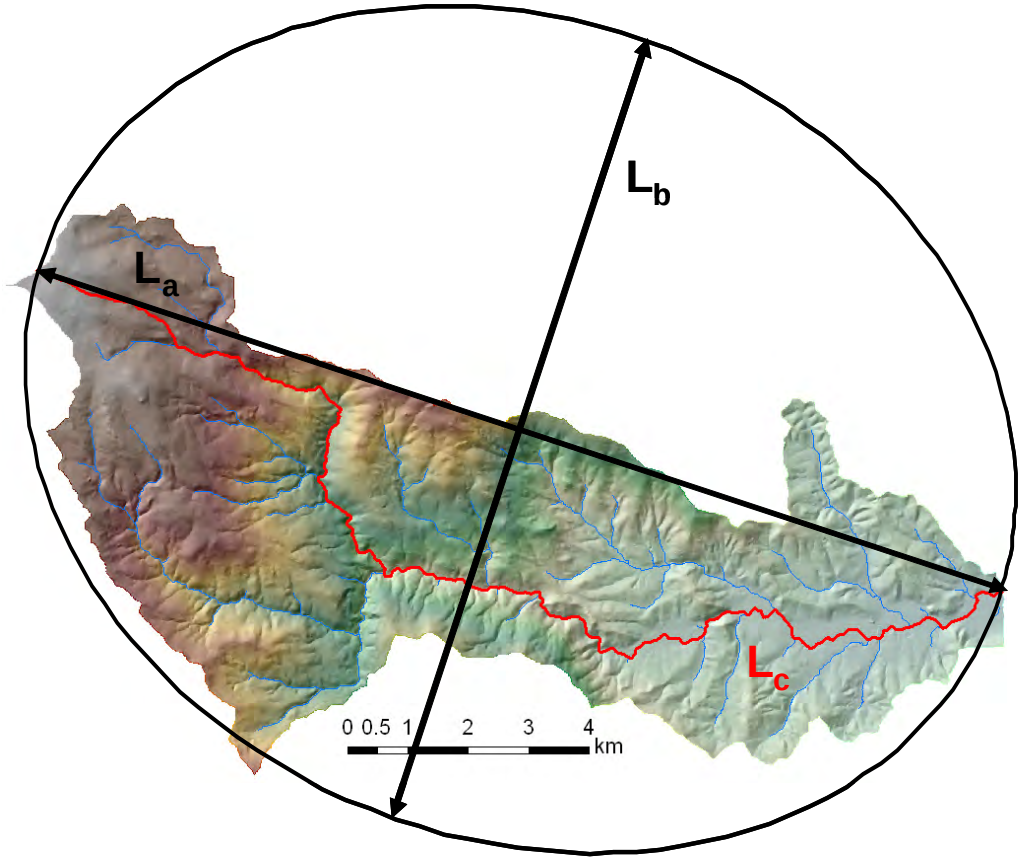

Figure 4-7: Definition of the basin ellipse. Red river is the main stem of the catchment with the length L_c, L_a is the long axis of the catchment, L_b the short axis (Catchment: Weiße Sulm, Eastern Koralpe).

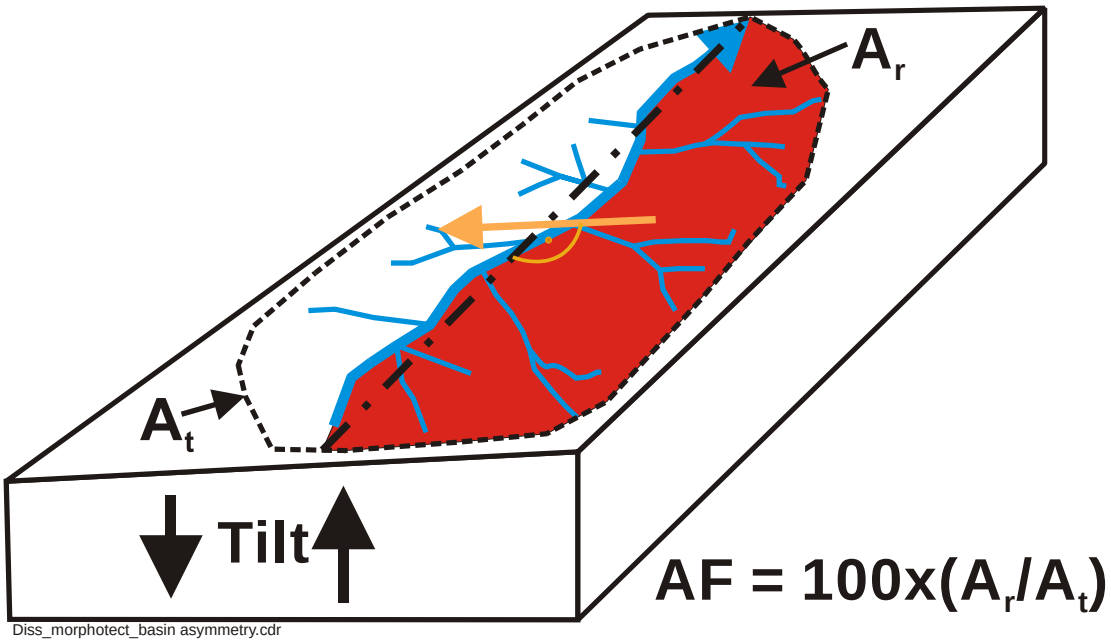

Figure 4-8: Basin asymmetry factor AF after Hare & Gardner (1984), a possible indicator for tilting (sketch modified after Keller and Pinter, 2002). A_r is area of right basin half, A_t is total basin area. Orange arrow indicates direction of tilt in plan view, perpendicular to general drainage direction (dash-dotted line).

4.2.5.4 LONGITUDINAL RIVER PROFILES

Longitudinal river profiles are cross sectional plots of a river's elevation from its source to its mouth (Keller and Pinter, 2002). Rivers in equilibrium are called "graded" (e.g. Hamblin and Christiansen, 1995) and show a smooth, concave longitudinal profile with steeper gradient near the source, getting continuously flatter towards the mouth (Figure 4-9). Disturbances of this equilibrium result in new adjustments of the system to achieve a new state of equilibrium and may be visible in the profiles as "knickpoints" or "knick zones". Such disturbances may be caused by active tectonics e.g. by displacement along a fault (e.g. Sung et al. 2000), by stream piracy, variations in the uplift rate of a region (Keller and Pinter, 2002), lithological variations along a river profile (Seidl et al., 1994; Burbank and Anderson, 2001) or even by human causes like the erection or operation of a hydro power scheme (Germanoski and Ritter, 1988, Mosley, 1984). The rates of knickpoint migration are not well known (e.g. Seidl et al., 1994; Burbank and Anderson, 2001). Mosely (1984) documented a 2 m high knickpoint, caused by lowering of the local base level, to migrate 1 km in less than three months in an alluviated valley. Knickpoint propagated in basaltic rocks of Hawaii for more than 2 mm per year (Seidl et al., 1994). For the northwestern Himalaya river incision rates into bedrock, calculated from abandoned river-cut terraces, yielded values of 2 to 12 mm/a (Burbank et al., 1996), indicating knickpoint recession rates of up to 1 m/a (Burbank and Anderson, 2001). Whipple et al. (2000) described incision rates into bedrock (Jurassic sandstone and siltstone) of 0.01 to 0.1 mm per year. Rates of 10m/ka were derived from cosmogenic ^{10}Be data in a landscape of active normal faulting (Commins et al., 2006).

All the causes for knickpoint formation except erodibility contrasts in the bedrock of a reach can be subsumed under the term "changes in base level". The concept of base level was introduced by Powell (1875). Base level is the elevation at which a river is no longer able to erode below its bed. Normally this is the sea level, also called the *ultimate base level* (e.g. Bloom, 1998). In contrast, the *local base level* is formed by regional water surfaces like lakes (Burbank and Anderson, 2001). For the Koralpe region the ultimate base level is the Black Sea. The Mur, the Lavant and the Drau (Drava) represent local base levels in the surrounding basins. Further local base levels are the artificial water reservoirs within the Koralpe (Figure 4-33). In this study, knickpoints were identified in profiles by visual examination. To assess their regional distribution, their location is shown in maps and compared to the location of lithological boundaries and fault zones. Additionally the knickpoints were analysed for their elevation distribution.

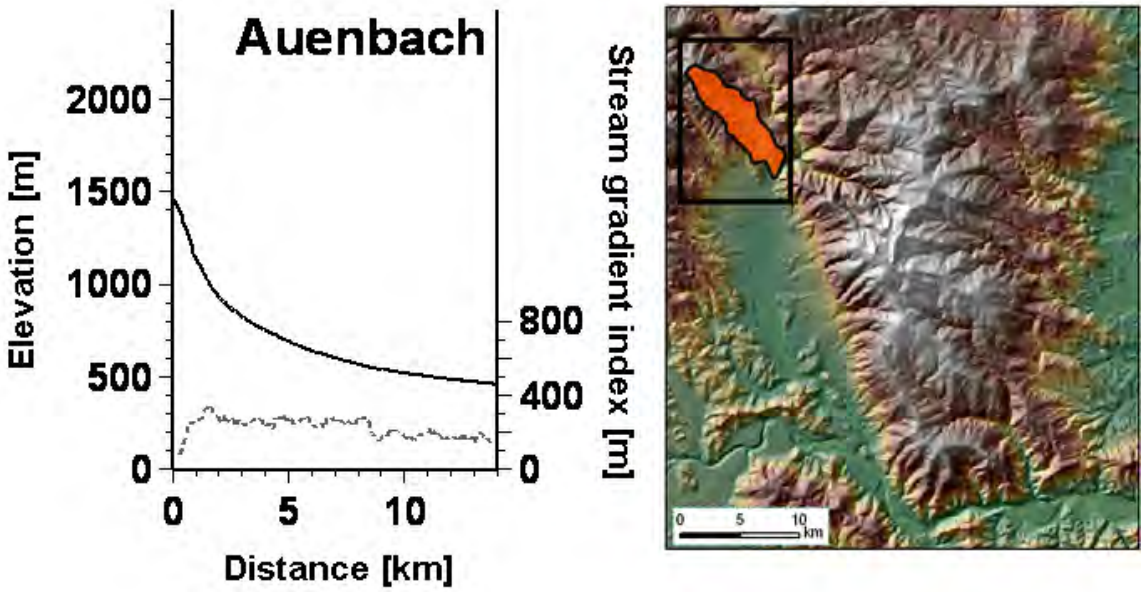

Figure 4-9: Example of a graded river profile (Auenbach) from the NW working area. The catchment follows the Lavanttal fault. Map on the right side shows location of catchment (red area). For the definition of the stream gradient index refer to Figure 4-11 and the text below.

To compare the different river profiles and to identify abnormal river stretches and knickpoints several indices were calculated: The *concavity index* (Snow and Slingerland, 1987) is defined as $C_A = A_1/A_2$ (Figure 4-10), not to be mixed up with the concavity index used in the slope-area relationship (Sklar and Dietrich, 1998; Kirby et al., 2003). A_1 is the area between the profile curve and a straight line connecting the profile endpoints and A_2 is the triangular area above the straight line connecting the two endpoints of the profile (Snow and Slingerland, 1987). If the straight line intersects the profile curve (convex profile) then this part of A_1 above the straight line is taken as a negative value, reducing the overall area of A_1. C_A was calculated for normalized river profiles. According to Snow and Slingerland (1987), C_A is significantly affected by discharge, sediment discharge and sediment diameter. A C_A theoretical value of 0 represents a straight line. C_A becomes larger, the more concave a river gets (Radoane et al., 2003). Generally concavity should increase with the age of the river (Snow and Slingerland, 1987), as the profile approaches an equilibrium ("graded river"). However, Radoane et al. (2003) showed that there are deviations in linear-exponential equilibrium profiles, if tectonic uplift prevails over river erosion. Duvall et al. (2004) showed for the Santa Ynez Mountains (California) a strong relationship between concavity index and bedrock strength. Streams that cross areas rocks of different competence showed variable profile form.

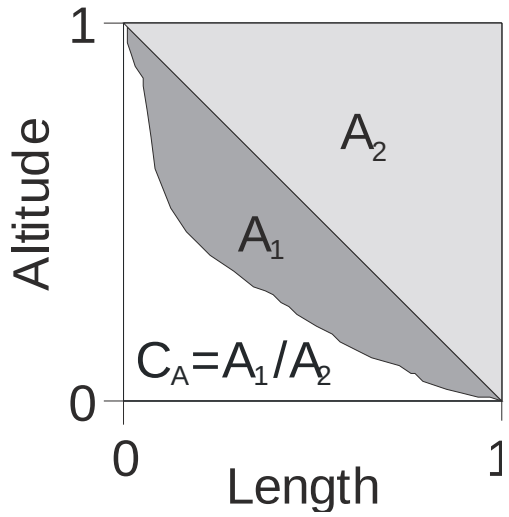

Figure 4-10: Concavity index C_A (Snow & Slingerland, 1987). A_1 represents the dark grey area above the longitudinal river profile, A_2 the triangular area above the straight line connecting the two endpoints of the profile. The two axes are normalized to allow a comparison of different river profiles.

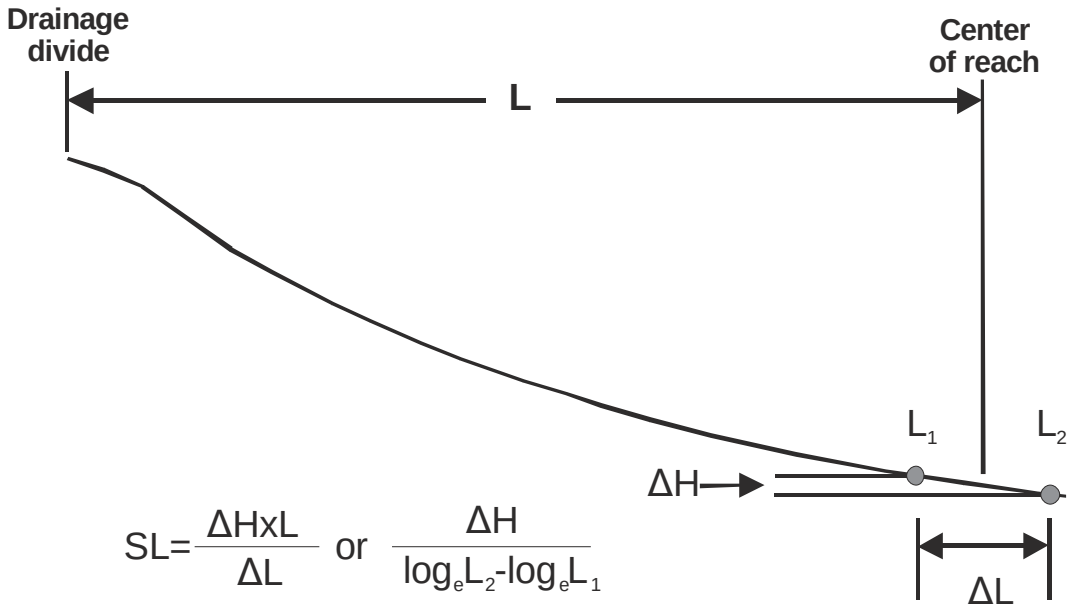

Figure 4-11: Definition of stream gradient index (after Hack, 1973, Figure 1).

The *stream gradient index* SL (Hack, 1973) is defined as shown in Figure 4-11. SL is calculated for the longest stream in a catchment. The stream gradient index indicates anomalously steep reaches of a stream and helps to compare streams of different sizes. It's sensitivity to changes in stream slope makes it a valuable tool in the study of active tectonics with a prevailing vertical displacement component (Keller, 1986). However, as it is also influenced by rock strength, discrimination from the effects of tectonics may be difficult.

For the calculation of SL, the river profiles were resampled in 100 m intervals. Due to its length, the profile of the river Lavant was resampled in 500 m intervals. For map

presentations of SL the coordinates of the midpoints of the reaches for which SL was calculated were taken.

4.2.6 MOUNTAIN FRONT SINUOSITY

Mountain front sinuosity S_{mf} is defined as the ratio of the length of the topographic mountain-piedmont junction (L_{mf}) to the overall length of the mountain front L resp. the range bounding geologic structure (Figure 4-12; Bull and McFadden, 1977; Bull, 2007). This index value is indicative for the tectonic activity along a mountain front. It reflects the balance between slope and stream processes and vertical active tectonics (Keller, 1986). A higher index indicates a more irregular mountain front. This index was introduced in arid regions (Bull and McFadden, 1977) with clearly defined mountain ranges bordered by clear pediment plains. Bull and McFadden (1977) defined three "tectonic activity classes" characterized by local base-level processes, typical (arid) landforms and exhibiting a typical range of mountain-front sinuosity. For class 1 ("Highly active") the sinuosity ranges from 1 to 1.5, for class 2 ("moderately active") from 1.5 to 3 and for class 3 ("inactive") from 3 to 10 (Bull, 2007).

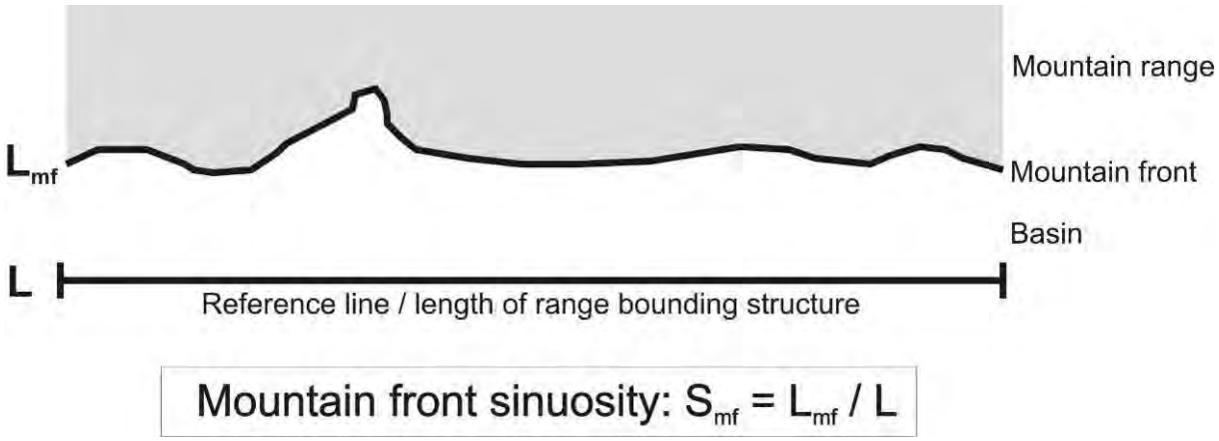

Figure 4-12: Mountain front sinuosity and the parameters involved in its calculation (after Keller and Pinter, 2002).

Mountain front sinuosity has been frequently used to asses the tectonic activity of mountain range boundary faults (Bull and McFadden, 1977; Cuong and Zuchiewicz, 2001; Verrios et al., 2004; Zovoili et al., 2004; Popotnig et al., 2007). Bull and McFadden (1977) noted that the value is depending on the scale and detail of the input data and the accuracy of geological mapping respectively. It is also obvious that the size of the mountain front section under investigation will have a severe influence on the outcome. Additional subjectivity arises from the designation of the mountain piedmont-junction (Burbank and Anderson, 2001), which is especially true in a non-arid setting as given by the case of the study area.

Difficulties in defining the mountain front arise along the eastern front of the Koralpe. Here, neotectonic activity is quite low (Reinecker, 2000). For the western slopes towards the Lavanttal the tectonic imprint of the Lavanttal fault is quite clear and a mountain front can be more clearly defined. First the index was calculated using the bedrock boundary as exposed in the geological maps. In areas with a massive slope

debris cover this leads to an over estimation of the mountain-front length. In a second step, the mountain front was redrawn across areas of mapped slope debris and mass movements. Alluvial valley floors incising far into the Koralpe were truncated near to the outer mountain front. These valleys can be considered as part of the foot wall block of the Lavanttal fault, and a truncation of their slope-valley floor junction emphasizes the mountain front (Bull, 2007).

If the location of a range-bounding fault is not known, the straight line connecting two points of the mountain-piedmont junction is used for L (Bull, 2007). The perimeter of isolated “inselbergs” has to be added to the mountain-piedmont junction. There is no clear definition of the reference length L, as it depends on the specific situation of the study site. In some cases L is shown as a tangent to the mountain front (Bull and McFadden, 1977), whereas in other cases it is a straight line connecting the two endpoints of the analysed mountain front stretch (Bull, 2007). In the best case it follows a visible fault line. In this work both ways were used to calculate the sinuosity value. However, self-similarity (fractality) of landscapes (Mandelbrot, 1967; Turcotte, 1997) implies that the mountain front sinuosity values are scale dependent. Application of this method has to consider this scale dependency (Keller and Pinter, 2002).

4.3 RESULTS

4.3.1 VISUAL GEOMORPHOLOGICAL INTERPRETATION

The Koralpe Range is characterized by steep slopes in the west and the south, whereas the eastern segment shows a gentler dipping slope (Figure 4-13). It exhibits a trapezoid shape in map view, with clearly defined western and southern mountain fronts. The eastern mountain front is strongly dissected by the drainage system, indicative for an inactive mountain front (e.g. Bull, 2007).

The drainage system of the Koralpe is characterized by gorgelike reaches, intersecting into the basement rocks (Figure 4-14). The most impressive ones are the Twimberg gorge and the Teigitsch gorge in the Northern Koralpe (Figure 4-13).

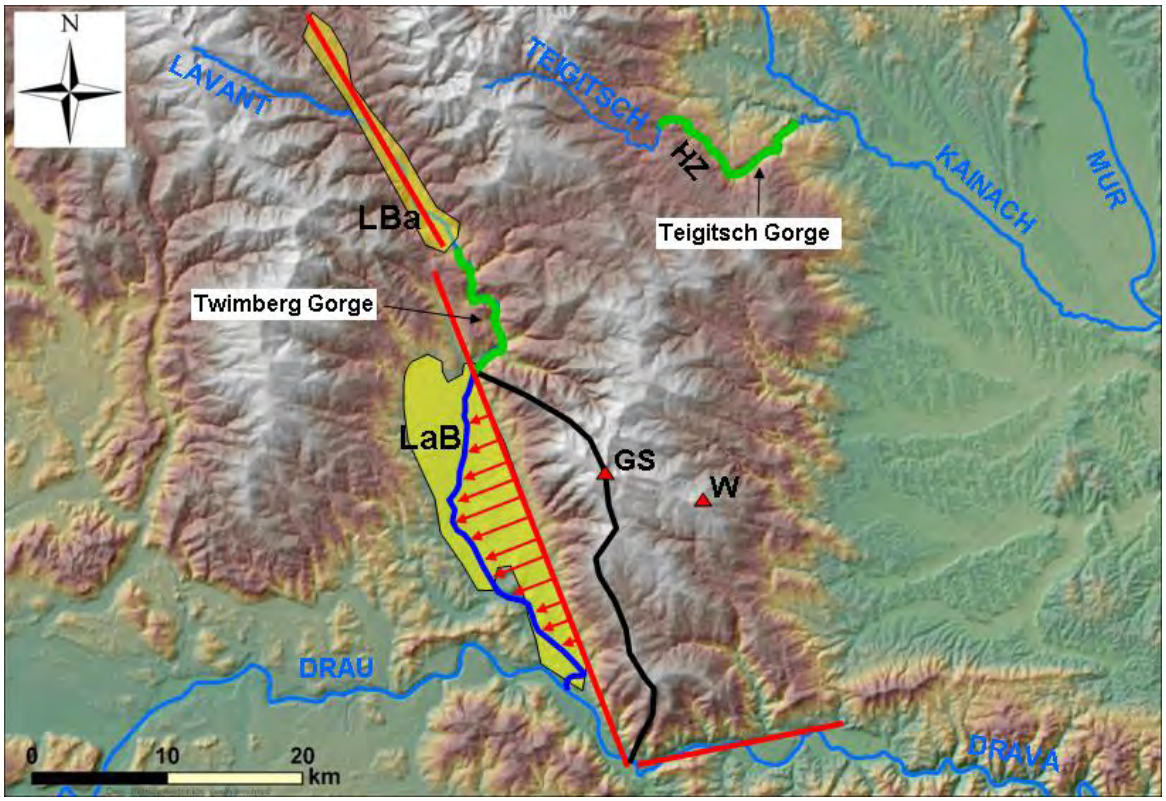

Figure 4-13: Overview map of the Koralpe and the adjacent Saualpe (96 m resolution DEM). Red lines mark the Lavanttal fault and a hypothetic fault along the southern margin of the Koralpe. Abbreviations in the map: HZ…Herzogberg, LBa…Bad St. Leonhard Basin, LaB…Lavanttal Basin, GS… Großer Speikkogel, W…Wolschenek.

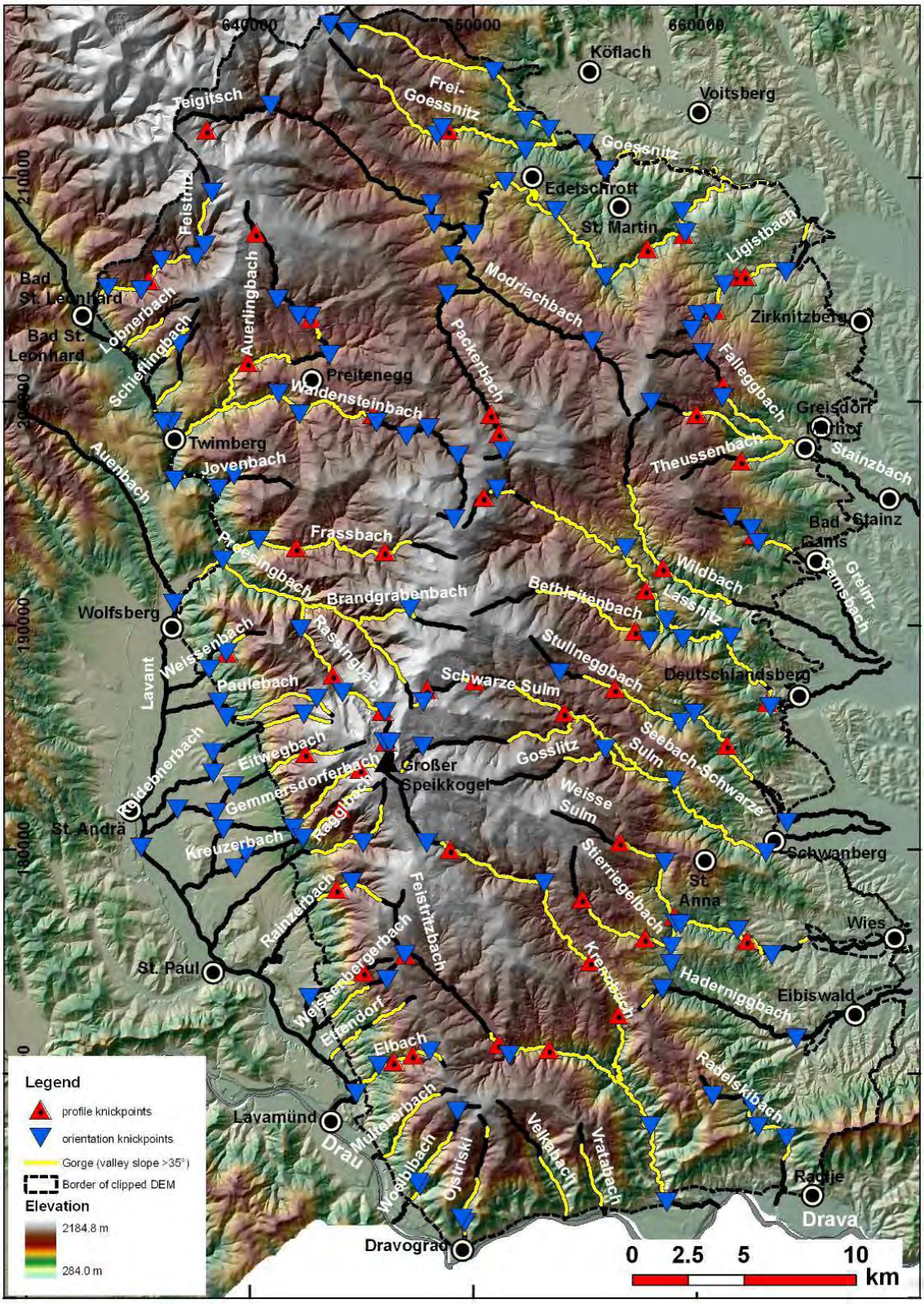

Figure 4-14: Combined hillshade-colour shaded visualization of the elevation data set and the main streams of the Koralpe. Yellow segments of the streams are characterized by steep, partly gorgelike valley slopes. Triangles mark profile knickpoints (red) and orientation knickpoints (blue).

The Twimberg gorge forms a transverse gorge, cutting through the metamorphic rocks of the Kor-Saualpe block and connecting the “Bad St. Leonhard Basin” and the “Lavanttal Basin” (Figure 4-13). Both basins are of Miocene age and essentially controlled by the Lavanttal fault system. This fault zone is characterised by cataclastic fault rocks with mechanical properties that are only fractions of their metamorphic protoliths. A width of several hundred meters has been documented for this fault zone in the exploratory tunnel for the Koralmtunnel (Fasching et al., 2008) and in the Gräberntunnel (Nowy and Bilak, 2003), the latter in the direct vicinity of the Twimberg Gorge. However, the Lavant river does not follow the fault zone resp. the shortest path connecting the two fault segments in this area (e.g. along the Auenbach, Figure 4-14).

Watershed gorges are frequently present in the realm of the Koralpe. The most prominent one, the Teigitsch, is found in the Northeastern Koralpe (Figure 4-13, Figure 4-14). Its course is characterised by two nearly rectangular changes in drainage direction from NE to SE, an indicator for basic structural control. The end of the gorge cuts through the NW-SE trending ridge of the Herzogberg in the SE and the Kreuzberg in the NW.

Along the Twimberg gorge WNW to W draining catchments show different drainage directions than the generally WSW draining catchments of the western slope of the Koralpe. East of Twimberg, the catchments of the Waldensteinbach, the Auerlingbach and towards the Styrian Basin the Teigitsch and the Gössnitz form a depression between the Koralpe in the south and the Stub- and Gleinalpe in the north. North of the Twimberg gorge, small, WSW draining catchments dominate the morphology along the eastern margins of the Bad St. Leonhard Basin.

Within the Lavanttal Basin the Lavant shifts is course from the eastern towards the western basin margin (Figure 4-13). The maximum deviation of the river from the western mountain front of the Koralpe coincides with the maximum elevation of the drainage divide of the Koralpe. Clearly visible in the elevation model are the large alluvial fans spreading from the Koralpe into the Lavanttal Basin. This indicates massive supply of sediment hindering a linear course of the river parallel to the Lavanttal fault (Figure 4-13). There is no systematic deflection of the creeks draining the western Koralpe, which would be an indication of neotectonic activity.

South of Lavamünd (mouth of the Lavant into the Drau / Drava) the slopes of the Koralpe exhibit triangular facets (Figure 4-15). Such facets may indicate normal faults along the mountain front (e.g. Bull, 2007) or erosional escarpments (Bull, 2007). In the present case both are possible, on the one hand the western margin of the Koralpe is clearly defined by the Lavanttal fault, and on the other hand the Drau (Drava) River borders the Koralpe south of Lavamünd. North of Lavamünd facets are still present; however the degree of dissection is much higher. With the widening of the valley towards the north the facets become still less obvious. This coincides with the above described shift of the Lavant River from the foot of the Koralpe towards the western basin margin (Figure 4-13).

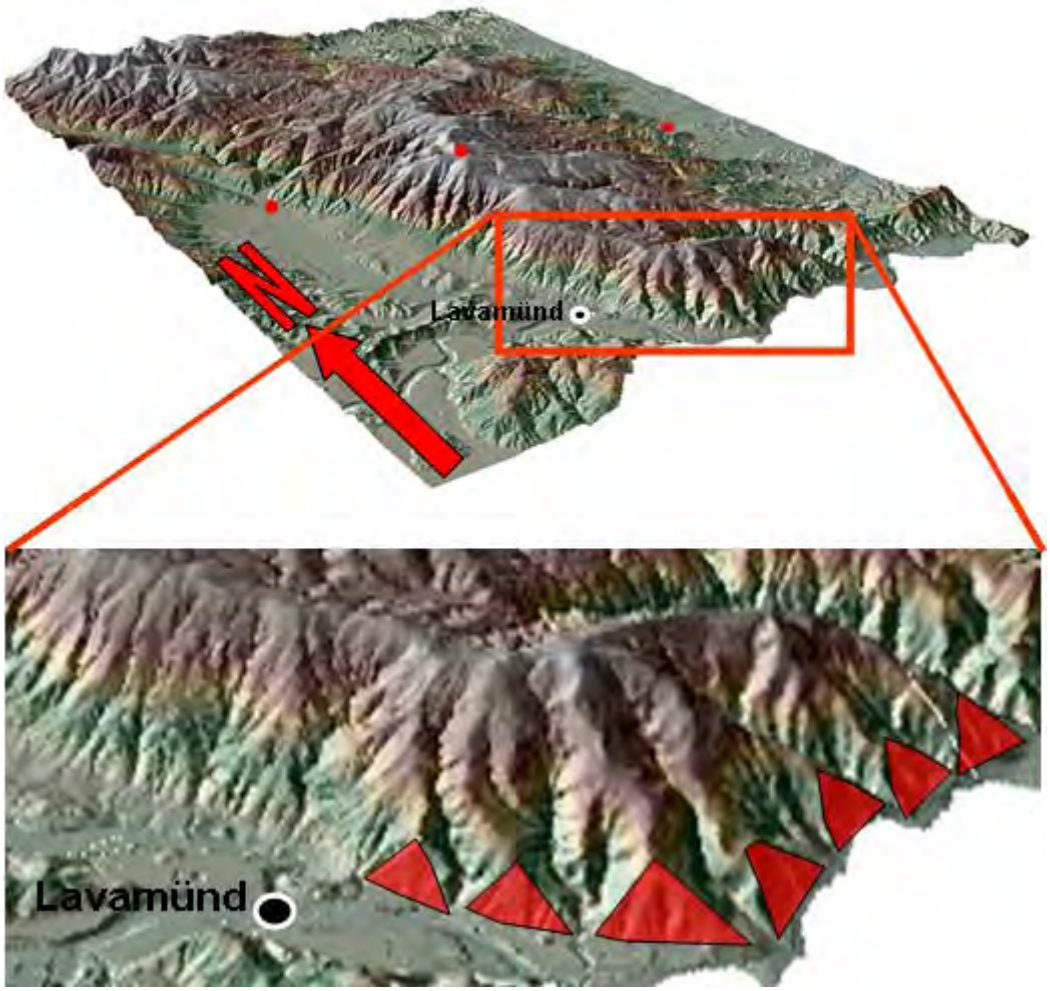

Figure 4-15: Colour shaded 3D view of the10 m DEM of the Koralpe. Note the asymmetric topography with the steep slopes towards W and the more gentle ones towards east. Detail shows triangular slope facets (red triangles) south of Lavamünd and along the Drau (Drava) valley

The hillshade visualization reveals a pronounced pattern of WNW trending linear features in the northern and eastern realm of the Koralpe. The NNW trending Lavanttal fault is clearly traceable in the hillshades (Figure 4-13, Figure 4-14).

Visualization allows the definition of six morphological domains ("morphounits") (Figure 4-16): The eastern Koralpe ("*Morphounit East*") encompasses the largest part of the working area. All of its catchments share the Mur River as a common receiving stream. The only exceptions are the Krennbach and the Feistritzbach (Bistrica), which, drain to the Drava (Drau) and incise deeply into the central eastern Koralpe. Based on their morphological impression the parts of these two catchments, north of the neighbouring to the Drava (Drau) draining catchments, are attributed to Morphounit East (Figure 4-16). Morphounit East is characterized by WNW-ESE trending valleys, which are separated by pronounced ridges. Yet several creeks show pronounced deviations from this rule of thumb (see chapter 4.3.7.1).

The depression like zone in the northern Koralpe, forming the transition towards the Stub- and Gleinalpe, is further discussed as "*Morphounit Northeast*". This zone is

drained by the catchments of the Waldensteinbach (draining to the Lavant River) and the Teigitsch (draining via the Kainach River to the Mur).

In the Northwest, the analysed DEM contains parts of the upper Lavant valley (Bad St. Leonhard Basin). Here a linear, fault controlled mountain front is developed. This region, consisting of a few smaller catchments of the Stubalpe, is subsumed as "*Morphounit Northwest*".

The Bad St. Leonhard Basin and the Lavanttal Basin are connected by the Twimberg gorge. Along this stretch the catchments of the Prössingbach and the Fraßbach, together with some smaller catchments, form the "*Morphounit Centralwest*".

From Wolfsberg, at the southern end of the Twimberg gorge, until Dravograd, the rivers, draining to the Lavant and the Drau (Drava), show, similar to Morphounit Northwest, a general, approximately SW directed drainage direction. The mountain front is clearly defined by the Lavanttal fault. Similar to the eastern Koralpe, the creeks show a high relief, yet within a much shorter horizontal distance. This zone will be discussed as "*Morphounit West*".

"*Morphounit South*" is formed by the catchments of the Koralpe, which drain to the Drava valley between Dravograd and Radlje, with the exception of the Krennbach/Feistritzbach catchments, which for the largest part are attributed to Morphounit East. The southern mountain front shows a linear trend too. It is assumed that this part of the Drava valley formed during Pliocene times, due to uplift of the Pohorje, causing the abandonment of an older river bed further south (Sölva et al., 2005b). This stretch of the Drava valley is probably associated with tectonic faulting too (Mioc, 1977), however seismicity in this region is low (e.g. Poljak et al., 2000, Anonymous, 2011) and faulting is poorly constrained.

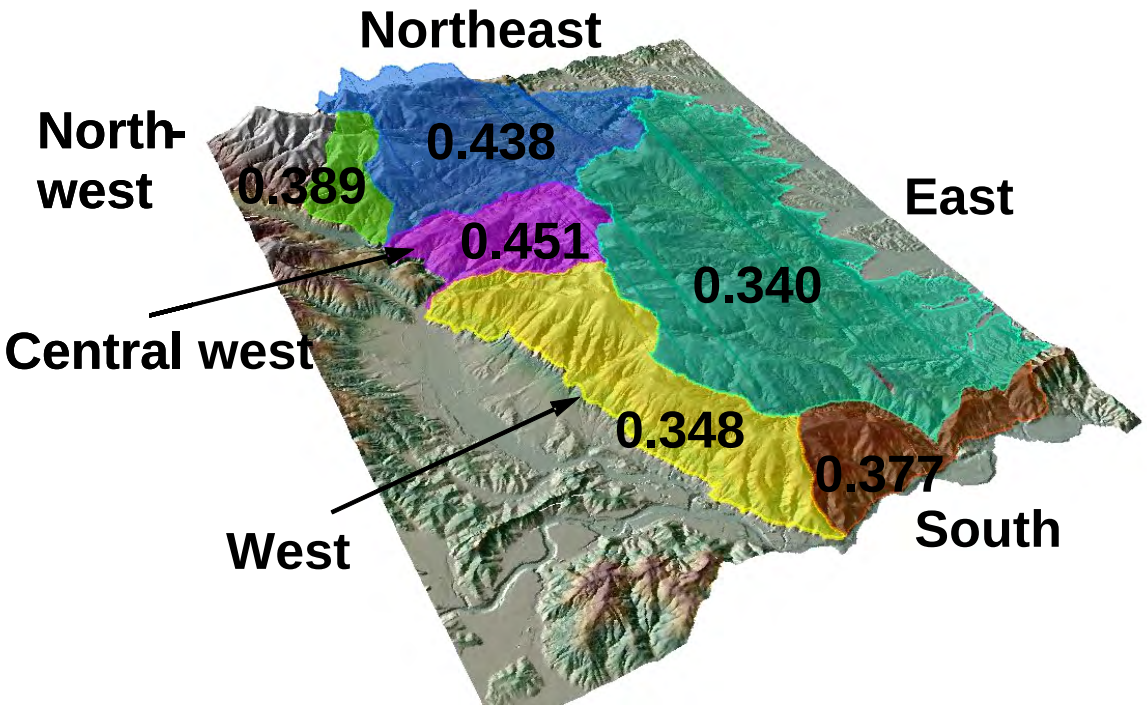

Figure 4-16: Colour-shaded 3D view of the10 m DEM of the Koralpe and a visual morphological division into six units. Numbers are the hypsometric integrals for the individual morphological units.

4.3.2 MOUNTAIN FRONT SINUOSITY

The transition of the Koralpe to the surrounding Neogene to Quaternary basins and the Drau (Drava) valley is, as described above, defined by mountain fronts, each showing a distinct appearance (Table 3, Figure 4-17). The sinuosity index of 2.2 for the entire western mountain front from Wolfsberg in the North to the bend of the river Drau (Drava) in the South (line No.2 in Figure 4-17) indicates a moderately active mountain front (Bull and McFadden, 1977; Bull, 2007). Based on morphotectonic considerations the western mountain front is divided into several segments: WSW-ENE trending faults with horizontal displacement seem to offset the mountain front several times (Figure 4-18). These faults are partly reflected in the lineament maps (Figure 4-55), but not yet verified in the field. The northern mountain front segment from Wolfsberg to Lavamünd has a sinuosity value of 2.3 to 2.4. This is slightly higher than the one for the entire segment (line No.2 in Figure 4-17), still indicating a moderately active mountain front. The southern segment from Lavamünd to the bend of the Drau (Drava) yields a lower value of 1.5 indicating a moderately to highly active mountain front. This is consistent with the values of 1.2 to 1.3 for the southern mountain front (Lines 8 and 9). According to the high sinuosity indices (3.9 to 4.4), the strongly dissected eastern mountain front represents an inactive mountain front of minor seismic activity (e.g. Reinecker and Lenhardt, 1999, Popotnig, 2009). However, in several places there are normal fault contacts between basement rocks and Neogene sediment (Chapter 3.2, Figure 3-16; Pischinger et al., 2008), confirming that also the eastern mountain front was locally fault controlled.

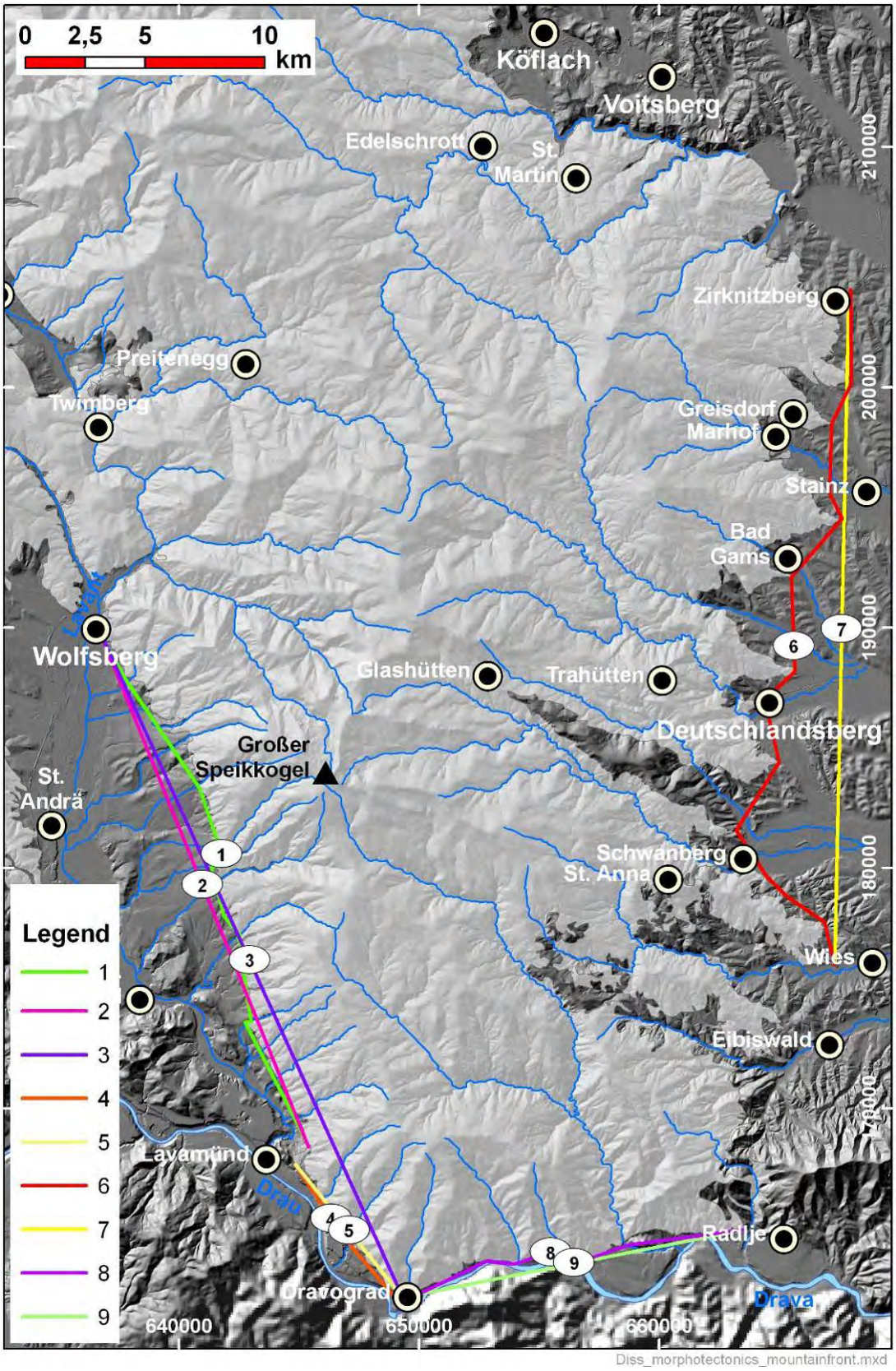

Figure 4-17: Mountain fronts of the Koralpe – Outline of the grey shaded areas represents the mountain front, coloured lines represent the reference lines for the mountain front sinuosity index calculation.

No.	Domaine	Location	baseline	L_{mf} [m]	L [m]	S_{mf}
1	West	Wolfsberg-Lavamünd	p	57361.9	25142.0	2.3
2	West	Wolfsberg-Lavamünd	l	57361.9	23492.1	2.4
3	West	Wolfsberg-Drau	l	69078.6	30788.0	2.2
4	West	Lavamünd-Drau	p	10482.9	7149.3	1.5
5	West	Lavamünd-Drau	l	10482.9	7108.2	1.5
6	East	Zirknitzberg-Wies	p	123185.8	31922.7	3.9
7	East	Zirknitzberg-Wies	l	123185.8	27898.5	4.4
8	South	Dravograd - Radlje ob Dravi	p	18258.3	14809.4	1.2
9	South	Dravograd - Radlje ob Dravi	l	18258.3	14549.7	1.3

baseline....referenceline type: p is a segmented polyline, l is a straight line
L_{mf}....length of mountain-front line, L....length of reference line, S_{mf}....mountain-front sinuosity

Table 3: Mountain front sinuosity values for the Koralpe. Numbers refer to Figure 4-17.

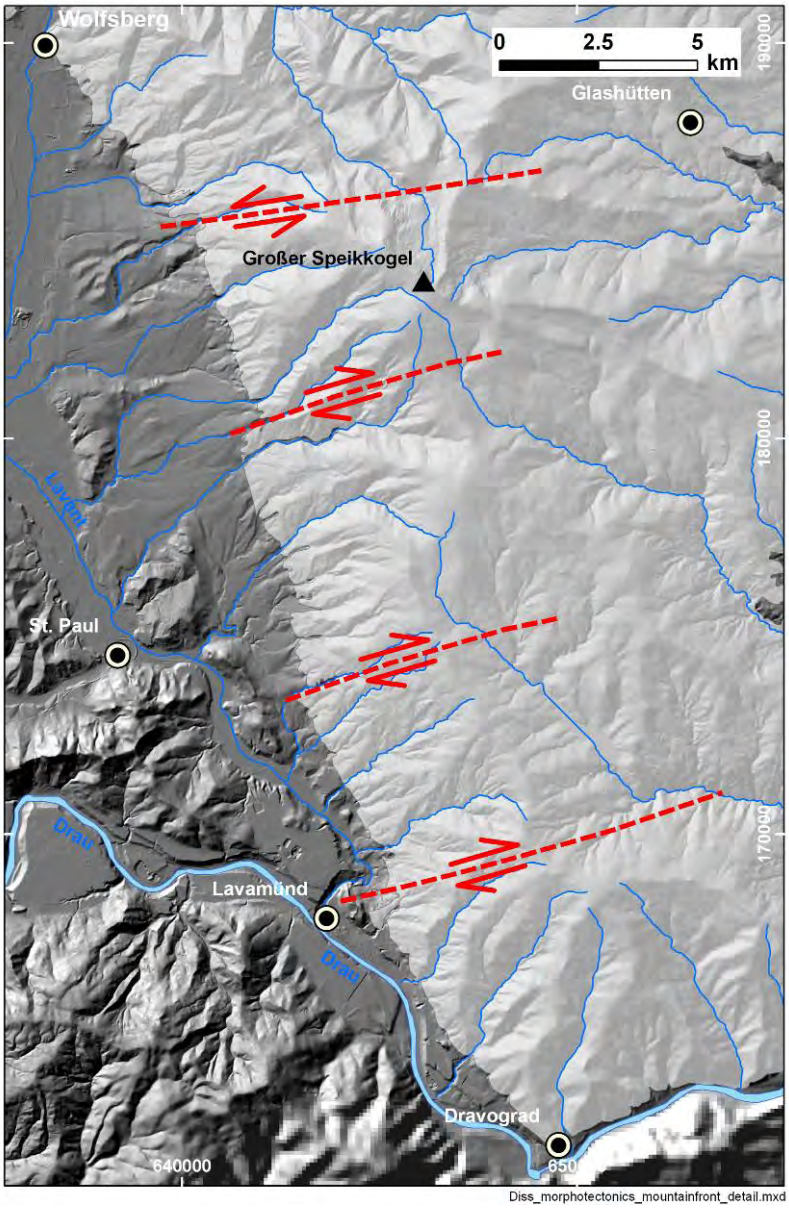

Figure 4-18: Western mountain front of the Koralpe and hypothetical faults with horizontal displacement. Light grey are marks the basement rocks.

4.3.3 HYPSOMETRY

The frequency distribution of the 10 m DEM (Figure 4-19) shows a peak at an altitude between 300 and 500 m a.s.l., which represents the basinal parts and a broad maximum between approx. 850 and 1050 m. Some minor peaks are caused by the presence of water reservoirs. The hypsometric integral (H_i) is smaller than 0.3 and the hypsometric curve has a concave shape (Table 4, Figure 4-19). To analyse a DEM of the Koralpe basement, the original data were clipped. This results in a more symmetric elevation distribution, but artefacts caused by water reservoirs are enhanced (Figure 4-19). The distribution is multimodal with a maximum between 860 and 1260 m. Further maximums are between 700 to 780 m and 400 to 420 m. Above the main maximum the distribution does not show such pronounced submaxima as below. However, the curve is not smooth. The truncation of the data set results in a higher H_i and a sigmoidal shaped hypsometric curve, with a convex middle part. According to Strahler (1952) and Keller and Pinter (2002), the shape of the curve and H_i indicate a relatively "mature" landscape, where a significant portion of land is present at higher elevations.

Relief maps were calculated for circular windows with radii of 100 m and 500 m (Figure 4-20). Within the Koralpe large areas with pronounced low relief are located in Morphounit Northeast and Morphounit East. These areas are better recognised in the relief map calculated with the larger window size. Less pronounced, elongated areas of low relief are visible in the ESE draining catchments of the eastern realm of the Koralpe. They define ridges separating the individual catchments and are better visible in the relief maps calculated with smaller window sizes (Figure 4-20).

The highest relief is found in Morphounit East and Morphounit West (Table 5). The highest mean elevation is found in the area of the Prössing catchment (Morphounit Central West). The northern units (northwest, northeast and central west) show a mean elevation >1000 m.

Dataset	N	A [km²]	Max [m]	Min [m]	Mean [m]	Median [m]	Mode [m]	sd [m]	Relief [m]	H_i
Entire DEM	22779189	2278	2185	284	849.2	790	468	387.4	1901	0.30
Clipped DEM	13151913	1315	2140	318	1006.7	1005	1078	347.5	1822	0.38
Eastern Alps	11288596	104821	3982	26.5	1282.6	1178	62	670.6	3956	0.32
Western Alps	8230119	76421	4780	-0.8	1427.0	1302	191	741.1	4781	0.30
Alps	19519499	181250	4780	-0.8	1343.5	1225	191	706.2	4781	0.28
Low Relief Area	1868697	17352	2426	110	866.4	807	437	432.7	2316	0.33
Tauern Window	818943	7604	3703	596	1962.9	1977	2007	523.1	3107	0.44

N... number of data, A...area, sd...standard deviation, H_i...hypsometric integral *Morphotectonics_DEM analysis.xls*

Table 4: Descriptive statistical parameters of the entire DEM and the DEM clipped to the outcropping basement rocks (DEM resolution is 10 m,) for the SRTM DEM of the Alps and several subsets (See Figure 4-28 for location).

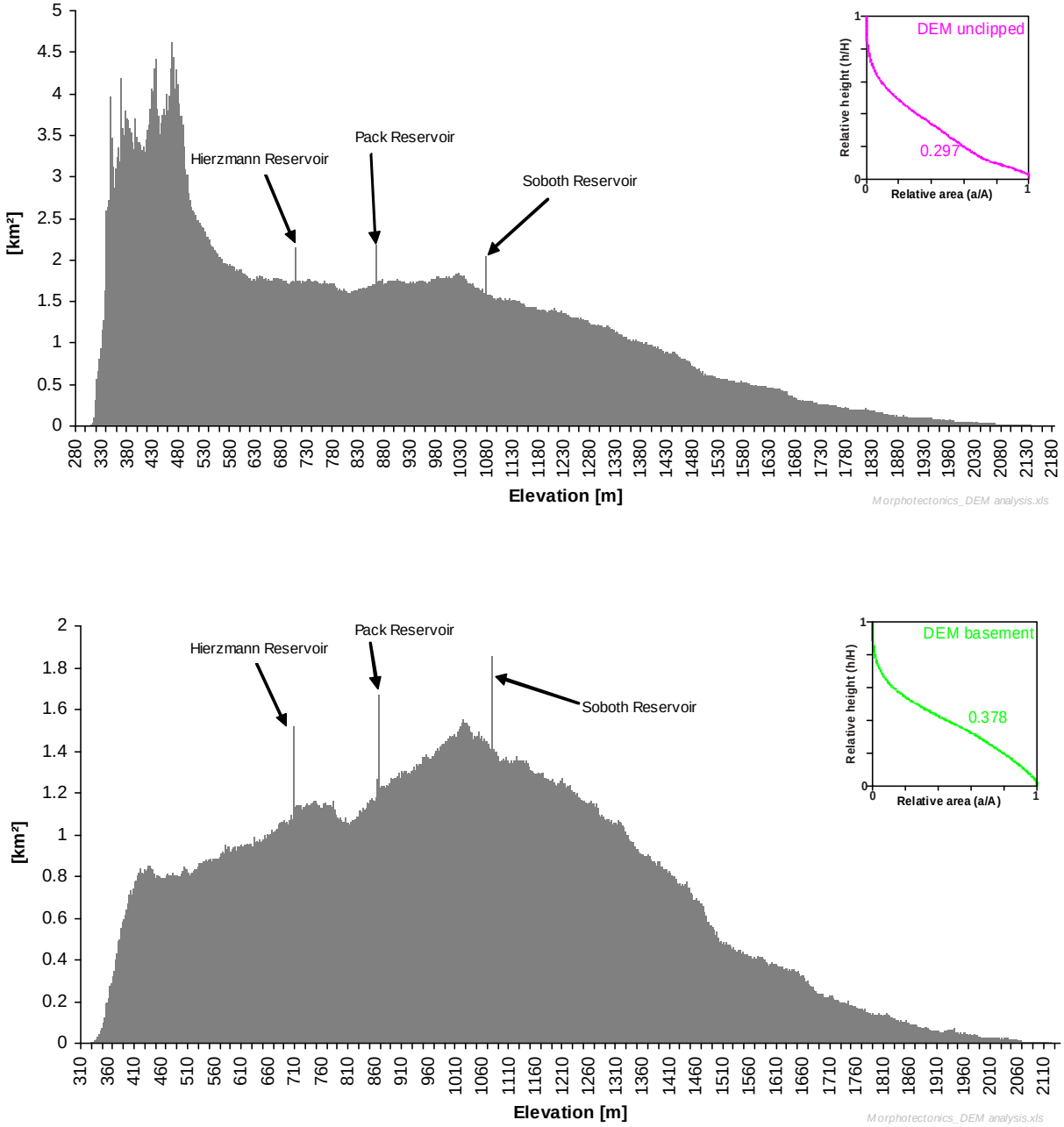

Figure 4-19: Frequency distribution of elevation for the entire DEM (upper graph) and for the DEM clipped to the basement rocks (lower graph) as depicted in Figure 4-14. Elevation interval is 1 m. Small insert on the right side shows their respective hypsometric curves and the hypsometric integral.

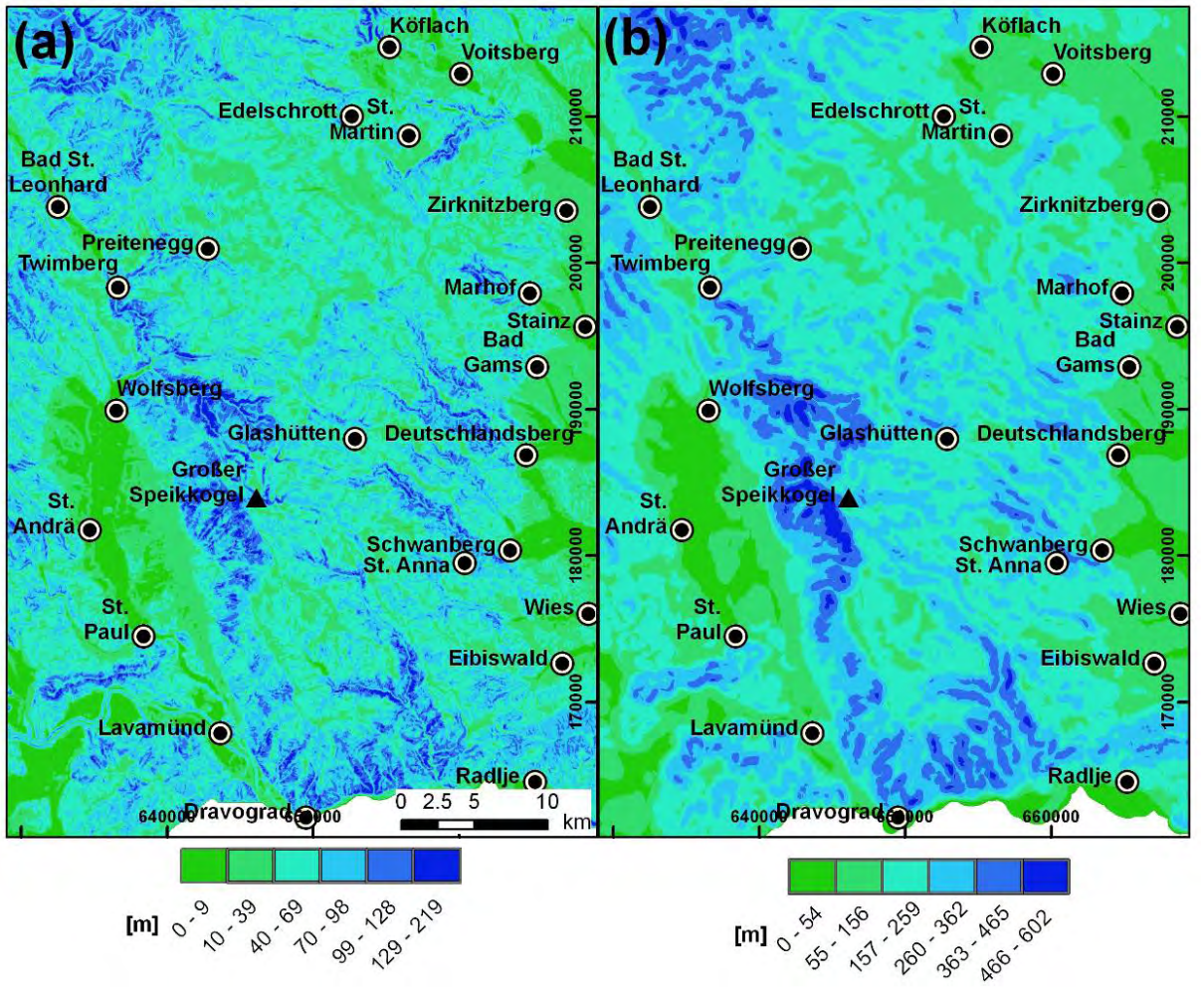

Figure 4-20: Relief maps calculated for circular windows with 100 m radius (a) and 500 m (b). Note scale dependence of relief from window size. Classification interval is one standard deviation.

	Morphounit	Min	Max	Relief	Mean	Median	Mode	sd	q25	q75	IQR
Elevation [m]	***South***	317.7	1520.2	1202.6	772.0	727	539.1	276.7	544.0	973.2	429.2
	East	328.9	2124.8	1795.9	945.4	920.5	1079*	364.8	638.7	1216.3	577.6
	Central west	464.0	2140.0	1676.0	1220.9	1206.7	1224.1	338.7	989.8	1476.2	486.4
	Northeast	364.1	1965.1	1601.0	1066.2	1067.3	865.2*	289.1	885.2	1261.9	376.7
	West	371.9	2139.8	1767.9	988.3	947.3	697.6	344.8	704.6	1217.7	513.1
	Northwest	600.1	1929.8	1329.7	1118.9	1074.6	1032.3	286.7	886.9	1324.9	438.0

sd……..standard deviation, q25...quartile at 25%, q75... quartile at 75%, IQR.....interquartile range

ZonalStats_morphounits.xls

Table 5: Descriptive statistics for the distribution of elevation in the six morphounits. Modes marked by an asterisk are misleading values as the elevation data contain water reservoirs and the most frequent values coincide with the reservoirs. See text for further information.

The elevation histograms for the individual morphounits (Figure 4-22) show two types of distribution. Morphounit Northeast and Central West show more or less symmetric frequency distributions, whereas the other four are characterised by asymmetric, right skewed distributions. This reflects the different shape of the morphounits with Morphounit Northeast and Morphounit Central West having narrow exits and the other four being characterised by wide mountain fronts towards the basins (Figure 4-16, Figure 4-21).

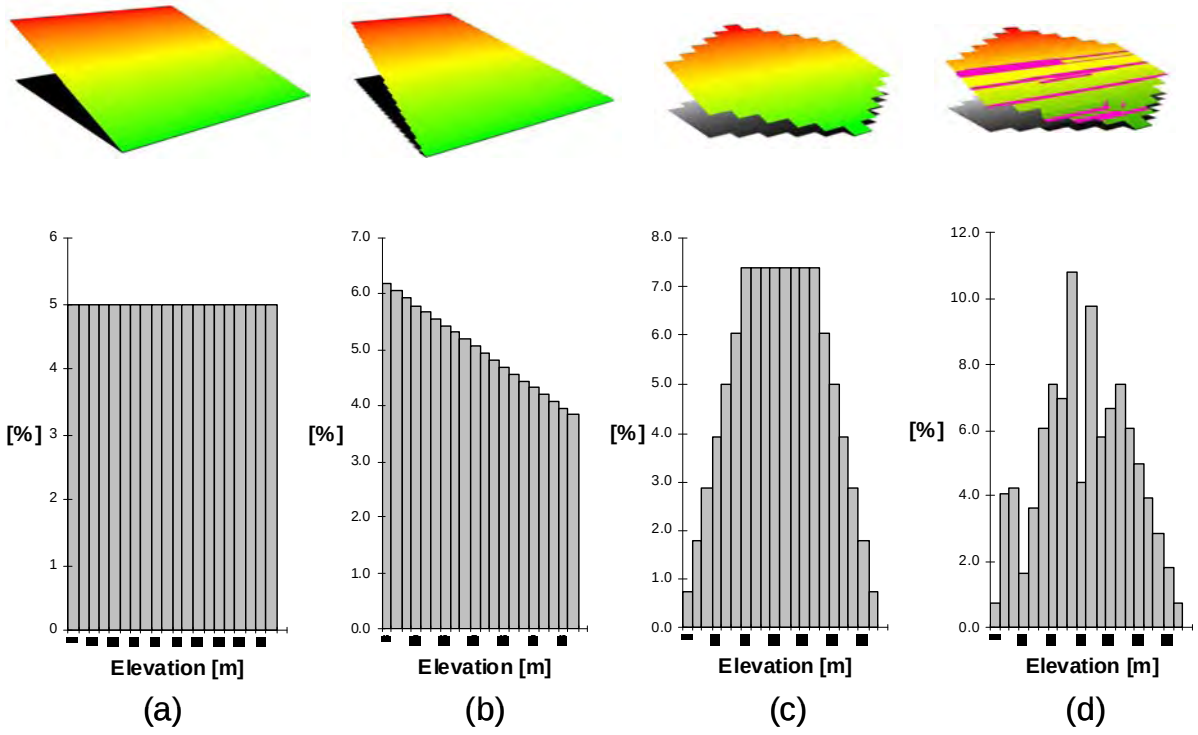

Figure 4-21 Frequency distribution for different shapes of hypothetic elevation models: (a) Inclined quadrangle, (b) upwards narrowing, (c) upwards widening, then narrowing, (d) upwards widening, then narrowing, pink areas indicate preferred elevation levels.

In Morphounit Northeast the mode of 865.2 m deviates strongly from the class 1020 to 1040 m, which is the largest class (Table 5). This is caused by the presence of water reservoirs, the largest of them, the Pack reservoir, is situated at this elevation. If the values of the reservoir are excluded from analysis the mode is calculated as 1030 m. Similarly, in Morphounit East the mode of 1079 m deviates strongly from the class 400 to 420 m, which is the class with the highest proportion of values. Again a reservoir is exactly situated at the mode value. After exclusion of the reservoir elevations the mode is calculated as 420 m.

The histograms are further characterised by several sub-maxima, which can be linked to morphological features contained in the different units. These represent on the one hand parts of the surrounding basins and on the other hand preferred levels of planation.

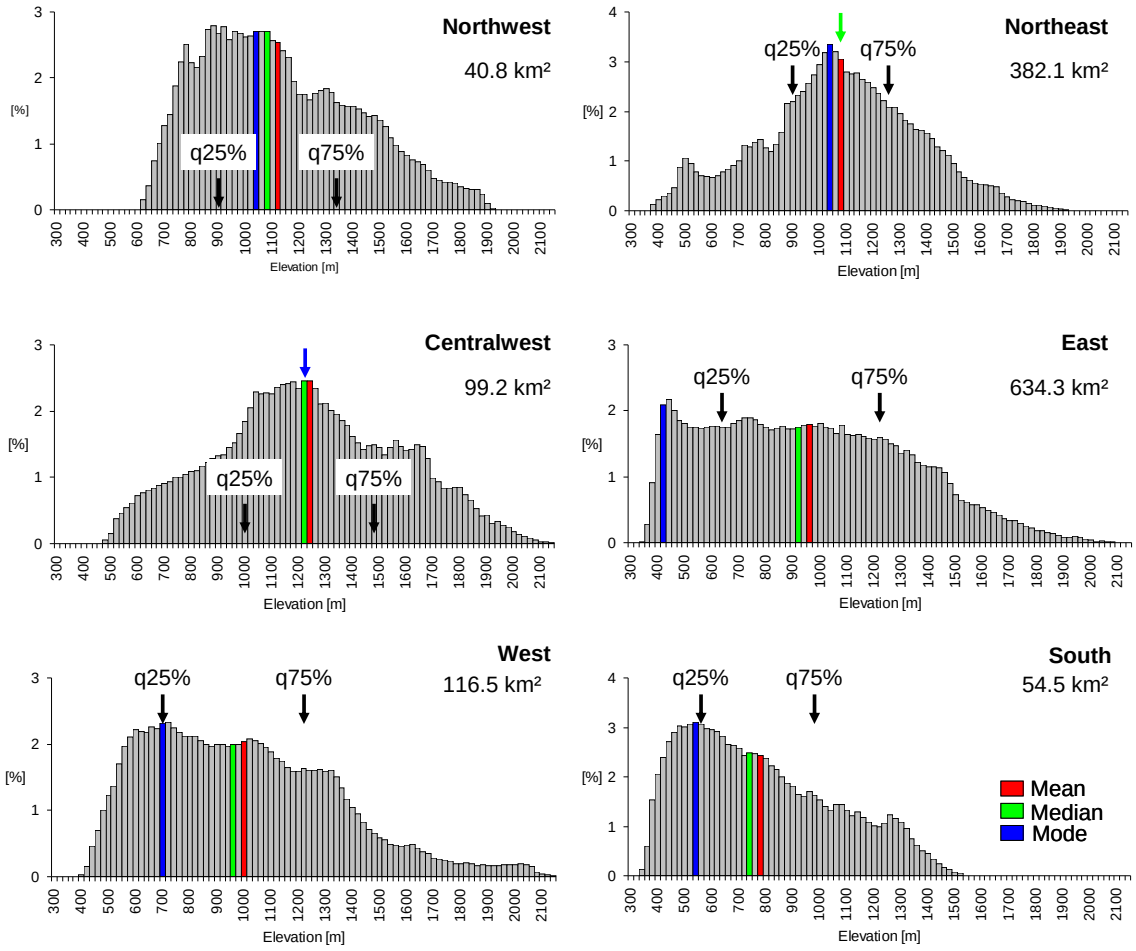

Figure 4-22: Elevation histograms for the six morphounits of the Koralpe. Class width is 20 m; values were extracted from 10 m DEM. Coloured columns mark the mean (red), the median (green) and the mode (blue). A coloured arrow marks classes which contain two of the central values. Arrows labelled q25% and q75% mark the first and the third quartile (see Table 5 for the exact values). Mode values show the values filtered for the water reservoir data as described in the text.

Hypsometry was performed for 71 catchments (Figure 4-23). The H_i values range predominantly between 0.4 and 0.5 (Table 6), with a minimum around 0.3 and a maximum at approx. 0.7. There are several zones with anomalous high values (Figure 4-23, Figure 6-2, Appendix). One zone is located along the southern Lavant valley (1 in Figure 4-23). Here, H_i values, between 0.5 and 0.6, are slightly higher than the values in the north. Further zones are found in the catchments of the Prössingbach and the Fraßbach (2 in Figure 4-23) draining to the Twimberg gorge of the Lavant river, in the Stainzbach along the eastern slope of the Koralpe (3 in Figure 4-23), and in several smaller catchments of the Gössnitz (4 in Figure 4-23).

H_i and catchment size are not correlated (Figure 4-25), although a correlation is indicated by the map picture (Figure 4-23) This result is not consistent with the findings of Willgoose and Hancock (1998) and Hurtrez et al. (1999) that hypsometry reflects landscape runoff and erosional processes and is strongly dependent on channel network structure and catchment geometry. Furthermore, the present analysis yields no relationship between H_i, catchment relief and several measures of catchment shape (see chapter 4.3.7.2).

A comparison of the H_i values of the individual morphounits shows that morphounit "*Central West*" shows the highest values, followed by unit "*Northeast*" with a similar value (Figure 4-16 and Table 6). All other units show a H_i below 0.4. This is consistent with their hypsometric curves (Figure 4-26). The convex shape of the curve indicates that within morphounits Northeast and Central West a higher proportion of area is at higher elevations than in the other units, which show a concave hypsometric curve.

Dataset	N	Mean	Min	Max	Median	g	sd	Unit
All	71	0.478	0.296	0.691	0.476	0.395	0.079	0.378
Northwest	4	0.435	0.382	0.488	0.434	0.084	0.046	0.389
Central west	5	0.591	0.509	0.687	0.575	0.445	0.069	0.451
West	20	0.480	0.387	0.592	0.491	0.149	0.059	0.348
East	25	0.441	0.296	0.575	0.442	0.028	0.075	0.34
Northeast	10	0.512	0.423	0.691	0.470	1.102	0.094	0.438
South	7	0.503	0.453	0.561	0.494	0.441	0.036	0.377

g... skewness, sd... standard deviation *catchments_koralpe_basement_01.xls*

Table 6: Statistical parameters of the hypsometric integral H_i (elevation-relief ratio E) for the catchments analysed. Zones are the same as in Figure 4-16. Values in column "Unit" are H_i values calculated for the entire DEM (basement) and the entire morphounit.

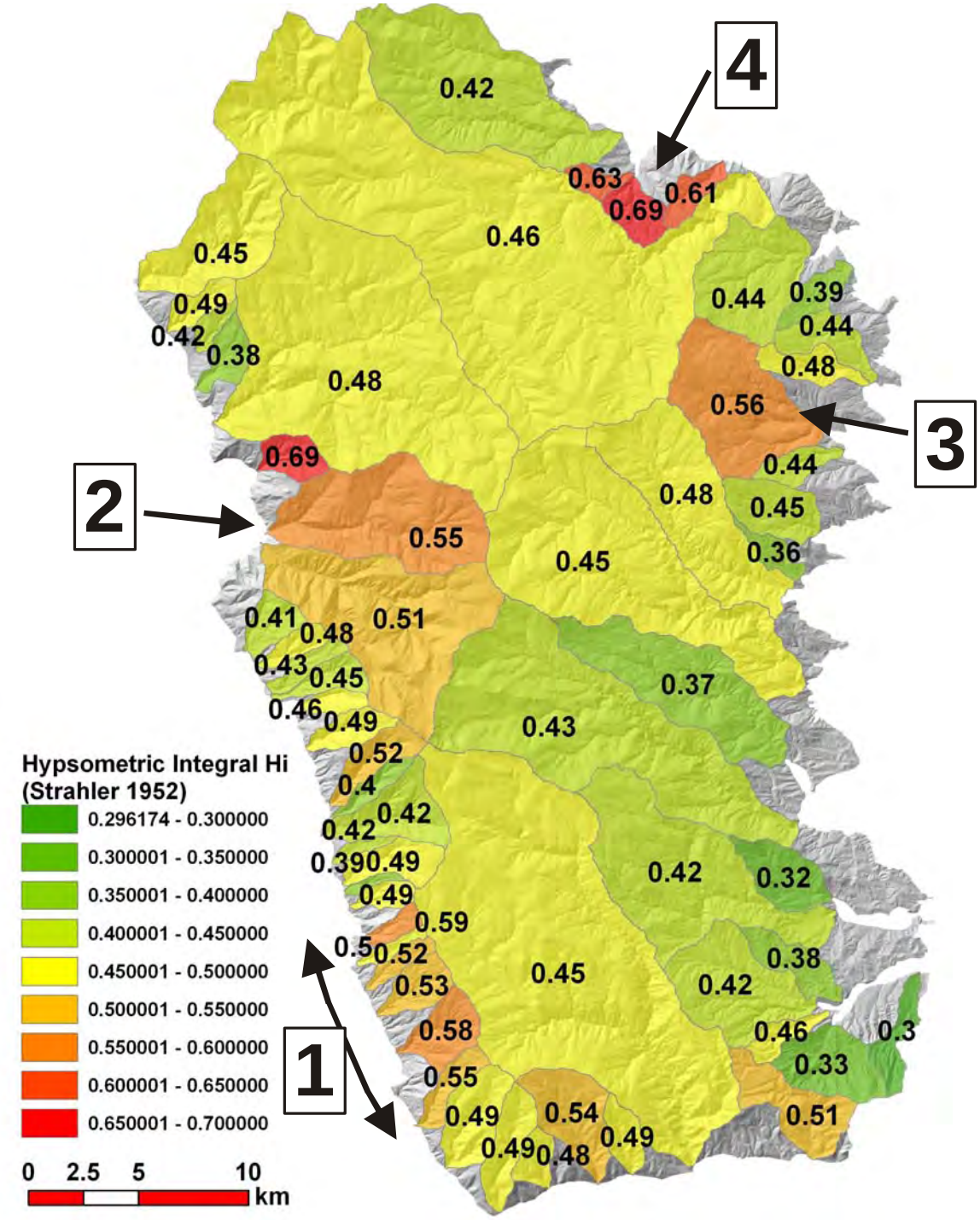

Figure 4-23: Regional distribution of hypsometric integral H_i (elevation-relief ratio E) calculated for individual catchments. Bold numbers and arrows indicate areas with higher H_i values: the southwestern Lavanttal (1), catchments along the Twimberg gorge of the river Lavant (2), the catchment of the Stainz River (3) and some small catchments on the northeastern margin of the Koralpe (4).

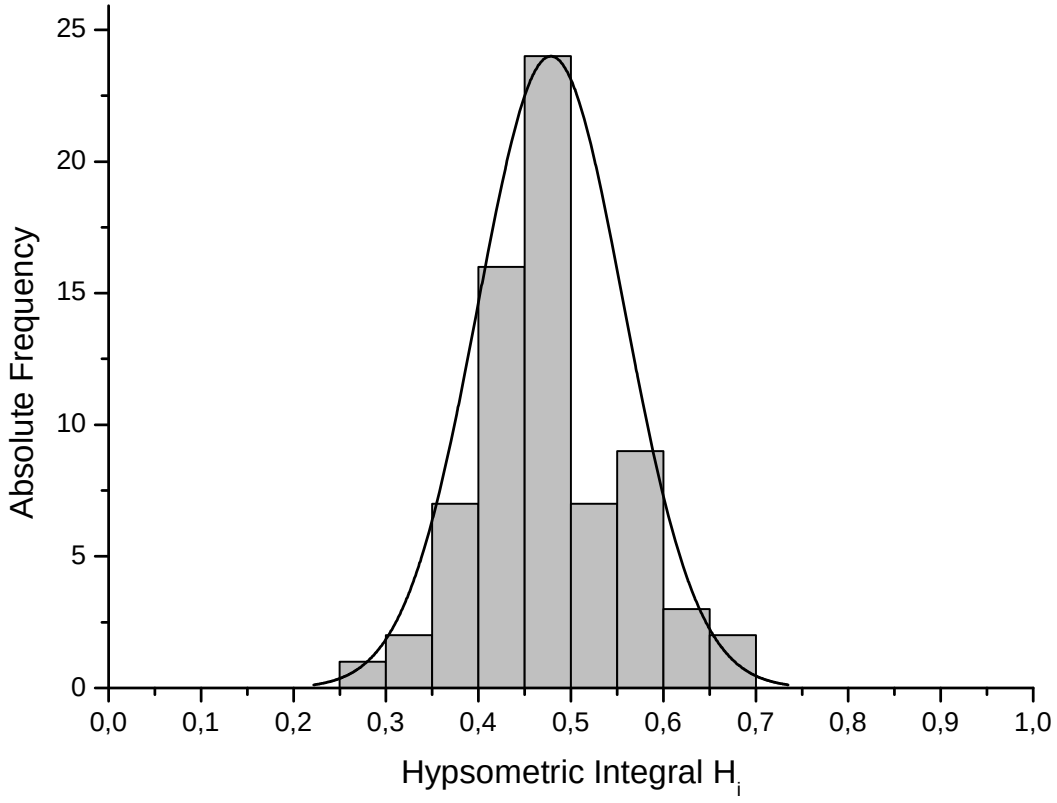

Figure 4-24: Histogram of the H_i values from all catchments of the Koralpe.

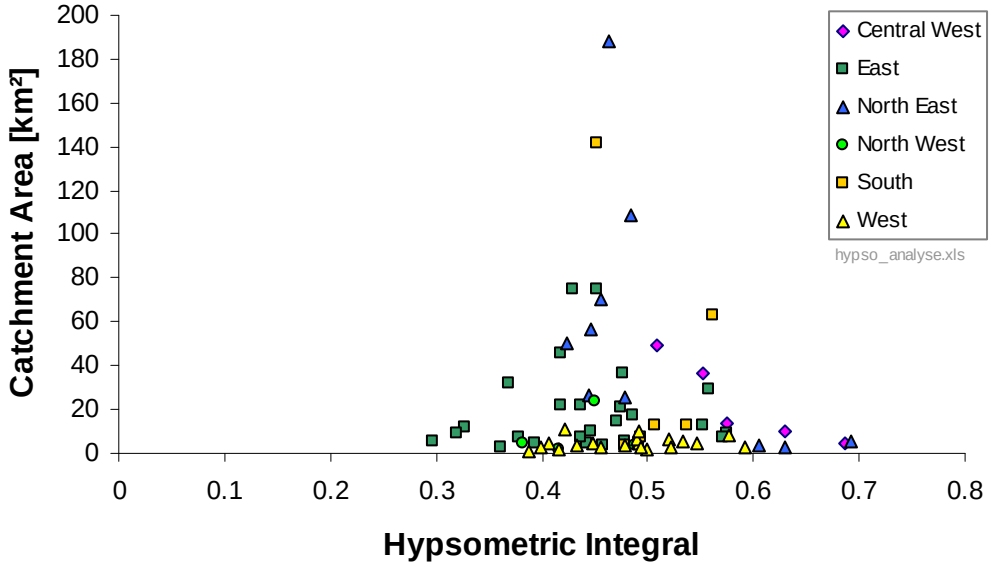

Figure 4-25: Scatter plot of catchment area against hypsometric integral H_i.

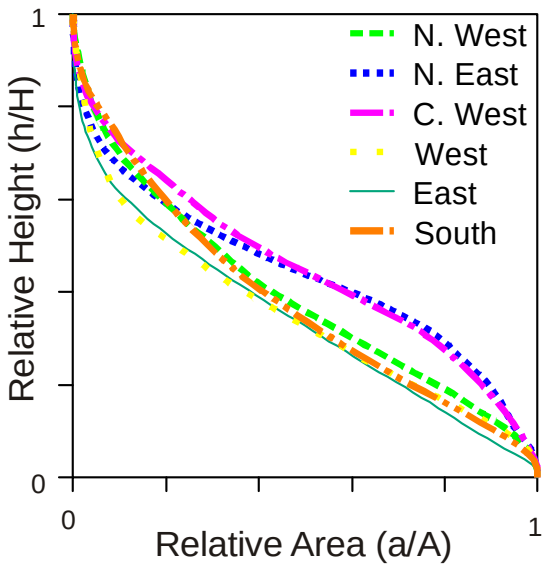

Figure 4-26: Hypsometric curves for the individual morphounits (refer to Table 6, column "unit" for the respective values of the hypsometric integral).

4.3.4 ELEVATION DATA OF THE ALPS

The DEM of the Koralpe can be considered as a sample of the DEM of the Alps (Figure 4-28). A comparison of diverse subsets (Eastern Alps, Western Alps, Tauern Window) with the data set of the Koralpe is considered to be helpful for the interpretation of the hypsometric properties of the Koralpe.

The SRTM data sets of the Alps, the Eastern and the Western Alps show quite similar shapes of their frequency resp. hypsometric curves (Figure 4-27a & b). All three data sets have their highest frequency between 800 and 900 m, however their mode is clearly lower than this value (Table 4). This results from the presence of large lakes within the Alps, whose frequency peaks are recognisable in the histograms with one meter class width (Figure 6-1, Appendix). The distributions are right skewed and the mean is always larger than the median. The Western Alps show a clear submaximum between 1900 and 2900 m, which is not present in the data set of the Eastern Alps.

The Koralpe, clipped to the basement rocks, shows a much narrower, more symmetric distribution, with its highest frequency between 1100 and 1200 m (Figure 4-27). This difference in hypsometry is also clearly visible in the colour coded elevation model of the Alps (Figure 4-28 a), where elevations drop east of the Tauern Window. This difference is enhanced in the relief map of the Alps (Figure 4-28 b), where a marked zone of lower relief is seen east of the Tauern Window. In the West, this zone is bordered by the Katschberg detachment between the Penninic and the Austroalpine units (Genser and Neubauer, 1989). In the North, it follows the fault bounded valley of the Mur and Mürz rivers. In the South, it is confined by the Drau (Drava) valley (partly parallel to the Mölltal fault) and the Periadriatic Line resp. the Lavanttal fault. In the east, it passes into the Pannonian Basin system, which is not included in the analysed elevation model. The elevation distribution in this zone

(labelled “Low Relief Area” in Figure 4-27) is similar to the one of the Koralpe. However, the abundant basinal parts contained in the “Low Relief Area” data set shift the distribution towards lower elevations.

The specific morphological situation of this area is highlighted by its contrast to the elevation distribution of the Tauern Window, which shows a much smoother, slightly left skewed outline of its frequency curve, with the median (1977 m) slightly higher than the mean (Figure 4-27a, Table 4). The mode of 2007 m is again influenced by the presence of reservoirs. A sub-maximum, especially visible in the elevation histogram with 1 m class interval (Figure 6-1, Appendix), is found between 820 and 870 m and marking pronounced, glacial oversteepened valleys. The hypsometric curve of the Tauern Window deviates clearly from the Koralpe and especially from the other data sets analysed (Figure 4-27b).

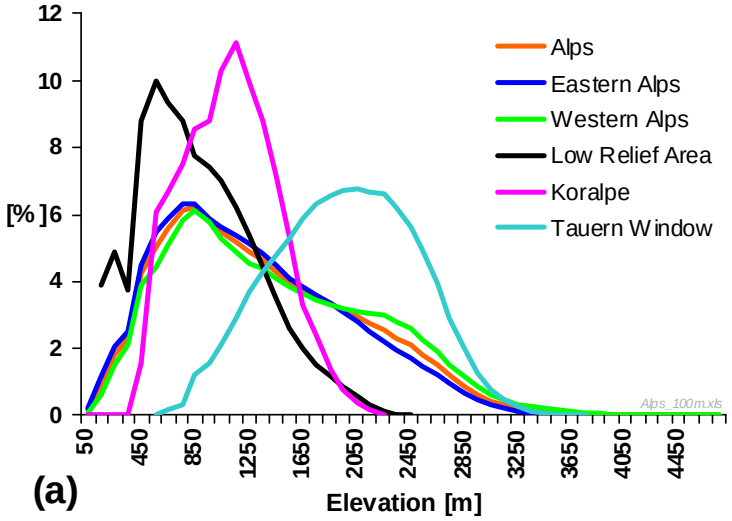

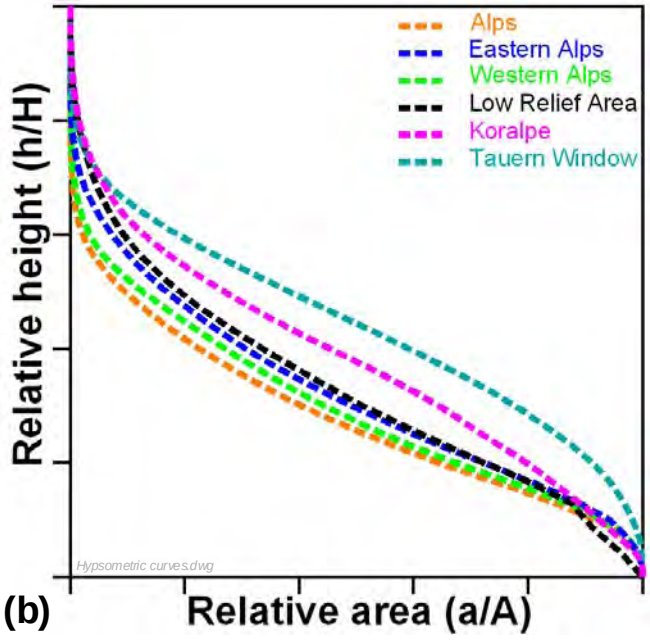

Figure 4-27 (previous page): (a) Frequency distribution and (b) hypsometric curves for the Alps, the Western Alps (including the respective parts of the southern Alps), the Eastern Alps (including the respective parts of the southern Alps), the Tauern Window, the low relief area east of the Tauern Window (all from the SRTM elevation data set) and the Koralpe (restricted to the basement parts, 10 m DEM). Class interval of the frequency distributions is 100 m. Refer to Figure 4-28 for location of the data sets.

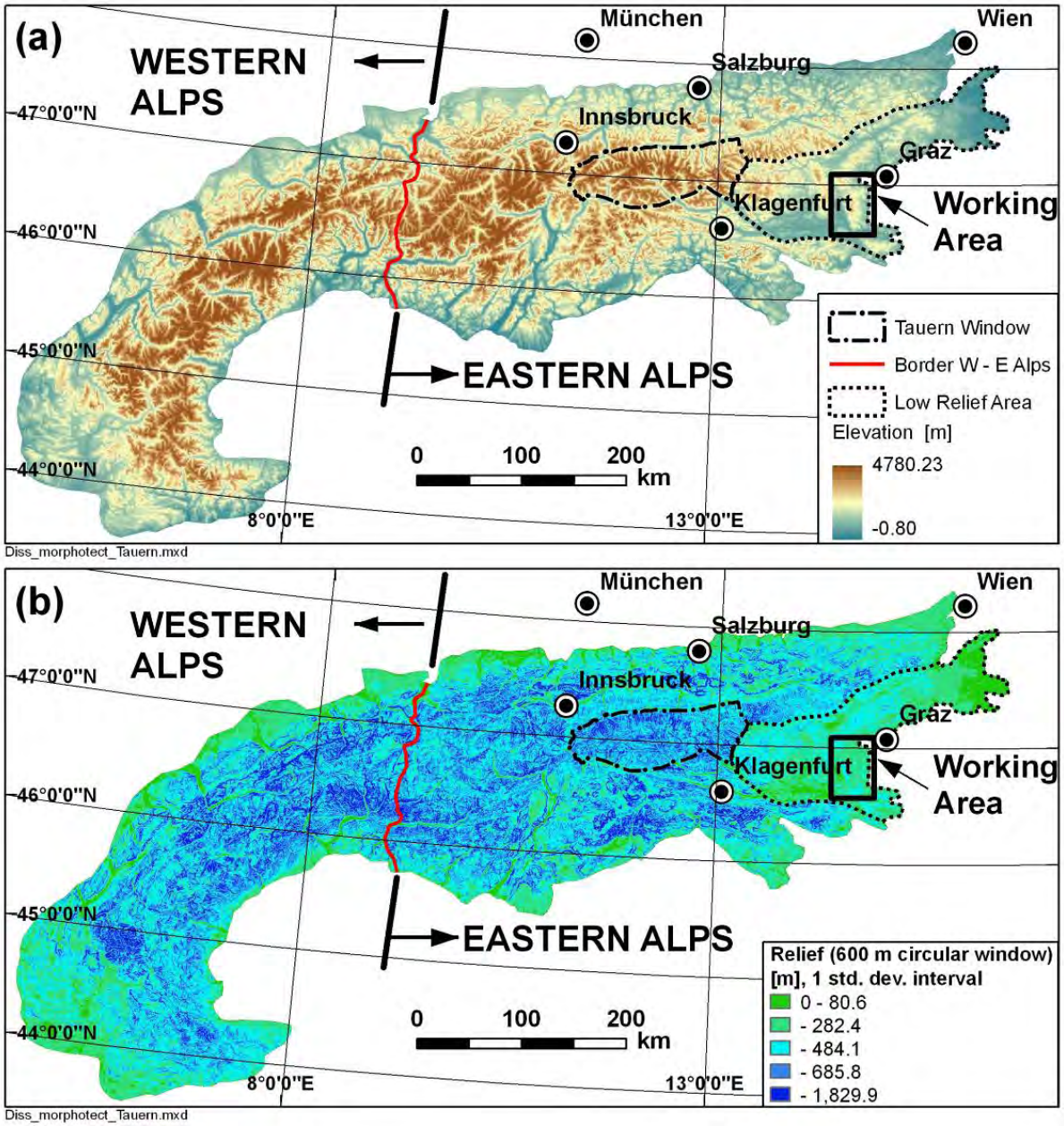

Figure 4-28: (a) Colour coded SRTM elevation model of the Alps (96 m resolution). (b) Relief map of the Alps, calculated from (a) in circular windows with 600 m radius.

4.3.5 ELEVATION DERIVATIVES

4.3.5.1 SLOPE GRADIENT

The frequency distributions of slope angles for the entire DEM and the clipped DEM (Figure 4-29) show differences attributable to the basins included in the unclipped data set. The slope gradient distribution for the Koralpe (clipped DEM in Figure 4-29) is positively skewed with the mean at 18° (Table 7). This is clearly lower than the mean slope angle of 28° to 34° representative for several mountain regions (Whipple et al., 1999). For the DEM (96 m resolution) of the entire Alps (Figure 4-30a) analysis yields a negatively skewed distribution with a mean slope angle of approx. 20° (Figure 4-29 & Table 7). The data set shows a second maximum at low slope gradient values resulting from basinal parts and lakes. Compared to the entire Alps, the distribution of slope gradients from the Koralpe is shifted towards lower slope angles. However, the Alps comprise a wide range of different lithologies with different erodibility and the Western and Eastern Alps show pronounced differences in their tectonic history. Therefore, their DEMs were analysed separately. Interestingly, there are only slight differences in their slope angle distribution (Figure 4-29).

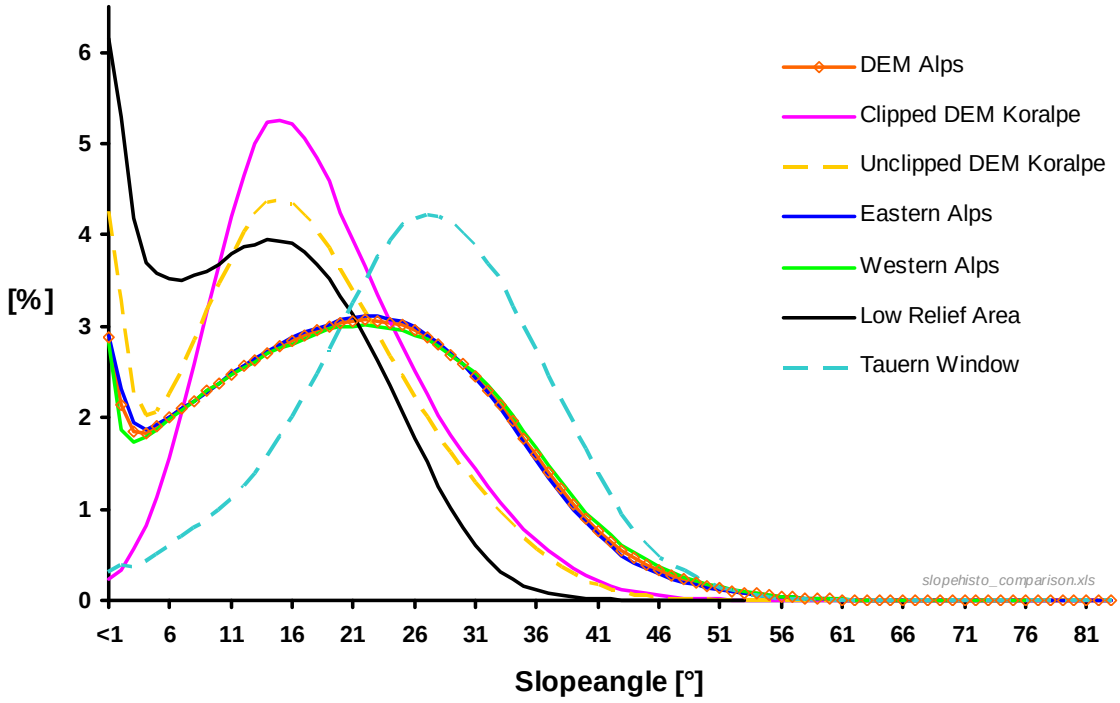

Figure 4-29: Frequency distribution of slope angle for the clipped and unclipped DEM of the Koralpe, the DEM for the entire Alps (96 m resolution), the Western and Eastern Alps, the Tauern Window and the paleosurface of which the Koralpe is a part. See Figure 4-28 for extend of the analysed DEMs.

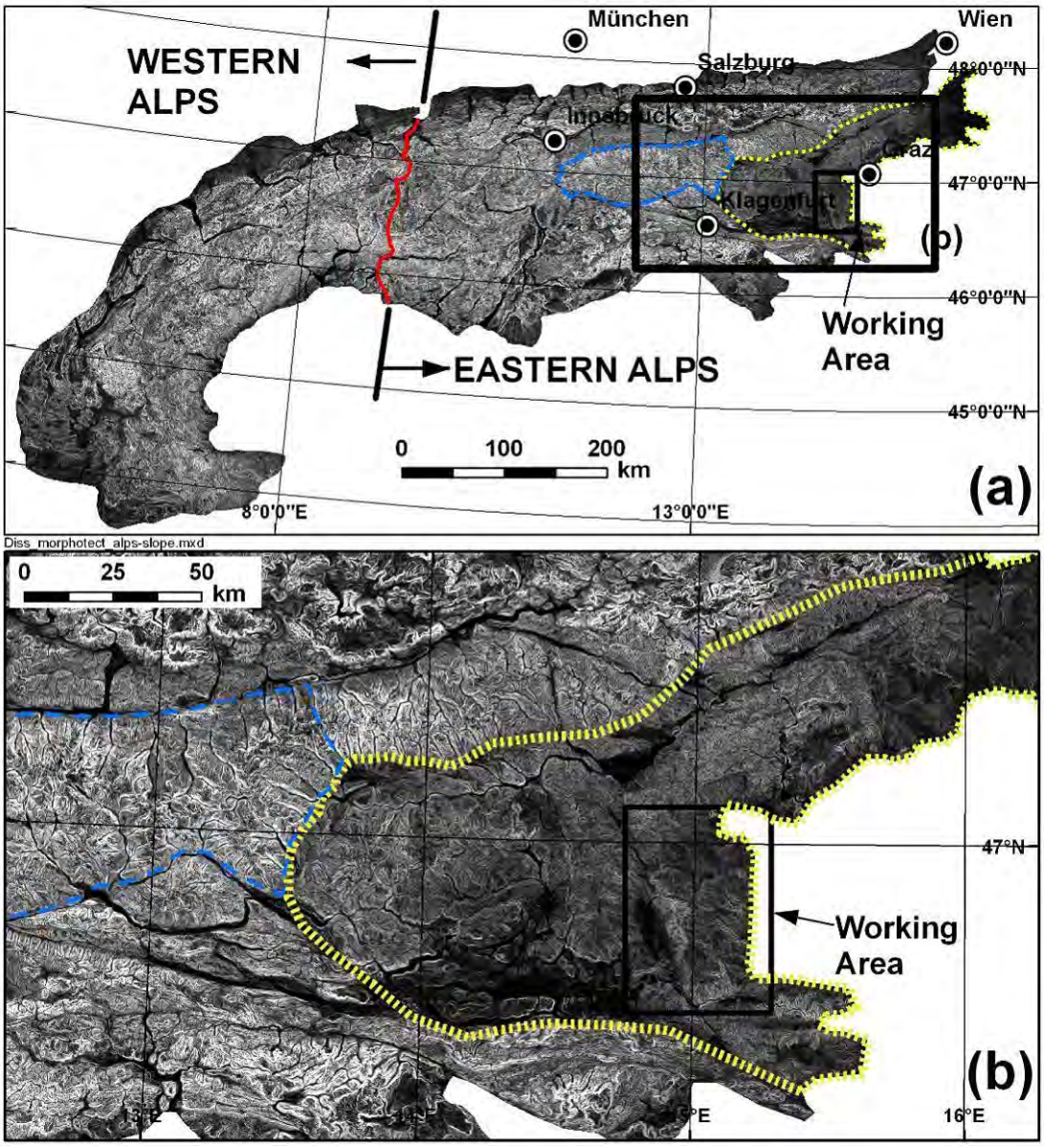

Figure 4-30: (a) Slope map of the Alps. Red line marks the border between Western and Eastern Alps, blue line the Tauern window and yellow line the low relief area of the Eastern Alps. (b) Detail of the Eastern Alps from the Tauern Window to the Styrian Basin.

Both, the unclipped DEM of the Koralpe and the DEM of the Alps show a clear peak of slope gradients lower than 4°, reflecting the valley and basin parts of the data sets. The general shift of the histogram of the Koralpe towards lower values indicates a more evolved relief for the Koralpe than for the majority of the Alps. This is supported by the distribution of elevation derivatives which reveals distinct distribution patterns for different tectonic units of the Eastern Alps (Székely et al., 1999; Székely, 2001; Székely et al., 2002). The Koralpe and the Gurktal Alps have a similar frequency distribution of slope (Székely, 2001). In the slope map of the Alps (Figure 4-30), the area east of the Tauern Window, including the Koralpe, is clearly recognisable as an area with low slope (Figure 4-29). On the contrary the Tauern Window shows a

slightly left skewed distribution of slope and a much higher mean slope than the other data sets (Figure 4-29 & Table 7).

Elevation model	N	Min [°]	Max [°]	Mean [°]	Median [°]	sd
Alps	19524652	0	82.6	20.3	20.1	11.6
Eastern Alps	11288596	0	82.6	20.1	19.9	11.4
Western Alps	8230133	0	75.0	21.2	20.4	11.6
Koralpe (unclipped)	22779189	0	74.8	15.7	15.2	9.2
Koralpe (clipped)	13151913	0	72.7	17.8	16.8	8.2
Low Relief Area	1868697	0	52.7	12.7	12.3	8.4
Tauern Window	818943	0	82.6	26.0	26.3	9.8

N…..data points, sd…standard deviation *Morphotectonics_DEM analysis.xls*

Table 7: Statistical parameters of slope angle for the seven data sets depicted in Figure 4-29.

The Koralpe Range is characterised by clear regional differences of slope angle distribution. This can be shown by a slope map (Figure 4-31) as well as by the distribution of the slope angle in different elevation classes (Figure 4-32, and Appendix, Figure 6-3, Figure 6-4 and Table 14). The slope map shows a zone of high slope gradient along the western slopes of the Koralpe. This zone is approx. 4 to 5 km wide, only along the Prössing catchment north of Wolfsberg it extends approx. 8 km into the Koralpe. It continues along the southern border of the Koralpe along the Drava (Drau) valley. Here it extends along the Feistritz-Krennbach catchment far into the interior of the Koralpe. The eastern morphological segment exhibits clearly flatter slope gradients than the west, incised by several NW-SE trending, partly gorge like tributaries. The northern part of the Koralpe is characterized by flat, partly plateau like areas, in which the Teigitsch in the east and the Waldensteinbach in the west incise, forming pronounced zones of high slope angles. Towards the Stub- and Gleinalpe, slope angles are continuously increasing.

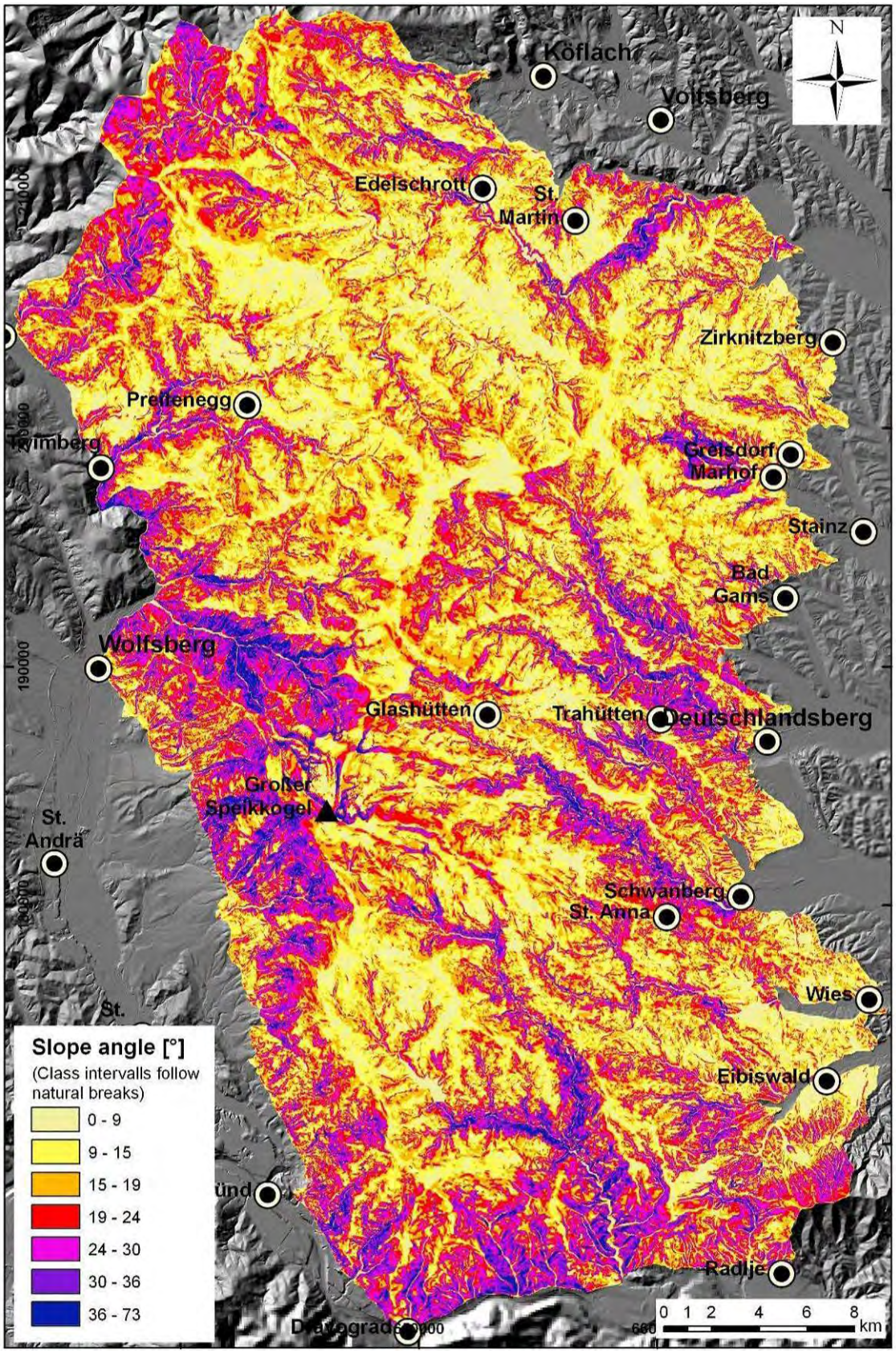

Figure 4-31: Slope map of the Koralpe, no filters or smoothing algorithms applied.

The relationship between elevation and slope angle is highlighted by Figure 4-32, for which descriptive statistics was calculated for 100 m elevation intervals (Table 14, Appendix). In the lowest class (up to 400 m) slope distribution obviously reflects the influence of the basin areas surrounding the range. Above that level, slope increases up to approx. 20° at 500 m a.s.l.. Above 820 m slope decreases to approx. 15-16° between 1040 m and 1480 m. Then the slope gradient increases again with increasing scatter of the data, which is reflected in the irregular shape of the curves (Figure 6-3, Appendix) and the increasing interquartile range for the elevation classes higher than 1700 m (Figure 4-32). In the summit region, the frequency distribution is irregular shaped. This effect may be caused by several factors. One is the decreasing number of data. Secondly, a morphological pronounced landscape changes its characteristics on a small scale, resulting in a multimodal distribution of slope gradient. This seems to be realistic for this region, characterised by the increasing presence of peaks respectively tors ("Felsofen"), by the presence of glacial landforms (Morawetz, 1952; Beck-Mannagetta, 1953; Summerfield 1991; Gosch, 2007) and by an increasing influence of exogenic processes.

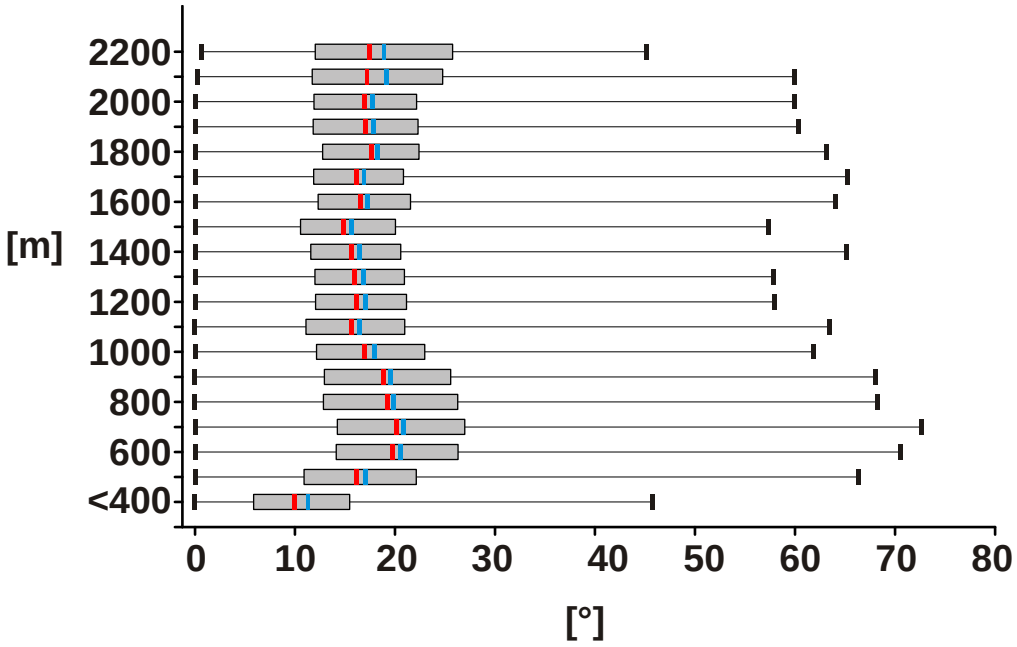

Figure 4-32: Box plots of slope gradient for 100 m elevation classes. Grey area marks interquartile range (25 and 75% quartile), red line the median and the blue line the mean value. Whiskers mark the minimum resp. the maximum values (see Table 14 for the individual values).

A map of areas with slope angles smaller than 10° highlights the widespread presence of flat areas (Figure 4-33). This is related to the paleolandforms preserved in the realm of the Koralpe (Winkler-Hermaden, 1957; Székely et al., 1999). In the northern Koralpe areas like the Lahnofen-Halterkogel (1100-1400 m a.s.l.), the Herzogberg (1000-1200 m), the watershed divide of Randlofen, Reinischkogel, Schrogentor together with the Freiländer Alm (1260-1500 m) and the area

Wöllmißberg-Edelschrott (600-800 m) form coherent areas of low slope angle (for location refer to Figure 4-33). Flat areas are also visible within the eastern Koralpe. Here, they follow frequently the WNW–ESE trending ridges, forming elongated, coherent areas. The flat areas detected in the western realm of the Koralpe are considerably smaller in size and are aligned in a step like manner along the WSW-ENE trending ridges (Figure 2-3). The lowest proportion of flat areas is delineated at the southern slope of the Koralpe, possibly indicating a younger morphology related to faulting and/or exhumation of the Pohorje Range (Mioc, 1977; Sölva et al., 2005a; Fodor et al., 2008; Robl et al., 2008). The histogram (Figure 4-34) of the flat areas shows a polymodal distribution indicating distinct planation levels. For the identification of these areas in the maps, the data were filtered for the elevation range of the individual planation levels. The peak around 390 m ("1" in Figure) is attributed to the transition of the Koralpe to the surrounding basins. Peak "2" represents areas on the eastern slope of the Koralpe (e.g. areas around Greisdorf and Greimkogel in the vicinity of Stainz and Bad Gams, Figure 4-34). Peak "3" mainly represents the area between Edelschrott and St. Martin am Wöllmißberg, north of the Teigitsch gorge. As an artefact, this peak also contains the reservoir of the Hirzmann dam at an elevation of 709 m. Similarly, with an elevation of 865 m the reservoir of the Pack dam is visible in the histogram ("4"). Peak "5" marks areas north of Marhof (approx. 880 to 930 m a.s.l.), which grade into neighbouring planation areas. The largest part of slopes < 10° is contained in the elevation classes around 1040 m and includes the pronounced paleosurfaces of Preitenegg and Herzogberg ("6"). These areas coincide with the mean elevation of the clipped DEM. Above this peak there is a marked frequency drop. The zone from 1080 m to 1470 m is characterized by several histogram peaks (7, 8, 9, and 10) forming a coherent zone of flat areas in map view (Figure 4-33), roughly coinciding with the "Glashütten" level (Winkler-Hermaden, 1957). The peak between 1090 and 1130 m ("7") includes e.g. areas along the Gressenberg in the Eastern Koralpe and areas east of Preitenegg in the Northern Koralpe. Further prominent levels are the Freiländer Alm and the Reinischkogel in the northern part of the Koralpe and the area north of St. Vinzenz in the southeastern Koralpe. Above 1470 m there is another pronounced drop in the frequency of flat areas. This is explainable by the general distribution of area with respect to elevation (Figure 4-19). Nevertheless, several peaks are still separable ("12" to "15" in Figure 4-34). These peaks mark planation features in the summit regions of the Koralpe and the southern Stubalpe.

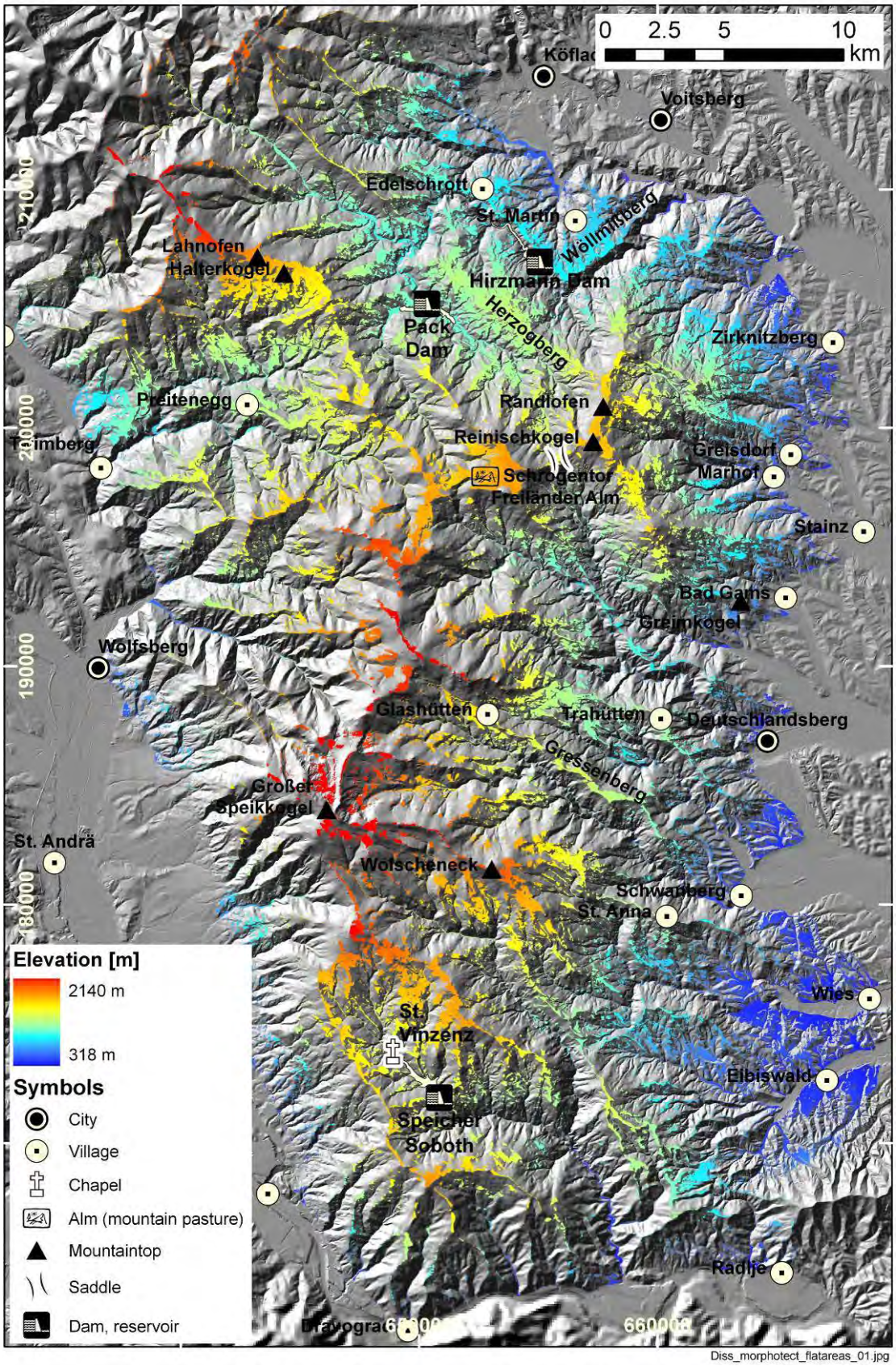

Figure 4-33: Elevation distribution of areas inclined < 10° in the Koralpe draped over a hillshade model of the Koralpe (10 m resolution). Zone of analysis is the same as in Figure 4-31.

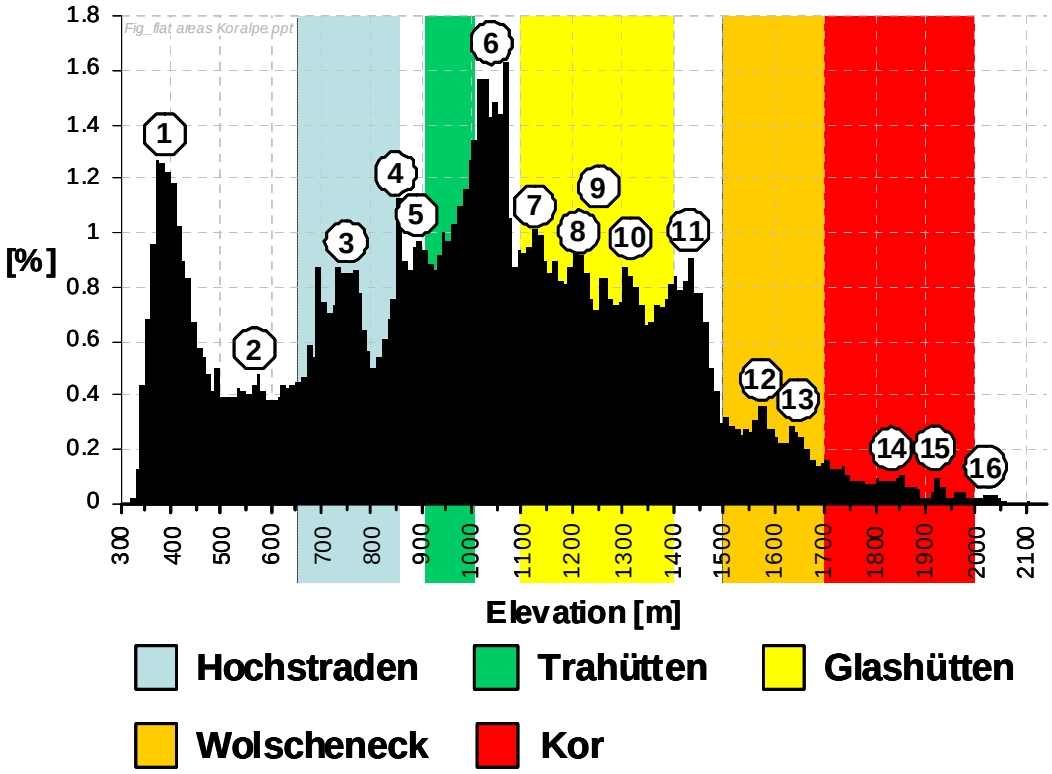

Figure 4-34: Elevation histogram of flat areas (slope gradient < 10°) derived from the clipped DEM of the Koralpe. Class width is 10 m. Numbers indicate locations described in the text. Colour bars indicate the planation levels ("Fluren") as described by Winkler-Hermaden (1957).

The histograms of slope angle for the morphounits reveal slightly skewed and smooth distributions (Figure 4-35). Morphounits East and Northeast show similar, slightly right skewed distributions. The other four morphounits are characterised by distributions shifted towards higher slope gradient values (Table 8).

	Morphounit	Min	Max	Mean	Median	Mode	sd	q25	q75	IQR
Slopeangle [°]	***South***	0.02	55.66	22.8	22.7	22.5	7.8	17.3	28.4	11.1
	East	0.00	72.66	17.2	16.2	14.9	7.9	11.4	22.2	10.8
	Central west	0.03	68.22	21.5	20.6	16.5	9.0	14.7	27.8	13.1
	Northeast	0.00	67.91	15.6	14.6	13.4	7.2	10.4	20.0	9.6
	West	0.04	68.06	22.2	21.6	20.4	8.2	16.0	27.8	11.8
	Northwest	0.09	52.97	19.7	19.6	18.1	7.4	14.6	24.8	10.2

sd.....standard deviation, q25...quartile at 25%, q75... quartile at 75%, IQR.....interquartile range *ZonalStats_morphounits.xls*

Table 8: Descriptive statistics for the distribution of slope angle in the six morphounits.

Above it has been shown, that the slope angle distribution varies with elevation and that distinct levels are associated with low slope angles. Below, this relation is analysed for the six morphounits (Figure 4-36, Figure 6-4, Appendix). The comparison of central values of slope angle reveals that Morphounit Northeast and

East, the units with the lowest central values of slope, show similar characteristics in their distribution of slope with respect to elevation. The minimum between 1000 and 1100 m corresponds to the planation surfaces of Herzogberg and Preitenegg and several smaller surfaces (e.g. Gressenberg, St. Anna ob Schwanberg) in the east. In the east and the northeast, the values are influenced by the presence of reservoirs. These are at elevations of 633, 708 and 865 m in the northeast and at 1079 m in the east (Figure 4-36).

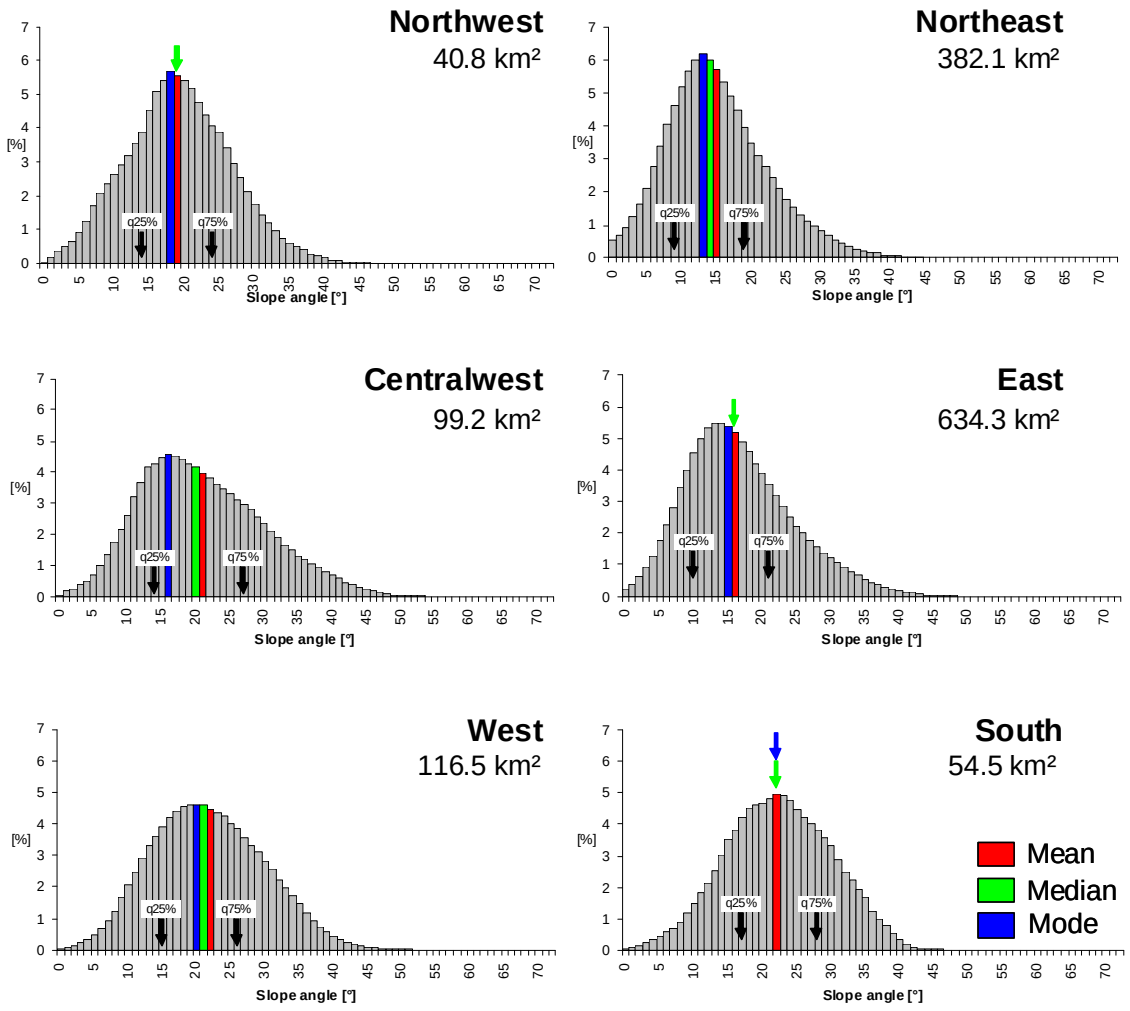

Figure 4-35: Slope histograms for the six morphounits of the Koralpe. Class width is 1°; values were extracted from 10m DEM. Arrows labelled q25% and q75% mark the first and the third quartile (see Table 8).

The minimum in the east and northeast at 1450 m is attributed to the Freiländer Alm and the Reinischkogel, along their common watershed, and to smaller areas in the southern part of Morphounit East. Above 1450 m the mean values increase, with a higher fluctuation.

Morphounit Central West shows a similar distribution of the mean slope with respect to elevation, but with generally higher values (Figure 4-36). The minimum between 1640 to 1660 m correlates with a planation surface along the watershed to

Morphounit Northeast. Between 1540 and 1900 m the values are similar to Morphounit East and Northeast.

Different characteristics are found in Morphounit Northwest. Here the values increase gradually from 16° between 600 and 620 m to 23° between 1220 and 1240 m. Above, the values fluctuate between 20 and 23° up to 1860 m and drop to 14° in the highest elevation class (2120 to 2140 m).

Morphounit West shows a gradual increase to 24° at 900 m and fluctuating values between 20° to 25°above, with a pronounced low between 1220 and 1440 m. In this section the curve is similar to the ones of Morphounit Northwest and Central West. Above 1840 to 1860 m the mean slope angle continuously declines to 15° and increases again to 20° between 2080 and 2120 m. This final peak is found in most of the morphounits with the exception of units South and Northwest, both of them do not reach the summit region of the Koralpe.

Morphounit South shows a sharp increase from 9° between 300 and 320 m up to 24° in 400 to 420 m. The mean slope angle remains in the range of 24° to 26° up to 920 to 940 m. This is similar to morphounit central west, where this maximum zone is narrower with respect to elevation and higher with respect to mean slope angle. Morphounit East shows a similar shape of the curve in this elevation range, but its mean slope angle is lower by approx. 5°. In morphounit south the values decrease above 940 m, only between 1160 and 1240 m the mean slope angle clearly exceeds 20°.

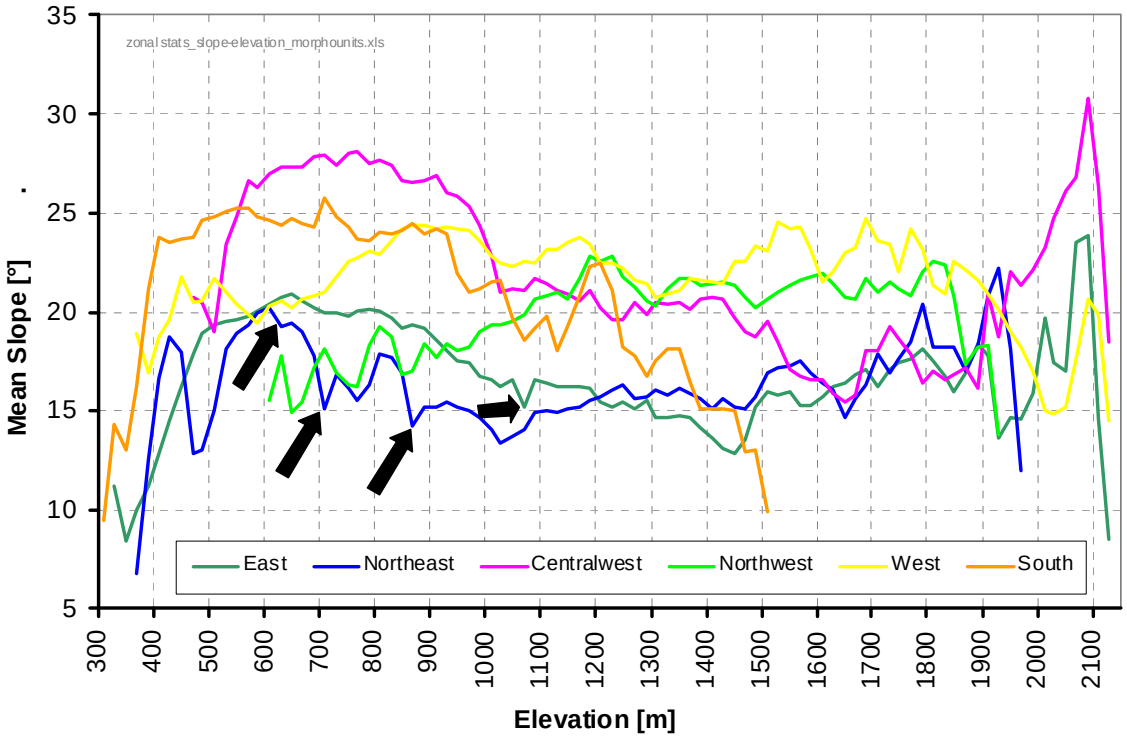

Figure 4-36: Comparison of the mean slope angle of the six morphounits for 20 m elevation intervals. Points represent the middle of the respective elevation class. Arrows mark data points influenced by the presence of reservoirs.

Further, analysis of slope gradient helps to reveal structurally controlled slopes. These are often related to the metamorphic foliation resulting in the formation of dip slopes and cuestas, especially in the Plattengneis areas of the eastern Koralpe (Figure 4-3, Figure 4-37). The large scale folds are clearly visible in the elevation and the slope data, with the best example, the “Seebach” syncline, clearly marked by asymmetric ridges (Figure 4-37).

Some pronounced linear slopes with steeper dip angles are linked to faults like the eastern slope of the Greimkogel, west of Bad Gams (Figure 4-38). Here the slope map helps to localise such features especially if slope angle in combination with slope aspect is used as a filter.

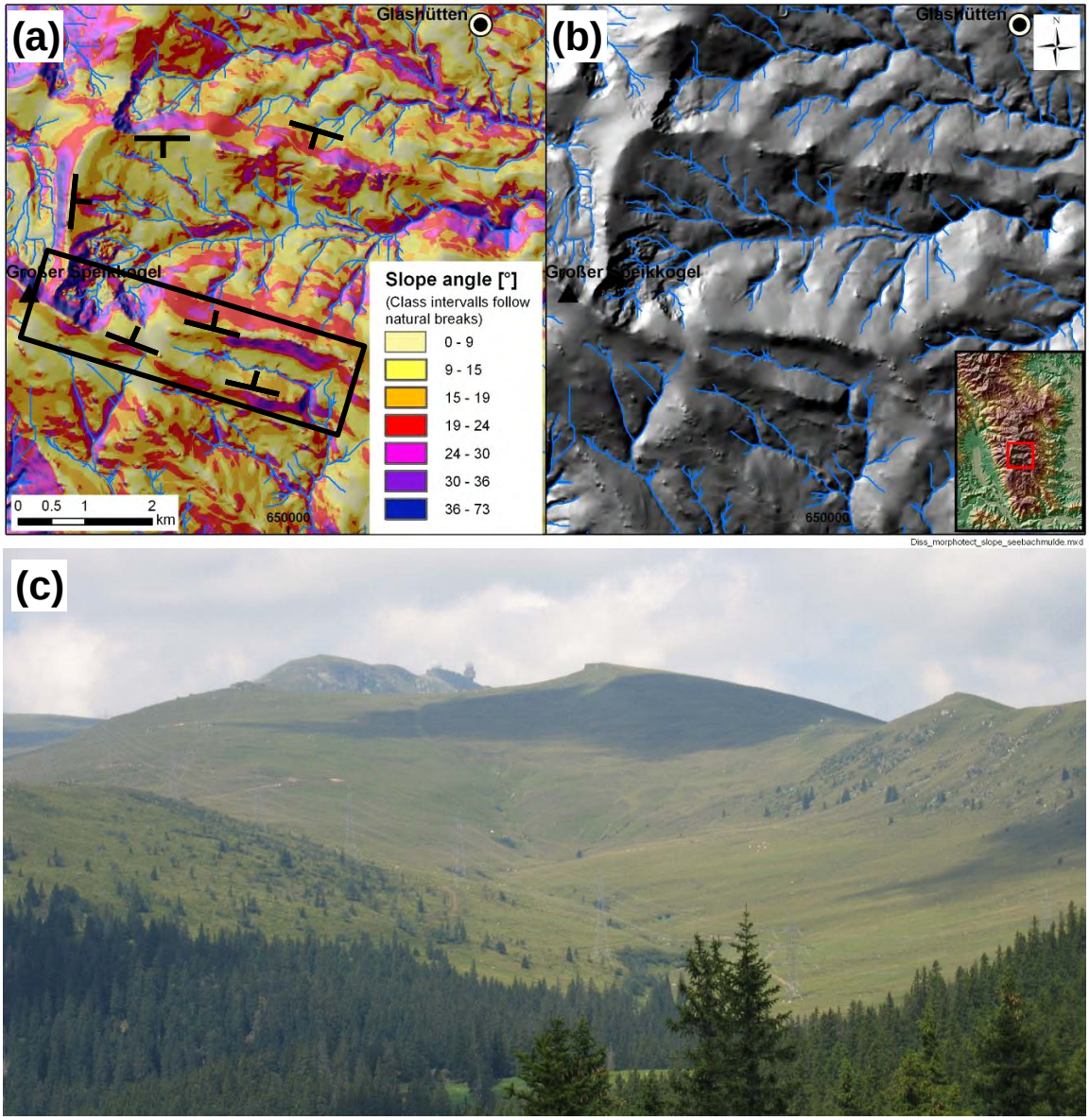

Figure 4-37: Foliation controlled slope geometry in the central Koralpe caused by a syncline in gneissic mylonite (“Plattengneis”) as reflected in the slope angle map with schematic dip symbols (a) and the hillshade (b). (c) Photograph of the northward dipping limb of the syncline (view towards WNW). Location is indicated by black rectangle in (a).

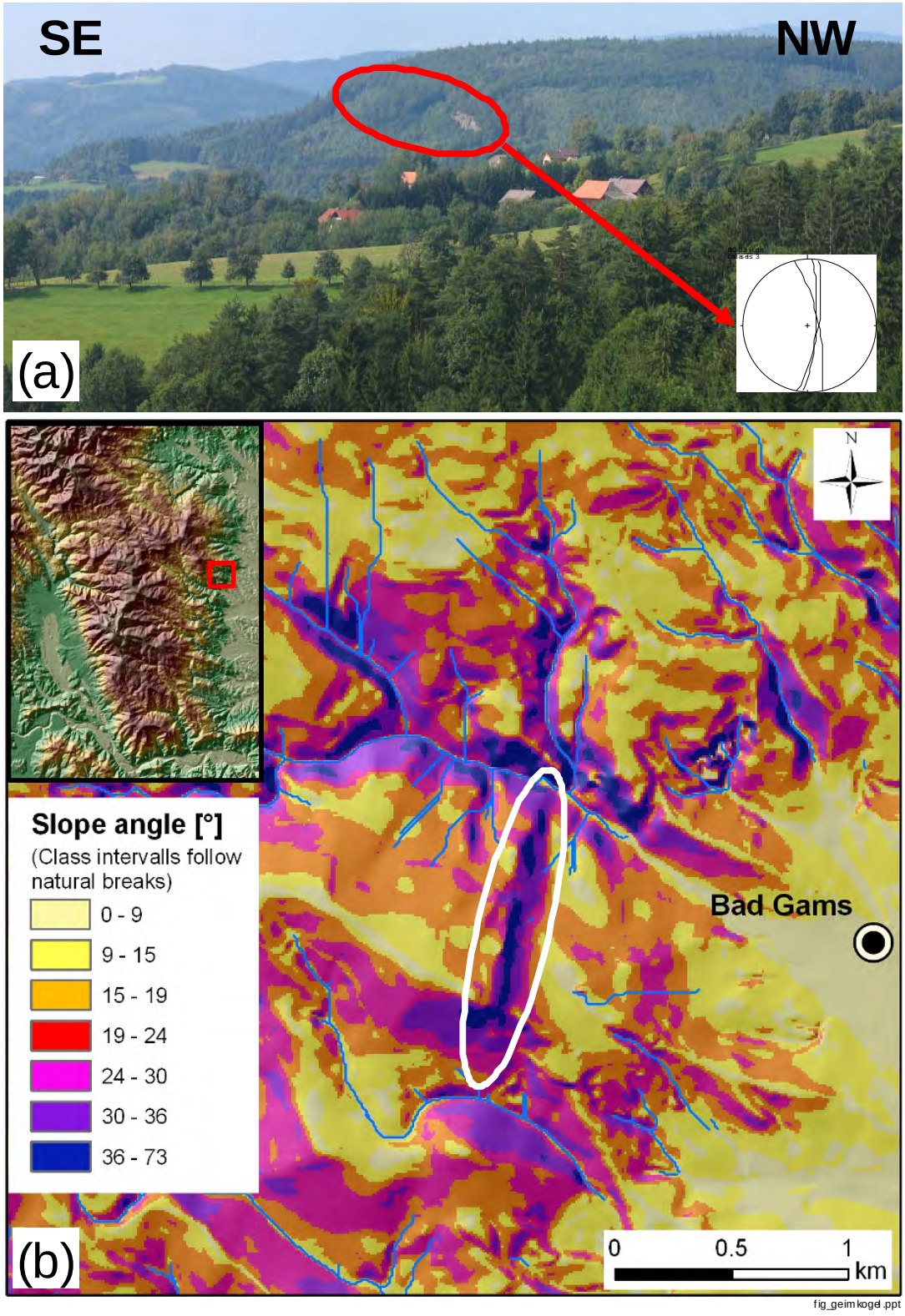

Figure 4-38: Fault controlled slope geometry at the eastern margin of the Koralpe (see insert for location). (a) View towards the fault bounded Greimkogel with the fault scarp marked by the red ellipse. Equal area (Lambert) projection (lower hemisphere) shows orientation data at that location. (b) Slope map of the area of the Greimkogel with its steeply eastwards dipping, fault bounded slope.

4.3.5.2 SLOPE ASPECT

Aspect analysis reveals a bimodal distribution, with maxima at 44° (NE) and 199° (SSW) respectively (Figure 4-39). N to NE and SSW dipping slopes are mainly found east of the main water divide and in the north (Figure 4-40) reflecting the general WNW-ESE trending drainage direction. SW to W dipping slopes are primarily found in the western realm of the range.

A preferred aspect may be indicative for the presence of structural controls in the bedrock geology, which have been already described for the northern Koralpe by Stiny (1925) and for the nearby Paleozoic of Graz by Flügel (1952). These controls include foliation, joints, fault planes and zones as well as strength contrasts of lithology. To assess the structural influence on slope orientation, metamorphic foliation as the basic, penetrative structure is compared to slope aspect. The foliation data set is derived from own measurements (259 outcrops) and from dip symbols of the geological maps (Beck-Mannagetta, 1980; Beck-Mannagetta et al., 1991; Beck-Mannagetta and Stingl, 2002). The rose diagrams of foliation dip direction and slope aspect (Figure 4-39) support the assumption of a basic structural control of the landscape. However, the aspect is locally uncorrelated to the foliation dip direction. This is explained by the fact that outcrops are rarely found in dip slope locations. Most outcrops are mapped along ridges or along cliffs on the opposing side of the dip slopes. This implies a pronounced under-representation of foliation measurements in dip slope locations. However, a structural control of slope orientation is observed in several places, especially along the large scale open folds of the “Plattengneis” mylonite (Figure 4-3, Figure 4-37).

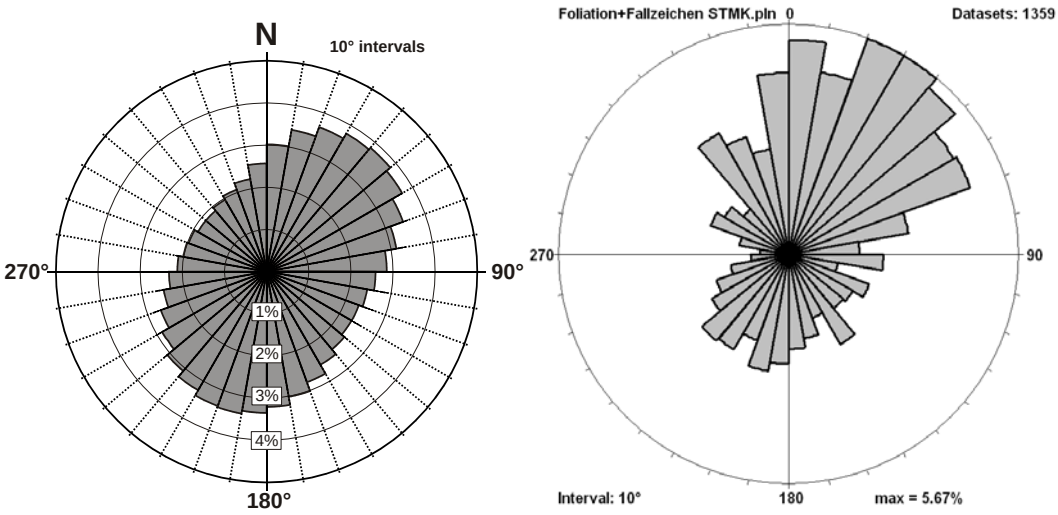

Figure 4-39: Rose diagram of slope aspect derived from the clipped DEM of the Koralpe (left diagram) and of the dip direction of foliation planes from the eastern realm of the Koralpe (right diagram).

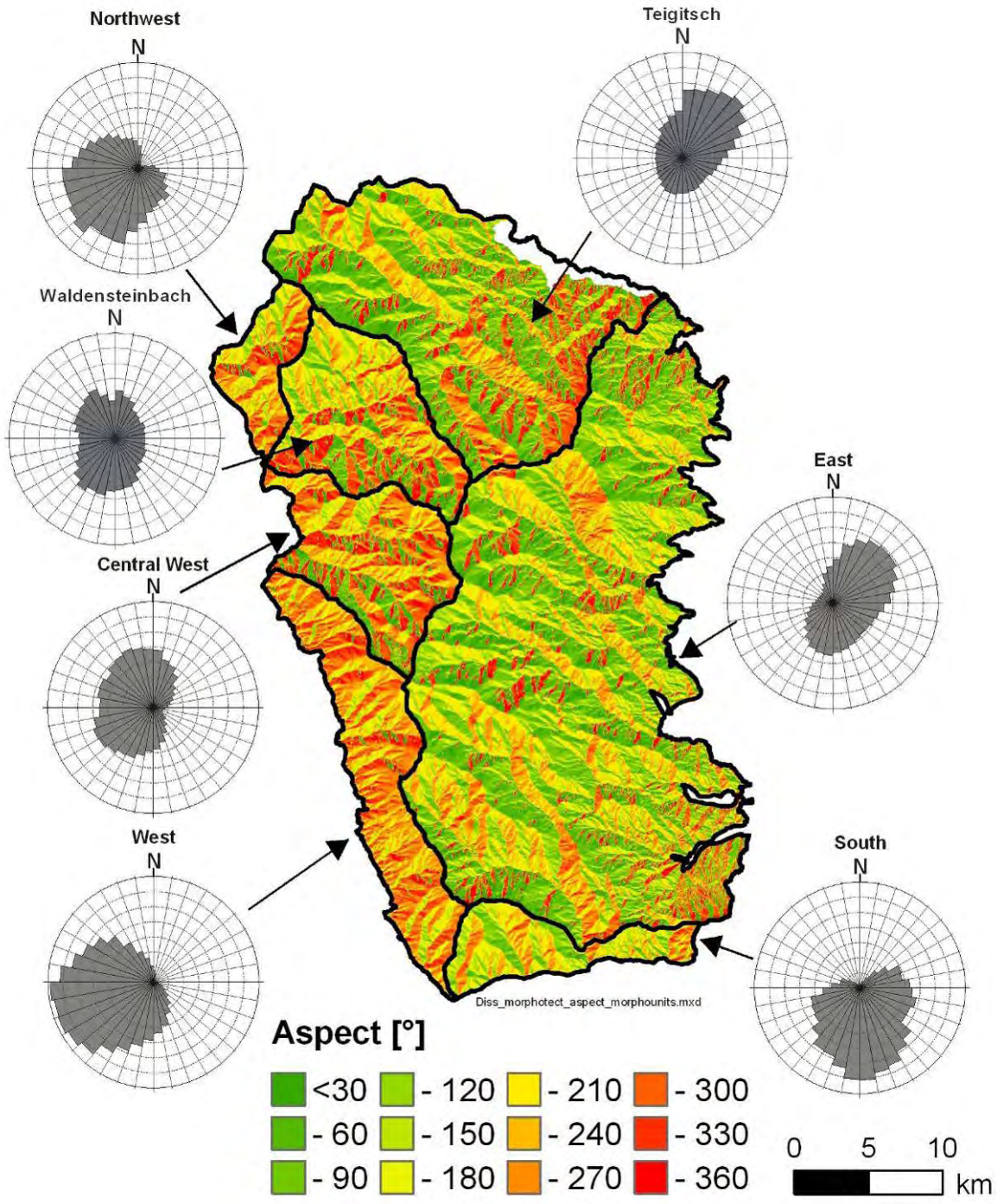

Figure 4-40: Slope aspect map classified in 30° intervals (north is towards 0°, clockwise classification) and draped over the hillshade of the Koralpe. Black lines mark the borders of the morphounits. Rose diagrams show the slope aspect of the six morphological units. Frequency interval in the circular histograms is two percent, the azimuth interval is 10°.

A regional comparison of *slope aspect* shows typical orientation patterns for the individual morphounits (Figure 4-40, Figure 4-41): Morphounit Northeast and East show slope orientations with prevailing NE to NNE and SW to SSW dipping slopes. Compared to the other morphological units they show a higher variation of aspect with two clear maxima in approximately opposing directions. However, in Morphounit Northeast this is due to the fact that it consists of two large catchments with opposing

drainage direction (Figure 4-41): The Teigitsch catchment is characterized by two maxima, one between N and E and one between SSE and SW, similar to Morphounit East. The Waldenstein catchment shows a high variation of aspect too and maxima between SSW - SW, and NNW - NNE. In contrast to these areas, morphounit Northwest and West show an unimodal distribution with the maximum towards SW. In Morphounit South aspect is characterized by one maximum too, with slopes dipping mainly towards southerly directions. Morphounit Central West shows a concentration of aspect values between S and NNE with several sub-maxima. These regional differences in aspect distribution may be indicative for a younger landscape in the Morphounits Northwest, Central West, West and South, with one broad maximum developed. In these regions the exogenic processes probably had not enough time to create a more mature landscape with a more pronounced drainage pattern. These regions are located, as described in previous chapters, along the active Lavanttal fault, the probably fault controlled Drava valley and along the transverse gorge of Twimberg.

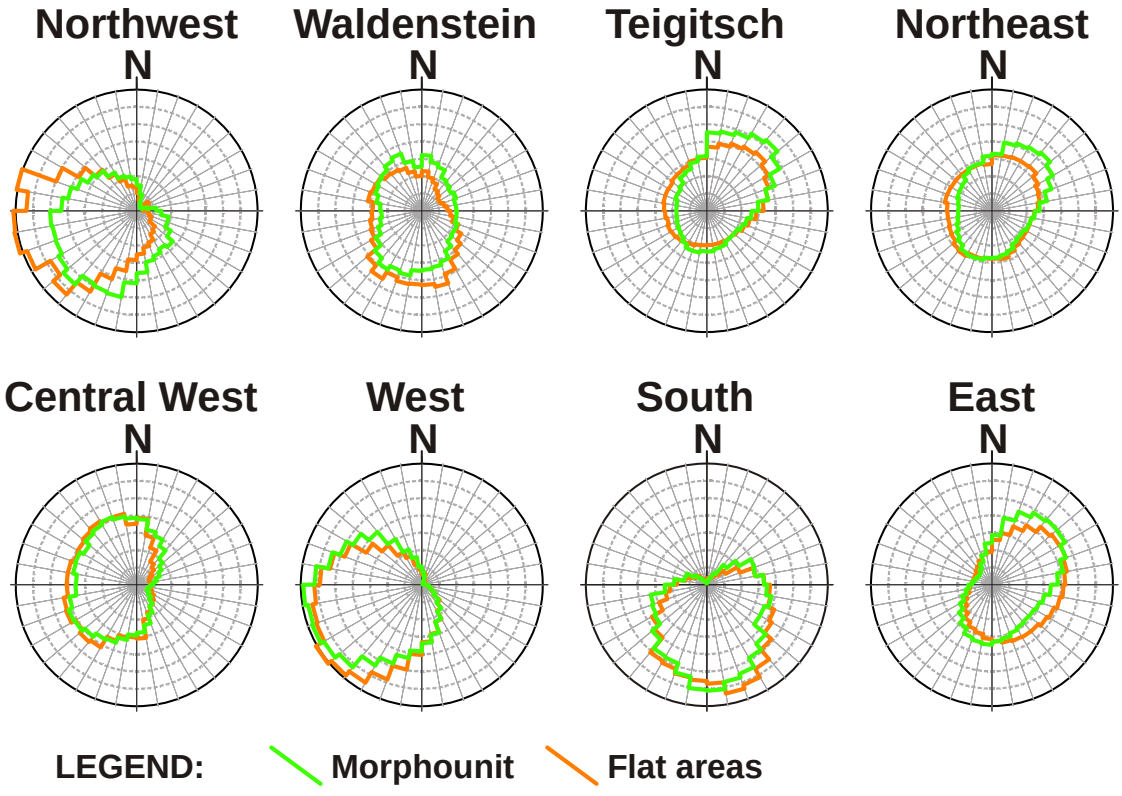

Figure 4-41: Aspect for the different morphounits of the Koralpe and comparison to the aspect of areas <10° slope gradient ("flat areas"). Frequency interval in the circular histograms is two percent, the azimuth interval is 10°.

To highlight the relationship between slope gradient and aspect, the slope angle distribution was determined for 30° aspect intervals (Figure 4-42 and Figure 6-5, Figure 6-6, Figure 6-7, Appendix). The shape of the frequency distribution curves is quite similar for all aspect classes. Differences exist mainly in the maximum of the aspect classes between 330° and 90° showing a higher frequency of slope gradients between 12° and 20°. The distributions of slope gradient are positively skewed

(mean > median > mode) for all aspect classes, with the mean between 17° and 19°, the median between 16° and 18° and the mode between 12° and 16°. The comparison (Figure 4-42, lower diagram) suggests that the aspect classes between 180° and 300° have higher slope gradient values than the rest. However, the mode does not reflect this trend. Increasing mean and median seem to reflect the steeper western and southern slopes as well as steep areas along the major creeks (Figure 6-5, Figure 6-6, Figure 6-7, Appendix). Further, this increase in slope angle coincides with slopes dipping into the opposite direction as foliation ("cuestas").

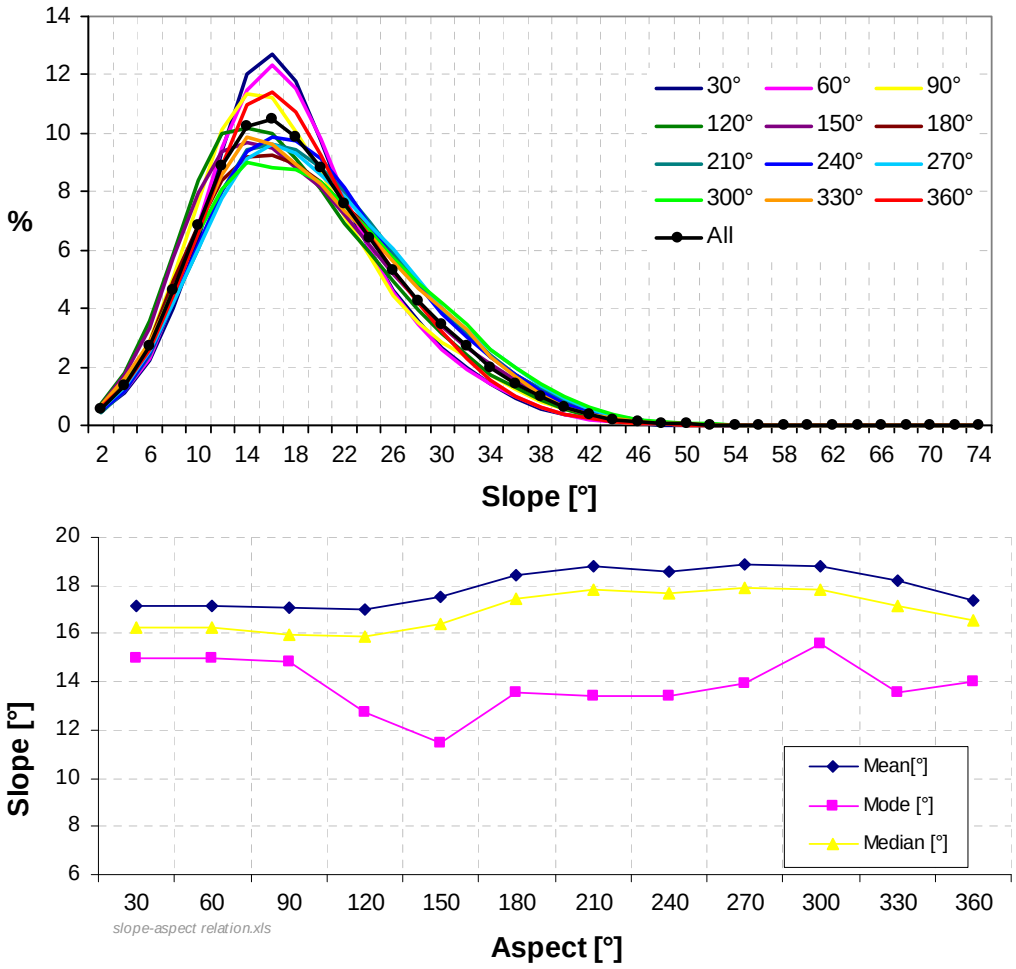

Figure 4-42: Relationship of slope gradient and slope aspect. Upper diagram shows slope gradient distribution for 30° aspect intervals. Lower diagram displays the relation of mean, median and mode values of the gradient in these aspect classes.

The aspect distribution in different slope gradient classes reveals pronounced differences between the individual classes (Figure 4-43, Figure 4-44). However, the aspect distribution of all slope gradient classes is strongly dominated by the two largest morphounits, the E and the NE, concealing the distributions of the smaller regions. Therefore the individual morphounits have been analysed separately.

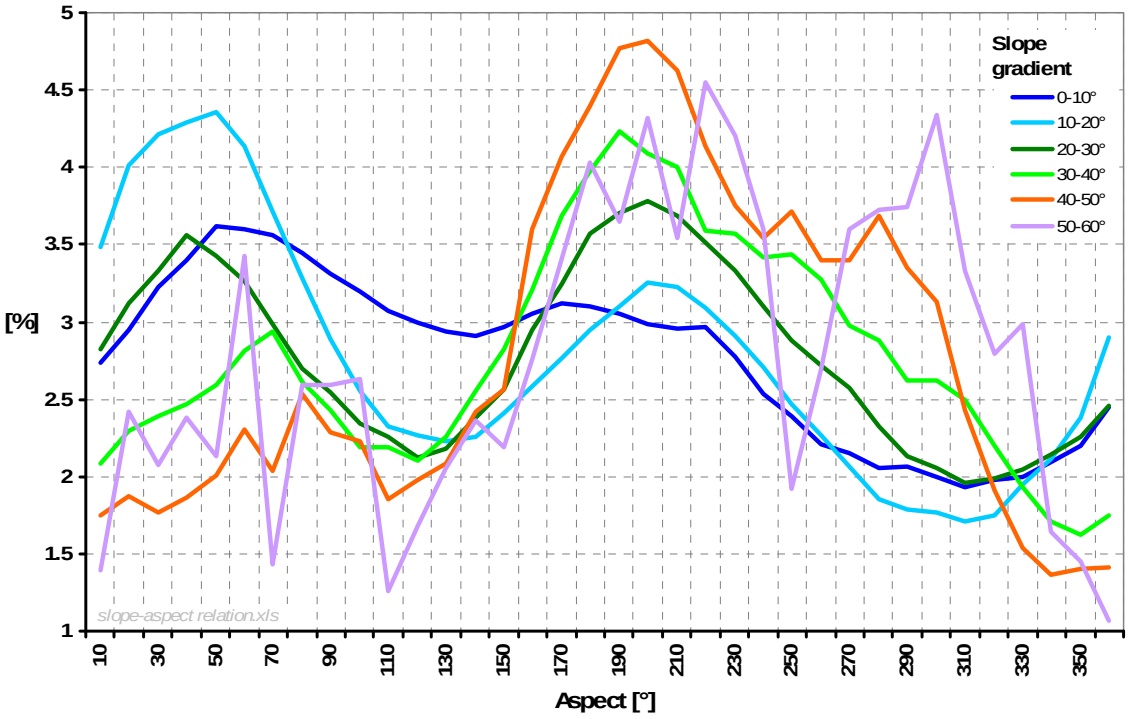

Figure 4-43: Frequency distribution of slope aspect for 10° slope gradient classes for the clipped DEM of the Koralpe.

The individual morphounits were analysed for 10° slope gradient classes too (Figure 4-45, Figure 4-46, Figure 4-47, Figure 4-48, Figure 4-49 and Figure 6-8, Figure 6-9, Figure 6-10, Figure 6-11, Figure 6-12, Figure 6-13 and Figure 6-14, all within the Appendix). Within slope gradient class 0 to10° Morphounits Northwest and West show very similar broad, unimodal distributions of aspect with their maxima towards WSW (Figure 4-45). Compared with the entire morphounit the distribution for the flat areas shows higher frequencies in aspects towards W-WSW for Morphounit Northwest, whereas in Morphounit West show practically the same distribution as the entire morphounit (Figure 4-41). Morphounit South is characterized by a unimodal aspect distribution in slope gradient class 0 to10° too. The peak is towards S-SSE. Compared to the entire data set, aspect is slightly shifted to more easterly directions (Figure 4-41). The “unimodal” aspect characteristics is maintained for Morphounits South and West up to a slope gradient class of 30°, for Morphounit Northwest up to 20° respectively (Figure 4-46, Figure 4-47). The latter is related to the lower number of data in this morphounit. Above, the distributions are controlled by regional morphological peculiarities and the decrease of data, being characterised by multiple, sharp peaks (Figure 4-48, Figure 4-49).

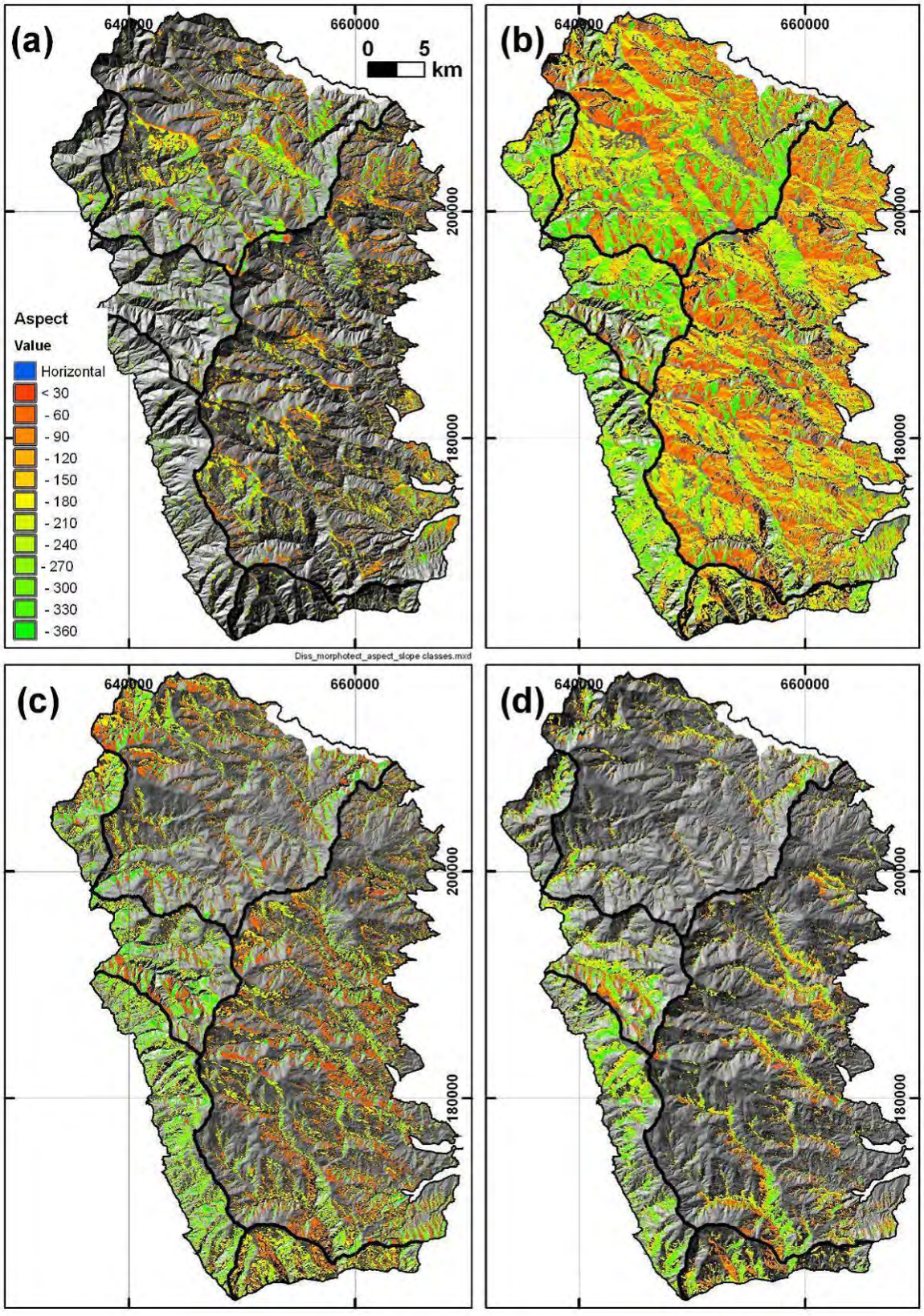

Figure 4-44: Slope aspect for 10° slope gradient classes: (a) 0-10°, (b) 10-20°, (c) 20-30° and (d) 30-40°. Legend is valid for all four maps.

For further analysis Morphounit Northeast, as above, is split into the Teigitsch catchment (draining to the Styrian Basin) and the Waldenstein catchment (draining to the Lavant River). In slope gradient class 0-10° these two catchments, Morphounit East and Morphounit Centralwest reach a maximum frequency which is ~3% lower than the one for the other three morphounits (Figure 4-45). In addition, their minima are not as low as the other ones. Overall, the spread of these data sets is more balanced, related to a better evolved drainage system and a high percentage of planation surfaces (between 18% and 24%), except for Morphounit Centralwest with a percentage of planation surfaces of only 8%. The flat areas within Teigitsch catchment show a very similar frequency distribution as the data for the entire data set, whereas in the Waldenstein catchment flat areas dip more frequently towards southerly directions (Figure 4-41). The flat areas in Morphounit East are characterized by higher frequencies of aspect towards E-SE.

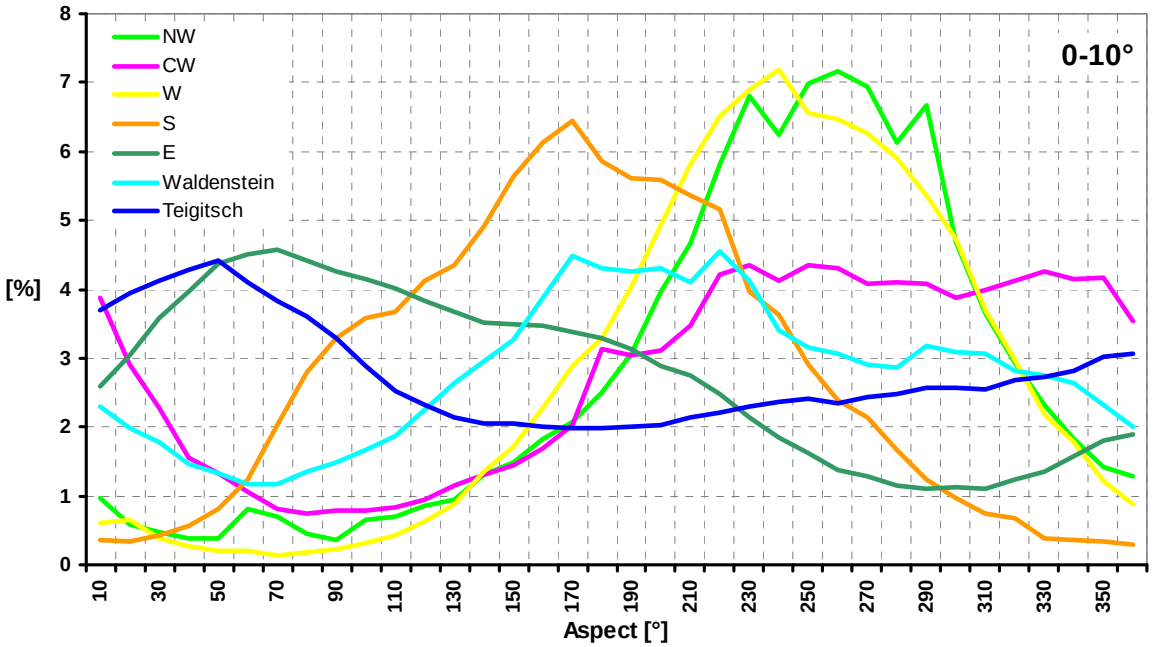

Figure 4-45: Slope aspect distribution within the individual morphounits for a slope gradient <= 10°.

Above 10° slope gradient the aspect distributions of the Waldenstein and Teigitsch catchments, as well as Morphounit East are characterized by two or more peaks (Figure 4-46). Morphounit East and the Teigitsch catchment show one pronounced peak towards NE and one less pronounced towards SSW-SW. The Waldenstein catchment shows one peak towards S-SW, a second towards NNW and a third towards N-NNE. Morphounit Centralwest shows a marked minimum towards ENE-ESE and a broad maximum from 190° to 30°with peaks at 240° and 350°, which is similar to the Waldenstein catchment. From 20° to 30° slope gradient Morphounit East and the Teigitsch retain their two peak distribution (Figure 4-47). The Waldenstein catchment shows a more balanced distribution with two remaining peaks. Morphounit Centralwest keeps its characteristics too. However, the peaks become less pronounced.

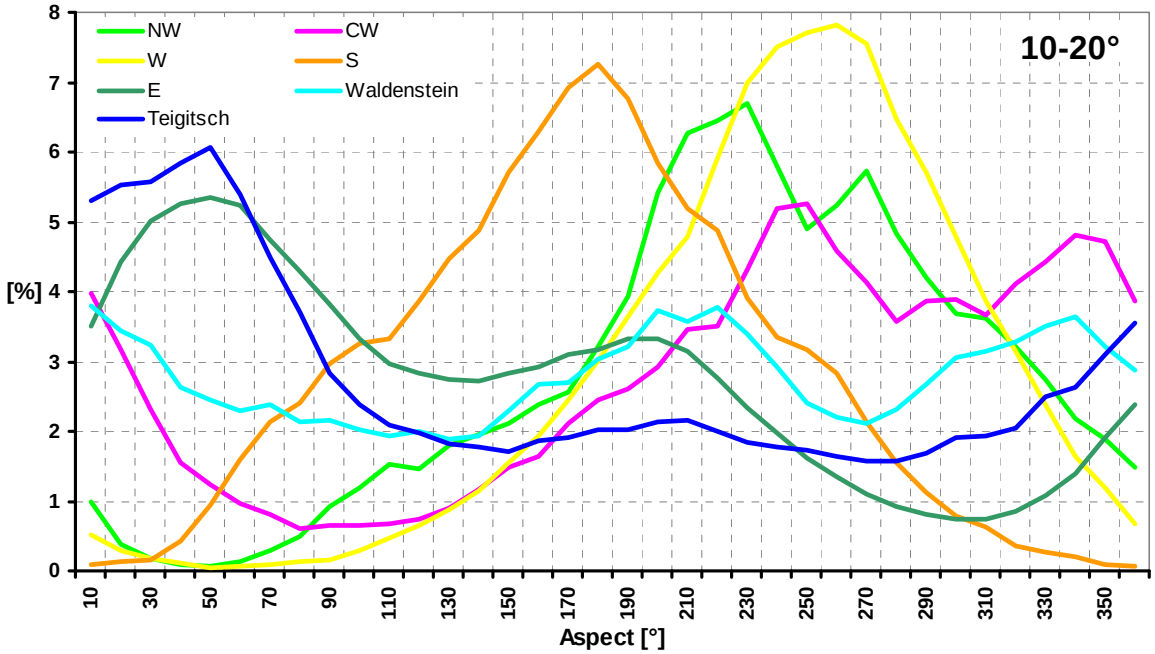

Figure 4-46: Slope aspect distribution within the individual morphounits for 10° to 20° slope gradient.

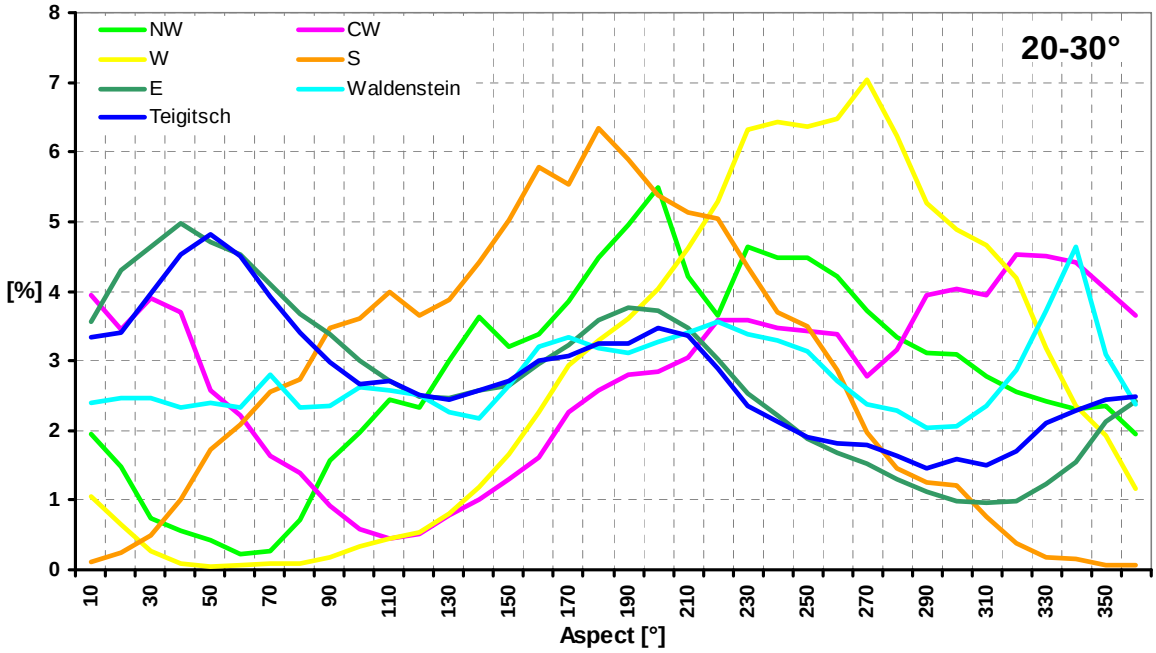

Figure 4-47: Slope aspect distribution within the individual morphounits for 20° to 30° slope gradient.

Above 30° slope gradient only Morphounit East keeps its distribution characteristics (Figure 4-48). The Teigitsch and the Waldenstein catchment are marked by one pronounced maximum towards S and one minor peak towards NNW. Morphounit Centralwest maintains its pronounced minimum towards ESE-SE. Two pronounced peaks mark slopes dipping towards SSW and W.

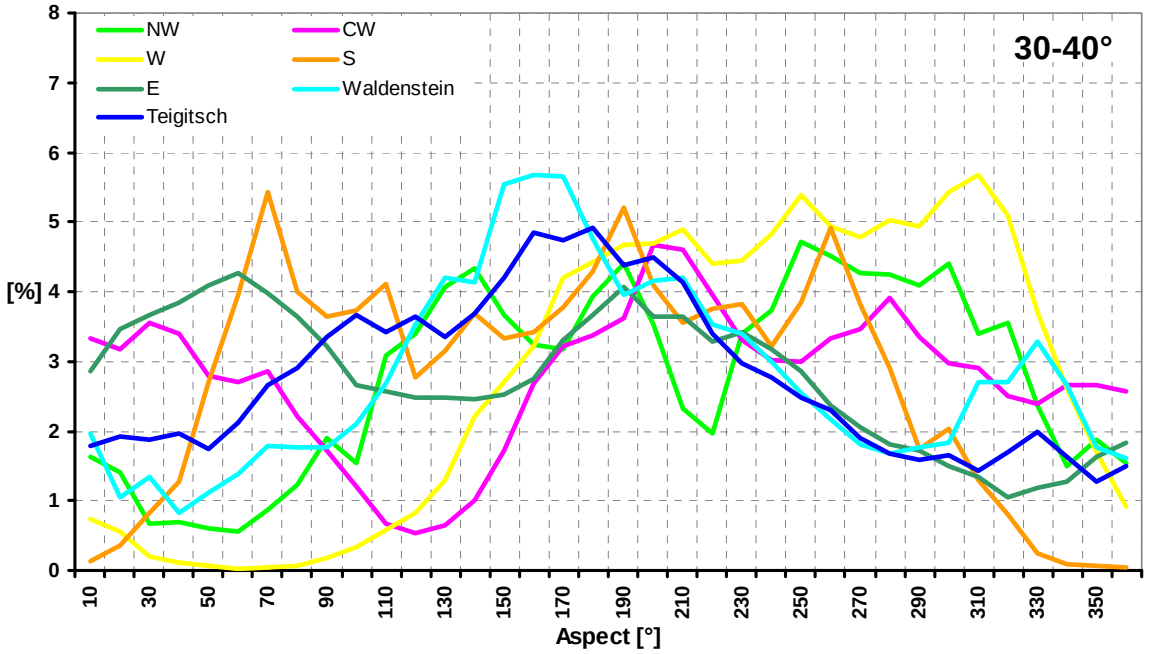

Figure 4-48: Slope aspect distribution within the individual morphounits for 30° to 40° slope gradient.

Slopes with a gradient steeper than 40° are rare. Within Morphounit Centralwest they reach ~3% and in Morphounit West ~2% of the unit area. All the other units show frequencies below 1%. Due to the low number of data the distributions represent rather singularities than general characteristics of the morphounits. The peaks coincide with steep, gorgelike stretches along the rivers (Figure 4-49).

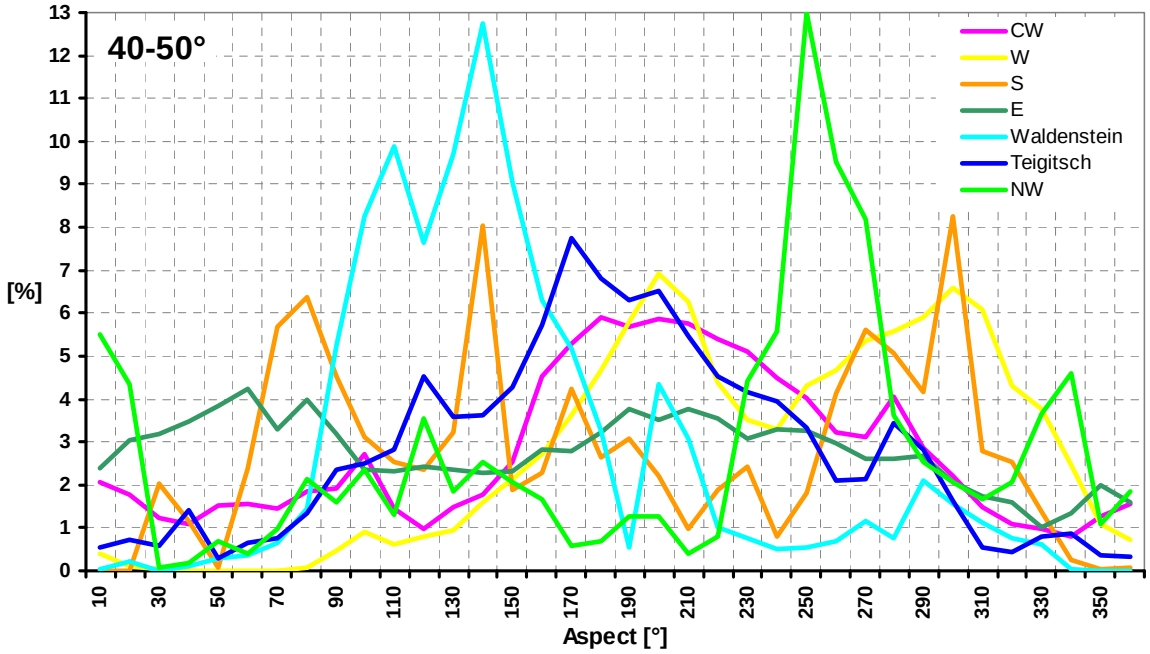

Figure 4-49: Slope aspect distribution within the individual morphounits for 40° to 50° slope gradient.

4.3.5.3 CURVATURE

Plan and profile curvatures (Figure 4-50, Figure 4-51) are approx. normal distributed (Figure 4-52). Unusual high values of curvature are rare and generally bound to cliffs, gorges or artificial structures like dams or quarries.

Profile curvature along ridgelines, peaks and tors (“Felsöfen”, remnants of ridges) is characterized by negative values, indicating upwardly convex landforms (Figure 4-51, Figure 4-53 a and c) while plan curvature exhibits positive values at the same location. The plan curvature map (Figure 4-50) is characterized by an intense fluctuation of convex and concave areas, reflecting the structuring of the landscape by innumerable, small-scaled ridges and trenches. The size of these areas is characteristic for certain regions of the Koralpe, with the larger ones in the higher regions and the slopes towards the Drau (Drava) valley and the smaller ones towards and in the surrounding basins. This may be indicative for the relative age and/or different (mass wasting) processes acting in different regions of the Koralpe. In the realm along the Drau (Drava) valley this may also be influenced by the fact that the DEM was here interpolated from 20 m contour lines, and may therefore lack a pronounced undulation in plan curvature. In the profile curvature map (Figure 4-51) the changes between convex and concave areas are less pronounced. The stream pattern is better visible in the profile curvature map, whereas the pattern of low order streams is better visible in the plan curvature map. The river courses are dominated by negative plan curvature and positive profile curvature. The human impact on the landscape is clearly reflected in the curvature data, especially for profile curvature, even in unpopulated, remote areas (roads for forestry). Smoothing of the input data reduces the visibility of the roads.

Curvature maps in combination with hillshade representations and adjusted transparency help to distinguish lineaments following ridges or valleys. This is especially true for the profile curvature map, as it enhances large-scale structures like ridges or major valleys. Difficulties in mapping lineaments from the curvature maps result from the dominant appearance of roads. The linear structures detectable in the profile curvature map correlate partly with the lineaments mapped from the hillshades and colour coded DEM combinations. According to Florinsky (1996), this suggests a predominating vertical displacement vector.

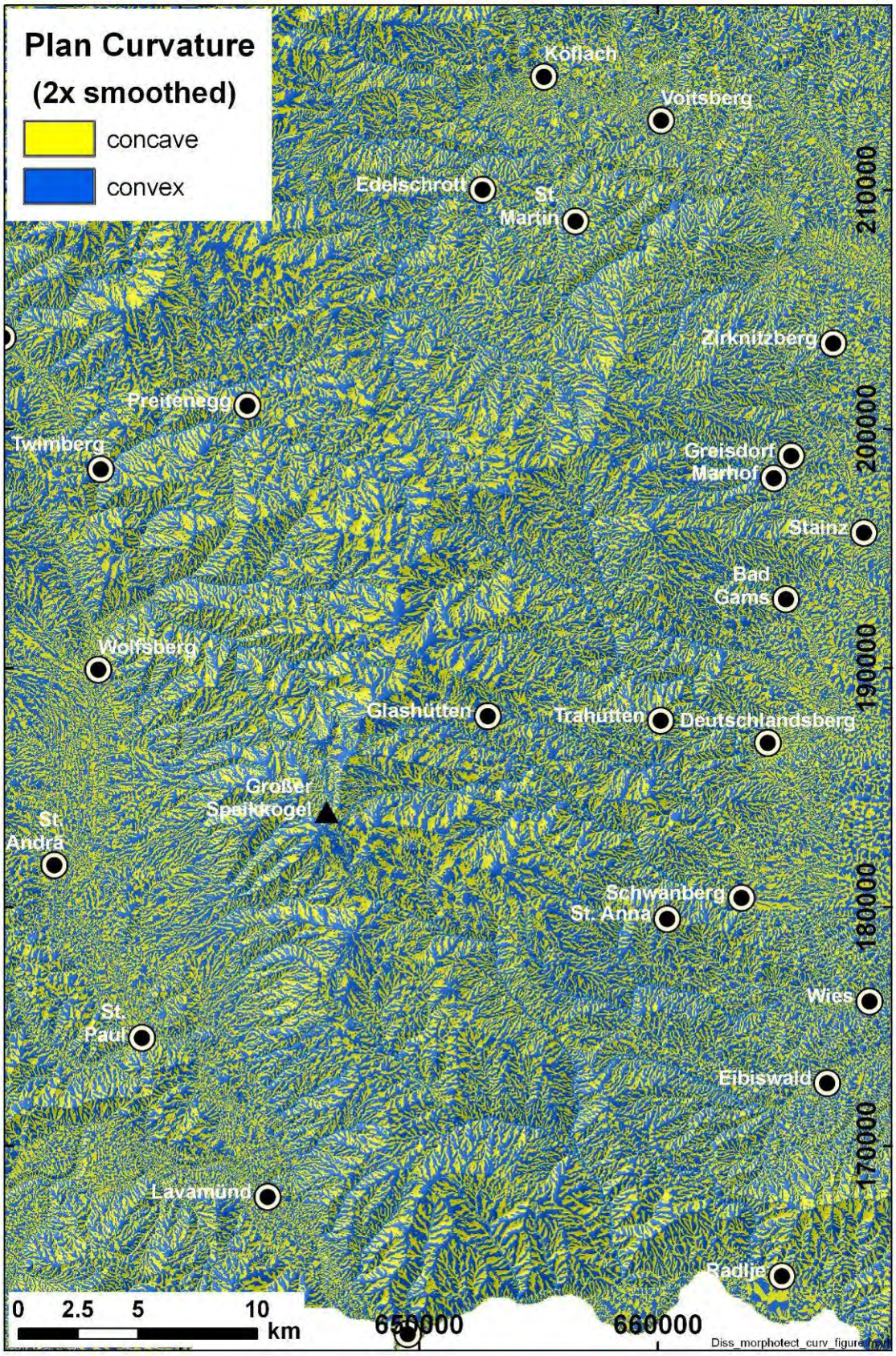

Figure 4-50: Plan curvature map of the Koralpe. Blue indicates convex areas ("ridges", positive landforms), yellow concave areas ("valleys", negative landforms). Morphology is enhanced by hillshade in the background.

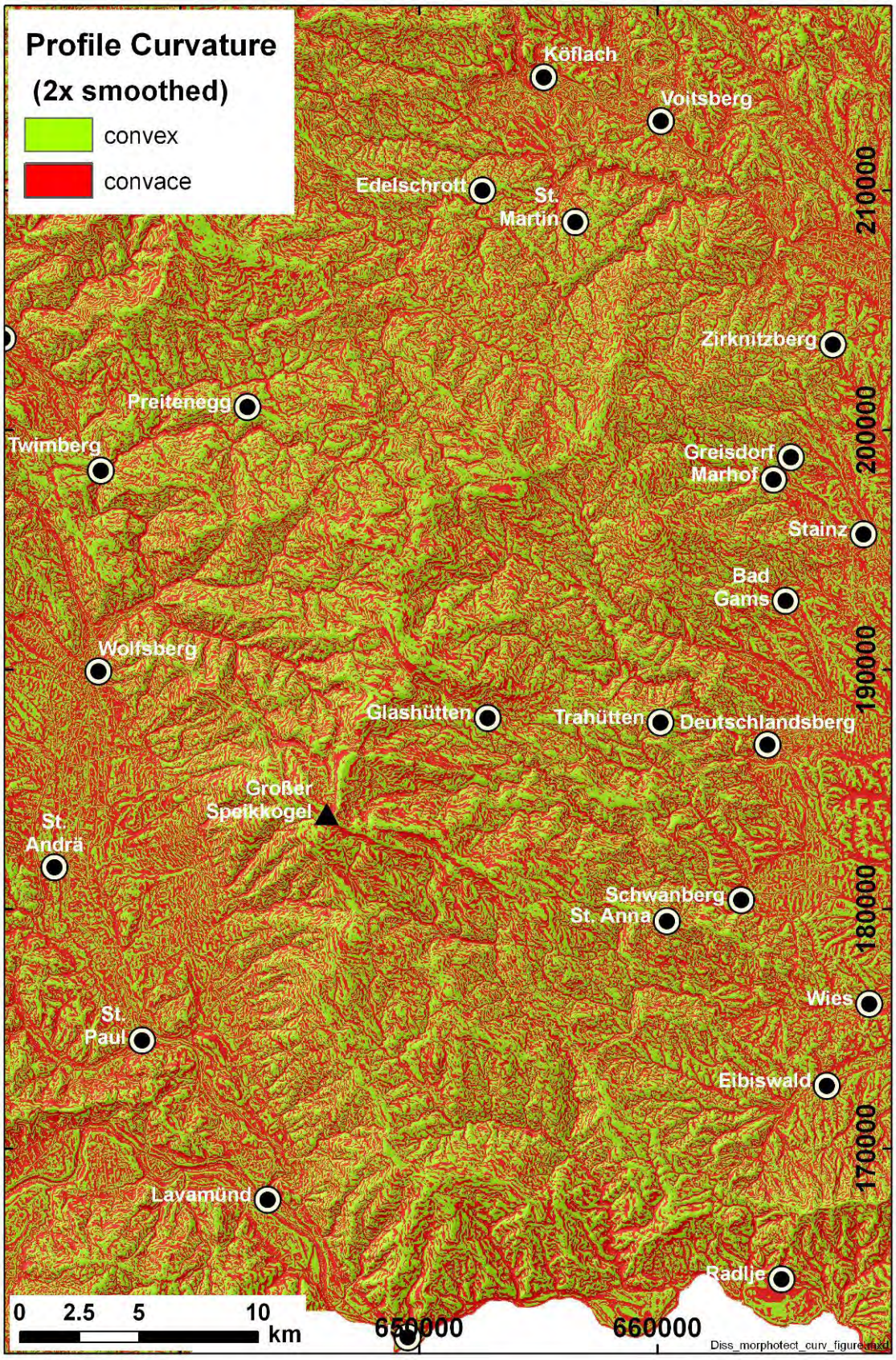

Figure 4-51: Profile curvature map of the Koralpe. Green indicates convex areas ("ridges", positive landforms), red concave areas ("valleys", negative landforms). Morphology is enhanced by hillshade in the background.

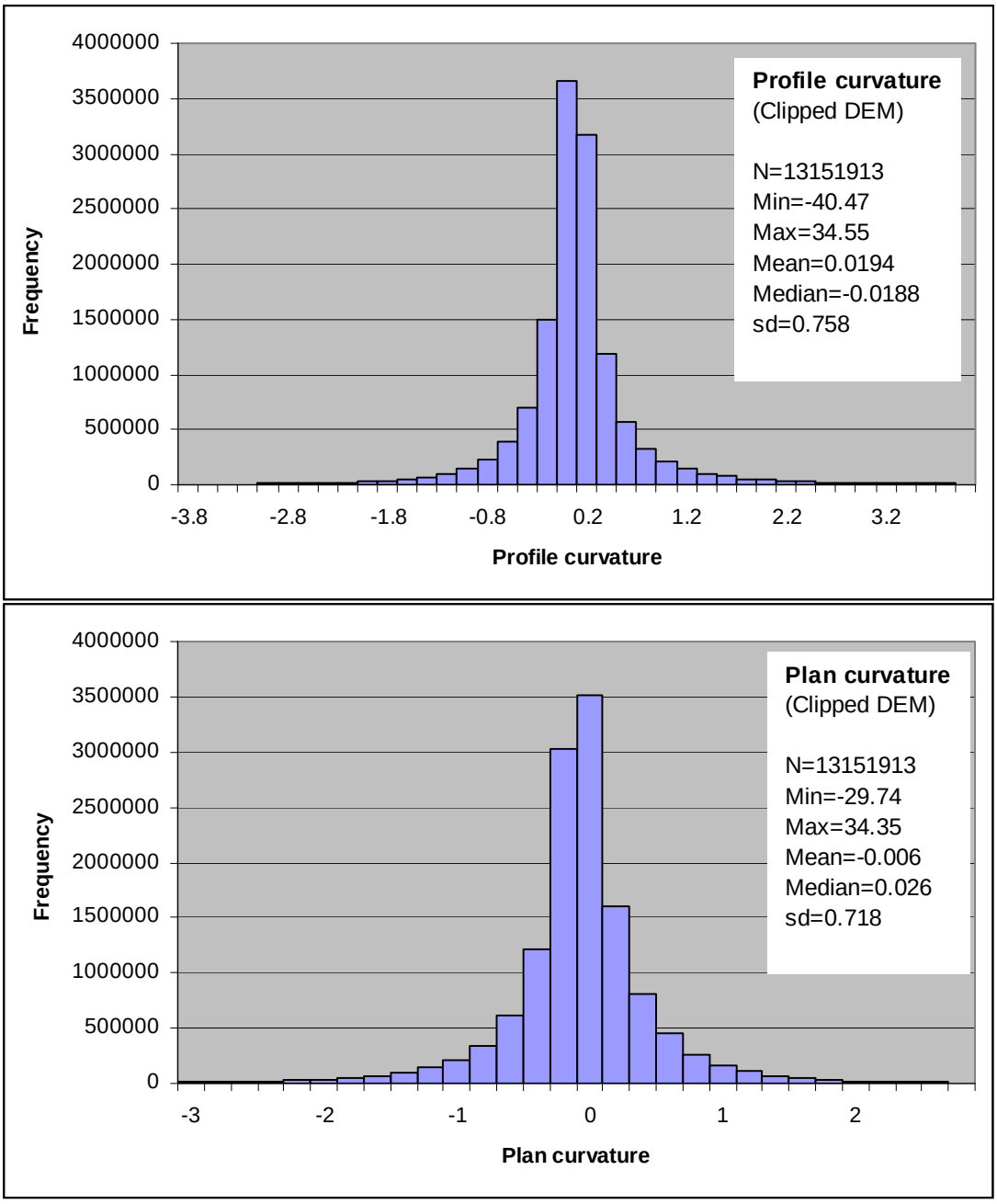

Figure 4-52: Histograms and basic statistics for plan and profile curvature. The histograms are truncated to omit the extreme values.

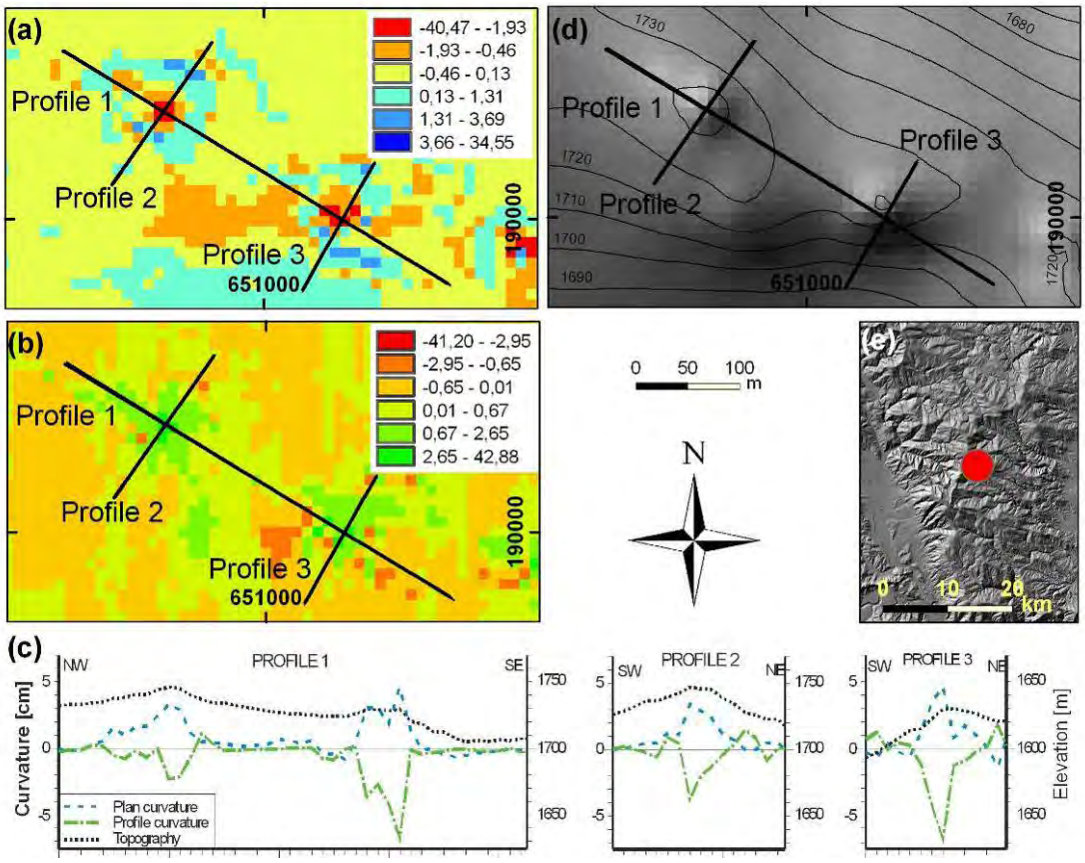

Figure 4-53: (a) Profile (negative values are convex, positive values are concave) and (b) plan curvature (negative values are concave, positive values are convex) map and (c) three curvature sections across two peaks in the central realm of the Koralpe and (d) the respective hillshaded elevation model with 10 m contour lines. (e) Overview hillshade of the Koralpe, red point indicates location of the area.

Plan and profile curvature were used to classify the slope shape into the nine classes defined in Figure 4-4. Curvature values were grouped as concave for positive values, as convex for negative values and as linear for zero values. Two example areas were chosen to illustrate the results of the classification (Figure 4-54). The map is dominated by combinations of convex and concave profile and plan curvature (Figure 4-54 b), which partly reflect a fold structure. Combinations with linear curvature are rare and are mostly related to larger water surfaces incorporated in the elevation model (Figure 4-54 a).

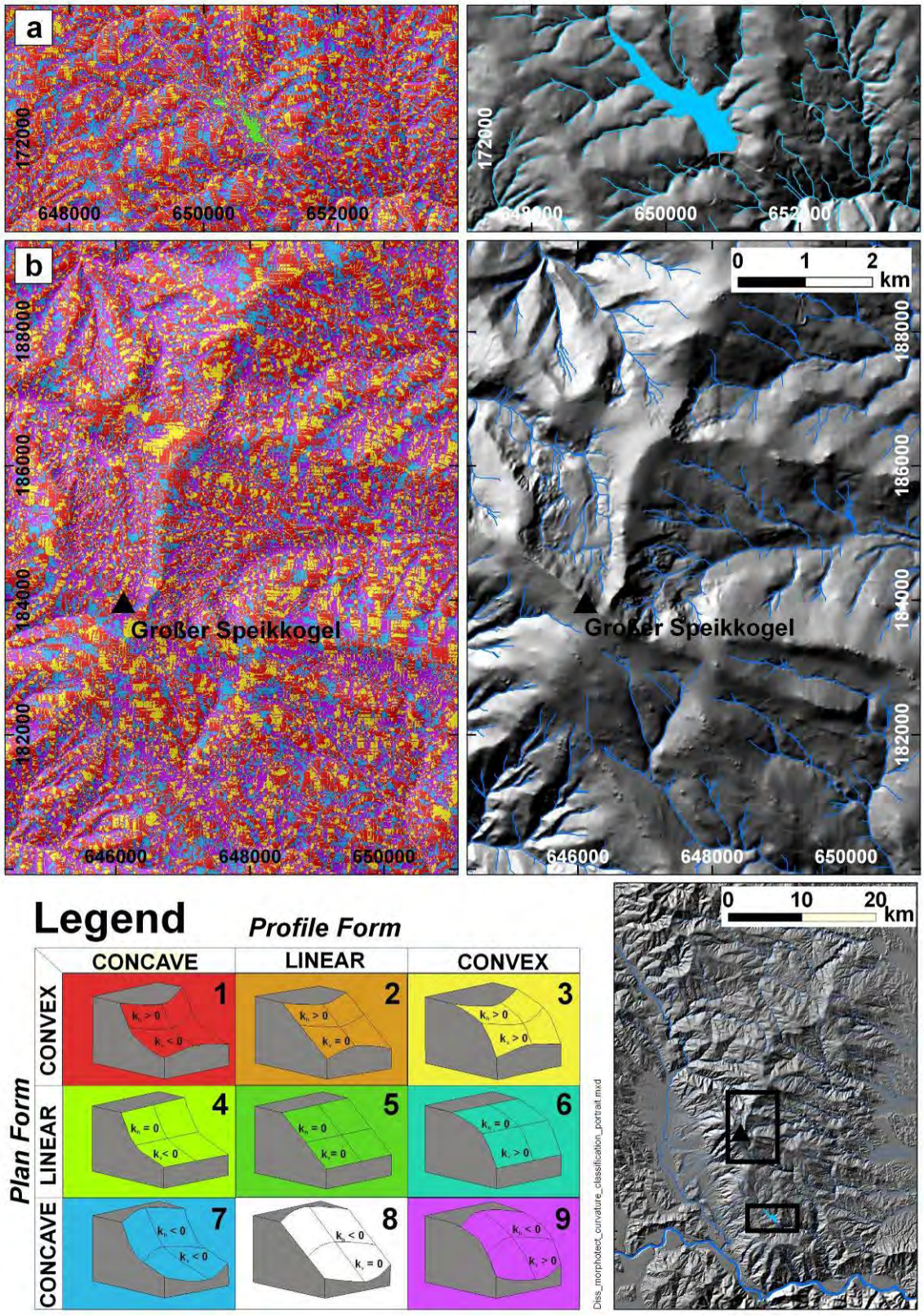

Figure 4-54: Examples of curvature classification maps as a transparent overlay over a hillshade and the respective hillshade: (a) Reservoir "Soboth": a rare location of curvature classes 2, 4, 5 and 6. (b) Summit region of the Koralpe with the "Seebach" mylonite syncline east of the summit (black triangle). Classes depicted in the legend are according to Figure 4-4, following Summerfield (1991) and Florinsky (2000). Overview map at the lower right shows location of (a) and (b) in the Koralpe Range.

A comparison of the curvature classification for the individual morphounits shows that the frequency of combinations of concave and convex forms is very similar for each combination class throughout the different morphounits (Table 9). Generally combinations of concave profile curvature and convex plan curvature prevail with frequencies between 31 and 36 %. Combinations of convex profile curvature and concave plan curvature show frequencies between 26 and 29%. Convex-convex combinations are within 1.4 % (18.9% to 20.3%), similarly to concave-concave combinations with a range of 1.3% (17.9 to 19.6%). This distribution reflects the dense drainage pattern of the Koralpe which is associated with concave plan forms and the intense structuring of the landscape by ridges, separating the individual drainage paths. Further, this similar distribution in areas different in size and location reflects the "self similarity" of the landscape at different scales (Mandelbrot, 1967; Turcotte, 1997).

		Profile Curvature [%]			Data Set
		Concave	Linear	Convex	
Plan Curvature [%]	Convex	33.5	0.0005	20.3	DEM 10m
	Linear	0.0058	0.0037	0.0066	
	Concave	18.3	0.0006	28.0	
	Convex	34.9	0.0001	19.5	DEM clipped
	Linear	0.0032	0.0041	0.0031	
	Concave	18.6	0.0001	26.9	
	Convex	33.9	0	20.2	West
	Linear	0.00017	0	0.0001	
	Concave	18.4	0.0002	27.4	
	Convex	31.3	0	20.2	NW
	Linear	0	0	0	
	Concave	19.6	0	29.0	
	Convex	34.6	0.0002	19.4	NE
	Linear	0.0032	0.0018	0.0029	
	Concave	19.0	0.0003	27.0	
	Convex	32.6	0	19.6	Central West
	Linear	0.0002	0	0.0004	
	Concave	19.1	0	28.7	
	Convex	35.0	0	18.9	South
	Linear	0.0002	0	0	
	Concave	17.9	0	28.2	
	Convex	35.8	0.0001	19.5	East
	Linear	0.0051	0.0080	0.0052	
	Concave	18.3	0.0001	26.4	

Curvature classes distribution.xls

Table 9: Percentages of profile and plan curvature classes for the individual morphounits and the entire DEM (clipped and unclipped).

4.3.6 LINEAMENT ANALYSIS

The Koralpe is dominated by WNW-ESE to NW-SE trending lineaments (Figure 4-55 & Figure 4-56). These lineament directions are observed in all data sources and all mapping scales. A second clear maximum is given by NNE-SSW to NE-SW trending lineaments in the combined 1:50.000 and 1:25.000 mapping and in the 1:100.000 mapping. The mapping on the 10 m resolution DEM at a scale of 1:200.000 yields a different result. Here this second cluster is trending NE-SW. This difference can be explained by a bias towards longer lineaments, trending NE-SW, introduced by the smaller mapping scale and towards shorter lineaments, trending more frequently WNW-ESE, in larger mapping scales (Figure 4-57). This shortcoming could possibly be compensated by introducing length thresholds for each mapping scale and by creating a synoptic lineament layer containing all lineaments from all mapping scales.

Frequency distribution and statistical parameters confirm this effect (Figure 4-56). Length binning of the lineament data in the 1:50.000 scale shows that the orientation distribution for lineaments longer than 5000 m corresponds to the results from the 1:200.000 scale mapping (Figure 4-56 & Figure 4-57). For the 1:100.000 scale mapping on the 96 m SRTM elevation model this coincidence is not observed, which can be attributed to the different data source, mapping scale and the “human” factor. In the combined 1:50.000 and 1:25.000 mapping, the length distribution shows predominantly features between 500 and 3000 m. Lineaments with lengths >5000 m are preferably trending NNW-SSE to NNE-SSW, WNW-ESE and WSW-ENE. These maxima coincide with the main orientations of outcropping fault planes and foliation planes (Figure 4-58), supporting a general structural control of surface morphology. A priori the identified lineaments may be caused by both structures, emphasizing a careful genetic interpretation of lineaments and a validation by a field check.

Regional distribution of lineaments can be studied by lineament density maps (see chapter 4.2.4, Kim et al., 2004). The three lineament maps were analysed by calculating the sum of the length of all lineaments contained within circular windows with 1, 2 and 3 km radii, using the line density function of ArcGIS (Figure 4-59). For comparison, this density was normalized by the largest density (Figure 4-60).

The highest density is found in the eastern and the northeastern Koralpe (Figure 4-16), the regions with the highest proportion of paleosurfaces. Generally, lineaments in the Koralpe can be regarded as a morphological expression of subsurface structure. This morphological expression is enhanced by contrasts in rock strength and erodibility. Differences in time of exposure to exogenic processes may also exert a significant influence in moulding the bedrock structures. Consequently a high lineament density does not necessarily represent areas of intense faulting or fracturing.

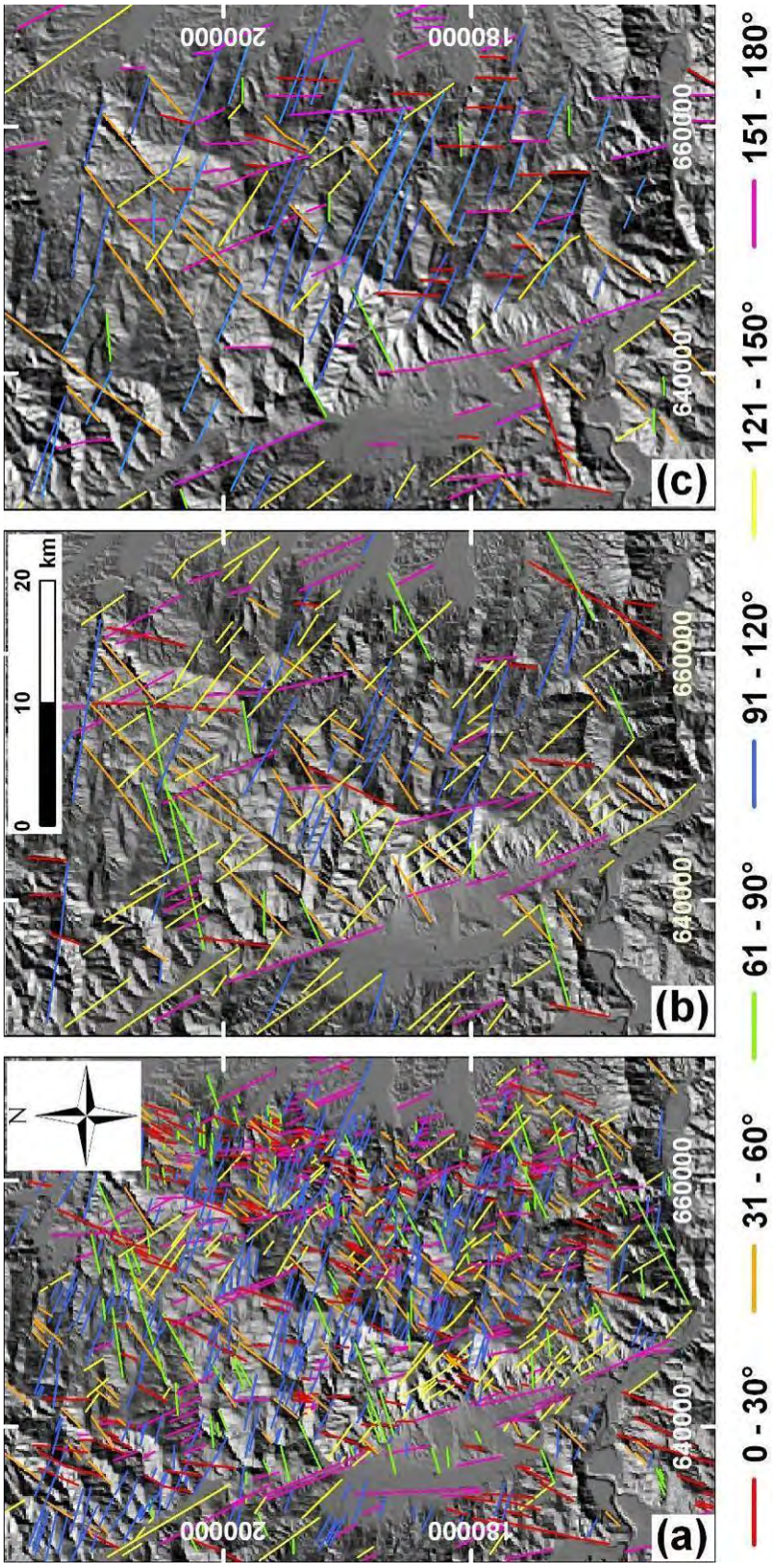

Figure 4-55: Lineament maps of the Koralpe Range, derived from 10 m resolution DEM (a & b) and from 96 m resolution SRTM DEM (c). All maps are at the same scale. Mapping scale is 1:50.000 for (a), 1:200.000 for (b) and 1:100.000 for (c).

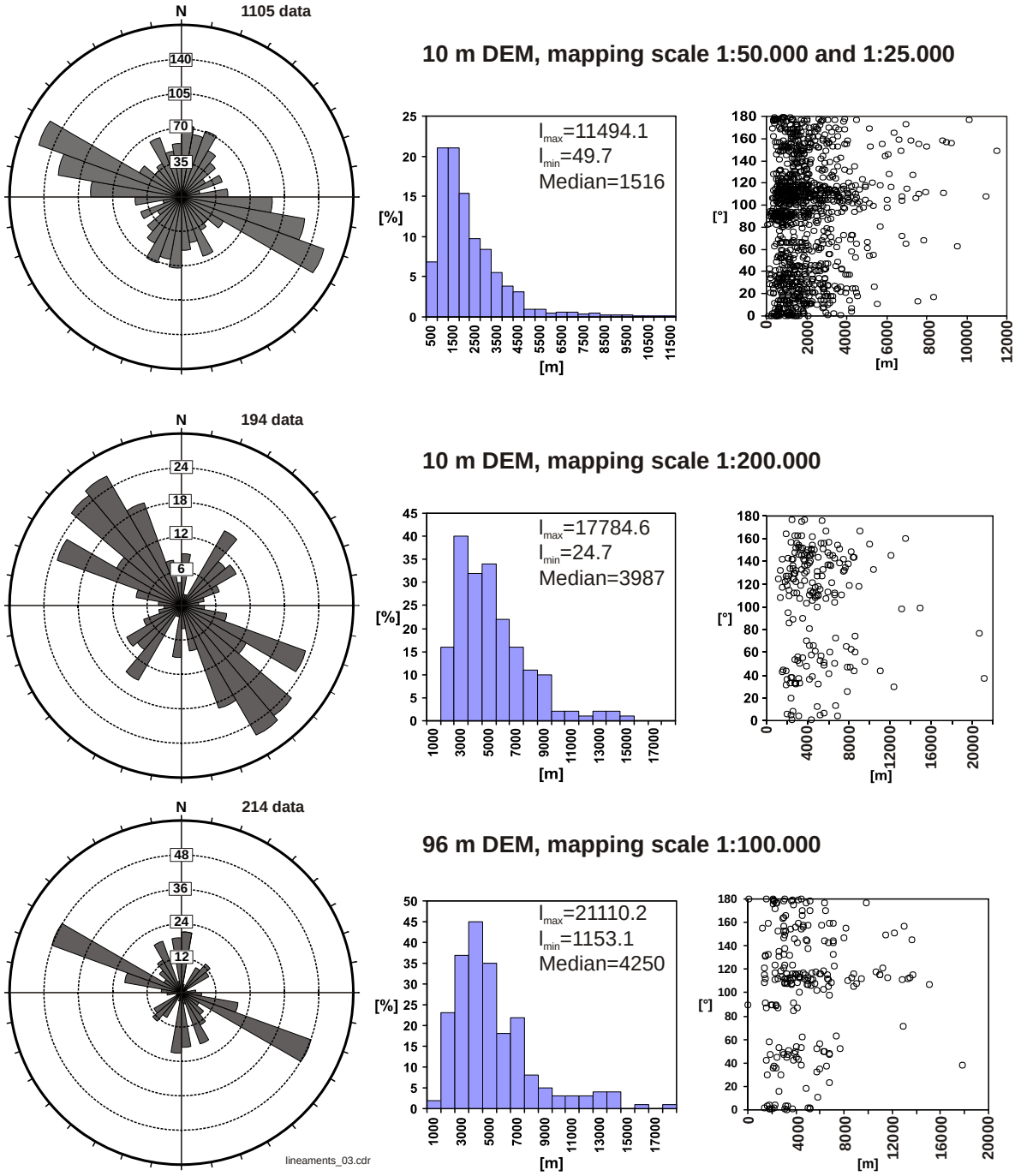

Figure 4-56: Rose diagrams of strike direction, histogram of length distribution and scatter plot of both for lineaments mapped in different scales on the 10 m DEM (upper two diagrams) and on the 96 m DEM (lowest diagram).

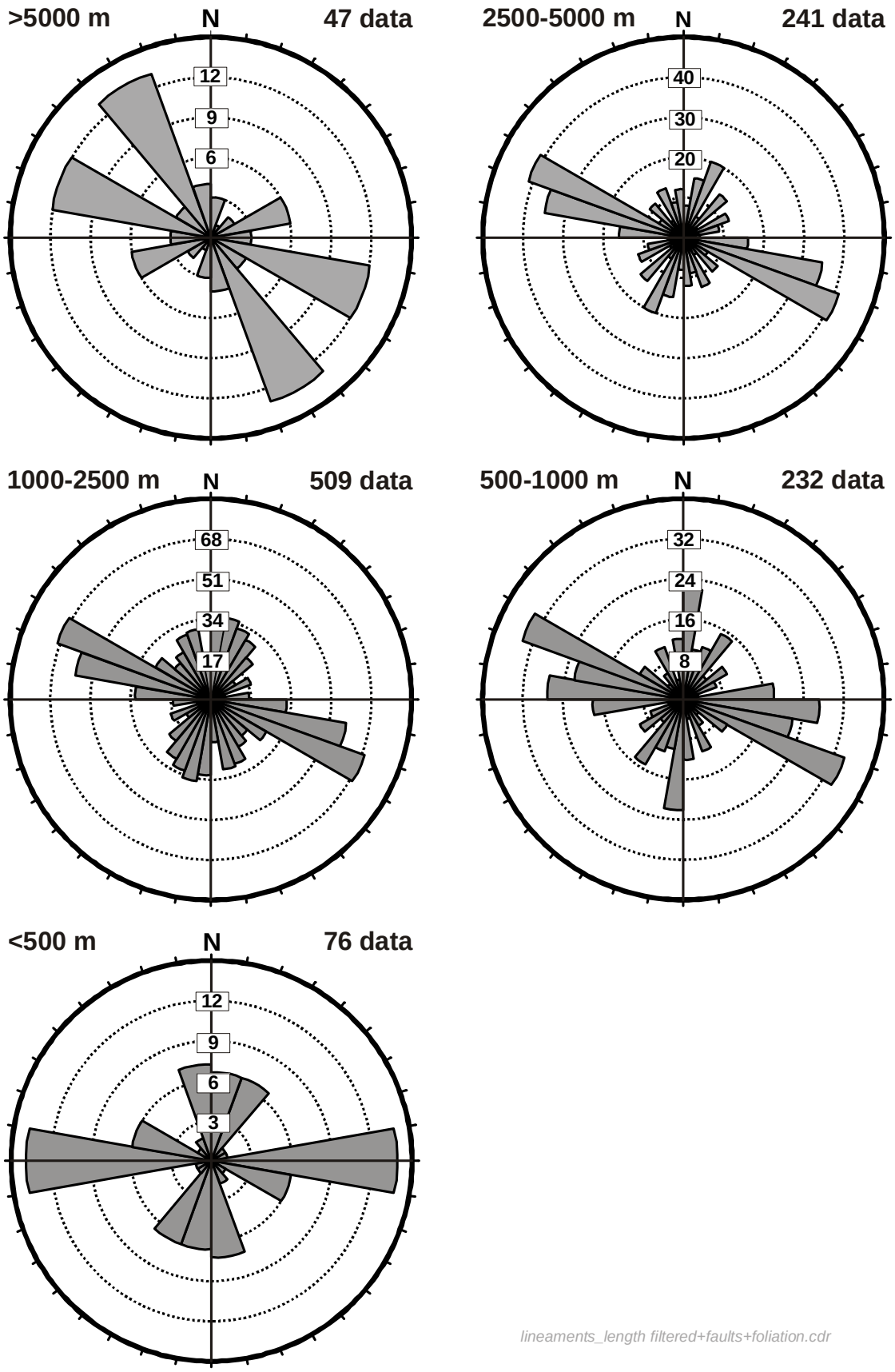

Figure 4-57: Rose diagrams (trend) of lineaments derived from the 10m DEM (mapping in 1:25.000 & 1:50.000) grouped into five length intervals (>5000 m, 5000-2500 m, 2500-1000 m, 1000-500 m and <500 m).

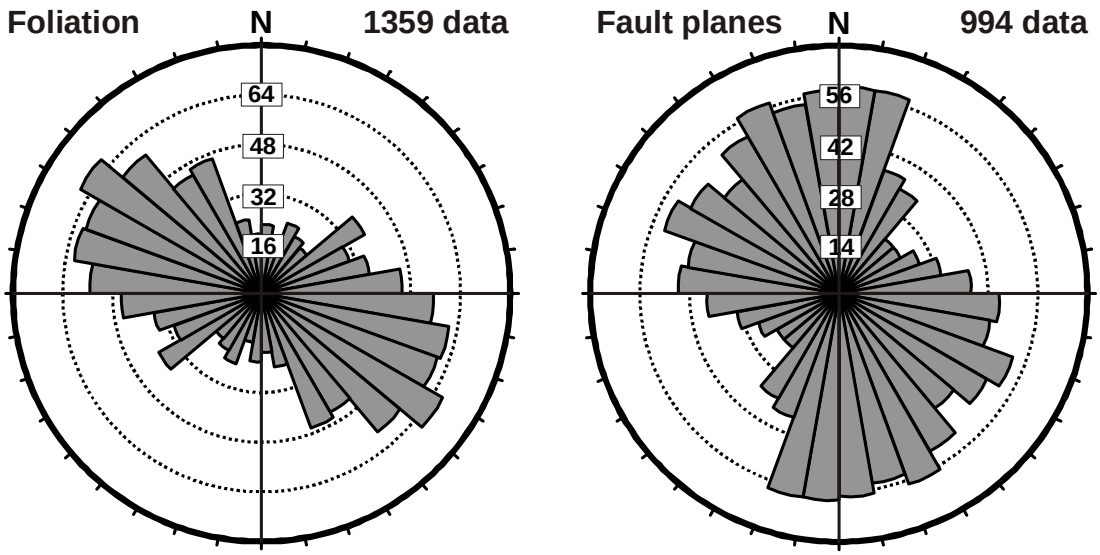

Figure 4-58: Rose diagrams for the strike direction of foliation (own outcrop measurements and map data Beck-Mannagetta, 1980; Beck-Mannagetta et al., 1991; Beck-Mannagetta and Stingl, 2002) and fault planes (own outcrop measurements, see also Rantitsch et al. (2009)).

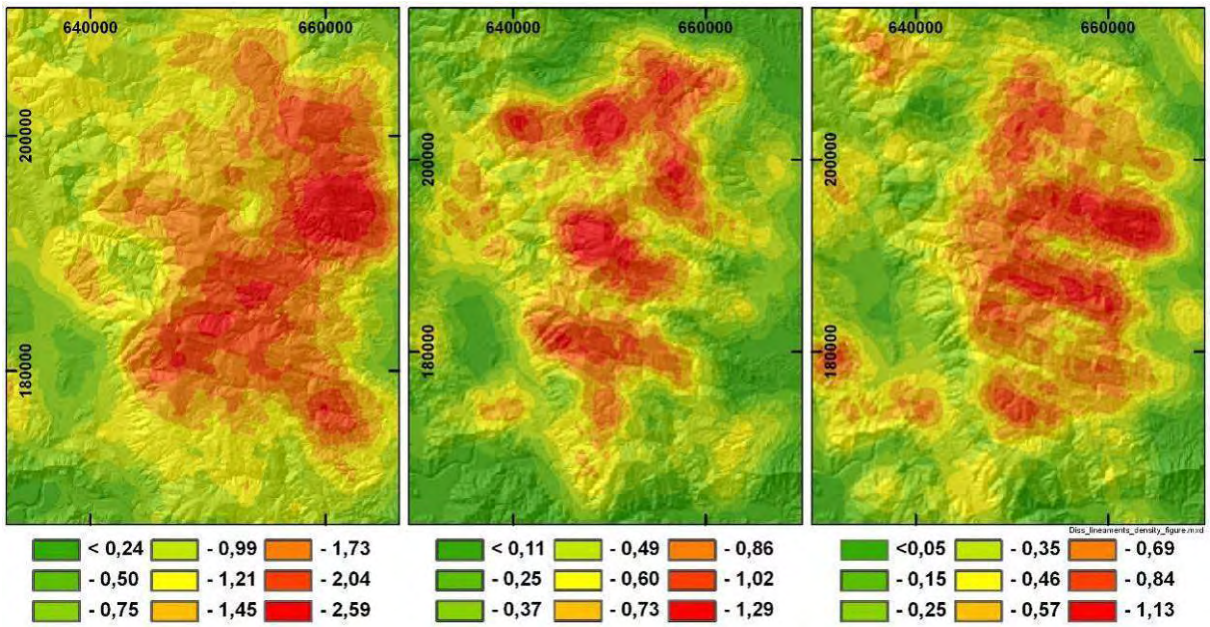

Figure 4-59: Lineament length density map derived from 10 m resolution DEM (a & b) and from 96 m resolution SRTM DEM. Search radius is 3 km. (a) lineaments mapped in scale 1:25.000 and 1:50.000, (b) lineaments mapped in scale 1:200.000 and (c) in 1:100.000. Units are km per km².

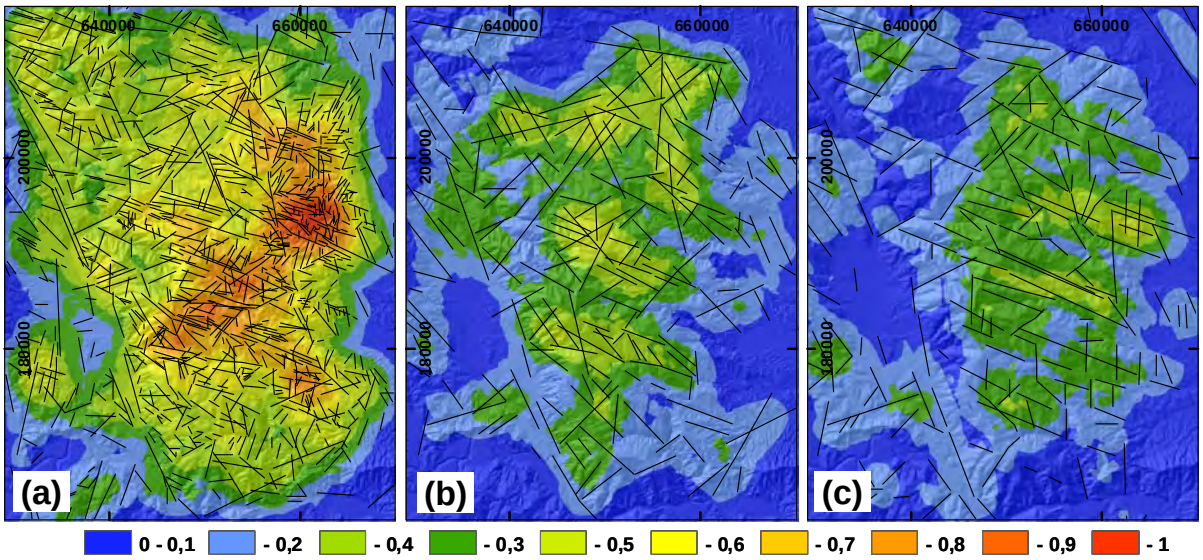

Figure 4-60: Normalized lineament length density map derived from 10 m resolution DEM (a & b) and from 96 m resolution SRTM DEM (c). Search radius is 3 km. (a) lineaments mapped in scale 1:25.000 and 1:50.000, (b) lineaments mapped in scale 1:200.000 and (c) in 1:100.000. Units are km per km².

4.3.7 DRAINAGE SYSTEM ANALYSIS

4.3.7.1 STREAM AND DRAINAGE PATTERN

Székely (2001) noted that the drainage pattern of the Eastern Alps is rather trellis-like or contorted due to glaciation and dendritic patterns are primarily observed in non-glaciated areas. On a first glance, the low order tributaries of the main streams of the Koralpe may be termed dendritic (Figure 4-61 a). However, the main streams show distinct drainage orientation changes by angular river bends, indicating a structural control of their course (Figure 4-62, Figure 4-61). Generally, in the eastern Koralpe the main streams follow the strike of the foliation and the axes of large scale fold structures. Structural control is also evident for smaller rivers like the Greim-Gamsbach (Figure 4-61 c), where the stream course is controlled by steeply dipping, nearly orthogonal discontinuity sets and the flat, approximately W-E striking foliation. Structural control of the Teigitsch's course (see Figure 4-62), the longest river in the realm of the Koralpe, has already been demonstrated by Stiny (1925). As structural control of drainage is clearly evident over large areas of the Koralpe it is more adequately described as contorted, trellis or subdendritic (see Zernitz, 1932 and Howard, 1967 for detailed description), similarly to the areas glaciated during the last glaciation. Structural control of drainage is partly masked by a high frequency of low order streams. This is explained by a mature landscape and a thick cover of slope debris, which promotes a dendritic drainage as long as a stream does not incise into bedrock.

Some prominent angular river knees are located in the Eastern Koralpe (Figure 4-61 b). Here, the Lassnitz, the Stullneggbach, the Schwarze Sulm and the Weiße Sulm (from North to South) change their drainage orientation from ESE to SE to S. The Stierriegelbach, a tributary of the Weiße Sulm, changes its drainage direction towards northerly directions before its confluence. These river knees are located at elevations between 500 m and 780 m and are aligned along a NNE-SSW to N-S trending curve (Figure 4-61 b). A second zone of aligned orientation changes are found at the entrance of the rivers south of the Wildbach into the Styrian Basin. It marks the change from anisotropic metamorphic rocks to the more isotropic sediments. Tectonic controls like faults, discontinuity pattern, foliation, fold structures or active faulting and/or tilting may be responsible for such phenomena. Drainage rearrangement processes like river capture, beheading and diversion (Bishop, 1995), which act simultaneously to structural controls, have also been shown to cause angular river knees ("elbow of capture", Summerfield 1991).

Drainage direction and orientation of foliation, the penetrative fabric element, where analysed to reveal possible causes for these river knees (Figure 4-63). For the Schwarze and Weiße Sulm the orientation of foliation and the general drainage direction of the reaches coincide fairly well. For the Lassnitz foliation and drainage direction are quite similar for the upstream reach, but do not coincide for the reach downstream of the river knee, although foliation trends more southerly east of the

river knee. In the case of the Stullneggbach, foliation strikes quite similar along the western and the eastern river segment. Again the drainage direction of the upstream reach fits better to the strike of foliation than does the downstream reach. Both reaches show two clusters of foliation orientation, indicating the presence of fold structures or of a second foliation.

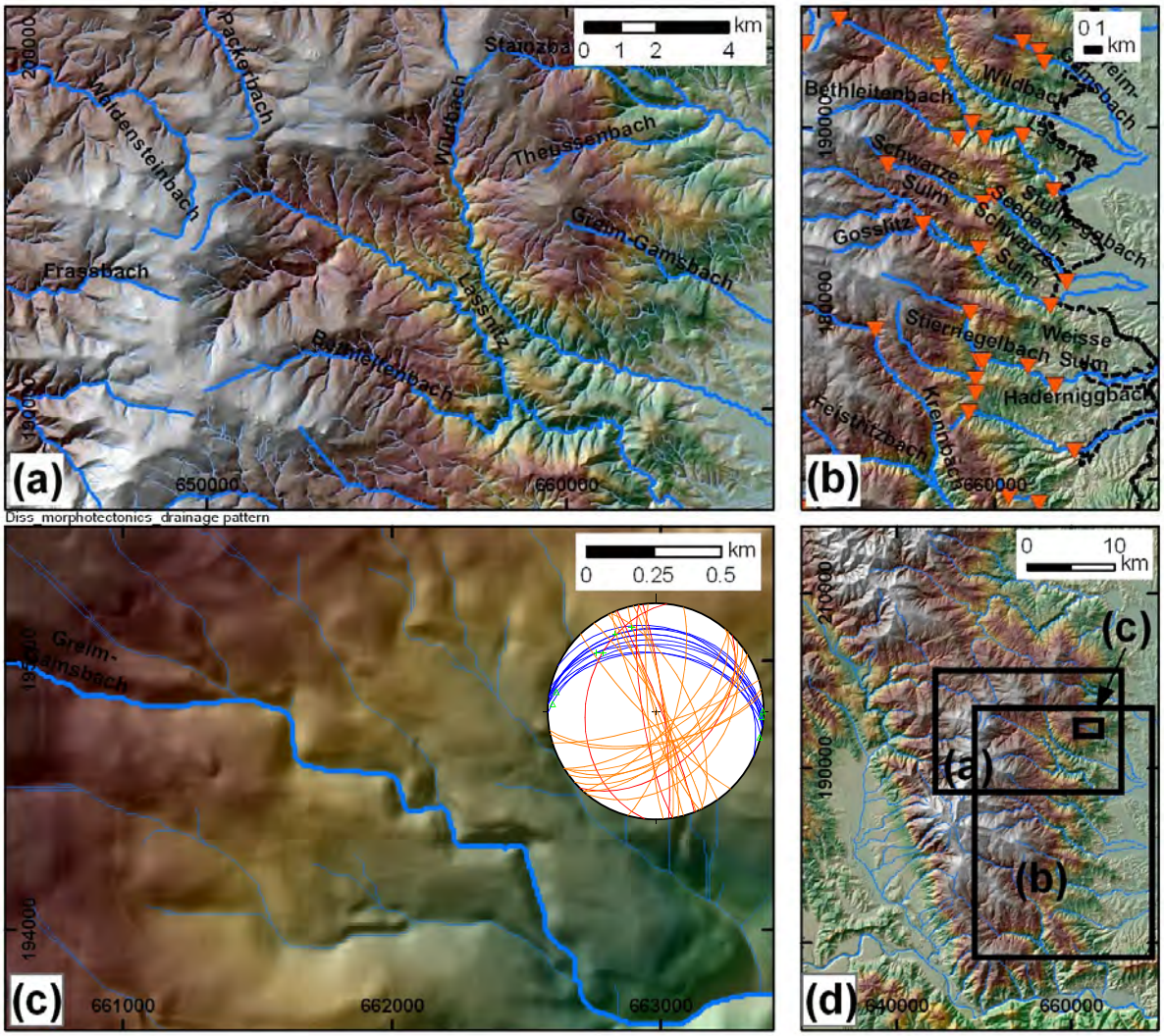

Figure 4-61: Stream resp. drainage patterns in the Eastern Koralpe at different scales:
(a) Catchment of Lassnitz and Wildbach with dendritic to subdendritic drainage pattern of low order streams and partly abnormal stream pattern of the high order streams indicating some basic structural control.
(b) Pronounced river knees (red triangles) indicate structural and/or lithological control.
(c) Greim-Gamsbach: River course follows orthogonal fracture sets in the flatly north dipping bedrocks ("Plattengneis"). Schmidt net (lower hemisphere) shows field measurements of foliation (blue) and shear fractures (orange and red) from this area.
(d) Location of maps (a) to (c).

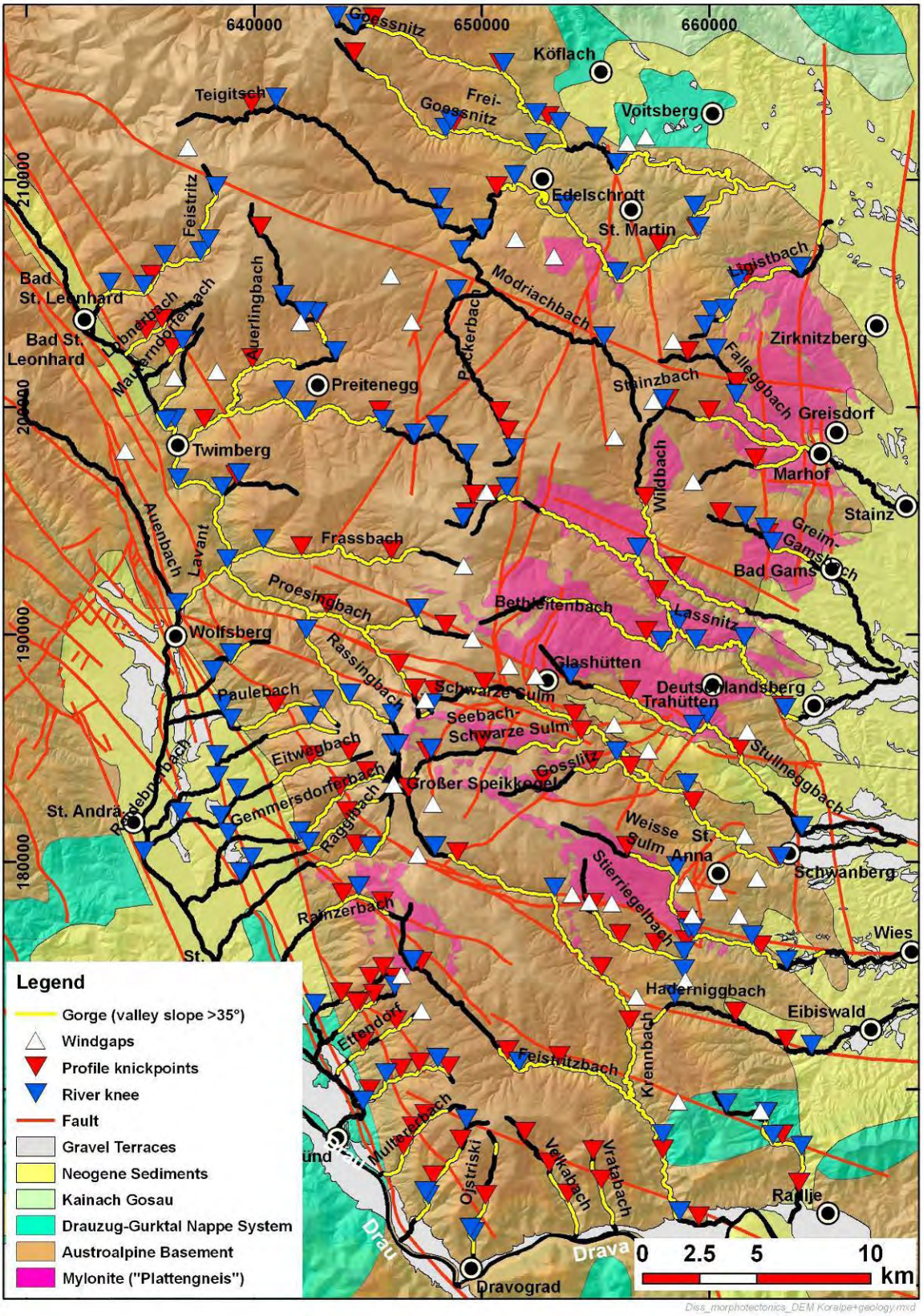

Figure 4-62: Geological map of the Koralpe with the main drainage pattern. White triangles mark possible wind gaps, blue triangles mark pronounced river knees (orientation knickpoints) and red triangles mark knickpoints in longitudinal river profiles.

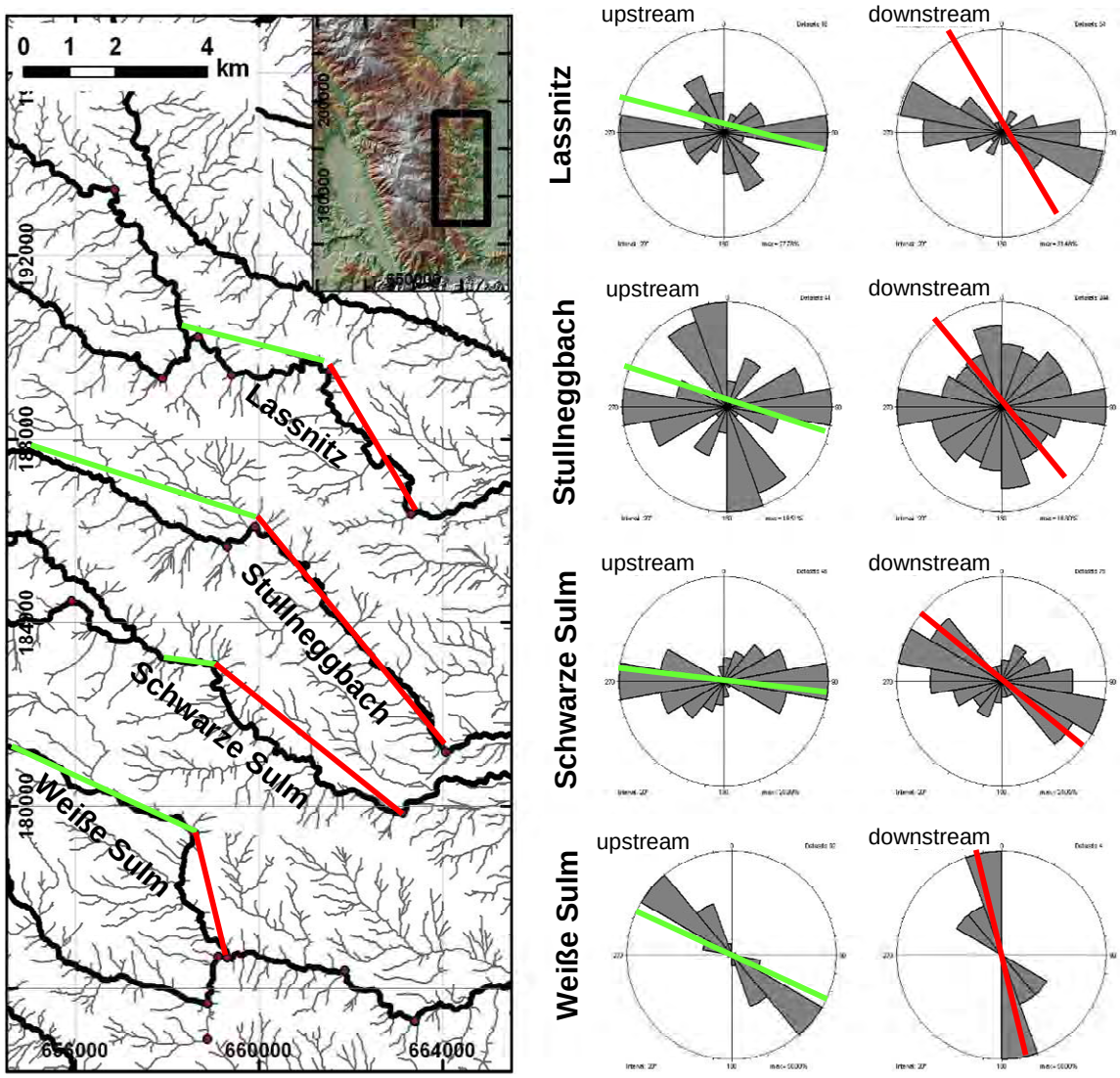

Figure 4-63: Changes of drainage direction in the Eastern Koralpe in relation to the foliation. Green lines mark reaches upstream, red lines reaches downstream of the river knees, which were used for a comparison to foliation strike in the rose diagrams. Foliation data are own field data, data from the field mappings for the Koralmtunnel (courtesy of 3G ZT GmbH and ÖBB-Infrastruktur AG) and from the geological maps 1:50.000 of the Geologische Bundesanstalt.

A comparison with the regional fault pattern (Figure 4-62) shows that in the upstream reaches, the Lassnitz, the Stullneggbach and the Schwarze Sulm flow parallel to or follow WNW-ESE trending dextral strike slip faults, reactivated as normal faults (Chapter 3.3). This is also true for the Modriachbach in the northern Koralpe, the Krennbach in the central Koralpe and the Weiße Sulm south of St. Anna up to Wies and several other river segments. The southeast to south trending river segments in Figure 4-63 do not follow faults. Furthermore no fault has been mapped that links the river bends or indicates a common, neotectonic offset of the rivers. If these river bends would be caused by such a major fault, the rivers would follow it for a certain distance. This is true for the Weiße Sulm and the Stierriegelbach, which turn abruptly from a WNW-ESE to a N-S drainage direction (Figure 4-61 b) before joining and turning to an ESE directed drainage direction. A suspected normal fault in the

catchment of the Schwarze Sulm could be extended to the river knee of the Weiße Sulm, but lacks field evidence. Furthermore, the contact between mylonite and mica schist strikes partly parallel to the N-S stretch of the Weiße Sulm (Figure 4-62 resp. Beck-Mannagetta and Stingl, 2002).

In addition to structural controls the presence of wind gaps in the vicinity of river knees indicates stream capture for some of the rivers (Figure 4-62 and Figure 4-64). In the southern Koralpe the Krennbach incises from the Drau (Drava) deeply into the central Koralpe. Morphological saddles, interpreted as wind gaps, and abrupt changes in drainage direction indicate that the Krennbach captured the Feistritzbach, the upstream reaches of the Haderniggbach, the Weiße Sulm and the Stierriegelbach. All captured rivers previously drained into the Styrian Basin. The timing of these drainage rearrangement can be linked to the shift of the Drau (Drava) into its present valley (Sölva et al., 2005b) during the Pliocene.

A very prominent morphological saddle called “Schrogentor” is located at the watershed between the Teigitsch catchment and the Wildbach (Figure 4-65). This saddle may be interpreted as a wind gap too, marking an old river course. In the 3D visualization of the DEM the “Schrogentor” seems to connect the upper part of the Teigitsch and the Modriachbach in the northern Koralpe with the Wildbach in the eastern Koralpe. At the pronounced bend of the Wildbach morphology allows the continuation of this paleoriver in a N-S direction (Figure 4-65).

The catchments resulting from stream capture often are characterized by a higher channel index CI (Figure 4-68 d). The highest CI values are found along the Waldensteinbach, the Teigitsch, the Wildbach and the Lassnitz, some of the largest catchments within the Koralpe. These catchments form a coherent, NW-SE striking zone in the northern and northeastern Koralpe. Rivers along the western and southern slopes show a low CI. This is also reflected in the statistical parameters of CI, calculated for the individual morphounits (Table 10).

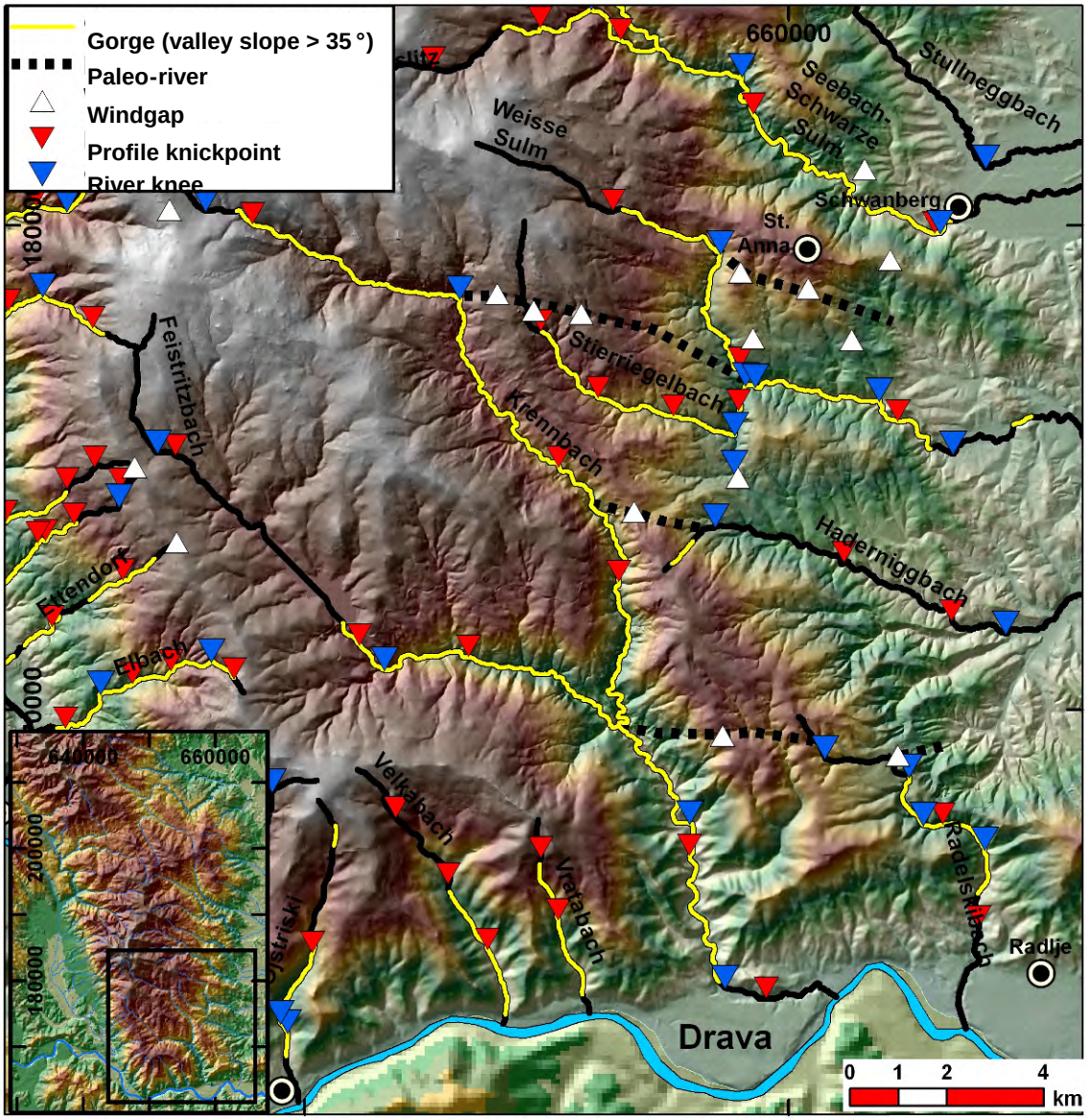

Fig_morphotect_Krennbach.ppt

Figure 4-64: Stream pattern of the southern Koralpe. The Krennbach incises deeply from Drava (Drau) river into the Koralpe, possibly capturing the Feistritzbach, the Hadernigg bach and the Weiße Sulm/Stierriegelbach, which all drain towards the Styrian Basin. The dashed bold lines indicate possible former course of rivers.

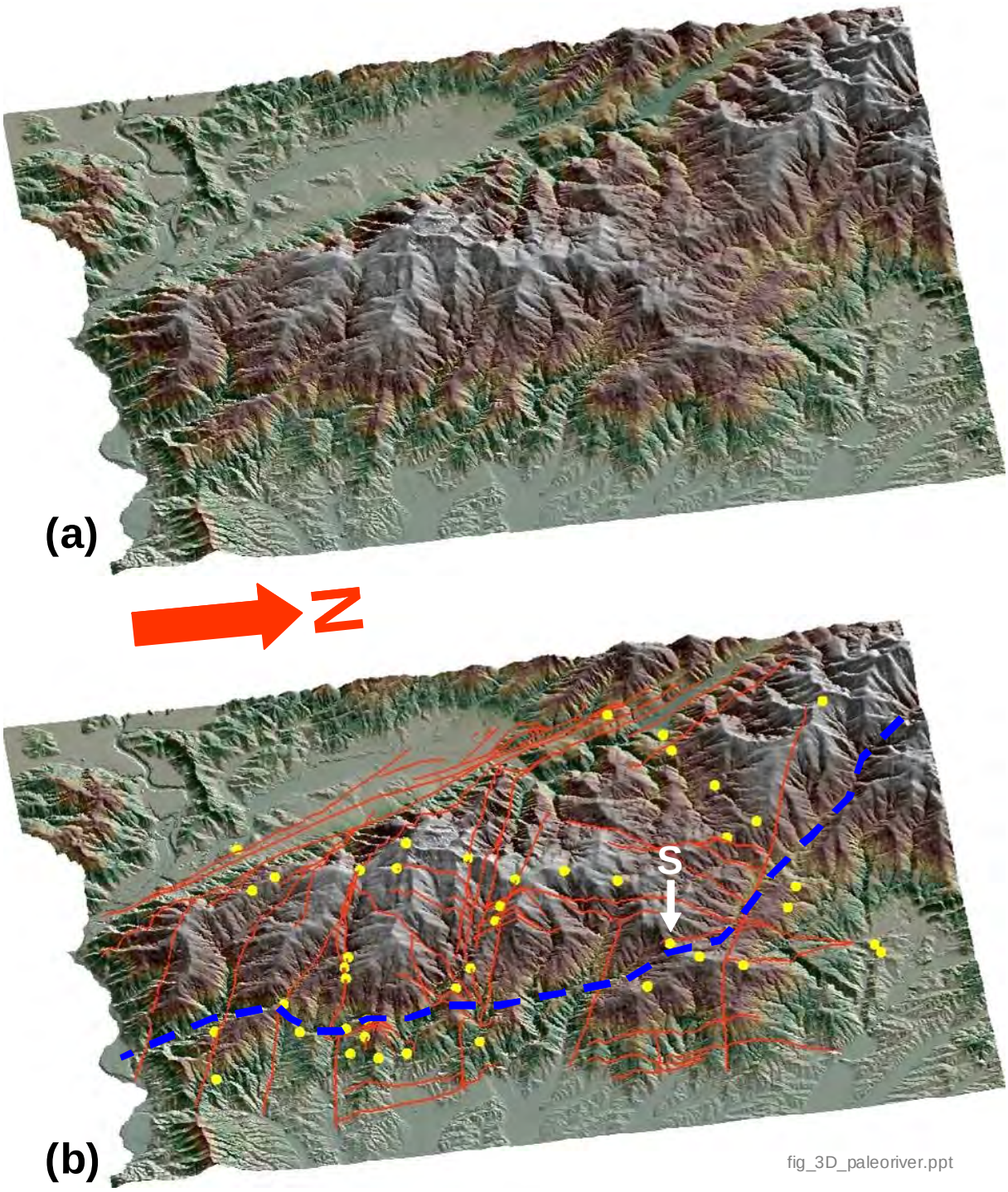

Figure 4-65: (a) 3D visualization of the DEM of the Koralpe (combined hillshade and colour-coded DEM). (b) 3D DEM plus fault pattern and possible course of an approx. N-S trending paleoriver. Note the pronounced saddle (wind gap?) at the watershed marked with arrow and "S" (Schrogentor). Yellow points mark possible wind gaps.

	Morphounit	Min	Max	Range	Mean	Median	sd	q25	q75	IQR	γ_1	N
Basin axes ratio	Northwest	0.51	1.04	0.53	0.76	0.73	0.24	0.59	0.90	0.31	0.36	4
	Central west	0.48	1.04	0.56	0.84	0.88	0.23	0.77	1.03	0.27	-1.05	5
	West	0.28	1.42	1.14	0.65	0.56	0.35	0.38	0.75	0.37	1.06	20
	South	0.44	1.10	0.66	0.74	0.81	0.28	0.47	0.95	0.48	0.03	7
	East	0.38	2.39	2.01	0.79	0.64	0.42	0.48	0.94	0.46	2.23	29
	Northeast	0.60	1.93	1.34	1.08	1.03	0.46	0.71	1.14	0.43	1.01	10
Horton's Form Facto	Northwest	0.23	0.40	0.17	0.30	0.29	0.07	0.27	0.32	0.05	1.03	4
	Central west	0.22	0.46	0.25	0.38	0.42	0.10	0.35	0.43	0.08	-1.34	5
	West	0.14	0.53	0.39	0.28	0.26	0.12	0.19	0.36	0.17	0.68	20
	South	0.22	0.51	0.29	0.34	0.33	0.09	0.29	0.37	0.08	1.02	7
	East	0.15	1.10	0.95	0.34	0.28	0.19	0.22	0.38	0.15	2.69	29
	Northeast	0.22	0.71	0.50	0.42	0.36	0.19	0.26	0.57	0.31	0.44	10
Elongation ratio	Northwest	0.54	0.72	0.18	0.62	0.61	0.07	0.58	0.64	0.05	0.82	4
	Central west	0.53	0.77	0.24	0.69	0.74	0.10	0.66	0.74	0.08	-1.49	5
	West	0.43	0.82	0.39	0.59	0.57	0.12	0.50	0.68	0.19	0.38	20
	South	0.53	0.81	0.27	0.65	0.64	0.09	0.61	0.68	0.08	0.70	7
	East	0.44	1.18	0.74	0.64	0.60	0.16	0.53	0.69	0.16	1.90	29
	Northeast	0.53	0.95	0.43	0.72	0.68	0.16	0.57	0.85	0.28	0.31	10
Channel index	Northwest	1.12	1.48	0.35	1.22	1.15	0.17	1.13	1.24	0.12	1.93	4
	Central west	1.22	1.29	0.08	1.24	1.24	0.03	1.22	1.24	0.03	1.29	5
	West	1.09	1.35	0.26	1.20	1.18	0.08	1.14	1.25	0.11	0.52	20
	South	1.08	1.42	0.34	1.23	1.14	0.14	1.12	1.36	0.24	0.40	7
	East	1.13	1.65	0.52	1.32	1.29	0.14	1.22	1.35	0.14	1.07	29
	Northeast	1.13	1.92	0.79	1.43	1.34	0.26	1.13	1.57	0.44	0.77	10
Mod. Basin Asymmetry	Northwest	7.75	31.71	23.95	17.42	15.10	11.64	8.01	24.51	16.50	0.55	4
	Central west	4.58	13.53	8.94	9.56	9.20	3.94	7.04	13.44	6.40	-0.12	5
	West	1.04	26.74	25.70	7.73	4.34	8.51	2.92	6.78	3.86	1.78	20
	South	4.22	22.69	18.47	11.37	11.55	6.86	5.76	14.81	9.05	0.64	7
	East	0.14	25.16	25.02	10.11	9.44	7.36	3.79	13.93	10.14	0.46	29
	Northeast	3.22	33.30	30.08	17.07	15.87	11.59	5.89	27.16	21.27	0.05	10

sd...standard dev., q25...quartile 25%, q75... quartile 75%, IQR.....interq. range, γ_1...skewness, N...data number *catchments_koralpe_basement_01.xls*

Table 10: Summary statistics of the following basin shape resp. stream parameters: basin axes ratio, Horton's form factor, elongation ratio, channel index and modified basin asymmetry.

4.3.7.2 BASIN SHAPE AND SYMMETRY

The largest part of the catchments shows slight asymmetries (Figure 4-66, Table 10, Table 16 appendix). However, the Teigitsch, the Waldensteinbach, the Lassnitz, the Weiße Sulm and the Feistritz and some smaller catchments show elevated asymmetry. The northern Koralpe forms a coherent region of asymmetric basins. A second zone is formed by the Feistritzbach and the Weiße Sulm in the southern Koralpe. No tilt related asymmetry, resulting in preferred asymmetry towards a certain direction, is recognised. Basin asymmetry is frequently observed in basins, with strong morphological indicators for stream capture. Therefore, stream piracy results in more complex basin geometries, whereas small, symmetric basins along the southwestern margin of the Koralpe coincide with a high hypsometric integral and a low channel index. This is also reflected in Morphounit West, which shows the lowest mean and median value of the modified basin asymmetry index (Table 10).

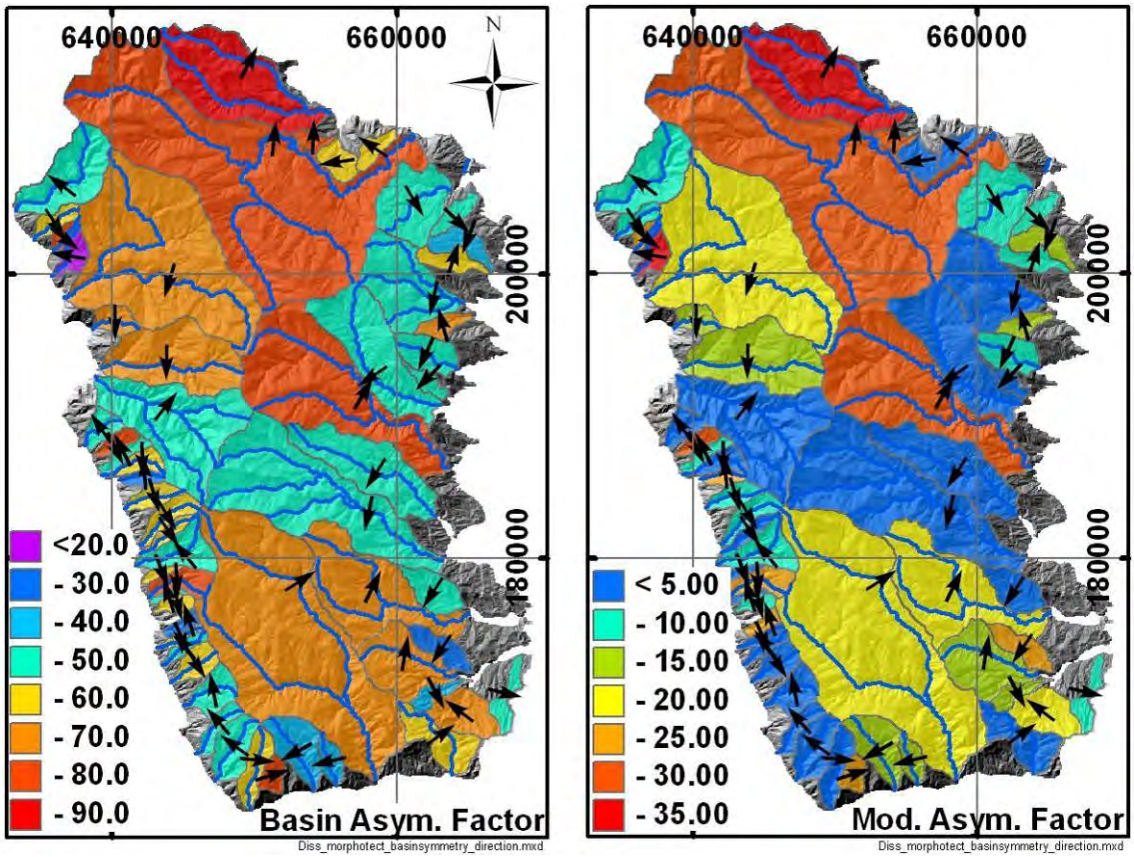

Figure 4-66: Asymmetry of drainage basins in the realm of the Koralpe: Basin asymmetry factor (AF) (left) and modified asymmetry AF_{mod} (right). A basin asymmetry factor >50 indicates a tilt to the left resp. that the right half of the basin is larger than the left one, view direction downstream. An AF_{mod} of 0 marks perfect symmetry, whereas 50 represents the maximum possible asymmetry. Black arrows indicate direction of hypothetic tilt resp. of shift of the stream. Basins which are a sub basin of a larger basin are not shown.

The basin shape ratios used in the present study (Basin axes ratio, Elongation ratio, Form factor, see chapter 4.2.5.3 for explanation) are correlated (Figure 4-67).

The *basin axes ratio* shows that many basins are slightly elongated parallel to the drainage axis (Figure 4-68 a, Table 10). Some smaller catchments are strongly elongated. They are found along the Lavant valley (Morphounit West), causing the lowest means and medians of all morphounits. In contrast several single basins are widened perpendicular to the drainage direction.

The *elongation ratio* map (Figure 4-68 b) shows a similar picture and confirms the concentration of strongly elongated catchments along the Lavant valley.

This picture is confirmed by *Horton's form factor*. However, the respective map (Figure 4-68 c) shows a homogeneous picture of elongated basins in the eastern and northeastern realm of the Koralpe too. Here, large basins with a form factor between 0.2 and 0.4 form a coherent belt.

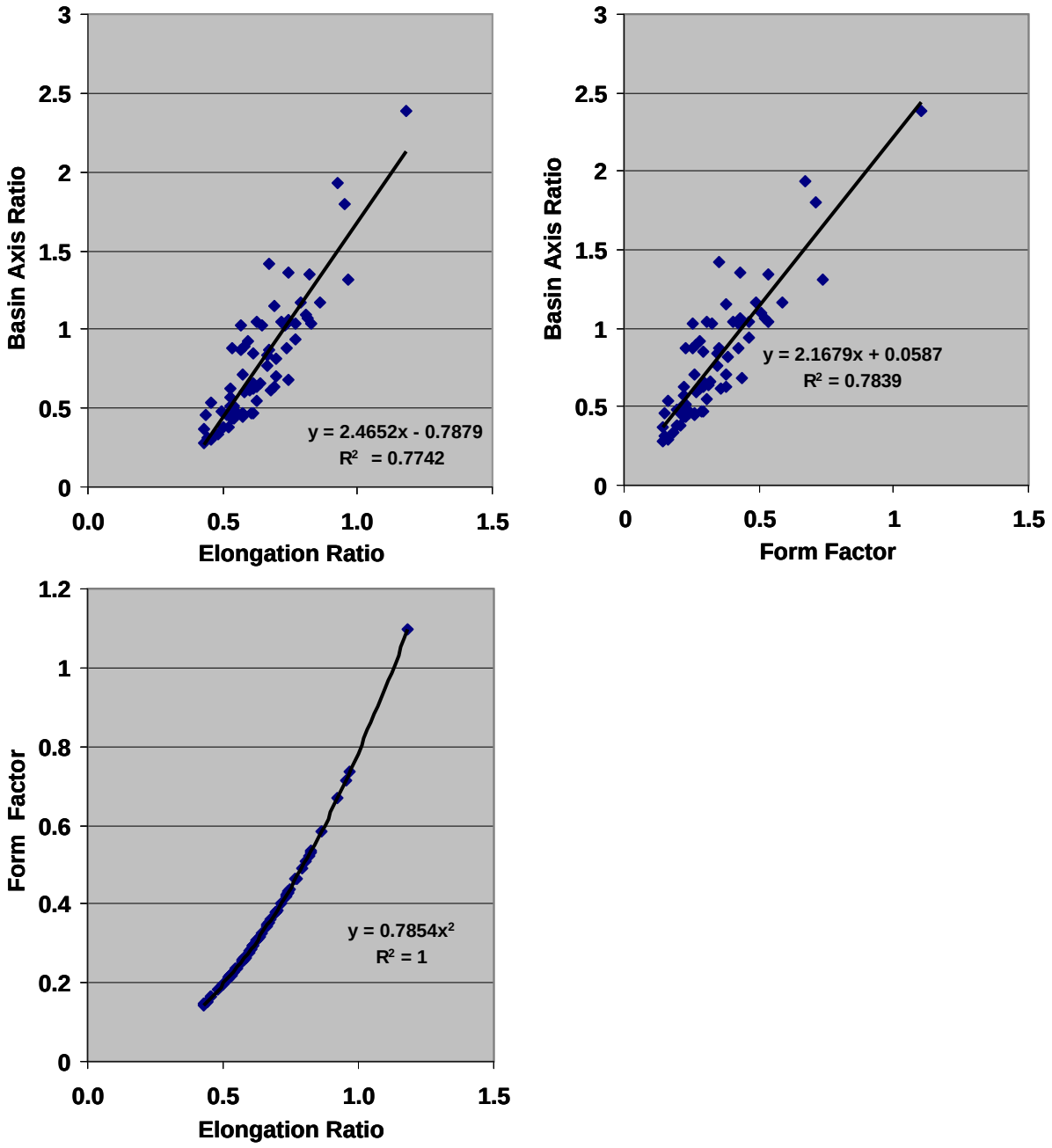

Figure 4-67: Scatter plots for the basin shape factors.

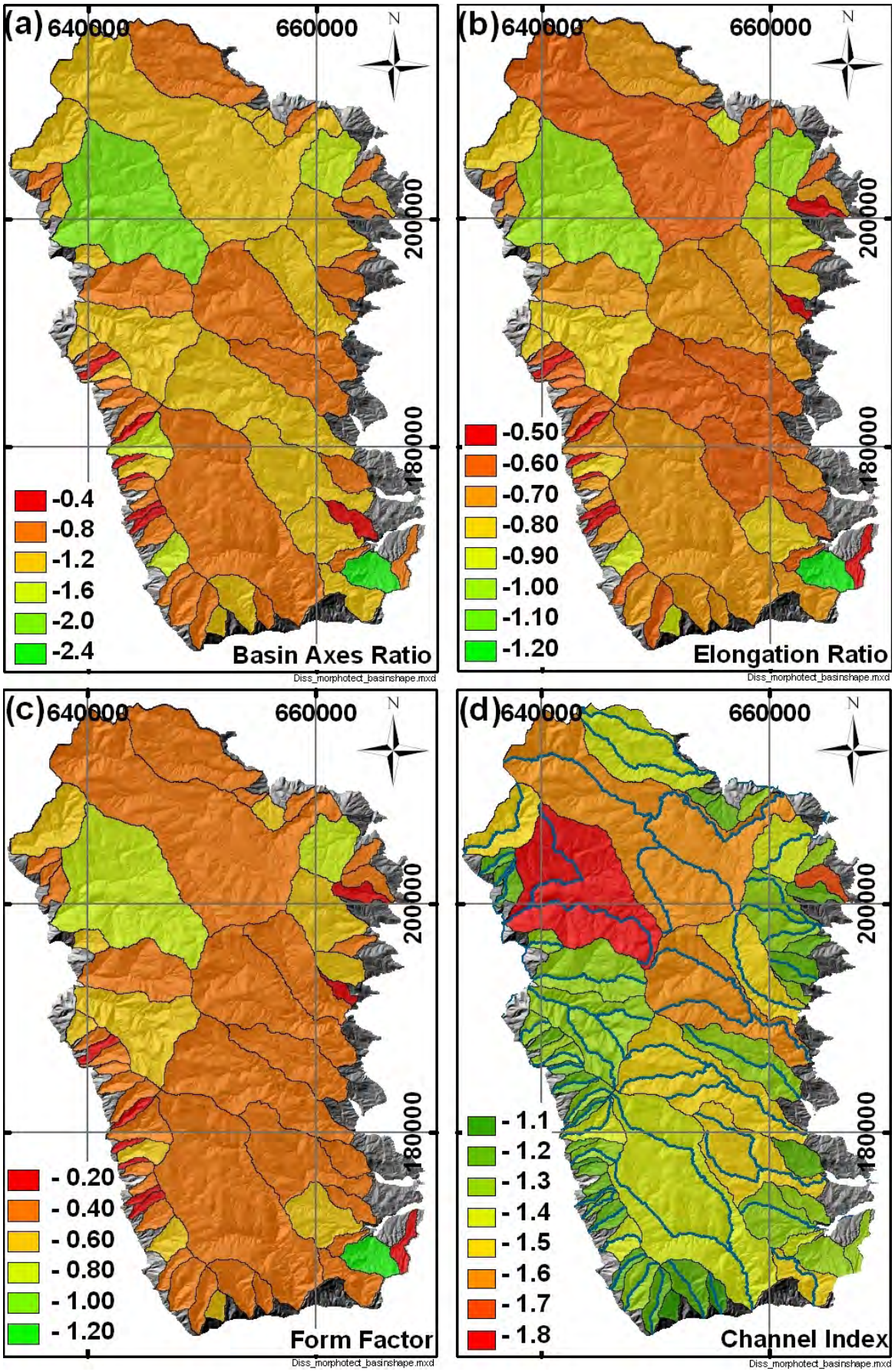
(a)
640000
660000
N
200000
180000
-0.4
-0.8
-1.2
-1.6
-2.0
-2.4
Basin Axes Ratio
Diss_morphotect_basinshape.mxd
(b)
640000
660000
N
200000
180000
-0.50
-0.60
-0.70
-0.80
-0.90
-1.00
-1.10
-1.20
Elongation Ratio
Diss_morphotect_basinshape.mxd
(c)
640000
660000
N
200000
180000
- 0.20
- 0.40
- 0.60
- 0.80
- 1.00
- 1.20
Form Factor
Diss_morphotect_basinshape.mxd
(d)
640000
660000
N
200000
180000
- 1.1
- 1.2
- 1.3
- 1.4
- 1.5
- 1.6
- 1.7
- 1.8
Channel Index
Diss_morphotect_basinshape.mxd

Figure 4-68 (previous page): Basin shape factors and the channel index for the Koralpe (sub basins are not shown):
(a) Basin axes ratio: values < 1 indicate basins elongated parallel to the drainage direction, values > 1 indicate elongation perpendicular to the drainage direction.
(b) Elongation ratio (Schumm, 1956): The lower the value the more elongated is the basin. A value of 1 indicates a rounded basin.
(c) Form Factor (Horton, 1932): F equals unity for a square and approaches a theoretical value of 1.273 for a perfect circle (Zavoianu, 1985). The lower the value the more elongated the basin is.
(d) Channel index (Mueller, 1968): The higher the value the longer is the stream with respect to the line connecting source and mouth. (CI=1: perfectly straight river; CI=2: river is two times longer than reference line)

Figure 4-69 (next page): Normalized longitudinal river profiles for 52 catchments of the Koralpe and the Lavant. Profiles are colour-coded according to their respective morphounit (see Figure 4-16). Order of profiles is approximately from north to south. Numbers refer to Table 17 (Appendix). ”D” marks location of dams.

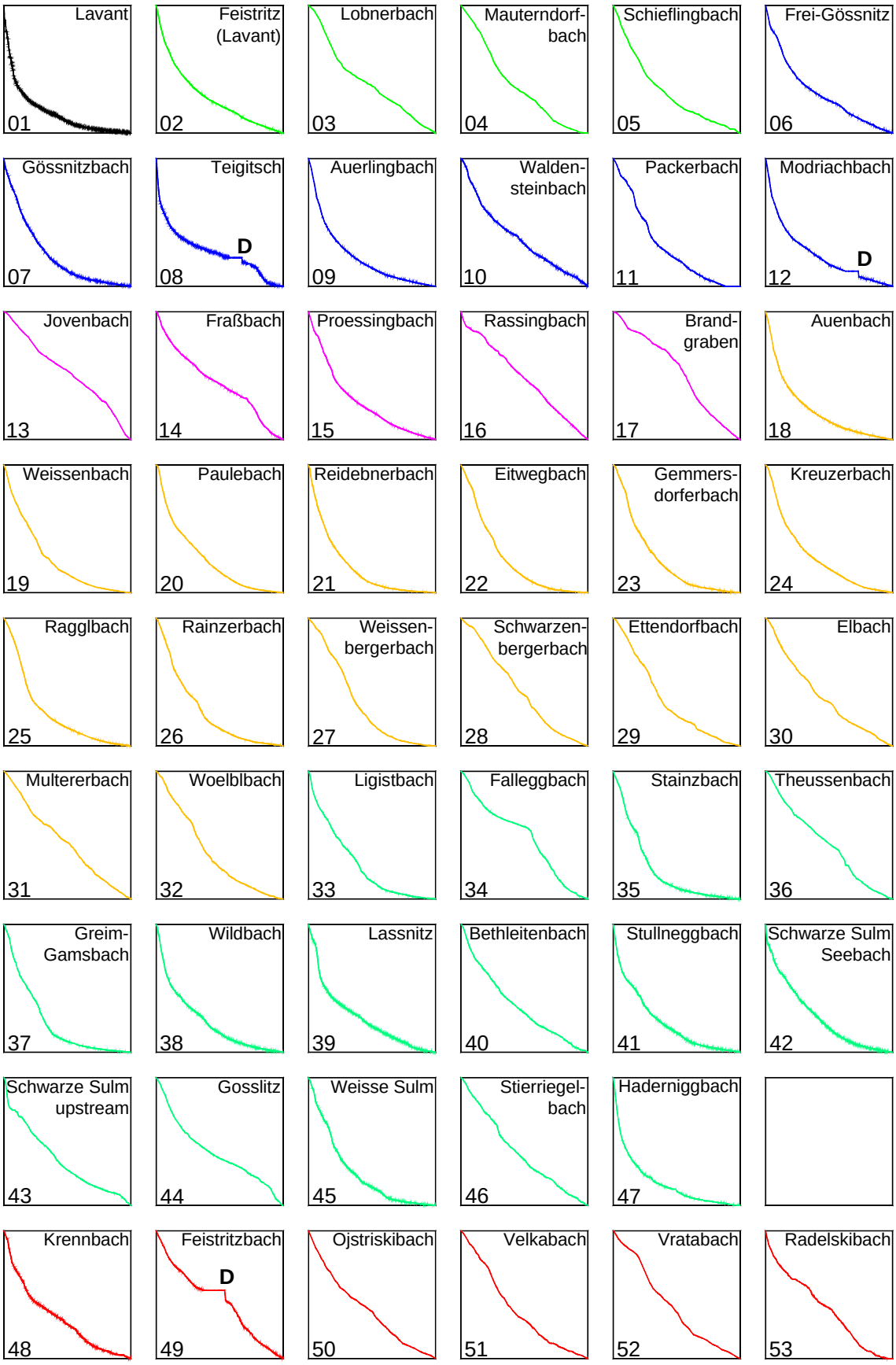
Lavant
01
Feistritz (Lavant)
02
Lobnerbach
03
Mauterndorf-bach
04
Schieflingbach
05
Frei-Gössnitz
06
Gössnitzbach
07
Teigitsch
D
08
Auerlingbach
09
Walden-steinbach
10
Packerbach
11
Modriachbach
D
12
Jovenbach
13
Fraßbach
14
Proessingbach
15
Rassingbach
16
Brand-graben
17
Auenbach
18
Weissenbach
19
Paulebach
20
Reidebnerbach
21
Eitwegbach
22
Gemmers-dorferbach
23
Kreuzerbach
24
Ragglbach
25
Rainzerbach
26
Weissen-bergerbach
27
Schwarzen-bergerbach
28
Ettendorfbach
29
Elbach
30
Multererbach
31
Woelblbach
32
Ligistbach
33
Falleggbach
34
Stainzbach
35
Theussenbach
36
Greim-Gamsbach
37
Wildbach
38
Lassnitz
39
Bethleitenbach
40
Stullneggbach
41
Schwarze Sulm Seebach
42
Schwarze Sulm upstream
43
Gosslitz
44
Weisse Sulm
45
Stierriegel-bach
46
Haderniggbach
47
Krennbach
48
Feistritzbach
D
49
Ojstriskibach
50
Velkabach
51
Vratabach
52
Radelskibach
53

4.3.7.3 LONGITUDINAL RIVER PROFILES

The normalized longitudinal river profiles (Figure 6-15, Appendix) allow a comparison between the individual rivers (Figure 4-69). Most of them show a graded, upwardly concave profile associated with a positive concavity index C_A (see Chapter 4.2.5.4 for explanation, Figure 4-70, Table 17). Some of the profiles exhibit pronounced knickpoints with a low C_A. The distribution of the C_A is negatively skewed. Most of the values range between 0.1 and 0.6 (Figure 4-70).

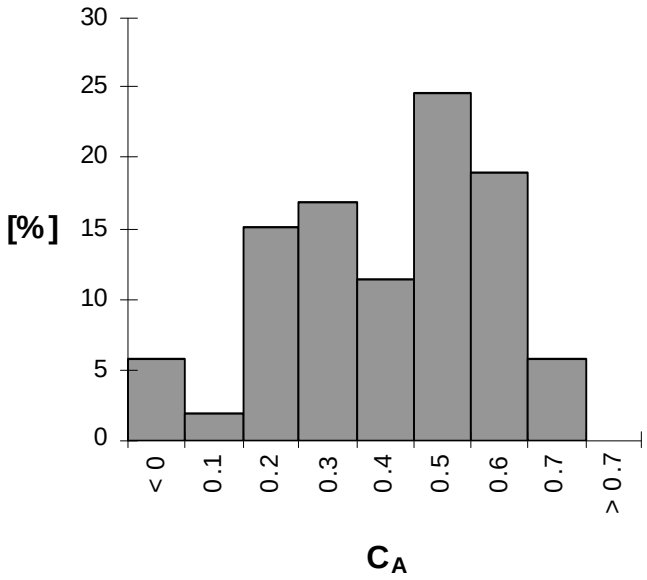

	C_A
Min	-0.05
Max	0.68
Mean	0.36
Median	0.39
Mode	0.44
SD	0.19
25% Q	0.23
75% Q	0.50

Figure 4-70: Frequency distribution of the normalized concavity index C_A and some measures for its distribution.

The regional distribution of C_A is characterised by low values along tributaries to the Drau (Drava) valley from Lavamünd to Dravograd and further to Radlje and along tributaries of longer streams in the interior of the Koralpe (Figure 4-73). They are related either to a more linear profile form or to profiles characterised by pronounced knickpoints. The C_A-map (Figure 4-73) indicates a correlation with stream length, the size of the catchment and with stream order. However, this could not be verified. An inverse linear relation can be established with the Hypsometric integral, which describes how elevation is distributed in a catchment (Figure 4-71).

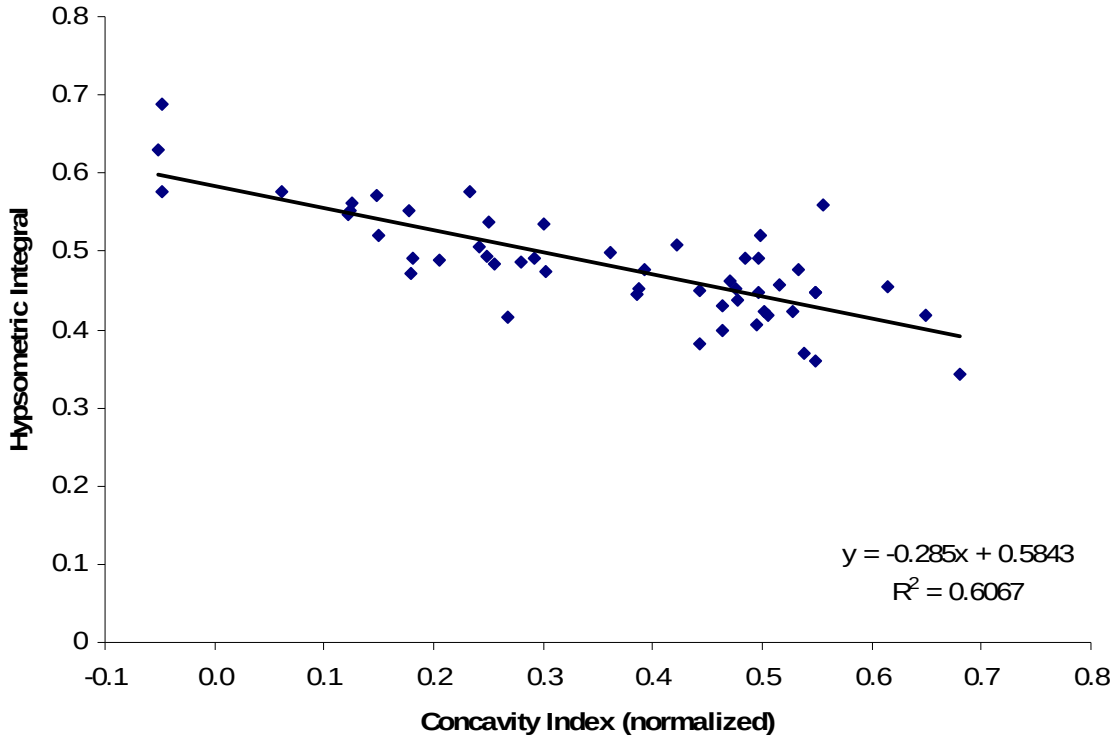

Figure 4-71: Scatter plot for the concavity index C_A and the hypsometric integral H_i.

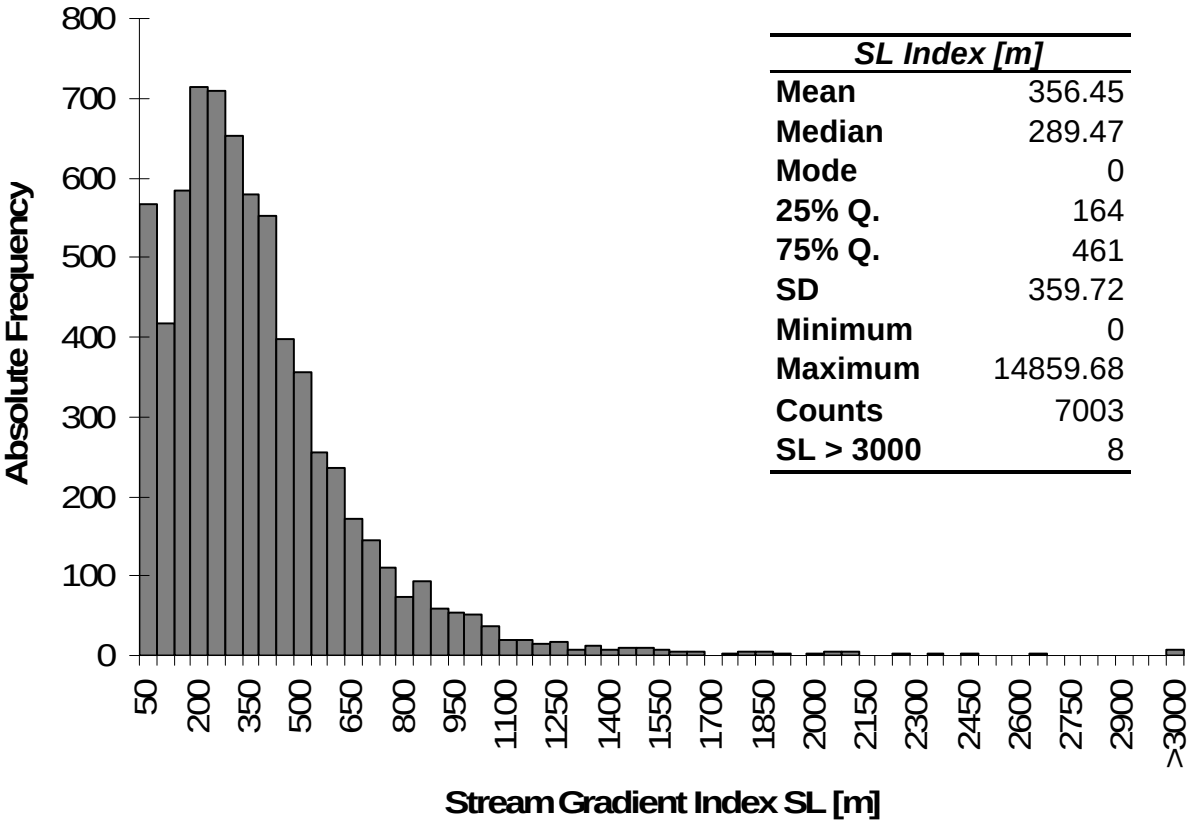

SL Index [m]	
Mean	356.45
Median	289.47
Mode	0
25% Q.	164
75% Q.	461
SD	359.72
Minimum	0
Maximum	14859.68
Counts	7003
SL > 3000	8

Figure 4-72: Histogram of the stream gradient index SL. Histogram is truncated at SL=3000, 8 values are larger than 3000.

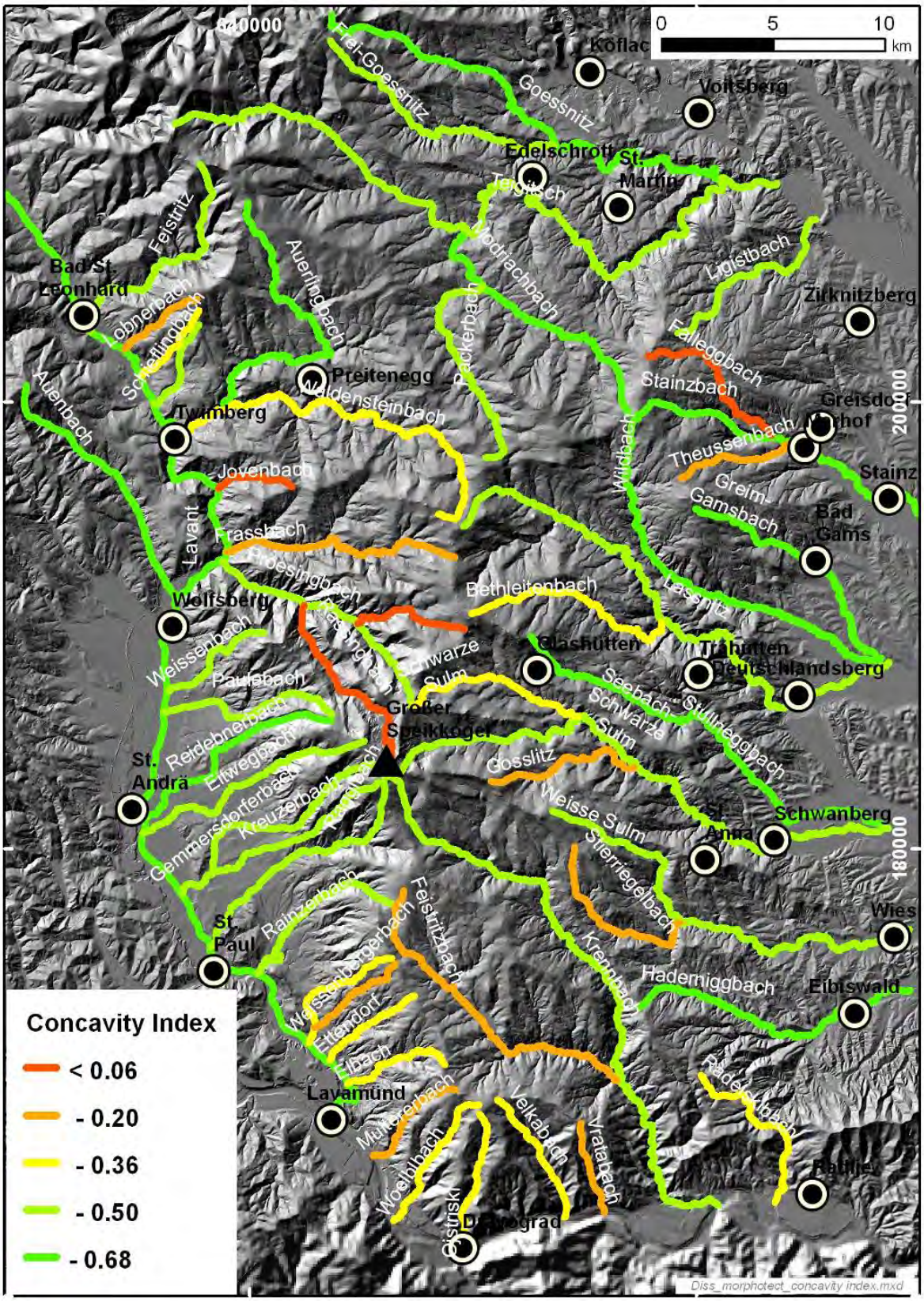

Figure 4-73: Normalized concavity index map for the 53 analysed streams (Table 17).

To identify abnormal steep stretches within a river profile the stream gradient index (SL) was plotted together with the longitudinal river profiles (Figure 6-15, Appendix). 50% of the SL data range between 164 and 461 m (Figure 4-72). The Median is 289 m and the most frequent single value (mode) is zero. The latter is caused by the water reservoirs along the analysed rivers (Teigitsch, Packer Bach, Feistritzbach), which plot as horizontal lines in the long profiles. Of the eight highest values four are related to the four large dams in the area of the Koralpe. The other four coincide with knickpoints in the long profiles and/or in the plan view of the rivers. All of them are located in the catchments of the Teigitsch and of the Krennbach resp. of their tributaries.

The Lavant, representing the local base level for most of the rivers on the western slopes of the Koralpe, shows a decline in the stream gradient index SL at the beginning of the Twimberg gorge. The gorge itself is characterized by a rise of the SL values, between the confluences with the Waldensteinbach and the Prössingbach. No longitudinal river knickpoint is associated with this SL peak. South of the gorge the SL gradually declines. Within the Koralpe an increase in SL is often associated with pronounced river knickpoints (Figure 6-15, Appendix) and gorgelike valleys (valley slopes frequently >35°, Figure 4-75). To give a regional overview, the SL values along the individual tributaries were interpolated by local polynomial interpolation (implemented in ArcGIS 9.1) to a stream gradient map (Figure 4-76). The interpolation yields a belt of elevated SL values between 300 and 571 m which follows the outline of the Koralpe. This belt surrounds an area elongated in north - south direction with lower values and the minimum in the area of the Packer Bach and the Modriachbach. This area coincides with the paleosurfaces preserved in the northern Koralpe, but also in higher regions of the eastern Koralpe. The regions with the highest values are located along the Teigitsch gorge in the northeastern Koralpe and in the southern Koralpe upstream of the junction of Krennbach and Feistritzbach. The interpolated values outside the analysed area are regarded as not reliable as no SL values have been calculated e.g. west of the Lavant or along the Drau (Drava).

Most of the profile knickpoints detected are situated within a belt of increased SL values and within the gorge like stretches of the rivers. 113 knickpoints were extracted from the longitudinal river profiles (Appendix: Table 18 and Figure 6-15). Some of these knickpoints are clearly recognisable in the longitudinal profiles (e.g. Fraßbach, Nr. 14 in Figure 4-69) others become evident only after comparison with the SL curve. All knickpoints extracted were checked for errors in the DEM as a possible cause for the knickpoint. Furthermore, they were compared to the topographic maps and to aerial photographs to detect possible human causes. To detect possible geological causes the knickpoints were plotted on a map and compared to the regional geological maps of the Koralpe and to a synoptic layer of known faults. Possible causes (lithology, base level, structure) deducible from this data are listed in Table 18 (Appendix).

The elevation histogram of the knickpoints shows a multimodal distribution (Figure 4-78 a), with the highest concentration between 700 and 800 m. A second peak is situated between 1100 and 1200 m. Above 1300 m the frequency of knickpoints is

declining abruptly. The knickpoints are not randomly distributed within the working area.

Some knickpoints are situated at the end of gorgelike stretches (Figure 4-75, Figure 4-76 and Figure 4-77). For some of the knickpoints a lithological control is evident, an example is the catchment of the Stainzbach with two tributaries (Figure 4-74 a & b). Here, pronounced knickpoints (Figure 4-74 a) are found close to the contact of a mylonite ("Stainzer Plattengneis") to overlying mica schist (Figure 4-74 b). Due to the flatly dipping strata the knickpoints are located at similar elevations. The strength contrast between these two lithologies is pronounced (Table 11). Generally the strength contrast and the pronounced strength anisotropy of these rocks related to the penetrative metamorphic foliation (Blümel et al., 1999; Brosch et al., 2000) are thought to be a major cause for the disequilibria in the longitudinal river profiles of the Koralpe (Rantitsch et al., 2009). The pattern of knickpoints in several catchments of the Koralpe indicates that changes in base level may also be a possible cause. Such a situation can be observed along the Krennbach and its tributary the Feistritzbach. Here three levels of knickpoints are situated at approximately similar distance from their confluence (Figure 4-75, Figure 4-76, Figure 4-77). In the eastern Koralpe from the Wildbach southwards to the catchment of the Schwarze Sulm a slightly curved front of knickpoints indicates a propagating front of knickpoints running parallel to the mountain front. These knickpoints are found at elevations ranging from 606 m (Wildbach) to 879 m (Stullneggbach), with increasing elevation from north to south (Figure 4-77).

Lithology	Frequency	Uniaxial compressive strength [MPa]			
		Min	Max	Mean	Median
Amphibolite/ Eclogite	12	29.25	301.87	135.08	121.60
"Augengneis"	10	38.99	173.40	117.99	118.87
Gneiss	45	14.83	185.24	104.82	105.20
"Plattengneis"	16	31.47	193.71	116.69	121.66
Gneiss-micaschist group	40	16.04	143.55	71.90	67.50
Silikatmarmor	14	65.40	172.71	109.80	104.37
Marmor	5	72.15	138.55	94.12	87.63
Pegmatite*	3	102.03, 111.05, 130.17			

*only three values, no statistics but individual values are given

Table 11: Uniaxial compressive of the main lithotypes of the Koralpe strength (data from site investigations of the Koralmtunnel, by courtesy of the ÖBB-Infrastruktur AG).

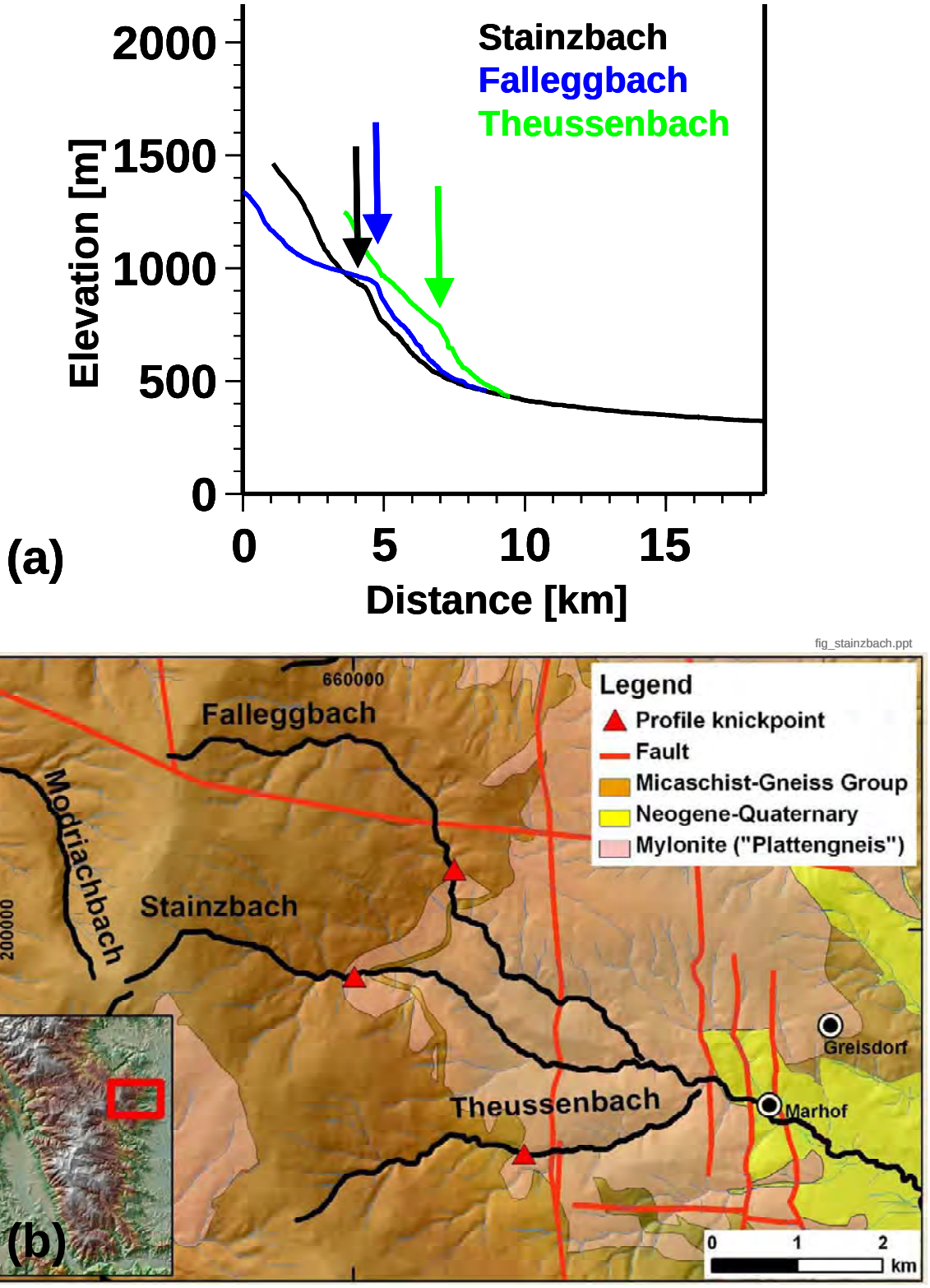

Figure 4-74: (a) River profiles from the catchment of the Stainzbach, Eastern Koralpe and (b) the respective geological map (after Beck-Mannagetta, 1986 and own field mappings).

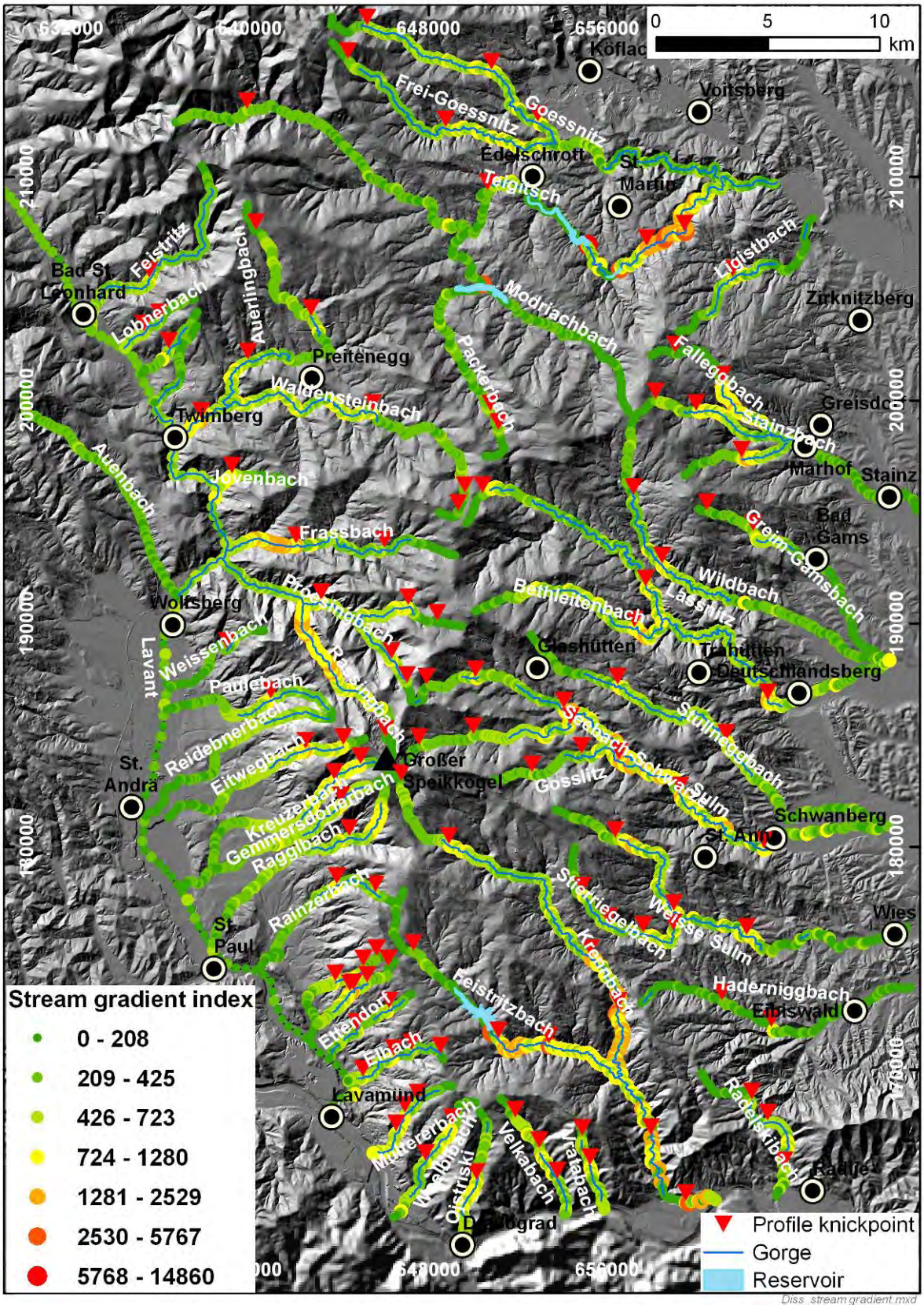

Figure 4-75: Stream gradient index distribution along the rivers of the Koralpe. Red triangles mark knickpoints in the longitudinal profiles of the rivers, blue lines mark gorgelike river stretches (valley slopes >35°).

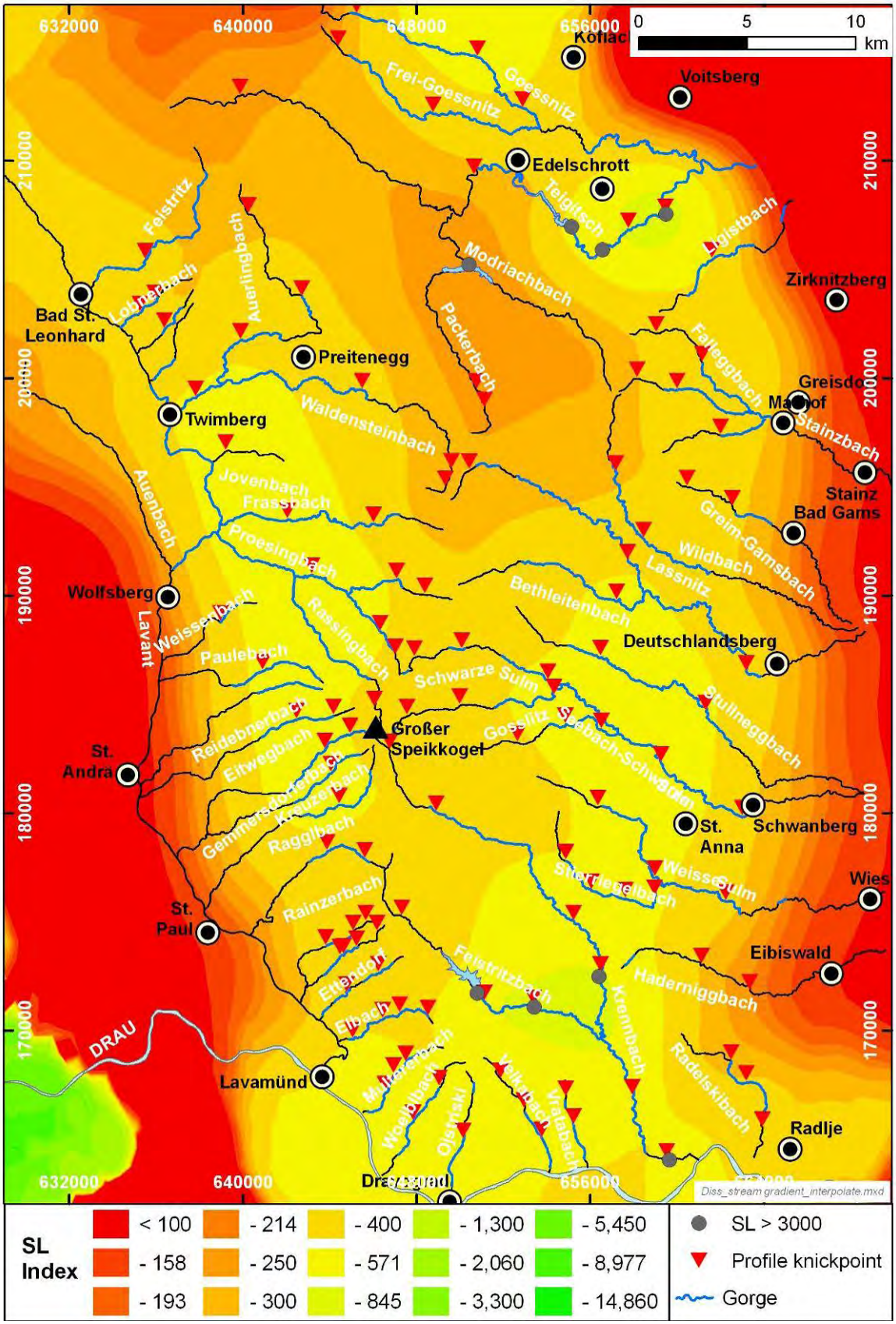

Figure 4-76: Contour map of the stream gradient index SL. Map is interpolated from data points along the shown rivers (Local Polynomial Interpolation).

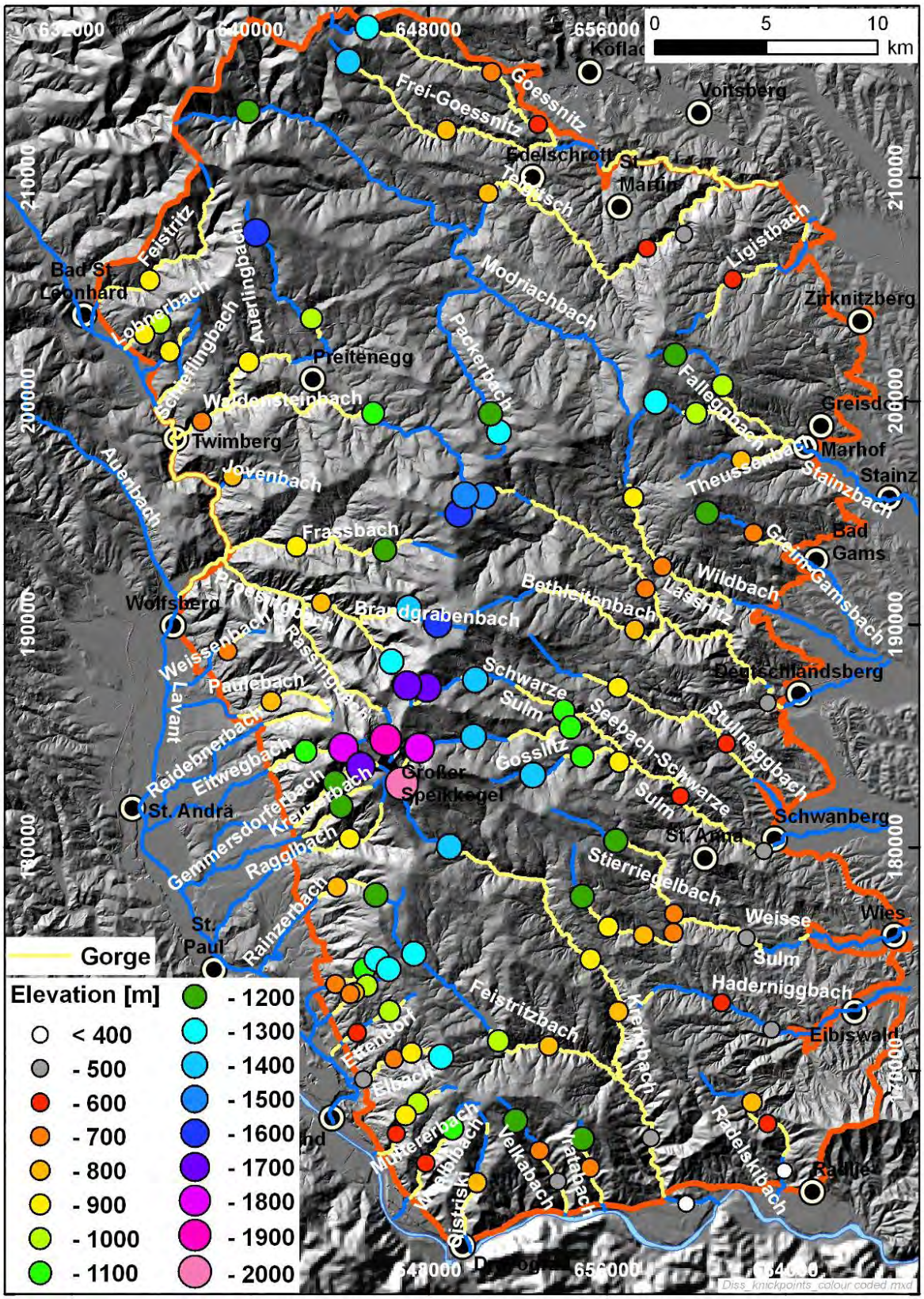

Figure 4-77: Regional distribution of longitudinal river knickpoints and gorge like river sections. The knickpoints are coded by colour and size for their elevation. Yellow lines mark gorge like stretches (valley slope >35°) of the analysed rivers.

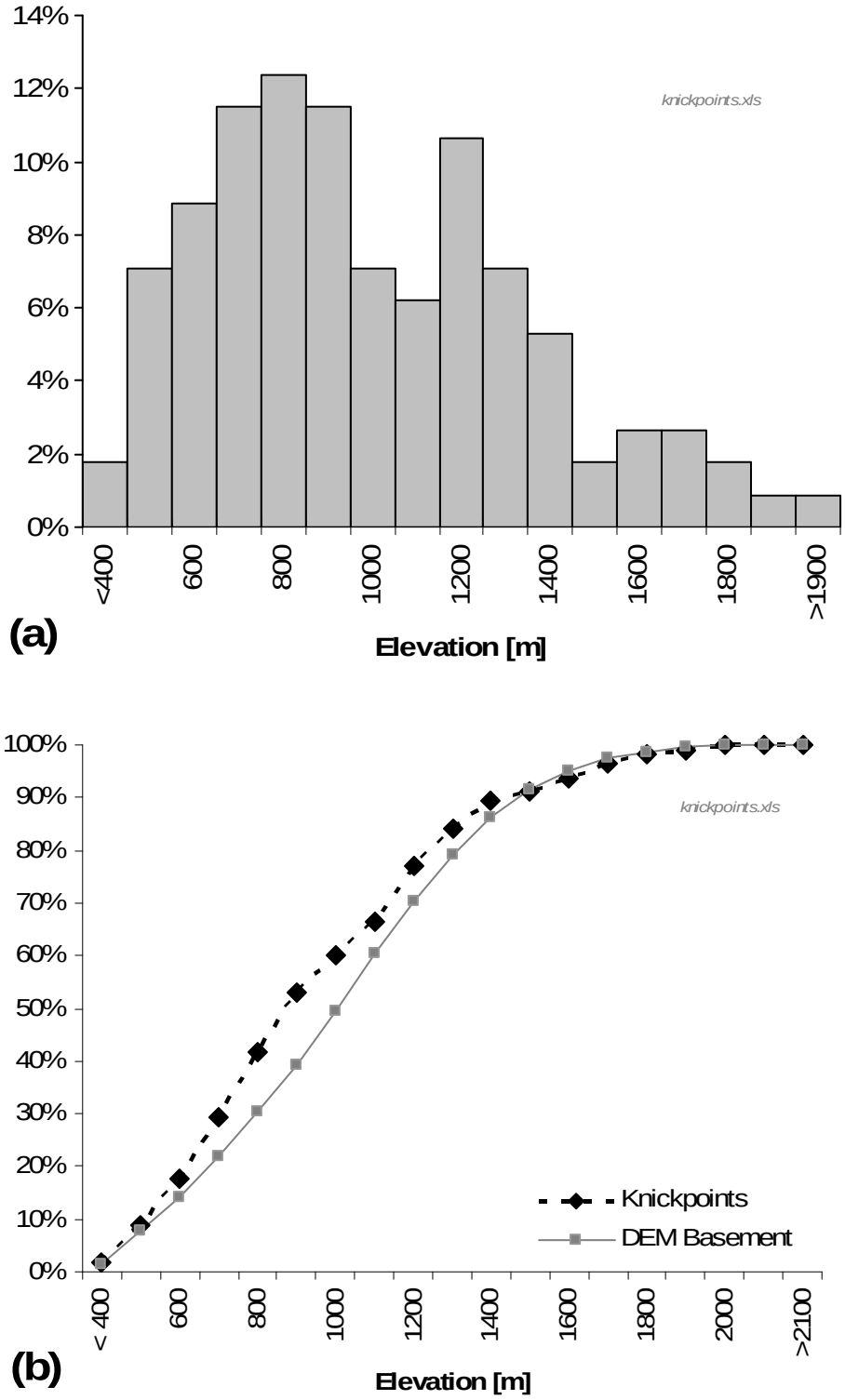

Figure 4-78: (a) Histogram of the elevation distribution of the longitudinal river profile knickpoints in the realm of the Koralpe. Class interval is 100m. (b) Comparison of the cumulative frequency of the elevation distribution of knickpoints and of the DEM clipped to the basement rocks.

4.4 DISCUSSION

The morphological evolution of the Koralpe and the neighbouring parts of the Eastern Alps is still not well understood. There is agreement in literature that the Koralpe block was tilted. However, timing of this event is already a topic not commonly agreed upon. The present analysis contributes only little to the “timing problem” associated with the geomorphological evolution of the Koralpe, as no dating methods have been applied. However, defining the geomorphological characteristics is a prerequisite to understand this evolution. Further, we have to understand the controls exerted by the basement rocks and their structures on the geomorphology to establish a profound geomorphological evolution for this part of the Eastern Alps.

Based on 10 m resolution elevation data this study discusses the morphotectonics resp. geomorphology of the Koralpe. This includes visualization of elevation data, analysis of hypsometry and of elevation derivatives and the determination of lineaments. Further, the drainage system is discussed with respect to its stream and drainage pattern, its shape and symmetry as well as its river profiles.

Visualization of the elevation data indicates the presence of domains (“morphounits”) with similar geomorphological characteristics. This is supported by the analysis of elevation and its derivatives, revealing characteristic distributions for the individual morphounits. Elevation histograms and hypsometric curves reflect the overall distribution of land (area) with respect to elevation. This has been discussed by Szekely (2001) in a two dimensional approach for some basic landforms. However, the overall shape (outline) of a region has a marked influence on the frequency distribution: Units with a relatively narrow drainage exit have less area at lower elevations compared to units which have a broader or several outlets. The symmetric histograms and the convex hypsometric curves of Morphounit Centralwest and Northeast (Figure 4-22, Figure 4-26) reflect such narrow outlets, widening in the middle and narrowing towards the highest elevations. Morphounit East, on the other hand, is characterized by an asymmetric distribution, caused by the broad outlet towards the Styrian Basin and the gradually narrowing of the unit towards its watershed. Similarly, the morphounits Northwest, West and South all show broad outlets resulting in asymmetric elevation histograms, with peaks indicating “preferred” elevation classes. Areas of low relief are frequently present in the eastern and northern Koralpe and reflected as anomalies (peaks) in the elevation histograms and by lower slope angles in the respective elevation classes. The differences in geomorphology resp. the tectonic setting are also traceable in the slope aspect distribution, with a much higher variation of slope aspect in relatively older, more mature areas.

The slope angle analysis reveals structural controls of the Koralpe‘s morphology, too. These controls are frequently related to the metamorphic foliation and the large scale fold structures of the Koralpe and result in the formation of dip slopes and cuestas (Figure 4-37). Locally, linear slopes with steep gradient can be correlated to fault scarps (Figure 4-38).

The strong morphological impact of the metamorphic foliation ("dip slopes") is also reflected in the similar directional statistics of foliation and aspect. However, due to an under representation of foliation measurements in dip slope locations, a correlation could not be verified by GIS analysis but is clearly deducible from field evidence.

Furthermore, structural control of the landscape is indicated by a pronounced lineament pattern. Lineament mapping on visualizations of elevation and its derivatives yields two maxima of lineaments. WNW-ESE to NW-SE trending lineaments dominate in all length classes. A second maximum is formed by NNW-SSE to NE-SW trending lineaments. The mapping scale clearly influences the results: A larger mapping scale causes a length bias towards longer lineaments. Especially the eastern, but also the northeastern morphological unit show higher lineament densities than the rest of the Koralpe. For the eastern unit this can be related to the large scale fold structure with WNW-ESE trending fold axes and the pronounced morphological impact of the metamorphic foliation. Higher lineament density in these areas is further caused by a higher frequency of shorter lineaments, which can be explained by a stronger structuring of the landscape by exogenic processes, possibly also reflecting the age of the landscape. For the Koralpe, lineaments can generally be regarded as a morphological expression of subsurface structure. This includes not only tectonic faults, representing zones of weakness, but also metamorphic foliation and the large scale fold structures of the Koralpe. This morphological expression is additionally enhanced by contrasts in rock strength and erodibility between the different lithologies. The lineament pattern correlates well with the regional strike of metamorphic foliation but also with the fault pattern described in part one of this thesis. According to the interpretation of the field data (Chapter 3.3), the WNW-ESE trending faults were probably formed during Ottnangian to Karpatian time as strike slip faults and were several times reactivated during successive stages of brittle deformation as normal as well as strike slip faults. The NNW-SSE to NE-SW trending faults represent mainly normal faults which predominately formed from the Karpatian onwards.

In combination with hillshade representations and adjusted transparency, curvature maps showed to be useful tools for the identification of lineaments following ridges or valleys. The linear structures detectable in the profile curvature map correlate better with the lineaments (mapped from hillshades and colour-coded DEM combinations) than the ones from the plan curvature do. According to Florinsky (1996), this indicates that lineaments really representing tectonic faults would rather represent elements with a predominating vertical displacement vector. However, this does not imply active normal faulting along those lineaments, although normal faults form the most frequent fault elements in the realm of the Koralpe.

The Koralpe's DEM displays a trapezoid shape in plan view (Figure 4-13): Linear mountain fronts define the western and southern margin of the Koralpe and are partly marked by triangular facets and low mountain front sinuosity. Additionally, the western mountain front seems to be offset by WSW-ENE trending faults with predominating dextral sense of shear in map view. Linear mountain fronts and triangular facets indicate active faulting and/or young erosion. Both seem possible

along the southern Lavanttal Basin and the Drau (Drava) valley. The triangular facets along the southern Lavanttal Basin and the Drau (Drava) valley are better preserved than along the northern Lavanttal Basin. This indicates that young erosional activity is the principal agent for preserving the mountain front in these areas. This is supported by the fact that the spur of the Lavanttal fault zone ("Koralmrandstörung", Herzog and Kahler, 1978; Reischenbacher, 2008) is masked by debris fans, which urge the Lavant River to the western valley side. Additionally, hypsometric analysis yields elevated values for the catchments of the southern Lavant valley and parts of the Drau (Drava) valley. However, neotectonic activity of the Lavanttal Fault Zone with a horizontal slip rate of ~1mm/yr (Vrabec et al., 2006) did not result in a clear trace. Generally the Koralpe and the surrounding basins are characterized by low seismicity (Grünthal and GSHAP Region 3 Working Group, 1999). In contrast, the eastern mountain front is strongly dissected and normal faults (Chapter 3.2 resp. Pischinger et al., 2008) do not have a neotectonic amount of slip to maintain a linear mountain front. In the north, the Koralpe does not show a mountain front but a depression-like transition zone towards the Stubalpe reaching from north of Twimberg at the southern end of the Bad St. Leonhard Basin to Wöllmißberg north of the Teigitsch gorge (Figure 4-33).

The Koralpe does not only show a peculiar shape in map view, but also a typical asymmetric topography in W-E cross-sections from the northern edge of the Lavanttal Basin southwards (Figure 2-1). This is attributed to Miocene block rotation resp. tilting during Miocene extrusion (Neubauer and Genser, 1990; Kurz et al., 2011). The northern Koralpe does not show this asymmetry, indicating that this area was not tilted or that post-tilt surface processes have modified this region. Furthermore, foliation data from the northern Koralpe do not show the ESE dipping fold axes of the eastern Koralpe, commonly interpreted to be a result of block rotation. This difference necessitates that tilting has to be accommodated either by distinct fault zones, which have been exposed in tunnel headings of the northern Koralpe (e.g. Brosch, 1982; Brosch, 1983, and own mappings) or by multiple, smaller fractures. Timing of tilting is poorly constrained. Winkler-Hermaden (1957) assigns tilting to a period from the uppermost Sarmatian (~12 Ma) to the Middle Pannonian (~9 Ma), followed by uplift up to the Quaternary. Friebe (1991) correlates block rotation with the "Styrian Unconformity", which is attributed to the uppermost Karpatian. According to Kurz et al. (2011) thermochronological data indicate block rotation prior to the Sarmatian (>12 Ma).

Tilting around a N–S trending rotation axis (Winkler-Hermaden, 1957; Neubauer and Genser, 1990) would probably not affect the symmetry of W-E trending catchments, especially in a region with a pronounced bedrock structure. Consequently it is not traceable by basin asymmetry. Additionally, the time span from the proposed tilting to the present (probably >12 Ma, cf. Kurz et al., 2011) seems too long to preserve such effects (Robl et al., 2008) in the catchment shape.

Bull (2009) described in detail the differences in basin shape for the Panamint Range in southeastern California, which experienced eastward tilting during the Pleistocene. The tectonic setting is similar to the Koralpe with active (normal) faulting in the West

and relative tectonic quiescence in the East. In the case of the Panamint Range the basins east of the water divide exhibit larger circularities than the ones in the west. Such a pattern is also reflected in the shape ratios for the Koralpe: The shape ratios constrain more elongated catchments for morphounit west than for morphounit east. Yet the differences are not as pronounced as could be expected from their different tectonic setting. Several basins are widened perpendicular to the general drainage direction, which again is an indicator of drainage capture processes or strong structural controls. Generally the basin axis ratio showed to be more sensitive to differences in shape than the other ratios, as the range of its values is wider. The image of more elongated basins in morphounits NW, W, and S is also reflected in their channel index C_i, which is significantly lower in these morphounits. Still it seems doubtful, if this trend can be related to Miocene tilting of the Koralpe, because larger circularities and higher C_i values are also observed in the NE, where the asymmetric morphology, attributed to Miocene tilting is not present. Furthermore, the paleosurfaces of this region do not reflect a tilt into a preferred direction as do the ones in morphounit east. However, the regional differences in stream and basin shape could also be related to the differences in age or in structure of the morphounits. E.g. within morphounit east the large fold structures with gently ESE dipping fold axes favour the development of drainage in an ESE direction, whereas such large scale fold structures are missing within the NE.

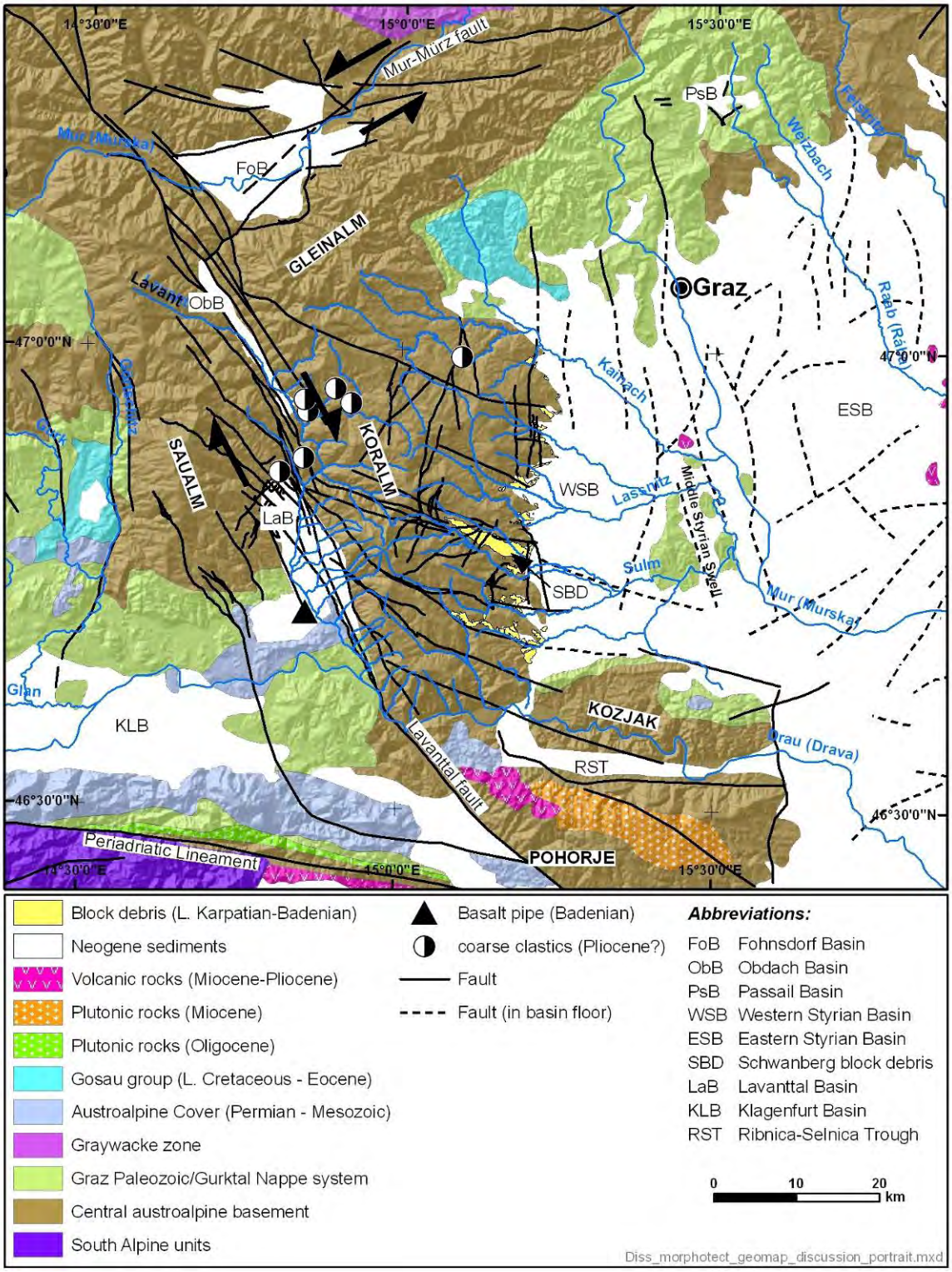

Figure 4-79: Geological map of the Koralpe and adjacent areas, including the main faults active during the Miocene and the main drainage pattern in this region. Geology compiled from Beck-Mannagetta, 1952; Weissenbach, 1978a; Weissenbach, 1978b; Becker, 1979; Beck-Mannagetta, 1980; Kröll, 1988; Beck-Mannagetta et al., 1991; Egger et al., 1999; 1999; Strauss et al., 2001; Beck-Mannagetta and Stingl, 2002, mappings by 3G ZT GmbH (courtesy of ÖBB Infrastruktur Bau GmbH) and own mappings.

Analysis of the Koralpe's elevation data reveals the presence of wide areas of low relief and low slope gradient, especially within the northern and the eastern Koralpe. The west and the south show a relatively low proportion of low slope angle. The latter are related to active tectonics (Lavanttal fault resp. Drau (Drava) valley) and/or intense erosional processes are associated with higher slope gradients than the rest of the Koralpe.

Extraction of the filtered elevation data to a histogram reveals preferred levels of planation (Figure 4-34). These areas have widely been interpreted as remnants of paleosurfaces (e.g. Winkler-Hermaden, 1957; Frisch et al., 2000b). These different levels of planation ("Fluren") were associated by Arthur Winkler-Hermaden to different epochs from the Neogene up to the Pleistocene (Table 1). Thermochronological constraints from distinct cave levels within the Graz Paleozoic were brought forward (Wagner et al., 2011), giving minimum ages for the Hochstraden level (~3.4 Ma) and the Trahütten level (~4 Ma). For the Glashütten level no corresponding cave level is known. A coherent uplift of the "Styrian Block" for the last 4-5 Ma is inferred under the assumption, that fragmentation of this block had been finished during the Miocene (Wagner et al., 2011).

The levels proposed by Winkler-Hermaden (e.g. 1957) partly show a good correlation to the flat areas mirrored in the elevation histogram, partly a correlation is not possible (Figure 4-80). However, the maximum concentration of flat areas between 1010 and 1070 m is neither contained within the range of the Trahütten level (900 to 100m a.s.l. according to Winkler-Hermaden, 1957), nor within the one for the Glashütten level (1100 to 1400 m a.s.l.). Additionally, map analysis (Figure 4-33, Figure 4-81) shows, that the flat areas of the northern and eastern Koralpe are often connected to each other and no separation by steeper sections is observed. This promotes the interpretation that they may represent remnants of a former, coherent landscape, rather than distinct levels of planation from different geological epochs. The age of this possible paleolandscape can be assumed to be younger than ~12 Ma (Sarmatian) and older than the ~3.4 to 4 Ma (Pliocene, Wagner et al., 2011). This coherent landscape was subsequently modified by exogenic processes and possibly further fragmented by faulting and differential uplift (Wagner, 2010). The present interpretation is similar to Frisch et al. (2000b) who argued in favour of a coherent Early Miocene paleosurface ("Pre-extrusion surface") east of the Tauern Window. This surface is named "Nock surface", correlating with Winkler-Hermadens "Kor" level (elevations higher than 1700 m a.s.l.), a rarely preserved level within the Koralpe. The presence of a pre-extrusion surface is reflected in red, lateritic soils and Neogene gravels preserved in the area of the Saualpe and other regions of the Eastern Alps, which represent a "terrestric" phase between the Middle Eocene and the Middle Miocene (Thiedig and Weissenbach, 1975). Generally the term "paleosurface" is misleading, as the whole area termed "Nock Surface" is better considered as a former, coherent and structured landscape and not as a single planation surface. It could be replaced by the term "paleolandscape", as it was discussed by Widdowson (1997).

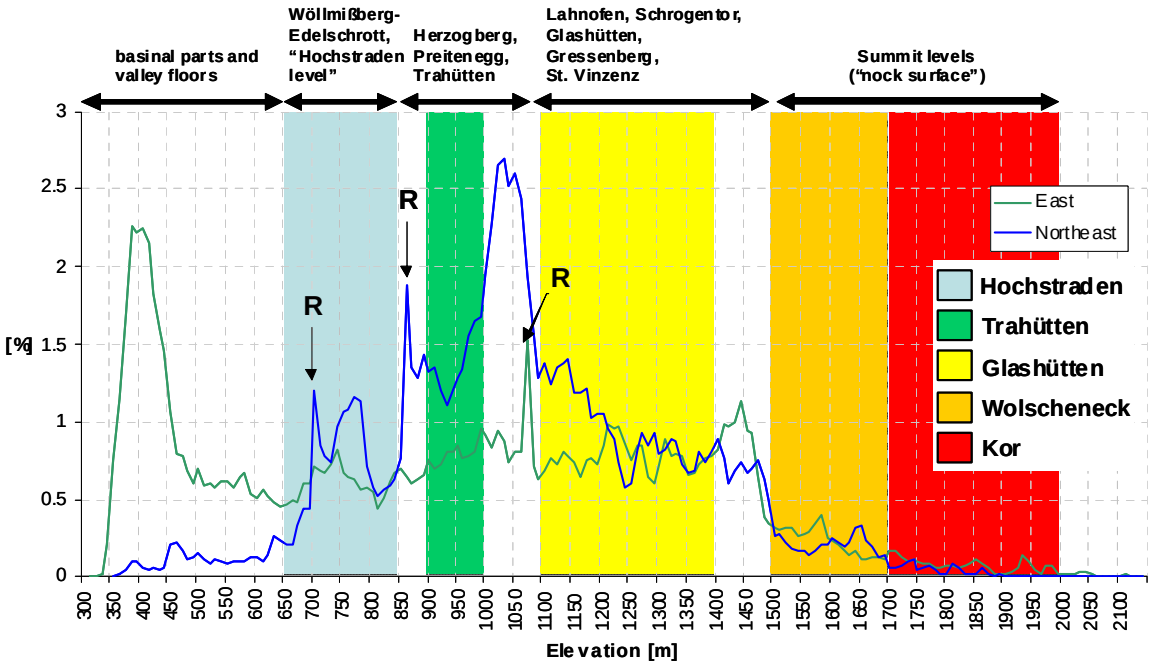

Figure 4-80: Frequency distribution of areas with slope gradient <10° in 10 m elevation classes for Morphounits East and Northeast. Coloured background indicates the planation levels after Winkler-Hermaden (1957). Black arrows mark subdivision based on the histogram. Arrows marked with "R" indicate reservoir areas.

The widespread presence of low relief areas within the Koralpe reflects its being part of a large low relief zone east of the Tauern Window (Figure 4-28), which is clearly visible in the respective elevation data. This is additionally reflected in the hypsometric curve and integral of the Koralpe.

The outline of this low relief zone is bordered in the W by the Katschberg fault (Exner, 1949). In the S it follows the Mölltal fault and is continued towards E by the front of the Karawanken range at the southern margin of the Klagenfurt Basin up to the southern margin to the Pohorje Range (Figure 1-3). The northern border (from the Katschberg fault onwards) parallels roughly the valleys of the Mur and the Mürz river respectively, running approx. 5 to 13 km north of the valley within the southward slopes of the Niedere Tauern. The segment between the Katschberg fault and the Fohnsdorf Basin parallels the so called "Niedere Tauern Southern fault system" (Reinecker, 2000), a part of the Mur-Mürz fault system. East of the Palten-Liesing valley it follows approximately the border between the Northern Calcareous Alps (Mürztal nappe) and the Greywacke zone (Noric nappe) up to the "Wiener Neustätter Bucht", a part of the Vienna Basin. The eastern border follows the contact of the Eastern Alps to the sedimentary units of the surrounding Neogene basins. This zone coincides with an area characterized by Apatite fission track (AFT) ages between 51 and 30 Ma (cf. Wölfler et al., 2011 and references therein). In contrast to this, the Tauern Window and the Niedere Tauern exhibit AFT ages from 20 to 07 Ma and from 23 to 14 Ma respectively (cf. Wölfler et al., 2011 and references therein).

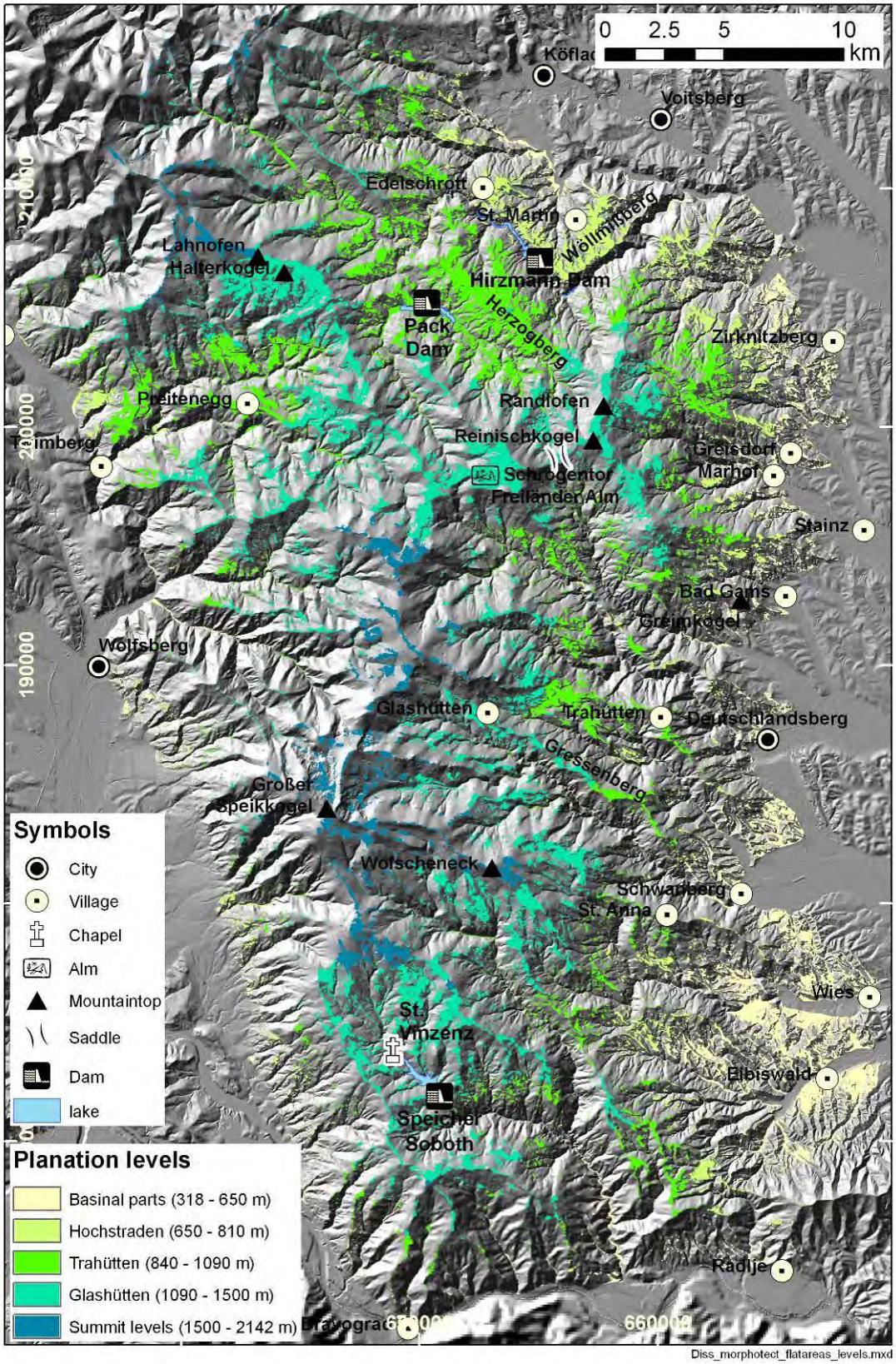

Figure 4-81: Areas <10° slope gradient within the realm of the Koralpe and assignment to different levels of planation according to the elevation histogram (Figure 4-34).

Before lateral extrusion, drainage is thought to have occurred mainly from south to north (Frisch et al., 1998). Dunkl et al. (2005) proposed that rivers in the Eastern Alps, as a result of lateral extrusion, followed mainly W-E trending faults (Paleo-Drau (Drava), Paleo-Mur-Mürz and Paleo-Enns). Today's course of the Mur was a result of stream piracy after the Mid-Miocene (e.g. Wagner, 2010). Earlier drainage of the Mur river probably was conducted via the Mürz valley to the Pannonian basin system, but drainage via the Lavant valley to the Drau (Drava) is also possible (Dunkl et al., 2005).

The presence of gorges is clearly reflected in the relief and slope maps, indicating lowering of the base level. The most impressive ones are the gorges of Twimberg (Lavant River), of the Teigitsch, the Krennbach, the Lassnitz and the Schwarze Sulm. The local relief from the valley floor to the accompanying ridges reaches up to approx. 450 m meters for the Teigitsch and several other creeks dissect a relief of several hundred meters too (Figure 4-20). This phenomenon is not restricted to the Koralpe. Prominent examples of gorges are found around the Styrian Basin (e.g. Raabklamm and Weizklamm). In the case of the Twimberg gorge, the question arises why the river cuts through a ridge of resistant crystalline rocks instead of following the cataclastic rocks of the Lavanttal fault system. Such transverse or discordant drainage may be a result of antecedence, superposition or simple headward erosion but also of stream piracy (Summerfield 1991; Stokes and Mather, 2003; Douglass and Schmeeckle, 2007; Stokes et al., 2008). For the Twimberg gorge it seems possible that the Paleo-Lavant initially followed the spur of the Lavanttal Fault Zone. During evolution of the drainage system an easterly tributary possibly captured successively the catchments of the Prössingbach, the Fraßbach and the largest one, the Waldensteinbach, which formerly drained to the Paleo-Lavant (= Auenbach). Finally, this tributary could have reached the Basin of Bad St. Leonhard (= Obdach Basin), capturing its own main stream.

The age of the Koralpe's gorges is poorly constrained. It is inferred that incision began at the end of the Miocene about 5 to 6 Ma b.p. (Wagner, 2010; Legrain et al., 2011). This coincides with a phase of pronounced activity of the Lavanttal fault (Vrabec et al., 2006). Sedimentary markers constrain the maximum age of incision. One of them is the Schwanberg block debris (Badenian, 16 to 12.5 Ma, Nebert, 1989), several hundred meters above the present surface level of the Styrian Basin. As these sediments are cut through by the gorges of the Eastern Koralpe, incision must be younger than Badenian. Block debris and gravel at higher elevations have been reported by several authors (e.g. Stiny, 1925; Beck-Mannagetta, 1980; Beck-Mannagetta et al., 1991) from the northern Koralpe (Preitenegg, Wöllmißberg, Figure 4-79). Their age is presumably Pliocene or late Miocene (Beck-Mannagetta, 1980; Beck-Mannagetta et al., 1991). These sediments indicate that the Koralpe once must have been a place of (fluvial) sedimentation and that incision must be younger than this age. Within the Western Styrian Basin, Sarmatian (12.7-11.5 Ma) sediments are only preserved in rare places, indicating pronounced Post-Sarmatian erosion. Within the Lavanttal Basin, Sarmatian Sediments are better preserved. The overlying Pannonian (?) gravel beds (cf. Reischenbacher, 2008), indicate uplift and erosion in a northern to north easterly source area. South of the entrance of the Lassnitz into the

Styrian Basin a gravel terrace of early Pleistocene age (Beck-Mannagetta et al., 1991, approx. 1.8 Ma) approx. 40 m above the present level of the river, indicates incision of the river of at least the same amount. The resulting hypothetic incision rate of 0.02 mm/a is compatible with the cosmogenic-derived 10Be denudation rates of Legrain et al. (2011). Wagner (2010) postulated a mean incision rate for the river Mur of 0.125 mm for the last 4 Ma.

Further, geomorphological analysis focused on the stream and drainage pattern. As described above, structural control of drainage is clearly evident over large areas of the Koralpe. This results in a contorted, trellis or subdendritic drainage pattern (see Zernitz, 1932 and Howard, 1967), similarly to the areas glaciated during the last glaciation. Low order streams running in the thick slope debris blanket display a dendritic pattern as long as they do not incise into bedrock. This intense structuring of the landscape by low order streams is especially reflected in the plan curvature map, characterized by an intense fluctuation of convex and concave areas.

Two girdles of prominent angular river knees are located in the eastern Koralpe (Figure 4-61 b). The first is located 3 to 7 km from the entrance into the Styrian basin associated with a change of drainage orientation from ESE to SE and partly S. Structural control related to changes in orientation of metamorphic foliation may be responsible, but is not clear for all river knees. In places, a fault control can not be excluded. However, up to now there is no field evidence for offset or deflection by a common fault. Wind gaps in the vicinity of the river knees indicate stream capture processes during drainage evolution. But also antecedence or superposition from a nowadays eroded sedimentary cover onto the basement rocks may be possible explanations (Figure 4-82). Remnants of a sedimentary cover are found in several places of the eastern and the northern Koralpe, advocating superposition as a possible cause (Figure 4-79).

The second zone of aligned river knees is located at the entrance of the rivers south of the Wildbach into the sedimentary rocks of the Styrian Basin. They are probably caused by differences in lithology and structure between the Austroalpine basement rocks of the Koralpe and the Neogene sedimentary rocks of the Styrian Basin (Figure 4-62, Figure 4-82).

The Koralpe shows a general WNW-ESE strike of foliation and a pronounced large scale fold structure with fold axes dipping gently (~10°, Putz et al., 2006) towards ESE. The bordering Neogene beds of the Styrian Basin are nearly horizontal or are gently dipping towards NE – SE. Furthermore, they have a much higher erodibility than the metamorphic rocks of the Koralpe. This is reflected in differences of their uniaxiale compressive strength by factors of 20 and more (Table 11, Table 12). Additionally, structures like faults and joints are widely missing within the Styrian Basin. Hence a structural control on drainage is mainly to be expected from the sedimentary bedding planes and only in places from the sparsely distributed faults. This lack of structural control may imply that the rivers within the Styrian Basin developed primarily as consequent rivers. Structural control may have resulted on a

large scale from the tectonic style of the Styrian Basin, which is characterized by normal faults ("Horst-Graben" style, Figure 4-79).

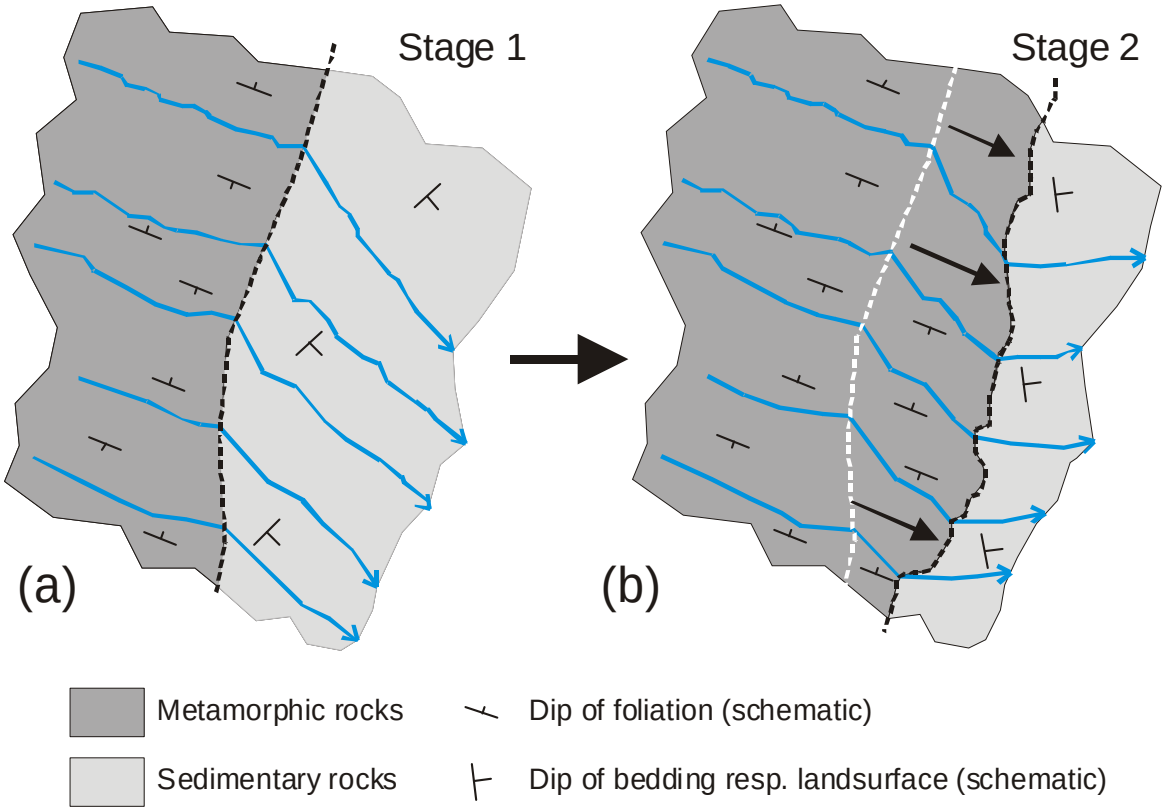

Figure 4-82: Possible development of river knees in the eastern Koralpe caused by erosion of sedimentary cover and change in dip of sedimentary strata or topography. Superposition on the underlying metamorphic rocks preserves their original course.

	All Samples	Siltstone		Sandstone	
		Normal	Concretion	Normal	Concretion
	[MPa]	[MPa]	[MPa]	[MPa]	[MPa]
Mean	3.7	2.9	15.8	1.8	8.8
Median (q50%)	2.7	2.7	15.6	1.6	8.8
Quartile 25%	1.5	2.0	13.6	1.0	7.9
Quartile 75%	3.8	3.8	16.1	2.6	9.3
Min	0.1	0.1	7.9	0.3	7.0
Max	26.5	6.0	26.5	3.7	11.0
Number	***89***	***50***	***6***	***29***	***4***

Table 12: Uniaxial strength of Neogene sedimentary rocks from the Styrian Basin (Data from Koralmtunnel project, used by courtesy of ÖBB Infrastruktur AG).

Within the Eastern and Northern Koralpe wind gaps indicate possible remnants of a NW-SE trending paleoriver from the Stubalpe through the eastern Koralpe towards the Drava valley (Figure 4-65). This has already been indicated by Sölch (1928). This hypothetic river may have been active, before it was captured by eastward directed drainage of the Mur catchment (Figure 4-83). It seems possible that remnants of this paleo-drainage system are preserved in locations, mainly along the watersheds of the present drainage basins. This is also indicated by remnants of fluvial sediments described in locations on top of the paleosurfaces, especially in the northern Koralpe (e.g. Stiny, 1925; Beck-Mannagetta, 1948; Beck-Mannagetta, 1980; Beck-Mannagetta et al., 1991). The Pliocene to Miocene age of these sediments, although poorly constrained, indicates a capture event after this time span.

Successive phases of stream capture are very probable for the Koralpe (Morawetz, 1964; Morawetz, 1984), resulting in catchment geometries marked by a higher channel index and frequently by a pronounced basin asymmetry. Restructuring of the drainage pattern by the catchment of the Krennbach, progressing from the Southern Koralpe into the central Koralpe, was probably triggered by the shift of the Drava River in its present position (Figure 4-83). According to Sölva et al. (Sachsenhofer, 1996; Sölva et al., 2005b), the maximum age of the shift of the Drau (Drava) into its present position is constraint by Pliocene (5-2 Ma b.p.) river sediments in its paleo-channel. Subsequent incision and stream capture of the Krennbach diverted several rivers formerly draining to the Styrian Basin towards the Drau (Drava) valley.

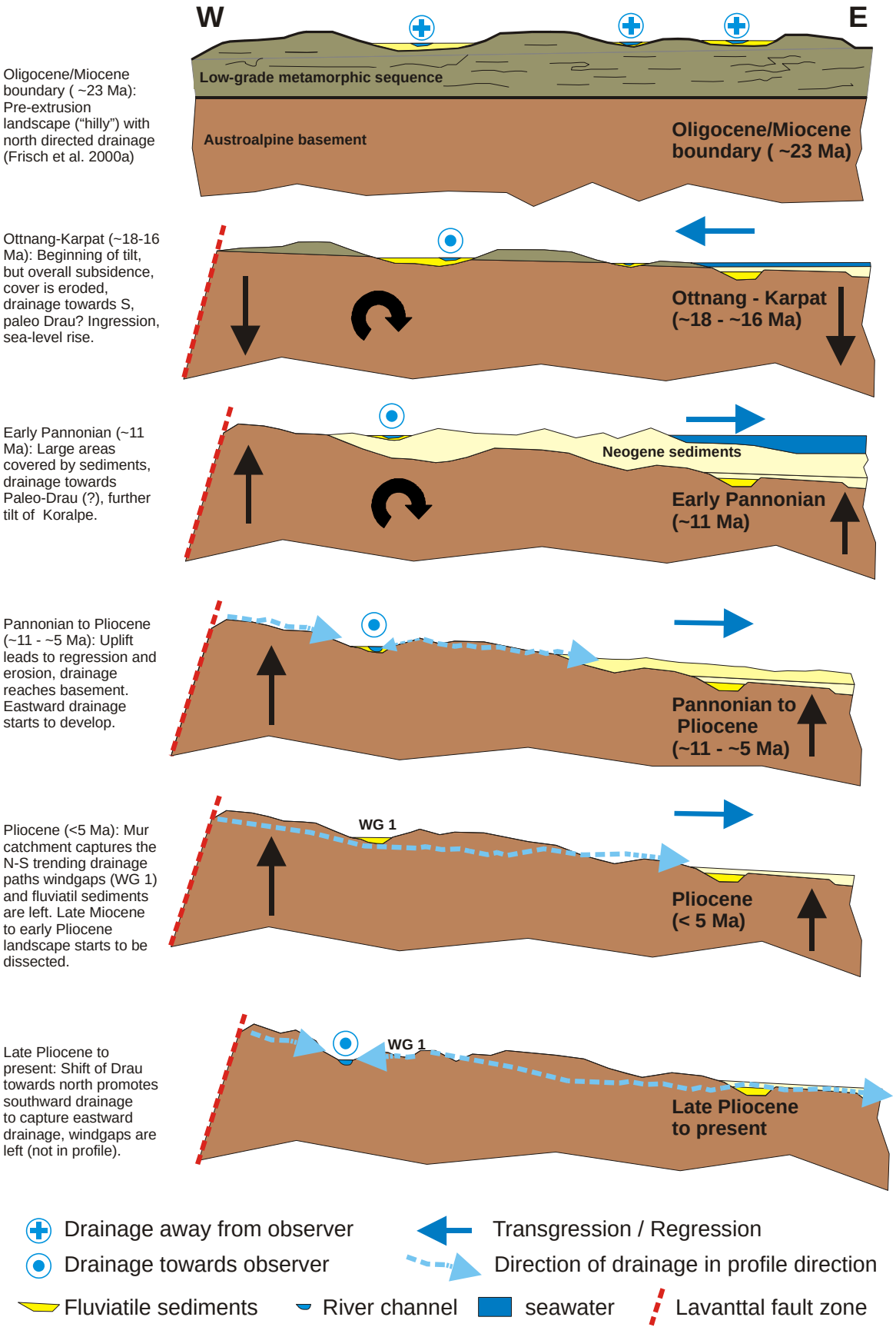

Figure 4-83: Schematic scheme for drainage evolution within the Koralpe from the Oligocene boundary up to the present (not to scale).

Most of the analysed rivers show a graded, upwardly concave longitudinal profile associated with a positive concavity index C_A. C_A ranges from –0.05 to 0.68, indicating the presence of non-steady state profiles (Snow and Slingerland, 1987). River profiles associated with low C_A values are often characterized by pronounced knickpoints or by a linear profile form. The regional distribution of C_A shows a concentration of low values along tributaries to the Drau (Drava) valley from Lavamünd to Dravograd and further to Radlje and along some of the tributaries to the longer creeks in the interior of the Koralpe.

The calculation of the stream gradient index (SL) reveals zones of increased gradient, usually coinciding with a low C_A. Again an increase in SL is often associated with pronounced river knickpoints and gorgelike valleys. The interpolation to a stream gradient map (Figure 4-76) yields a belt of elevated SL values of 300 m to 571 m, which follows the outline of the Koralpe and its typical morphology. It surrounds an area elongated in north - south direction with clearly lower values and a minimum in the area of the Packer Bach and the Modriachbach with values of 193 m to 214 m. This area coincides with the paleolandscape preserved in the northern Koralpe, but also in higher regions of the eastern Koralpe. This indicates that these areas have not yet been submitted to severe erosive restructuring. Most of the knickpoints detected in the longitudinal river profiles are situated within this belt of increased SL index values and within the gorge like stretches of the rivers at elevations from 700 to 800 m and from 1100 to 1200 m.

The SL map, the systematic distribution of some of the knickpoints and the systematic presence of gorges suggest that changes in base level may be a common cause for the some of the knickpoints. However, a rough control with the available geological data (lithology, structure, mass wasting processes etc.) reveals, even without a thorough field check, that multiple causes may be responsible for the formation of the knickpoints. This multi-causality of knickpoint origin is confirmed by several studies around the world in very different settings (Bishop et al., 2005; Crosby and Whipple, 2006; Larue, 2008; Phillips et al., 2010 and references cited therein). For the Koralpe clear lithological control can be shown for several major knickpoints (e.g. Stainzbach and its tributaries, Figure 4-74). This strong influence of lithology is additionally reflected in the hypsometric curve and integral of these catchments. To our opinion it is beyond question that mechanical anisotropy and rock structure exert a significant influence on the shape of the river profiles within the Koralpe. Hence base level processes can not be used as the single explanation for the presence of knickpoints within the Koralpe's river profiles, as it is indicated in recent research papers (Legrain et al., 2011). Rantitsch et al. (2009) did not see evidence for systematically migrating knickpoints and assumed a general equilibrium state of the Koralpe Range. Their analysis of slope-area data yielded no breaks corresponding to the knickpoints in the longitudinal river profiles, indicating a non-tectonic origin. Yet a north to south directed increase of the steepness values was observed, advocating higher uplift rates in the central Koralpe. According to Rantisch et al. (2009), this trend seems to be traceable in Paleogene low temperature geochronology and the Late Cretaceous metamorphic field gradient. A stable, long-term pattern of exhumation and uplift is therefore proposed by Rantitsch et al. (2009). As a consequence Rantitsch et al. (2009)

suggested that the analysed stream profiles reflect rather the long-term average (~10 Ma) than the short-term (1-5 Ma) landscape evolution. This is supported by Robl et al. (2008), who showed in their analysis of the major rivers of the Eastern Alps, that only changes younger than 5 Ma are mirrored in the longitudinal profiles.

Generally, GIS-based visualization and analysis of elevation data, including analysis of the drainage system, are state of the art tools which may be used to assist with the early stages of site investigation. With the increasing availability of high resolution data (e.g. LIDAR data) this becomes also true for smaller project sizes. Elevation analysis may assist in the identification of fault zones, may yield information on bedrock structure and on regional strength contrasts. Additionally, geomorphological peculiarities may reveal possible neotectonic activity and, depending on the resolution of the used elevation data, also mass wasting processes.

The elevation data of the Koralpe yield a hypsometric integral and a hypsometric curve which, according to Strahler (1952), both would indicate a mature equilibrium landscape. However, their use as a proxy for landscape maturity has to be considered carefully (Willgoose and Hancock, 1998; Hurtrez et al., 1999), as H_i and hypsometric curve are influenced by several catchment parameters like e.g. catchment geometry and channel network. Additionally scale dependency is indicated in literature (Willgoose and Hancock, 1998; Hurtrez et al., 1999; Cheng et al., 2012). In the case of the Koralpe this scale dependency is probably masked by lithological and structural controls, but basin hypsometry may be scale independent in a steady-state topography too (Cheng et al., 2012). With the application of GIS techniques hypsometric curve and integral are quickly calculated from digital elevation data. From a field geologists point of view they are helpful tools to reveal areas with hypsometric or morphological peculiarities, rather than indicators for some stage of landscape development. Such peculiarities may reflect lithological and structural differences, as well as active tectonics or mass wasting processes.

At several locations of the Koralpe the morphological impact of fault zones is evident and was verified by tunnel headings or core drillings (e.g. Figure 1-1 b). However, this does not imply that every morphological saddle, planation surface, gully, valley or break in slope gradient is linked to a fault or fault zone. Especially a region like the Koralpe, which was exposed to exogenic forces over a long time span and which is characterised by a pronounced bedrock structure and lithological contrasts, will develop similar landforms. Hence, such landforms may be used as indicators, but suspected fault zones have to be verified by detailed subsurface investigations to avoid erroneous interpretations. This is also valid for the identified lineaments, because an unreflective parallelisation of lineaments and fault zones may lead to an over estimation of fault density. Mapping of indicator landforms and lineaments may be automated by algorithms (e.g. Dikau, 1988; Dikau, 1989; Wood, 1996; Bolongaro-Crevenna et al., 2005; Schmidt and Andrew, 2005; Smith and Clark, 2005; Arrell et al., 2007 and Raghavan et al., 1993; Arenas Abarca, 2006), allowing to analyse large data sets. However, if a specific area has to be judged, results from automated detection procedures must not be accepted unconsidered because they may be far from the actual truth.

4.5 CONCLUSIONS

The presented study uses GIS techniques to analyse the geomorphology resp. the morphotectonics of the Koralpe. Visualizations of digital elevation data showed to be extremely helpful to gain a quick overview of a region with respect to its geomorphology and morphotectonics.

A possible neotectonic control of the western and southern mountain front of the Koralpe is deducible from the visualizations of digital elevation data and mountain front sinuosity. However, fluviatile forces enhance the mountain fronts in places. In the West, the outline of the Koralpe is controlled by the Lavanttal Fault Zone, causing a linear mountain front. For the southern mountain front a control by fault elements parallel to the mountain front has yet to be constrained by geological field work. The eastern mountain front can be termed tectonically inactive.

GPS measurements and seismic activity along the (northern) Lavanttal Fault Zone support neotectonic activity (Reinecker and Lenhardt, 1999; Vrabec et al., 2006; Caporali et al., 2008). However, neotectonic activity is not large enough to leave a clear fault trace within the large debris fans at the eastern margin of the Lavanttal Basin. Furthermore, the Lavant river at present does not have a transport capacity large enough to maintain its course along the zone of maximum depth (= maximum subsidence) of the basin, and its course is deviated to the western side of the basin.

The systematic presence of gorges indicates a lowering of the base level. Such gorges are observed all around the Styrian Basin.

Furthermore, the DEM of the Koralpe reveals large areas of low relief, especially in the northern and the eastern morphounit. The comparison with the elevation data of the Alps confirm, that the Koralpe belongs to a fault-bounded zone of low relief and low slope gradient east of the Tauern Window.

The hypsometric integral and curve for the Koralpe indicate a mature equilibrium landscape (Strahler, 1952). Apart from such debatable descriptions, hypsometric analysis showed to be a helpful tool to detect hypsometric peculiarities, which are either linked to relatively younger erosional processes, to lithological controls or possible neotectonic activity.

Slope angle analysis shows large areas of low slope angle especially in the northern and the eastern Koralpe. These areas are commonly interpreted as preferred levels of planation with a Upper Sarmatian to Pliocene age (Winkler-Hermaden, 1957; Wagner et al., 2011). However, in the northern and the eastern Koralpe they do not represent isolated planation surfaces but form continuous zones. Therefore these planation surfaces are proposed to represent remnants of a single paleolandscape with a probable Upper Miocene to Pliocene age (Frisch et al., 2000b).

The Koralpe's geomorphology is fundamentally controlled by the penetrative metamorphic foliation, causing a pronounced anisotropy in the mechanical rock properties. Orientation of foliation controls especially slope inclination and orientation.

In the eastern and central Koralpe orientation and shape of slopes accentuates the underlying large scale fold structure. On the contrary, the northern Koralpe is characterized by plateau formation and successive landforms due to a frequently nearly horizontal foliation.

Morphological impact (formation of saddles, passes, gullies and linear valleys) of faults and fault zones is verifiable in certain locations (e.g. the Herzogberg of the northern Koralpe). However, the morphological impact of faults within the interior of the Koralpe is difficult to discern from the one caused by lithological contrasts or structural elements like foliation or joints. Due to the strong structural and lithological controls it seems not probable that fault related neotectonic activity could possibly be identified from specific landforms in the Koralpe's interior, especially as deformation rates can be assumed to be very low.

The river pattern of the Koralpe exhibits strong evidence of structural controls too. The presence of wind gaps and angular river knees underline the importance of stream capture processes for the development of the Koralpe's drainage system. The systematic changes in river orientation in the eastern Koralpe constrain the presence of other processes like superposition from an eroded sedimentary cover of the Koralpe. Systematic changes in river orientation at the entrance into the sediments of the Styrian Basin support the idea of superposition.

The course of paleorivers may be inferred in several places from aligned wind gaps and linear valleys, indicating a reorganisation of drainage from a N-S direction to a WNW-ESE direction. Pliocene shift of the Drau (Drava) in its present position triggered a renewed reorganisation to N-S directed drainage by stream capture.

Generally, tilting of the Koralpe is mainly advocated by the topographic profile in W-E direction from the Saualpe to the Mur River. However, such a typical topography is not present in the northern Koralpe. The necessary differential movements between these two regions could have been accommodated by WNW-ESE striking fault zones encountered during tunnelling in the northern Koralpe. Tilting of the Koralpe is not reflected in a preferred asymmetry of catchments. However, the basin asymmetry factor turned out to be a helpful tool for the detection of stream capture processes. Furthermore, several basin shape indices and also the channel index yield elongated basins for the western Koralpe, which could be interpreted as a result of tilting.

Knickpoints are frequently present in the longitudinal river profiles of the Koralpe. They are associated with low concavity indices and an increase in the stream gradient index SL. A belt of high SL values around the Koralpe contains most of the knickpoints, frequently associated to gorgelike river stretches. This advocates changes in base level as a common cause knickpoint origin. However, some of the knickpoints are clearly associated to contrasts in lithology. Slope-area plots indicate a non-tectonic knickpoint origin (Rantitsch et al., 2009). Hence multi-causality of knick point origin is, due to its geological structure, its lithological contrasts and the tectonical framework, a probable scenario for the Koralpe.

5 REFERENCES

Anderson, E.M., 1951. The dynamics of faulting and dyke formation with applications to Britain. Oliver and Boyd, Edinburgh, 206 pp.

Angelier, J., 1994. Fault Slip Analysis and Palaeostress Reconstruction. In: P.L. Hancock (Editor), Continental Deformation. Pergamon Press, Oxford, pp. 53-100.

Angelier, J. and Goguel, J., 1979. Sur une methode simple de determination des axes principaux des contraintes pour une population de failles. Comptes Rendus Hebdomadaires des Seances de l'Academie des Sciences, Serie D: Sciences Naturelles, 288(3): 307-310.

Angelier, J. and Mechler, P., 1977. Sur une methode graphique de recherche des contraintes principales egalement utilisables en tectonique et en seismologie : la methode des diedres droits. A graphic method applied to the localization of principal stresses for fault tectonics and seismology; the right dihedral method. Bulletin de la Societe Geologique de France, 19(6): 1309-1318.

Anonymous, 2011. WP3: Risk analysis (Date of accesss: 2011-01-09).

Arenas Abarca, M.A., 2006. Lineament extraction from digital terrain models. Master Thesis Thesis, Enschede, The Netherlands.

Arrell, K.E., Fisher, P.F., Tate, N.J. and Bastin, L., 2007. A fuzzy c-means classification of elevation derivatives to extract the morphometric classification of landforms in Snowdonia, Wales. Computers & Geosciences, 33(10): 1366-1381.

Balogh, K., Ebner, F. and Ravasz, C., 1994. K/Ar-Alter tertiärer Vulkanite der südöstlichen Steiermark und des südlichen Burgenlands. In: H. Lobitzer, G. Csaszar and A. Daurer (Editors), Jubiläumsschrift 20 Jahre geologische Zusammenarbeit Österreich-Ungarn. Geologische Bundesanstalt, Vienna, pp. 55-72.

Bárdossy, A. and Schmidt, F., 2002. GIS approach to scale issues of perimeter-based shape indices for drainage basins. Hydrological Sciences Journal, 47(6): 931-942.

Barnett, P. and Shirota, J., 2004. Lake Nipigon Region geoscience Initiative (LNRGI): Lineament Analysis Project; poster, Ontariao Exploration and Geoscience. Ontario Geological Survey.

Barton, N., 2000. TBM Tunnelling in Jointed and Faulted Rock. A. A. Balkema, Rotterdam, 172 pp.

Becker, L.P., 1979. Geologische Karte der Republik Österreich 1:50.000 - 162 Köflach. Geologische Bundesanstalt, Wien.

Becker, L.P., 1980. Geologische Karte der Republik Österreich 1:50.000 - Erläuterungen zu Blatt 162 Köflach. Geologische Bundesanstalt, Wien, 57 pp.

Beck-Mannagetta, P., 1948. Zur Morphotektonik des Koralpenostrandes. Mitteilungen der Geographischen Gesellschaft in Wien, 90(12-17).

Beck-Mannagetta, P., 1952. Zur Geologie und Paläontologie des Tertiärs des unteren Lavanttales. Jahrbuch der Geologischen Bundesanstalt, 95: 1-102.

Beck-Mannagetta, P., 1953. Die eiszeitliche Vergletscherung der Koralpe (Alpen-Ostrand). Zeitschrift fuer Gletscherkunde und Glazialgeologie, 2(2): 263-277.

Beck-Mannagetta, P., 1980. Geologische Karte der Republik Österreich 1:50.000 - 188 Wolfsberg. Geologische Bundesanstalt, Wien.

Beck-Mannagetta, P., 1986. Blatt 189 Deutschlandsberg Bericht 1985 über geologische Aufnahmen auf Blatt 189 Deutschlandsberg. Jahrbuch der Geologischen Bundesanstalt, 129(2): 463-464.

Beck-Mannagetta, P., Eisenhut, M., Ertl, V. and Homann, O., 1991. Geologische Karte der Republik Österreich 1:50.000 - 189 Deutschlandsberg. Geologische Bundesanstalt, Wien.

Beck-Mannagetta, P. and Stingl, K., 2002. Geologische Karte der Republik Österreich 1:50.000 - 206 Eibiswald. Geologische Bundesanstalt, Wien.

BEV, 2006. Digitales Höhenmodell (DGM) - Höhenraster (dgm-hr.pdf). Bundesamt für Eich- und Vermessungswesen, pp. 3.

Bishop, P., 1995. Drainage rearrangement by river capture, beheading and diversion. Progress in Physical Geography, 19(4): 449-473.

Bishop, P., Hoey, T.B., Jansen, J.D. and Lexartza Artza, I., 2005. Knickpoint recession rate and catchment area: the case of uplifted rivers in Eastern Scotland. Earth Surface Processes and Landforms, 30(6): 767-778.

Blenkinsop, T.G., 2006. Kinematic and dynamic fault slip analyses: implications from the surface rupture of the 1999 Chi-Chi, Taiwan, earthquake. Journal of Structural Geology, 28(6): 1040-1050.

Bloom, A.L., 1998. Geomorphology: A Systematic Analysis Of Late Cenozoic Landforms. Waveland Press inc., Long Grove, Illinois.

Blümel, M., Brosch, F.J. and Fasching, A., 1999. Investigations on fabrics and related mechanical properties of a highly anisotropic gneiss, International Congress on Rock Mechanics, Paris / France, pp. 1001-1005.

Bojar, H.-P., Bojar, A.-V., Mogessie, A., Fritz, H. and Thalhammer, O.A.R., 2001. Evolution of veins and sub-economic ore at Strassegg, Paleozoic of Graz,

Eastern Alps, Austria: evidence for local fluid transport during metamorphism. Chemical Geology, 175: 757–777.

Bolongaro-Crevenna, A., Torres-Rodriguez, V., Sorani, V., Frame, D. and Arturo Ortiz, M., 2005. Geomorphometric analysis for characterizing landforms in Morelos State, Mexico. Geomorphology, 67(3-4): 407-422.

Bott, M.H.P., 1959. The mechanics of oblique slip faulting. Geological Magazine, 96(2): 109-117.

Braun, R., 2003. In situ stress and parameter determination using core samples, 7. Workshop Bohrlochgeophysik und Gesteinsphysik, Hannover.

Brekke, T.L. and Howard, T.R., 1973. Functional classification of gouge materials from seams and faults in relation to stability problems in underground openings, Department of Civil Engineering, Institute of Transport and Traffic Engineering, Berkely.

Brodie, K., Fettes, D. and Harte, B., 2007. Structural terms including fault rock terms. In: D. Fettes and J. Desmons (Editors), Metamorphic Rocks - A Classification and Glossary of Terms. Cambridge University Press, Cambridge, pp. 24-31.

Brodie, K.H., Fettes, D., Harte, B. and Schmid, R., 2002. Towards a unified nomenclature in metamorphic petrology: 5. Structural terms including fault rocks. A proposal on behalf of the IUGS Sucommission on the Systematics of Metamorphic Rocks. Provisional recommendations, web version of 31.10.2002. IUGS Subcommission on the Systematics of Metamorphic Rocks (SCMR), pp. 8.

Brosch, F.J., 1982. Zur Baugeologie des Kalcherkogeltunnels. Mitteilungen der Gesellschaft der Geologie und Bergbaustudenten in Österreich, 28: 177-200.

Brosch, F.J., 1983. Der tektonische Bau des Kalcherkogels in der Koralpe (Steiermark/Kärnten). Mitteilungen der Österreichischen Geologischen Gesellschaft, 76: 101-132.

Brosch, F.-J., Pischinger, G., Steidl, A., Vanek, R. and Decker, K., 2001. Improved site investigation results by kinematic discontinuity analysis on drill cores. In: P. Särkkä and P. Eloranta (Editors), Rock Mechanics a challenge for society - ISRM Regional Symposium EUROCK 2001. Swets & Zeitlinger Lisse, Espoo/Finland, pp. 41-45.

Brosch, F.J., Schachner, K., Blumel, M., Fasching, A. and Fritz, H., 2000. Preliminary investigation results on fabrics and related physical properties of an anisotropic gneiss. Journal of Structural Geology, 22(11-12): 1773-1787.

Brox, D. and Hagedorn, H., 1999. Extreme deformation and damage during the construction of large tunnels. Tunnelling and Underground Space Technology, 14(1): 23-28.

Brückl, E. et al., 2007. Crustal structure due to collisional and escape tectonics in the Eastern Alps region based on profiles Alp01 and Alp02 from the ALP 2002 seismic experiment. Journal of Geophysical Research, 112(B06308, doi:10.1029/2006JB004687).

Buchroithner, M.F., 1984. Karte der Landsatlineamente von Österreich 1:500.000. Geologische Bundesanstalt, Wien.

Bull, W.B., 2007. Tectonic Geomorphology of Mountains: A New Approach to Paleoseismology. Blackwell Publishing, Oxford.

Bull, W.B., 2009. Tectonically Active Landscapes. Wiley-Blackwell, 326 pp.

Bull, W.B. and McFadden, L.D., 1977. Tectonic geomorphology north and south of the Garlock Fault, California. In: D.O. Doehring (Editor), Geomorphology in Arid Regions. George Allen & Unwin, pp. 115-138.

Burbank, D.W. and Anderson, R.S., 2001. Tectonic geomorphology. Blackwell Science, Oxford, 274 pp.

Burbank, D.W. et al., 1996. Bedrock incision, rock uplift and threshold hillslopes in the northwestern Himalayas. Nature, 379(6565): 505-510.

Bürgi, C. and Parriaux, A., 1999. Cataclastic fault rocks in underground works: project AlpTransit-Lötschberg and other sites in the Alps. In: S. Löw and R. Wyss (Editors), Vorerkundung und Prognose der Basistunnels am Gotthard und am Lötschberg. A.A.Balkema, Zürich.

Bürgi, C., Parriaux, A. and Franciosi, G., 2001. Geological characterization of weak cataclastic fault rocks with regards to the assessment of their geomechanical properties. Quarterly Journal of Engineering Geology and Hydrogeology, e4(2): 225-232.

Cannon, P.J., 1976. Generation of explicit parameters for a quantitative geomorphic study of the Mill Creek drainage basin. Oklahoma Geological Notes, 38(1): 3-17.

Caporali, A. et al., 2009. Surface kinematics in the Alpine-Carpathian-Dinaric and Balkan region inferred from a new multi-network GPS combination solution. Tectonophysics, Accepted manuscript.

Caporali, A. et al., 2008. Geokinematics of Central Europe: New insights from the CERGOP-2/Environment Project. Journal of Geodynamics, 45(4-5): 246-256.

Casas, A.M. et al., 2000. LINDENS: A program for lineament length and density analysis. Computers & Geosciences, 26(9-10): 1011-1022.

Chen, Y.-C., Sung, Q. and Cheng, K.-Y., 2003. Along-strike variations of morphotectonic features in the Western Foothills of Taiwan: tectonic implications based on stream-gradient and hypsometric analysis. Geomorphology, 56(1-2): 109-137.

Cheng, K.-Y., Hung, J.-H., Chang, H.-C., Tsai, H. and Sung, Q.-C., 2012. Scale independence of basin hypsometry and steady state topography. Geomorphology, 171-172: 1-11.

Chester, F.M., Friedman, M. and Logan, J.M., 1985. Foliated cataclasites. Tectonophysics, 111(1-2): 139-146.

Chester, F.M. and Logan, J.M., 1987. Composite planar fabric of gouge from the Punchbowl Fault, California. Journal of Structural Geology, 9(5-6): 621-634.

Chester, F.M. and Logan, J.M., 1998. Shear band fabric in gouge. In: A.W. Snoke, J. Tullis and V.R. Todd (Editors), Fault related rocks. Princeton University Press, Princeton, pp. 68-69.

Cladouhos, T.T., 1999. A kinematic model for deformation within brittle shear zones. Journal of Structural Geology, 21(4): 437-448.

Cladouhos, T.T., 1999b. A kinematic model for deformation within brittle shear zones. Journal of Structural Geology, 21(4): 437-448.

Commins, D.C., Gupta, S., Phillips, W. and Schaefer, J., 2006. Styles and rates of knickpoint migration from cosmogenic Be-10 in a landscape of active normal faulting. Geophysical Research Abstracts, 8(09886): 1.

Cox, R.T., 1994. Analysis of drainage-basin symmetry as a rapid technique to identify areas of possible Quaternary tilt-block tectonics; an example from the Mississippi Embayment. Geological Society of America Bulletin, 106(5): 571-581.

Crosby, B.T. and Whipple, K.X., 2006. Knickpoint initiation and distribution within fluvial networks: 236 waterfalls in the Waipaoa River, North Island, New Zealand. Geomorphology - The Hydrology and Geomorphology of Bedrock Rivers, 82(1-2): 16-38.

Cuong, N.Q. and Zuchiewicz, W.A., 2001. Morphotectonic properties of the Lo River Fault near Tam Dao in North Vietnam. Natural Hazards and Earth System Sciences, 1: 15-22.

Decker, K., 1996. Miocene tectonics at the Alpine-Carpathian junction and the evolution of the Vienna basin. Mitteilungen der Gesellschaft der Geologie und Bergbaustudenten in Österreich, 41: 33-44.

Dikau, R., 1988. Entwurf einer Geomorphographisch-Analytischen Systematik von Reliefeinheiten, Arbeitsbericht im Rahmen des DFG-Schwerpunktprogramms "Digitale Geowissenschaftliche Kartenwerke", Geographisches Institut der Universität Heidelberg, Heidelberg.

Dikau, R., 1989. Computergestützte Reliefmodellierung als Kern einer Digitalen Geomorphologischen Basiskarte. Geowissenschaftliche Mitteilungen der TU Wien, 33: 51-59.

Doblas, M., 1998. Slickenside kinematic indicators. Tectonophysics, 295(1-2): 187-197.

Douglas, D.H. and Peucker, T.K., 1973. Algorithms for the reduction of the number of points required to represent a digitized line or its caricature. The Canadian Cartographer, 10(2): 112-122.

Douglass, J. and Schmeeckle, M., 2007. Analogue modeling of transverse drainage mechanisms. Geomorphology, 84(1-2): 22-43.

Drury, S.A., 1993. Image interpretation in geology. Chapman & Hall, London, 283 pp.

Dunkl, I. and Frisch, W., 2002. Thermochronologic constraints on the Late Cenozoic exhumation along the Alpine and West Carpathian margins of the Pannonian basin. EGU Stephan Mueller Special Publication Series, 3: 135-147.

Dunkl, I., Kuhlemann, J., Reinecker, J. and Frisch, W., 2005. Cenozoic relief evolution of the Eastern Alps – constraints from apatite fission track age-provenance of Neogene intramontane sediments. Austrian Journal of Earth Sciences, 98: 92-105.

Duvall, A., Kirby, E. and Burbank, D., 2004. Tectonic and lithologic controls on bedrock channel profiles and processes in coastal California. Journal of Geophysical Research, 109: F03002.

Ebner, F. and Rantitsch, G., 2000. Das Gosaubecken von Kainach—ein Überblick. Mitteilungen der Gesellschaft der Geologie und Bergbaustudenten in Österreich, 44: 157-172.

Ebner, F. and Sachsenhofer, R.F., 1995. Palaeogeography, subsidence and thermal history of the Neogene Styrian Basin (Pannonian basin system, Austria). Tectonophysics, 242(1-2): 133-150.

Egger, H. et al., 1999. Geologische Übersichtskarte der Republik Österreich 1:1500 000. Geologische Bundesanstalt, Wien.

Egger, S., 2007. Strukturelle Analyse des Schwanberger Blockschutt Beckens im Hinblick auf die Achse des Koralm-Basistunnel. Magisterarbeit Thesis, Technische Universität Graz, Graz, 68 pp.

Ekneligoda, T.C. and Henkel, H., 2006. The spacing calculator software--A Visual Basic program to calculate spatial properties of lineaments. Computers & Geosciences, 32(4): 542-553.

Evans, I.S., 1981. General Morphometry. In: A. Goudie (Editor), Geomorphological Techniques. George Allen & Unwin, London, pp. 31-37.

Exner, C., 1949. Beitrag zur Kenntnis der jungen Hebung der östlichen hohen Tauern. Mitteilungen der Österreichischen Geographischen Gesellschaft, 91(10-12): 186-196.

Fairhurst, C., 2003. Stress estimation in rock: a brief history and review. International Journal of Rock Mechanics and Mining Sciences, 40(7-8): 957-973.

Fasching, F., Wurzwaller, S. and Pischinger, G., 2008. The Lavanttal fault - tunnelling through a major fault zone of the Eastern Alps - PANGEO 2008: Kurzfassungen und Abstracts. Journal of Alpine Geology, 49: 24.

Faulkner, D.R., Mitchell, T.M., Rutter, E.H. and Cembrano, J., 2008. On the structure and mechanical properties of large strike-slip faults. In: C.A.J. Wibberley, W. Kurz, J. Imber, R.E. Holdsworth and C. Collettini (Editors), The Internal Structure of Fault Zones: Implications for Mechanical and Fluid-Flow Properties. Geological Society Special Publications. Geological Society, London, pp. 139-150.

Florinsky, I.V., 1996. Quantitative topographic method of fault morphology recognition. Geomorphology, 16(2): 103-119.

Florinsky, I.V., 1998. Combined analysis of digital terrain models and remotely sensed data in landscape investigations. Progress in Physical Geography, 22(1): 33-60.

Florinsky, I.V., 2000. Relationships between topographically expressed zones of flow accumulation and sites of fault intersection: analysis by means of digital terrain modelling. Environmental Modelling and Software, 15(1): 87-100.

Flügel, H., 1952. Über die Zusammenhänge zwischen Klüftung und Talnetz im Grazer Bergland. Geologie und Bauwesen, 18: 195-200.

Flügel, H.W. and Neubauer, F., 1984. Steiermark - Erläuterungen zur Geologischen Karte der Steiermark 1:200.000. Geologie der Österreichischen Bundesländer in kurzgefassten Einzeldarstellungen. Geologische Bundesanstalt, Wien, 127 pp.

Fodor, L. et al., 2008. Miocene emplacement and rapid cooling of the Pohorje pluton at the Alpine-Pannonian-Dinaridic junction, Slovenia. Swiss Journal of Geosciences, 101(0): 255-271.

Fodor, L. and POSIHU Research Group, 2003. Miocene exhumation of the Pohorje-Kozjak Mts., Slovenia (Alpine-Pannonian transition). Geophysical Research Abstracts, 5: 11814.

Frank, W., 1987. Evolution of the Austroalpine elements in the Cretaceous. In: H.W. Flügel and P. Faupl (Editors), Geodynamics of the Eastern Alps. Deuticke, pp. 379–406.

Frank, W. et al., 1983. Die Entwicklungsgeschichte von Stub- und Koralpenkristallin und die Beziehung zum Grazer Paläozoikum., Die frühalpine Entwicklungsgeschichte der Ostalpen. Jahresbericht 1982 Hochschulschwerpunkt S15, Graz, pp. 263-293.

Frank, W., Kralik, M., Scharbert, S. and Thöni, M., 1987. Geochronological data from the Eastern Alps. In: H.W. Flügel and P. Faupl (Editors), Geodynamics of the Eastern Alps. Deuticke, Vienna, pp. 272-281.

Friebe, J.G., 1990. Neotektonik an der mittelsteirischen Schwelle (Österreich): Die "Steirische Phase". In: K.G. Institut für Geologie und Paläontologie (Editor), TSK III - 3. Symposium für tektonik,

Strukturgeologie, Kristallingeologie im deutschsprachigen Raum. Institut für Geologie und Paläontologie, KFU Graz, Graz, pp. 73-76.
Friebe, J.G., 1991. Neotektonik an der Mittelsteirischen Schwelle (Oesterreich): Die "Steirische Phase". Zentralblatt für Mineralogie, Geologie und Paläontologie . Teil 1: Geologie und Paläontologie, 1: 41-54.
Friedman, M., Logan, J.M. and Shimamoto, T., 1998. Cataclastic fabrics in experimental shear zones. In: A.W. Snoke, J. Tullis and V.R. Todd (Editors), Fault-related rocks: a photographic atlas. Princeton University Press, Princeton, pp. 70-71.
Frisch, W., Dunkl, I. and Kuhlemann, J., 2000a. Post-collisional orogen-parallel large-scale extension in the Eastern Alps. Tectonophysics, 327(3-4): 239-265.
Frisch, W., Kuhlemann, J., Dunkl, I. and Brugel, A., 1998. Palinspastic reconstruction and topographic evolution of the Eastern Alps during late Tertiary tectonic extrusion. Tectonophysics, 297(1-4): 1-15.
Frisch, W., Kuhlemann, J., Dunkl, I. and Székely, B., 2001. The Dachstein paleosurface and the Augenstein Formation in the Northern Calcareous Alps - a mosaic stone in the geomorphological evolution of the Eastern Alps. International Journal of Earth Sciences, 90(3): 500-518.
Frisch, W., Székely, B., Kuhlemann, J. and Dunkl, I., 2000b. Geomorphological evolution of the Eastern Alps in response to Miocene tectonics. Zeitschrift für Geomorphologie Neue Folge, 44(1): 103-138.
Froitzheim, N., Plasienka, D. and Schuster, R., 2008. Alpine tectonics of the Alps and Western Carpathians. In: T. McCann (Editor), The Geology of Central Europe. The Geological Society, London, pp. 1141-1232.
Fürlinger, W., 1978. Geologische Vorerkundung und baugeologische Erfahrungen - ein kritischer Vergleich am Beispiel des Mitterbergtunnels. Rock Mechanics, Suppl. 7: 3-11.
Gapais, D., Cobbold, P.R., Bourgeois, O., Rouby, D. and de Urreiztieta, M., 2000. Tectonic significance of fault-slip data. Journal of Structural Geology, 22(7): 881-888.
Genser, J. and Neubauer, F., 1989. Low angle normal faults at the Eastern margin of the Tauern Window (Eastern Alps). Mitteilungen der Österreichischen Geologischen Gesellschaft, 81: 233–243.
Germanoski, D. and Ritter, D.F., 1988. Tributary response to local base level lowering below a dam. Regulated Rivers: Research & Management, 2(1): 11-24.
Ghisetti, F., 2000. Slip partitioning and deformation cycles close to major faults in southern California: Evidence from small-scale faults. Tectonics, 19(1): 25-43.
Goldsworthy, M. and Jackson, J., 2001. Migration of activity within normal fault systems: examples from the Quaternary of mainland Greece. Journal of Structural Geology, 23(2-3): 489-506.
Gollner, H., Schirnik, D. and Tschelaut, W., 1987. The Problem of the Southalpine clasts in the "Mittelsteirische Gosau". In: H.W. Flügel and P. Faupl (Editors), Geodynamics of the Eastern Alps. Deuticke, Wien, pp. 156-163.
Goricki, A. and Harer, G., 2004. Spannungsmessung für das Projekt Koralmtunnel - Methoden, Ergebnisse, Diskussion. In: R. Poisel and E. Tentschert (Editors), 2nd Coll. Rockmech. - Theory and Practice. Mitteilungen für Ingenieurgeologie und Geomechanik Band 6, pp. 55-65.
Gosch, G., 2007. Strukturelle und morphologische Charakterisierung von Felsöfen auf der Koralpe. Masterthesis Thesis, Technische Universität Graz, Graz, 73 pp.
Götzinger, G., 1913. Neue Funde von Augensteinen auf den östlichen Kalkhochalpenplateaus. Verhandlungen der geologischen Reichsanstalt: 61-65.
Graf, F., Kohl, T., Mégel, T., Rybach, L. and Fuchs, R., 2001. Hydraulic-Geothermal Modelling of Koralm Tunnel into Rock Mass Classification. Felsbau, 19(6): 54-59.
Grasemann, B., Martel, S. and Passchier, C., 2005. Reverse and normal drag along a fault. Journal of Structural Geology, 27(6): 999-1010.
Grasemann, B., Stuwe, K. and Vannay, J.-C., 2003. Sense and non-sense of shear in flanking structures. Journal of Structural Geology, 25(1): 19-34.
Gravelius, H., 1914. Flußkunde. Grundriß der gesamten Gewässerkunde, erster Band. Göschen, Berlin und Leipzig, 176 pp.
Gross, M. et al., 2007. The Neogene of the Styrian Basin – Guide to Excursions. Joannea - Geologie und Paläontologie, 9: 117-193.
Grünthal, G. and GSHAP Region 3 Working Group, 1999. Seismic hazard assessment for Central, North and Northwest Europe: GSHAP Region 3. Annali di Geofisica, 42(6): 999-1011.

Gülcan, S., 2005. Lineament analysis from satellite images north-west of Ankara. master thesis Thesis, Middle East Technical University, Ankara, 76 pp.
Gupta, R.P., 2003. Remote Sensing Geology. Springer, Berlin, 655 pp.
Habler, G. and Thöni, M., 2001. Preservation of Permo-Triassic low-pressure assemblages in the Cretaceous high-pressure metamorphic Saualpe crystalline basement (Eastern Alps, Austria). Journal of Metamorphic Geology, 19(6): 679–697.
Hack, J.T., 1973. Stream-profile analysis and stream-gradient index. Journal of Research of the U. S. Geological Survey, 1(4): 421-429.
Haimson, B.C., 1993. The hydraulic fracturing method of stress measurement: theory and practice. In: J.A. Hudson (Editor), Comprehensive Rock Engineering. Pergamon Press, Oxford, pp. 395-412.
Haimson, B.C. and Cornet, F.H., 2003. ISRM Suggested Methods for rock stress estimation--Part 3: hydraulic fracturing (HF) and/or hydraulic testing of pre-existing fractures (HTPF). International Journal of Rock Mechanics and Mining Sciences, 40(7-8): 1011-1020.
Hamblin, W.E. and Christiansen, E.H., 1995. Earth's Dynamic Systems. Prentice-Hall, Englewood Cliffs, 710 pp.
Hare, P.W. and Gardner, T.W., 1984. Geomorphic indicators of vertical neotectonism along converging plate margins, Nicoya Peninsula, Costa Rica. In: M. Morisawa and J.T. Hack (Editors), 15th Annual Binghamton Geomorphology Symposium. Allen and Unwin, pp. 90–104.
Harer, G. and Riedmüller, G., 1999. Assessment of Ground Condition for the Koralm Tunnel during the Early Stage of Planning. Felsbau, 17(5): 367-380.
Harlin, J.M., 1978. Statistical moments of the hypsometric curve and its density function. Mathematical Geology, 10(1): 59-72.
Haslinger, C., Krauss, S. and Stangl, G., 2007. The Intra-Plate Velocities of GPS Permanent Stations of the Eastern Alps. Vermessung & Geoinformation, 2/2007: 66-72.
Heidbach, O. et al., 2009. The World Stress Map based on the database release 2008. Commission for the Geological Map of the World, Paris.
Heitzmann, P., 1985. Kakirite, Kataklasite, Mylonite - Zur Nomenklatur der Metamorphite mit Verformungsgefügen. Eclogae geol. Helv., 78(2): 273-286.
Hejl, E., 1997. 'Cold spots' during the Cenozoic evolution of the Eastern Alps: thermochronological interpretation of apatite fission-track data. Tectonophysics, 272(2-4): 159-173.
Hejl, E., 1998. Über die känozoische Abkühlung und Denudation der Zentralalpen östlich der Hohen Tauern - Apatit-Spaltspuranalyse. Mitteilungen der Österreichischen Geologischen Gesellschaft, 89 (1996): 179-199.
Hergarten, S., Wagner, T. and Stüwe, K., 2010. Age and Prematurity of the Alps Derived from Topography. Earth and Planetary Science Letters, 297: 453-460.
Heritsch, H., 1980a. Einführung zu Problemen der Petrologie der Koralpe. Mitteilungen der Abteilung Geologie, Paläontologie und Bergbau am Landesmuseum Joanneum, 41: 9-44.
Heritsch, H., 1980b. Exkursion: Petrologie des Kristallins der Koralpe. Mitteilungen der Abteilung Geologie, Paläontologie und Bergbau am Landesmuseum Joanneum, 41: 87-92.
Herzog, U. and Kahler, F., 1978. Geologische Ergebnisse geophysikalischer Messungen im Kohlentertiär südlich von Wolfsberg im Lavanttal (Kärnten). Carinthia II, 168/88: 47-54.
Hobbs, W.H., 1904. Lineaments of the Atlantic border region. Geological Society of America Bulletin, 15: 483–506.
Hobbs, W.H., 1912. Earth features and their meaning - an introduction to geology for the student and the general reader. Macmillan, 506 pp.
Hoek, E., Marinos, P. and M., B., 1998. Applicability of the geological strength index (GSI) classification for very weak and sheared rock masses. The case of the Athens Schist Formation. Bulletin of Engineering Geology and the Environment, 57(2): 151-160.
Höfer, H., 1894. Die geologischen Verhältnisse der St. Pauler Berge in Kärnten. Sitzungsberichte der Wiener Akademie der Wissenschaften, 103: 467-487.
Homann, O., 1962. Das kristalline Gebirge im Raume Pack - Ligist. Mineralogisches Mitteilungsblatt des Landesmuseums Joanneum Graz, 2/1962: 21-62.
Hoogerduijn Strating, E.H. and Vissers, R.L.M., 1998. Microstructures in natural serpentinite gouges. In: A.W. Snoke, J. Tullis and V.R. Todd (Editors), Fault-related rocks: a photographic atlas. Princeton University Press, Princeton.
Horton, R.E., 1932. Drainage basin characteristics. Transactions, 13: 350-361.

Horton, R.E., 1945. Erosional development of streams and their drainage basins, hydrophysical approach to quantitative morphology. Geol Soc Am Bull, 56(3): 275-370.
Howard, A.D., 1967. Drainage analysis in geologic interpretation: A summation. The American Association of Petroleum Geologists Bulletin, 51(11): 2246-2259.
Howarth, D.F. and Rowlands, J.C., 1986. Development of an index to quantify rock texture for qualitative assessment of intact rock properties. Geotechnical Testing Journal, 9: 169-179.
Huang, M.-L., 2006. EZ Profiler 9.1. http://arcscripts.esri.com/details.asp?dbid=13688.
Hurtrez, J.E., Sol, C. and Lucazeau, F., 1999. Effect of drainage area on hypsometry from an analysis of small-scale drainage basins in the Siwalik Hills (Central Nepal). Earth Surface Processes and Landforms, 24(9): 799-808.
Jarvis, R.S., 1981. Specific Geomorphometry. In: K.S. Richards (Editor), Geomorphological Techniques. Allen & Unwin, London, pp. 42-46.
Jelinek, J., 2006. Application of Newly Developed ArcGIS Software Extensions for Localization of Faults and Natural Zones of Methane's Escape by Morphotectonic Analysis (Moravosilesian Region). GeoLines, 20: 60 - 63.
Jenson, S.K. and Domingue, J.O., 1988. Extracting Topographic Structure from Digital Elevation Data for Geographic Information System Analysis. PHOTOGRAMMETRIC ENGINEERING AND REMOTE SENSING, 54(11): 1593-1600.
Jordan, G., 2003. Morphometric analysis and tectonic interpretation of digital terrain data: a case study. Earth Surface Processes and Landforms, 28(8): 807-822.
Jordan, G., Meijninger, B.M.L., Hinsbergen, D.J.J.v., Meulenkamp, J.E. and Dijk, P.M.v., 2005. Extraction of morphotectonic features from DEMs: Development and applications for study areas in Hungary and NW Greece. International Journal of Applied Earth Observation and Geoinformation, 7(3): 163-182.
Keller, E.A., 1986. Investigation of active tectonics: use of surficial earth processes, Active tectonics: Impact on Society. Studies in Geophysics. National Academy Press, Washington, D.C., pp. 136-147.
Keller, E.A. and Pinter, N., 2002. Active Tectonics: Earthquakes, Uplift, and Landscape. Prentice Hall, Upper Saddle River, NJ, 362 pp.
Kieslinger, A., 1928a. Die Lavanttaler Störungszone. Jahrbuch der Geologischen Bundesanstalt, 78: 499-528.
Kieslinger, A., 1928b. Geologie und Petrographie der Koralpe, 9: der Bau der Koralpe und seine Beziehungen zu den Nachbargebieten. Sitzungsberichte Akademie der Wissenschaften Mathematisch-Naturwissenschaftliche Klasse Abteilung 1, 137(7): 491-532.
Kim, G.-B., Lee, J.-Y. and Lee, K.-K., 2004. Construction of lineament maps related to groundwater occurrence with ArcView and Avenue(TM) scripts. Computers & Geosciences, 30(9-10): 1117-1126.
Kirby, E., Whipple, K., Tang, W. and Chen, Z., 2003. Distribution of active rock uplift along the eastern margin of the Tibetan Plateau: Inferences from bedrock channel longitudinal profiles. Journal of Geophysical Research, 108(B4): 2217.
Kleinschmidt, G. and Ritter, U., 1976. Geologisch-petrographischer Aufbau des Koralpenkristallins südlich von Soboth/Steiermark-Kärnten (Raum Hühnerkogel—Laaken). Carinthia II, 166/86: 57-91.
Kleinschmidt, G., Seeger, M. and Thiedig, F., 1989. Geologische Karte der Republik Österreich 1:50.000 - 205 Sankt Paul im Lavanttal. Geologische Bundesanstalt, Wien.
Klima, K., Riedmüller, G. and Stattegger, K., 1988. Statistical Analysis of Clay Mineral Assemblages in Fault Gouges. Clays and Clay Minerals, 36(No. 3): 277-283.
Koch, G., 1990. Tonmineralverteilungen in hydrothermal stark beeinflussten Scherzonen der suedlichen Koralpe. Diplomarbeit Thesis, Karl-Franzens Universität Graz, Graz, 47 pp.
Koike, K., Nagano, S. and Ohmi, M., 1995. Lineament analysis of satellite images using a Segment Tracing Algorithm (STA). Computers & Geosciences, 21(9): 1091-1104.
Kollmann, K., 1964. Jungtertiär im Steirischen Becken. Mitteilungen der Österreichischen Geologischen Gesellschaft, 57(2): 479-632.
Krenn, K., Fritz, H., Mogessie, A. and Schaflechner, J., 2008. Late Cretaceous exhumation history of an extensional extruding wedge (Graz Paleozoic Nappe Complex, Austria). International Journal of Earth Sciences, 97(6): 1331-1352.
Krohe, A., 1987. Kinematics of Cretaceous nappe tectonics in the Austroalpine basement of the Koralpe region (eastern Austria). Tectonophysics, 136(3-4): 171-196.

Kröll, 1988. Steirisches Becken-Südburgenländische Schwelle - Reliefkarte des prätertiären Untergrundes. Geologische Bundesanstalt, Wien.

Kuhlemann, J., Frisch, W., Székely, B., Dunkl, I. and Kázmér, M., 2002. Post-collisional sediment budget history of the Alps: tectonic versus climatic control. International Journal of Earth Sciences, 91(5): 818-837.

Kühni, A. and Pfiffner, O.A., 2001. The relief of the Swiss Alps and adjacent areas and its relation to lithology and structure: topographic analysis from a 250-m DEM. Geomorphology, 41(4): 285-307.

Kurz, W. and Fritz, H., 2003. Tectonometamorphic Evolution of the Austroalpine Nappe Complex in the Central Eastern Alps—Consequences for the Eo-Alpine Evolution of the Eastern Alps. International Geology Review, 45(12): 1100-1127.

Kurz, W., Fritz, H., Tenczer, V. and Unzog, W., 2002. Tectonometamorphic evolution of the Koralm Complex (Eastern Alps): constraints from microstructures and textures of the 'Plattengneis' shear zone. Journal of Structural Geology, 24(12): 1957-1970.

Kurz, W., Pischinger, G. and Wölfler, A., 2009. Final exhumation and uplift of the Koralm basement (Eastern Alps) and its relation to the evolution of the Styrian Basin, Tectonics and Sedimentation, Bonn.

Kurz, W., Wölfler, A., Rabitsch, R. and Genser, J., 2011. Polyphase movement on the Lavanttal Fault Zone (Eastern Alps): reconciling the evidence from different geochronological indicators. Swiss Journal of Geosciences, 104(2): 323-343.

Lague, D., Davy, P. and Crave, A., 2000. Estimating uplift rate and erodibility from the area-slope relationship: Examples from Brittany (France) and numerical modelling. Physics and Chemistry of the Earth, Part A: Solid Earth and Geodesy, 25(6â€“7): 543-548.

Larue, J.-P., 2008. Effects of tectonics and lithology on long profiles of 16 rivers of the southern Central Massif border between the Aude and the Orb (France). Geomorphology, 93(3-4): 343-367.

Laws, S., 2001. Structural, geomechanical and petrophysical properties of shear zones in the Eastern Aar massif, Switzerland. doctoral thesis Thesis, Swiss Federal Institute of Technology, Zürich, 121 pp.

Leber, D., Peresson, H. and Häusler, H., 1997. Fault Patterns Derived from RS-, DEM-, 3D-Seismic- and Microtectonic Data:The Vienna Basin (Austria).

Legrain, N., Stüwe, K., Dixon, J.L., Von Blanckenburg, F. and Kubik, P., 2011. Large scale, small amplitude, post-Miocene surface uplift in the non-glaciated Eastern Alps: river profiles analysis and cosmogenic-derived 10Be denudation rates. Geophysical Research Abstracts, 13(EGU2011-10708, EGU General Assembly 2011): 1.

Lifton, N.A. and Chase, C.G., 1992. Tectonic, climatic and lithologic influences on landscape fractal dimension and hypsometry: implications for landscape evolution in the San Gabriel Mountains, California. Geomorphology, 5(1-2): 77-114.

Lindquist, E.S., 1994a. The strength and deformation properties of melange. PhD dissertation Thesis, University of California, Berkley.

Lindquist, E.S. and Goodman, R.E., 1994. Strength and deformation properties of a physical model melange. In: P.P. Nelson and S.E. Laubach (Editors), PROCEEDINGS OF THE 1ST NORTH AMERICAN ROCK MECHANICS SYMPOSIUM. Balkema, Austin/Texas, pp. 843-850.

Lippolt, H.J., Baranyi, I. and Todt, W., 1975. Das Kalium-Argon Alter des Basalts vom Lavant-Tal in Kärnten. Der Aufschluss, 26: 238-242.

Lister, G.S. and Snoke, A.W., 1984. S-C Mylonites. Journal of Structural Geology, 6(6): 617-638.

Litscher, H., 1978. Ein Beitrag zur Geologie der südlichen Koralpe (geotechnische Untersuchungen am Sperrenstandort Krumbach). Carinthia II, 168/88: 71-74.

Liu-Zeng, J., Klinger, Y., Sieh, K., Rubin, C. and Seitz, G., 2006. Serial ruptures of the San Andreas fault, Carrizo Plain, California, revealed by three-dimensional excavations. Journal of Geophysical Research, 111(B02306): doi:10.1029/2004JB003601.

Logan, J.M., Friedman, M., Higgs, N., Dengo, C. and Shimamoto, T., 1979. Experimental studies of simulated gouge and their application to studies of natural zones. US Geological Survey Open-file Report 791239, US Geological Survey.

Lopes Cardozo, G.G.O. and Behrmann, J.H., 2006. Kinematic analysis of the Upper Rhine Graben boundary fault system. Journal of Structural Geology, 28(6): 1028-1039.

Löw, S., Frei, B., Laws, S. and Lützenkirchen, V., 1999. Zur Hydrogeologie von Störzonen im östlichen Aar- und Gotthard-Massiv. In: S. Löw and R. Wyss (Editors), Vorerkundung und Prognose der Basistunnels am Gotthard und am Lötschberg. A.A.Balkema, Zürich, pp. 185-194.

Luo, W., 1998. Hypsometric analysis with a geographic information system. Computers & Geosciences, 24(8): 815-821.

Luo, W., 2000. Quantifying Groundwater Sapping Processes with a Hypsometric Analysis Technique. Journal of Geophysical Research, 105(1): 1685-1694.

Luo, W., 2002. Hypsometric Analysis of Margaritifer Sinus and Origin of Valley Networks. Journal of Geophysical Research - Planets, 107(E10).

Lützenkirchen, V., 2003. Structural geology and hydrogeology of brittle fault zones in the central and eastern Gotthard massif, Switzerland, Swiss Federal Institute of Technology, Zürich, 264 pp.

Mähr, L., 1990. Mikrogefügeuntersuchungen an kataklastischen Gesteinen der südlichen Koralpe. Doctoral Thesis Thesis, Graz University of Technology, Graz, 70 pp.

Mandelbrot, B.B., 1967. How long is the coast of Britain? Statistical self-similarity and fractional dimension. Science, 156: 636-638.

Mandl, G., 2000. Faulting in brittle rocks - an introduction to the mechanics of tectonic faults. Springer, Berlin, 434 pp.

Mark, R., 1992. Multidirectional, oblique-weighted, shaded-relief image of the Island of Hawaii. OF-92-422.

Marrett, R. and Allmendinger, R.W., 1990. Kinematic analysis of fault-slip data. Journal of Structural Geology, 12(8): 973-986.

Márton, E. et al., 2002. Miocene to Quaternary deformation in NE Slovenia: complex paleomagnetic and structural study. Journal of Geodynamics, 34(5): 627-651.

Márton, E., Kuhlemann, J., Frisch, W. and Dunkl, I., 2000. Miocene rotations in the Eastern Alps -- palaeomagnetic results from intramontane basin sediments. Tectonophysics, 323(3-4): 163-182.

Massironi, M., 1999. Fault network reconstruction by satellite remote-sensing investigation, 4th Workshop on Alpine Geological Studies. Tübinger Geowissenschaftliche Arbeiten Series A, Tübingen/Germany, pp. 19 - 23.

Mayer, L., 1986. Tectonic Geomorphology of Escarpments and Mountain Fronts. In: M. Commission on Physical Sciences, and Applications (Editor), Active tectonics: Impact on Society. Studies in Geophysics. National Academy Press, Washington, D.C., pp. 125-135.

Medley, E.W., 1994. The Engineering Characterization of Melanges and Similar Block-in-Matrix Rocks (Bimrocks). Ph.D. dissertation Thesis, University of California, Berkeley, 175 pp.

Meschede, M., 1994. Methoden der Strukturgeologie. Ferdinand Enke Verlag Stuttgart, 169 pp.

Metz, K., 1976. Bruchsysteme und Westbewegungen in den östlichen Zentralalpen. Mitteilungen der Österreichischen Geologischen Gesellschaft, 69: 27-47.

Miller, V.C., 1953. A quantitative geomorphic study of drainage basin characteristics in the Clinch Mountain area, Virginia and Tenessee. Tech. Report No. 3., Office of Naval Research, Geography Branch.

Mioc, P., 1977. Geologic Structure of the Drava Valley between Dravograd and Selnica. Geologija, 20: 193-230.

Mitchell, R.S., 1985. Dictionary of rocks. Van Nostrand Reinhold Company Inc., New York, 228 pp.

Molnar, P. and England, P., 1990. Late Cenozoic uplift of mountain ranges and global climate change: chicken or egg? Nature, 346(6279): 29-34.

Moore, I.D., Grayson, R.B. and Ladson, A.R., 1991. Digital terrain modelling: A review of hydrological, geomorphological, and biological applications. Hydrological Processes, 5(1): 3-30.

Morawetz, S., 1952. Periglaziale Erscheinungen auf der Koralpe (steirisches Randgebirge). Mitteilungen der Geographischen Gesellschaft in Wien, 94(5-8): 252-257.

Morawetz, S., 1964. Zur Frage der Talentwicklung auf der Ostabdachung der Koralpe im Steirischen Randgebirge. Mitteilungen der Österreichischen Geographischen Gesellschaft, 106: 204-208.

Morawetz, S., 1984. Abdachung, Stockwerkbau, Kamm- und Talentwicklung auf dem Ostabfall der Koralpe im Steirischen Randgebirge, Wiener Geographische Schriften, pp. 13-26.

Morisawa, M., 1958. Measurement of Drainage-Basin Outline Form. The Journal of Geology, 66(5): 587-591.

Mosley, M.P., 1984. Response of the Ohau River and delta to lake level lowering. Earth Surface Processes and Landforms, 9(2): 181-187.

Mueller, J.E., 1968. An introduction to the hydraulic and topographic sinuosity indexes. Annals of the Association of American Geographers, 58(2): 371-385.
Nebert, K., 1983. Zyklische Gliederung der Eibiswalder Schichten (Südweststeiermark). Jahrbuch der Geologischen Bundesanstalt, 126(2): 259-285.
Nebert, K., 1989. Das Neogen zwischen Sulm und Lassnitz (Suedweststeiermark). Jahrbuch der Geologischen Bundesanstalt Wien, 132(4): 727-743.
Neubauer, F., 1991. Kinematic indicators in the Koralm and Saualm eclogites (Eastern Alps). Zentralblatt für Mineralogie, Geologie und Paläontologie, Teil I: Allgemeine, Angewandte, Regionale und Historische Geologie, 1991(1): 139-155.
Neubauer, F., Dallmeyer, R.D., Dunkl, I. and Schirnik, D., 1995. Late Cretaceous exhumation of the metamorphic Gleinalm dome, Eastern Alps: kinematics, cooling history and sedimentary response in a sinistral wrench corridor. Tectonophysics, 242(1-2): 79-98.
Neubauer, F. et al., 2000. Structural evolution within an extruding block: model and application to the Alpine-Pannonian system. In: F.K. Lehner and J.L. Urai (Editors), Aspects of Tectonic Faulting: Festschrift in Honour of Georg Mandl. Springer, pp. 141-1 53.
Neubauer, F. and Genser, J., 1990. Architektur und Kinematik der östlichen Zentralalpen - eine Übersicht. Mitteilungen des Naturwissenschaftlichen Vereins für Steiermark, 120: 203-219.
Neubauer, F. and Höck, V., 2000. Aspects of Geology in Austria and Adjoining Areas: Introduction. Mitteilungen der Österreichischen Geologischen Gesellschaft, 92 (1999): 7-14.
Neumüller, E., Pischinger, G. and Rappold, M., 2003. Overbreak remedy at the Herzogberg. Tunnels and Tunnelling International, 35(1): 20-23.
Nieto-Samaniego, A.F. and Alaniz-Alvarez, S.A., 1997. Origin and tectonic interpretation of multiple fault patterns. Tectonophysics, 270(3-4): 197-206.
Nievoll, J., 1985. Die bruchhafte Tektonik entlang der Trofaiachlinie (Östliche Zentralalpen, Österreich). Jahrbuch der Geologischen Bundesanstalt, 127(4): 643-671.
Nowy, W. and Bilak, A., 2003. A2 Südautobahn Abschnitt Twimberg - Wolfsberg, Gräbern Tunnel Weströhre - Baugeologische Dokumentation und Beratung - Schlußbericht, Österreichische Autobahnen und Schnellstraßen GesmbH, Wien/Klosterneuburg.
Oberlander, T.M., 1984. Origin of drainage structures transverse to structures in orogens. In: M. Morisawa and J.T. Hack (Editors), 15th Annual Binghamton Geomorphology Symposium. Allen and Unwin, pp. 156-182.
Ohmori, H., 1993. Changes in the hypsometric curve through mountain building resulting from concurrent tectonics and denudation. Geomorphology, 8(4): 263-277.
O'Leary, D.W., Friedman, J.D. and Pohn, H.A., 1976. Lineament, linear, lineation: Some proposed new standards for old terms. Geological Society of America Bulletin, 87(10): 1463–1469.
Orife, T. and Lisle, R.J., 2006. Assessing the statistical significance of palaeostress estimates: simulations using random fault-slips. Journal of Structural Geology, 28(6): 952-956.
Pacher, F. and Riepl, K., 1978. Über die chemische Zusammensetzung von Gneisen und Glimmerschiefern der Koralpe, Steiermark. Mitteilungen des Naturwissenschaftlichen Vereins für Steiermark, 108: 45-54.
Passchier, C.W., 2001. Flanking structures. Journal of Structural Geology, 23(6-7): 951-962.
Passchier, C.W. and Trouw, R.A.J., 1996. Microtectonics. Springer Verlag, Berlin-Heidelberg, 289 pp.
Peacock, D.C.P., Knipe, R.J. and Sanderson, D.J., 2000. Glossary of normal faults. Journal of Structural Geology, 22(3): 291-305.
Penck, W., 1924. Die morphologische Analyse: Ein Kapitel der physikalischen Geologie. Engelhorn, Stuttgart, 283 pp.
Peresson, H. and Decker, K., 1997. Far-field effects of Late Miocene subduction in the Eastern Carpathians: E-W compression and inversion of structures in the Alpine-Carpathian-Pannonian region. Tectonics, 16(1): 38-56.
Peresson, H. and Decker, K., 1998. Tektonische Auswertungen von Digitalen Fernerkundungs- und Höhendaten - Trassenkorridor Koralmtunnel, Geozentrum - Institut für Geologie Universität Wien, Vienna.
Petit, J.P., 1987. Criteria for the sense of movement on fault surfaces in brittle rocks. Journal of Structural Geology, 9(5-6): 597-608.
Peucker, T.K. and Douglas, D.H., 1975. Detection of Surface-Specific Points by Local Parallel Processing of Discrete Terrain Elevation Data. Computer Graphics And Image Processing, 4: 375-387.

Phillips, J.D. et al., 2010. Origin and interpretation of knickpoints in the Big South Fork River basin, Kentucky-Tennessee. Geomorphology, 114(3): 188-198.
Pike, R.J. and Wilson, S.E., 1971. Elevation-relief ratio, hypsometric integral, and geomorphic area-altitude analysis. Geological Society of America Bulletin, 82(4): 1079-1083.
Piller, W.E., Harzhauser, M. and Mandic, O., 2007. Miocene Central Paratethys stratigraphy – current status and future directions. Stratigraphy, 4(2/3): 151-168.
Pischinger, G. et al., 2005. Brittle faulting in the Koralm region - results from the site investigation for the Koralmtunnel. In: S. Löw (Editor), Symposium Geologie Alptransit - Programm Abstracts, Zürich, pp. 81-82.
Pischinger, G., Brosch, F.-J., Kurz, W. and Rantitsch, G., 2006. Normal faulting in a rigid basin boundary block – field evidence from the Koralm Complex (Eastern Alps). PANGEO Austria 2006. Innsbruck University Press Conference Series, Innsbruck, pp. 250–251.
Pischinger, G. et al., 2008. Fault slip analysis in the Koralm Massif (Eastern Alps) and consequences for the final uplift of “cold spots” in Miocene times. Swiss Journal of Geosciences, doi: 10.1007/s00015-008-1277-x: 235-254.
Poljak, M., Zivcic, M. and Zupancic, P., 2000. The Seismotectonic Characteristics of Slovenia. Pure and Applied Geophysics, 157(1-2): 37-55.
Pollard, D.D. and Aydin, A., 1988. Progress in understanding jointing over the past century. Geological Society of America Bulletin, 100: 1181-1204.
Pollard, D.D., Saltzer, S.D. and Rubin, A.M., 1993. Stress inversion methods: are they based on faulty assumptions? Journal of Structural Geology, 15(8): 1045-1054.
Popotnig, A., 2009. Kinematik und tektonische Geomorphologie der Lavanttal-Störung. Masterthesis Thesis, Universität Wien, Vienna, 92 pp.
Popotnig, A., Decker, K. and Grasemann, B., 2007. Active kinematics and tectonic geomorphology of the Lavanttal Fault. Geophysical Research Abstracts, 9(A-03270).
Powell, J.W., 1875. Exploration of the Colorado River of the West and its tributaries : Explored in 1869, 1870, 1871, and 1872, under the direction of the secretary of the Smithsonian institution. Smithsonian Institution, Washington D.C., 462 pp.
Puch, T., 1995. Spaltspurendatierungen an Apatit und Zirkon als Tracer tektonischer Prozesse im Bereich Koralpe-Saualpe-Krappfeld(Kärnten/Österreich), Ostalpen. Master thesis Thesis, Universität Graz, 124 pp.
Putz, M., Stüwe, K., Jessell, M. and Calcagno, P., 2006. Three-dimensional model and late stage warping of the Plattengneis Shear Zone in the Eastern Alps. Tectonophysics, 412(1-2): 87-103.
Rabitsch, R., Wölfler, A. and Kurz, W., 2007. Fission track dating in fault zones: an example from the Eastern Alps. Geophysical Research Abstracts, 9.
Radoane, M., Radoane, N. and Dumitriu, D., 2003. Geomorphological evolution of longitudinal river profiles in the Carpathians. Geomorphology, 50(4): 293-306.
Raghavan, V., Wadatsumi, K. and Masumoto, S., 1993. Automatic extraction of lineament information from satellite images using digital elevation data. Natural Resources Research, 2(2): 148-155.
Ramsay, J.G. and Huber, M.I., 1987. The Techniques of Modern Structural Geology. Volume 2: Folds and fractures, 2. Academic Press, London, 309 - 700 pp.
Rantitsch, G. and Mali, H., 2006. The geological structure of the Late Cretaceous Graden normal fault (Eastern Alps). Mitteilungen des Naturwissenschaftlichen Vereins für Steiermark, 135: 25-31.
Rantitsch, G., Pischinger, G. and Kurz, W., 2009. Stream profile analysis of the Koralm Range (Eastern Alps). Swiss Journal of Geosciences, 102(1): 31-41.
Rantitsch, G., Sachsenhofer, R.F., Hasenhüttl, C., Russegger, B. and Rainer, T., 2005. Thermal evolution of an extensional detachment as constrained by organic metamorphic data and thermal modeling: Graz Paleozoic Nappe Complex (Eastern Alps). Tectonophysics, 411: 57-72.
Ratschbacher, L., Frisch, W., Linzer, H.-G. and Merle, O., 1991b. Lateral extrusion in the Eastern Alps, part 2: structural analysis. Tectonics, 10(2): 257-271.
Ratschbacher, L., Frisch, W., Neubauer, F., Schmid, S.M. and Neugebauer, J., 1989. Extension in compressional orogenic belts: The eastern Alps. Geology, 17(5): 404-407.
Ratschbacher, L., Merle, O., Davy, P. and Cobbold, P., 1991a. Lateral Extrusion in the Eastern Alps, Part 1: Boundary Conditions and Experiments scaled for Gravity. Tectonics, 10(2): 245-256.
Reinecker, J., 2000. Stress and Deformation: Miocene to present-day tectonics in the eastern alps. Tübinger Geowissenschaftliche Arbeiten, A(55): 128.

Reinecker, J. and Lenhardt, W.A., 1999. Present-day stress field and deformation in eastern Austria. International Journal of Earth Sciences, 88(3): 532-550.
Reinecker, J., Tingay, M. and Müller, B., 2003. Borehole breakout analysis from four arm caliper logs. World Stress Map Project.
Reischenbacher, D., 2008. Beckenentwicklung und Bildung von Kohleflözen und organisch-reichen Sedimenten am Beispiel des neogenen Lavanttaler Beckens. PhD Thesis, Montanuniversität Leoben, Leoben, 295 pp.
Reischenbacher, D. et al., 2007. Early Badenian paleoenvironment in the Lavanttal Basin (Mühldorf Formation; Austria): Evidence from geochemistry and paleontology. Austrian Journal of Earth Sciences, 100(202-229).
Reischenbacher, D. and Sachsenhofer, R., 2012. Basin formation during the post-collisional evolution of the Eastern Alps: the example of the Lavanttal Basin, International Journal of Earth Sciences. Springer Berlin / Heidelberg, pp. 1-27.
Reischenbacher, D. and Sachsenhofer, R.F., 2006. Das Sarmat im Lavanttaler Becken. In: M. Tessadri-Wackerle (Editor), Pangeo Austria 2006. Conference Series. Innsbruck University Press, Innsbruck/Austria, pp. 266-267.
Reiter, F. and Acs, P., 1996-2007. TectonicsFP - Computer Software for Structural Geology, Innsbruck.
Research, J. and GIS-STMK, 1999. Provisorische Geologische Karte der Republik Österreich 1:50.000 - 161 Knittelfeld. Geologische Bundesanstalt, Wien.
Riedmüller, G., Brosch, F.-J., Klima, K. and Medley, E.W., 2001. Engineering Geological Characterization of Brittle Faults and Classification of Fault Rocks. Felsbau, 19(4): 13-19.
Riedmüller, G. and Schwaighofer, B., 1978. Beziehungen zwischen Tonmineralverteilung und tektonischer Beanspruchung in der Kesselbach-Krumbach-Störung (südliche Koralpe). Carinthia II, 168/88: 75-79.
Robl, J., Hergarten, S. and Stüwe, K., 2008. Morphological Analysis of the Drainage System in the Eastern Alps. Tectonophysics, 460(1-4): 263-277.
Rosenberg, C.L., Brun, J.-P., Cagnard, F. and Gapais, D., 2007. Oblique indentation in the Eastern Alps: Insights from laboratory experiments. Tectonics, 26.
Rutter, E.H., H., M.R., Hall, S.H. and White, S.H., 1986. Comparative microstructures of natural and experimentally produced clay-bearing fault gouges. Pure and Applied Geophysics, 124(1-2): 3-30.
Sachsenhofer, R.F., 1996. The Neogene Styrian Basin: An Overview. Mitteilungen der Gesellschaft der Geologie und Bergbaustudenten in Österreich, 41: 19-32.
Sachsenhofer, R.F., Dunkl, I., Hasenhüttl, C. and Jelen, B., 1998. Miocene thermal history of the southwestern margin of the Styrian Basin: vitrinite reflectance and fission-track data from the Pohorje/Kozjak area (Slovenia). Tectonophysics, 297(1-4): 17-29.
Sachsenhofer, R.F., Jelen, B., Hasenhüttl, C., Dunkl, I. and Rainer, T., 2001. Thermal history of Tertiary basins in Slovenia (Alpine-Dinaride-Pannonian junction). Tectonophysics, 334(2): 77-99.
Sachsenhofer, R.F., Kogler, A., Polesny, H., Strauss, P. and Wagreich, M., 2000. The Neogene Fohnsdorf Basin: basin formation and basin inversion during lateral extrusion in the Eastern Alps (Austria). International Journal of Earth Sciences, 89(2): 415-430.
Sachsenhofer, R.F., Lankreijer, A., Cloetingh, S. and Ebner, F., 1997. Subsidence analysis and quantitative basin modelling in the Styrian Basin (Pannonian Basin System, Austria). Tectonophysics, 272(2-4): 175-196.
Sandau, W., 1981. Untersuchungen zur Petrographie und Tektonik in der südlichen Koralpe / Österreich. Diplomarbeit Thesis, Technische Universität Darmstadt, Darmstadt, 82 pp.
Scheidegger, A.E., 2004. Morphotectonics. Springer, 197 pp.
Schmid, S.M., Fügenschuh, B., Kissling, E. and Schuster, R., 2004. Tectonic map and overall architecture of the Alpine orogen. Eclogae Geologicae Helvetiae, 97(1): 93-117.
Schmid, S.M. and Handy, M.R., 1991. Towards a Genetic Classification of Fault Rocks: Geological Usage and Tectonophysical Implications. In: D.W. Müller (Editor), Controversies in modern geology. Academic Press, London, pp. 339-361.
Schmidt, J. and Andrew, R., 2005. Multi-scale landform characterization. Area, 37(3): 341-350.
Schmitz, D. et al., 1989. Core Orientation in the KTB pilot well. Scientific Drilling(1): 150-155.
Schneider, T.R., 1997. Behandlung der Störzonen beim Projekt des Gotthard-Basistunnels. Felsbau, 15(6): 489-495.

Scholz, C.H., 1990. The mechanics of earthquakes and faulting. Cambridge University Press, Cambridge, 439 pp.
Schumm, S.A., 1956. Evolution of drainage systems and slopes in badlands at Perth Amboy, New Jersey. Geological Society of America Bulletin, 67: 597-646.
Schuster, R. and Kurz, W., 2005. Eclogites in the Eastern Alps: High-pressure
metamorphism in the context of Alpine orogeny. Mitteilungen der Österreichischen Mineralogischen Gesellschaft, 150: 183–198.
Seefeldner, E., 1926. Zur Morphologie der Salzburger Alpen. Geogr. Jahresber. aus Österreich, 13: 107-149.
Seidl, M.A., Dietrich, W.E. and Kirchner, J.W., 1994. Longitudinal Profile Development into Bedrock: An Analysis of Hawaiian Channels. Journal of Geology, volume 102: 457-474.
Sibson, R.H., 1977. Fault rocks and fault mechanisms. Journal of the geological Society of London, 133: 191-213.
Sklar, L.S. and Dietrich, W.E., 1998. River longitudinal profiles and bedrock incision models: Stream power and the influence of sediment supply. In: E.E. Wohl (Editor), Rivers over rock: Fluvial processes in bedrock channels. American Geophysical Union Monograph, pp. 237-260.
Smith, G.H., 1935. The relative relief of Ohio. Geographical Review, 25(2): 272-284.
Smith, M.J. and Clark, C.D., 2005. Methods for the visualization of digital elevation models for landform mapping. Earth Surface Processes and Landforms, 30(7): 885-900.
Snow, R.S. and Slingerland, R.L., 1987. Mathematical modeling of graded river profiles. Journal of Geology, 95(1): 15-33.
Snyder, N., Whipple, K., Tucker, G. and Merrits, D., 2000. Landscape response to tectonic forcing: DEM analysis of stream profiles in the Mendocino triple junction region, northern California. Geological Society of America Bulletin, 112(8): 1250-1263.
Sölva, H., Grasemann, B., Thoni, M., Thiede, R. and Habler, G., 2005a. The Schneeberg Normal Fault Zone: Normal faulting associated with Cretaceous SE-directed extrusion in the Eastern Alps (Italy/Austria). Tectonophysics, 401(3-4): 143-166.
Sölva, H., Stüwe, K. and Strauss, P., 2005b. The Drava River and the Pohorje Mountain Range (Slovenia): Geomorphological Interactions. Mitteilungen des Naturwissenschaftlichen Vereins für Steiermark, 134: 45-55.
Sperner, B., Ratschbacher, L. and Ott, R., 1993. Fault-striae analysis: A turbo pascal program package for graphical presentation and reduced stress tensor calculation. Computers & Geosciences, 19(9): 1361-1388.
Steidl, A., Goricki, A., Schubert, W. and Riedmüller, G., 2001. Geological and Geotechnical Ground Chracterisation for the Koralm Tunnel Route Selection. Felsbau, 19(6): 14-21.
Stiny, J., 1925. Gesteinsklüftung im Teigitschgebiet. Tschermaks Mineralogische u. Petrographische Mitteilungen, 38: 464-478.
Stoddart, D.R., 1965. The shape of atolls. Marine Geology, 3(5): 369-383.
Stokes, M. and Mather, A.E., 2003. Tectonic origin and evolution of a transverse drainage: the Río Almanzora, Betic Cordillera, Southeast Spain. Geomorphology, 50(1-3): 59-81.
Stokes, M., Mather, A.E., Belfoul, A. and Farik, F., 2008. Active and passive tectonic controls for transverse drainage and river gorge development in a collisional mountain belt (Dades Gorges, High Atlas Mountains, Morocco). Geomorphology, 102(1): 2-20.
Strahler, A.N., 1952. Hypsometric (area-altitude curve) analysis of erosional topography. Geological Society of America Bulletin, 63(11): 1117-1141.
Strahler, A.N., 1957. Quantitative analysis of watershed geomorphology. Transactions of the American Geophysical Union, 38: 913-920.
Strauss, P., Wagreich, M., Decker, K. and Sachsenhofer, R., 2001. Tectonics and sedimentation in the Fohnsdorf-Seckau Basin (Miocene, Austria): from a pull-apart basin to a half-graben. International Journal of Earth Sciences, 90(3): 549-559.
Summerfield , M.A., 1991. Global Geomorphology. Prentice Hall, 537 pp.
Summerfield , M.A., 2000. Geomorphology and Global Tectonics. John Wiley & Sons Ltd., 368 pp.
Sung, Q., Chen, Y.-C., Tsai, H., Chen, Y.-G. and Chen, W.-S., 2000. Comparison Study on the Coseismic Deformation of the 1999 Chi-Chi Earthquake and Long-term Stream Gradient Changes along the Chelungpu Fault in Central Taiwan. Terrestrial, Atmospheric and Oceanic Sciences, 11(3): 735-750.
Suppe, J., 1985. Principles of structural geology. Prentice-Hall, Englewood Cliffs, NJ, 537 pp.

Szekely, B., 2001. On the surface of the Eastern Alps - a DEM study. Tübinger Geowissenschaftliche Arbeiten, 60: 1-157.

Székely, B., 2001. On the surface of the Eastern Alps - a DEM study. Tübinger Geowissenschaftliche Arbeiten, 60: 1-157.

Székely, B., Frisch, W., Dunkl, I. and Kuhlemann, J., 1999. DEM-based statistical methods of surface evaluation; considerations and results for the Eastern Alps. In: B. Szekely, W. Frisch, I. Dunkl and J. Kuhlemann (Editors), 4th workshop on Alpine geological studies, Sept. 21-24, 1999. Tuebinger Geowissenschaftliche Arbeiten. Reihe A, Geologie, Palaeontologie, Stratigraphie. Universität Tübingen, Institut und Museum für Geologie und Paläontologie, Tübingen / Germany, pp. 41-42.

Székely, B., Reinecker, J., Dunkl, I., Frisch, W. and Kuhlemann, J., 2002. Neotectonic movements and their geomorphic response as reflected in surface parameters and stress patterns in the Eastern Alps. EGU Stephan Mueller Special Publication Series, 3: 149-166.

Tenczer, V. and Stüwe, K., 2003. The metamorphic field gradient in the eclogite type locality, Koralpe region, Eastern Alps. Journal of Metamorphic Geology, 21(4): 377-393.

Thöni, M. and Miller, C., 1996. Garnet Sm–Nd data from the Saualpe and the Koralpe (Eastern Alps, Austria): chronological and P–T constraints on the thermal and tectonic history. Journal of Metamorphic Geology, 14(4): 453-466.

Tingay, M., Reinecker, J. and Müller, B., 2008. Borehole breakout and drilling-induced fracture analysis from image logs. World Stress Map Project, pp. 8.

Tollmann, A., 1959. Der Deckenbau der Ostalpen aufgrund der Neuuntersuchung des zentralalpinen Mesozoikums. Mitteilungen der Gesellschaft der Geologie und Bergbaustudenten in Österreich, 10: 1-62.

Tollmann, A., 1963. Ostalpensynthese. F. Deuticke, Wien, 256 pp.

Tollmann, A., 1968. Die palaogeographische, palaomorphologische und morphologische Entwicklung der Ostalpen. Mitteilungen der Osterreichischen Geographischen Gesellschaft, I-II: 224-244.

Tollmann, A., 1969. Die Bruchtektonik in den Ostalpen. Geologische Rundschau, 59(1): 278-288.

Tollmann, A., 1976. Schräger Durchgang und Steirisches Hügellland - Geologie-Morphologie. In: L. Beckel (Editor), Österreich im Satellitenbild. Otto Müller Verlag, Salzburg, pp. 96-98.

Tollmann, A., 1977. Die Zentralalpen. Die Geologie von Österreich, 1. Deuticke, Wien, 766 pp.

Turcotte, D.L., 1997. Fractals and chaos in geology and geophysics. Cambridge University Press, New York, 370 pp.

Turner, F.J., 1953. Nature and dynamic interpretation of deformation lamellae in calcite of three marbles. American Journal of Science, 251: 276-298.

Twidale, C.R., 2004. River patterns and their meaning. Earth-Science Reviews, 67(3-4): 159-218.

Twiss, R.J. and Moores, E.M., 2007. Structural Geology. W.H. Freeman and Company, New York, 736 pp.

Twiss, R.J. and Unruh, J.R., 1998. Analysis of fault-slip inversions: Do they constrain stress or strain rate? Journal of Geophysical Research, 103(B6): 12205–12222.

Übleis, M., 2007. Tektonische Analyse und Hydraulische Auswirkungen im Bereich des Koralm - Basistunnels. Magisterarbeit Thesis, Technische Universität Graz, Graz, 125 pp.

Van Husen, D., 1987. Die Ostalpen in den Eiszeiten. Aus der geologischen Geschichte Österreichs - Populärwissenschaftliche Veröffentlichungen der Geologischen Bundesanstalt, Wien, 24 pp.

Vanek, R., Pischinger, G. and Brosch, F.J., 2001. Kinematic Discontinuity Analysis. Felsbau, 19(6): 31-36.

Verrios, S., Zygouri, V. and Kokkalas, S., 2004. Morphotectonic analyis in the Eliki fault zone (Gulf of Corinth, Greece). Bulletin of the Geological Society of Greece, 36: 1706-1715.

von Blanckenburg, F. and Davies, J.H., 1995. Slab breakoff: A model for syncollisional magmatism and tectonics in the Alps. Tectonics, 14(1): 120-131.

Vörösmarty, C.J., Fekete, B.M., Meybeck, M. and Lammers, R.B., 2000. Geomorphometric attributes of the global system of rivers at 30-minute spatial resolution. Journal of Hydrology, 237(1-2): 17-39.

Vrabec, M. and Fodor, L., 2005. Structural styles at the northeastern corner of the Adriatic microplate. In: N. Pinter, G. Grenerczy, J. Weber and D. Medak (Editors), Proceedings of the NATO Advanced Research Workshop on The Adria Microplate: GPS Geodesy, Active Tectonics and Hazards. IV. Earth and Environmental Sciences. Springer, Veszprem, Hungary, pp. 151-168.

Vrabec, M., Pavlovic Preseren, P. and Stopar, B., 2006. GPS study (1996–2002) of active deformation along the Periadriatic fault system in northeastern Slovenia: tectonic model. Geologica Carpathica, 57(1): 57-65.

Wagner, T., 2010. Young uplift in the non-glaciated parts of the Eastern Alps - Geomorphological and geochronological constraints. PhD Thesis, Karl-Franzens University, Graz, 162 pp.

Wagner, T. et al., 2010a. Young uplift in the non-glaciated parts of the Eastern Alps. Earth and Planetary Science Letters, 295(1-2): 159-169.

Wagner, T. et al., 2011. Correlations of cave levels, stream terraces and planation surfaces along the River Mur-"Timing of landscape evolution along the eastern margin of the Alps. Geomorphology, Geomorphology and Natural Hazards in Karst Areas, 134(1-2): 62-78.

Wagner, T., Fritz, H., Stüwe, K. and Fabel, D., 2010b. Pliocene to Pleistocene faulting at the transition between Alps and Pannonian Basin: Constraints from dating fault activity by the 26Al/10Be burial age method. International Journal of Earth Sciences, submitted manuscript: 19.

Wakabayashi, J. and Medley, E.W., 2004. Geological Characterization of Melanges for Practitioners. Felsbau, 22(5): 10-18.

Walcott, R.C. and Summerfield, M.A., 2008. Scale dependence of hypsometric integrals: An analysis of southeast African basins. Geomorphology, 96(1â€“2): 174-186.

Wallace, R.E., 1951. Geometry of shearing stress and relation to faulting. Journal of Geology, 59(2): 118-130.

Wallbrecher, E., 1986. Tektonische und gefügeanalytische Arbeitsweisen. Ferdinand Enke Verlag, Stuttgart, 244 pp.

Weber, L. and Weiss, A., 1983. Bergbaugeschichte und Geologie der österreichischen Braunkohlenvorkommen. Archiv für Lagerstättenforschung der Geologischen Bundesanstalt, 4. Geologische Bundesanstalt, Wien, 317 pp.

Weissenbach, N., 1978a. Geologische Karte der Saulpe, Nord (Kärnten) 1:25.000. Geologische Bundesanstalt, Wien.

Weissenbach, N., 1978b. Geologische Karte der Saulpe, Süd (Kärnten) 1:25.000. Geologische Bundesanstalt, Wien.

Wells, S.G. et al., 1988. Regional variations in tectonic geomorphology along a segmented convergent plate boundary pacific coast of Costa Rica. Geomorphology, 1(3): 239-265.

Whipple, K.X., Kirby, E. and Brocklehurst, S.H., 1999. Geomorphic limits to climate-induced increases in topographic relief. 401(6748): 39-43.

Whitten, D.G.A. and Brooks, J.R.V., 1972. The Penguin Dictionary of Geology. Penguin Books, London, 509 pp.

Widdowson, M., 1997. The geomorphological and geological importance of palaeosurfaces. In: M. Widdowson (Editor), Palaeosurfaces: Recognition, Reconstruction & Palaeoenvironmental Interpretation. GSL Special Publications. The Geological Society of London, London, pp. 1-11.

Willgoose, G. and Hancock, G., 1998. Revisiting the hypsometric curve as an indicator of form and process in transport-limited catchment. Earth Surface Processes and Landforms, 23(7): 611-623.

Winkler, A., 1926. Zur geomorphologischen und geologischen Entwicklungsgeschichte der Ostabdachung der Zentralalpen in der Miozänzeit. Geologische Rundschau, 17: 36-68.

Winkler-Hermaden, A., 1957. Geologisches Kräftespiel und Landformung. Springer, 822 pp.

Wise, D.U. et al., 1984. Fault related rocks: Suggestion for terminology. Geology, 12: 391-394.

Wobus, C. et al., 2003. Tectonics from topography; procedures, promise, and pitfalls. In: S.D.H. Willett, N.; Brandon, M.T.; Fisher, D.M. (Editor), Penrose conference on Tectonics, climate, and landscape evolution. Special Paper - Geological Society of America. Geological Society of America, Taroko Gorge, Taiwan, pp. 55-74.

Wölfler, A., Kurz, W., Danišík, M. and Rabitsch, R., 2010. Dating of fault zone activity by apatite fission track and apatite (U/Th)/He thermochronometry: a case study from the Lavanttal fault system (Eastern Alps). Terra Nova, 22(4): 274-282.

Wölfler, A., Kurz, W., Fritz, H. and Stüwe, K., 2011. Lateral extrusion in the Eastern Alps revisited: Refining the model by thermochronological, sedimentary, and seismic data. Tectonics, 30(4): TC4006.

Wood, J., 1996. The geomorphological characterisation of digital elevation models. Ph.D. Thesis, University of Leicester, Leicester, 185 pp.

Zavoianu, I., 1985. Morphometry of drainage basins. Developments in water science, 20. Elsevier, Amsterdam, 238 pp.

Zernitz, E.R., 1932. Drainage patterns and their significance. The Journal of Geology, 40: 498–521.
Zevenbergen, L.W. and Thorne, C.R., 1987. Quantitative analysis of land surface topography. Earth Surface Processes and Landforms, 12(1): 47-56.
Zhang, X., -G., Han, W.-F. and Nie, D.-X., 1986. Engineering geological classification of fault rocks, Fifth International IAEG Congress. Balkema, Buenos Aires, pp. 479-486.
Zoback, M.D. et al., 2003. Determination of stress orientation and magnitude in deep wells. International Journal of Rock Mechanics and Mining Sciences, 40(7-8): 1049-1076.
Zovoili, E., Konstantinidi, E. and Koukouvelas, I.K., 2004. Tectonic Geomorphology of Escarpments: The cases of Kompotades and Nea Anchialos Faults. Bulletin of the Geological Society of Greece, 36: 1716-1725.

6 APPENDIX

Outcrop-ID	Easting	Northing	Altitude	Method	N	N_{biv}	P [°]		B [°]		T [°]		Theta [°]	R	Event
							dipdir	dip	dipdir	dip	dipdir	dip			
1	663924	196819	531	PT, NDA	4	0	48	72	275	8	181	15	35	0.435	D1-2
1	663924	196819	531	PT, NDA	15	4	138	83	5	5	280	5	35	0.422	D2
5	663787	192855	695	Extension	3	0	270	89	360	1	90	1			D2
7	643581	186454	1554	PT	3	0	227	79	332	1	61	9	30		D2
7	643581	186454	1554	PT	3	0	236	15	123	55	336	31	30		D3-1
7	643581	186454	1554	PT, NDA	4	0	297	80	28	2	121	10	30	0.578	D3-2
8	647102	190757	1384	PT, NDA	15	3	160	76	283	8	11	14	20	0.455	D1-2
9	647176	190763	1364	PT, NDA	8	3	145	69	306	13	40	6	30	0.487	D1-2
10	647070	190665	1384	PT, NDA	6	0	143	88	293	19	27	10	30	0.539	D1-2
22	644596	182403	1351	PT	3	0	173	21	326	69	79	6	35		D1-1
24	661794	193955	803	PT	4	1	212	43	22	51	303	2	30		D3-1
26	662236	194433	772	PT	3	0	84	81	342	2	251	7	30		D2
30	645204	175958	1159	PT, NDA	5	0	283	75	116	14	24	4	30	0.49	D1-2
47	641508	182275	779	PT, NDA	5	1	222	62	353	17	86	20	30	0.508	D2
49	660446	210288	400	PT, NDA	6	1	123	57	347	24	246	19	30	0.471	D2
49	660446	210288	400	conjug	12	0	143	88	53	1	323	2			D3-2
50	655925	184494	957	PT, NDA	12	4	51	43	193	48	308	16	30	0.519	D3-1
52	662334	198465	480	PT	5	4	33	23	273	83	126	7	30		D3-1
53	662576	198465	480	PT, NDA	5	1	34	41	190	47	292	13	30	0.513	D3-1
69	649017	207767	824	PT	3	0	252	74	156	2	66	17	30		D2
70	649543	207315	821	PT, NDA	4	0	332	69	186	17	93	11	30	0.506	D2
71	653276	203732	941	PT	3	0	343	7	128	89	69	5	30		D1-1
72	654254	204047	944	PT, NDA	6	2	69	80	169	2	256	10	30	0.524	D2
72	654254	204047	944	PT, NDA	9	0	144	1	42	78	234	17	30	0.539	D1-1
73	645808	181306	1385	PT, NDA	7	0	242	54	120	22	17	32	30	0.46	D1-2
74	645026	181295	1156	PT, NDA	10	5	140	82	318	9	47	1	30	0.505	D2
75	641028	173255	351	PT, NDA	22	0	186	11	44	77	277	10	30	0.521	D1-1
75	641028	173255	351	PT, NDA	4	0	319	73	112	14	204	7	42	0.427	D1-2
75	641028	173255	351	PT, NDA	12	0	215	6	96	79	306	10	30	0.502	D3-1
75	641028	173255	351	PT, NDA	15	0	240	87	20	4	110	2	30	0.436	D3-2
76	665673	207869	360	PT, NDA	7	0	193	70	349	19	82	7	30	0.525	D2
78	665609	208009	360	Extension	6		260	89	350	1	80	1			D2
78	665609	208009	360	Extension	3		324	89	54	1	144	1			D3-2
79	656552	183317	1003	extension	7		93	79	183	1	273	11			D2
80	654290	182897	1408	PT, NDA	5	0	62	82	273	8	182	3	30	0.483	D1-2
80	654290	182897	1408	PT	3	0	230	50	23	37	124	15	30		D3-1
83	654524	184073	1104	PT	3	0	335	72	85	5	175	16	30		D1-2
83	654524	184073	1104	PT, NDA	4	0	118	76	215	3	306	15	30	0.504	D3-2
83	654524	184073	1104	PT, NDA	6	0	73	5	187	79	335	8	30	0.528	D3-1
84	656922	183178	962	PT, NDA	11	0	102	75	240	11	332	11	30	0.484	D3-2
87	663564	197707	485	PT	3	0	6	24	217	62	100	9	30		D3-1
87	663564	197707	485	PT	3	0	265	79	357	3	88	11	30		D2
88	663482	198540	519	PT, NDA	8	1	190	83	16	6	286	1	30	0.514	D2
91	664252	199059	483	PT, NDA	7	1	79	77	193	3	288	12	30	0.457	D2
92	663094	199115	604	PT	3	0	184	76	17	13	286	3	30		D2
96	665011	197074	434	PT, NDA	7	0	116	79	10	4	281	11	38	0.496	D2
105	653654	203296	946	PT, NDA	6	1	93	58	264	25	350	7	30	0.502	D1-2
111	644448	183782	1512	PT, NDA	12	0	259	59	45	27	142	15	30	0.46	D3-2
113	643169	180605	916	PT, NDA	22	7	49	73	288	9	198	12	30	0.503	D1-2
114	642505	180715	820	PT, NDA	6	0	89	76	241	12	332	4	30	0.419	D3-2
114	642505	180715	820	PT, NDA	9	0	299	76	129	13	39	3	30	0.518	D1-2
114	642505	180715	820	PT, NDA	8	0	91	15	318	71	187	10	30	0.543	D4
116	643499	190857	787	PT, NDA	16	4	210	56	84	16	345	26	30	0.487	D1-2
116	643499	190857	787	PT	3	0	163	52	5	36	267	11	30		D1-1
117	643312	190960	846	PT, NDA	5	0	175	56	3	36	270	3	30	0.452	D2
118	642288	191188	677	PT, NDA	12	0	258	79	65	13	155	5	30	0.416	D1-2
122	641852	191822	835	PT, NDA	9	1	166	67	31	17	295	16	30	0.503	D3-2
125	641585	191533	708	extension	5	0	121	59	31	1	301	31			D3-2
127	641605	191508	670	PT	3	1	126	58	35	9	292	31	30		D3-2

Table 13 (continued on next page)

Outcrop-ID	Easting	Northing	Altitude	Method	N	N_{biv}	P [°]		B [°]		T [°]		Theta [°]	R	Event
							dipdir	dip	dipdir	dip	dipdir	dip			
129	641008	191033	796	PT, NDA	10	0	153	22	14	62	248	16	30	0.398	D1-1
129	641008	191033	796	PT, NDA	6	0	133	64	12	10	278	22	30	0.443	D2
133	640619	191656	582	PT, NDA	13	2	13	1	172	88	284	2	46	0.412	D3-1
134	643312	190960	846	PT, NDA	19	0	295	72	26	0	114	17	32	0.503	D3-2
134	643312	190960	846	PT, NDA	5	0	206	33	7	56	110	7	42	0.502	D3-1
134	643312	190960	846	PT	3	0	315	40	156	46	53	12	32		D1-1
137	643185	189360	1264	PT, NDA	8	2	152	32	11	47	254	23	30	0.522	D1-1
137	643185	189360	1264	PT, NDA	6	1	231	78	111	6	18	7	30	0.504	D1-2
140	643147	189657	1290	kex, conjug	4	0	192	59	31	29	296	6			D3-2
142	662283	197361	687	PT, NDA	18	0	111	86	10	1	284	4	30	0.412	D2
142	662283	197361	687	PT, NDA	5	0	177	21	328	69	82	15	30	0.587	D1-1
147	646630	164609	420	PT	3	1	342	51	171	49	83	0	30		D1-1
153	643033	184644	1299	PT, NDA	6	0	285	85	109	4	20	1	30	0.524	D1-2
153	643033	184644	1299	PT, NDA	8	0	159	72	344	18	253	2	30	0.503	D2
153	643033	184644	1299	PT	4	3	193	12	25	58	98	22	30		D3-1
155	642137	172272	431	PT	5	3	317	4	209	70	48	6	30		D1-1
158	661345	184999	610	PT	3	0	71	81	184	4	274	9	30		D2
160	661532	184990	627	PT	3	0	268	71	100	19	9	4	30		D1-2
161	655900	187379	950	PT, NDA	8	0	225	76	3	10	94	9	30	0.515	D2
163	660863	185328	593	PT, NDA	9	1	129	79	5	7	276	9	30	0.492	D2
164	658552	185624	728	PT, NDA	7	1	69	1	155	0	221	89	70	0.49	D4
164	658552	185624	728	PT, NDA	5	0	4	4	239	82	92	7	30	0.487	D1-1
166	666079	194998	552	PT, NDA	14	0	355	65	139	21	234	9	30	0.483	D2
166	666079	194998	552	PT, NDA	7	3	289	18	83	70	197	8	30	0.516	D4
167	666222	195122	495	Extension	6	0	250	89	160	1	70	1			D2
172	657335	206228	624	PT	3	0	32	78	169	8	261	11	30		D2
173	662431	209863	393	PT, NDA	7	0	129	53	277	32	17	16	30	0.495	D1-2
175	636706	197628	647	PT, NDA	8	3	179	16	320	69	87	9	30	0.501	D1-1
175	636706	197628	647	PT	5	2	66	74	330	2	240	14	30		D2
177	638417	195115	584	PT	3	0	156	18	13	68	251	14	30		D1-1
177	638417	195115	584	PT	3	0	210	62	90	14	352	22	30		D1-2
178	636596	197512	620	PT	3	1	196	61	329	32	76	17	30		D2
186	660723	191011	515	PT, NDA	9	0	9	11	187	78	278	2	30	0.538	D1-1
187	659822	191359	568	PT	5	2	132	74	12	5	282	19	20		D3-2
187	659822	191359	568	PT, NDA	13	4	0	3	98	77	271	7	20	0.668	D1-1
190	663218	184495	771	PT	7	4	345	3	10	89	75	1	25		D1-1
192	637814	199201	717	PT, NDA	6	0	143	51	8	30	263	22	30	0.507	D2
193	638250	199468	717	PT	3	0	332	28	75	23	195	51	30		D1-1
195	644347	179775	1034	PT, NDA	6	1	350	82	111	8	204	8	30	0.447	D1-2
204	657747	193401	667	PT, NDA	5	1	345	73	153	14	250	2	30	0.474	D2
207	660402	191534	519	PT	3	1	29	13	287	52	126	27	30		D3-1
214	659807	191581	501	PT	6	4	352	12	158	73	262	2	30		D1-1
215	664345	185080		PT, NDA	8	0	88	78	349	2	258	12	30	0.46	D2
216	663811	184927		PT	4	3	176	5	336	71	85	17	30		D1-1
220	650377	182333	1574	PT	3	0	129	23	263	61	30	19	30		D1-1
222	659330	185505	681	PT, NDA	6	1	150	5	21	79	239	11	30	0.511	D1-1
223	660685	184075	630	PT, NDA	7	0	113	82	290	10	20	4	30	0.489	D1-2
224	639826	199759	730	PT,NDA	10	0	320	7	53	45	222	41	30	0.493	D1-1
224	639826	199759	730	PT, NDA	4	0	123	53	310	38	217	2	30	0.483	D1-2
225	633483	185458	472	PT	5	3	73	9	287	69	164	10	30		D3-1
226	663955	184694	563	PT	29	7	108	50	344	27	238	27	45		D2
226	663955	184694	563	PT	6	0	338	78	81	2	172	11	40		D1-2
227	663183	184861	664	PT	27	3	205	55	23	39	111	4	40		D3-2
227	663183	184861	664	PT	3	0	125	60	312	30	218	6	30		D1-2
227	663183	184861	664	PT	4	0	7	14	99	18	240	71	30		D3-1
228	658129	183153	650	PT	19	0	46	52	167	22	271	30	35		D2
228	658128.5	183153	650.455	PT	15	0	121	70	237	8	329	18	32		D3-2
228	658128.5	183153	650.455	PT	17	0	340	77	102	9	188	14	35		D1-2
229	655507.6	185555.5	981.77	PT	12	0	253	71	87	19	352	7	32		D1-2

Table 13 (continued on next page)

Outcrop-ID	Easting	Northing	Altitude	Method	N	N_{biv}	P [°]		B [°]		T [°]		Theta	R	Event
							dipdir	dip	dipdir	dip	dipdir	dip	[°]		
229	655507.6	185555.5	981.77	PT	8	0	197	18	96	38	305	47	26		D3-1
230	649069.8	184805.2	1465.56	PT	9	0	251	75	70	13	165	3	30		D1-2
230	649069.8	184805.2	1465.56	PT	18	0	72	81	18	1	282	13	40		D2
231	644176.6	183776	1473.04	PT	4	2	180	51	14	29	281	11	35		D2
232	642857.9	182093.9	926.372	PT	10	2	184	79	277	6	16	14	38		D1-2
232	642857.9	182093.9	926.372	PT	9	2	172	67	2	8	271	4	38		D2
233	659741.8	183436.5	930.21	PT	22	0	12	74	113	4	196	15	26		D1-2
233	659741.8	183436.5	930.21	PT	16	0	43	65	216	25	306	7	36		D3-2
233	659741.8	183436.5	930.21	PT	18	0	15	4	105	49	296	45	30		D3-1
233	659741.8	183436.5	930.21	PT	12	0	88	7	171	29	338	56	30		D4
234	651250.7	183919.2	1510.56	PT	60	0	301	86	99	5	189	5	35		D1-2
234	651250.7	183919.2	1510.56	PT	91	0	178	69	3	24	272	3	46		D2
234	651250.7	183919.2	1510.56	PT	13	0	155	17	54	30	265	54	35		D1-1
234	651250.7	183919.2	1510.56	PT	6	0	255	2	354	61	157	29	35		D3-1
235	641981.6	180586.5	700.67	PT	13	0	350	76	100	4	189	14	50	0.507	D1-2
235	641981.6	180586.5	700.67	PT	18	0	355	78	154	12	245	0	52	0.498	D2
235	641981.6	180586.5	700.67	PT	12	0	47	81	229	9	138	2	64	0.542	D3-2
236	656711	181761.2	1233.02	PT	19	0	150	33	13	49	252	23	40	0.511	D1-1
236	656711	181761.2	1233.02	PT	12	0	213	71	91	11	356	13	30	0.564	D1-2
236	656711	181761.2	1233.02	PT	5	0	109	77	330	10	241	8	42	0.53	D2
236	656711	181761.2	1233.02	PT	4	0	52	17	266	72	146	9	30	0.231	D3-1
236	656711	181761.2	1233.02	PT	6	0	211	0	113	2	107	86	40	0.48	D3-1
237	650458.8	181155	1374.76	PT	3	0	162	3	284	87	76	2	30		D1-1
237	650458.8	181155	1374.76	PT	16	0	142	69	355	18	259	11	30	0.505	D2
237	650458.8	181155	1374.76	PT	21	0	158	19	46	50	258	34	30	0.503	D1-1
237	650458.8	181155	1374.76	PT	7	0	50	12	190	72	324	11	20	0.567	D3-1
237	650458.8	181155	1374.76	PT	26	0	197	51	35	38	299	10	30	0.519	D3-2
238	647255.7	180773	1581.38	PT	4	0	217	66	80	17	347	15	30	0.443	D1-2
238	647255.7	180773	1581.38	PT	5	0	68	21	333	11	216	66	30	0.475	D4
238	647255.7	180773	1581.38	PT	3	0	201	1	111	29	292	60	30		D3-1
238	647255.7	180773	1581.38	PT	3	0	164	16	52	56	256	32	30		D1-1
238	647255.7	180773	1581.38	PT	18	0	246	66	99	21	4	13	48	0.464	D1-2
238	647255.7	180773	1581.38	PT	25	0	253	70	29	13	123	13	54	0.452	D3-2
238	647255.7	180773	1581.38	PT	3	0	217	7	128	11	339	79	30		D3-1
239	647255.7	180773	1581.38	PT	9	0	258	73	40	14	132	17	68	0.578	D3-2
239	647255.7	180773	1581.38	PT	4	0	280	67	125	17	38	6	54	0.516	D1-2
240	654045.3	181267	1545.4	PT	55	0	137	72	347	15	255	11	50	0.448	D2
240	654045.3	181267	1545.4	PT	3	0	220	12	99	64	314	22	30		D3-1
240	654045.3	181267	1545.4	PT	13	0	254	60	39	23	133	17	78	0.485	D3-2
240	654045.3	181267	1545.4	PT	6	0	186	75	33	13	302	6	30	0.433	D3-2
240	654045.3	181267	1545.4	PT	7	0	218	61	44	30	313	2	80	0.47	D3-2
240	654045.3	181267	1545.4	PT	5	0	100	15	2	24	212	63	20	0.465	D4

Table 13: Coordinates of outcrop locations used for paleostress analysis with detailed orientations of the principal stress / strain axes determined for each location. Coordinates are in Austrian BMN M34 system. N...total number of data, Nbiv ... number of bivalent data, PT…PT method after Turner (1953), NDA… numerical dynamical analysis after Spang (1972), secfrac…kinematic deduced from secondary fractures e.g. Riedel fractures, Kex…extension fractures (gashes), con…conjugated shear fractures; P...compression axis, B...intermediate axis, T...extension axis, Theta...angle of internal friction, R...shape factor of the paleostress ellipsoid calculated with the numerical dynamical analysis (NDA) after Spang (1972). PT and NDA were calculated with TectonicsFP (Reiter and Acs 1996-2001).

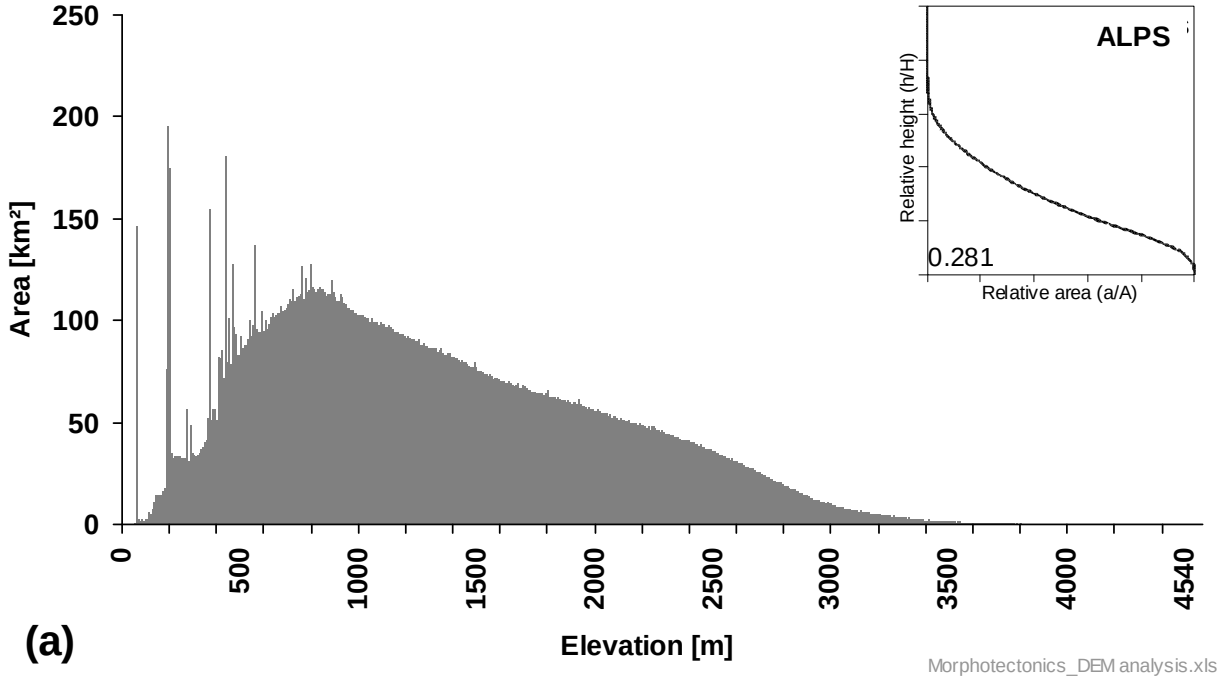

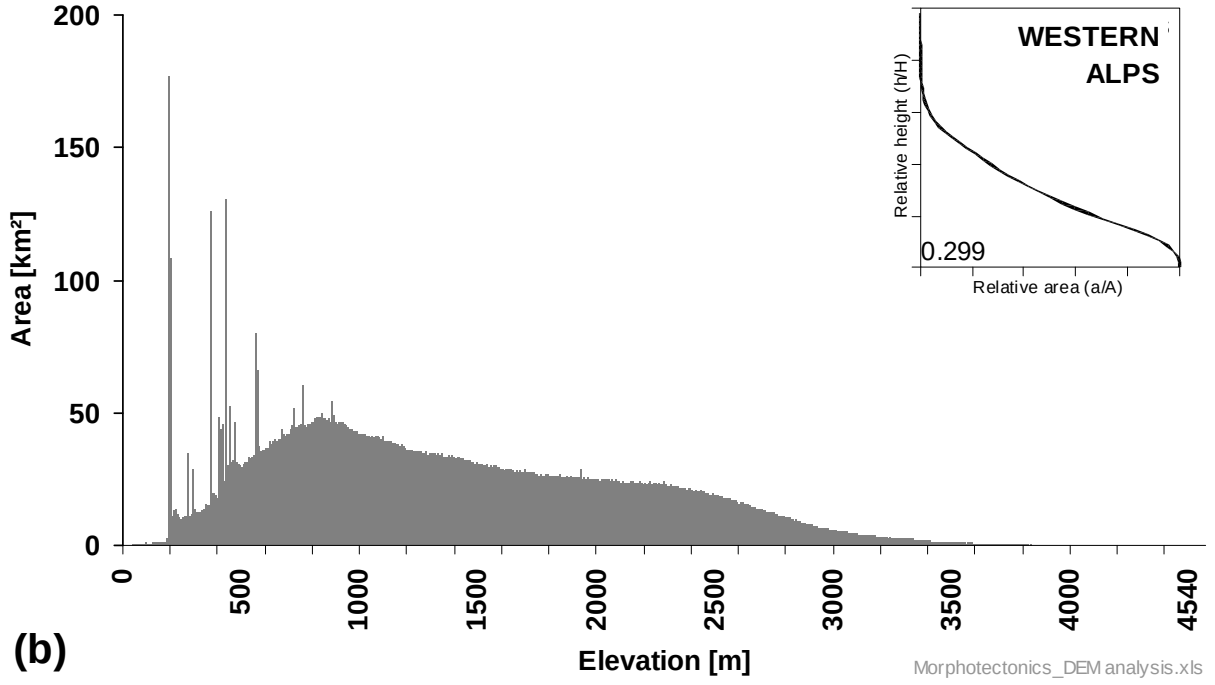

Figure 6-1: Histograms of the SRTM elevation model for the Alps (a), the Western Alps (b), the Eastern Alps (c) and the Tauern Window (d).

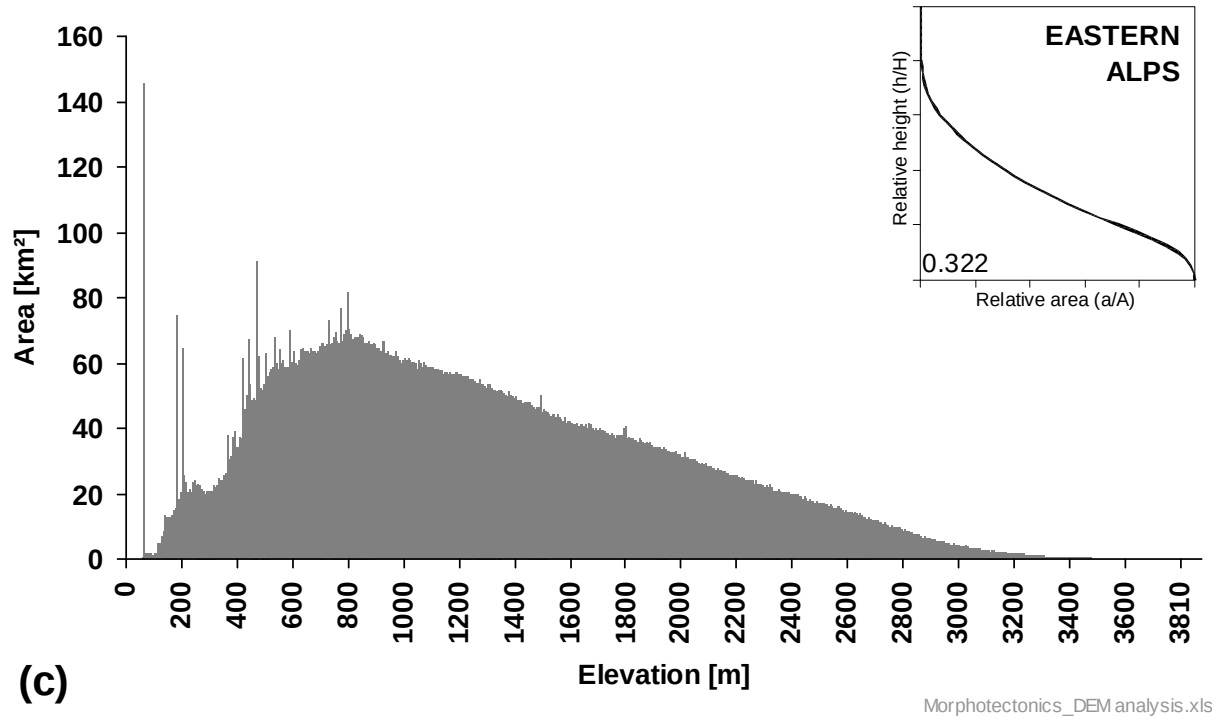

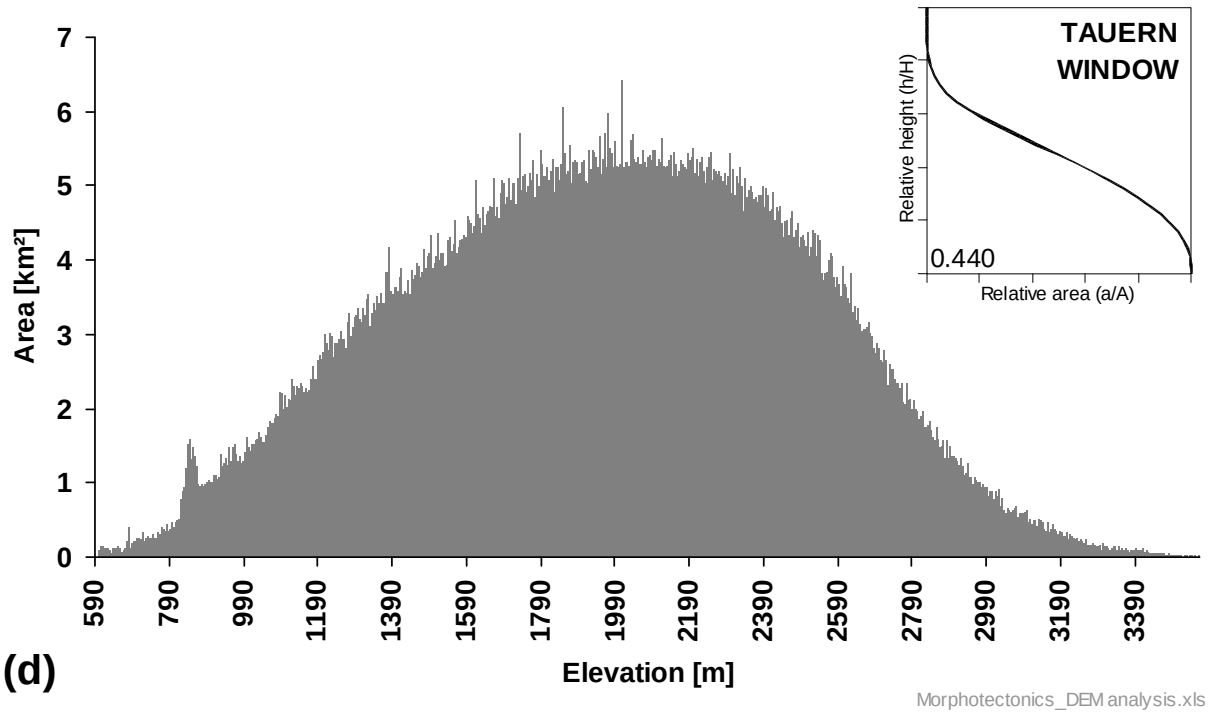

Figure 6-1 (continued)

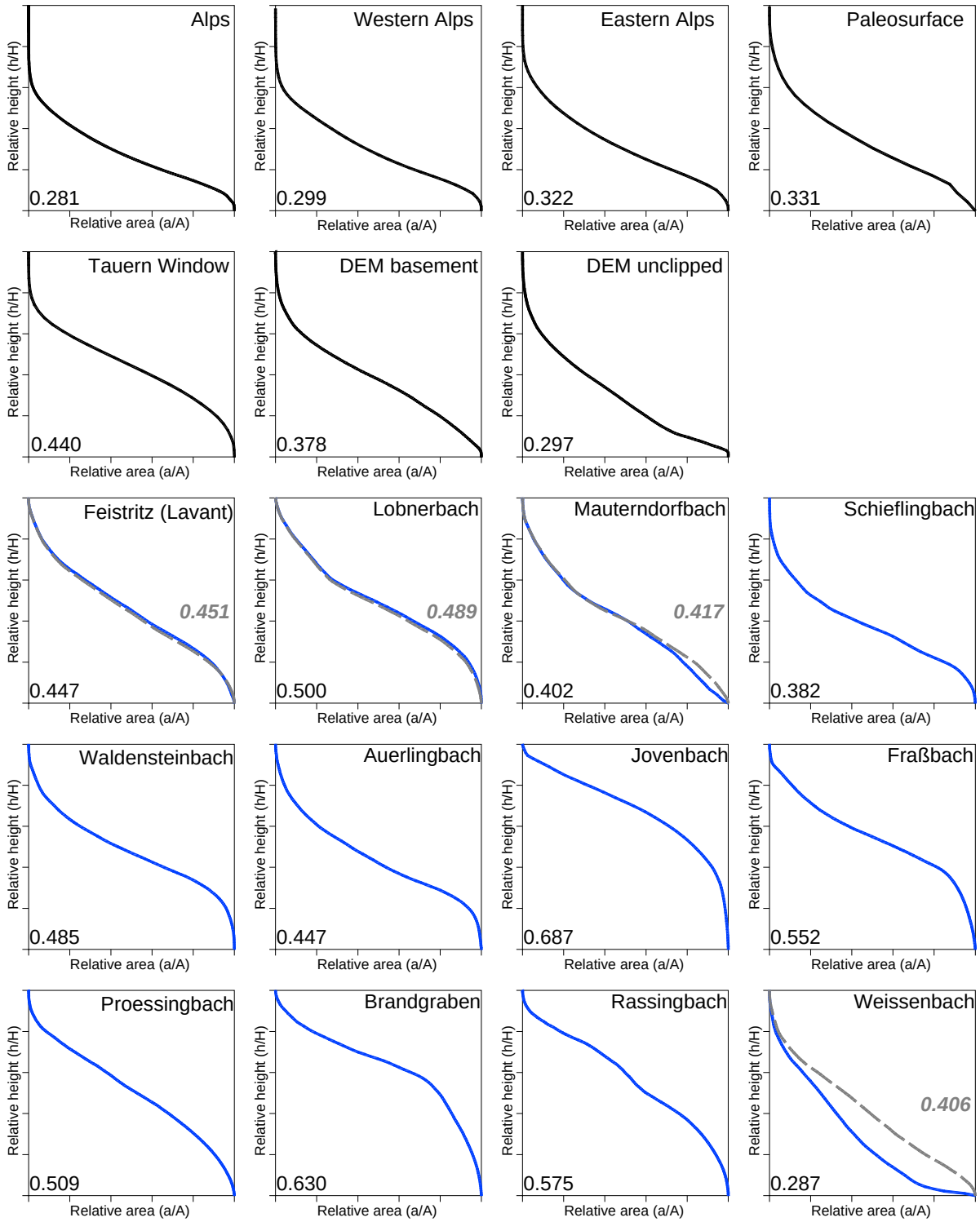

Figure 6-2: Hypsometric curves of the used DEMs (96m and 10 m) and the individual catchments of the Koralpe. Blue lines mark hypsometric curves including data from the basins surrounding the basement rocks of the Koralpe, grey dashed lines represent only the catchments truncated to the basement rocks. Numbers depicted within the graphs are the respective hypsometric integrals, grey cursive numbers represent the ones derived for the basement parts of the catchments.

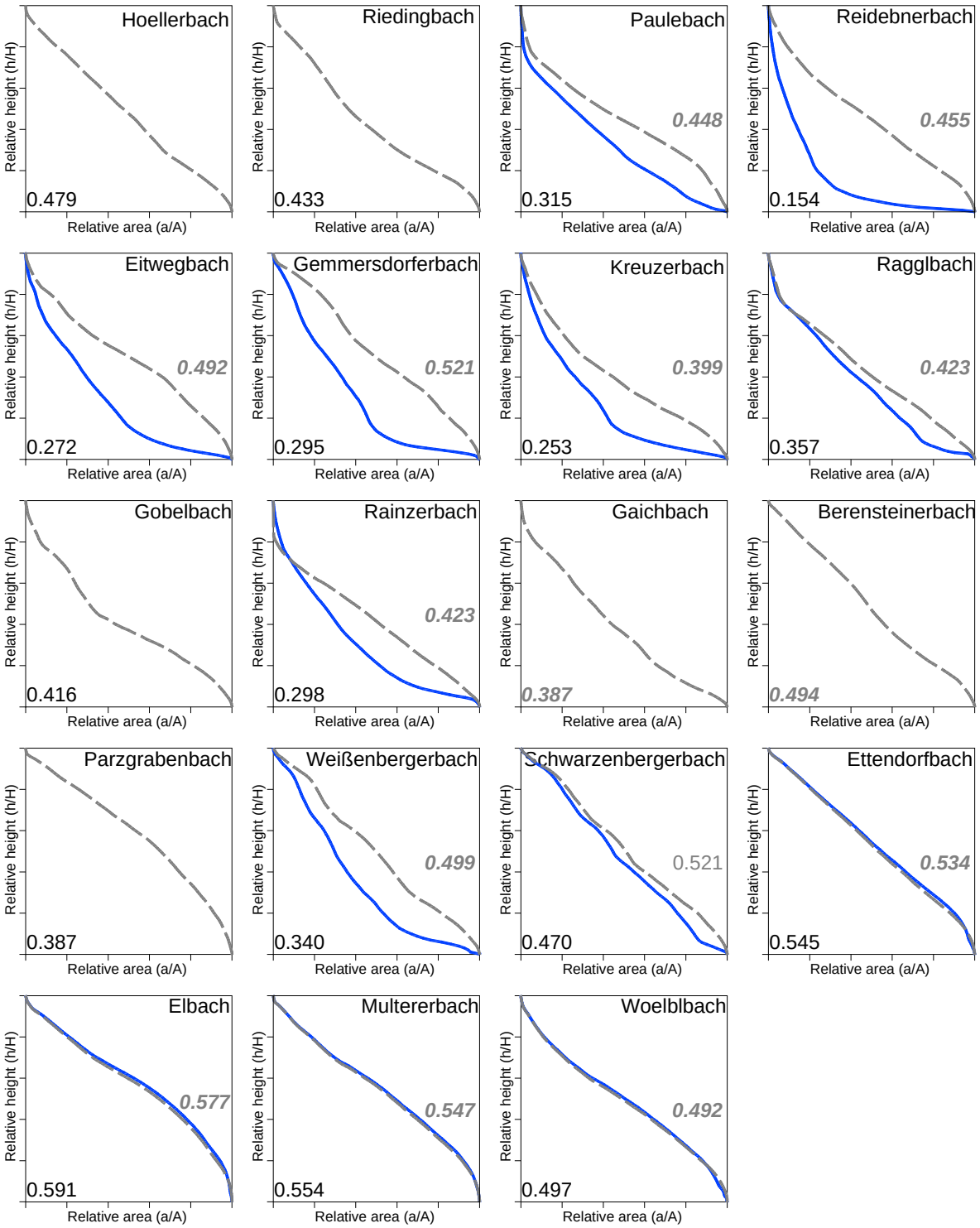

Figure 6-2 (continued)

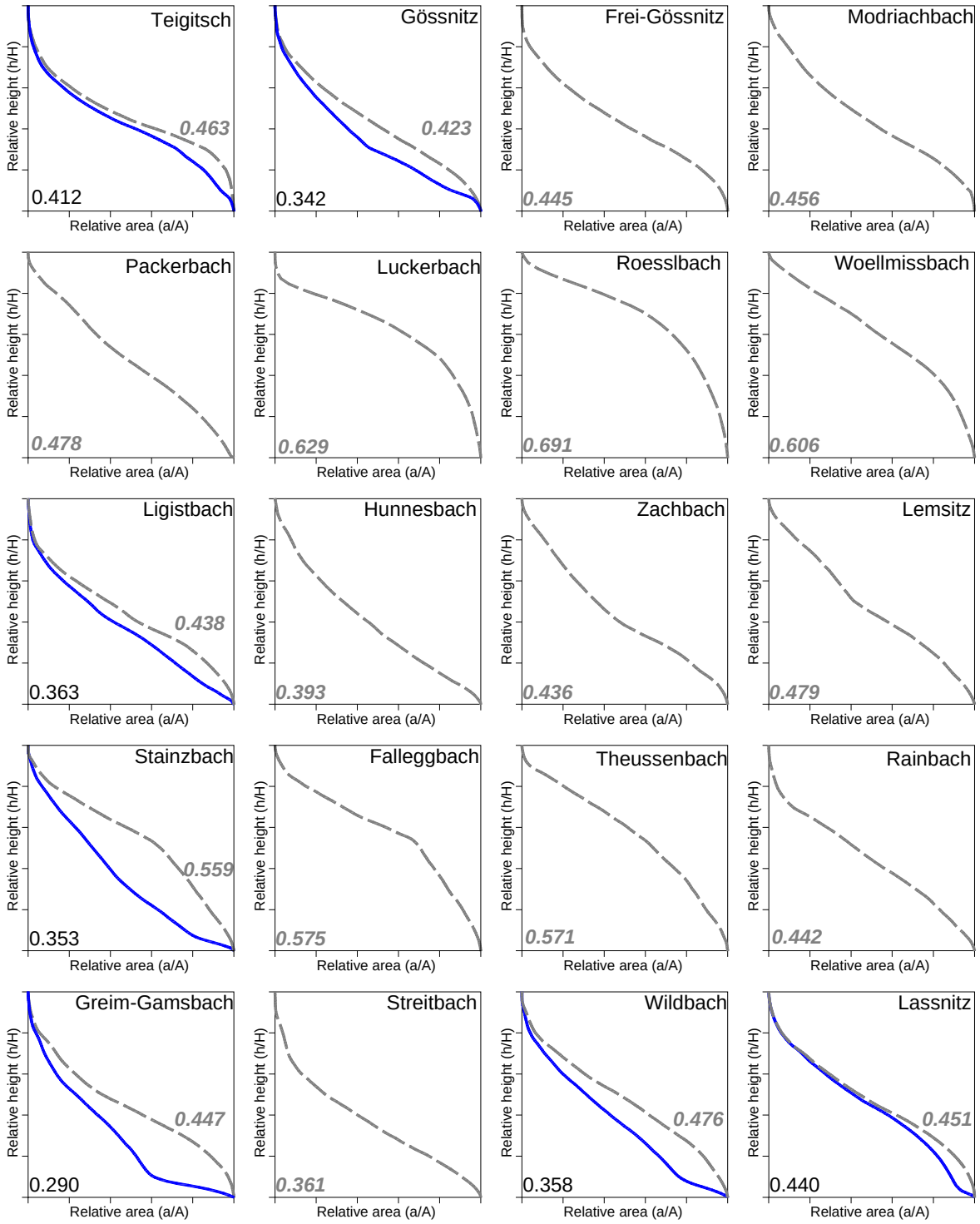

Figure 6-2 (continued)

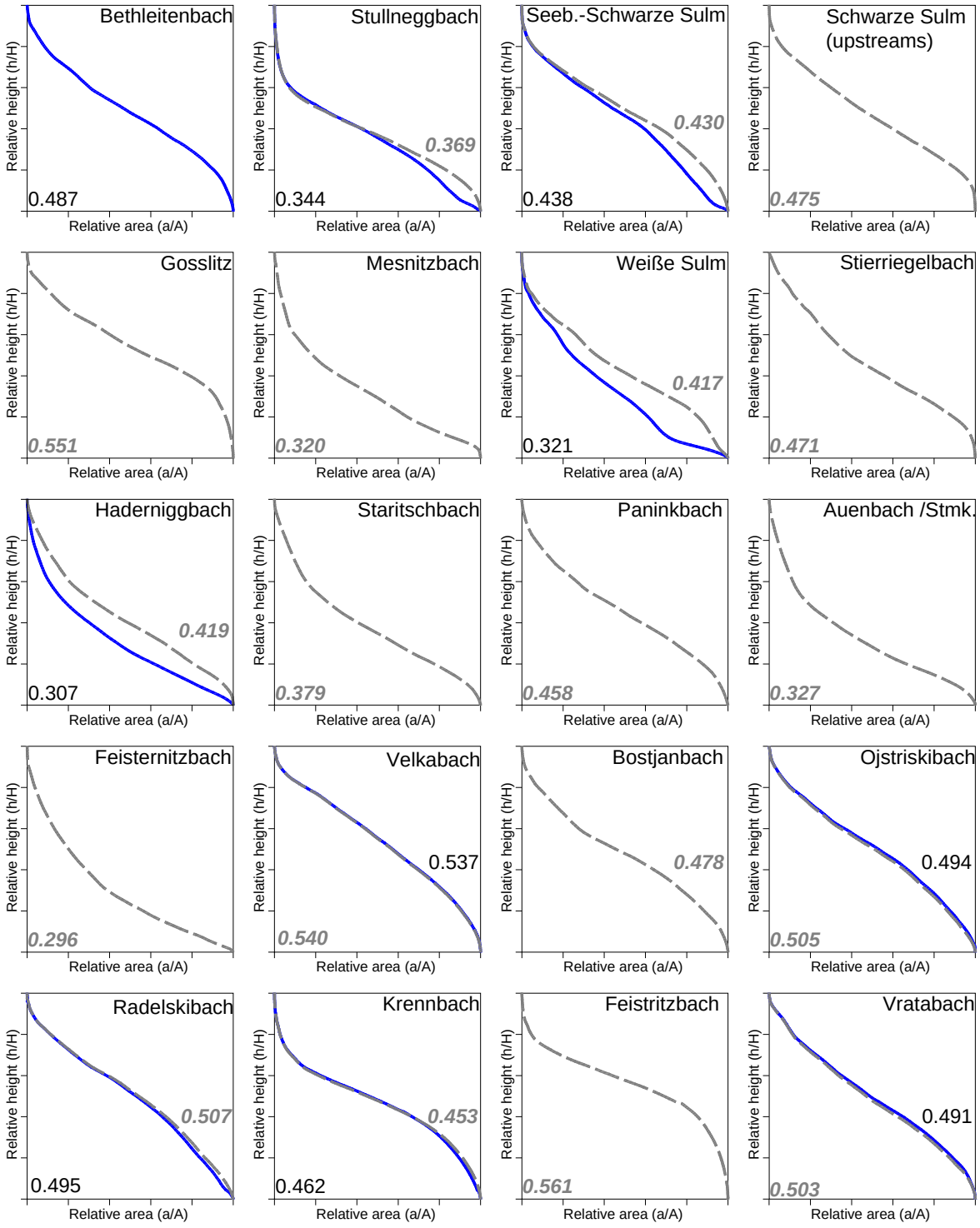

Figure 6-2 (continued)

Elevation class [m]	N	Min [°]	Max [°]	Mean [°]	σ [°]	Skewness	Kurtosis	q 25%	Median	q 75%	IQR
<400	202149	0.004	45.71	11.35	7.28	0.96	3.79	5.86	9.91	15.48	9.62
500	797198	0.020	66.34	17.11	8.36	0.55	2.99	10.92	16.13	22.13	11.21
600	873131	0.100	70.50	20.50	8.59	0.35	2.71	14.12	19.73	26.30	12.18
700	986889	0.056	72.66	20.85	8.68	0.34	2.74	14.24	20.14	26.98	12.74
800	1124768	0.000	68.23	19.85	9.11	0.31	2.61	12.86	19.24	26.28	13.42
900	1156003	0.000	68.06	19.57	8.72	0.37	2.79	12.95	18.83	25.56	12.61
1000	1351462	0.023	61.82	17.98	7.97	0.59	3.21	12.15	16.97	22.98	10.83
1100	1457989	0.000	63.44	16.49	7.71	0.64	3.59	11.11	15.61	20.97	9.87
1200	1308168	0.032	57.99	17.10	7.22	0.77	3.83	12.07	16.10	21.15	9.08
1300	1160328	0.030	57.82	16.87	7.02	0.66	3.62	12.00	16.00	20.95	8.95
1400	941368	0.032	65.13	16.48	6.90	0.64	3.53	11.59	15.67	20.58	9.00
1500	698956	0.040	57.35	15.69	7.11	0.57	3.21	10.55	14.86	20.04	9.49
1600	430646	0.084	64.01	17.27	6.90	0.58	3.43	12.32	16.53	21.56	9.24
1700	316039	0.064	65.25	16.89	7.07	0.77	4.15	11.88	16.11	20.85	8.97
1800	179310	0.109	63.18	18.23	7.69	0.64	3.73	12.77	17.66	22.41	9.64
1900	101492	0.035	60.40	17.82	8.44	0.76	3.88	11.82	17.02	22.31	10.49
2000	48317	0.027	59.98	17.77	8.53	0.75	3.73	11.90	16.94	22.17	10.27
2100	16327	0.270	59.95	19.18	9.68	0.76	3.04	11.73	17.20	24.77	13.04
2200	1371	0.679	45.11	18.88	9.37	0.35	2.44	12.03	17.42	25.77	13.74

σ..standard deviation, q25%....lower quartile, q75%....upper quartile, IQR….interquartile range

Table 14: Descriptive statistics of the slope angle for 100 m elevation intervals.

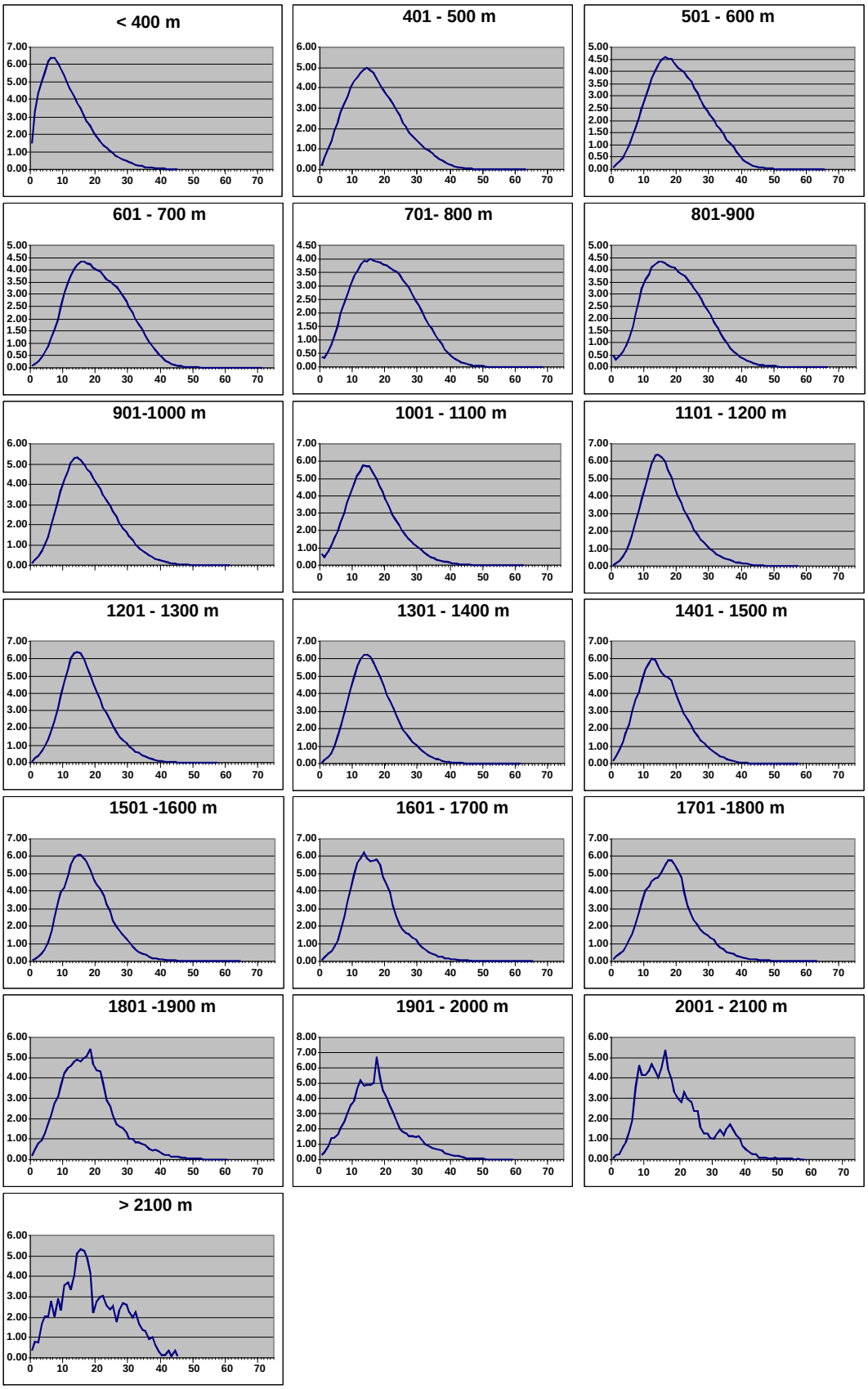

Figure 6-3: Distribution of slope angle in 100 m elevation intervals for the Koralpe.

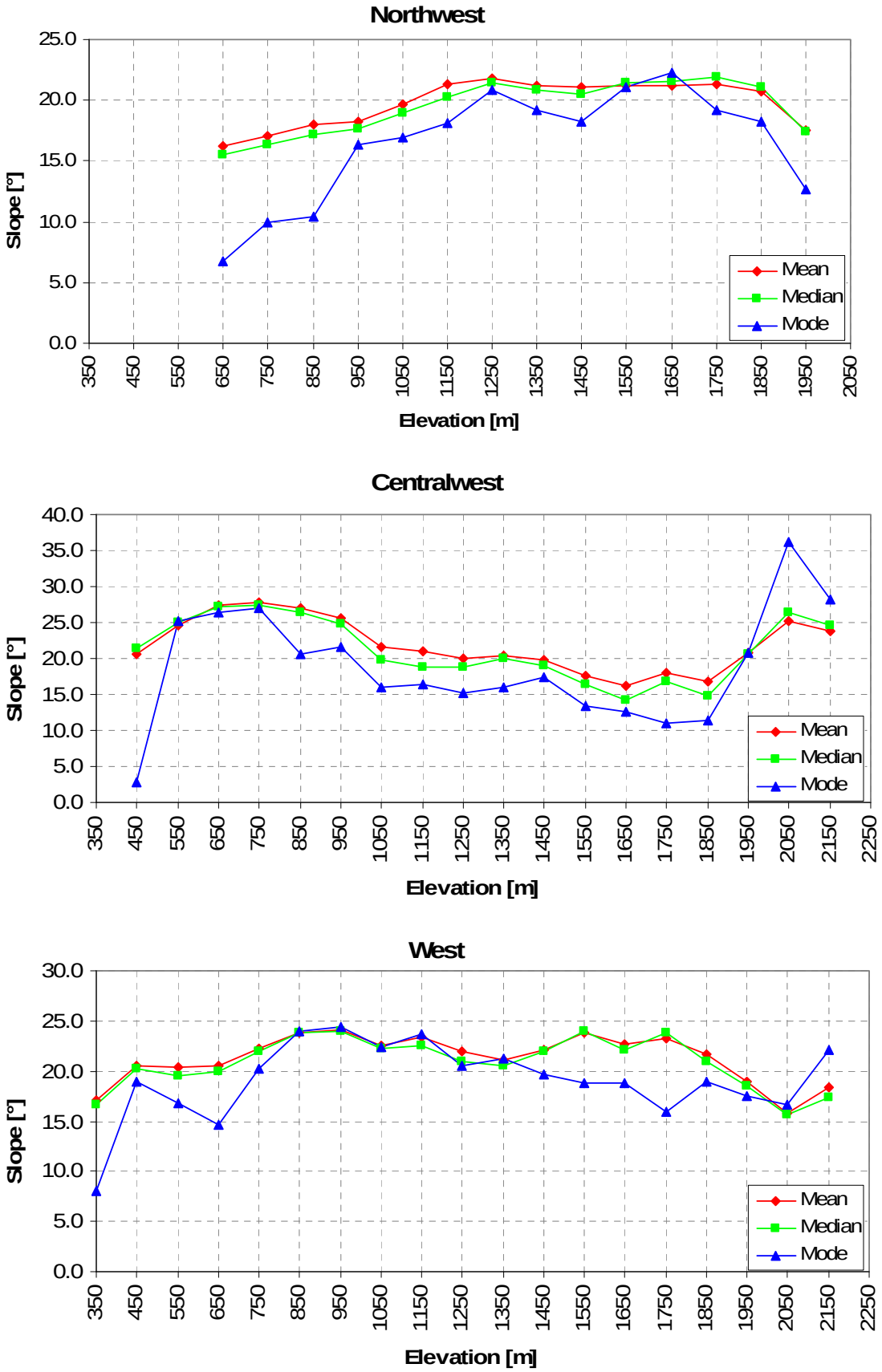

Figure 6-4: Central values of statistical distribution for the slope angle of the individual morphounits calculated for 100 m intervals of elevation. Elevation values mark the middle of the respective class.

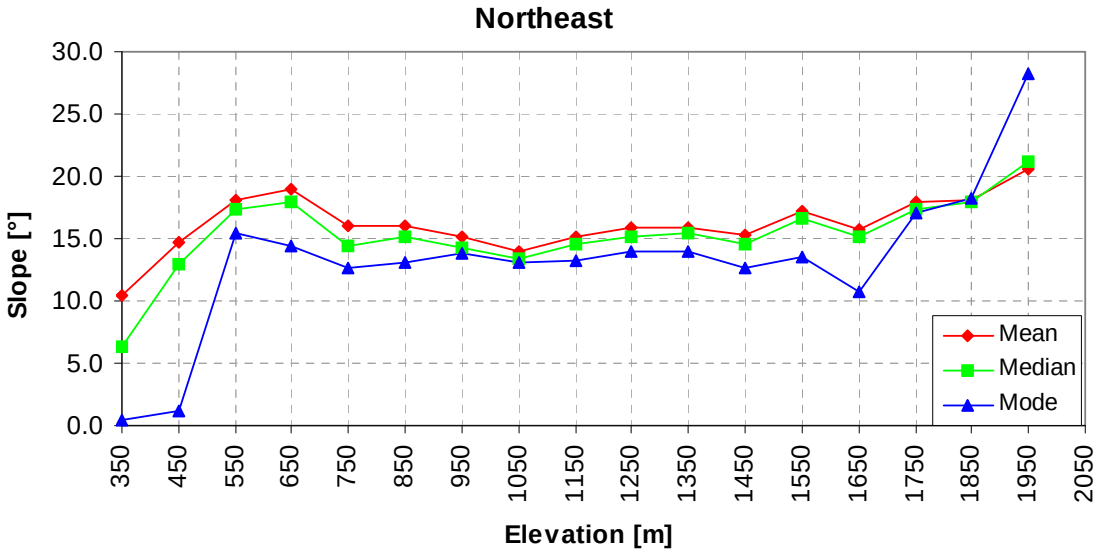

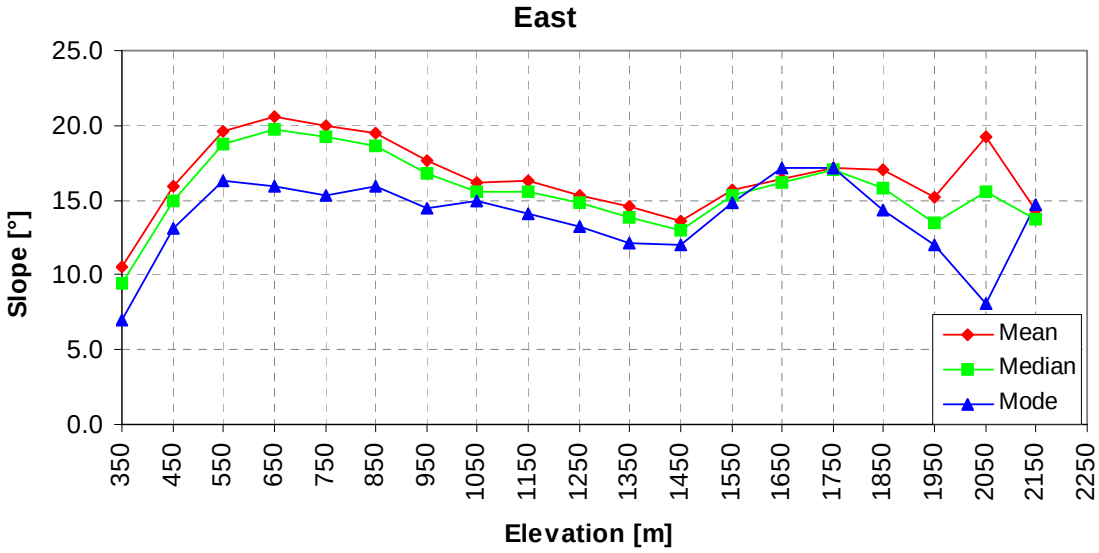

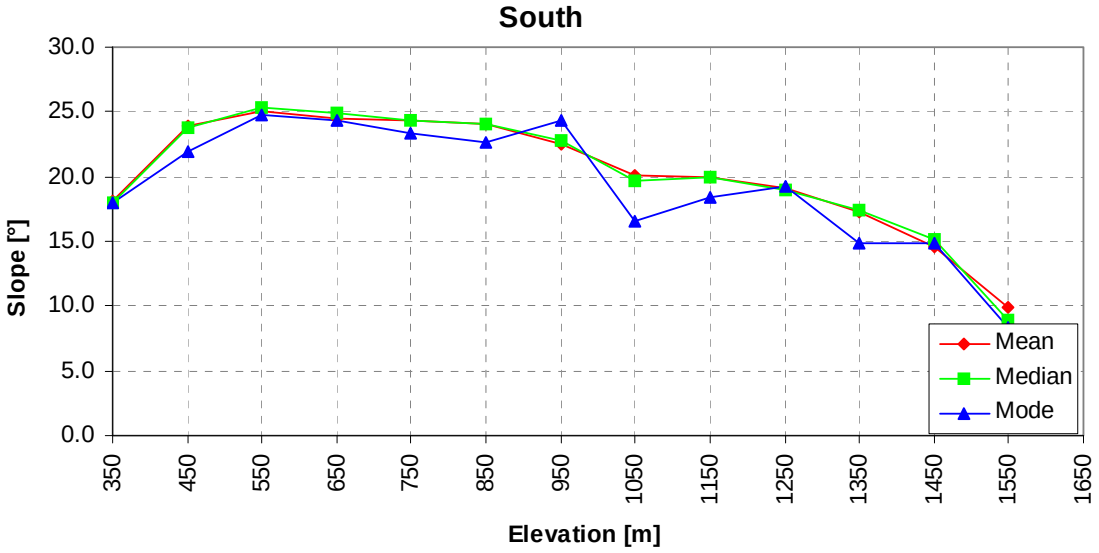

Figure 6-4 (continued)

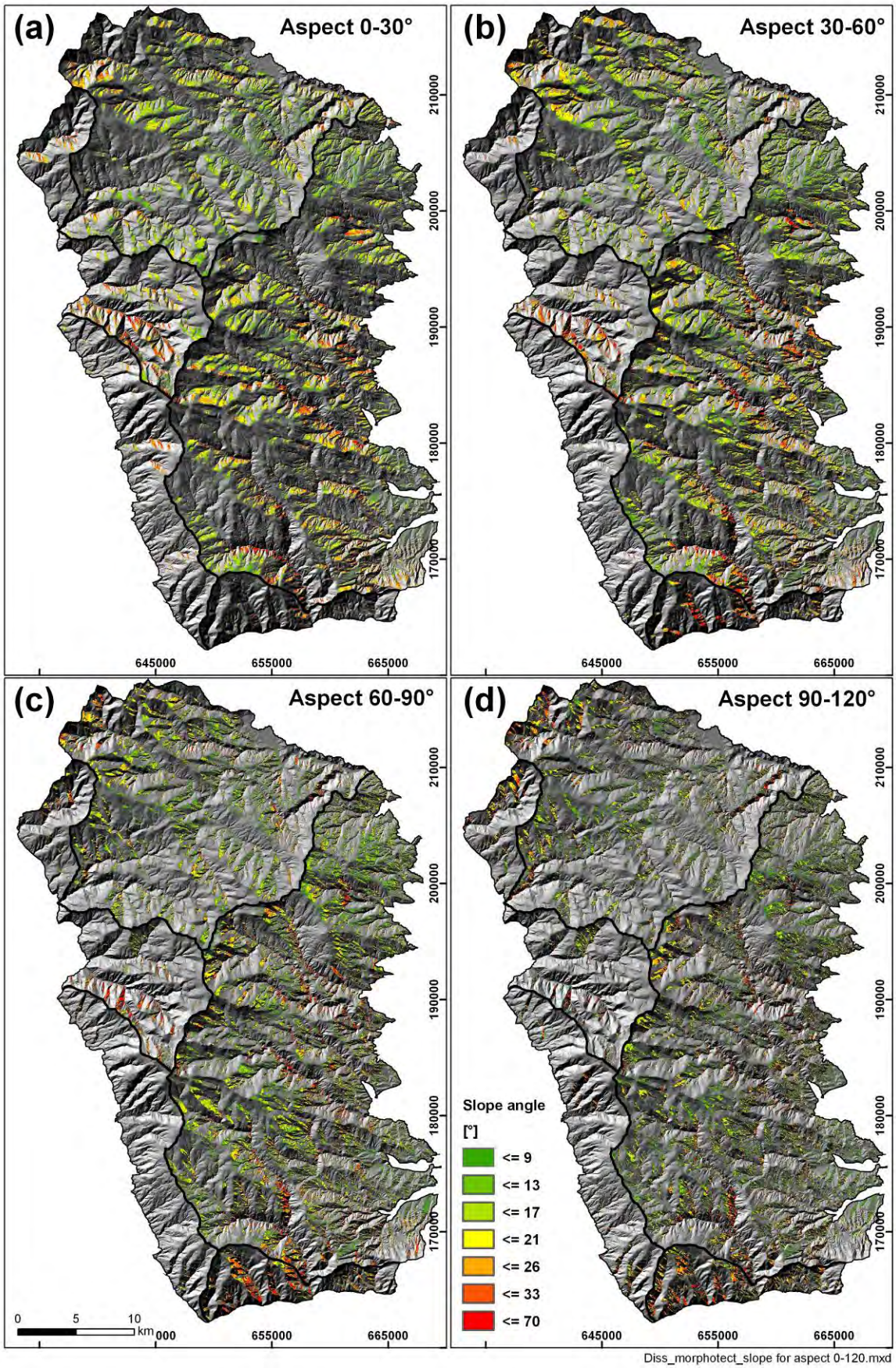

Figure 6-5: Slope gradient map (10° intervals) for 30° slope aspect intervals: (a) aspect 0 to 30°, (b) 30° to 60°, (c) 60° to 90° and (d) 90° to 120°.

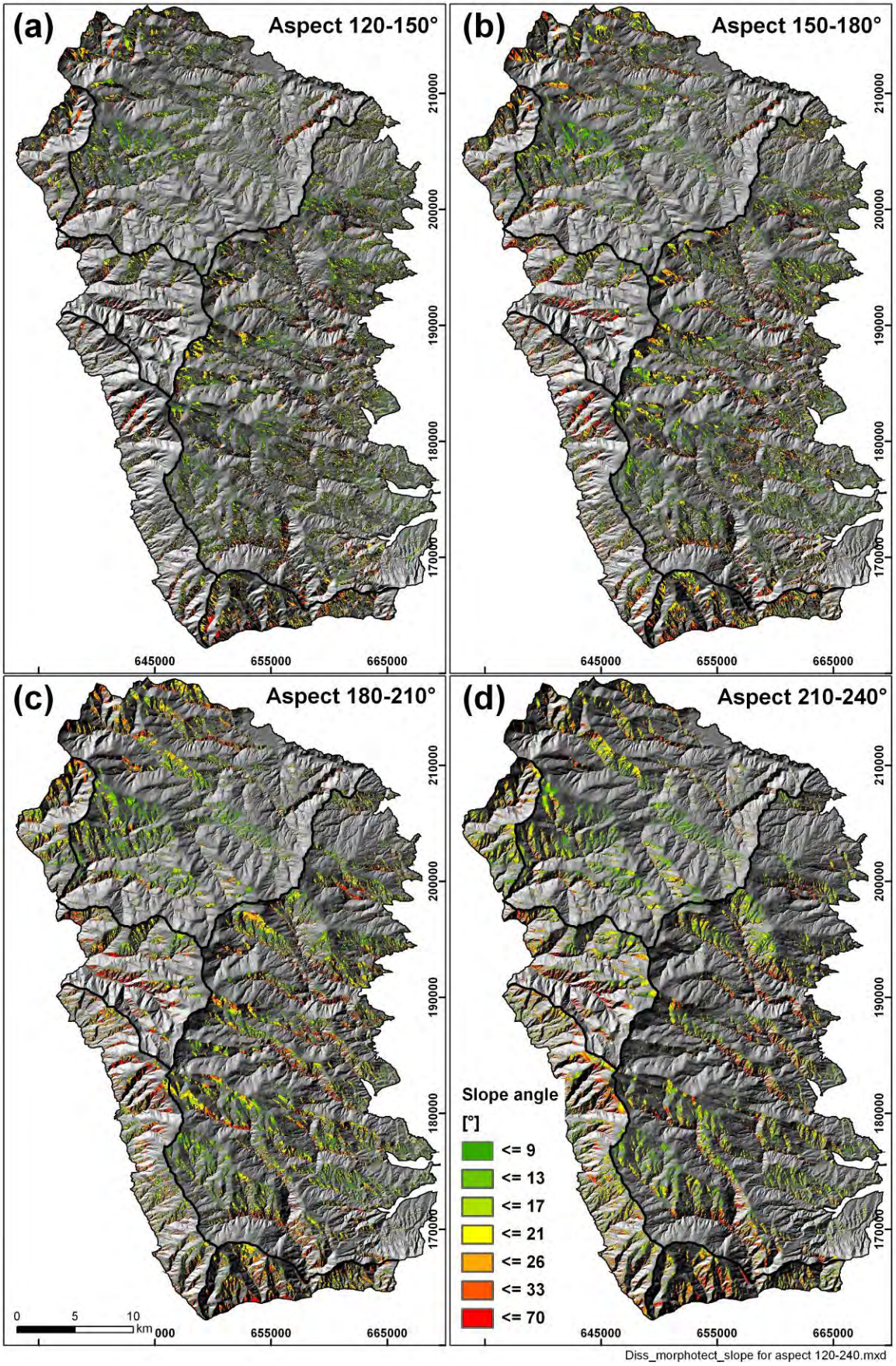

Figure 6-6: Slope gradient map (10° intervals) for 30° slope aspect intervals: (a) aspect 120° to 150°, (b) 150° to 180°, (c) 180° to 210° and (d) 210° to 240°.

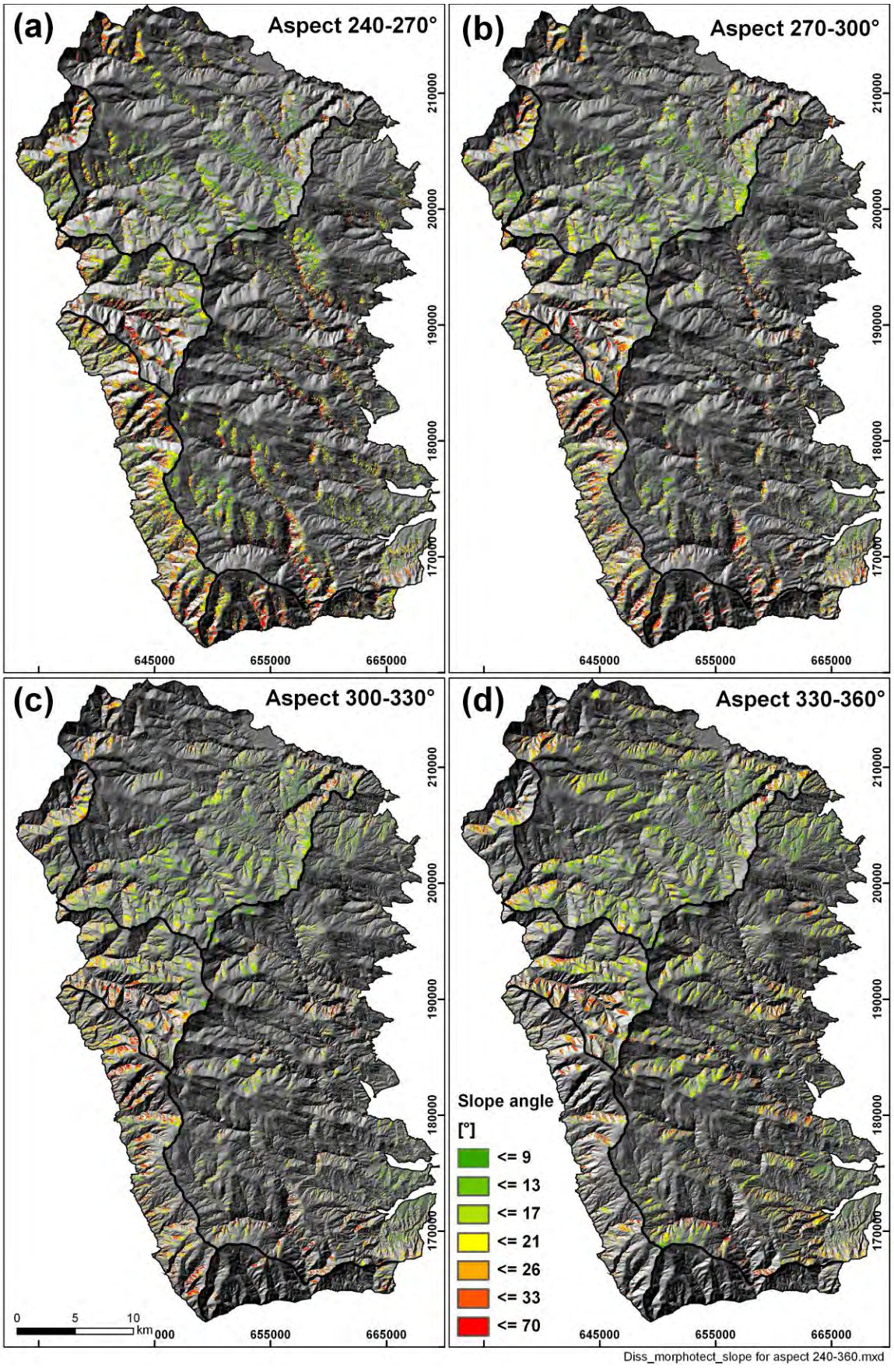

Figure 6-7: Slope gradient map (10° intervals) for 30° slope aspect intervals: (a) aspect 240° to 270°, (b) 270° to 300°, (c) 300° to 330° and (d) 330° to 360°.

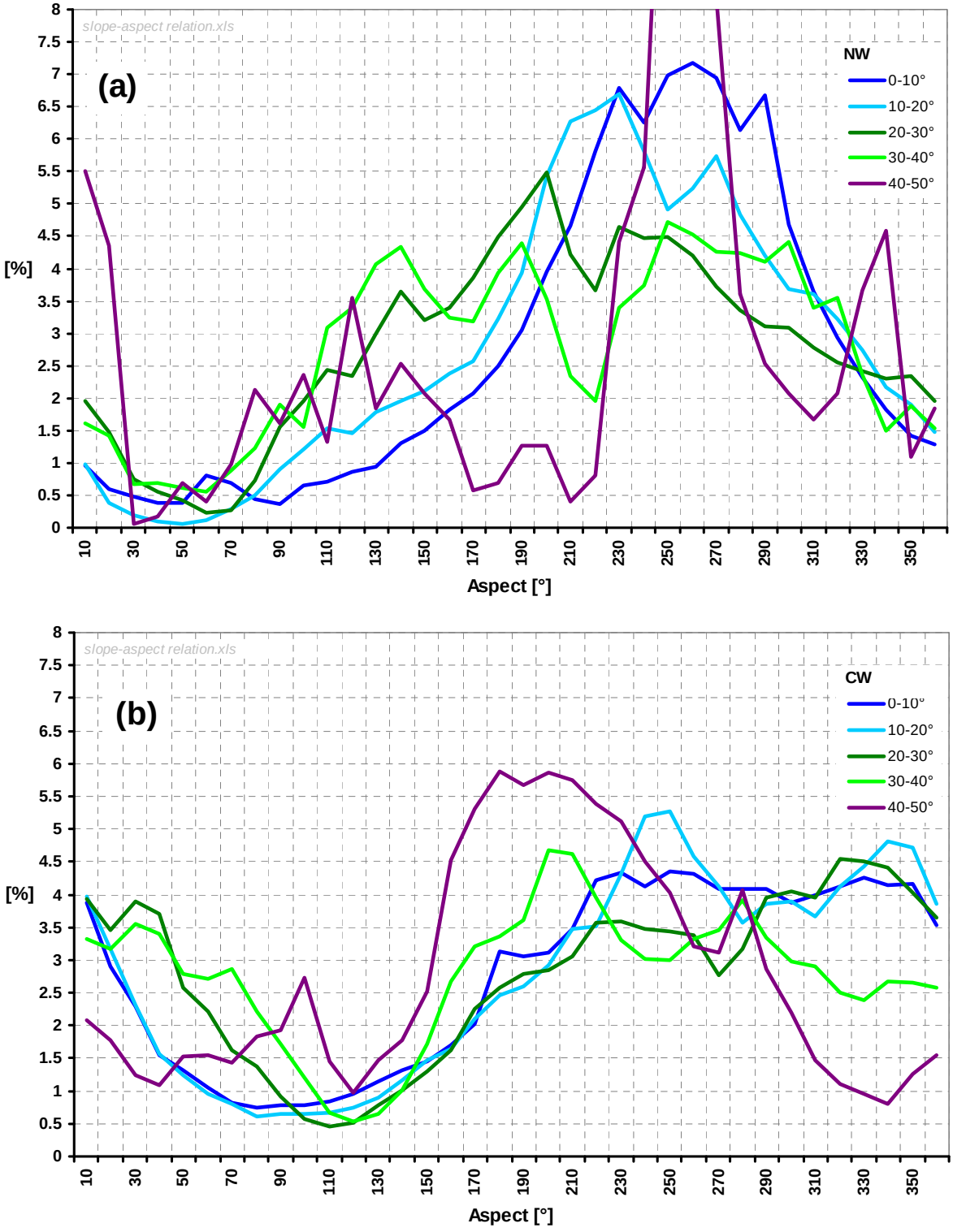

Figure 6-8: Distribution of slope aspect within 10° slope gradient classes for the individual morphounis:. (a) Northwest (NW), (b) Central West (CW), (c) West, (d) South, (f) Northeast (NE).

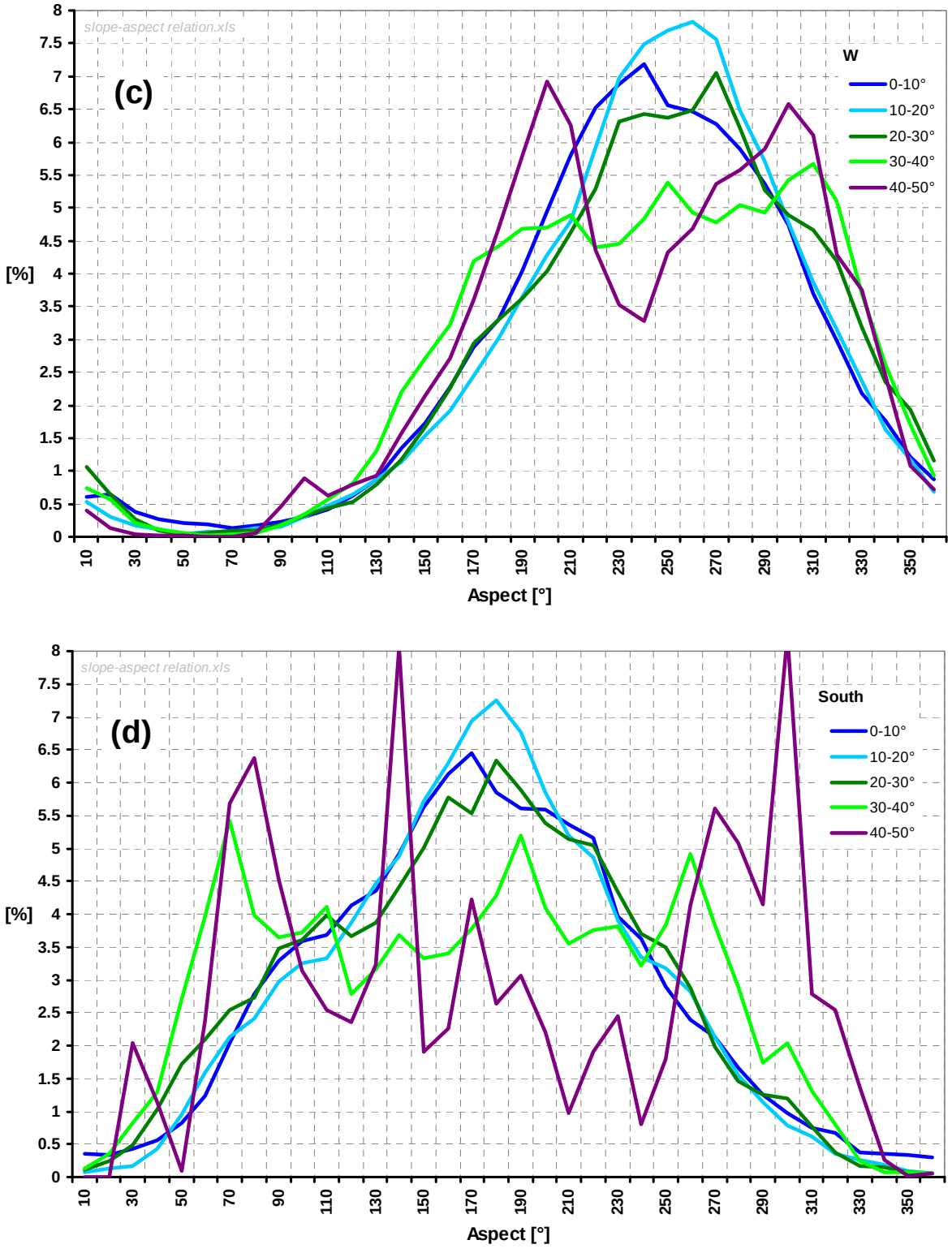

Figure 6-8 (continued)

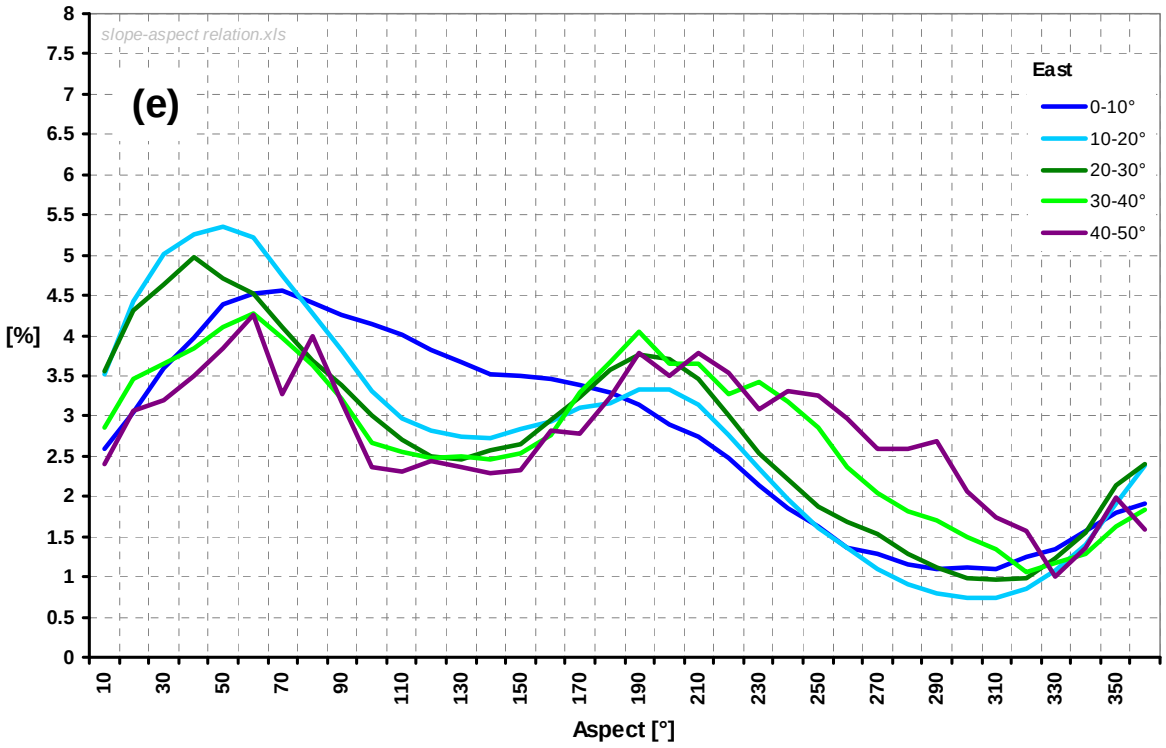

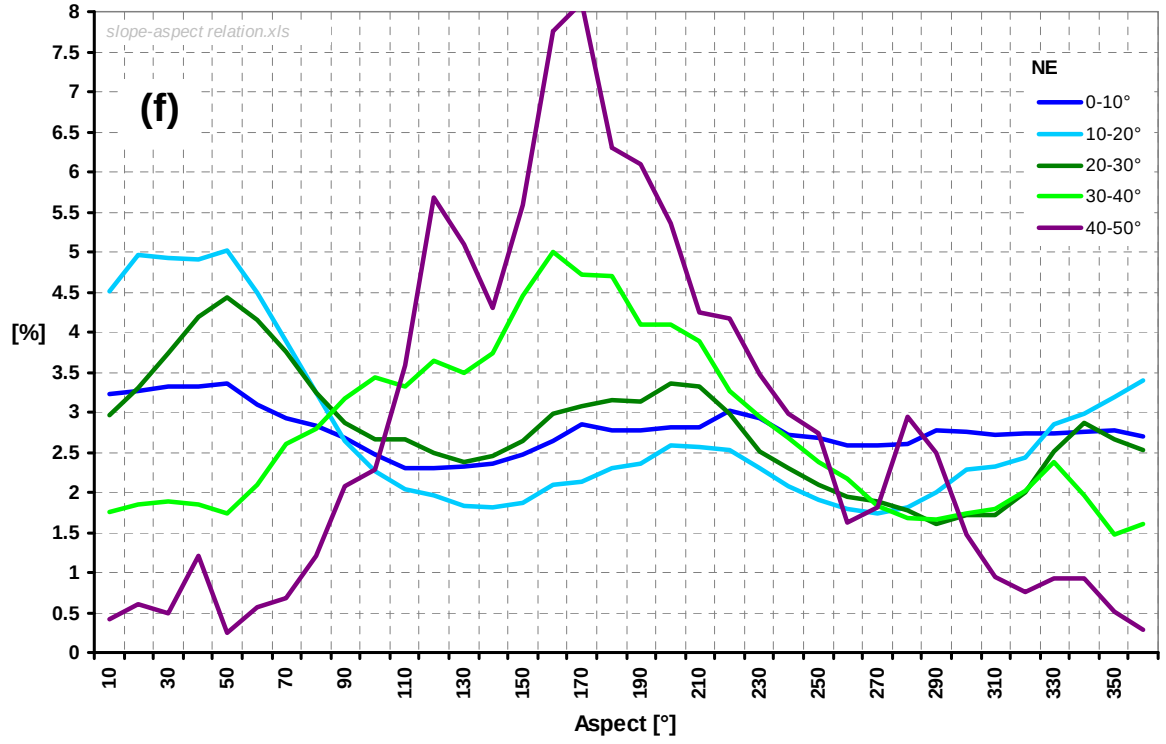

Figure 6-8 (continued)

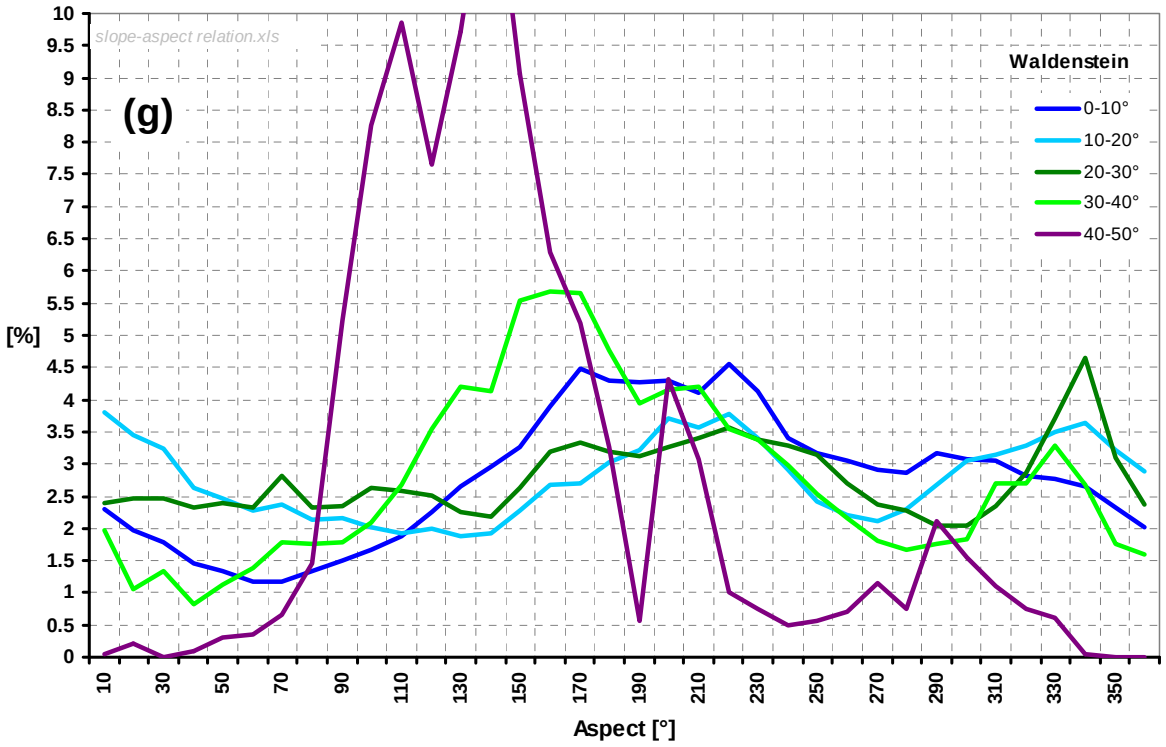

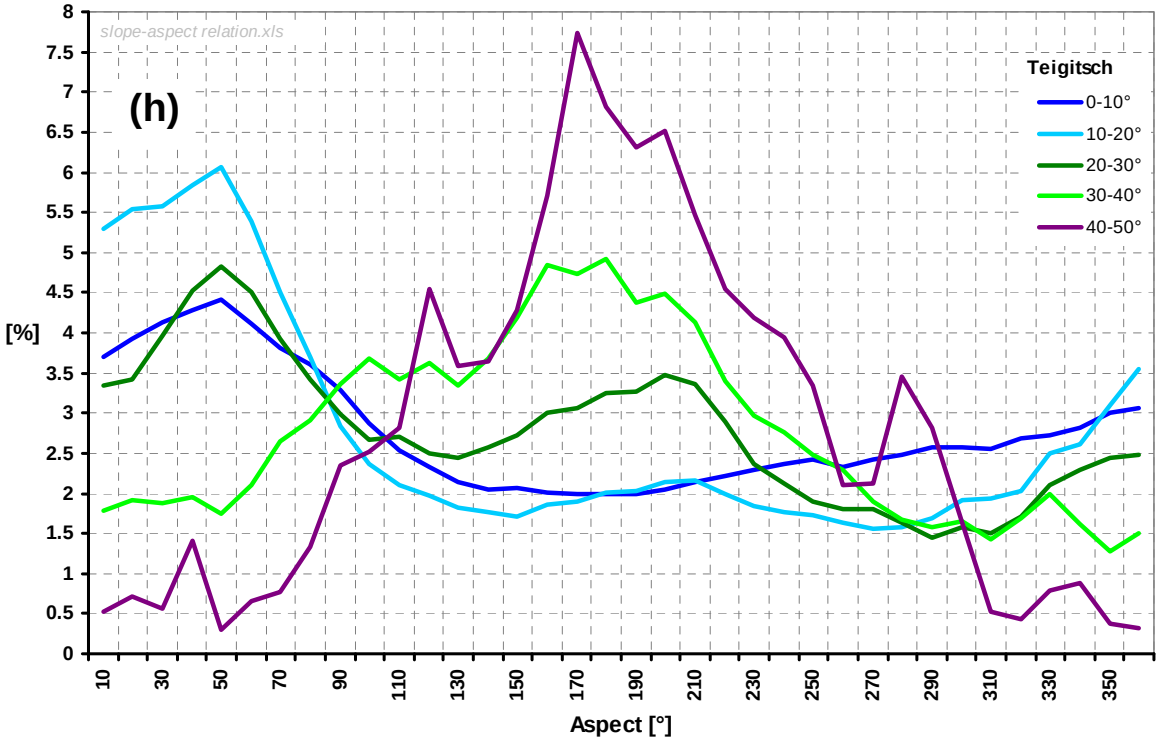

Figure 6-8 (continued)

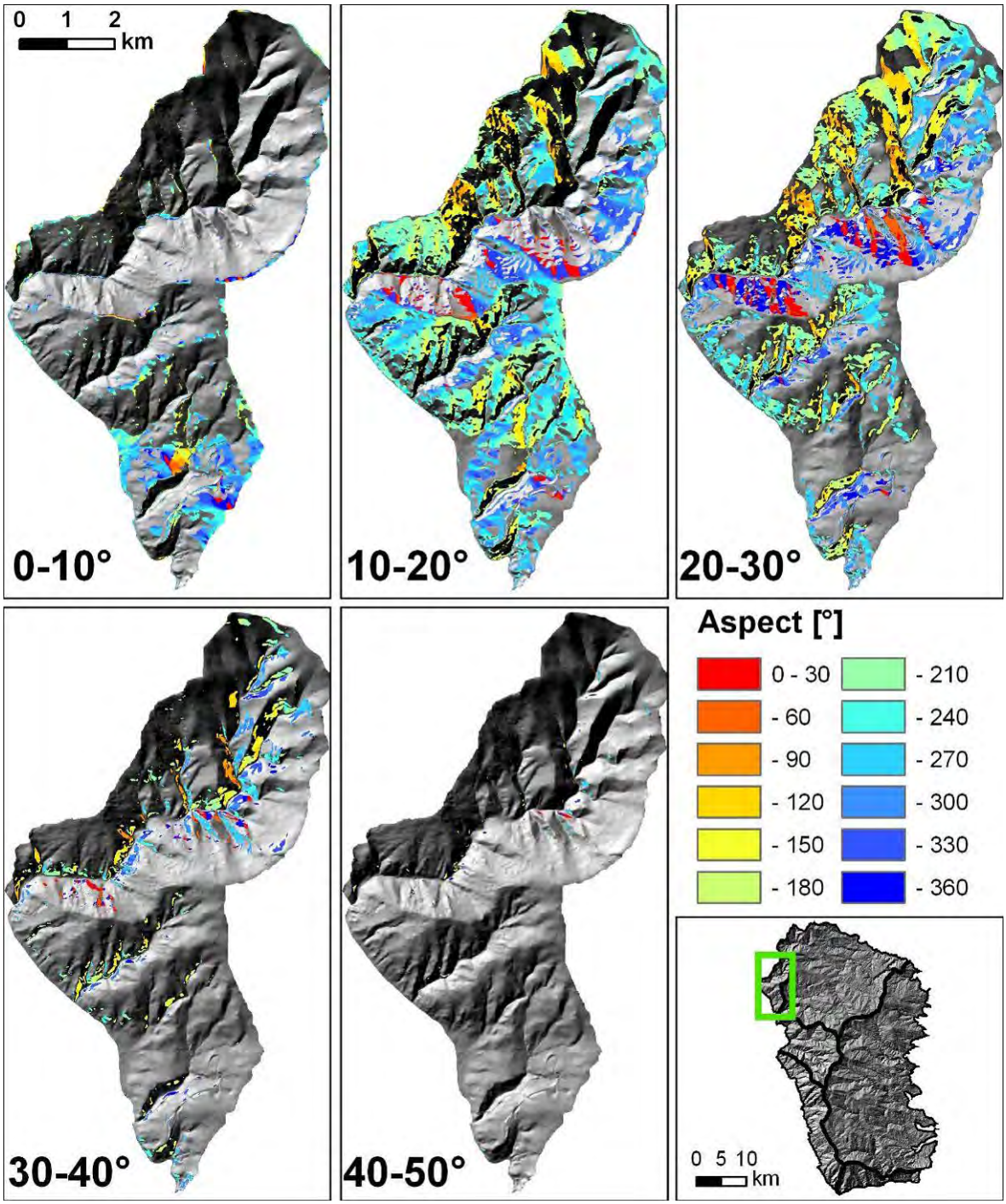

Figure 6-9: Slope aspect distribution for slope angles from 0° to 50° in morphounit Northwest.

Figure 6-10 (next page): Slope aspect distribution for slope angles from 0° to 50° in Morphounit Centralwest.

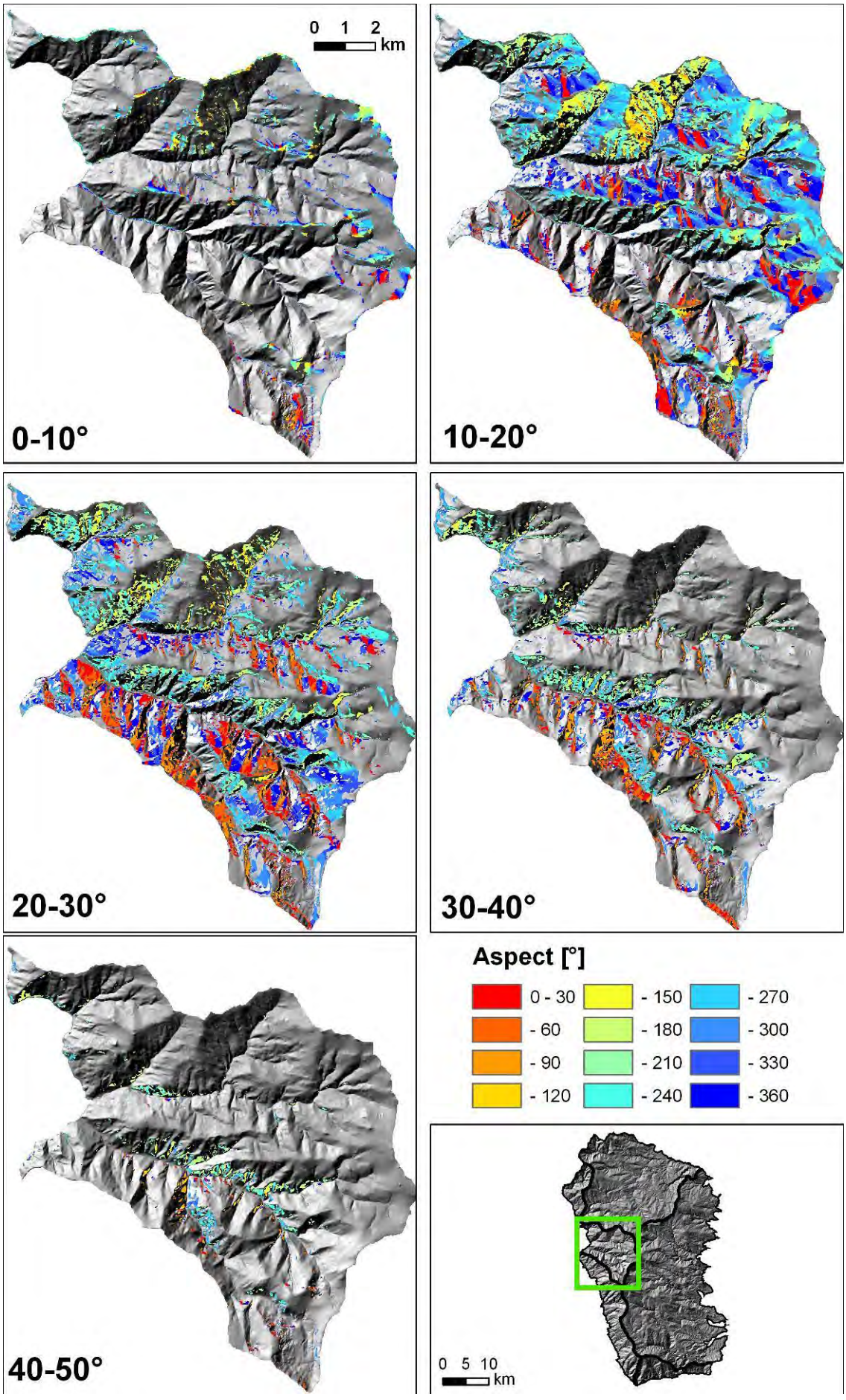
0 1 2
km
0-10°
10-20°
20-30°
30-40°
40-50°
Aspect [°]
0 - 30
- 60
- 90
- 120
- 150
- 180
- 210
- 240
- 270
- 300
- 330
- 360
0 5 10
km

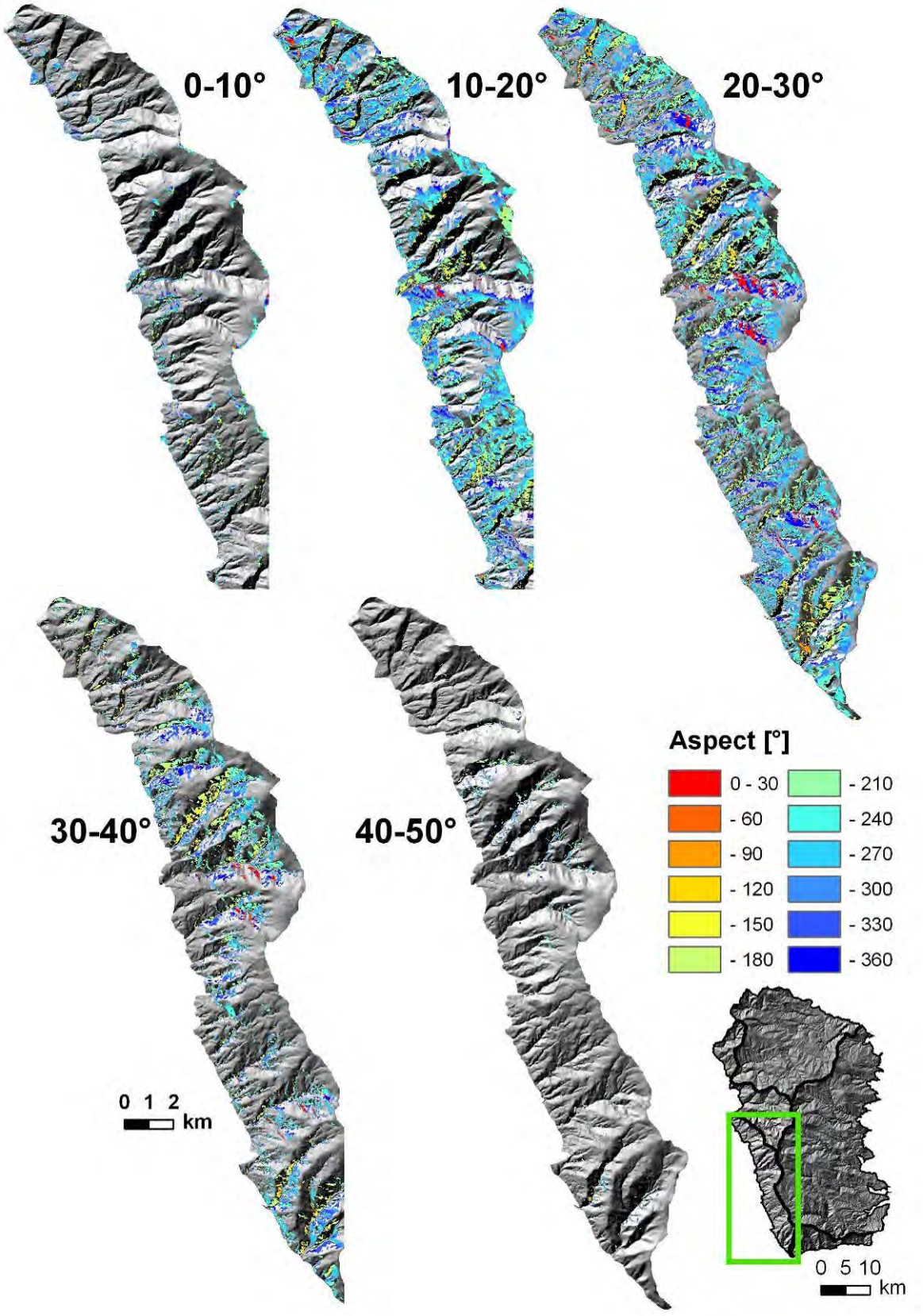

Figure 6-11: Slope aspect distribution for slope angles from 0° to 50° in Morphounit West.

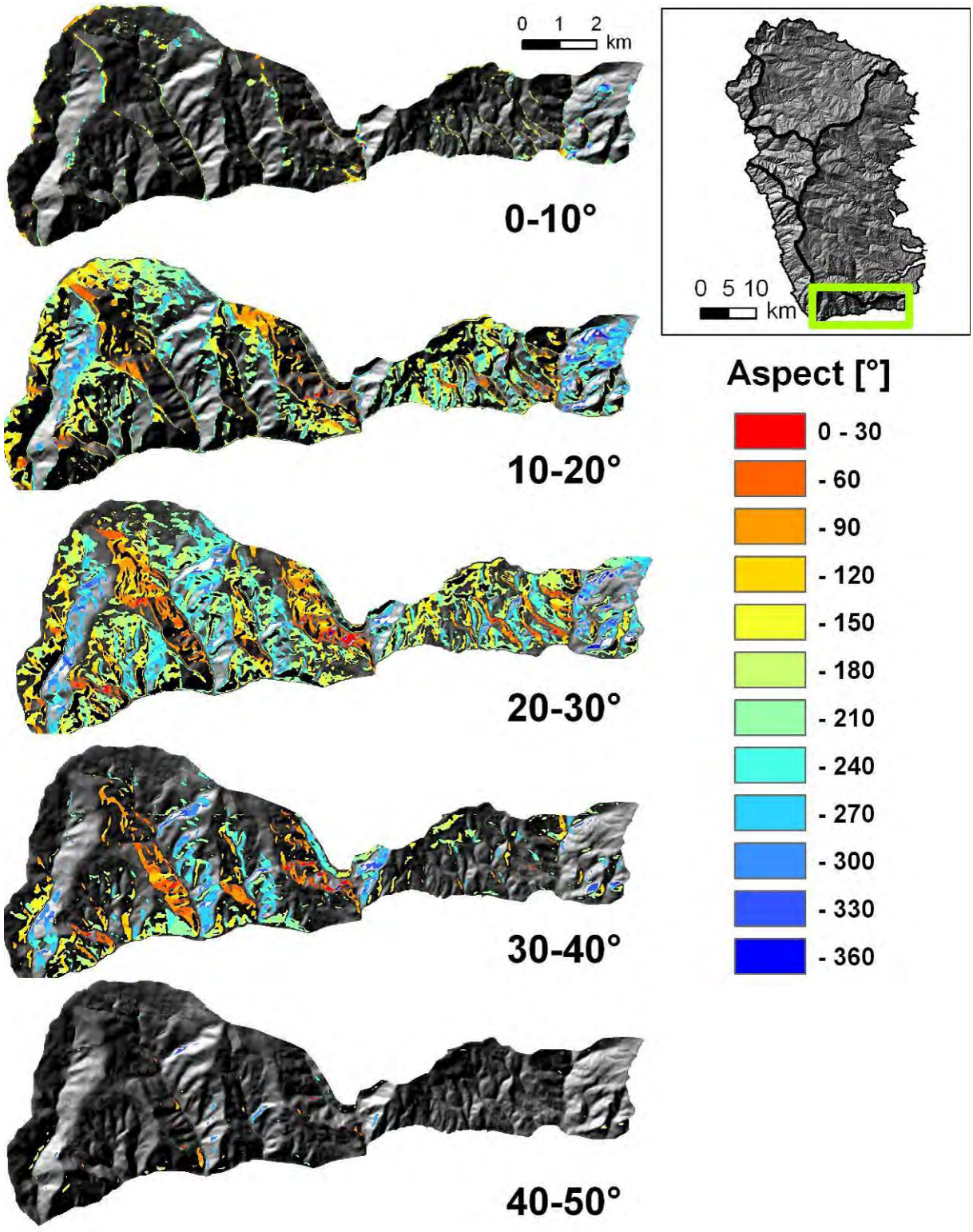

Figure 6-12: Slope aspect distribution for slope angles from 0° to 50° in Morphounit South.

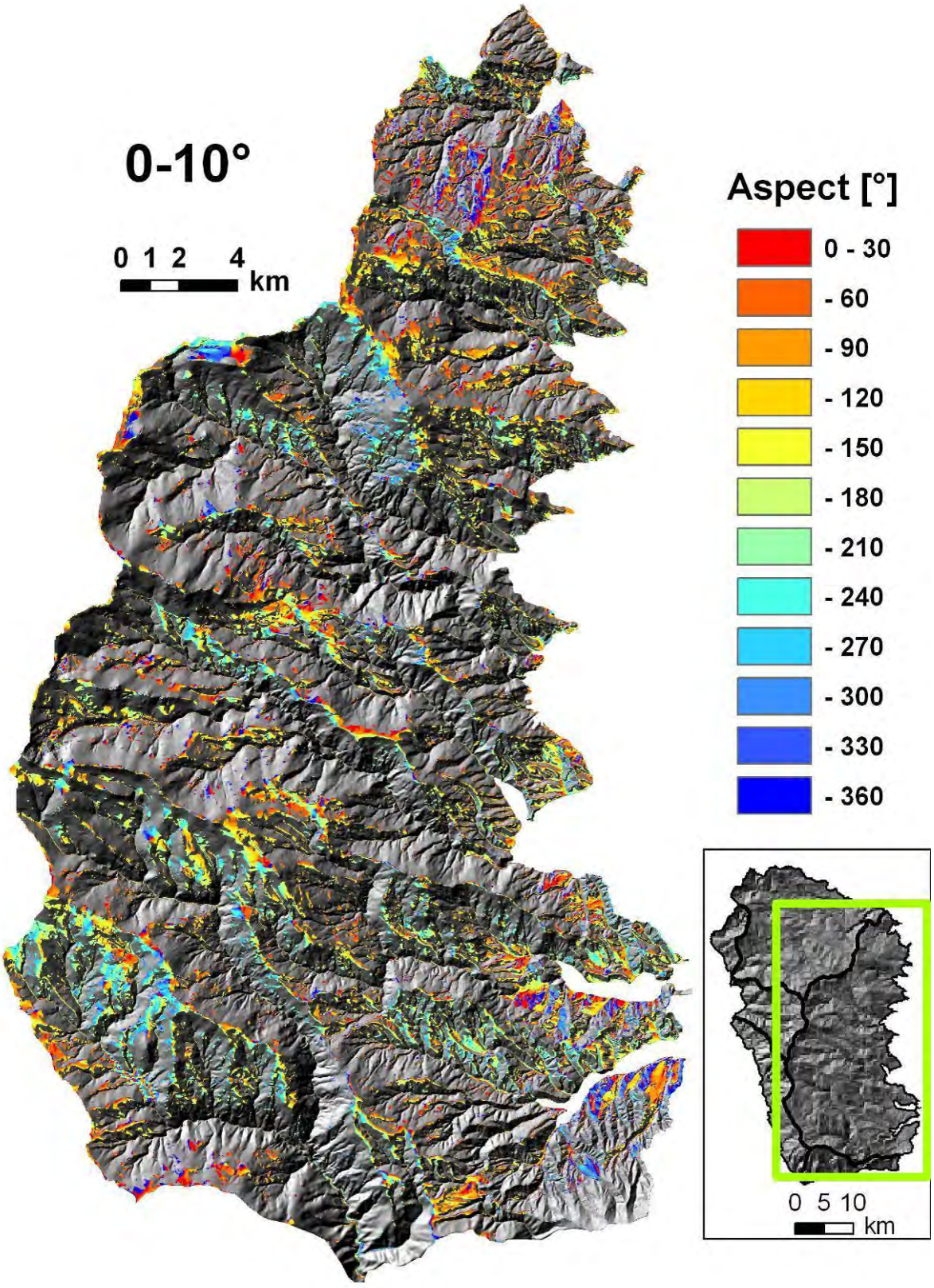

Figure 6-13 (a): Slope aspect distribution for slope angles from 0 to 10° in Morphounit East.

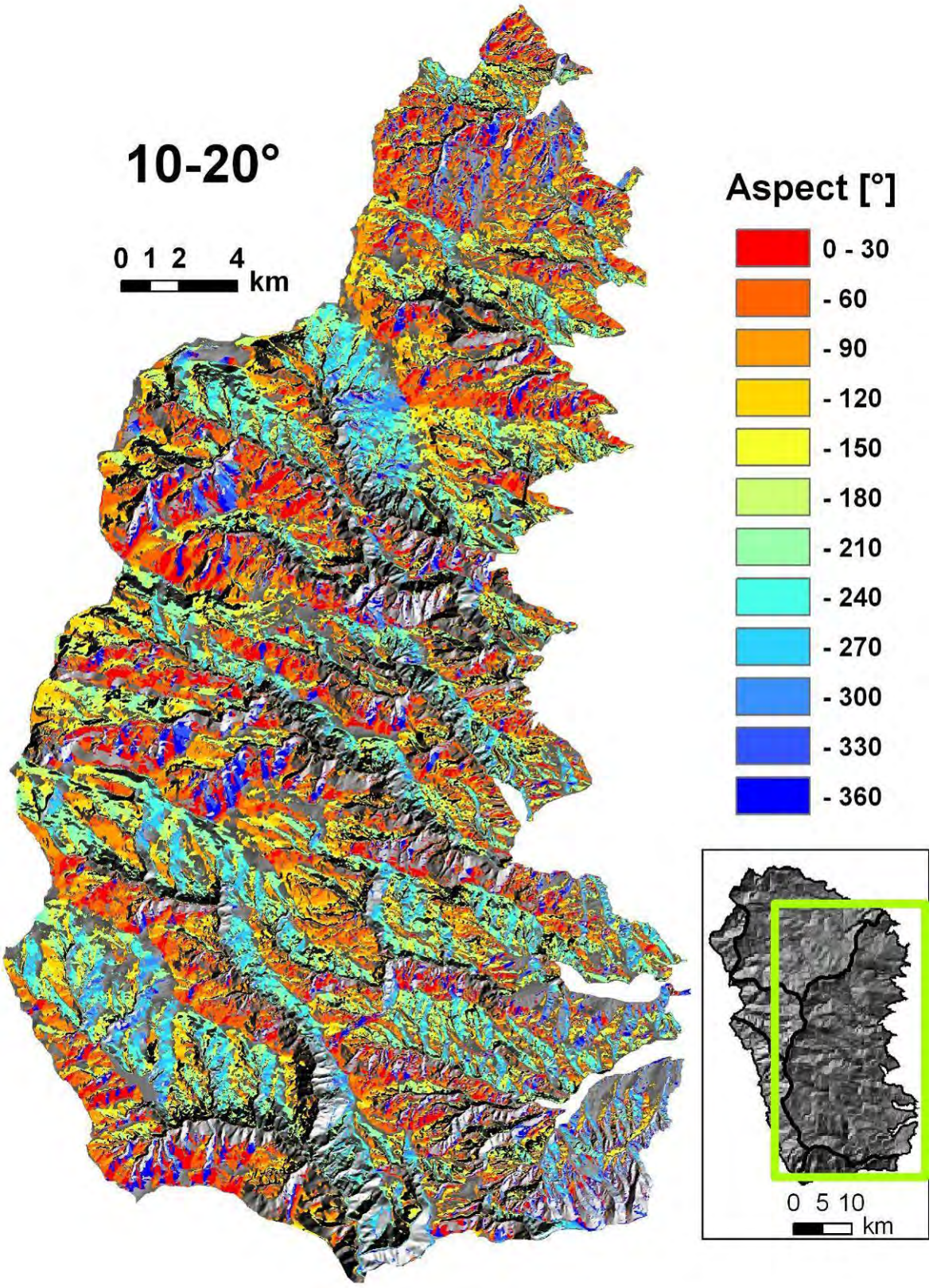

Figure 6-13 (b): Slope aspect distribution in Morphounit East for slope angles from 10 to 20°.

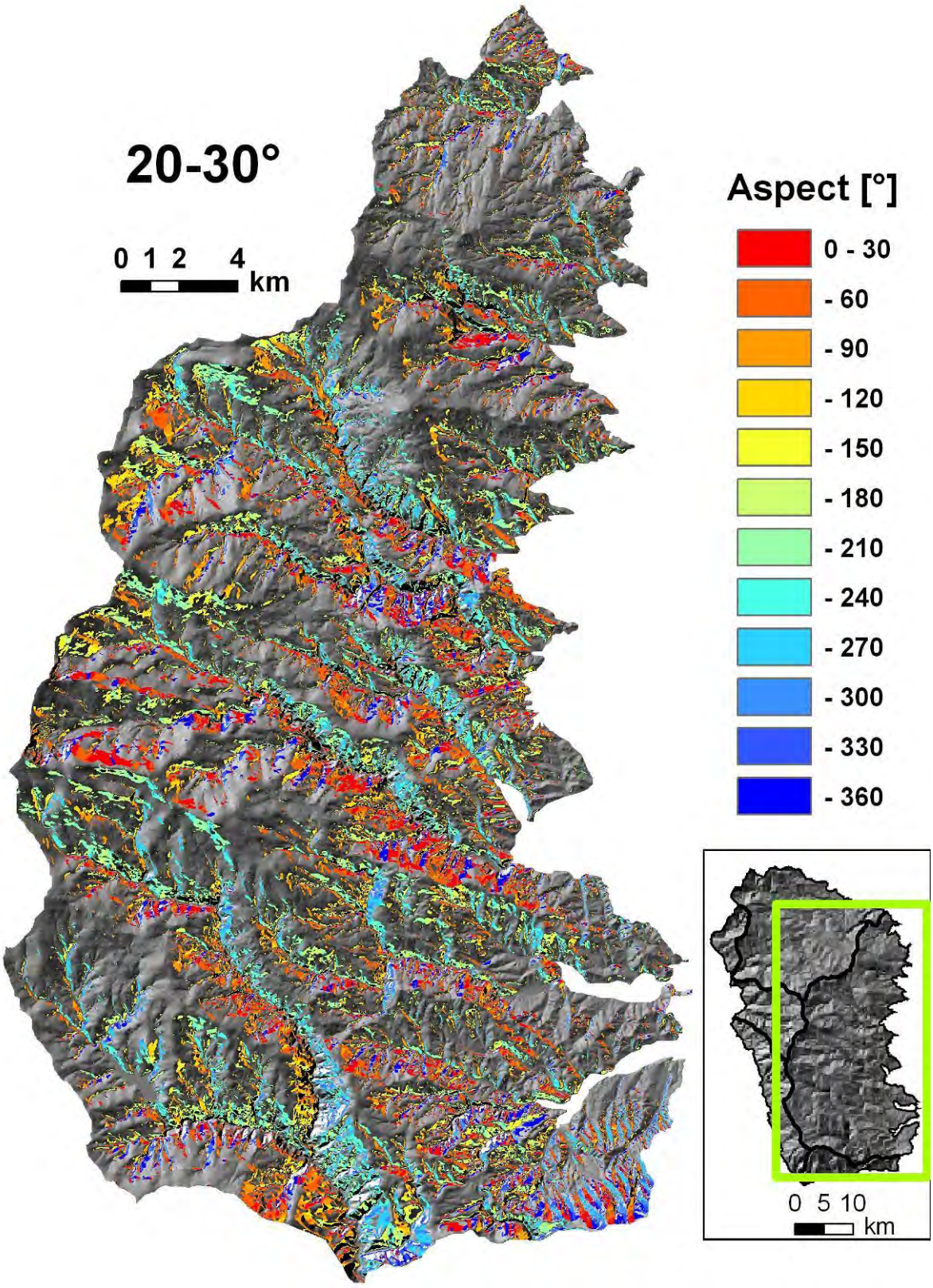

Figure 6-13 (c): Slope aspect distribution in Morphounit East for slope angles from 20 to 30°.

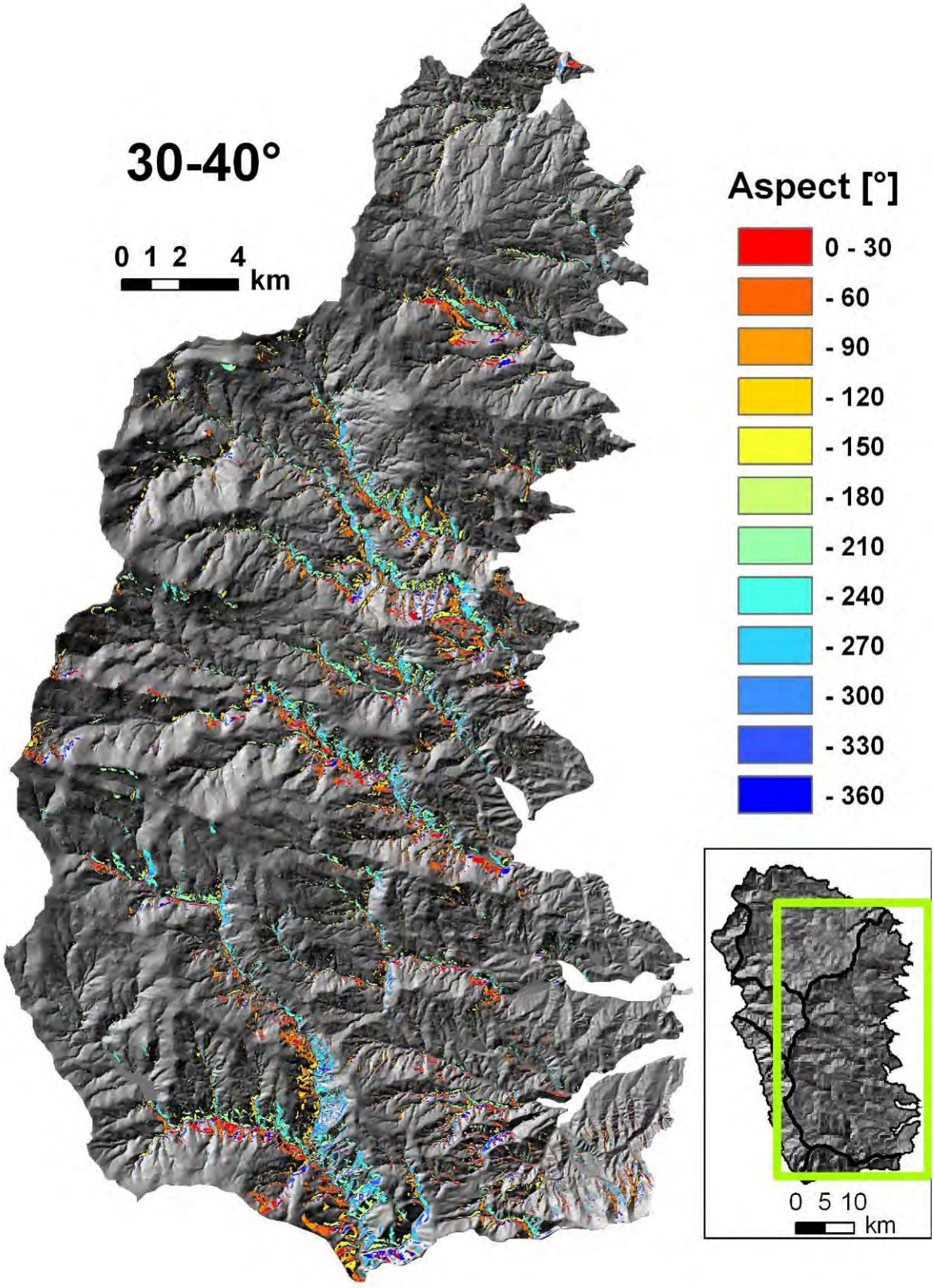

Figure 6-13 (d): Slope aspect distribution in Morphounit East for slope angles from 30 to 40°.

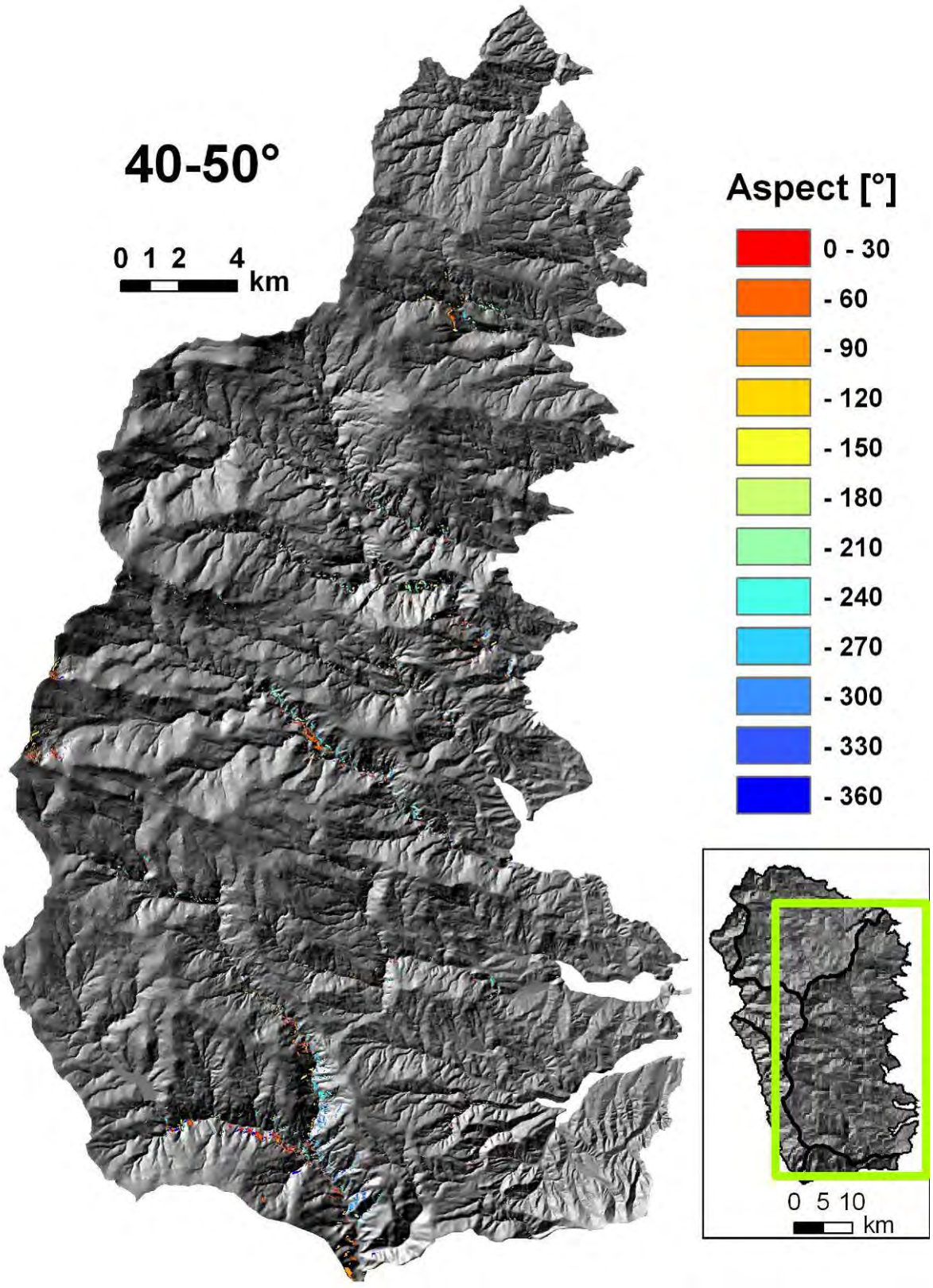

Figure 6-13 (e): Slope aspect distribution in Morphounit East for slope angles from 40 to 50°.

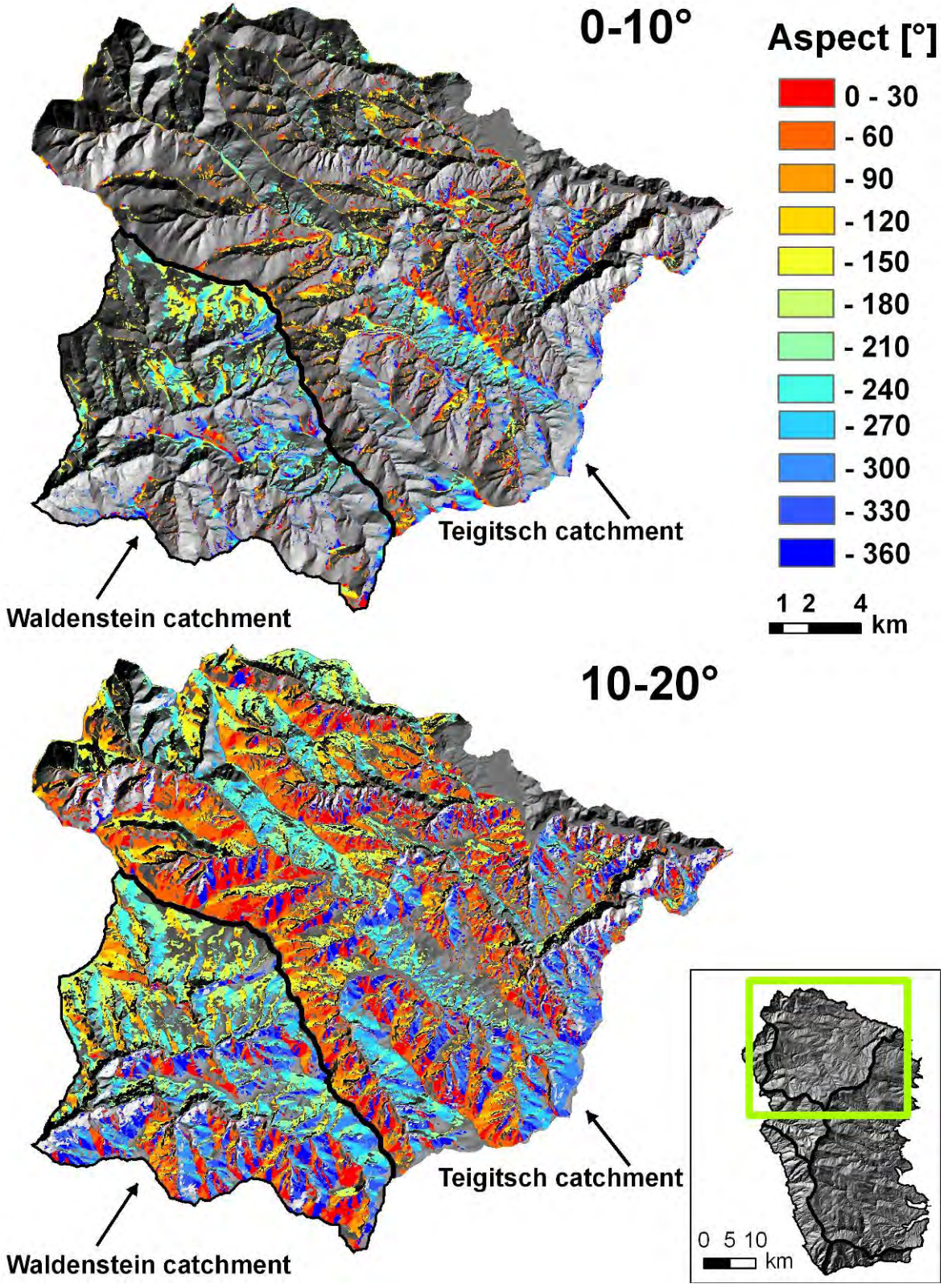

Figure 6-14 (a): Slope aspect distribution in Morphounit Northeast for slope angles from 0 to 10° and 10 to 20°.

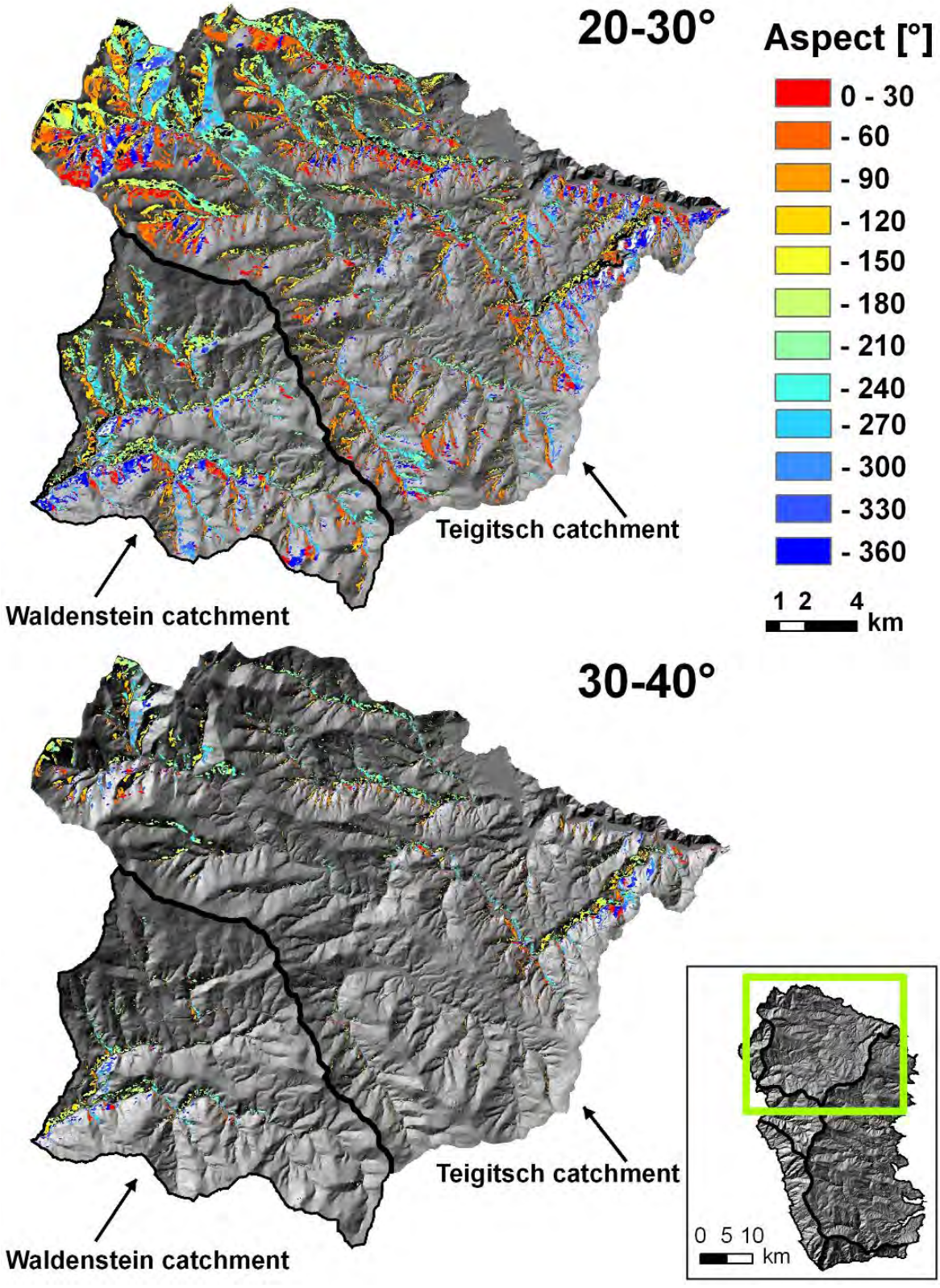

Figure 6-14 (b): Slope aspect distribution in Morphounit Northeast for slope angles from 20 to 30° and from 30 to 40°.

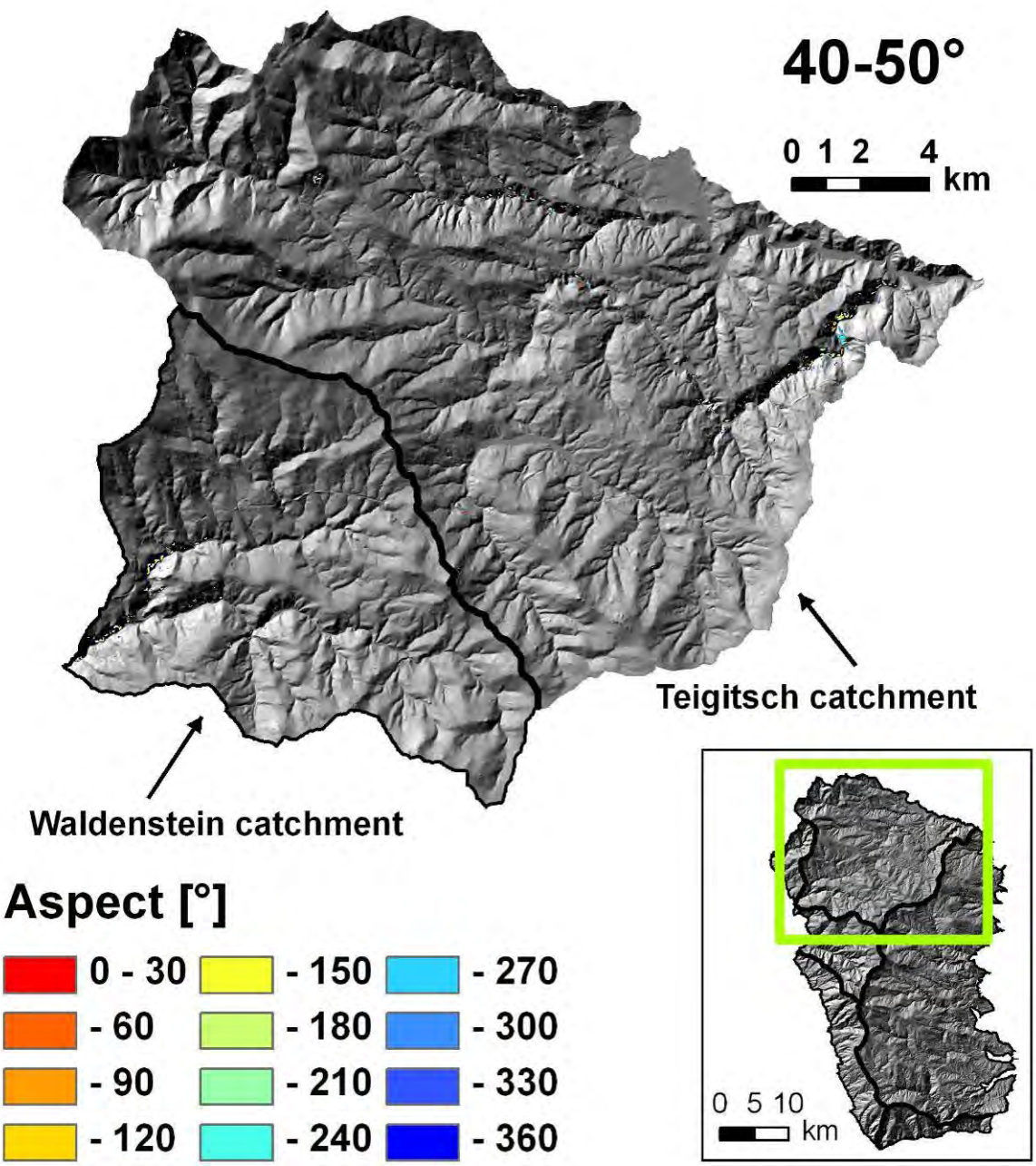

Figure 6-14 (c): Slope aspect distribution in Morphounit Northeast for slope angles from 40 to 50°. Data points are barely visible due to the low number of data. Data are located along the main drainage paths of the morphounit.

Catchmentname	A_b [km²]	L_c [km]	Strahler Order	Shreve Order	H_{min} [m]	H_{max} [m]	H_{mean} [m]	H_{sd} [m]	Relief [m]	H_i
Feistritz (Lavanttal)	23.58	11.31	4	174	732.4	1929.8	1272.2	255.4	1197.3	0.45
Lobnerbach	4.10	4.31	4	36	681.1	1490.5	1076.5	168.3	809.4	0.49
Ligistbach	21.88	7.15	5	163	398.5	1286.1	786.9	178.2	887.6	0.44
Mauterndorfbach	2.25	3.53	3	15	685.6	1386.6	977.8	150.0	701.1	0.42
Stainzbach	29.39	9.12	5	212	409.8	1463.6	998.4	277.7	1053.8	0.56
Greim-Gamsbach	9.68	5.63	4	66	438.9	1361.6	851.1	187.8	922.8	0.45
Wildbach	36.36	15.14	5	268	405.3	1549.7	950.0	250.0	1144.4	0.48
Weissenbach	4.88	4.04	4	48	480.1	1342.0	830.1	196.7	861.8	0.41
Paulebach	4.53	5.55	4	36	550.8	1752.3	1089.1	247.9	1201.5	0.45
Lassnitz	75.01	25.81	5	551	384.4	1853.8	1047.6	303.7	1469.4	0.45
Reidebnerbach	2.67	3.59	3	16	717.8	1825.0	1221.9	261.5	1107.3	0.46
Eitwegbach	4.81	5.04	4	45	678.7	2070.0	1363.8	324.4	1391.3	0.49
Stullneggbach	31.80	15.18	5	232	429.6	1725.2	907.4	213.5	1295.6	0.37
Gemmersdorferbach	6.26	6.05	4	51	677.6	2139.8	1439.5	394.7	1462.2	0.52
Kreuzerbach	3.11	5.26	3	22	676.6	2065.1	1230.3	325.3	1388.5	0.40
Seebach- Schwarze Sulm	75.30	24.87	5	612	409.4	2125.0	1147.5	408.1	1715.6	0.43
Ragglbach	11.41	7.44	4	94	571.3	2067.2	1203.4	352.7	1495.9	0.42
Rainzerbach	6.67	5.14	4	46	516.9	1758.2	1125.9	324.1	1241.3	0.49
Weissenbergerbach	1.88	4.01	2	10	483.0	1392.2	936.6	258.4	909.3	0.50
Weisse Sulm	45.82	17.99	5	301	361.6	1697.1	918.7	321.3	1335.5	0.42
Schwarzenbergerbach	2.74	4.69	3	16	435.5	1381.7	928.9	264.0	946.2	0.52
Ettendorfbach	5.86	4.52	4	42	417.6	1363.7	923.0	248.3	946.1	0.53
Haderniggbach	21.94	8.83	5	146	400.1	1183.4	728.1	174.8	783.3	0.42
Elbach	7.93	5.22	4	46	411.1	1414.6	989.9	232.6	1003.5	0.58
Multererbach	4.50	5.41	3	30	375.8	1446.9	961.4	256.3	1071.1	0.55
Krennbach	141.93	30.79	6	1037	354.1	2123.3	1155.0	375.1	1769.2	0.45
Woelblbach	10.33	6.32	4	81	404.9	1520.2	953.1	257.6	1115.3	0.49
Vratabach	4.36	4.21	4	32	366.4	1366.3	857.3	234.0	999.9	0.49
Velkabach	12.74	6.84	5	107	344.9	1513.5	972.4	270.4	1168.7	0.54
Ojstriskibach	7.70	6.67	3	57	379.6	1520.2	942.7	265.8	1140.7	0.49
Gössnitzbach	50.21	17.07	5	346	458.0	1703.1	984.6	295.5	1245.2	0.42
Radelski Bach	12.89	8.92	4	74	335.8	1017.2	681.3	160.7	681.4	0.51
Frei-Gössnitz	26.73	14.30	5	192	495.8	1652.2	1010.4	253.1	1156.4	0.44
Proessingbach	48.99	12.98	5	373	487.4	2140.0	1329.2	359.1	1652.6	0.51
Rassingbach	13.85	10.32	4	113	688.7	2140.0	1523.6	324.7	1451.3	0.58
Brandgraben	9.78	5.95	4	61	916.5	1865.3	1514.6	186.9	948.8	0.63
Falleggbach	9.50	8.63	4	72	456.6	1420.4	1011.1	216.1	963.8	0.58
Theussenbach	7.20	5.87	4	52	436.9	1362.4	964.9	223.3	925.5	0.57
Jovenbach	4.99	3.99	5	46	539.1	1270.9	1042.1	134.9	731.7	0.69
Fraßbach	36.35	12.77	5	266	491.4	1798.8	1212.4	244.8	1307.4	0.55
Waldensteinbach	108.83	21.70	6	746	601.2	1777.4	1171.0	205.9	1176.2	0.48
Auerlingbach	56.74	17.71	6	362	699.7	1777.4	1181.5	200.1	1077.6	0.45
Teigitsch	187.83	41.92	6	1356	379.1	1965.1	1113.4	308.9	1586.0	0.46
Schieflingbach	4.92	4.76	4	37	626.5	1280.2	876.4	114.6	653.6	0.38
Auenbach (Stmk.)	12.12	4.28	4	89	395.0	1052.0	610.1	137.8	656.9	0.33
Feistemitzbach	5.38	7.11	3	37	350.3	1052.9	558.4	161.7	702.6	0.30
Staritschbach	6.91	7.06	4	46	377.1	810.7	541.4	93.5	433.7	0.38
Mesnitzbach	9.17	6.43	4	68	370.6	1070.1	594.5	143.0	699.6	0.32
Streitbach	3.08	5.45	4	19	420.3	1150.6	683.6	150.5	730.3	0.36
Rainbach	4.20	5.04	4	31	407.5	1131.9	727.8	158.4	724.4	0.44
Luckerbach	2.65	3.77	3	16	465.1	849.3	707.0	73.6	384.2	0.63

A_b…Basin area, L_c…stream length, H_{min}…minimum elevation of basin,
H_{max}… maximum elevation of basin, H_{sd}…standard elevation of elevation, H_i…Hypsometric Integral,

Table 15: Basis properties of catchments in the realm of the Koralpe. Values are for the catchments truncated by the border of the basement rocks to the surrounding sedimentary basins.

Catchmentname	A_b [km²]	L_c [km]	Strahler Order	Shreve Order	H_{min} [m]	H_{max} [m]	H_{mean} [m]	H_{sd} [m]	Relief [m]	H_i
Roesslbach	5.65	3.66	4	37	471.78	806.92	703.51	71.20	335.13	0.69
Woellmissbach	4.08	4.79	3	30	398.28	795.21	638.84	91.14	396.93	0.61
Hunnesbach	4.49	5.75	4	34	385.08	953.87	608.57	139.89	568.79	0.39
Zachbach	6.95	7.84	4	41	390.76	1009.72	660.71	149.72	618.96	0.44
Lemsitz	5.56	6.21	3	39	395.93	1080.45	723.67	171.12	684.52	0.48
Parzgrabenbach	2.45	3.04	3	21	569.07	1424.59	1075.35	214.99	855.52	0.59
Berensteinerbach	2.78	3.44	4	22	528.38	1444.55	981.04	255.78	916.17	0.49
Gaichbach	1.11	2.83	3	6	526.36	1373.80	854.47	222.22	847.44	0.39
Gobelbach	1.59	3.77	3	11	549.61	1250.41	841.04	163.58	700.80	0.42
Riedingbach	3.35	5.37	3	22	503.68	1424.49	902.06	237.64	920.81	0.43
Hoellerbach	3.22	3.91	3	25	521.97	1413.47	949.28	237.31	891.50	0.48
Paninkbach	3.62	5.39	3	22	391.77	944.69	644.78	118.68	552.92	0.46
Bostjanbach	3.65	2.89	4	29	375.36	1261.77	798.87	189.12	886.41	0.48
Bethleitenbach	17.24	11.49	4	124	599.95	1853.71	1210.47	268.79	1253.76	0.49
Modriachbach	70.03	15.06	6	520	791.00	1517.48	1122.48	160.88	726.48	0.46
Goslitz	12.71	8.31	4	98	710.94	1768.25	1293.91	200.19	1057.31	0.55
Stierriegelbach	14.58	9.47	4	99	563.14	1450.59	981.16	203.62	887.45	0.47
Packerbach	25.50	12.11	5	191	865.39	1517.48	1176.96	164.45	652.09	0.48
Schwarze Sulm upstream	20.64	9.69	4	157	942.05	1955.47	1423.51	207.92	1013.42	0.48
Feistritzbach	62.93	17.07	5	434	491.79	1758.89	1202.46	206.96	1267.10	0.56

A_b…Basin area, L_c…stream length, H_{min}…minimum elevation of basin,

H_{max}… maximum elevation of basin, H_{sd}…standard elevation of elevation, H_i…Hypsometric Integral,

Table 15 (continued)

Table 16 (next page): Morphometric properties of catchments and streams of the Koralpe (this and previous page). Values are for the catchments truncated by the border of the basement rocks to the surrounding sedimentary basins.

Catchmentname	AF	AF_{mod}	L_a [km]	L_b [km]	CI	L_b/L_a	A_b/A_e	F	E_r
Feistritz (Lavanttal)	42.25	7.75	7.65	7.99	1.48	1.04	0.49	0.40	0.72
Lobnerbach	58.10	8.10	3.81	2.35	1.13	0.62	0.58	0.28	0.60
Ligistbach	41.40	8.60	5.45	7.15	1.31	1.31	0.72	0.74	0.97
Mauterndorfbach	72.11	22.11	3.14	1.60	1.12	0.51	0.57	0.23	0.54
Stainzbach	49.58	0.42	7.49	7.98	1.22	1.07	0.63	0.52	0.82
Greim-Gamsbach	43.61	6.39	4.71	3.22	1.20	0.68	0.81	0.44	0.75
Wildbach	46.62	3.38	10.23	8.54	1.48	0.83	0.53	0.35	0.66
Weissenbach	48.04	1.96	3.16	3.68	1.28	1.17	0.53	0.49	0.79
Paulebach	51.42	1.42	4.47	3.92	1.24	0.88	0.33	0.23	0.54
Lassnitz	75.16	25.16	16.26	10.45	1.59	0.64	0.56	0.28	0.60
Reidebnerbach	26.22	23.78	3.21	1.43	1.12	0.44	0.74	0.26	0.58
Eitwegbach	55.95	5.95	4.51	2.19	1.12	0.49	0.62	0.24	0.55
Stullneggbach	47.72	2.28	12.07	5.41	1.26	0.45	0.62	0.22	0.53
Gemmersdorferbach	59.76	9.76	4.93	3.49	1.23	0.71	0.46	0.26	0.57
Kreuzerbach	51.96	1.96	4.63	1.30	1.13	0.28	0.66	0.15	0.43
Seebach- Schwarze Sulm	48.62	1.38	16.88	15.05	1.47	0.89	0.38	0.26	0.58
Ragglbach	41.41	8.59	5.68	8.05	1.31	1.42	0.32	0.35	0.67
Rainzerbach	70.11	20.11	3.98	4.11	1.29	1.03	0.52	0.42	0.73
Weissenbergerbach	54.05	4.05	3.52	1.11	1.14	0.32	0.62	0.15	0.44
Weisse Sulm	68.87	18.87	12.84	11.83	1.40	0.92	0.38	0.28	0.59
Schwarzenbergerbach	48.30	1.70	3.88	1.30	1.21	0.34	0.69	0.18	0.48
Ettendorfbach	53.93	3.93	3.93	2.49	1.15	0.63	0.76	0.38	0.69
Haderniggbach	63.93	13.93	6.86	6.43	1.29	0.94	0.63	0.47	0.77
Elbach	46.85	3.15	3.86	5.20	1.35	1.35	0.50	0.53	0.82
Multererbach	47.16	2.84	4.52	2.33	1.20	0.52	0.55	0.22	0.53
Krennbach	67.37	17.37	22.28	10.52	1.38	0.47	0.76	0.29	0.60
Woelblbach	48.85	1.15	5.22	3.66	1.21	0.70	0.69	0.38	0.70
Vratabach	37.76	12.24	3.84	1.81	1.10	0.47	0.80	0.30	0.61
Velkabach	38.45	11.55	6.02	5.27	1.14	0.87	0.51	0.35	0.67
Ojstriskibach	54.22	4.22	5.86	2.57	1.14	0.44	0.65	0.22	0.53
Gössnitzbach	83.30	33.30	13.10	8.63	1.30	0.66	0.57	0.29	0.61
Radelski Bach	54.47	4.47	6.30	6.45	1.42	1.03	0.40	0.33	0.64
Frei-Gössnitz	61.54	11.54	11.06	6.90	1.29	0.62	0.45	0.22	0.53
Proessingbach	45.42	4.58	10.68	11.04	1.22	1.03	0.53	0.43	0.74
Rassingbach	42.96	7.04	7.99	3.82	1.29	0.48	0.58	0.22	0.53
Brandgraben	59.20	9.20	4.80	4.21	1.24	0.88	0.62	0.42	0.74
Falleggbach	53.79	3.79	6.59	3.76	1.31	0.57	0.49	0.22	0.53
Theussenbach	59.44	9.44	4.96	3.10	1.18	0.63	0.60	0.29	0.61
Jovenbach	63.53	13.53	3.28	3.42	1.22	1.04	0.57	0.46	0.77
Fraßbach	63.44	13.44	10.26	7.85	1.24	0.77	0.57	0.35	0.66
Waldensteinbach	68.95	18.95	12.35	22.22	1.76	1.80	0.51	0.71	0.95
Auerlingbach	37.20	12.80	9.21	17.80	1.92	1.93	0.44	0.67	0.92
Teigitsch	77.54	27.54	27.10	27.82	1.55	1.03	0.32	0.26	0.57
Schieflingbach	18.29	31.71	4.08	3.47	1.17	0.85	0.44	0.30	0.61
Auenbach (Stmk.)	66.19	16.19	3.32	7.93	1.29	2.39	0.59	1.10	1.18
Feistemitzbach	40.35	9.65	5.74	3.10	1.24	0.54	0.38	0.16	0.46
Staritschbach	28.68	21.32	5.71	2.16	1.24	0.38	0.71	0.21	0.52
Mesnitzbach	49.86	0.14	5.37	3.54	1.20	0.66	0.62	0.32	0.64
Streitbach	48.13	1.87	4.50	2.07	1.21	0.46	0.42	0.15	0.44
Rainbach	60.93	10.93	4.47	2.06	1.13	0.46	0.58	0.21	0.52
Luckerbach	76.01	26.01	3.22	2.81	1.17	0.87	0.37	0.26	0.57

AF...Basin asymmetry factor (Hare & Gardner, 1984); AF_{mod}…basin asymmetry recalculated to a value range of 0 (symmetric) to 50 (asymmetric); L_a…axis of basin ellipse = length of straight line connecting stream pour point and origin (projected to watershed); L_b...axis of ellipse defined by maximum width of basin along the line normal to L_a; CI...channel index (Mueller, 1968) where $CI=L_c/L_a$; L_b/L_a…basin axes ratio or ellepticity index (Stoddard, 1965); A_b/Ae…basin ellipse ratio where A_b=basin area and A_e=area of basin ellipse defined by l_a and l_b; F…form factor (Horton, 1932) where $F=A_b/L_a$^2; E_r…elongation ratio (Schumm, 1956) where E_r= diameter of circle of the same size as the basin/L

Catchmentname	AF	AF_{mod}	L_a [km]	L_b [km]	CI	L_b/L_a	A_b/A_e	F	E_r
Roesslbach	53.64	3.64	3.24	3.38	1.13	1.04	0.66	0.54	0.83
Woellmissbach	54.01	4.01	3.92	2.34	1.22	0.60	0.57	0.27	0.58
Hunnesbach	44.69	5.31	4.47	2.02	1.29	0.45	0.63	0.22	0.53
Zachbach	36.40	13.60	4.76	4.97	1.65	1.04	0.37	0.31	0.62
Lemsitz	55.09	5.09	5.35	2.56	1.16	0.48	0.52	0.19	0.50
Parzgrabenbach	26.39	23.61	2.61	1.60	1.16	0.61	0.75	0.36	0.68
Berensteinerbach	55.39	5.39	2.99	1.91	1.15	0.64	0.62	0.31	0.63
Gaichbach	45.37	4.63	2.60	0.77	1.09	0.30	0.71	0.16	0.46
Gobelbach	51.04	1.04	3.32	1.22	1.14	0.37	0.50	0.14	0.43
Riedingbach	43.22	6.78	4.13	1.58	1.30	0.38	0.65	0.20	0.50
Hoellerbach	76.74	26.74	3.51	1.63	1.11	0.46	0.72	0.26	0.58
Paninkbach	36.32	13.68	3.98	1.75	1.35	0.44	0.66	0.23	0.54
Bostjanbach	72.69	22.69	2.67	2.93	1.08	1.10	0.59	0.51	0.81
Bethleitenbach	70.88	20.88	8.51	3.93	1.35	0.46	0.66	0.24	0.55
Modriachbach	20.28	29.72	10.94	12.76	1.38	1.17	0.64	0.59	0.86
Goslitz	71.44	21.44	6.44	3.55	1.29	0.55	0.71	0.31	0.62
Stierriegelbach	58.85	8.85	5.82	7.91	1.63	1.36	0.40	0.43	0.74
Packerbach	46.78	3.22	7.68	8.14	1.58	1.06	0.52	0.43	0.74
Schwarze Sulm upstream	39.76	10.24	7.39	8.51	1.31	1.15	0.42	0.38	0.69
Feistritzbach	42.95	7.05	12.80	10.41	1.33	0.81	0.60	0.38	0.70

AF...Basin asymmetry factor (Hare & Gardner, 1984); AF_{mod}…basin asymmetry recalculated to a value range of 0 (symmetric) to 50 (asymmetric); L_a…axis of basin ellipse = length of straight line connecting stream pour point and origin (projected to watershed); L_b...axis of ellipse defined by maximum width of basin along the line normal to L_a; CI...channel index (Mueller, 1968) where CI=L_c/L_a; L_b/L_a…basin axes ratio or ellepticity index (Stoddard, 1965); A_b/Ae…basin ellipse ratio where A_b=basin area and A_e=area of basin ellipse defined by l_a and l_b; F…form factor (Horton, 1932) where F=A_b/L_a^2; E_r…elongation ratio (Schumm, 1956) where E_r= diameter of circle of the same size as the basin/L

Table 16 (continued)

ID	Name	A [km²]	L [km]	Strahler	Shreve	C_A	H_{max} [m]	H_{min} [m]	Relief [m]	Morpho unit	Subbasin to
1	Lavant	972.5	77.2	7	5301	0.68	2280.2	339.3	1941.0	Lavant	Drau
2	Feistritz (Lavanttal)	24.4	12.9	4	180	0.44	1925.4	681.1	1244.3	NW	Lavant
3	Lobnerbach	4.1	4.5	4	36	0.20	1424.8	661.3	763.5	NW	Lavant
4	Mauterndorfbach	2.6	4.4	3	18	0.27	1350.6	640.2	710.4	NW	Lavant
5	Schieflingbach	4.9	4.8	4	37	0.44	1225.7	627.1	598.6	NW	Lavant
6	Gössnitzbach	82.6	27.1	5	598	0.53	1617.0	381.0	1236.0	NE	Teigitsch
7	Frei Gössnitz	26.7	14.3	5	192	0.39	1652.0	495.0	1157.0	NE	Gössnitzbach
8	Teigitsch	273.3	45.0	6	1976	0.47	1585.0	363.0	1222.0	NE	Kainach
9	Auerlingbach	56.7	17.7	6	362	0.55	1751.4	699.7	1051.7	NE	Lavant
10	Waldensteinbach	108.8	21.7	6	746	0.26	1649.1	601.0	1048.1	NE	Lavant
11	Packerbach	25.5	12.1	5	191	0.39	1364.5	790.9	573.6	NE	Modriachbach
12	Modriachbach	70.0	15.1	6	520	0.52	1416.0	791.0	625.0	NE	Teigitsch
13	Jovenbach	5.0	4.0	3	5	-0.05	1157.5	535.5	622.0	CW	Lavant
14	Fraßbach	36.4	12.8	5	266	0.12	1608.9	491.0	1117.9	CW	Lavant
15	Proessingbach	49.0	13.0	5	373	0.42	1971.7	487.4	1484.3	CW	Lavant
16	Rassingbach	13.9	10.3	4	113	-0.05	2109.5	684.8	1424.7	CW	Proessingbach
17	Brandgraben	9.8	6.0	4	61	-0.05	1665.3	916.4	748.8	CW	Proessingbach
18	Auenbach (Lavanttal)	27.0	13.9	5	222	0.55	1470.7	463.0	1007.7	W	Lavant
19	Weissenbach	8.0	6.1	5	79	0.49	1189.7	431.0	758.7	W	Lavant
20	Paulebach	16.4	9.4	4	124	0.50	1700.2	421.6	1278.5	W	Lavant
21	Reidebnerbach	18.7	12.1	5	121	0.61	1751.2	398.1	1353.1	W	Lavant
22	Eitwegbach	19.7	11.4	5	138	0.50	2069.6	405.6	1664.0	W	Lavant
23	Gemmersdorferbach	20.0	14.0	4	143	0.50	2040.1	384.4	1655.7	W	Lavant
24	Kreuzerbach	7.3	9.8	3	45	0.46	2011.1	415.3	1595.7	W	Gemmersdorferb.
25	Ragglbach	16.5	13.4	4	130	0.50	2054.4	377.7	1676.7	W	Lavant
26	Rainzerbach	28.9	10.2	6	210	0.48	1489.3	367.3	1122.0	W	Lavant
27	Weissenbergerbach	8.4	6.4	4	49	0.36	1355.7	359.8	995.9	W	Lavant
28	Schwarzenbergerbach	3.3	5.6	3	20	0.15	1359.4	370.8	988.5	W	Weissenbergerb.
29	Ettendorfbach	6.1	5.5	4	42	0.30	1312.8	359.6	953.2	W	Lavant
30	Elbach	8.1	5.9	4	46	0.23	1381.5	354.6	1026.9	W	Lavant
31	Multererbach	4.6	5.7	3	30	0.12	1425.1	341.0	1084.0	W	Drau
32	Woelblbach	10.9	7.8	4	86	0.29	1478.5	339.0	1139.6	W	Drau
33	Ligistbach	33.9	10.7	5	262	0.48	950.1	353.1	597.0	E	Kainach
34	Falleggbach	9.5	8.6	4	72	0.06	1339.1	456.6	882.5	E	Stainzbach
35	Stainzbach	73.2	17.4	6	542	0.56	1463.5	323.5	1140.0	E	Lassnitz
36	Theussenbach	7.2	5.9	4	52	0.15	1093.5	430.0	663.5	E	Stainzbach
37	Greim-Gamsbach	20.0	13.4	4	143	0.55	1063.9	327.0	736.9	E	Lassnitz
38	Wildbach	70.9	22.8	5	537	0.53	1446.5	326.7	1119.9	E	Lassnitz
39	Lassnitz	86.3	32.2	5	648	0.48	1625.2	323.7	1301.6	E	Sulm
40	Bethleitenbach	17.2	11.5	4	124	0.28	1852.8	599.4	1253.4	E	Lassnitz
41	Stullneggbach	39.0	23.8	5	281	0.54	1603.8	345.4	1258.4	E	Sulm
42	Seebach- Schwarze Sulm	89.4	31.5	5	726	0.46	2071.3	345.1	1726.2	E	Sulm
43	SchwarzeSulm upstream	20.6	9.7	4	157	0.30	1960.7	939.5	1021.2	E	Seebach-SSulm
44	Gosslitz	12.7	8.3	4	98	0.18	1767.8	710.9	1056.8	E	Seebach-SSulm
45	Weisse Sulm	72.4	24.2	5	517	0.50	1597.9	325.6	1272.3	E	Sulm
46	Stierriegelbach	14.6	9.5	4	99	0.18	1438.5	563.1	875.4	E	Weisse Sulm
47	Haderniggbach	64.0	16.0	5	446	0.65	1109.0	338.0	771.0	E	Sulm
48	Krennbach	147.6	33.7	6	1086	0.39	2040.1	311.8	1728.3	S	Drau
49	Feistritzbach	62.9	17.1	5	434	0.13	1451.2	491.1	960.1	S	Krennbach
50	Ojstriskibach	7.8	7.1	3	57	0.25	1517.8	341.6	1176.2	S	Drau
51	Velkabach	12.8	6.9	5	107	0.25	1414.4	339.6	1074.8	S	Drau
52	Vratabach	4.4	4.5	4	32	0.18	1346.0	327.6	1018.4	S	Drau
53	Radelski Bach	13.4	9.7	4	78	0.24	1005.7	330.5	675.2	S	Drau

Table 17: Longitudinal river profiles and some of their properties, sorted according to the morphological units. Data are for the streams not clipped to the basement rocks.
A… catchment size, L….length of reach, C_A…normalized concavity index, H_{max}, H_{min}… maximum resp. minimum elevation of reach

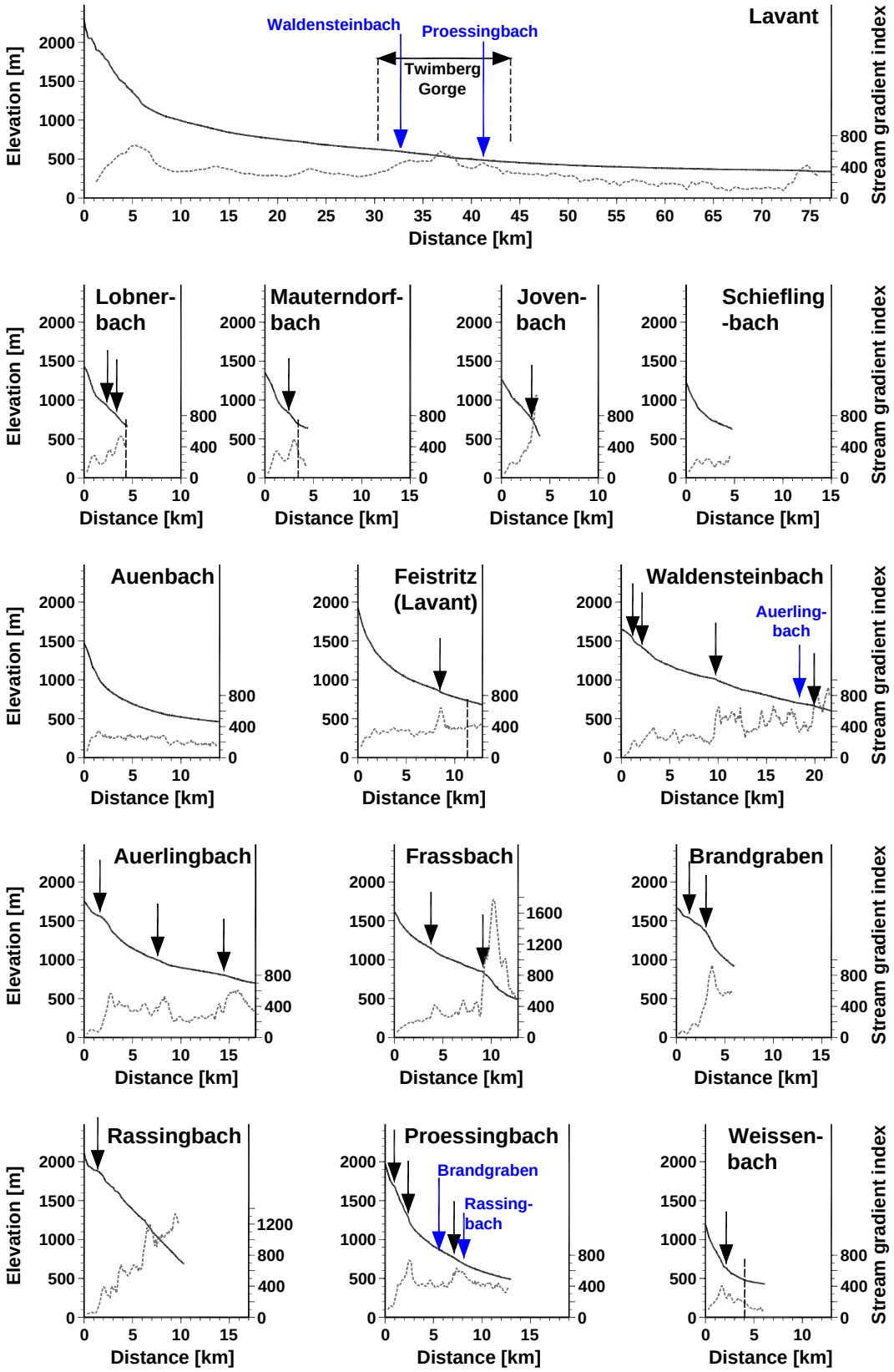

Figure 6-15: Longitudinal stream profiles (8 x vertical exaggeration, solid black lines) and stream gradient index (dashed grey lines, after Hack 1973) for 55 streams of the Koralpe. Black arrows indicate river knickpoints identified in the profiles by visual interpretation. Blue arrows indicate junction with major tributaries. Black, dashed lines show border between crystalline and sedimentary rocks.

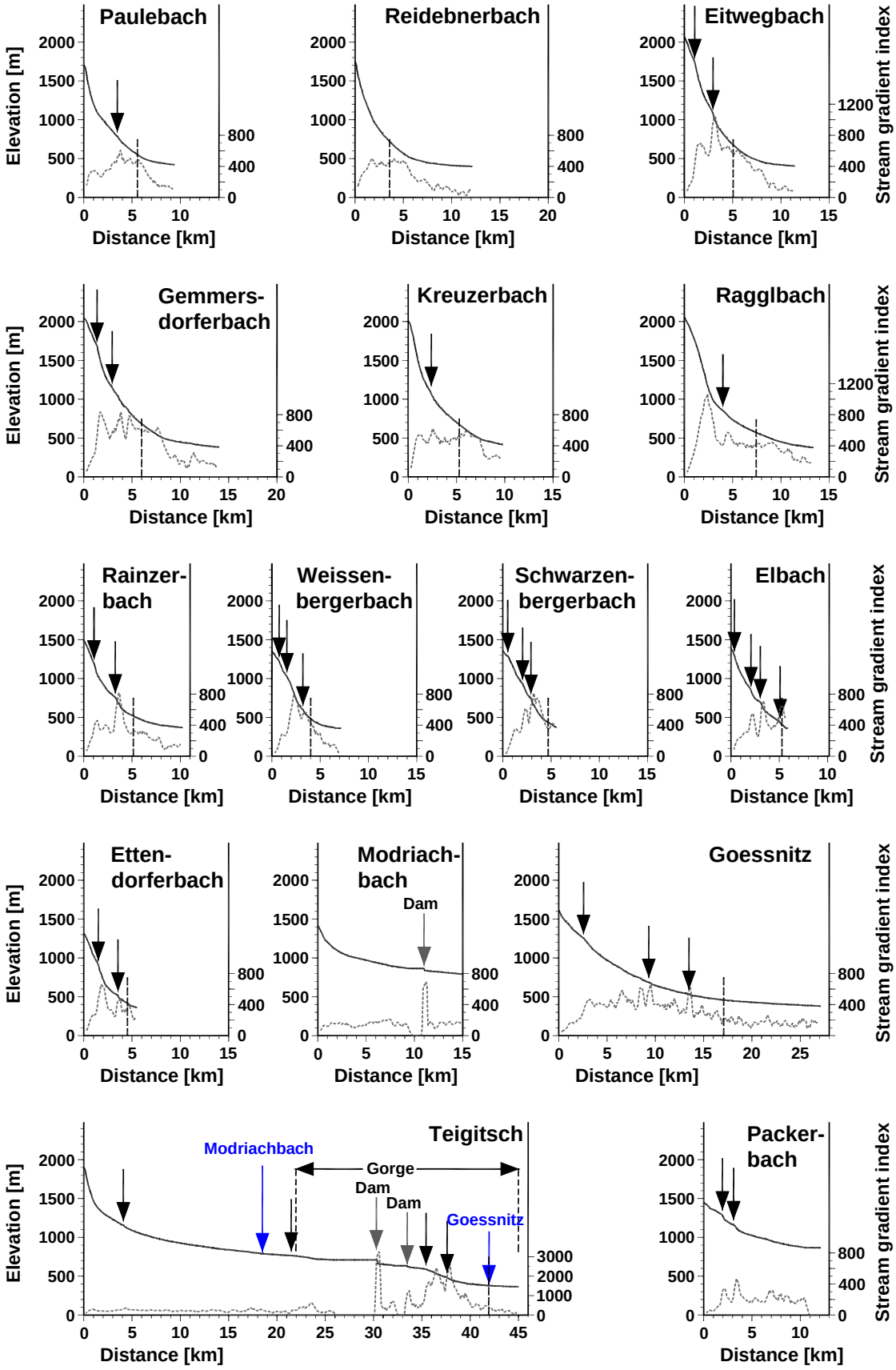

Figure 6-15 (continued)

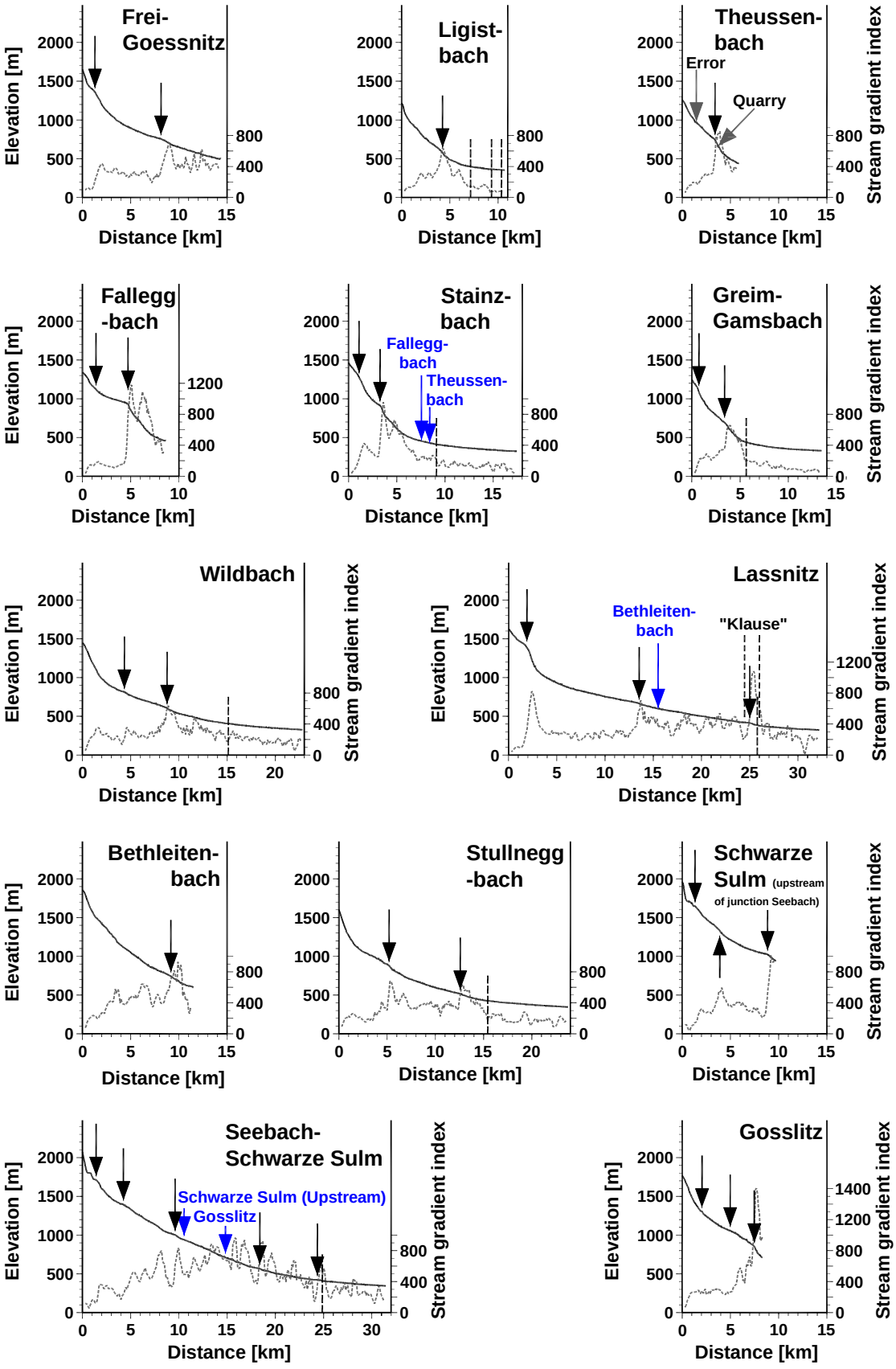

Figure 6-15 (continued)

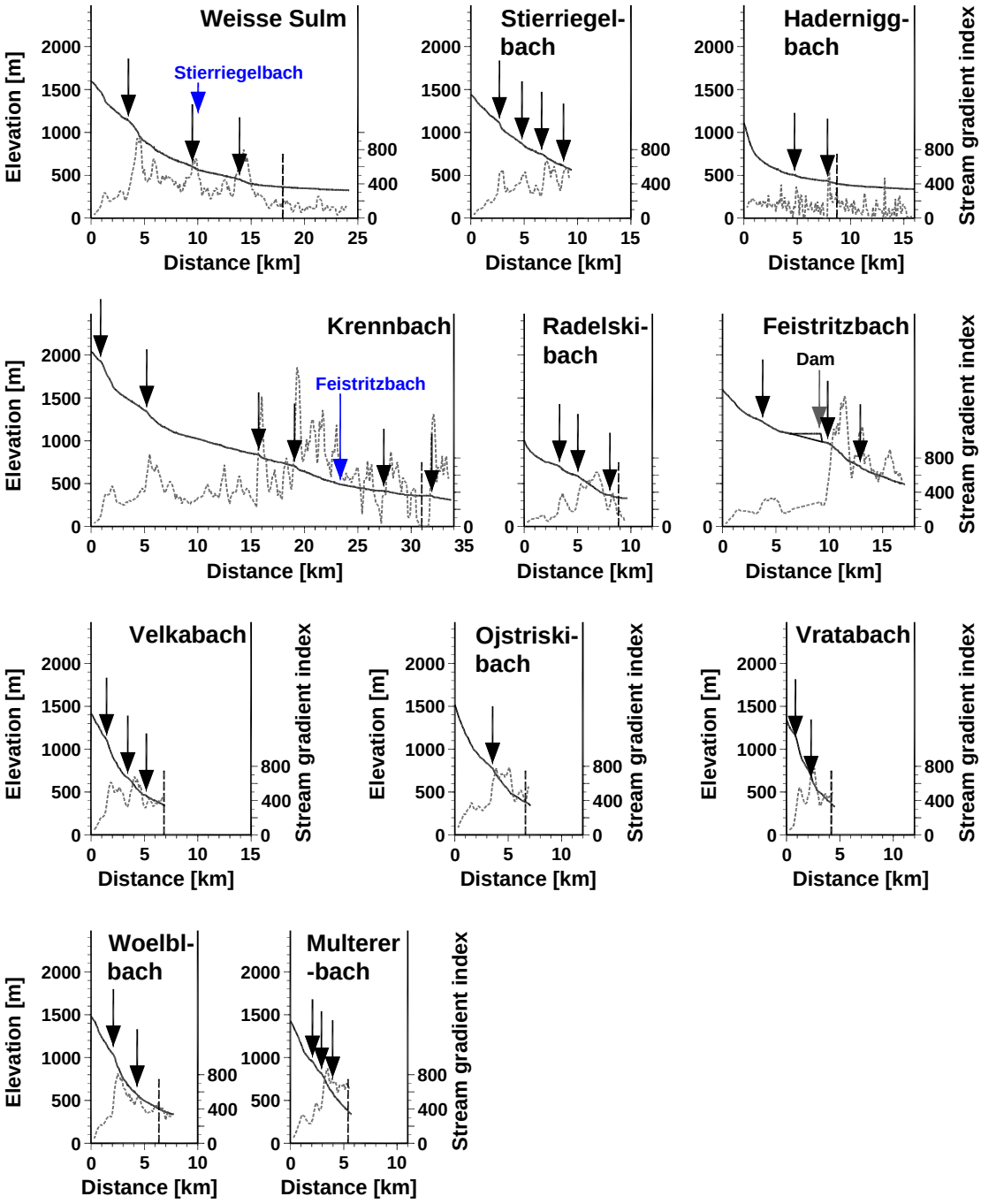

Figure 6-15 (continued)

Stream	Easting [m]	Northing [m]	Altitude [m]	Distance [m]		Region	Cause	Lithology	Comment
				from mouth	to fault				
Packerbach	651150.00	198590.00	1287.73	10998.92	Unknown	Northeast	Unknown	Gneissic mica schist	
Packerbach	650780.00	199430.00	1162.76	9812.94	Unknown	Northeast	Unknown	Quarzitic gneiss	Situated in area with changing dip directions
Goessnitz	645260.00	216730.00	1253.78	24518.01	Unknown	Northeast	Unknown	Gneiss	
Goessnitz	650820.00	214740.00	689.56	17784.02	Unknown	Northeast	Unknown	Gneiss	Change in dip direction?
Goessnitz	652910.00	212400.00	536.31	13634.71	Unknown	Northeast	Lithology?	Gneiss	Next to Pegmatite
Frei-Goessnitz	648780.00	212150.00	755.43	6148.93	Unknown	Northeast	Unknown	Gneissic mica schist	Pegmatitic
Frei-Goessnitz	644410.00	215210.00	1359.65	12998.31	Unknown	Northeast	Unknown	Gneissic mica schist	Pegmatitic
Teigitsch	639880.00	212970.00	1154.85	40926.48	Unknown	Northeast	Unknown	Gneiss	
Teigitsch	650660.00	209320.00	766.30	23548.77	Unknown	Northeast	Unknown	Gneiss	
Teigitsch	657780.00	206830.00	589.75	10454.57	740	Northeast	Unknown	Gneissic mica schist	Changes in lithology, foldstructures?
Teigitsch	659470.00	207480.00	485.34	7412.48	Unknown	Northeast	Unknown	Gneissic mica schist	166m from litho border, change in drainage direction
Ligistbach	661630.00	205460.00	577.69	6430.47	Unknown	Northeast	Unknown	Mylonite ("Plattengneis")	
Theussenbach	662030.00	197360.00	748.49	2490.16	<400	East	Lithology	Mylonite ("Plattengneis")	Next to quarry
Falleggbach	661180.00	200710.00	929.17	3896.61	Unknown	East	Lithology	Gneiss	At border Plattengneiss/Hirscheggergneis
Falleggbach	659050.00	202070.00	1124.34	7227.52	Unknown	East	Unknown	Slope debris	
Stainzbach	660010.00	199450.00	915.42	14165.50	Unknown	East	Lithology	Mylonite ("Plattengneis")	
Stainzbach	658184.48	199975.65	1279.57	16339.50	Unknown	East	Unknown	Slope debris	
Greim-Gamsbach	662560.00	194070.00	698.50	10089.24	<450	East	Structure?	Mylonite ("Plattengneis")	Directly in prolongation of fault
Greim-Gamsbach	660480.00	194990.00	1138.73	12849.49	Unknown	East	Unknown	Slope debris	
Wildbach	658480.00	192600.00	605.98	14020.38	>1000m	East	Unknown	Mylonite ("Plattengneis")	In vicinity of pegmatites, strike of foliation parallel to river
Wildbach	657190.00	195670.00	814.74	18452.41	Irrelevant	East	Lithology	Quarzitic gneiss	Situated in resistant lithology
Lassnitz	650440.00	195750.00	1418.58	30471.88	Irrelevant	East	Lithology	Quarzitic gneiss	Knickpoint in Waldensteinbach in 800m distance, same lithological border, old mining activity?
Lassnitz	657730.00	191580.00	667.11	18673.60	550	East	Base level?	Mylonite ("Plattengneis")	Next to border to Quarzitic gneiss
Lassnitz	663210.00	186490.00	405.66	6963.90	12	East	Lithology?	Mylonitic Gneiss	Situated in more resistant lithology near the border to mica schist
Bethleitenbach	657240.00	189760.00	744.88	2317.44	Irrelevant	East	Base level	Mylonite ("Plattengneis")	Appr. same distance from junction with Lassnitz as knickpoint in Lassnitz
Stullneggbach	656490.00	187180.00	879.30	18534.31	25	East	Unknown	Quarzitic gneiss	260m from Pegmatite
Stullneggbach	661350.00	184660.00	517.40	11167.65	26	East	Unknown	Gneissic mica schist	Ahnhernschlosstönung, appr.270m from blockdebris basin
Schwarze Sulm upstream	647920.00	187170.00	1647.33	8394.65	8	East	Glacial	Moraine	Next to Moraine wall
Schwarze Sulm upstream	650110.00	187520.00	1331.79	5833.99	154	East	Glacial	Slope debris	127m from end of Moraine
Schwarze Sulm upstream	654070.00	186110.00	1024.53	869.12	<190m	East	Base level	Quarzitic gneiss	At appr. same distance from junction with Seebach as knickpoint along Seebach
Seebach-Schwarze Sulm	647590.00	184470.00	1712.39	30033.17	158	East	Glacial	Moraine	Großes Kar, Moraine walls
Seebach-Schwarze Sulm	650010.00	184960.00	1395.58	27208.36	81	East	Glacial	Moraine	Near to Moraine walls
Seebach-Schwarze Sulm	654360.00	185390.00	1002.97	21845.21	7	East	Lithology? Base level?	Quarzitic gneiss	Near to pegmatite appr. same distance from junction with SSulm as knickpoint along SSulm
Seebach-Schwarze Sulm	659280.00	182290.00	567.59	13056.12	130	East	Lithology? Base level?	Mylonitic Gneiss	Next to border with mica schist
Seebach-Schwarze Sulm	663030.00	179840.00	423.50	7092.13	Irrelevant	East	Base level	Alluvium	Approx. 410m from Styrian basin (similar to Lassnitz)

knickpoints.xls

Table 18: Table of the knickpoints identified in the river long profiles of the Koralpe.

Table 18 (continued)

Stream	Easting [m]	Northing [m]	Altitude [m]	Distance [m]		Region	Cause	Lithology	Comment
				from mouth	to fault				
Vratabach	654890.0	166940.0	1159.2	3695.5	Unknown	South	Base level	Unknown	Same distance from Drau river as knickpoints in Krennbach, Vratabach und Ojstriski
Vratabach	655250.0	165650.0	691.3	2231.5	Unknown	South	Base level	Unknown	Correlates to knickpoints in Krennbach, Velka, Vratabach und Radelski
Feistritz (Lavanttal)	635500.0	205420.0	872.7	6442.6	590	Northwest	Unknown	Gneissic mica schist	Vicinity to Lavanttal fault system
Waldensteinbach	649340.0	194970.0	1540.5	20549.4	Unknown	Central West	Unknown	Gneissic mica schist	Vicinity to Quarzitic gneiss
Waldensteinbach	649630.0	195770.0	1428.7	19621.0	Unknown	Central West	Lithology	Quarzitic gneiss	Knickpoint in Lassnitz in 800m distance, at same lithological border
Waldensteinbach	645510.0	199450.0	1009.5	11934.8	Unknown	Central West	fold	Gneissic mica schist	300m to Pegmatite, foldstructure?
Waldensteinbach	637820.0	199090.0	665.8	1715.6	1000	Central West	Unknown	Gneissic mica schist	
Auerlingbach	640270.0	207540.0	1558.9	17087.9	256	Central West	Unknown	Quarzitic gneiss	200m to amphibolite
Auerlingbach	642740.0	203700.0	995.0	11126.0	2000	Central West	Unknown	Quarzitic gneiss	200m to lithoborder (pegmatite, micaschist)
Auerlingbach	639920.0	201750.0	801.3	4290.6	256	Central West	Lithology	Mica schist	Lithological border Garnet-Micaschist to Gneissic mica schist
Fraßbach	646030.0	193320.0	1147.5	9576.5	3720	Central West	Lithology	Gneissic mica schist	Lithoborder Quarzitic gneiss-Gneissic mica schist
Fraßbach	642070.0	193490.0	843.7	4214.1	79	Central West	Fault?	Gneissic mica schist	Change in dip direction, between two faults
Brandgraben	648410.0	190040.0	1535.1	4619.6	1250	Central West	Unknown	Alluvium	Pronounced normal fault slickensides
Brandgraben	647110.0	190730.0	1360.7	2891.8	1400	Central West	Unknown	Quarzitic gneiss	
Rassingbach	646080.0	184830.0	1885.2	8953.9	826	Central West	Glacial	Moraine	Glacial morphology
Proessingbach	647050.0	187250.0	1687.3	12031.2	Irrelevant	Central West	Glacial	Moraine	Glacial morphology
Proessingbach	646340.0	188330.0	1286.2	10592.6	Irrelevant	Central West	Glacial	Mica schist ("Paramorphosenschiefer") / Moraine	Glacial morphology
Proessingbach	643200.0	190960.0	767.8	5854.2	105	Central West	Unknown	Gneissic mica schist	Vicinity to E to SE dipping normal fault
Weissenbach	638970.0	188790.0	635.7	4695.8	25	West	Lithology + fault	Orthogneiss (granitic)	Border Orthogneis(Wolfsberger Granite) to Gneissic mica schist
Paulebach	640940.0	186540.0	787.2	5929.2	Unknown	West	Unknown	Gneissic mica schist	157 m to Amphibolite
Eitwegbach	642490.0	184300.0	1079.8	2962.4	129	West	Lithology	Quarzitic gneiss	19 m to border with Mica schist ("Paramorphosenschiefer")
Eitwegbach	644189.0	184470.0	1741.2	1073.0	380	West	Lithology	Mica schist ("Paramorphosenschiefer")	41m from border to Quarzitic gneiss
Gemmersdorferbach	644960.0	183620.0	1686.3	12626.4	567	West	Lithology	Pegmatite	At border to Paramorphosenaschiefer
Gemmersdorferbach	643790.0	182910.0	1151.1	11048.5	18	West	Lithology + fault	Quarzitic gneiss	Vicinity to fault and marble
Kreuzerbach	644080.0	181850.0	1102.0	7501.1	50	West	Unknown	Quarzitic gneiss	50 m to NNW-SSE trending, and 24m to NE-SW trending fault
Ragglbach	644460.0	180400.0	854.0	9419.1	3	West	Unknown	Quarzitic gneiss	Next to fault
Rainzerbach	645630.0	177880.0	1194.7	9175.9	125	West	Unknown	Mylonite ("Plattengneis")	At border to slope debris
Rainzerbach	643890.0	178240.0	756.8	6967.9	48	West	Unknown	Quarzitic gneiss	Vicinity to lavanttal fault system

knickpoints.xls

Table 18 (continued)

Stream	Easting [m]	Northing [m]	Altitude [m]	Distance [m]		Region	Cause	Lithology	Comment
				from mouth	to fault				
Vratabach	654890.0	166940.0	1159.2	3695.5	Unknown	South	Base level	Unknown	Same distance from Drau river as knickpoints in Krennbach, Vratabach und Ojstriski
Vratabach	655250.0	165650.0	691.3	2231.5	Unknown	South	Base level	Unknown	Correlates to knickpoints in Krennbach, Velka, Vratabach und Radelski
Feistritz (Lavanttal)	635500.0	205420.0	872.7	6442.6	590	Northwest	Unknown	Gneissic mica schist	Vicinity to Lavanttal fault system
Waldensteinbach	649340.0	194970.0	1540.5	20549.4	Unknown	Central West	Unknown	Gneissic mica schist	Vicinity to Quarzitic gneiss
Waldensteinbach	649630.0	195770.0	1428.7	19621.0	Unknown	Central West	Lithology	Quarzitic gneiss	Knickpoint in Lassnitz in 800m distance, at same lithological border
Waldensteinbach	645510.0	199450.0	1009.5	11934.8	Unknown	Central West	fold	Gneissic mica schist	300m to Pegmatite, foldstructure?
Waldensteinbach	637820.0	199090.0	665.8	1715.6	1000	Central West	Unknown	Gneissic mica schist	
Auerlingbach	640270.0	207540.0	1558.9	17087.9	256	Central West	Unknown	Quarzitic gneiss	200m to amphibolite
Auerlingbach	642740.0	203700.0	995.0	11126.0	2000	Central West	Unknown	Quarzitic gneiss	200m to lithoborder (pegmatite, micaschist)
Auerlingbach	639920.0	201750.0	801.3	4290.6	256	Central West	Lithology	Mica schist	Lithological border Garnet-Micaschist to Gneissic mica schist
Fraßbach	646030.0	193320.0	1147.5	9576.5	3720	Central West	Lithology	Gneissic mica schist	Lithoborder Quarzitic gneiss-Gneissic mica schist
Fraßbach	642070.0	193490.0	843.7	4214.1	79	Central West	Fault?	Gneissic mica schist	Change in dip direction, between two faults
Brandgraben	648410.0	190040.0	1535.1	4619.6	1250	Central West	Unknown	Alluvium	Pronounced normal fault slickensides
Brandgraben	647110.0	190730.0	1360.7	2891.8	1400	Central West	Unknown	Quarzitic gneiss	
Rassingbach	646080.0	184830.0	1885.2	8953.9	826	Central West	Glacial	Moraine	Glacial morphology
Proessingbach	647050.0	187250.0	1687.3	12031.2	Irrelevant	Central West	Glacial	Moraine	Glacial morphology
Proessingbach	646340.0	188330.0	1286.2	10592.6	Irrelevant	Central West	Glacial	Mica schist ("Paramorphosenschiefer") / Moraine	Glacial morphology
Proessingbach	643200.0	190960.0	767.8	5854.2	105	Central West	Unknown	Gneissic mica schist	Vicinity to E to SE dipping normal fault
Weissenbach	638970.0	188790.0	635.7	4695.8	25	West	Lithology + fault	Orthogneiss (granitic)	Border Orthogneis(Wolfsberger Granite) to Gneissic mica schist
Paulebach	640940.0	186540.0	787.2	5929.2	Unknown	West	Unknown	Gneissic mica schist	157 m to Amphibolite
Eitwegbach	642490.0	184300.0	1079.8	2962.4	129	West	Lithology	Quarzitic gneiss	19 m to border with Mica schist ("Paramorphosenschiefer")
Eitwegbach	644189.0	184470.0	1741.2	1073.0	380	West	Lithology	Mica schist ("Paramorphosenschiefer")	41m from border to Quarzitic gneiss
Gemmersdorferbach	644960.0	183620.0	1686.3	12626.4	567	West	Lithology	Pegmatite	At border to Paramorphosenaschiefer
Gemmersdorferbach	643790.0	182910.0	1151.1	11048.5	18	West	Lithology + fault	Quarzitic gneiss	Vicinity to fault and marble
Kreuzerbach	644080.0	181850.0	1102.0	7501.1	50	West	Unknown	Quarzitic gneiss	50 m to NNW-SSE trending, and 24m to NE-SW trending fault
Ragglbach	644460.0	180400.0	854.0	9419.1	3	West	Unknown	Quarzitic gneiss	Next to fault
Rainzerbach	645630.0	177880.0	1194.7	9175.9	125	West	Unknown	Mylonite ("Plattengneis")	At border to slope debris
Rainzerbach	643890.0	178240.0	756.8	6967.9	48	West	Unknown	Quarzitic gneiss	Vicinity to lavanttal fault system

knickpoints.xls

Stream	Easting [m]	Northing [m]	Altitude [m]	Distance [m]		Region	Cause	Lithology	Comment
				from mouth	to fault				
Weissenbergerbach	645100.0	174550.0	1028.9	6360.9	50	West	Landslide	Mylonitic Gneiss	Landslide! Vicinity to lavanttal fault system
Weissenbergerbach	645670.0	175000.0	1226.9	6414.9	40	West	Fault?	Mylonitic Gneiss	Vicinity to lavanttal fault system
Weissenbergerbach	643830.0	173880.0	600.2	3950.0	0	West	Fault?	Mylonitic Gneiss	Vicinity to lavanttal fault system
Schwarzenbergerbach	646200.0	174540.0	1288.4	5067.6	56	West	Unknown	Mylonitic Gneiss	56 m to fault, 112 m to Gneissic mica schist
Schwarzenbergerbach	645250.0	173820.0	933.4	3528.5	312	West	Lithology	Gneissic mica schist	Next to border to Quarzitic gneiss and Pegmatite
Schwarzenbergerbach	644650.0	173490.0	748.1	2673.2	67	West	Unknown	Mylonitic Gneiss	Vicinity to lavanttal fault system
Schwarzenbergerbach	644490.0	173440.0	669.3	2470.1	220	West	Unknown	Mylonitic Gneiss	Vicinity to lavanttal fault system
Elbach	645070.0	169610.0	435.6	782.3	140	West	Unknown	Alluvium	Vicinity to lavanttal fault system
Elbach	646450.0	170530.0	694.3	2832.3	110	West	Unknown	Gneissic mica schist	Vicinity to lavanttal fault system and amphibolite
Elbach	648550.0	170630.0	1298.2	5507.5	186	West	Unknown	Gneissic mica schist	Vicinity to lavanttal fault system
Elbach	647250.0	170800.0	848.8	3794.8	201	West	Lithology	Pegmatite	Vicinity to lavanttal fault system
Ettendorferbach	646250.0	172670.0	911.2	4012.2	100	West	Unknown	Mylonitic Gneiss	100 m to Pegmatite resp. Gneissic mica schist
Ettendorferbach	644790.0	171710.0	513.6	1966.7	139	West	Landslide?	Gneissic mica schist	Vicinity to Lavanttal fault system
Lobnerbach	635950.0	203500.0	939.9	2202.3	25	Northwest	Unknown	Gneissic mica schist	Vicinity to Lavanttal fault system
Lobnerbach	635260.0	203000.0	821.3	1234.9	100	Northwest	Unknown	Gneiss, disthenbearing	Vicinity to Lavanttal fault system
Mauterndorfbach	636390.0	202240.0	822.4	1859.2	617	Northwest	Unknown	Gneissic mica schist	Vicinity to Pegmatite (70m)
Jovenbach	639210.0	196640.0	755.7	861.8	Unknown	Northwest	Unknown	Gneissic mica schist	Vicinity to pegmatite (125m)
Woelblbach	649070.0	167420.0	1036.5	5665.3	<330	West	Base level	Micaschist	Correlates with knickpoints in neighbouring streams (Drau base level)
Woelblbach	647870.0	165840.0	568.9	3427.7	120	West	Base level	Gneissic mica schist	Correlates with knickpoints in neighbouring streams (Drau base level)
Multererbach	647520.0	168530.0	955.6	3648.7	36	West	Base level	Gneissic mica schist	Correlates with knickpoints in neighbouring streams (Drau base level)
Multererbach	646960.0	168000.0	816.0	2810.6	243	West	Base level	Gneissic mica schist	Correlates with knickpoints in neighbouring streams (Drau base level)
Multererbach	646560.0	167150.0	590.7	1765.6	56	West	base level?	Gneissic mica schist	Correlates with knickpoints in neighbouring streams (Drau base level)

knickpoints.xls

Table 18 (continued)

7 LIST OF PUBLICATIONS

Articles

Brosch, F.J. and Pischinger, G., 2012 (submitted). Small- to meso-scale brittle rock structures and the determination of “paleostress” axes - Examples from the Koralm region (Styria/Carinthia). Austrian Journal of Earth Sciences: pp 47.

Pischinger, G. et al., 2008b. Fault slip analysis in the Koralm Massif (Eastern Alps) and consequences for the final uplift of “cold spots” in Miocene times. Swiss Journal of Geosciences, doi: 10.1007/s00015-008-1277-x: 235-254.

Rantitsch, G., Pischinger, G. and Kurz, W., 2009. Stream profile analysis of the Koralm Range (Eastern Alps). Swiss Journal of Geosciences, 102(1): 31-41.

Posters, Presentations and Abstracts

Brosch, F.J., Pischinger, G. and Vanek, R., 2004. Application and Methodology of Kinematic Discontinuity Analysis on Drill Cores. In: B. Hubmann and W.E. Piller (Editors), Pangeo Austria. Berichte des Instituts für Erdwissenschaften Karl-Franzens-Universität Graz.9: 94-97.

Fasching, F., Wurzwaller, S. and Pischinger, G., 2008. The Lavanttal fault - tunnelling through a major fault zone of the Eastern Alps - PANGEO 2008: Kurzfassungen und Abstracts. Journal of Alpine Geology, 49: 24.

Pischinger, G. et al., 2005a. Brittle faulting in the Koralm region - results from the site investigation for the Koralmtunnel. In: S. Löw (Editor), Symposium Geologie Alptransit - Programm Abstracts, Zürich, pp. 81-82.

Pischinger, G., Goricki, A., Vanek, R. and Brosch, F.J., 2005b. Paleostress analysis and in-situ stress measurements – an evaluation of results and methods from the investigation campaign for the Koralm Tunnel (Austria), EGU General Assembly 2005. European Geosciences Union, Vienna, pp. 06243.

Pischinger, G., Brosch, F.-J., Kurz, W. and Rantitsch, G., 2006. Normal faulting in a rigid basin boundary block – field evidence from the Koralm Complex (Eastern Alps). PANGEO Austria 2006. Innsbruck University Press Conference Series, Innsbruck, pp. 250–251.

Pischinger, G., Kurz, W. and Brosch, F.J., 2008a. A cold block in an extrusional corridor – The Neogene tectonic evolution of the Koralm Massif (Eastern Alps). PANGEO 2008: Kurzfassungen und Abstracts. Journal of alpine geology, 49: 80-81.

Pischinger, G., 2010. Sprödtektonik und Morphotektonik als Methoden in der Ingenieurgeologie. Vortrag am 01.07.2010 in der Vortragsreihe der Fakultät für Bauingenieurwissenschaften, TU Graz.

Pischinger, G., Wurzwaller, S., Fasching, F., Pack, G. and Harer, G., 2012. Koralmtunnel lots KAT1 and KAT2: The Neogene of the Styrian Basin. In: G. Friedl and H. Steyrer (Editors), Pangeo Austria 2012 - geo.wissenschaft plus praxis. Eigenverlag der Universität Salzburg, Salzburg, pp. 111-112.